



# UNIVERSIDAD DE GRANADA

Facultad de Ciencias

Departamento de Química Orgánica

Programa de Doctorado en Química

**SÍNTESIS Y CARACTERIZACIÓN EN DISOLUCIÓN Y SOBRE SUPERFICIES  
METÁLICAS DE NANOESTRUCTURAS GRAFÉNICAS CURVAS**

**IN-SOLUTION AND ON-SURFACE SYNTHESIS AND CHARACTERIZATION  
OF CURVED GRAPHENIC NANOESTRUCTURES**

MEMORIA DE TESIS DOCTORAL

Presentada por

**FEDERICO VILLALOBOS ROMERO**

bajo la supervisión de

JUAN MANUEL CUERVA CARVAJAL Y CARLOS SÁNCHEZ SÁNCHEZ

para optar al título de

**DOCTOR POR LA UNIVERSIDAD DE GRANADA**

con mención **INTERNACIONAL**

Editor: Universidad de Granada. Tesis Doctorales  
Autor: Federico Villalobos Romero  
ISBN: 978-84-1195-621-5  
URI: <https://hdl.handle.net/10481/97736>

*A mi padre, a mi madre  
y a mi tati.*

RESUMEN/SUMMARY

Graphene is known for its remarkable properties derived from its  $sp^2$  hybridized carbon atoms and delocalized  $\pi$ -electrons. Traditionally, applications of graphene have leveraged these properties. However, a significant limitation of graphene is its lack of an inherent band gap, which is crucial for semiconducting materials. This absence prevents graphene from effectively switching on and off, a necessary function for transistors and other semiconductor devices. In this regard, different strategies for modifying graphene's band structure have already been described in the literature, encompassing: (i) the electron confinement in smaller graphene nanostructures or graphene nanoribbons, (ii) by subjecting graphene to mechanical strain or (iii), by hydrogenating graphene with certain patterns.

This thesis provides an in-depth exploration into the synthesis and characterization of graphene nanostructures on top of a Au(111) surface under ultra high vacuum conditions (UHV), with a particular focus on studying the generated properties in this graphene nanostructures due to the inducement of curvature in them. This research is significant as it delves into the less explored aspect of how curvature influences graphene's electronic, magnetic, and optical properties, thereby expanding its potential applications in nanoelectronics and optoelectronics.

The thesis was developed under the guidance of Juan Manuel Cuerva Carvajal and Carlos Sánchez Sánchez, spanning two laboratories at the University of Granada (FQM367) and at the Materials Science Institute in Madrid (ICMM-CSIC). Additionally, collaborations were established with other groups and laboratories for various measurements and experiments, including the Instituto de Nanociencia y Materiales de Aragón (INMA), the Regional Centre of Advanced Technologies and Materials in Olomouc, Czech Republic, and the Institute of Physics of the Czech Academy of Sciences in Prague, Czech Republic.

The manuscript is organized into six chapters: Introduction, Objectives, Results, Experimental Methods, Conclusions, and Annexes. The Introduction delves into the electronic properties of graphene and graphenic nanostructures, as well as their synthetic methodologies. It provides a detailed explanation of how curvature affects the properties of these materials and explores various methods to induce curvature in  $sp^2$  graphenic nanostructures. Additionally, the chapter reviews already reported syntheses of other curved nanographenes, graphene nanoribbons, and cycloarenes, highlighting their emerging electronic and magnetic properties.

Significant findings from the thesis include the study of the thermal stability of high-membered rings, used to synthesize saddle-shaped graphene nanostructures from various molecular precursors and under different reaction conditions on a gold surface. Mechanistic studies of the rearrangements of these high-membered rings at high temperatures reveal several key factors in the field of on-surface synthesis: the importance of the initial diastereomeric configuration, the role of adatoms in on-surface reactions, and the impact of surface-induced symmetry breakage.

The second section of the Results chapter, which focuses on the synthesis of a family of cycloarenes on surfaces, represents a state-of-the-art advancement in both precursor design and comprehensive characterization using scanning probe microscopy methods. This research significantly enhances the understanding of magnetically active molecules. The study investigates the interactions between free radicals and underlying surfaces, explores the relationship between size enlargement and structural curvature, and delves into electronic properties such as global aromaticity.

In the final section of the Results the interaction between free radicals in non-hexagonal rings and the surface beneath them is underscored again. It is demonstrated that these interactions may create curvature in the graphenic structures due to a mismatch between the distances of the surface lattice and the distance between radicals in a molecule, modifying the electronic properties, particularly the bandgap.

The Experimental Methods chapter is divided in two sections, as the thesis utilized both in-solution and on-surface methodologies. The in-solution section involves the description of the chemical reactions for designing and functionalizing the prior graphene precursors of the final curved nanostructures. Every intermediate and every final precursor were fully characterized by current in-solution methods as: nuclear magnetic resonance, infrared spectroscopy, high-resolution mass spectrometry or x-ray diffraction. The on-surface section describes the experimental setup to generate the final nanomaterials on surface and under UHV conditions utilized in the laboratory from the Materials Science Institute of Madrid. As well, this section delves into the basics of the main utilized techniques for the characterization of the materials on surface as the scanning tunnelling microscopy, the atomic force microscopy or the x-ray photoemission spectroscopy. In addition, the basic concepts of the molecular manipulation with the probe of the scanning tunnelling microscope are also addressed in this section.

The thesis concludes that curvature is a critical factor that can be manipulated to customize the properties of graphene-based materials for specific applications. This chemical ability to control curvature paves the way for designing materials with desired electronic and optical properties, potentially leading to breakthroughs in electronics, spintronics, sensors, and other technological areas. The thesis is a testament to the innovative spirit of research, pushing the boundaries of what is possible with one of the most promising materials of the 21st century.

Finally, the Annex chapter provides additional information on different experiments discussed in the Results chapter, relevant bibliographic references, and computational calculations. It also includes a list of publications resulting from the doctoral thesis.

El grafeno es conocido por sus notables propiedades, derivadas de sus átomos de carbono con hibridación  $sp^2$ , y de sus electrones  $\pi$  deslocalizados. Sin embargo, una limitación importante del grafeno es la ausencia inherente de una brecha de energía, crucial para la aplicación de los materiales semiconductores. Esta falta impide que el grafeno pueda encenderse y apagarse con eficacia, una función necesaria para los transistores y otros dispositivos. En este sentido, en bibliografía se han descrito diferentes estrategias para modificar la estructura de bandas del grafeno: (i) a través del confinamiento de electrones en nanoestructuras más pequeñas o nanoribbons de grafeno, (ii) a partir del sometimiento del grafeno a tensiones mecánicas, o (iii) con la hidrogenación del grafeno con patrones específicos.

En este sentido, esta tesis profundiza en la síntesis y caracterización de nanoestructuras de grafeno sobre una superficie de Au(111) en condiciones de ultra alto vacío (UHV), con especial atención a las propiedades generadas en estas nanoestructuras debido a la inducción de curvatura. Esta investigación aborda cómo la curvatura influye en las propiedades electrónicas, magnéticas y ópticas en nanoestructuras de grafeno, ampliando así sus posibles aplicaciones en nanoelectrónica y optoelectrónica.

La tesis se ha desarrollado bajo la dirección de Juan Manuel Cuerva Carvajal y Carlos Sánchez Sánchez, en dos centros diferentes: el laboratorio FQM367 de la Universidad de Granada (UGR), y por otro lado el Instituto de Ciencia de Materiales de Madrid (ICMM-CSIC). Además, durante el transcurso de la misma, se han establecido colaboraciones con otros grupos y laboratorios para realizar diversas medidas y experimentos, entre ellos: el Instituto de Nanociencia y Materiales de Aragón (INMA), the Regional Centre of Advanced Technologies and Materials en Olomouc, República Checa, o the Institute of Physics of the Czech Academy of Sciences en Praga, República Checa.

El manuscrito está organizado en seis capítulos: Introducción, Objetivos, Resultados, Métodos Experimentales, Conclusiones y Anexos. La Introducción profundiza en las propiedades electrónicas del grafeno y las de las nanoestructuras grafénicas, así como en sus metodologías sintéticas. Ofrece una visión detallada de cómo la curvatura puede modificar las propiedades de estos materiales, y explora los diferentes métodos para inducir curvatura en nanoestructuras grafénicas tipo  $sp^2$ . Además, en este capítulo se lleva a cabo una revisión de otras estrategias de síntesis de nanografenos curvos, nanocintas de grafeno y cicloarenos ya descritas en bibliografía, destacando sus emergentes propiedades electrónicas y magnéticas.

Entre los hallazgos más significativos de la tesis se incluye el estudio de la estabilidad térmica de anillos superiores (heptagonales y octogonales) utilizados para sintetizar nanoestructuras de grafeno con curvatura tipo silla de montar a partir de varios precursores moleculares y bajo diferentes condiciones de reacción sobre una superficie de oro. Los estudios mecanísticos de los reordenamientos observados en estos anillos superiores a altas temperaturas revelan varios factores clave en el campo de la síntesis en superficie: la importancia de la configuración diastereomérica inicial, el papel de los adátomos en las reacciones en superficie y el impacto de la ruptura de simetría inducida por la superficie.

La segunda sección del capítulo de Resultados, que se centra en la síntesis de una familia de cicloarenos sobre superficies, representa un avance tanto en el diseño de precursores como en la caracterización exhaustiva mediante métodos de microscopía de efecto túnel y de fuerzas

atómicas. Esta investigación mejora significativamente la comprensión de las moléculas magnéticamente activas en superficies a través del estudio de las interacciones entre estas y radicales libres. Además, explora la relación entre el aumento de tamaño en las estructuras y la curvatura de las mismas, y profundiza en propiedades electrónicas como la aromaticidad global.

En la sección final de los Resultados se destaca nuevamente la interacción entre los radicales libres en anillos no hexagonales y la superficie subyacente. Se demuestra que estas interacciones pueden crear curvatura en las estructuras grafénicas debido a un desajuste entre las distancias las distancias entre átomos en la superficie y la distancia entre radicales en una molécula, modificando así las propiedades electrónicas, en particular el bandgap.

El capítulo de Métodos Experimentales se divide en dos secciones, ya que en la tesis se utilizaron metodologías tanto en disolución como en superficies. La sección dedicada a los métodos en disolución describe las rutas y protocolos experimentales para diseñar y funcionalizar los precursores de las nanoestructuras grafénicas curvas. Cada intermedio y cada precursor final se caracterizó mediante métodos como la resonancia magnética nuclear, la espectroscopia infrarroja, la espectrometría de masas de alta resolución o la difracción de rayos X. La sección relacionada con los métodos en superficie describe el equipo experimental utilizado para generar los nanomateriales finales en superficie y en condiciones de UHV en el Instituto de Ciencia de Materiales de Madrid. También se profundiza en los fundamentos de las principales técnicas utilizadas para la caracterización de los materiales en superficie, como la microscopía de efecto túnel, la microscopía de fuerzas atómicas y la espectroscopia de fotoemisión de rayos X. Además, se abordan conceptos básicos relacionados con la manipulación atómica y molecular llevada a cabo con la punta del microscopio de efecto túnel.

La tesis concluye que la curvatura es un factor crítico que puede manipularse para modular las propiedades de los materiales basados en grafeno para aplicaciones específicas. Esta capacidad de controlar la curvatura facilita el camino para el diseño de materiales con las deseadas propiedades electrónicas, ópticas y magnéticas, lo que podría conducir a grandes avances en electrónica, espintrónica, nuevos sensores y otras aplicaciones en áreas tecnológicas. La tesis es un testimonio del espíritu innovador de la investigación, que amplía los límites de lo posible con uno de los materiales más prometedores del siglo XXI.

Finalmente, el capítulo de Anexos ofrece información adicional sobre varios experimentos tratados en el capítulo de Resultados, referencias bibliográficas relevantes y cálculos computacionales. También incluye una lista de publicaciones derivadas de la tesis doctoral.



## ABBREVIATIONS AND ACRONIMS

<b>2D</b>	Two-Dimension(al).
<b>3D</b>	Three-Dimension(al).
<b>AC</b>	Alternating Current.
<b>ACID</b>	Anisotropy of the Induced Current Density.
<b>AFM</b>	Atomic Force Microscopy.
<b>AM-AFM</b>	Amplitude Modulation Mode Atomic Force Microscopy.
<b>APCI</b>	Atmospheric-pressure Chemical Ionization.
<b>ATR</b>	Attenuated Total Reflectance
<b>AWA</b>	Annulene Within Annulene.
<b>BE</b>	Binding Energy.
<b>BR-STM</b>	Bond Resolved Scanning Tunneling Microscopy.
<b>Bpin</b>	Boron Pinacolate.
<b>CASSCF</b>	Complete Active Space Self-Consistent Field.
<b>CB</b>	Conduction Band.
<b>CDH</b>	Cyclodehydrogenation.
<b>COSY</b>	Correlation Spectroscopy.
<b>COT</b>	Cyclooctatetraene.
<b>CSIC</b>	Centro Superior de Investigaciones Científicas
<b>DAC</b>	Digital-Analog Converter.
<b>DC</b>	Direct Current.
<b>DCM</b>	Methylene chloride.
<b>DDQ</b>	2,3-Dichloro-5,6-dicyano-1,4-benzoquinone.
<b>DEPT</b>	Distortionless Enhancement by Polarization Transfer.
<b>DFT</b>	Density Functional Theory.
<b>DMF</b>	Dimethyl Formamide.
<b>DMRG</b>	Density Matrix Renormalization Group.
<b>DOS</b>	Density of States.
<b>DSP</b>	Digital Signal Processor.

<b>ESI</b>	Electrospray Ionization.
<b>EtOAc</b>	Ethyl Acetate.
<b>FM-AFM</b>	Frequency Modulation Mode Atomic Force Microscopy.
<b>GAFF</b>	General Amber Force Field.
<b>GC</b>	Gas Chromatography.
<b>HMBC</b>	Heteronuclear Multiple Bond Correlation.
<b>HOMO</b>	Highest Unoccupied Molecular Orbital.
<b>HR-MS</b>	High-Resolution Mass Spectrometry.
<b>HSQC</b>	Heteronuclear Single Quantum Coherence Spectroscopy.
<b>IR</b>	Infrared.
<b>LDOS</b>	Local Density of States.
<b>LUMO</b>	Lowest Unoccupied Molecular Orbital.
<b>MALDI</b>	Matrix-assisted Laser Desorption/Ionization.
<b>MeCN</b>	Acetonitrile.
<b>MRCI</b>	Multireference Configuration Interaction.
<b>nc-AFM</b>	Non-Contact Atomic Force Microscopy.
<b>NEVPT</b>	N–Electron Valence Perturbation Theory.
<b>NICS</b>	Nucleus-Independent Chemical Shift.
<b>NMR</b>	Nuclear Magnetic Resonance.
<b>NO</b>	Natural Orbital.
<b>OSS</b>	On-Surface Synthesis.
<b>PAH</b>	Polycyclic Aromatic Hydrocarbon.
<b>PI</b>	Proportional-Integral Controller.
<b>PS</b>	Photoemission spectroscopy.
<b>PTCDA</b>	Perylenetetracarboxylic Dianhydride.
<b>Py</b>	Pyridine.
<b>r.t.</b>	Room Temperature.
<b>SOMO</b>	Single Occupied Molecular Orbital.
<b>SONO</b>	Single Occupied Natural Orbital.

<b>SPM</b>	Scanning Probe Microscopy.
<b>STM</b>	Scanning Tunneling Microscopy.
<b>STS</b>	Scanning Tunneling Spectroscopy.
<b>SUMO</b>	Single Unoccupied Molecular Orbital.
<b>TBAF</b>	Tetra-n-butylammonium fluoride.
<b>TBDMSO</b>	Tert-Butyldimethylsilyl Ether.
<b><sup>t</sup>Bu</b>	Tert-Butyl.
<b>TfOH</b>	Trifluoromethanesulfonic acid.
<b>THF</b>	Tetrahydrofuran.
<b>TOF</b>	Time of Flight.
<b>UHV</b>	Ultra High Vacuum.
<b>UPS</b>	Ultraviolet Photoelectron Spectroscopy.
<b>VB</b>	Valence Band.
<b>XPS</b>	X-ray Photoelectron Spectroscopy.

## TABLE OF CONTENTS

# Table of Contents

RESUMEN/SUMMARY .....	7
ABBREVIATIONS AND ACRONIMS.....	15
TABLE OF CONTENTS.....	21
1 INTRODUCTION.....	27
1.0 Materials.....	29
1.1 Graphene.....	31
1.2 Graphenic Nanostructures .....	35
1.2.1 Nanographenes .....	35
1.2.2 Cycloarenes.....	37
1.2.3 Synthetic Approaches .....	39
1.3 Curvature .....	46
1.3.1 Helical curvature – Steric interactions.....	50
1.3.2 Lattice defects – Inner strain .....	52
2 OBJECTIVES.....	75
3 RESULTS.....	81
3.1 Saddle-Shape Curvature into Graphene Nanostructures by the Incorporation of Higher-Membered Rings.....	84
3.1.1 Graphene Nanoribbons From Precursors Containing a Seven-Membered Ring....	86
3.1.2 A Non-Benzenoid Graphene Nanoribbon from a Precursor Containing an Eight-Membered Ring.....	97
3.1.3 Graphenic Polymers from Precursors Containing a Seven-Membered Ring.....	113
3.2 Tuning the Structure, Curvature and Properties of a Cyclopenta-Ring-Fused Oligo(m-Phenylene) Macrocyclic Family Through Structure Enlargement.....	122
3.2.1 Synthetic Strategy.....	125
3.2.2 P8 Macrocycle .....	130
3.2.3 P9 Macrocycle .....	140
3.2.4 P10 Macrocycle.....	152
3.2.5 P11 Macrocycle.....	164
3.2.6 P12 Macrocycle.....	171
3.3 A Cyclopentaannulated Chevron-Like Graphene Nanoribbon Composed of Nanodomes .....	183

4 EXPERIMENTAL METHODS.....	197
4.1 In-Solution Synthesis and Characterization.....	200
4.2.1 General Information.....	200
4.2.2 Synthesis and Characterization of the Prepared Compounds.....	201
4.2.1 X-Ray Diffraction Structure .....	229
4.2.1 Representative NMR of the Prepared Compounds.....	231
4.2 On-Surface Synthesis Methods and Characterization Techniques .....	272
4.2.1 Experimental Set-Up .....	272
4.2.2 Sample Preparation Methods .....	274
4.2.3 Scanning Tunneling Microscopy and Spectroscopy .....	277
4.2.4 Atomic Force Microscopy .....	284
4.2.5 Atomic-Molecular Manipulation.....	287
4.2.6 Tip Functionalization & High-Resolution Images.....	294
4.2.7 Photoemission Spectroscopy.....	298
5 CONCLUSIONS.....	301
6 ANNEXES.....	307

# 1 INTRODUCTION



## 1.0 Materials

The history of humanity can be categorized from various perspectives and under different points of view. Without trying to be pretentious with this doctoral thesis, one of them is the materials used in each era. Materials have been fundamental to the development of human civilization, playing a pivotal role in our technological, cultural, and economic evolution. From the Stone Age to the present day, the progression of the material science reflects the broader story of human ingenuity and adaptation.

The first usages of materials by humans dates back to the Stone Age, around 2.6 million years ago. During this period, early humans used stones to create tools and weapons. For example, the flint, a hard and sharp stone, became the material of choice due to its ability to be chipped into precise shapes, suitable for cutting and hunting<sup>1</sup>. Some years after, the discovery and utilization of fire was a turning point in the use and craft of materials. It paved the way for the discovery of ceramics. Around 30,000 BCE, humans began crafting pottery from clay, using fire to harden it and create durable containers for storing food or water<sup>2</sup>.

The Bronze Age (around 3300 BCE) and the Iron Age (around 1200 BCE) were the birth of the metallurgy. These periods were characterized by the development and use of metal tools and weapons, which revolutionized agriculture, warfare, and craftsmanship. The discovery of smelting, the process of extracting metal from ore, was a transformative advancement. Bronze, an alloy of copper and tin, was among the first metals to be widely used due to its hardness and durability<sup>3</sup>. Iron, which requires higher temperatures to smelt than bronze, eventually became the dominant material for tools and weapons. The superior strength and abundance of iron contributed to its widespread adoption, leading to significant societal changes. The Iron Age saw the rise of powerful empires and the development of infrastructure such as roads and aqueducts, which were made thanks to iron tools<sup>4</sup>.

During the Middle Ages (500-1500 CE), the material science saw important developments. The use of materials such as glass and textiles became more sophisticated. These innovations led to the creation of stained-glass windows, which not only served to aesthetic purposes in cathedrals, but also had practical applications in scientific instruments like early telescopes and microscopes<sup>5</sup>. The Renaissance (14th to 17th century) saw significant advancements in metallurgy, particularly in the refinement of iron into steel, which became essential for the development of the initial industrial activities. Leonardo da Vinci's studies on material strength and mechanical properties laid the groundwork for modern engineering principles<sup>6</sup>.

The Industrial Revolution (18th to 19th century) marked a profound change in the use of materials driven by mechanization and mass production. The development of steel, a more versatile and stronger material than iron, was central to this transformation. Innovations such

---

<sup>1</sup> S. H. Ambrose, *Science*, **2001**, 291, 1748–1753.

<sup>2</sup> P. M. Rice, *Journal of Archaeological Method and Theory*, **1999**, 6, 1-53.

<sup>3</sup> J. D. Muhly, *Transactions of the Connecticut Academy of Arts and Sciences.*, **1973**, 43, 155-535.

<sup>4</sup> R. F. Tylecote, *The Early History of Metallurgy in Europe*, Longman, London, **1987**.

<sup>5</sup> M. Woods, M. B. Woods, *Glass: From the First Mirrors to Fiber Optics*, Twenty-First Century Books, **2011**.

<sup>6</sup> H. Petroski, H. (1992). *The Evolution of Useful Things*. Alfred A. Knopf. **1992**

as the Bessemer process (1856), which allowed for the mass production of steel, revolutionized construction, transportation, and manufacturing industries. And in the late 19th and early 20th centuries, the development of polymers opened new frontiers in material science. The invention of synthetic polymers as the Bakelite (1907) paved the way for the modern plastics industry. These materials offered unprecedented versatility and were used in a wide range of applications, from household goods to industrial components<sup>7</sup>.

The big advancements in chemistry, physics, and engineering in the 20th century enabled an exponential growth in material science. The discovery and development of semiconductors, such as silicon, revolutionized electronics and computing with the advent of the Information Age: modern electronics, computers, smartphones, a myriad of digital devices... The latter half of the century also had significant developments in composite materials and nanotechnology. Composites, which combine two or more materials to create superior properties, found applications in aerospace, automotive, and sports industries. Nanomaterials, characterized by their nanoscale dimensions and unique properties, opened new possibilities in medicine, electronics, and environmental sustainability<sup>8</sup>. The development of this new research field was predicted back in December of 1959, when Richard Feynman gave a talk called “There’s Plenty of Room at the Bottom” at an annual meeting of the American Physical Society at Caltech. In this famous lecture, Feynman laid the conceptual foundations and challenges for the field now called nanotechnology when he imagined a day when things could be miniaturized — when huge amounts of information could be encoded onto increasingly small spaces, and when machinery could be made considerably smaller and more compact.

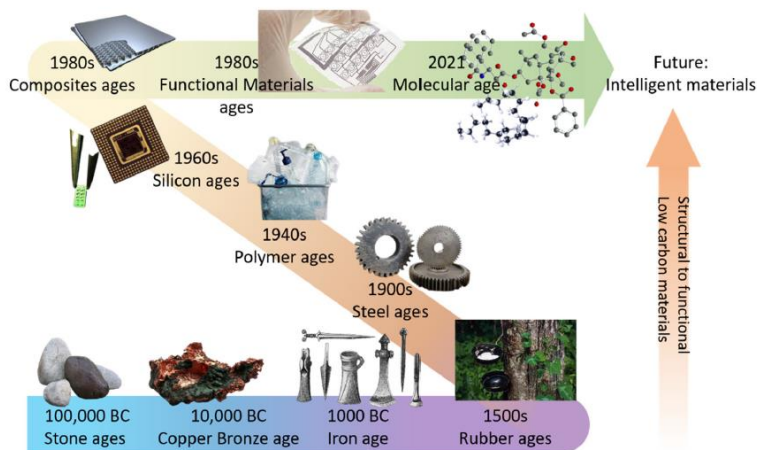


Figure 1. The history of materials. Image reproduced with permission of MDPI<sup>9</sup>.

<sup>7</sup> J. L. Meikle, *American Plastic: A Cultural History*. Rutgers University Press, 1995.

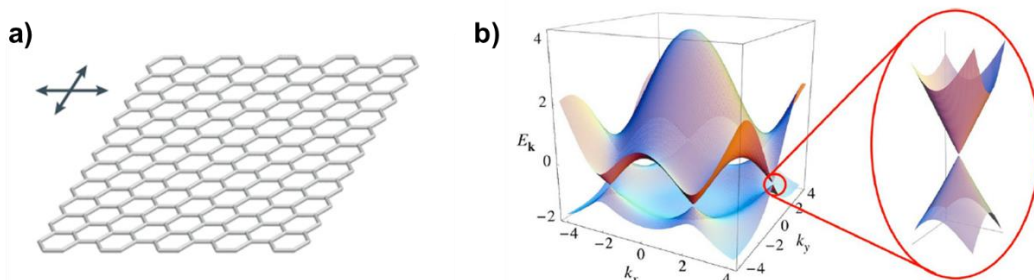
<sup>8</sup> B. Bhushan, *Springer Handbook of Nanotechnology*, Springer, 2017.

<sup>9</sup> L. Jingcheng, V. S. Reddy, W. A. D. M. Jayathilaka, A. Chinnappan, S. Ramakrishna, R. Ghosh, *Polymers*, 2021, 13, 1427.

## 1.1 Graphene

In this context, one of those nanomaterials that in the last years has been the focus of extensive research is graphene, isolated and characterized by K. S. Novoselov, A. K. Geim, and their colleagues in 2004<sup>10</sup>. Their groundbreaking work involved isolating graphene and investigating its electric field effects in atomically thin carbon films, ultimately leading to the award of the Nobel Prize in Physics in 2010<sup>11</sup>. Among all its applications, the low electrical resistivity, high thermal conductivity, high current carrying capability, besides other excellent mechanical properties, make graphene a serious candidate to replace conventional materials in nanoelectronics, as it can be produced on a large scale.

The structure of graphene can be described as a single layer of carbon atoms arranged in a flat honeycomb-like hexagonal lattice, as depicted in **Figure 2 a**. Each carbon atom in graphene exhibits a  $sp^2$  hybridization and forms direct bonds with other three carbon atoms, creating three  $\sigma$  bonds. Additionally, each carbon atom possesses a non-hybridized  $p$  orbital perpendicular to the  $sp^2$  hybrid orbitals, participating in a  $\pi$  bond. This arrangement results in the delocalization of electrons across the surface of the hexagonal lattice through a delocalized  $\pi$  orbital.



**Figure 2.** a) Graphene structure. b) Graphene's band structure. Reproduced with permission of MDPI<sup>12</sup>.

The unique electronic properties of graphene stem from the delocalization of electrons. Since 1947, numerous efforts have been made to elucidate the electronic characteristics of graphite, with its band theory being established using a monolayer (graphene) as a model<sup>13</sup>. From an electronic point of view, graphene is classified as a zero-gap semiconductor, wherein the conduction band and the valence band converge at a single point known as the Dirac point. At this point, each carbon atom intersects with both bands. The valence band is densely populated with electrons, positioning the Fermi level at the Dirac point (see **Figure 2 b**). Consequently,

<sup>10</sup> K. S. Novoselov, A. K. Geim, S. V. Morozov, D. Jiang, Y. Zhang, S. V. Dubonos, I. V. Grigorieva, A. A. Firsov, *Science*, **2004**, *306*, 666-669.

<sup>11</sup> a) A. K. Geim, *Angew. Chem. Int. Ed.*, **2011**, *50*, 6966-6985. b) K. S. Novoselov, *Angew. Chem. Int. Ed.*, **2011**, *50*, 6986-7002.

<sup>12</sup> A. Maffucci, G. Miano, *Applied Sciences*, **2014**, *4*, 305-317.

<sup>13</sup> P. R. Wallace, *Phys. Rev.*, **1947**, *71*, 622-634.

alterations in the gate voltage ( $V_g$ ) induce shifts in the Fermi level ( $E_F$ ), leading to a swift decrease in resistivity ( $\rho$ ), thus exhibiting an ambipolar electric field effect.

However, graphene presents a disadvantage, exhibiting an on/off ratio of  $\approx 10$ . Although it is a record value for a semimetal<sup>14</sup>, it is too low for many applications both in high-frequency signal amplification and in digital electronics<sup>15</sup>. The fact that graphene transistors do not properly turn off is a direct consequence of the lack of a bandgap. In this regard, room-temperature digital-logic applications are considered to require bandgaps of 0.4 eV or more<sup>15</sup>.

To tackle this issue, one may therefore wonder: is it possible to open a bandgap in graphene's electronic structure that is sufficiently large for these applications without sacrificing other properties? The answer is yes. In this regard, different strategies for modifying graphene's band structure have already been described in the literature, encompassing: (i) the electron confinement in smaller graphene nanoflakes or graphene nanoribbons (GNRs)<sup>16</sup>, (ii) by subjecting graphene to mechanical strain<sup>17</sup>, (iii) by hydrogenating graphene with certain patterns<sup>18</sup>, or (iv), by the growth of graphene on different substrates<sup>19</sup>. In this doctoral thesis, we are interested in the chemical synthesis and design of nanomaterials, and therefore, we will delve in the strategy of opening a bandgap through the confinement of electrons in smaller and tailored GNRs or graphene nanoflakes. So, first, we will briefly describe the structure, properties and synthesis of some of these graphenic nanostructures.

### Graphene Nanoribbons

Graphene nanoribbons are essentially narrow strips of graphene. They extend the remarkable properties of graphene, such as its high electrical conductivity and mechanical strength, into a format that offers a more feasible and controlled tunability of its bandgap, which is normally harder to do in graphene. As stated before, this tunability arises from the quantum confinement of the electrons, and from the edge effects due to the edge topology. Therefore, the electronic properties of the GNRs are significantly influenced by their length, width, edge, inclusion of heteroatoms or defects (in form of non-hexagonal rings) or presence of curvature (depicted in **Figure 3**).

---

<sup>14</sup> A. K. Geim, *Rev. Mod. Phys.*, **2011**, *83*, 851.

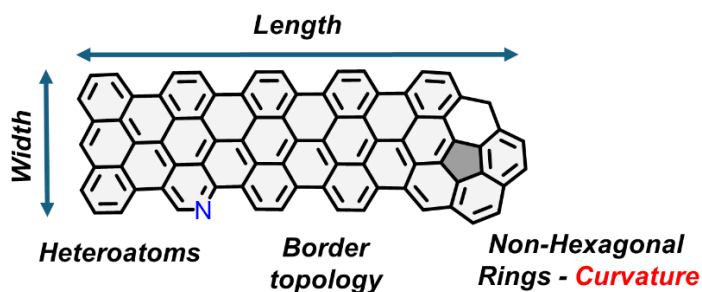
<sup>15</sup> Schwierz, *Nat. Nanotechnol.*, **2010**, *5*, 487.

<sup>16</sup> L. Talirz, P. Ruffieux, R. Fasel, *Adv. Mater.*, **2016**, *28*, 6222–6231.

<sup>17</sup> F. Schwierz, *Nat. Nanotechnol.*, **2010**, *5*, 487–496.

<sup>18</sup> **a)** H. Gao, L. Wang, J. Zhao, F. Ding, J. Lu, *J. Phys. Chem. C*, **2011**, *115*, 3236–3242. **b)** R. Balog, B. Jørgensen, L. Nilsson, M. Andersen, E. Rienks, M. Bianchi, M. Fanetti, E. Lægsgaard, A. Baraldi, S. Lizzit, Z. Sljivancanin, F. Besenbacher, B. Hammer, T. G. Pedersen, P. Hofmann, L. Hornekær, *Nature Mater.*, **2010**, *9*, 315–319.

<sup>19</sup> **a)** S. Y. Zhou, G.-H. Gweon, A. V. Fedorov, P. N. First, W. A. De Heer, D.-H. Lee, F. Guinea, A. H. Castro Neto, A. Lanzara, *Nature Mater.*, **2007**, *6*, 770–775. **b)** G. Giovannetti, P. A. Khomyakov, G. Brocks, P. J. Kelly, J. Van Den Brink, *Phys. Rev. B*, **2007**, *76*, 073103.



**Figure 3.** Potential strategies for derivatization of the graphene lattice to induce new properties.

The edge topology of the GNRs plays a crucial role in determining their electronic and magnetic properties. Some of the already synthesized edge geometries are depicted in **Scheme 1**, encompassing armchair<sup>20</sup> (**2** and **4**), zigzag<sup>21</sup> (**6** or **8**), chevron-like<sup>20</sup> (**10**) or cove<sup>22</sup> (**12**), among others. Regarding the armchair topology, the edges of the nanoribbon run parallel to the direction of the carbon-carbon bonds, appearing as a series of "armchair" shapes along the edge. Armchair GNRs (aGNRs) are known for exhibiting a semiconducting behaviour that varies predictably with the ribbon's width. The band gap in armchair nanoribbons inversely correlates with the width<sup>16</sup>, making them highly valuable for applications where precise control of electronic properties is necessary.

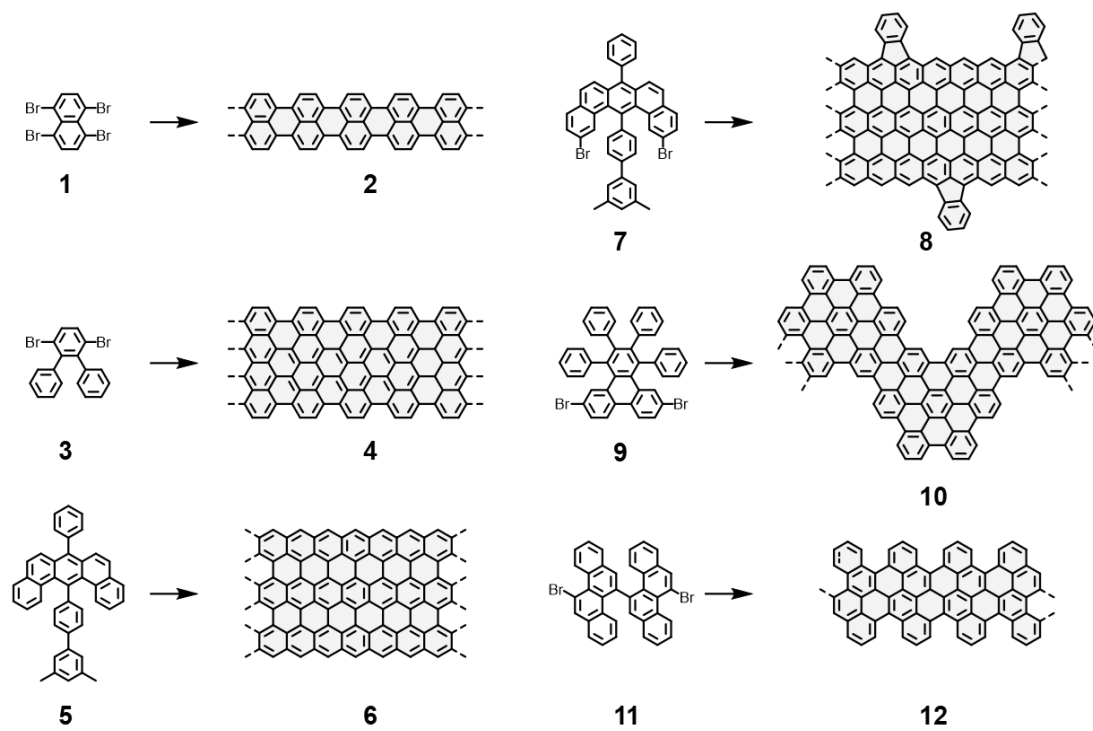
On the other hand, zigzag GNRs (zGNRs) feature edges that run perpendicular to the carbon-carbon bonds, forming a "zigzag" pattern. These nanoribbons display metallic properties due to the presence of localized edge states. Interestingly, zGNRs exhibit magnetic properties at the edges under certain conditions, potentially useful for spintronic devices.

Chevron-like GNRs feature a V-shaped pattern along their edges, leading to unique electronic properties that can be engineered for specific applications. They are very versatile as the in-solution synthesis for the precursor allows an "easily" chemical derivatization. Finally, cove-edged GNRs, named after their concave edge pattern, possess a curved edge structure, and display distinct properties, particularly in their interaction with light and other electromagnetic fields.

<sup>20</sup> J. Cai, P. Ruffieux, R. Jaafar, M. Bieri, T. Braun, S. Blankenburg, M. Muoth, A. P. Seitsonen, M. Saleh, X. Feng, K. Müllen, R. Fasel, *Nature*, **2010**, *466*, 470–473.

<sup>21</sup> P. Ruffieux, S. Wang, B. Yang, C. Sánchez-Sánchez, J. Liu, T. Dienel, L. Talirz, P. Shinde, C. A. Pignedoli, D. Passerone, T. Dumslaff, X. Feng, K. Müllen, R. Fasel, *Nature*, **2016**, *531*, 489–492.

<sup>22</sup> J. Liu, B.-W. Li, Y.-Z. Tan, A. Giannakopoulos, C. Sanchez-Sanchez, D. Beljonne, P. Ruffieux, R. Fasel, X. Feng, K. Müllen, *J. Am. Chem. Soc.* **2015**, *137*, 6097–6103.

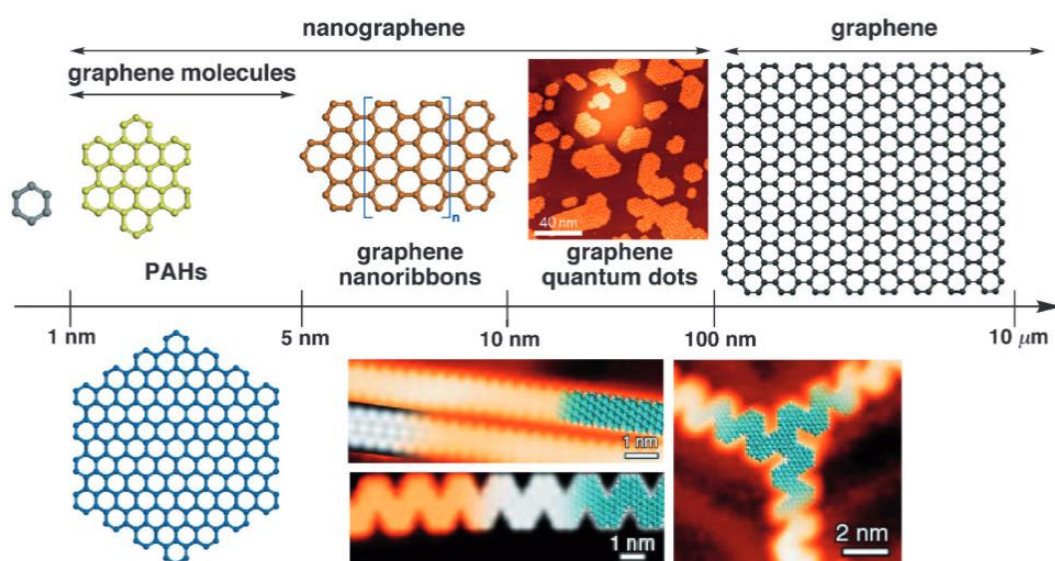


**Scheme 1.** Different examples of synthesized graphene nanoribbons encompassing armchair, zigzag, chevron-like and cove topologies.

## 1.2 Graphenic Nanostructures

### 1.2.1 Nanographenes

Beyond the before stated definitions, graphene and GNRs can be conceptualized as a repeating arrangement of benzene molecules interconnected by covalent bonds. Therefore, benzene serves as the fundamental building block not only for graphene but also for various other structures such as polycyclic aromatic hydrocarbons (PAHs), GNRs, and graphene quantum dots, as depicted in **Figure 4**.



**Figure 4.** Schematic representation of graphene terminology defined according to their size. Reproduced with permission from SpringerNature<sup>23</sup>.

Following the Müllen's nomenclature<sup>23</sup>, PAHs are aromatic hydrocarbons containing two or more fused benzene rings. Molecules, essentially composed of benzene rings, but also bearing non-hexagonal rings or heteroatoms, are also categorized as PAHs. In these compounds, all atoms exhibit  $sp^2$  hybridization, like graphene, and the  $p_z$  orbital of each carbon atom overlaps with those of its neighbors, forming alternating double bonds within a conjugated system. As the number of fused benzene rings increases to a certain threshold and the molecule's length exceeds 1 nm but not more than 5 nm, these compounds can be regarded as graphene-like molecules. The smallest known graphene-based molecule is the hexa-peri-hexabenzocoronene (HBC), which comprises thirteen fused benzene rings. These nanoscale molecules belong to a

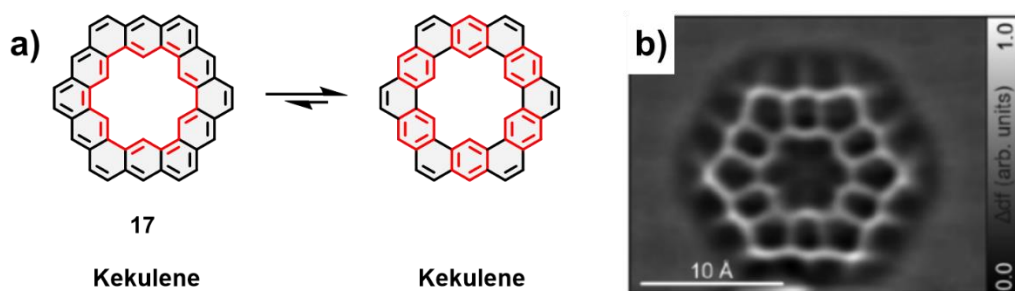
<sup>23</sup> L. Chen, Y. Hernandez, X. Feng, K. Müllen, *Angew. Chem. Int. Ed.*, **2012**, *51*, 7640–7654.





### 1.2.2 Cycloarenes

In addition, and for the purposes of this doctoral thesis, there is another relevant family of compounds worthy to remark, the cycloarenes. They are fully annulated  $\pi$ -conjugated macrocycles (they can be regarded as porous nanographenes too) with interesting electronic structures, optoelectronic properties, and diverse molecular geometries. The textbook example of cycloarene is the Kekulene **17**, a macrocycle that comprises 12 circularly fused benzene rings, see **Figure 5 a**. In this sense, the electronic structure of **17** has been the subject of an intriguing debate for decades<sup>28</sup>. On the one hand, kekulene can be formulated as a combination of two annulene perimeters bridged by radial single bonds, as depicted with black and red colors in the left resonant form of the **Figure 5 a**. These currents show global aromaticity<sup>29</sup> or antiaromaticity depending on the  $[4n+2]$  Huckel's rule. Such systems, in which an annulene is concentric to other annulene, are referred as AWA<sup>30</sup>, and they are very scarce in PAHs molecules. On the other hand, **17** may also be considered as a regular benzenoid system where just a specific way of annulation led to a macrocyclic structure where the Clar's sextet rule<sup>31</sup> governs its electronic structure, cancelling the AWA-like system. The Clar's sextets can be localized as illustrated in the resonant form on the right in the **Figure 5 a**.



**Figure 5.** Kekulene. **a)** Possible resonant forms of kekulene. **b)** High-resolution nc-AFM image of kekulene on top of a Cu(111) surface. Reproduced with permission from ACS Publications<sup>32</sup>.

Kekulene was successfully synthesized by Staab and Diederich in 1978<sup>33</sup>, being a landmark in the field of arenes chemistry. Analysis via single-crystal X-ray and <sup>1</sup>H NMR spectroscopy unveiled that the  $\pi$ -electrons in **17** primarily localize on individual benzenoid rings (resonant form on the right in **Figure 5 a**) rather than being delocalized throughout the entire macrocyclic framework. Moreover, kekulene stands as the smallest macrocyclic nanographene, positioning

<sup>28</sup> J. Aihara, *Bull. Chem. Soc. Jpn.*, **1976**, *49*, 1429–14230.

<sup>29</sup> **a)** M. Rickhaus, M. Jirasek, L. Tejerina, H. Gotfredsen, M. D. Peeks, R. Haver, H.-W. Jiang, T. D. W. Claridge, H. L. Anderson, *Nat. Chem.*, **2020**, *12*, 236–241. **b)** C. Liu, Y. Ni, X. Lu, G. Li, J. Wu, *Acc. Chem. Res.*, **2019**, *52*, 2309–2321.

<sup>30</sup> **a)** T. K. Dickens, R. B. Mallion, *Croat. Chem. Acta*, **2014**, *87*, 221–232. **b)** T. K. Dickens, R. B. Mallion, *Croat. Chem. Acta*, **2013**, *86*, 387–406.

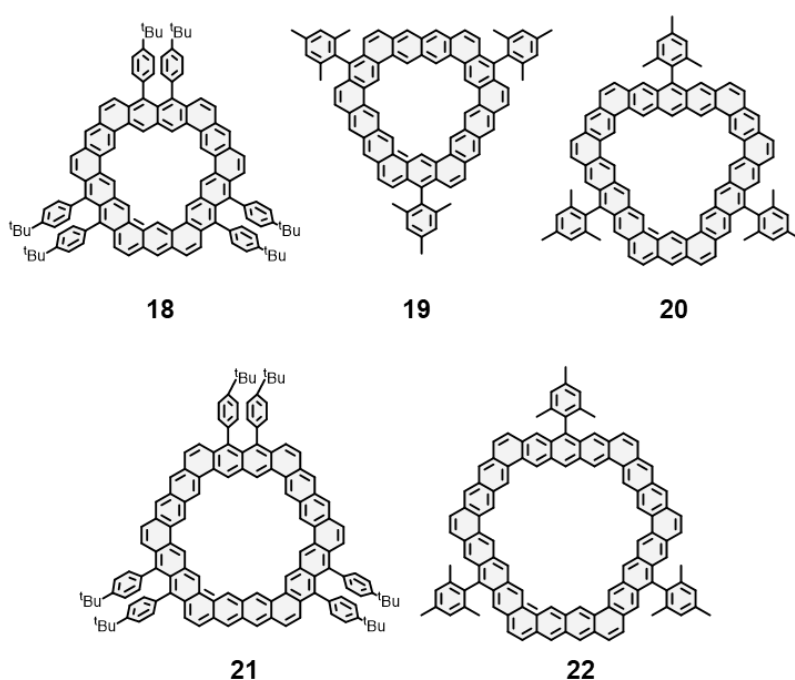
<sup>31</sup> E. Clar, *The Aromatic Sextet*, John Wiley & Sons LTD, London, New York, Sydney, Toronto, **1972**.

<sup>32</sup> I. Pozo, Z. Majzik, N. Pavliček, M. Melle-Franco, E. Guitián, D. Peña, L. Gross, D. Pérez, *J. Am. Chem. Soc.*, **2019**, *141*, 15488–15493.

<sup>33</sup> H. A. Staab, F. Diederich, *Chem. Ber.*, **1983**, *116*, 3487–3503.

cycloarenes as model molecules for studying and comprehending defects in graphene or porous graphene<sup>34</sup>. After 40 years from the first synthesis of the kekulene, Peña et al. revisited the synthesis of kekulene with an improved synthetic route in 2019<sup>32</sup>. Kekulene was analyzed by means of SPM (**Figure 5 b**), obtaining comparable results to those of Staab et al. in 1978. The resonant form of kekulene is governed by the Clar's sextet theory, and hence, no evidence of an AWA system is found in this cycloarene. In this doctoral thesis, we will revisit the concept of AWA, as it has been an important result for us.

In addition, Wu et al.<sup>35</sup> prepared a series of planar edge-extended (**Scheme 3**) kekulenes, from **18** to **22**. In this work, they investigated their size- and symmetry-dependent electronic structures (frontier molecular orbitals, aromaticity) and physical properties (optical and electrochemical) by various spectroscopic measurements, assisted by theoretical calculations.



**Scheme 3.** Extended kekulene molecules prepared by Wu et al<sup>35</sup>.

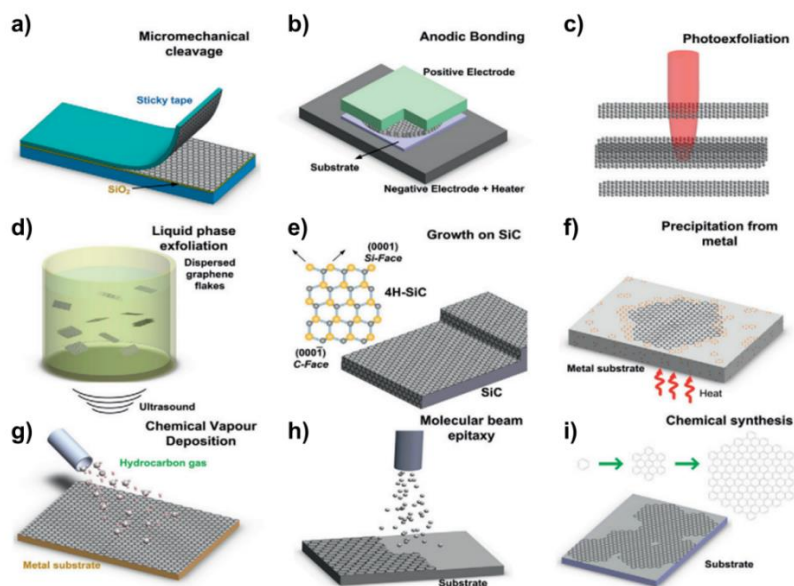
<sup>34</sup> C. Moreno, M. Vilas-Varela, B. Kretz, A. Garcia-Lekue, M. V. Costache, M. Paradinas, M. Panighel, G. Ceballos, S. O. Valenzuela, D. Peña, A. Mugarza, *Science*, **2018**, *360*, 199–203.

<sup>35</sup> W. Fan, Y. Han, X. Wang, X. Hou, J. Wu, *J. Am. Chem. Soc.*, **2021**, *143*, 13908–13916.

### 1.2.3 Synthetic Approaches

#### Top-down strategies:

Until the moment, some examples of graphene nanostructures have been shown, but nothing in relation of their synthesis have been stated. In this regard, there are two main strategies for the preparation of graphene nanoribbons or nanographenes. If the starting material is macroscopic, such as graphene or graphite, the methodology is described as top-down. Conversely, if the starting material consists of low molecular weight building blocks that are subsequently connected through chemical reactions, the approach is termed bottom-up. **Figure 6** shows a brief summary of some of these top-down and bottom-up strategies to synthesize GNRs and nanographenes.



**Figure 6.** Schematic illustration of the main strategy for the synthesis of graphene and nanographenes. **a)** Micromechanical cleavage. **b)** Anodic bonding. **c)** Photoexfoliation. **d)** Liquid phase exfoliation. **e)** Growth on SiC. **f)** Segregation/precipitation from carbon containing metal substrate. **g)** Chemical vapor deposition. **h)** Molecular Beam epitaxy. **i)** Chemical synthesis. Reproduced with permission of Elsevier<sup>36</sup>.

Among the top-down strategies, there are three worthy to be described due to their usage in the synthesis of GNRs and graphene nanoflakes. Firstly, the lithography, or also understood as cutting a graphene/graphite precursor to give narrow GNRs. It is based in the degradation of graphene with oxygen plasma. Those parts of the graphene unprotected without a Si nanowire

<sup>36</sup> F. Bonaccorso, A. Lombardo, T. Hasan, Z. Sun, L. Colombo, A. C. Ferrari, *Mater. Today*, **2012**, *15*, 564-589.

are eliminated with the oxygen plasma, and hence, stripes of graphene or GNRs, with different lengths and rough control in the topology of the borders are obtained<sup>37</sup>.

The second method is the liquid phase exfoliation of graphite via sonication. In this strategy the graphite is exfoliated under high temperatures ( $> 1000$  °C) followed by the dispersion of the formed nanographenes in an organic solvent with the presence of a polymer<sup>38</sup>. The last strategy is based in the unzipping of carbon nanotubes with highly oxidant reagents or plasma<sup>39</sup>.

As commented before, the properties of the GNRs and the nanographenes are highly dependent on their structure, and although the top-down methodologies can be fast, scalable and efficient, they exhibit several drawbacks due to the lack of control in the size, structure and functionalization of the nanographenes.

### In-Solution Synthesis

Conversely, bottom-up methodologies do care about the structural perfection on GNRs and nanographenes. There are two main methodologies within the bottom-up strategies: in-solution synthesis and on-surface synthesis.

Despite the current problems of solubility of GNRs and planar nanographenes, and hence, the difficulties in characterizing these products under in-solution methods, recent research has demonstrated that synthesizing nanographenes in solution is, indeed, feasible. In addition, these methodologies can be scaled up to produce gram-scale quantities of GNRs that are over 100 nm long and can be dispersed in organic solvents for characterization and processing in liquid phase. The edge topologies of the GNRs can vary depending on the monomer structures used<sup>40</sup>.

In this regard, there are three main strategies or reactions that have been employed under in-solution methodologies for the construction of graphenic nanostructures: the cyclotrimerization reaction, the Diels-Alder reaction and the oxidative cyclodehydrogenation reaction, as depicted in **Scheme 4**. In this regard, K. Müllen et al.<sup>41</sup> developed a synthetic strategy (**Scheme 4 a**) to obtain hexaphenylbenzene intermediates employing diphenylacetylene and octacarbonyl dicobalt. These conditions are compatible with different functionalizations of the precursors for further extensions or derivatizations of the nanographenes. However, due to the lack of regioselectivity<sup>42</sup> in this procedure, another strategy (**Scheme 4 b**) has been extensively used based on the Diels-Alder cycloaddition<sup>43</sup> between a cyclopentadienene and a diphenylacetylene. This strategy also enables the functionalization of the precursors for further derivatizations. Normally, after one of the previous two reactions, the final step is an intramolecular oxidative

---

<sup>37</sup> J. Bai, X. Duan, Y. Huang, *Nano Lett.*, **2009**, *9*, 2083-2087.

<sup>38</sup> X. Li, X. Wang, L. Zhang, S. Lee, H. Dai, *Science*, **2008**, *319*, 1229-1232.

<sup>39</sup> D. V. Kosynkin, A. L. Higginbotham, A. Sinitskii, J. R. Lomeda, A. Dimiev, B. K. Price, J. M. Tour, *Nature*, **2009**, *458*, 872-877.

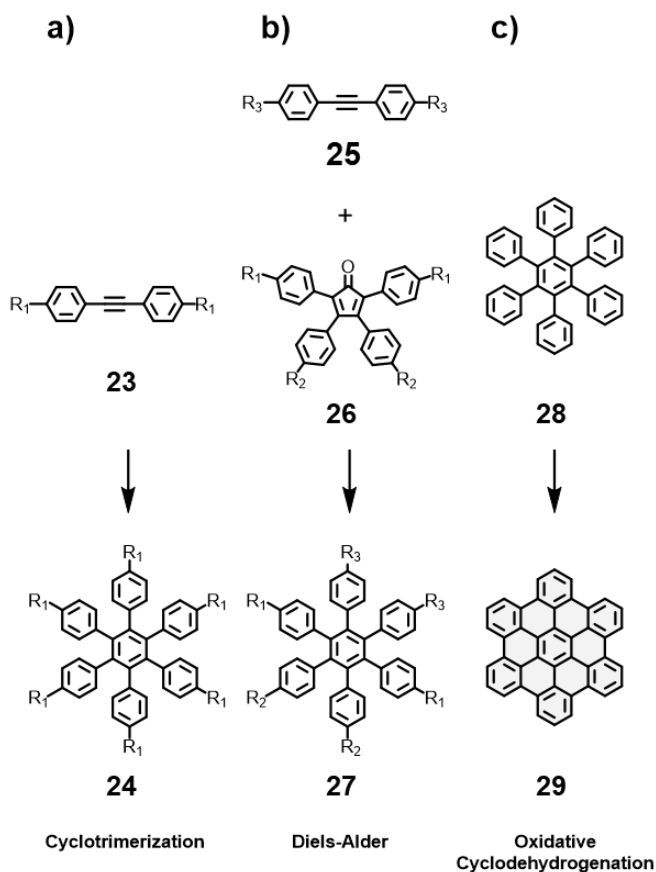
<sup>40</sup> **a)** A. Narita, X.-Y. Wang, X. Feng, K. Müllen, *Chem. Soc. Rev.*, **2015**, *44*, 6616-6643. **b)** A. Narita, Z. Chen, Q. Chen, K. Müllen, *Chem. Sci.*, **2019**, *10*, 964-975.

<sup>41</sup> M. Müller, H. Mauermann-Düll, M. Wagner, V. Enkelmann, K. Müllen, *Angew. Chem. Int. Ed. Engl.*, **1995**, *34*, 1583-1586.

<sup>42</sup> G. Domínguez, J. Pérez-Castells, *Chem. Soc. Rev.*, **2011**, *40*, 3430-3444.

<sup>43</sup> M. Müller, C. Kübel, K. Müllen, *Chem. Eur. J.*, **1998**, *4*, 2099-2109.

cyclodehydrogenation or Scholl reaction<sup>44</sup>, in which the fully conjugation of the structure is achieved (**Scheme 4 c**).



**Scheme 4.** Different strategies/reactions used in wet chemistry to build nanographenes.

In addition, it is worthy to mention other synthetic strategies due to the broad possibilities that offer in the construction of other topologies of graphenic nanostructures as: (i) the approach based in aryne chemistry by Peña et al.<sup>45</sup>, (ii) the annulative  $\pi$ -extension reactions (APEX)<sup>46</sup>, (iii)

<sup>44</sup> **a)** M. Grzybowski, K. Skonieczny, H. Butenschön, D. T. Gryko, *Angew. Chem. Int. Ed.*, **2013**, *52*, 9900–9930. **b)** Y. Zhang, S. H. Pun, Q. Miao, *Chem. Rev.*, **2022**, *122*, 14554–14593.

<sup>45</sup> **a)** D. Pérez, D. Peña, E. Guitián, *Eur. J. Org. Chem.* **2013**, 5981–6013. **b)** I. Pozo, E. Guitián, D. Pérez, D. Peña, *Acc. Chem. Res.* **2019**, *52*, 2472–2481.

<sup>46</sup> **a)** K. Ozaki, K. Kawasumi, M. Shibata, H. Ito, K. Itami, *Nat. Commun.*, **2015**, *6*, 6251. **b)** Y. Koga, T. Kaneda, Y. Saito, K. Murakami, K. Itami, *Science*, **2018**, *359*, 435–439. **c)** H. Ito, Y. Segawa, K. Murakami, K. Itami, *J. Am. Chem. Soc.*, **2019**, *141*, 3–10.

the benzannulation-cyclodehydrogenation approach<sup>47</sup> or (iv), those based on Suzuki-Miyaura<sup>48</sup> or Yamamoto couplings<sup>49</sup>.

### On-Surface Synthesis

Alternatively, in the last years on-surface synthesis (OSS)<sup>50</sup> has flourished as a bottom-up strategy for fabricating intricate molecular nanostructures with atomic precision. Unlike conventional solution-based methods, OSS is based on performing chemical transformations directly on top of substrates. Typically, OSS has been conducted on top of catalytic coinage metals as Au(111), Ag(111), Cu(111), but also on top of insulators as NaCl<sup>51</sup>, or semiconductors as SnSe<sup>52</sup> or TiO<sub>2</sub><sup>53</sup>. This unique approach alters the idiosyncrasy of reactivity with respect to the in-solution synthesis, from 3D to 2D, bringing other possibilities over traditional wet chemistry.

OSS offers the chance to perform experiments in ultra-high vacuum (UHV) conditions, i.e. 1·10<sup>-10</sup> mbar, and at cryogenic temperatures, enabling the synthesis and study of highly unstable compounds that would be unachievable via conventional wet chemistry. For instance, the synthesis of intriguing compounds as: macrocycles<sup>54</sup>, triangulenes<sup>55</sup>, the biphenylene carbon allotrope<sup>56</sup>, graphyne-based structures<sup>57</sup>, cyclo[n]carbons allotropes<sup>58</sup> or the Clar's goblet<sup>59</sup> have been tackled thanks to the OSS. Due to the UHV conditions and the cryogenic temperatures, normally, there is no need to use bulky protecting groups for the most reactive molecules, as is typically required in solution-phase chemistry. This approach prevents the alteration of the intrinsic properties of the synthesized molecules that can occur with protecting groups<sup>60</sup>. In

<sup>47</sup> H. Arslan, F. J. Uribe-Romo, B. J. Smith, W. R. Dichtel, *Chem. Sci.*, **2013**, *4*, 3973–3978.

<sup>48</sup> X. Yang, X. Dou, A. Rouhanipour, L. Zhi, H. J. Räder, K. Müllen, *J. Am. Chem. Soc.*, **2008**, *130*, 4216–4217.

<sup>49</sup> M. G. Schwab, A. Narita, Y. Hernandez, T. Balandina, K. S. Mali, S. De Feyter, X. Feng, K. Müllen, *J. Am. Chem. Soc.*, **2012**, *134*, 18169–18172.

<sup>50</sup> **a)** S. Clair, D. G. De Oteyza, *Chem. Rev.*, **2019**, *119*, 4717–4776. **b)** X. Zhang, Q. Zeng, C. Wang, *Nanoscale*, **2013**, *5*, 8269. **c)** J. Méndez, M. F. López, J. A. Martín-Gago, *Chem. Soc. Rev.*, **2011**, *40*, 4578. **d)** Q. Shen, H.-Y. Gao, H. Fuchs, *Nano Today*, **2017**, *13*, 77–96.

<sup>51</sup> N. Pavliček, A. Mistry, Z. Majzik, N. Moll, G. Meyer, D. J. Fox, L. Gross, *Nature Nanotech.*, **2017**, *12*, 308–311.

<sup>52</sup> F. Frezza, A. Sánchez-Grande, S. Canola, A. Lamancová, P. Mutombo, Q. Chen, C. Wäckerlin, K.-H. Ernst, M. Muntwiler, N. Zema, M. Di Giovannantonio, D. Nachtigallová, P. Jelínek, *Angew. Chem. Int. Ed.*, **2024**, e202405983.

<sup>53</sup> C. Sánchez-Sánchez, J. I. Martínez, V. Lanzilotto, G. Biddau, B. Gómez-Lor, R. Pérez, L. Floreano, M. F. López, J. Á. Martín-Gago, *Nanoscale*, **2013**, *5*, 11058.

<sup>54</sup> F. Xiang, S. Maisel, S. Beniwal, V. Akhmetov, C. Ruppenstein, M. Devarajulu, A. Dörr, O. Papaianina, A. Görling, K. Y. Amsharov, S. Maier, *Nat. Chem.*, **2022**, *14*, 871–876.

<sup>55</sup> J. Su, M. Telychko, S. Song, J. Lu, *Angew. Chem. Int. Ed.*, **2020**, *59*, 7658 – 7668.

<sup>56</sup> Q. Fan, L. Yan, M. W. Tripp, S. R. Kachel, M. Chen, A. S. Foster, U. Koert, P. Liljeroth, J. M. Gottfried, *Science*, **2021**, *372*, 852–856.

<sup>57</sup> **a)** X. Yu, L. Cai, M. Bao, Q. Sun, H. Ma, C. Yuan, W. Xu, *Chem. Commun.*, **2020**, *56*, 1685–1688. **b)** X. Li, H. Zhang, L. Chi, *Adv. Mater.*, **2019**, *31*, 1804087.

<sup>58</sup> **a)** Y. Gao, F. Albrecht, I. Rončević, I. Ettetdgui, P. Kumar, L. M. Scriven, K. E. Christensen, S. Mishra, L. Righetti, M. Rossmannek, I. Tavernelli, H. L. Anderson, L. Gross, *Nature*, **2023**, *623*, 977–981. **b)** K. Kaiser, L. M. Scriven, F. Schulz, P. Gawel, L. Gross, H. L. Anderson, *Science*, **2019**, *365*, 1299–1301. **c)** F. Albrecht, I. Ronc, I. Tavernelli, S. Mishra, H. L. Anderson, L. Gross, *Science*, **2024**, *384*, 677–682.

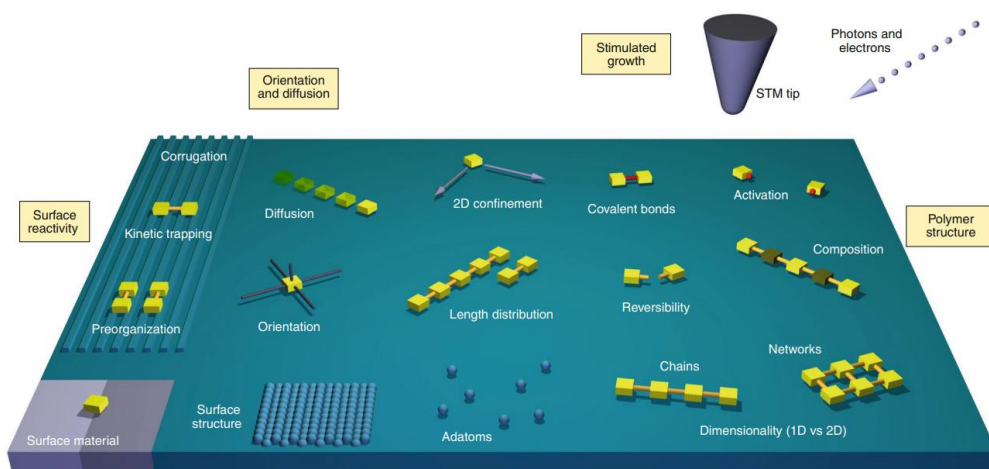
<sup>59</sup> S. Mishra, D. Beyer, K. Eimre, S. Kezilebieke, R. Berger, O. Gröning, C. A. Pignedoli, K. Müllen, P. Liljeroth, P. Ruffieux, X. Feng, R. Fasel, *Nat. Nanotechnol.*, **2020**, *15*, 22–28.

<sup>60</sup> R. Casares, Á. Martínez-Pinel, S. Rodríguez-González, I. R. Márquez, L. Lezama, M. T. González, E. Leary, V. Blanco, J. G. Fallaque, C. Díaz, F. Martín, J. M. Cuerva, A. Millán, *J. Mater. Chem. C*, **2022**, *10*, 11775–11782.

addition, it is noteworthy to remark how the problem of the solubility is also solved in the OSS, enabling the synthesis of conjugated organic polymers, graphene nanoribbons or other insoluble nanographenes.

Furthermore, surface confinement facilitates the application of highly surface-specific characterization techniques as the scanning probe microscopy<sup>61</sup> (SPM), beyond others. This technique (SPM) allows single-atom-molecule observation, characterization and manipulation, thus, elucidating, at the atomic-level, reaction mechanisms and structures (the description of the SPM techniques and their possibilities is detailedly addressed in the Experimental Methods chapter).

Related to the on-surface reactivity, **Figure 7** summarizes some of the main characteristics of this “new field of research”. In general, there are three main strategies to activate the molecules when conducting a chemical reaction on top of a surface: thermally, with light or with the tip of the probe. Due to the importance of the latter in this doctoral thesis, there is a specific section dedicated to tip-induced reactions and manipulations in the Methods chapter.



**Figure 7.** Key aspects of on-surface polymerization. Reproduced with permission from SpringerNature<sup>62</sup>.

In the realm of the on-surface described reactions, some thermally reaction mechanisms encompass the Ullmann coupling<sup>63</sup>, the Glaser coupling<sup>64</sup>, the Sonogashira coupling<sup>65</sup>, the Diels-Alder reaction<sup>66</sup> or the cyclodehydrogenation, among others. On the other hand, some

<sup>61</sup> K. Bian, C. Gerber, A. J. Heinrich, D. J. Müller, S. Scheuring, Y. Jiang, *Nat. Rev. Methods Primers*, **2021**, *1*, 36.

<sup>62</sup> L. Grill, S. Hecht, *Nat. Chem.*, **2020**, *12*, 115–130.

<sup>63</sup> L. Grill, M. Dyer, L. Lafferentz, M. Persson, M. V. Peters, S. Hecht, *Nature Nanotech.*, **2007**, *2*, 687–691.

<sup>64</sup> H. Gao, H. Wagner, D. Zhong, J. Franke, A. Studer, H. Fuchs, *Angew. Chem. Int. Ed.*, **2013**, *52*, 4024–4028.

<sup>65</sup> C.-H. Shu, Y. He, R.-X. Zhang, J.-L. Chen, A. Wang, P.-N. Liu, *J. Am. Chem. Soc.*, **2020**, *142*, 16579–16586.

<sup>66</sup> J. Castro-Esteban, F. Albrecht, S. Fatayer, D. Pérez, L. Gross, D. Peña, *Angew. Chem. Int. Ed.*, **2021**, *60*, 26346–26350.

reported tip-induced rearrangements include skeletal rearrangements<sup>67</sup>, the Bergman cyclization<sup>68</sup>, debrominations<sup>69</sup> or C-H activations<sup>70</sup>. Finally, although photochemical reactions have been less explored to date, some described reactions are the diacetylene polymerization<sup>71</sup>, the carbon halogen activation<sup>72</sup>, the alkyne coupling<sup>73</sup> or the [4+4] cycloaddition<sup>74</sup>.

Beyond the way of activating the molecules on top of the surfaces, there are some key general factors related to the reactivity in the OSS that are also worthy to remark. Essentially, all these factors rely on the dimensional restriction from a 3D to a 2D environment, which is the big difference when wet chemistry and on-surface synthesis are compared. Some of these factors are:

- The self-assembly of the molecules on the surfaces. These arrangements are orchestrated by surface chemistry and intermolecular interactions<sup>75</sup> and may have big implications on the properties of the generated surface (depending on the self-assembly patterns the electronic properties may change) and on the subsequent reactions<sup>76</sup>.
- The balance between adsorption energy and molecular diffusion. This balance may dictate intramolecular versus intermolecular reactions. For instance, while dehydrogenative polymerization and cyclodehydrogenation occur for different PAHs hydrocarbons on the rather inert Au(111) surface (with efficient molecular diffusion), only the cyclodehydrogenation process is observed for the same molecules on the more reactive Pt(111), that strongly reduces diffusion<sup>77</sup>.
- The orientation and crystallographic surface structure, which can affect the catalytic activity of the surface. For instance, dimers and trimers of anthracene are formed by

---

<sup>67</sup> N. Pavlíček, P. Gawel, D. R. Kohn, Z. Majzik, Y. Xiong, G. Meyer, H. L. Anderson, L. Gross, *Nature Chem.*, **2018**, *10*, 853–858.

<sup>68</sup> B. Schuler, S. Fatayer, F. Mohn, N. Moll, N. Pavlíček, G. Meyer, D. Peña, L. Gross, *Nature Chem.*, **2016**, *8*, 220–224.

<sup>69</sup> a) S. Kawai, O. Krejčí, T. Nishiuchi, K. Sahara, T. Kodama, R. Pawlak, E. Meyer, T. Kubo, A. S. Foster, *Sci. Adv.*, **2020**, *6*, 8913. b) Q. Zhong, A. Ihle, S. Ahles, H. A. Wegner, A. Schirmeisen, D. Ebeling, *Nat. Chem.*, **2021**, *13*, 1133–1139.

<sup>70</sup> C. Zhao, Q. Huang, L. Valenta, K. Eimre, L. Yang, A. V. Yakutovich, W. Xu, J. Ma, X. Feng, M. Juríček, R. Fasel, P. Ruffieux, C. A. Pignedoli, *Phys. Rev. Lett.*, **2024**, *132*, 046201.

<sup>71</sup> A. Richter, V. Haapasilta, C. Venturini, R. Bechstein, A. Gourdon, A. S. Foster, A. Kühnle, *Phys. Chem. Chem. Phys.*, **2017**, *19*, 15172–15176.

<sup>72</sup> a) D. Sloan, Y.-M. Sun, H. Ihm, J. M. White, *J. Phys. Chem. B*, **1998**, *102*, 6825–6830. b) A. Basagni, L. Ferrighi, M. Cattelan, L. Nicolas, K. Handrup, L. Vaghi, A. Papagni, F. Sedona, C. D. Valentin, S. Agnoli, M. Sambi, *Chem. Commun.*, **2015**, *51*, 12593–12596.

<sup>73</sup> H.-Y. Gao, D. Zhong, H. Mönig, H. Wagner, P.-A. Held, A. Timmer, A. Studer, H. Fuchs, *J. Phys. Chem. C*, **2014**, *118*, 6272–6277.

<sup>74</sup> L. Grossmann, B. T. King, S. Reichlmaier, N. Hartmann, J. Rosen, W. M. Heckl, J. Björk, M. Lackinger, *Nat. Chem.*, **2021**, *13*, 730–736.

<sup>75</sup> a) J. V. Barth, G. Costantini, K. Kern, *Nature*, **2005**, *437*, 671–679. b) X. Zhou, J. Dai, K. Wu, *Phys. Chem. Chem. Phys.* **2017**, *19*, 31531–31539.

<sup>76</sup> Q. Chen, J. R. Cramer, J. Liu, X. Jin, P. Liao, X. Shao, K. V. Gothelf, K. Wu, *Angew. Chem. Int. Ed.*, **2017**, *129*, 5108–5112.

<sup>77</sup> A. L. Pinardi, G. Otero-Irurueta, I. Palacio, J. I. Martínez, C. Sanchez-Sanchez, M. Tello, C. Rogero, A. Cossaro, A. Preobrajenski, B. Gómez-Lor, A. Jancarik, I. G. Stará, I. Starý, M. F. Lopez, J. Méndez, J. A. Martín-Gago, *ACS Nano*, **2013**, *7*, 3676–3684.



cycloaddition on Au(111), but only dimers are generated on Au(100) due to its different surface corrugation<sup>78</sup>.

- The presence of adatoms. They can take part in the reaction mechanisms<sup>79</sup>, but they may also form part of organometallic polymers or complexes<sup>80</sup>.

---

<sup>78</sup> M. Koch, M. Gille, S. Hecht, L. Grill, *Surface Science*, **2018**, *678*, 194–200.

<sup>79</sup> **a)** Q. Li, B. Yang, J. Björk, Q. Zhong, H. Ju, J. Zhang, N. Cao, Z. Shi, H. Zhang, D. Ebeling, A. Schirmeisen, J. Zhu, L. Chi, *J. Am. Chem. Soc.*, **2018**, *140*, 6076–6082. **b)** J. Björk, C. Sánchez-Sánchez, Q. Chen, C. A. Pignedoli, J. Rosen, P. Ruffieux, X. Feng, A. Narita, K. Müllen, R. Fasel, *Angew. Chem. Int. Ed.*, **2022**, *61*, e202212354.

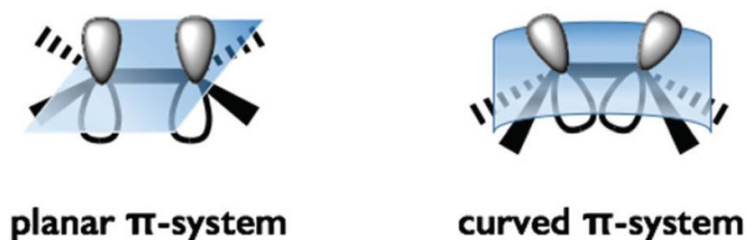
<sup>80</sup> M. Bieri, S. Blankenburg, M. Kivala, C. A. Pignedoli, P. Ruffieux, K. Müllen, R. Fasel, *Chem. Commun.*, **2011**, *47*, 10239.

### 1.3 Curvature

Among the different approaches for modifying or incorporating new properties in graphene-nanostructures (see **Figure 3**), this section delves into the use of the strategy based on the introduction of curvature in the  $sp^2$  structures. We will address issues like why the incorporation of curvature may alter the properties of graphene, which type of properties can be modified or which structural strategies have been used to generate curvature in these geometries. Additionally, we will briefly discuss some relevant examples of some already synthesized molecules, in solution and on surfaces, related to these topics. It is important to note that numerous examples have been reported in the literature, many of which could not be included in this doctoral thesis because of space restrictions. We will focus on some examples that properly illustrate the treated concepts.

#### How curvature modifies graphene properties

As stated before, the exceptional properties of graphene stem directly from the precise arrangement of carbon atoms and the presence of delocalized  $\pi$ -orbitals across its hexagonal lattice. Consequently, alterations to this periodicity are presumed to alter its properties. Introducing curvature in  $sp^2$  structures causes distortion of the  $p$ -conjugation due to an inefficient overlap of each  $p$ -orbital (**Figure 8**), prompting a local rehybridization of  $\sigma$  and  $\pi$ -orbitals. Hence, the electronic properties of curved graphene are susceptible to suffer modifications. In essence, this modifies the Dirac equation governing graphene's band theory with the possible introduction of transport gaps into graphene.



**Figure 8.** Distortion of the  $p$ -conjugation in curved systems due to an inefficient overlap of the  $p$ -orbitals. Reproduced with permission from RSC Publishing<sup>81</sup>.

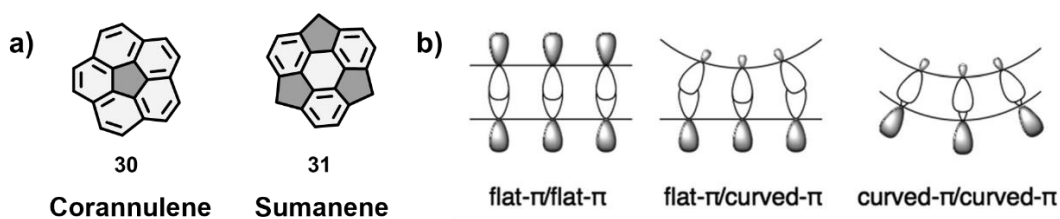
Similarly, several property modifications are also expected after the incorporation of curvature in nanographenes. For example, the energy shifts of the HOMO and LUMO levels (again due to the modified overlapping between orbitals), or the modification of the electron accepting properties<sup>81,82</sup>. In this regard, different examples of curved nanographenes with appealing

<sup>81</sup> M. Saito, H. Shinokubo, H. Sakurai, *Mater. Chem. Front.*, **2018**, 2, 635–661.

<sup>82</sup> **a)** S. H. Pun, Q. Miao, *Acc. Chem. Res.*, **2018**, 51, 1630–1642. **b)** I. R. Márquez, N. Fuentes, C. M. Cruz, V. Puente-Muñoz, L. Sotorriós, M. L. Marcos, D. Choquesillo-Lazarte, B. Biel, L. Crovetto, E. Gómez-Bengoá, M. T. González, R. Martín, J. M. Cuerva, A. G. Campaña, *Chem. Sci.*, **2017**, 8, 1068–1074.

unimolecular photophysical properties have already been described encompassing: a tuned fluorescence and phosphorescence in comparison with planar counterparts<sup>83</sup>, a thermally activated delayed fluorescence (TADF) or an enhanced two-photon absorption<sup>84</sup>.

The introduction of curvature may also induce dipole moments in the nanographenes despite the absence of polar functional groups in them. For example, the buckybowls (bowl-shaped) corannulene **30** and sumanene **31** (depicted in **Figure 9 a**), have a perpendicular axis dipole moment of 2.07 D and 2.70 D, respectively<sup>85</sup>. This dipole moment is directly related with the break of symmetry due to the curvature of their structures. In this sense, the related planar compound hexabenzocoronene (depicted in **Figure 4**) does not have any dipolar moment. In this regard, one can expect that ferroelectric materials could be developed from these buckybowls if they assemble in a one-dimensional fashion.



**Figure 9.** a) Positively curved molecules. b) Interaction of p orbitals depending on the curved geometry. Reproduced with permission from RSC Publishing<sup>86</sup>.

The dipole moment presented in curved PAHs also plays a role in their solubility, enhancing it in more polar solvents compared to their planar related compounds. In addition, **Figure 9 b** depicts how curved structures present a lower complementarity in the shape of the p orbitals, worsen the  $\pi$ - $\pi$  stacking<sup>87</sup> in comparison with the planar compounds. The better p-complementarity between structures, the easier to form stacks of nanographenes and the less soluble the molecule results. Therefore, it can be generally stated that curved structures enhance solubility.

On the other hand, introducing curvature in  $sp^2$  lattices also opens the door to an intriguing supramolecular chemistry. Nanographenes are generally electronically neutral, therefore, the interactions that dominate their assemblies are Van der Waals forces. As depicted before in **Figure 9 b**, the geometrical complementarity of the surfaces that interact in the supramolecular assemblies plays a determinant role in these interactions<sup>87</sup>. Indeed, the rotational and translational motion of the molecules in a stacked assembly is also dependent on the type of

<sup>83</sup> J. Luo, X. Xu, R. Mao and Q. Miao, *J. Am. Chem. Soc.*, **2012**, *134*, 13796–13803.

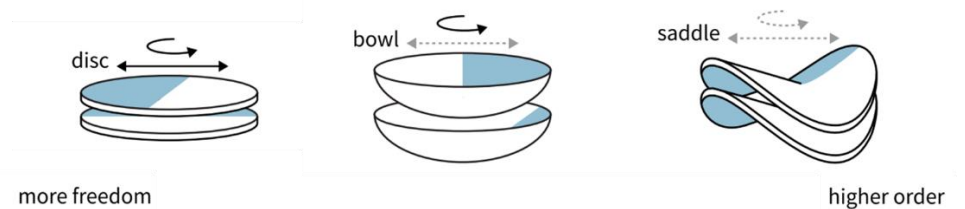
<sup>84</sup> a) S. Castro-Fernández, C. M. Cruz, I. F. A. Mariz, I. R. Márquez, V. G. Jiménez, L. Palomino-Ruiz, J. M. Cuerva, E. Maçóas, A. G. Campaña. *Angew. Chem. Int. Ed.*, **2020**, *59*, 7139-7145. b) H. Terrones, R. Lv, M. Terrones, M. S. Dresselhaus, *Rep. Prog. Phys.*, **2012**, *75*, 062501.

<sup>85</sup> D. R Lide, *CRC Handbook of Chemistry and Physics*, CRC Press: Boca Raton, FL, **2010**.

<sup>86</sup> M. Saito, H. Shinokubo, H. Sakurai, *Mater. Chem. Front.*, **2018**, *2*, 635–661.

<sup>87</sup> E. M. Pérez, N. Martín, *Chem. Soc. Rev.*, **2015**, *44*, 6425–6433.

curvature that the structures possess. **Figure 10** shows how going from a planar to a saddle geometry the stack loses freedom of motion and gains in order, paving the way to interesting curvature-dependent supramolecular assemblies. In this sense, Rickhaus et al.<sup>88</sup> designed a directional supramolecular polymer with the use of a saddle-shaped monomer. The direction and stack of the polymer was oriented by the curvature of the monomers. Alternatively, other hetero-supramolecular interactions have been reported in the literature as the one between fullerenes and curved PAHs, both positively<sup>89</sup> and negatively curved<sup>90</sup>.



**Figure 10.** Geometrical supramolecular interactions between planar-planar structures and curved-curved structures. Reproduced with permission from SpringerNature<sup>88</sup>.

Along with the introduction of a third dimension in the  $sp^2$  graphenic structures thanks to the incorporation of curvature, chirality and chiroptical properties<sup>91</sup> may emerge on them. Thus, optical rotation, circular dichroism or even circularly polarized luminescence may also appear. (**Figure 11**).

<sup>88</sup> J. F. Woods, L. Gallego, P. Pfister, M. Maaloum, A. Vargas Jentzsch, M. Rickhaus, *Nat. Commun.*, **2022**, *13*, 3681.

<sup>89</sup> For selected examples, see: **a)** A. Sygula, F. R. Fronczek, R. Sygula, P. W. R., M. M. Olmstead, *J. Am. Chem. Soc.*, **2007**, *129*, 3842–3843. **b)** D.-C. Yang, M. Li, C.-F. Chen, *Chem. Commun.*, **2017**, *53*, 9336–9339. **c)** M. Takeda, S. Hiroto, H. Yokoi, S. Lee, D. Kim, H. Shinokubo, *J. Am. Chem. Soc.*, **2018**, *140*, 6336–6342

<sup>90</sup> For selected examples, see: **a)** Z. Wang, F. Dötz, V. Enkelmann, K. Müllen, *Angew. Chem. Int. Ed.*, **2005**, *44*, 1247–1250. **b)** N. J. Tremblay, A. A. Gorodet-sky, M. P. Cox, T. Schiros, B. Kim, R. Steiner, Z. Bullard, A. Sattler, W.-Y. So, Y. Itoh, M. F. Toney, H. Ogasawara, A. P. Ramirez, I. Kymissis, M. L. Steigerwald, C. Nuckolls, *Chem Phys Chem.*, **2010**, *11*, 799–803. **c)** S. J. Kang, J. B. Kim, C.-Y. Chiu, S. Ahn, T. Schiros, S. S. Lee, K. G. Yager, M. F. Toney, Y.-L. Loo, C. Nuckolls, *Angew. Chem. Int. Ed.*, **2012**, *51*, 8594–8597. **d)** A. H. G. David, S. Míguez-Lago, C. M. Cruz, J. M. Cuerva, V. Blanco, A. G. Campaña, *Org. Mater.*, **2021**, *3*, 51–59,

<sup>91</sup> **a)** T. Mori, *Chem. Rev.* **2021**, *121*, 2373–2412. **b)** L. Arrico, L. Di Bari, F. Zinna, *Chemistry A European J* **2021**, *27*, 2920–2934.

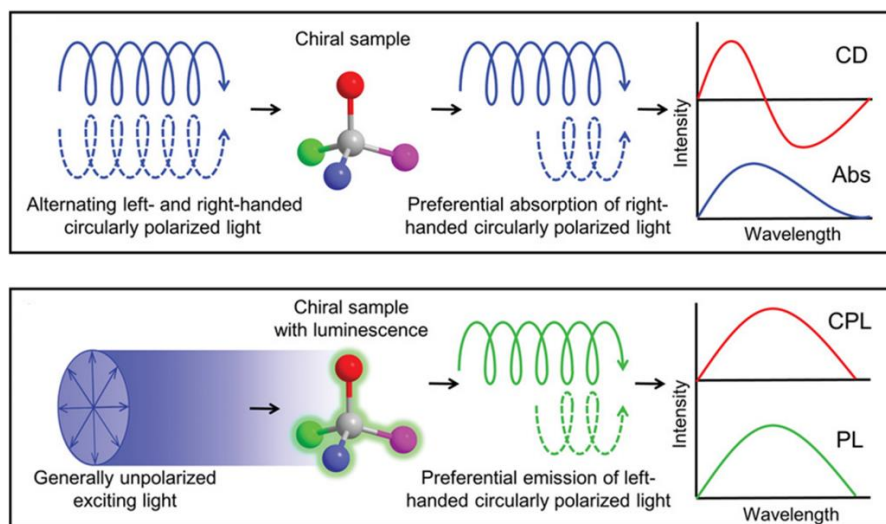


Figure 11. Quiroptical properties. Top, circular dichroism. Bottom, circularly polarized luminescence.

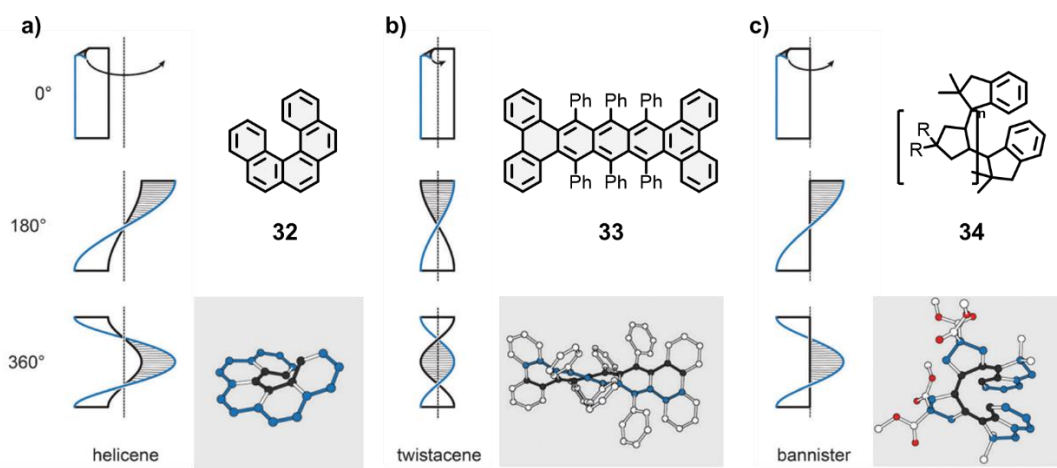
Finally, it is worth commenting that as curvature modifies the hybridization between orbitals, the introduction of curvature may also influence and tune the magnetic properties of the graphene nanoflakes. For instance, Yang et al. reported in 2010<sup>92</sup> a theoretical work based on first principle methods in which they investigated the effects of curvature on the magnetic properties of finite-length zigzag carbon nanotubes and curved nanographenes. Their results indicated a transition from antiferromagnetic to ferromagnetic coupling upon increasing the curvature, while a decrease in the magnetic moment upon the increase of curvature.

<sup>92</sup> Y. Yang, X. H. Yan, X. Shen, X. Zhang, Y. Xiao, *J. Phys. Chem. C*, **2010**, *114*, 7553–7557.

### 1.3.1 Helical curvature – Steric interactions

In order to induce curvature into graphene or into a graphene nanoflake, there are two main chemical approaches or strategies. The first approach is based on the steric interactions between rings or substituents in close proximity, which may induce a helical twist in the polyaromatic systems<sup>93</sup>.

The curvature or the helical conformation in the nanographenes is achieved by minimizing the steric interactions present in the hypothetical planar conformation. Against, there is an energy cost from the torsional strain, or deformation, induced upon twisting the structure. The main requirement for a molecule to adopt a helical conformation is therefore the right balance of the two forces, the first one (minimize the steric interactions) being the driving force. Consequently, it is necessary that the molecule is both rigid and flexible at the same time, and normally polyaromatic system do. The induced deformation is typically spread over a large number of bonds due to the relatively flexible core of these compounds. **Figure 12** illustrates three theoretical limiting cases of twisting a hypothetical graphene nanostructure depending on the position of the axis of twist.



**Figure 12.** The three limiting cases of twisting a graphene nanostructure depending on the axis of twist. Modified with permission of RSCPublishing<sup>93</sup>

The first type of helical molecule is depicted in **Figure 12 a** when a ribbon coils around an axis, which does not have an intersection with the ribbon. The molecular analogues are known as helicenes<sup>94</sup>, the most archetypal examples of helical polyaromatic systems. The steric interaction between overlapping or partially overlapping rings forces helicenes to adopt a helical

<sup>93</sup> M. Rickhaus, M. Mayor, M. Jurićek, *Chem. Soc. Rev.*, **2016**, *45*, 1542–1556.

<sup>94</sup> a) M. Gingras, *Chem. Soc. Rev.*, **2013**, *42*, 968–1006. b) M. Gingras, G. Félix and R. Peresutti, *Chem. Soc. Rev.*, **2013**, *42*, 1007–1050.

conformation, as in **32**, against the energy cost of the torsional strain induced in the helicene backbone.

The second type of helical molecules is depicted in **Figure 12 b** and features a twisting axis that is identical to the main axis of the untwisted planar molecule. When the ribbon is twisted around this axis, both edges have the same length. The closest molecular analogues are known as twistacenes<sup>95</sup>. Unfavorable steric interactions are achieved by introducing bulky groups around the periphery, as in **33**. The energy benefit of minimizing these steric interactions is optimized against the energy cost of distorting the conjugation and p-system from planarity.

The third type is depicted in **Figure 12 c**, where the twisting axis is one of the edges of the ribbon in its planar form. Twisting the ribbon around the twisting axis leads to a system similar to the case of a bannister. The structures of the known molecular bannister analogues normally consist of an oligo(para-phenylene)<sup>96</sup> or a phenylene–acetylene<sup>97</sup> backbone, and a linker bridging the terminal phenylene rings, forming a macrocycle encircling a “hollow” ribbon. Ring strain in the bannister systems induces the helically twisted conformation against the torsional strain generated in the oligo(para-phenylene) or phenylene-acetylene backbone, which is energetically less costly.

---

<sup>95</sup> R. A. Pascal Jr., *Chem. Rev.*, **2006**, *106*, 4809–4819.

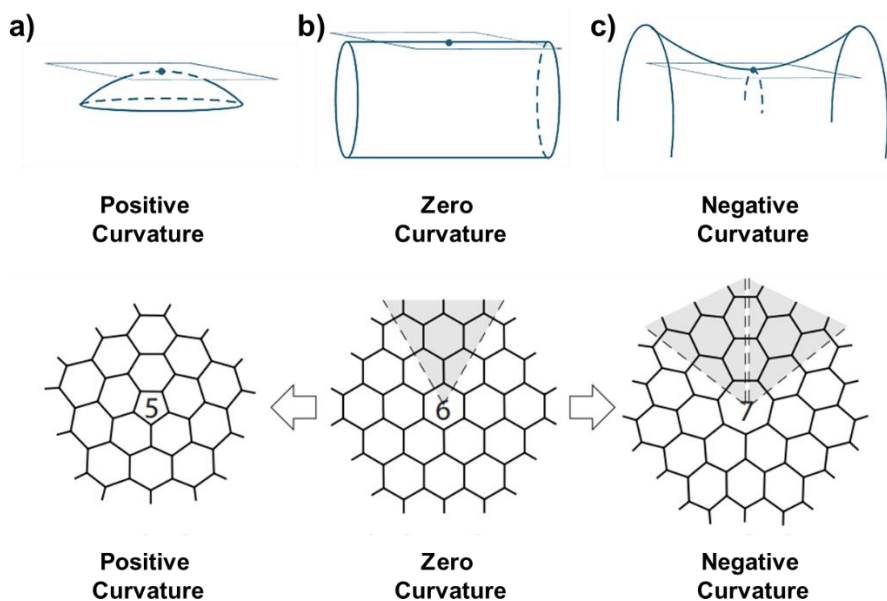
<sup>96</sup> **a)** B. Kiupel, C. Niederal, M. Nieger, S. Grimme and F. Vogtle, *Angew. Chem., Int. Ed.*, **1998**, *37*, 3031–3034. **b)** L. Eshdat, E. Shabtai, S. A. Saleh, T. Sternfeld, M. Saito, Y. Okamoto and M. Rabinovitz, *J. Org. Chem.*, **1999**, *64*, 3532–3537.

<sup>97</sup> **a)** S. Menning, M. Kramer, B. A. Coombs, F. Rominger, A. Beeby, A. Dreuw and U. H. F. Bunz, *J. Am. Chem. Soc.*, **2013**, *135*, 2160–2163. **b)** K. P. Baldwin, R. S. Simons, D. A. Scheiman, R. Lattimer, C. A. Tessier and W. J. Youngs, *J. Chem. Crystallogr.*, **1998**, *28*, 353–360.

### 1.3.2 Lattice defects – Inner strain

#### Gaussian Curvature

The second approach to induce curvature in  $sp^2$  carbon nanostructures is based on straining the geometries by the incorporation of non-benzenoid rings, as depicted in **Figure 13 a** (it is important to note that the incorporation of heteroatoms may also introduce strain into the structures, but this strategy is out of the scope of this doctoral thesis). In this regard, we can define the Gaussian curvature at a specific point of a structure as the degree to which a curved surface deviates from its tangent plane. Positive curvature occurs when the entire surface lies on one side of the tangent plane (top panel **Figure 13 a**). Conversely, negative curvature is present at a point when the surface is saddle-shaped, meaning that the tangent plane intersects the surface (top panel **Figure 13 b**). Between these two scenarios lies the zero curvature, where the surface aligns with the tangent plane along a line (top panel **Figure 13 c**). As depicted in the bottom panels of **Figure 13 a** and **Figure 13 c**, the graphenic structures show positive ('bowls') and negative ('saddles') Gaussian curvatures<sup>98</sup> respectively, in contrast to the zero Gaussian curvature displayed by the graphene, in the bottom panel of the **Figure 13 b**.



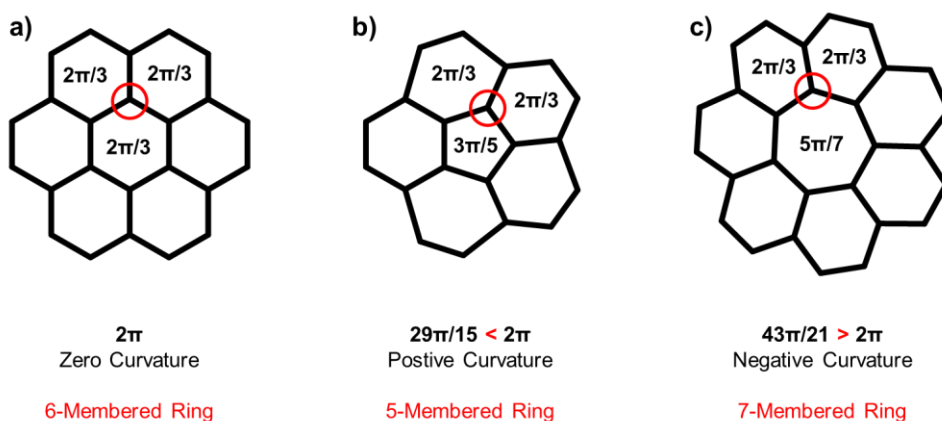
**Figure 13.** a) Curvature in a graphene lattice. b) Geometries of positive, zero and negative curvatures. Images modified with permission of <sup>98,99</sup>

<sup>98</sup> Y. Liu, B. I. Yakobson, *Nano Lett.*, **2010**, *10*, 2178-2183.

<sup>99</sup> O. V. Yazyev, S. G. Louie, *Phys. Rev. B*, **2010**, *81*, 195420.



For understanding the effect of inserting a non-hexagonal ring into a graphene lattice, we introduce the concept of *convex polygons*, which are defined as those in which all the interior angles are lower or equal to  $180^\circ$  ( $\pi$  radians). Thus, we can consider the graphene lattice as a polygonal surface (S) with carbon atoms located at each vertex of the different polygons composing it. Hence, as first approach, the polygonal curvature  $k(v)$  can be determined by the interior angles of the polygons at each vertex ( $v$ ) of S, and it is defined as  $k(v) = 2\pi - s(v)$ , where  $s(v)$  is the sum of the interior angles at each vertex, expressed in radians<sup>100</sup>. If  $k(v) < 0$ , a positive curvature will arise compensating the lack of the interior angles. When  $k(v) = 0$ , the structure will display zero curvature, and for  $k(v) > 0$  a negative curvature will be observed, as shown in **Figure 14**.



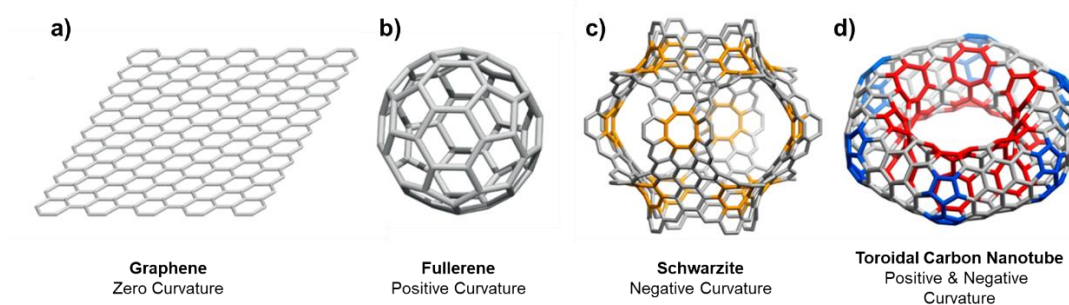
**Figure 14.** Dependence of the curvature in a graphene lattice with non-hexagonal “defects” on the interior angles of the polygonal regions. For example,  $29\pi/15$  in b) is the resulting sum of  $2\pi/3 + 2\pi/3 + 3\pi/5$ .

The interior angles of a regular convex polygon can be calculated as:  $a(v) = \pi(n - 2)/n$ , where  $n$  is the number of sides of the polygon. As shown in **Figure 14 a**, graphene presents a hexagonal lattice where each vertex is surrounded by three regular hexagons. Because the internal angle of a regular hexagon is  $2\pi/3$ , the polygonal curvature at each vertex of graphene is zero (the total sum of angles in a vertex is  $2\pi$ ). Conversely, the curvature in the vertex of a graphene flake with a five-membered ring, where each vertex is surrounded by two hexagons and one pentagon, presents a curvature  $k(v) = 29\pi/15 < 2\pi$ , thus being positive, as illustrated in **Figure 14 b**. Similar considerations can be regarded for a seven-membered ring embedded into a graphene lattice, where the total sum of angles will be greater than  $2\pi$ , **Figure 14 c**. It is noteworthy to remark that this model is useful but also simplistic. To have a more accurate prediction of the geometry of a molecule, especially in limiting examples, it should be also considered other electronic factors.

<sup>100</sup> G. A. Venema, *Polygonal Models and the Geometry of Space. In Foundations of Geometry*; Pearson. Boston, **2012**, Chapter 12.

### Curved Carbon Allotropes

In this context, remarkable curved carbon allotropes have been theoretically and/or experimentally described upon the introduction of the commented defects in a graphene lattice. For instance, fullerene<sup>101</sup>, which is a molecular 3D spherical  $sp^2$  carbon allotrope that displays positive curvature induced by the inclusion of five-membered rings (**Figure 15 b**). Fullerene attracted lot of attention due to its intriguing structure and wide possibilities of application. It can act encapsulating other molecules (endohedral fullerenes<sup>102</sup>), it can be used for biomedical purposes such as in photodynamic therapy<sup>103</sup> or as contrast agents, or it can be useful for advanced technologies due to its unique optoelectronic properties<sup>104</sup>.



**Figure 15.** Carbon allotropes displaying zero, positive and negative curvature.

Interestingly, negative curvature is featured in schwarzites (**Figure 15 c**) or carbon ‘foams’, which are theoretical porous  $sp^2$ -carbon allotropes proposed by Mackay and Terrones<sup>105</sup>. These structures contain seven- and/or eight-membered rings in addition to six-membered rings, and display an extended 3D network with promising properties and potential applications (on the basis of computational studies). In this regard, Tománek and co-workers<sup>106</sup> theoretically studied a negatively curved carbon nanotube junction, a model of a schwarzite, and found that it carried a net magnetic moment in its ground state. Alternatively, first-principles calculations suggested the potential application of carbon schwarzites in lithium-ion batteries as the anode materials, where the presence of pores in schwarzites can lead to three-dimensional lithium-ion diffusion pathways with relatively low energy barriers<sup>107</sup>.

In addition, an even more exotic surface topology is found in hypothetical toroidal carbon nanotubes<sup>108</sup> comprising five-, six-, and seven-membered rings as depicted in **Figure 15 d**. This

<sup>101</sup> H. W. Kroto, J. R. Heath, S. C. O’Brien, R. F. Curl, R. E. Smalley, *Nature*, **1985**, *318*, 162–163.

<sup>102</sup> A. A. Popov, S. Yang, L. Dunsch, *Chem. Rev.*, **2013**, *113*, 5989–6113.

<sup>103</sup> Z. Hu, C. Zhang, Y. Huang, S. Sun, W. Guan, Y. Yao, *Chemico-Biological Interactions*, **2012**, *195*, 86–94.

<sup>104</sup> J. F. Nierengarten, Synthesis of “Methanofullerenes for Materials Science and Biological Applications” chapter 4 in *Fullerenes: From Synthesis to Optoelectronic Properties*, Kluwer Academic Publishers, **2002**, pp. 51-79.

<sup>105</sup> A. L. Mackay, H. Terrones, *Nature*, **1991**, *352*, 762.

<sup>106</sup> N. Park, M. Yoon, S. Berber, J. Ihm, E. Osawa, D. Tománek, *Phys. Rev. Lett.*, **2003**, *91*, 237204.

<sup>107</sup> D. Odkhuu, D. H. Jung, H. Lee, S. S. Han, S.-H. Choi, R. S. Ruoff, N. Park, *Carbon*, **2014**, *66*, 39–47.

<sup>108</sup> F. Beuerle, C. Herrmann, A. C. Whalley, C. Valente, A. Gamburd, M. A. Ratner, J. F. Stoddart, *Chem. – Eur. J.*, **2011**, *17*, 3868–3875.

structure displays positive curvature on the outside, negative curvature on the inside of the torus, and zero curvature in between the two curved segments. Of special interest is the prediction of peculiar persistent currents<sup>109</sup> and exceptional magnetic responses<sup>110</sup> associated with these materials. Encapsulated systems containing fullerenes<sup>111</sup> or atomic metal loops<sup>112</sup> are described as potential gigahertz oscillators or composites with novel electro-magnetic properties.

### The [n]Circulene Family

In the last years, the study of curved graphene nanoflakes as small models of curved carbon allotropes have attracted the attention of the scientific community<sup>113</sup>. The synthesis of these molecules helped with the understanding of the mechanisms behind the generation of curvature and opened new avenues for exploring novel optoelectronic properties in graphene nanostructures. Within this context, the study of the [n]circulene family, and some of its related nanographenes, offers a direct pathway to understand how defects can induce strain and curvature in a graphene lattice. [n]circulenes, a subset of (PAHs), feature a central n-sided polygon surrounded entirely by fused six-membered benzenoid rings (see **Figure 16**).

---

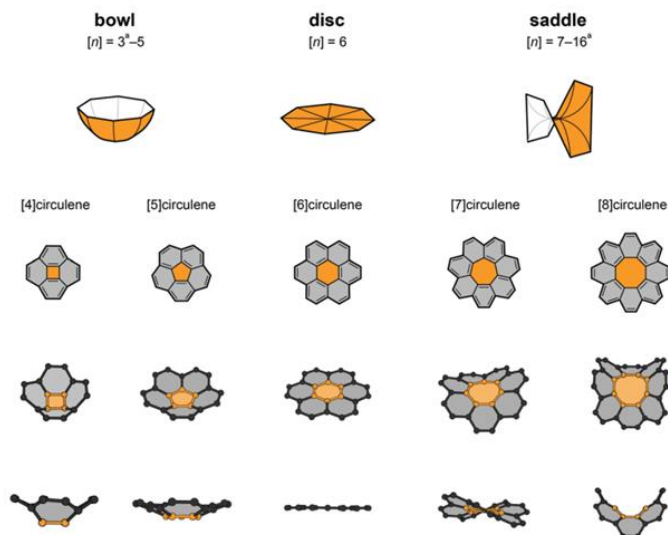
<sup>109</sup> **a)** M. F. Lin, D. S. Chuu, *Phys. Rev. B*, **1998**, *57*, 6731–6737. **b)** S. Latil, S. Roche, A. Rubio, *Phys. Rev. B*, **2003**, *67*, 165420. **c)** R. B. Chen, B. J. Lu, C. C. Tsai, C. P. Chang, F. L. Shyu, M. F. Lin, *Carbon*, **2004**, *42*, 2873–2878. **d)** C. C. Tsai, F. L. Shyu, C. W. Chiu, C. P. Chang, R. B. Chen, M. F. Lin, *Phys. Rev. B*, **2004**, *70*, 075411.

<sup>110</sup> **a)** M.-F. Lin, *J. Phys. Chem. Soc. Jpn.*, **1998**, *67*, 1094–1097. **b)** L. Liu, G. Y. Guo, C. S. Jayanthi, S. Y. Wu, *Phys. Rev. Lett.*, **2002**, *88*, 217206.

<sup>111</sup> T. A. Hilder, J. M. Hill, *J. Appl. Phys.*, **2007**, *101*, 064319.

<sup>112</sup> M. T. Lusk, N. Hamm, *Phys. Rev. B*, **2007**, *76*, 125422.

<sup>113</sup> **a)** Chaolumen, I. A. Stepek, K. E. Yamada, H. Ito, K. Itami, *Angew. Chem., Int. Ed.*, **2021**, *60*, 23508–23532. **b)** G. González Miera, S. Matsubara, H. Kono, K. Murakami, K. Itami, *Chem. Sci.*, **2022**, *13*, 1848–1868.



**Figure 16.** Schematic illustration of the change in curvature for structures of  $[n]$ circulenes ( $n = 4-8$ ). Reproduced with permission from RSCPublishing<sup>114</sup>.

Theoretical calculations<sup>115</sup> describe four types of  $[n]$ circulenes depending on their size (**Figure 17**): positively curved circulenes when  $n = 3 - 5$ <sup>116,117</sup>, planar if  $n = 6$ <sup>118</sup>, negatively curved circulenes when  $n = 7 - 16$ <sup>119,120</sup> and helical if  $n > 16$ . The geometrical change that the  $[n]$ circulene undergo upon the enlargement of its structure is motivated by the former arguments exposed in **Figure 14**. The strain of the structure, hence its geometry, is dependent on the internal angles of the polygons that form the  $[n]$ circulenes.

<sup>114</sup> M. Rickhaus, M. Mayor, M. Juriček, *Chem. Soc. Rev.*, **2017**, *46*, 1643–1660.

<sup>115</sup> H. Christoph, J. Grunenberg, H. Hopf, I. Dix, P. G. Jones, M. Scholtissek, G. Maier, *Chemistry A European J.*, **2008**, *14*, 5604–5616.

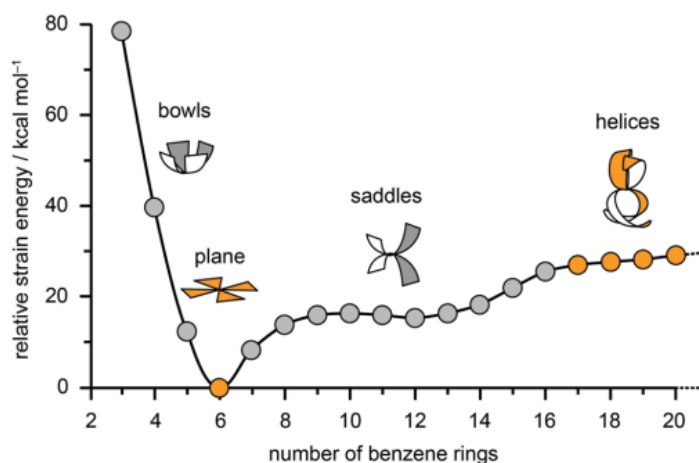
<sup>116</sup> Bharat, R. Bholra, T. Bally, A. Valente, M. K. Cyrański, Ł. Dobrzycki, S. M. Spain, P. Rempala, M. R. Chin, B. T. King, *Angew. Chem. Int. Ed.*, **2010**, *49*, 399–402.

<sup>117</sup> **a)** W. E. Barth, R. G. Lawton, *J. Am. Chem. Soc.*, **1966**, *88*, 380–381. **b)** L. T. Scott, M. M. Hashemi, M. S. Bratcher, *J. Am. Chem. Soc.*, **1992**, *114*, 1920–1921. **c)** A. Borchardt, A. Fuchicello, K. V. Kilway, K. K. Baldrige, J. S. Siegel, *J. Am. Chem. Soc.*, **1992**, *114*, 1921–1923. **d)** A. M. Butterfield, B. Gilomen, J. S. Siegel, *Org. Process Res. Dev.* **2012**, *16*, 664–676.

<sup>118</sup> J. K. Fawcett, J. Trotter, *Proc. R. Soc. London, Ser. A*, **1965**, 366–377.

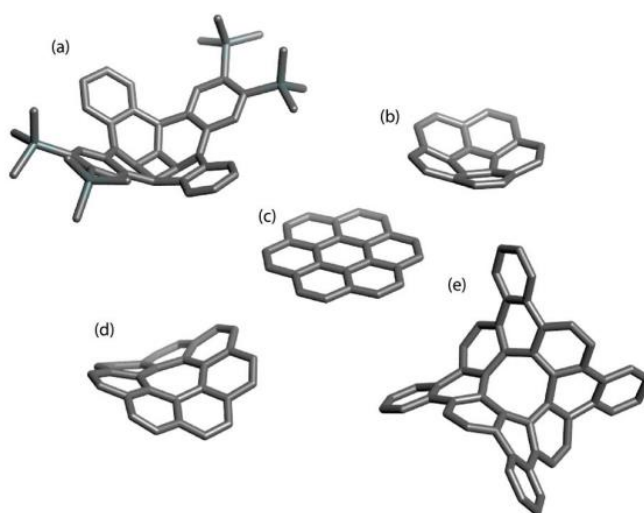
<sup>119</sup> K. Yamamoto, T. Harada, Y. Okamoto, H. Chikamatsu, M. Nakazaki, Y. Kai, T. Nakao, M. Tanaka, S. Harada, N. Kasai, *J. Am. Chem. Soc.*, **1988**, *110*, 3578–3584.

<sup>120</sup> C. Feng, M. Kuo, Y. Wu, *Angew. Chem. Int. Ed.*, **2013**, *52*, 7791–7794.



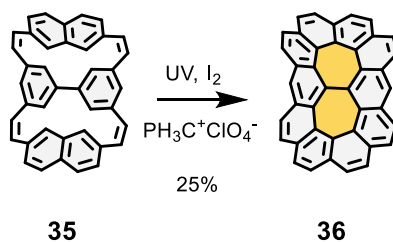
**Figure 17.** Energy diagram. Relative strain energy of [n]circulenes is plotted against the number of benzenoid rings (or sides of central polygon) that they possess. Reproduced with permission from RSCPublishing<sup>114</sup>.

Because of the strained character of positively and negatively curved [n]circulenes, their synthesis requires efficient processes that can build-up the strain in a stepwise manner. This synthetic challenge impedes the preparation of all the curved [n]circulenes, and to date only a handful of them, namely, [4]<sup>116</sup>, [5]<sup>117</sup>, [7]<sup>118</sup>, and [8]circulenes<sup>119</sup> have been addressed in solution. **Figure 18** captures the crystal structures from the synthesized extended [4]circulene, left top, to the extended [8]circulene, right bottom ([5], [6] and [7]circulenes have been successfully synthesized without the need of further extension of the structure).



**Figure 18.** X-ray crystal structures of the synthesized [n]circulenes. (a) A [4]circulene derivative. (b) [5]Circulene. (c) [6]Circulene. (d) [7]Circulene. (e) An [8]circulene derivative. Reproduced with permission from Thieme<sup>121</sup>.

In this context, the incorporation of single or combined non-benzenoid rings into more extended nanographenes has been utilized to distort structures and assess the impact of the curvature on their properties. Doing a comprehensive review of all the reported nanographenes with distortion bearing non-hexagonal rings is out of the scope of this doctoral thesis. Hence, I will focus and comment on the geometry and synthesis of some of the most remarkable examples. In this regard, the group of Ooka achieved the synthesis of **36** in 1991<sup>122</sup>, a related compound to the [7]circulene bearing two seven-membered rings through a final photocyclization step. It is assumed a pretty pronounced saddle-shaped curvature for the final compound (there is no reported analysis of X-ray diffraction).



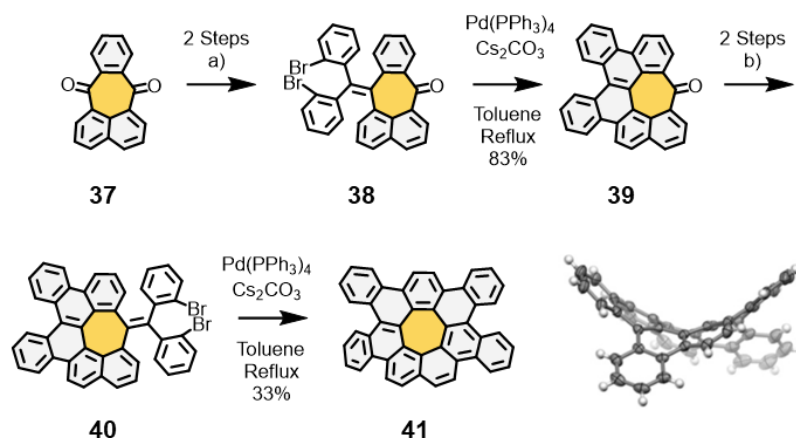
**Scheme 5.** Synthesis of a derivate of the [7]circulene bearing two seven-membered rings.

On the basis of the [7]circulene, some years later Miao and collaborators<sup>123</sup> yielded the synthesis of the extended [7]circulene **41** by ortho annulation. The synthesis of **41** was achieved from the dione **37**, which contained a seven-membered ring pre-formed by an intra-molecular Friedel–Crafts acylation. In this synthetic strategy, the annulation of the seven-membered ring was conducted sequentially, first in one ketone group and then in the other. The simultaneous annulations were not possible due to the steric hindrance caused by the inner curvature of the structure. The sequence of reactions to conduct the annulations encompassed a Ramirez olefination, a Suzuki coupling and Pd-catalyzed cyclization. Beyond the interesting saddle-shaped curvature exhibited by **41**, see crystal structure in **Figure 19**, it was also found that **41** functioned as a p-type semiconductor in thin-film transistors and could cocrystallize with C<sub>60</sub>.

<sup>121</sup> T. Hensel, N. Andersen, M. Plesner, M. Pittelkow, *Synlett*, **2015**, 27, 498–525.

<sup>122</sup> K. Yamamoto, Y. Saitho, D. Iwaki, T. Ooka, *Angew. Chem., Int. Ed. Engl.*, **1991**, 30, 1173–1174.

<sup>123</sup> X. Gu, H. Li, B. Shan, Z. Liu, Q. Miao, *Org. Lett.*, **2017**, 19, 2246–2249.

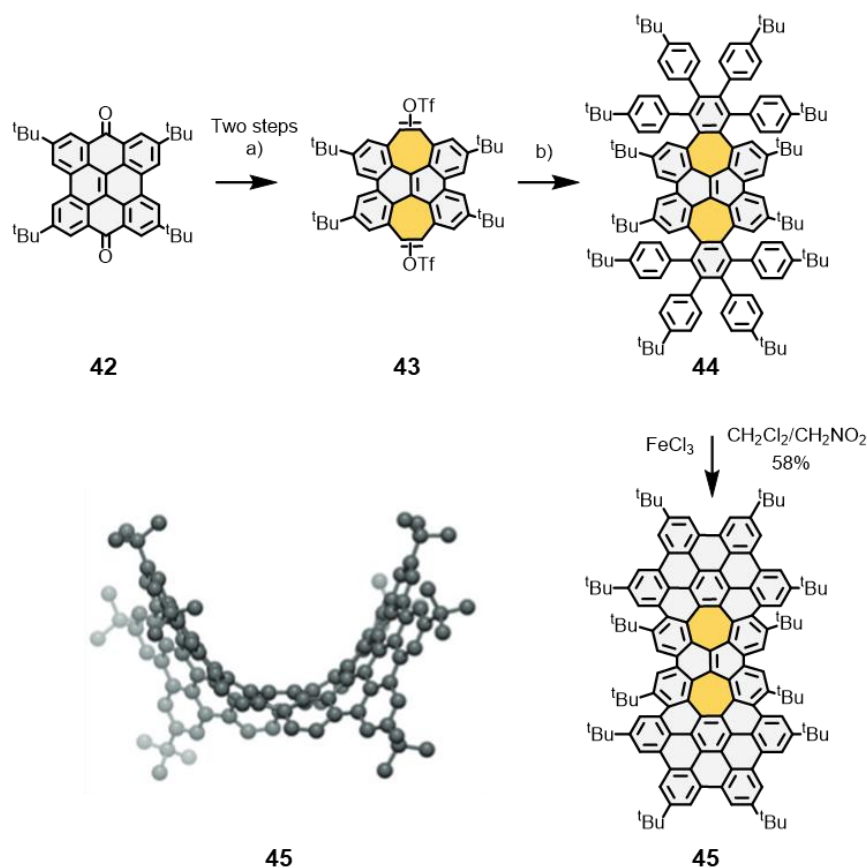


**Figure 19.** In-solution synthesis of the expanded derivative **41** of the [7]circulene with its crystal structure.

In 2018, the Miao's group<sup>124</sup> reported the aromatic saddle structure **45** ( $C_{86}$ ) containing a dipleiadiene core (**Figure 20**). For its synthesis, diketone **42** was used as the precursor. Sequential ring-expansion reaction, using trimethylsilyl-diazomethane, and treatment with LDA and triflic anhydride yielded ditriflate **43**, which subsequently, was also treated with potassium tert-butoxide to generate a strained diyne in situ. This diyne underwent twofold [4+2] Diels–Alder cycloaddition with cyclopentadienone to afford **44**, and finally, a cyclodehydrogenation reaction was performed with  $\text{FeCl}_3$  to assess the final distorted nanographene **45**. The X-ray diffraction analysis revealed that **45** is a severely curved saddle aromatic nanographene with a depth of 6.0 Å. Due to the curvature, the naphthalene moiety at the core of **45** exhibited a record out-of-plane bending deformation of 77.2°, which is significantly higher than even the 42.5° bending observed in the naphthalene moiety of  $C_{60}$ <sup>125</sup>. DFT calculations revealed the molecular dynamics of **45**, suggesting that its tert-butyl substituents stabilize its negative curvature, making it less flexible than its unsubstituted analogue.

<sup>124</sup> S. H. Pun, C. K. Chan, J. Luo, Z. Liu, Q. Miao, *Angew. Chem. Int. Ed.*, **2018**, *57*, 1581 – 1586.

<sup>125</sup> W. I. David, R. M. Ibberson, J. C. Matthewman, K. Prassides, T. J. S. Dennis, J. P. Hare, H. W. Kroto, R. Taylor, D. R. M. Walton, *Nature*, **1991**, *353*, 147 – 149



**Figure 20.** In-solution synthesis of distorted seven-membered rings-containing nanographene **45** and its x-ray diffraction structure.

Alternatively, in 2013, Itami, Scott, and co-workers<sup>126</sup> reported the unprecedented synthesis of the warped nanographene **47** (**Figure 21**). The biaryl precursor **46** was readily synthesized from commercially available corannulene by palladium-catalyzed C–H activation and subjected to cyclodehydrogenation with DDQ and TfOH, yielding the formation of five heptagons and five hexagons surrounding a corannulene core.

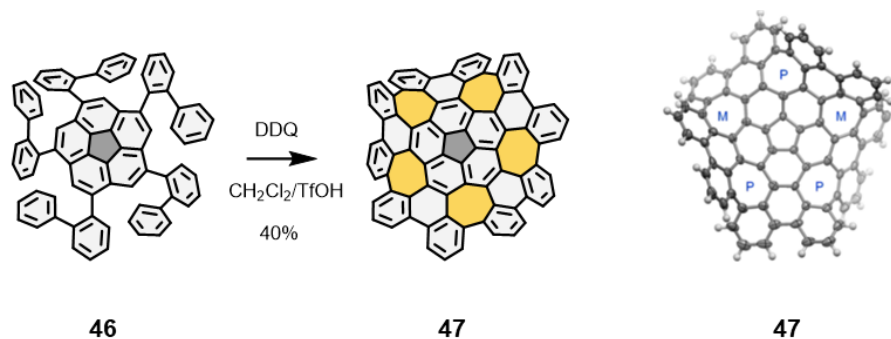
In addition, iridium-catalyzed C–H borylation of **47** was achieved, allowing for the synthesis of green- and red-emissive derivatives bearing electron-withdrawing and -donating groups, respectively<sup>127</sup>. A water-soluble derivative of **47** with applications in live-cell imaging and photoinduced cell death was also synthesized by a similar strategy, showcasing the promise of heptagon-embedded nanographenes in even unorthodox bioimaging contexts<sup>128</sup>.

<sup>126</sup> K. Kawasumi, Q. Zhang, Y. Segawa, L. T. Scott, K. Itami, *Nat. Chem.*, **2013**, *5*, 739–744.

<sup>127</sup> K. Kato, H.-A. Lin, M. Kuwayama, M. Nagase, Y. Segawa, L. T. Scott, K. Itami, *Chem. Sci.*, **2019**, *10*, 9038 – 9041.

<sup>128</sup> H.-A. Lin, Y. Sato, Y. Segawa, T. Nishihara, N. Sugimoto, L. T. Scott, T. Higashiyama, K. Itami, *Angew. Chem. Int. Ed.*, **2018**, *57*, 2874 – 2878.



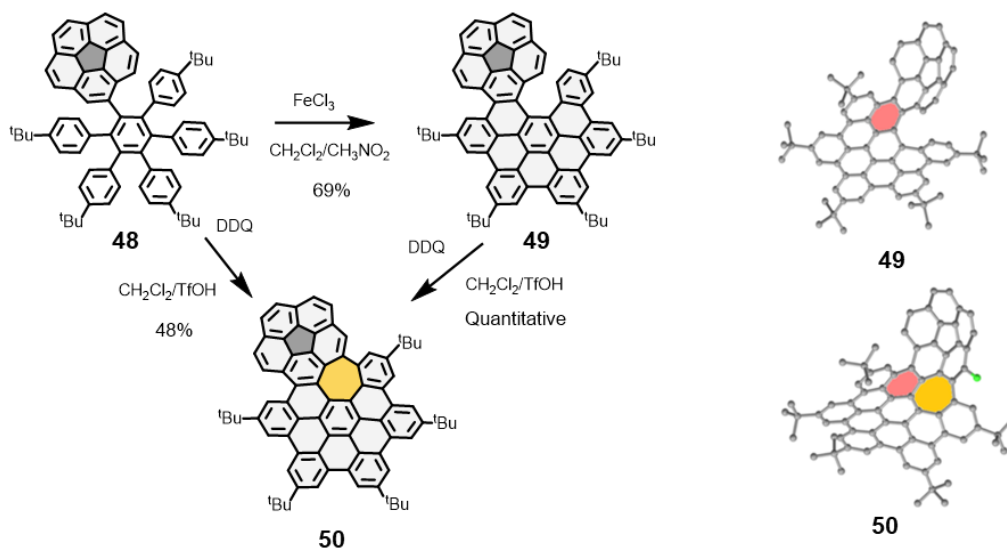


**Figure 21.** In-solution synthesis of the warped nanographene **47** bearing seven and five-membered rings and its x-ray diffraction structure.

Another example regarding curved structures combining non-benzenoid rings was reported in 2018 by the group of Martín and co-workers<sup>129</sup> who reported the cyclodehydrogenation of the hexaphenylbenzene derivative **48**, in which one of the phenyl groups was replaced by a corannulene unit (**Figure 22**). Two different products from the oxidative cyclization reaction of **48** were obtained depending on the reaction conditions. The use of traditional Scholl reaction conditions,  $\text{FeCl}_3$  in  $\text{CH}_2\text{Cl}_2$  at  $-50\text{ }^\circ\text{C}$ , yielded the partially cyclized product **49**. However, under the presence of DDQ and TfOH at  $0\text{ }^\circ\text{C}$ , compound **48** proceeded to give fully cyclized product **50**, with the formation of five hexagonal rings and one seven-membered ring. It was also reported that partially cyclized product **49** could be quantitatively converted into **50** under DDQ/TfOH conditions, indicating that heptagon formation proceeds subsequent to the hexagonal stitching up. Compared to a similar planar compound, namely the hexa-tert-butylhexa-peri-hexabenzocoronene (HBC)<sup>130</sup>, nanographene **50** exhibits increased solubility and better electron-accepting ability ( $-1.82\text{ V}$  vs.  $-2.10\text{ V}$  based on  $\text{Fc}/\text{Fc}^+$ ), as well as improved fluorescence quantum yield (25 % vs. 6 %) and red-shift emission (523 nm vs. 493 nm) due to its greater flexibility and larger p-surface area.

<sup>129</sup> J. M. Fernández-García, P. J. Evans, S. M. Rivero, I. Fernández, D. García-Fresnadillo, J. Perles, J. Casado, N. Martín, *J. Am. Chem. Soc.*, **2018**, *140*, 17188 – 17196.

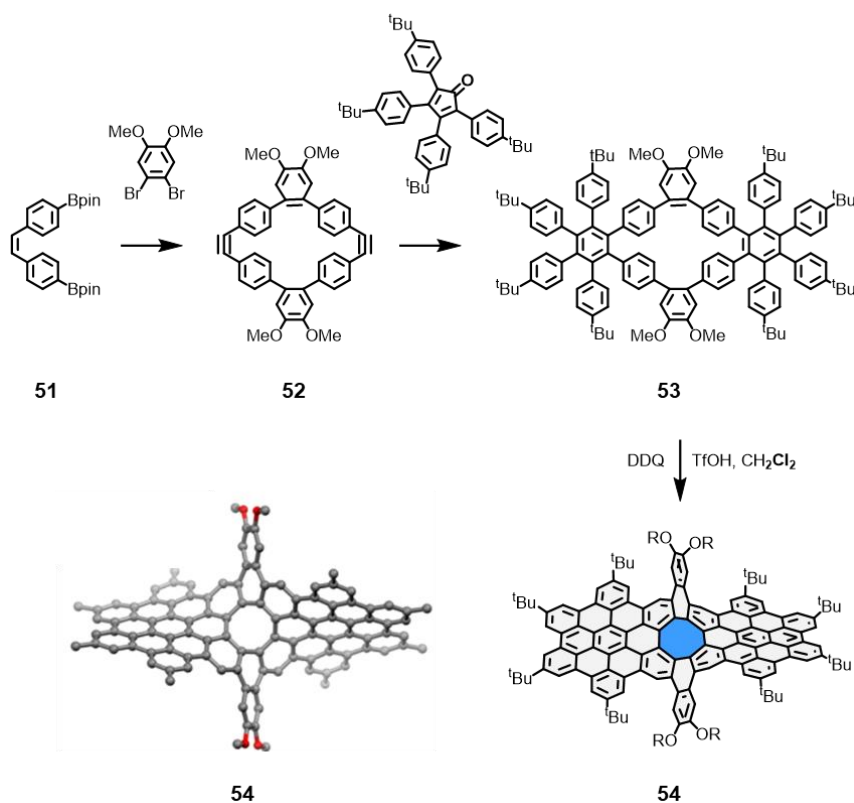
<sup>130</sup> R. Rathore, C. L. Burns, *J. Org. Chem.*, **2003**, *68*, 4071 – 4074.



**Figure 22.** In-solution synthesis of the hexabenzocoronene derivatives **49** and **50** with their corresponding x-ray diffraction structures.

As a final example of curved nanographene structures, Miao and coworkers synthesized a derivate of the [8]circulene consisting in 96  $\text{sp}^2$  carbon atoms<sup>131</sup>. After a Suzuki cross coupling reaction, precursor **52**, a macrocyclic diyne, underwent a Diels–Alder reaction with a cyclopentadienone derivative to afford the intermediate **53** bearing hexaarylbenzene moieties. Finally, the Scholl reaction with DDQ and TfOH resulted in the synthesis of the [8]circulene derivative **54** with the formation of a polycyclic twisted framework with a central eight-membered ring and hexabenzocoronene moieties (**Figure 23**). This work demonstrated the applicability of the “fold-in approach” to large molecular nanocarbons containing an eight-membered ring. The nanographene **54** presented a twisted geometry along two directions with end-to-end twists of  $142.4^\circ$  and  $140.2^\circ$  as revealed by X-ray crystallography. The authors reported a flexible structure at r.t. as found from the computational and experimental studies.

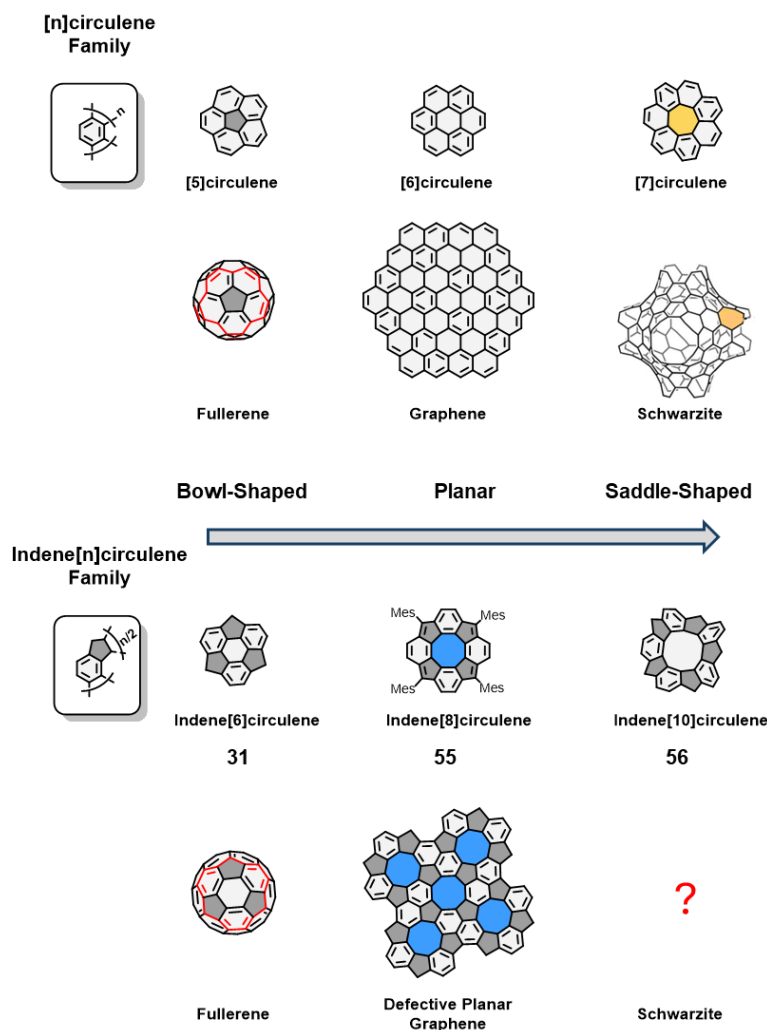
<sup>131</sup> K. Y. Cheung, C. K. Chan, Z. Liu, Q. Miao, *Angew. Chem. Int. Ed.*, **2017**, *56*, 9003–9007.



**Figure 23.** In-solution synthesis of the extended [8]circulene **54** with its x-ray diffraction structure.

### Combination of defects. Extending the Concept to Other Lattices

For a deeper understanding of non-hexagonal rings and curvature, it is valuable to examine the behavior of the indene[n]circulenes family, compounds related to the [n]circulene family. In these compounds, a benzene ring is replaced by a five-membered ring for every two benzene rings in the [n]circulene family. It is also possible to synthesize different indene[n]circulenes by modifying the size of the inner ring, for example, from a six-membered to a ten-membered ring (**31**, **55** and **56**), as shown in **Scheme 6** (lower panel).



**Scheme 6.** [n]circulene and indene[n]circulene families of compounds with their respective change in curvature dependent on size, and with their respective carbon allotropes.

As previously stated for the [n]circulenes, the indene[n]circulene family also exhibits a change in curvature that is dependent on the size of the rings that compose the PAH. In contrast to the planar [6]circulene, the indene[6]circulene **32** (also called sumanene<sup>132</sup>) exhibits a bowl-shaped curvature. In this regard, the sumanene is the counterpart of the [5]circulene. Indeed, both are the building blocks for the fullerene<sup>133</sup>, as shown in **Scheme 6**.

Conversely, the indene[8]circulene **56** exhibits a planar configuration (despite presenting an eight-membered ring and four five-membered rings in its structure) in contrast to the saddle-

<sup>132</sup> H. Sakurai, T. Daiko, T. Hirao, *Science*, **2003**, *301*, 1878–1878.

<sup>133</sup> M. Saito, H. Shinokubo, H. Sakurai, *Mater. Chem. Front.*, **2018**, *2*, 635–661.

shaped geometry presented in the [8]circulene. Tobe and collaborators<sup>134</sup> reported the in-solution synthesis of **56**, describing a planar geometry with a close-shell electronic structure characterized by remarkable antiaromaticity and accessible magnetically-active higher states. In this regard, there is a compensation of the angles among the eight-membered ring and the five-membered rings. Indene[8]circulene is the counterpart of the [6]circulene (in terms of planarity), and, interestingly, as shown in **Scheme 6**, it would be possible to build a planar lattice using **56** as the building block that would result in a defective planar graphene structure. Additionally, some related compounds to indene[8]circulene bearing heteroatoms have also been reported, exhibiting (the majority of them)<sup>135</sup> planar configurations (ketone derivatives<sup>136</sup>, oxo-derivatives<sup>137</sup> and hetero[8]circulenes functionalized with other heteroatoms<sup>138</sup>).

Lastly, to the best of our knowledge, the indene[10]circulene **57** has not been synthesized to date, but, hypothetically, it would display a saddle-shaped curvature as shown in **Scheme 6**. However, Tanaka et al.<sup>139</sup> succeeded in the synthesis of its aza-derivative that displayed the expected saddle-shaped curvature.

To provide a clearer understanding of the curvature shift in the indene[n]circulene systems, again, a simplified model is illustrated in **Figure 24**, highlighting the dependence of the curvature on the internal angles of the polygons. In this regard, the bowl-shaped curvature of the indene[6]circulene and the saddle-shaped curvature of **57** can be clearly understood due to a big deviation of the sum of their internal angles to the planar  $2\pi$  value ( $1.933\pi$  and  $2.067\pi$ , respectively). On the other hand, despite the fact that indene[8]circulene does not have perfect  $2\pi$  values for its internal angles ( $2.017\pi$ ), it is a planar compound (as has been commented from the experimental evidences). In this regard, the structure might be stabilized in the planar configuration, despite the small strain (deviation of the interior angles from  $2\pi$ ), due to the gain in energy associated to a better  $\pi$  conjugation.

---

<sup>134</sup> S. Nobusue, H. Miyoshi, A. Shimizu, I. Hisaki, K. Fukuda, M. Nakano, Y. Tobe, *Angew. Chem. Int. Ed.*, **2015**, *54*, 2090–2094.

<sup>135</sup> When the heteroatom is big enough at the five-membered rings (as Se or S, tetraselena[8] and tetrathia[8]), the hetero[8]circulene turns to display a saddle-shaped geometry.

<sup>136</sup> D. Hellwinkel, G. Reiff, *Angew. Chem., Int. Ed. Engl.*, **1970**, *9*, 527.

<sup>137</sup> V. B. R. Pedersen, S. K. Pedersen, Z. Jin, N. Kofod, B. W. Laursen, G. V. Baryshnikov, C. Nuckolls, M. Pittelkow, *Angew. Chem. Int. Ed.*, **2022**, *61*, e20221229.

<sup>138</sup> **a)** G. V. Baryshnikov, B. F. Minaev and V. A. Minaeva, *Russ. Chem. Rev.*, **2015**, *84*, 455. **b)** T. Hensel, N. N. Andersen, M. Plesner, M. Pittelkow, *Synlett*, **2016**, 498. **c)** N. N. Karaush, G. V. Baryshnikov, V. A. Minaeva, H. Ågren, B. F. Minaev, *Mol. Phys.*, **2017**, *115*, 2218. **d)** S. Kato, Y. Serizawa, D. Sakamaki, S. Seki, Y. Miyake, H. Shinokubo, *Chem. Commun.*, **2015**, *51*, 16944. **e)** Y. Nagata, S. Kato, Y. Miyake, H. Shinokubo, *Org. Lett.*, **2017**, *19*, 2718.

<sup>139</sup> Y. Matsuo, K. Kise, Y. Morimoto, A. Osuka, T. Tanaka, *Angew. Chem. Int. Ed.*, **2022**, *61*, e2021167

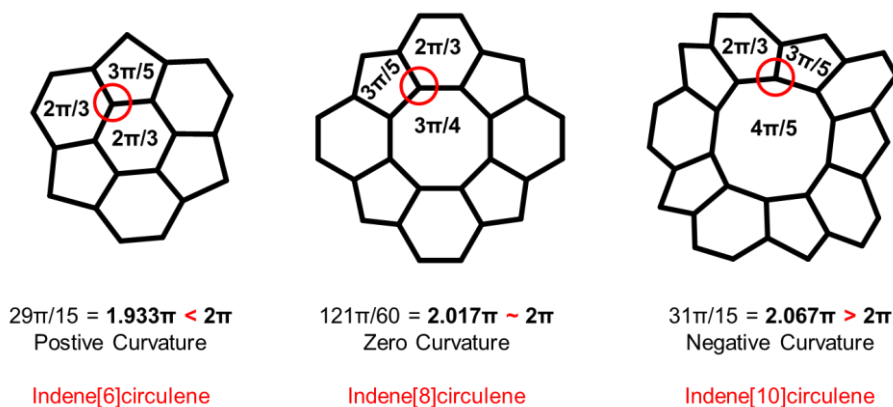


Figure 24. Analysis of the internal angles displayed in some compounds of the indene[n]circulene family.

In this context, it is worthy to remark that, in the last years, other relevant planar carbon lattices bearing different non-hexagonal rings have been theoretically described, as for example the carbon pentaheptite lattice (5-7)<sup>140</sup>, and the biphenylene network (4-6-8)<sup>141</sup>, see **Figure 25 b** and **c**. In both cases, these materials were predicted to present a metallic character. Gottfried et al. in 2021<sup>56</sup> achieved the on-surface synthesis and characterization of the biphenylene network carbon allotrope (4-6-8), see **Figure 25 d** and **e**, confirming the predicted metallic character of the structure, which presented a highly dependence on the width of the synthesized carbon stripe.

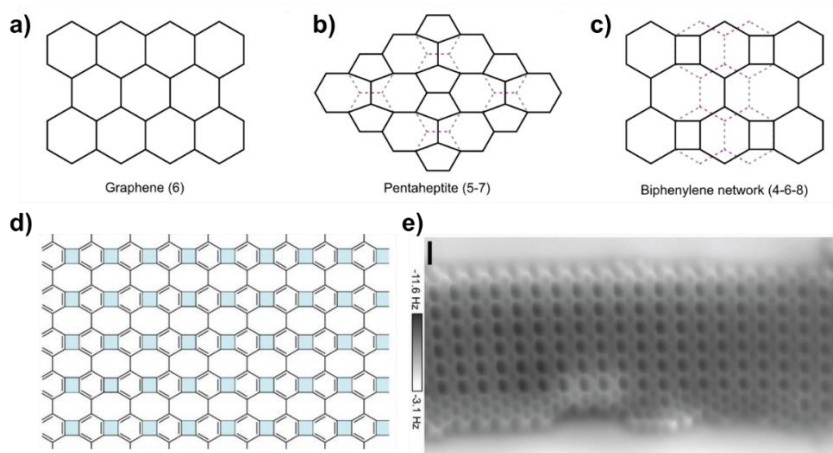
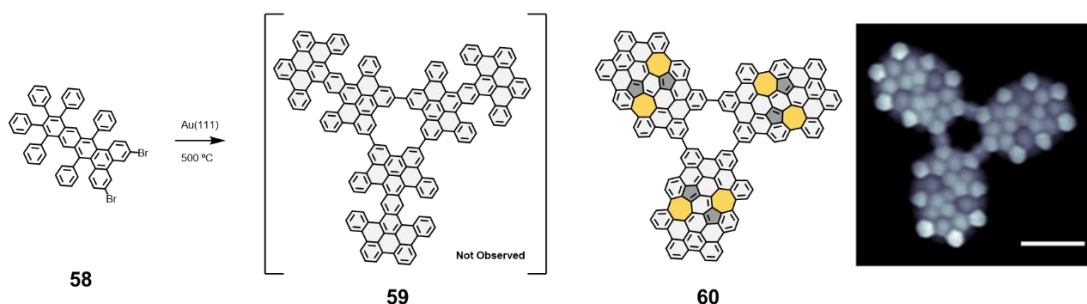


Figure 25. **a)** to **c)** Lattice structures of three planar carbon allotropes: graphene, carbon pentaheptite (5-7), and biphenylene network (4-6-8). The latter two formally result from graphene by reorganizing bonds (magenta dotted lines). **d)** and **e)** Chemical model and nc-AFM experimentally obtained image of the biphenylene network (4-6-8) on Au(111). Reproduced with permission from AAAS<sup>56</sup>.

<sup>140</sup> V. H. Crespi, L. X. Benedict, M. L. Cohen, S. G. Louie, *Phys. Rev. B*, **1996**, *53*, R13303–R13305.

<sup>141</sup> A. T. Balaban, C. C. Rentia, E. Ciupitu, *Rev. Roum. Chim.*, **1968**, *13*, 231–247.

In this sense, different nanographenes and GNRs with combinations of non-hexagonal rings have been synthesized in the literature. Again, this does not intend to be an exhaustive review but an illustration of related important examples. For more examples, the reader is invited to check references<sup>142</sup>. As depicted in **Figure 26**, Pascual, Peña et al.<sup>143</sup> in 2018 reported the surface-mediated Ullmann-type trimerization of dibromo-substituted precursor **58**, and the subsequent cyclodehydrogenation reaction resulting in the propeller-shaped nanographene **60** composed of three flat blades around a central pore (**Figure 26**). High-resolution STM images revealed the [18]annulene pore of the structure, while the two azulene moieties embedded within each of the three blades yielded a flat topography. The conjoined cove regions of the expected product **59**, which were predicted to induce a distortion and hinder the planar adsorption on the surface were not observed, suggesting that an alternative cyclization process occurred during the reaction, leading to the planar azulene-embedded nanographene **60**.



**Figure 26.** On-surface synthesis of a macrocycle bearing azulene moieties. BR-STM image reproduced with permission of ACS Publications<sup>143</sup>

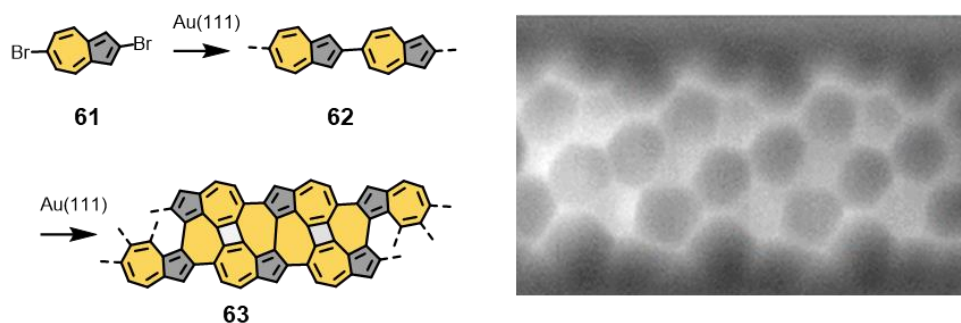
In 2019, Ebeling, Hilt, Hieringer, Gottfried, and co-workers<sup>144</sup> reported that the 2,6-polyazulene chain **62**, derived from surface-assisted Ullmann polymerization of 2,6-dibromoazulene **61**, could undergo lateral dehydrogenative fusion to form carbon nanoribbons. The formed species, nanoribbon **63** (**Figure 27**), were rich in 5-7 ring skeleton defects (phagraphene<sup>145</sup>). This carbon nanoribbon paves the way towards new non-alternant carbon allotropes with distinctive properties.

<sup>142</sup> c) T. G. Lohr, J. I. Urgel, K. Eimre, J. Liu, M. Di Giovannantonio, S. Mishra, R. Berger, P. Ruffieux, C. A. Pignedoli, R. Fasel, X. Feng, *J. Am. Chem. Soc.*, **2020**, *142*, 13565–13572. e) I. C.-Y. Hou, Q. Sun, K. Eimre, M. Di Giovannantonio, J. I. Urgel, P. Ruffieux, A. Narita, R. Fasel, K. Müllen, *J. Am. Chem. Soc.*, **2020**, *142*, 10291–10296. f) M. Liu, M. Liu, L. She, Z. Zha, J. Pan, S. Li, T. Li, Y. He, Z. Cai, J. Wang, Y. Zheng, X. Qiu, D. Zhong, *Nat Commun.*, **2017**, *8*, 14924.

<sup>143</sup> J. Hieulle, E. Carbonell-Sanromà, M. Vilas-Varela, A. Garcia-Lekue, E. Guitián, D. Peña, J. I. Pascual, *Nano Lett.*, **2018**, *18*, 418–423.

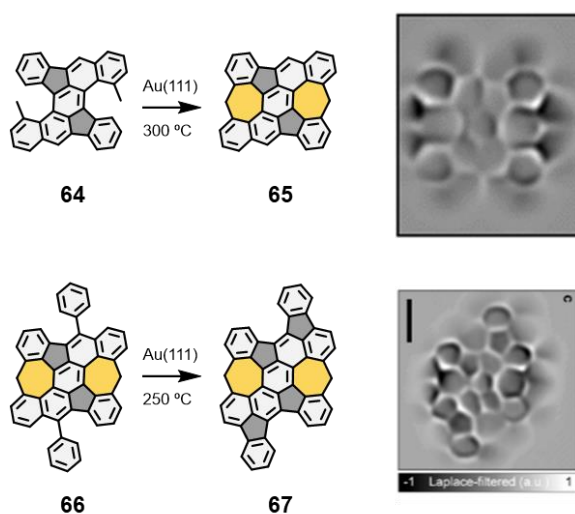
<sup>144</sup> Q. Fan, D. Martin-Jimenez, D. Ebeling, C. K. Krug, L. Brechmann, C. Kohlmeyer, G. Hilt, W. Hieringer, A. Schirmeisen, J. M. Gottfried, *J. Am. Chem. Soc.*, **2019**, *141*, 17713–17720.

<sup>145</sup> Z. Wang, X. F. Zhou, X. Zhang, Q. Zhu, H. Dong, M. Zhao, A. R. Oganov, *Nano Lett.*, **2015**, *15*, 6182–6186.



**Figure 27.** On-surface synthesis of GNRs embedding five-membered, seven-membered and four membered-rings. Nc-AFM image reproduced with permission of ACS Publications<sup>144</sup>

Alternatively, in 2018 and 2019, Feng, Müllen, Fasel, and co-workers reported the on-surface synthesis of novel nanocarbons bearing non-benzenoid rings such as the rubicene derivative **65** (Figure 28)<sup>146</sup>, and its pentagon-fused analogue **67** (Figure 28)<sup>147</sup>. PAHs **65** and **67** are non-alternant structural isomers of peri-tetracene with two embedded azulene units. Spin-polarized DFT calculations revealed that both **65** and **67** should exhibit open-shell singlet ground states, and **67** showed a narrow band gap (0.27 eV) and significant open-shell biradical character ( $y_0 = 0.92$ ), making them promising candidates for spintronic applications.



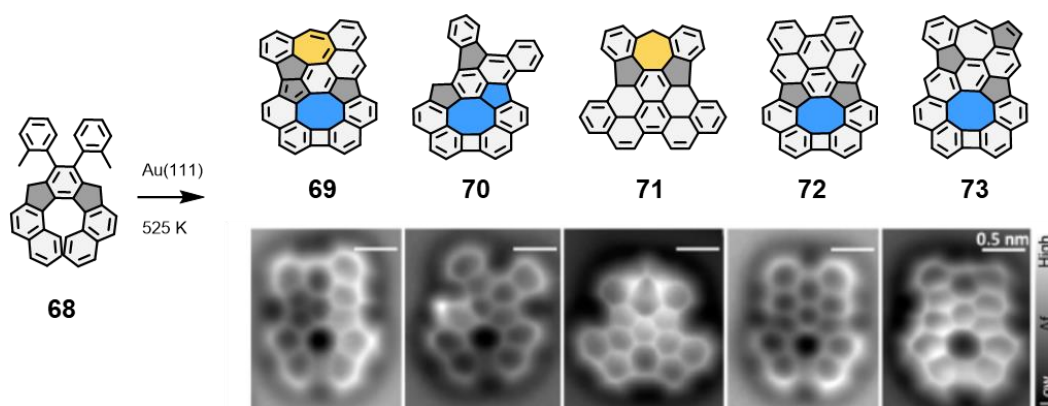
**Figure 28.** On-surface synthesis of rubicene derivatives on Au(111). Nc-AFM images reproduced with permission of ACS Publications<sup>146,147</sup>.

<sup>146</sup> S. Mishra, T. G. Lohr, C. A. Pignedoli, J. Liu, R. Berger, J. I. Urgel, K. Müllen, X. Feng, P. Ruffieux, R. Fasel, *ACS Nano*, **2018**, *12*, 11917 – 11927.

<sup>147</sup> J. Liu, S. Mishra, C. A. Pignedoli, D. Passerone, J. I. Urgel, A. Fabrizio, T. G. Lohr, J. Ma, H. Komber, M. Baumgarten, C. Corminboeuf, R. Berger, P. Ruffieux, K. Müllen, R. Fasel, X. Feng, *J. Am. Chem. Soc.*, **2019**, *141*, 12011 – 12020.



Finally, Mallada, Jelinek et al.<sup>148</sup> reported on the outcomes of the cyclodehydrogenation and ring closure reactions of the precursor **68** on top of a Au(111) surface. They observed the formation of different non-alternant PAHs bearing from four-membered rings to eight-membered rings, as depicted in **Figure 29**. Some of these products presented a peculiar ring current stabilizing aromatic character and all of them showed a close-shell and low bandgap electronic structure. Computationally, they also studied the influence and importance of the gold adatom in the rearrangement of some of the formed PAHs.



**Figure 29.** On-surface synthesis of nonalternant PAHs on Au(111). Nc-AFM images reproduced with permission of ACS Publications<sup>148</sup>.

To end up, as a conclusion, it can be stated that the combination of non-hexagonal rings in a graphene lattice may form distorted graphenic structures when they do not compensate curvatures, as presented in **Figure 21** or **Figure 22**. But planar structures are also possible to synthesize when a compensation of the internal angles is produced after the combination of higher and lower-membered rings, as stated in **Figure 27** or **Figure 28**.

As a second conclusion, the controlled enlargement of a PAH or a macrocyclic structure as the [n]circulene or the indeno[n]circulene families, exhibits different stages of curvature, going from a positive to a negative curvature passing through a zero curvature (theoretical studies<sup>115</sup> also describe a helical structure for larger geometries).

### Cycloarenes

Cycloarenes are not an exception to the previously mentioned strategies for generating curvature. Indeed, in the recent years, some curved cycloarenes have been reported in the literature following two main strategies: (i) enlarging or constricting the Kekulene structure, and (ii) incorporating non-benzenoid rings into the Kekulene geometry.

<sup>148</sup> B. Mallada, B. De La Torre, J. I. Mendieta-Moreno, D. Nachtigallová, A. Matěj, M. Matoušek, P. Mutombo, J. Brabec, L. Veis, T. Cadart, M. Kotora, P. Jelínek, *J. Am. Chem. Soc.*, **2021**, *143*, 14694–14702.

**Scheme 7** shows the curvature of some examples of enlarged or shortened Kekulenes. In this regard, Staab and Funhoff synthesized in 1986 the contracted kekulene **74** with 10 fused benzene rings<sup>149</sup>. Although a suitable crystal for X-Ray diffraction was not achieved in that work, it is assumed a curved geometry for the molecule due to the steric interactions of the hydrogens in the inner pore. In 2020, Müllen et al. prepared the extended Quintulene **75**<sup>150</sup>. It was a highly strained bowl-shaped molecule, which underwent dimerization in solution via  $\pi$ - $\pi$  stacking to form a metastable, but isolable bilayer complex. Although **75** was synthesized as an extended derivative, the curved bowl-shaped geometry arises from its geometrical constrain, which is shortened in comparison with the Kekulene **17**.

Some years before, in 2012, the King's group developed a higher heptagonal homologue, the Septulene<sup>151</sup> **76**. It contained 14 fused benzene rings and, although it was computationally predicted to exhibit a saddle-shaped curvature, it had a chair-conformation due to the interactions of the molecule in the crystal lattice. Finally, in 2016, Stępień and colleagues<sup>152</sup> achieved a higher octagonal homologue, the Octulene **77**, comprising 16 fused benzene rings. **77** presented a saddle-shaped geometry, and beyond its optoelectronic properties, it was interestingly utilized for binding chloride anions in its inner pore. Again, it is possible to observe in this series of compounds the already mentioned trend of going from a bowl-shaped to a saddle-shaped geometry passing through a planar structure in between (the Kekulene **17**) thanks to the enlargement of the structure.

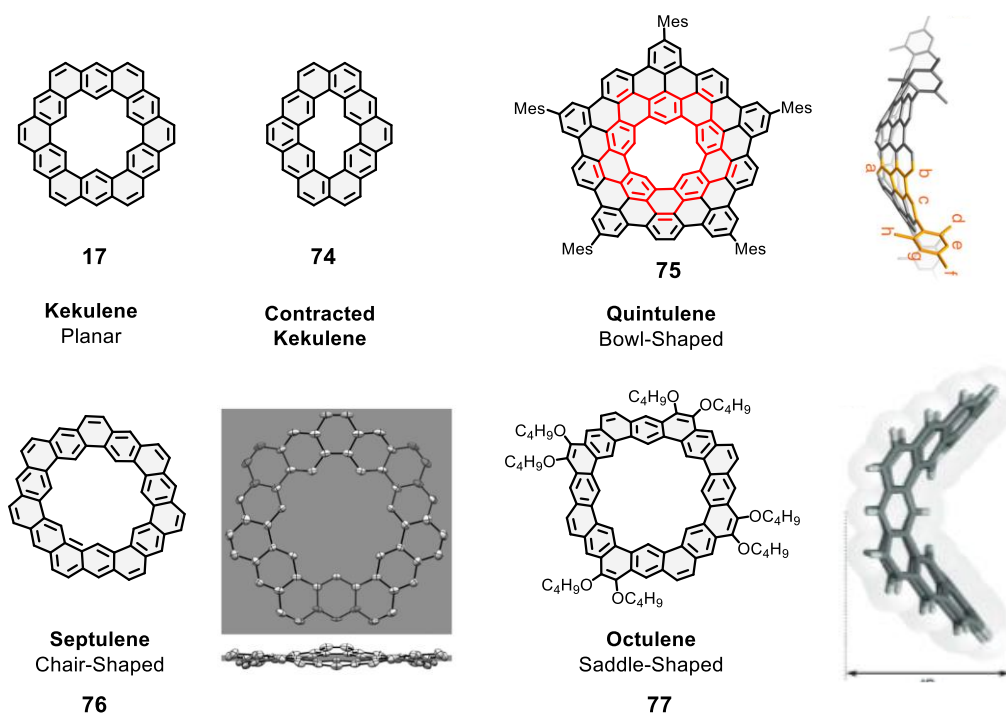
---

<sup>149</sup> D. J. H. Funhoff, H. A. Staab, *Angew. Chem. Int. Ed. Engl.*, **1986**, *25*, 742–744.

<sup>150</sup> H. Hou, X.-J. Zhao, C. Tang, Y.-Y. Ju, Z.-Y. Deng, X.-R. Wang, L.-B. Feng, D.-H. Lin, X. Hou, A. Narita, K. Müllen, Y.-Z. Tan, *Nat Commun* **2020**, *11*, 3976.

<sup>151</sup> B. Kumar, R. L. Viboh, M. C. Bonifacio, W. B. Thompson, J. C. Buttrick, B. C. Westlake, M. Kim, R. W. Zoellner, S. A. Varganov, P. Mörschel, J. Teteruk, M. U. Schmidt, B. T. King, *Angew. Chem. Int. Ed.*, **2012**, *51*, 12795–12800.

<sup>152</sup> M. A. Majewski, Y. Hong, T. Lis, J. Gregoliński, P. J. Chmielewski, J. Cybińska, D. Kim, M. Stępień, *Angew. Chem. Int. Ed.*, **2016**, *55*, 14072–14076.

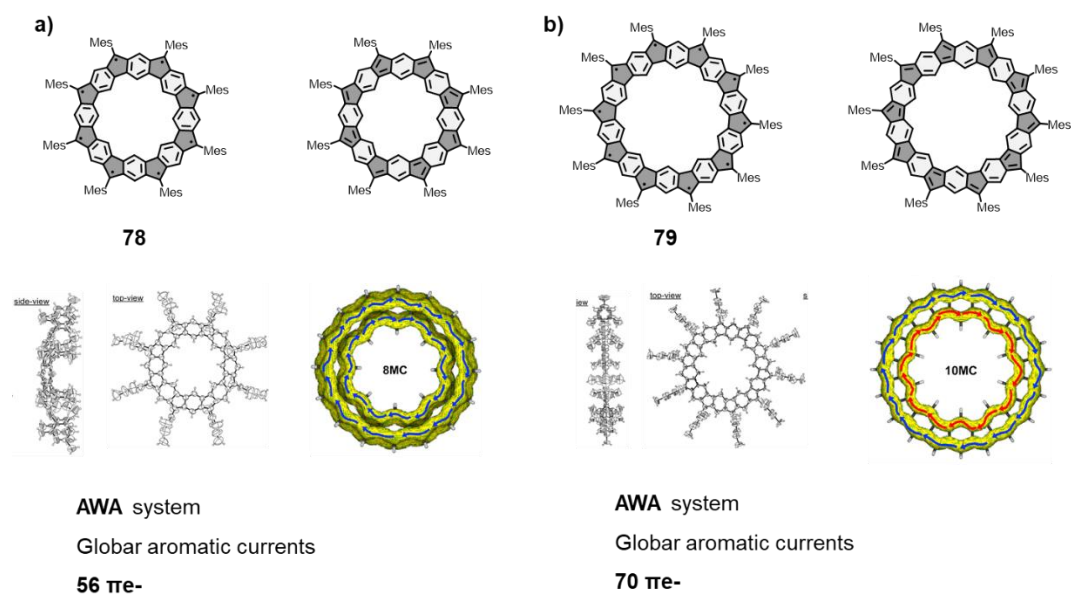


**Scheme 7.** Enlarged and shortened kekulene molecules with some of its X-ray diffraction crystal structures.

Simultaneously, different interesting cycloarenes bearing non-hexagonal rings were also reported. In 2018, Liu et al.<sup>153</sup> described the synthesis and characterization of two intriguing cyclopenta-ring-fused oligo(*m*-phenylene) macrocycles **78** and **79** depicted in **Figure 30**. The structure of these compounds is based on the combination of the same number of five-membered rings, hexagonal rings, and unpaired electrons. In principle, these radicals are located at the apex of the five-membered rings and are protected with mesityl groups due to the high reactivity of the unpaired electrons.

The analysis through X-ray diffraction revealed a truncated cone structure (positive curvature) for **78** and a planar geometry for **79**. Further investigations through magnetic measurements and quantum calculations revealed a singlet ground state for **78** and a triplet ground state for **79** both showing an AWA structure. As can be seen in the ACID plots in **Figure 30**, both molecules present two concentric aromatic ring currents, the direction of the currents being clockwise for both rings and molecules. These compounds mark the first examples of PAHs showing the exotic phenomenon of global aromaticity in two concentric ring currents (AWA), being a landmark for the field of arenes after the already commented localized electronic structure of kekulene **17**.

<sup>153</sup> C. Liu, M. E. Sandoval-Salinas, Y. Hong, T. Y. Gopalakrishna, H. Phan, N. Aratani, T. S. Heng, J. Ding, H. Yamada, D. Kim, D. Casanova, J. Wu, *Chem*, **2018**, *4*, 1586–1595.



**Figure 30.** Cyclopenta-ring-fused oligo(m-phenylene) macrocycles presenting the AWA system.

**Scheme 8** shows additional examples of other reported cycloarenes that bear non-benzenoid rings, heteroatoms and/or other topologies (the building blocks are depicted inside the boxes on the left side of the scheme). Similarly to the before commented cyclopenta-ring-fused oligo(m-phenylene) macrocycles, Wu et al.<sup>154</sup> synthesized two analogous compounds with the introduction of carbazole moieties. Compound **80** exhibited a bowl-shaped curvature and a tetraradicaloid behavior while compound **81** a saddle-shaped structure and a hexaradicaloid ground state. An AWA system was not observed in any of the two structures (note that the pure carbon macrocycles presented AWA structure). Both compounds had small excitation energy gaps and could be thermally populated to high-spin excited states, which results in an interesting magnetization behavior even at r.t..

On the other hand, Stepień and Mysliwiec in 2013<sup>155</sup> introduced a different topology for a heterocycloarene family that contained nitrogen atoms by incorporating carbazole units. In this regard, compound **82** was synthesized following a fold-in synthetic strategy and adopted a bowl-shaped geometry. The same group in 2015<sup>156</sup> conducted the enlargement of the same structure, resulting in a planar geometry for **83** with interesting optoelectronic properties.

Finally, it is worthy to remark the work developed in 2024 by Liu et al.<sup>157</sup>, where two different heterocycloarenes **84** and **85**, with an endo topology (some rings are facing the inner pore of the macrocycle), were synthesized exhibiting positive and negative curvature depending on their

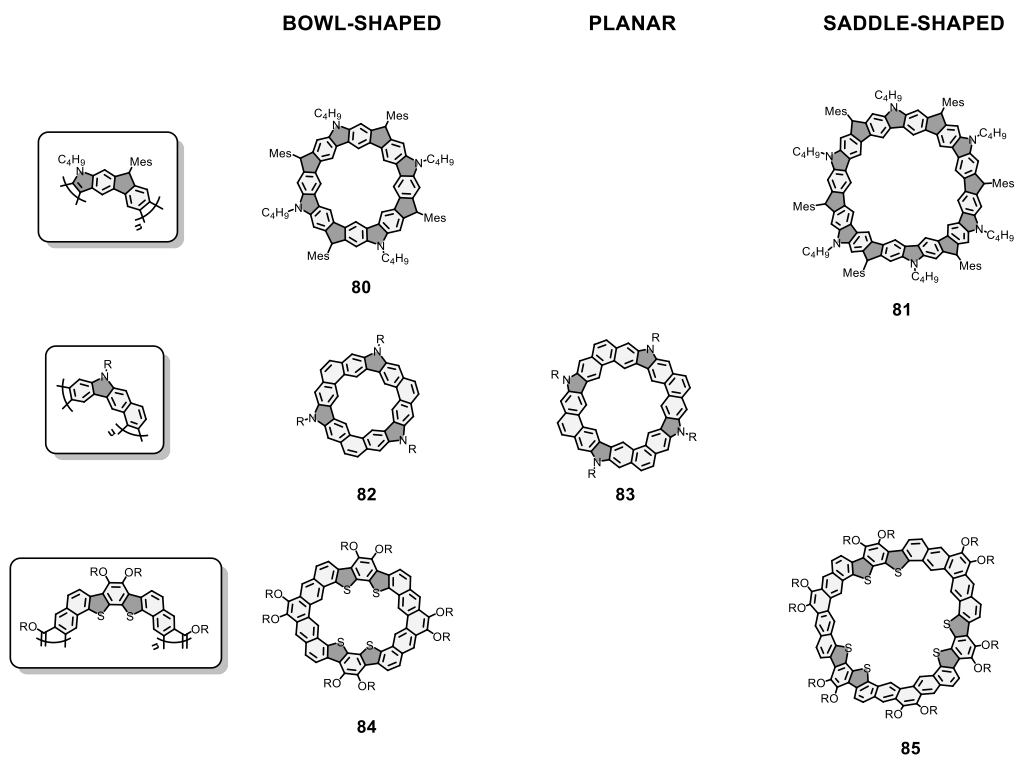
<sup>154</sup> S. Das, T. S. Heng, J. L. Zafra, P. M. Burrezo, M. Kitano, M. Ishida, T. Y. Gopalakrishna, P. Hu, A. Osuka, J. Casado, J. Ding, D. Casanova, J. Wu, *J. Am. Chem. Soc.*, **2016**, *138*, 7782–7790.

<sup>155</sup> D. Mysliwiec, M. Stepień, *Angew. Chem. Int. Ed.*, **2013**, *52*, 1713–1717.

<sup>156</sup> M. A. Majewski, T. Lis, J. Cybińska, M. Stepień, *Chem. Commun.*, **2015**, *51*, 15094–15097.

<sup>157</sup> D. An, R. Zhang, J. Zhu, T. Wang, Y. Zhao, X. Lu, Y. Liu, *Chem. Sci.*, **2024**, *15*, 4590–4601.

macrocycle size. In this regard, the synthetic strategy utilized was based on a periphery fusion strategy. Additionally, supramolecular affinities with  $C_{60}$  were tested for both macrocycles, showing an improved behavior for the bowl-shaped macrocycle **80**.



**Scheme 8.** Examples of heterocycloarenes exhibiting different curvatures.

As it has been stated for all the different topologies exposed in **Figure 30** and **Scheme 8**, again, it is observed a change in curvature from positive to negative (passing through a zero curvature) when the structures are enlarged.



**2 OBJECTIVES**





According to the information gathered in the Introduction chapter, where the state-of-art was described, curved graphenic nanostructures have a great potential to become one of the materials of the future due to their promising properties related to charge transport, light absorption and emission, or magnetism. However, their synthesis on top of metallic surfaces, which provide a unique environment for the exploration of new reaction pathways, synthetic strategies, and single-molecule characterization, has remained scarce thus far.

Therefore, the general objective of this thesis is:

**The synthesis of curved graphenic structures on top of metallic surfaces through the incorporation of non-benzenoid rings, and their subsequent characterization by on-surface techniques such as SPM or XPS.**

**The synthesis of curved graphenic structures on top of metallic surfaces through the incorporation of non-benzenoid rings, the understanding of the thermal and on-surface stability of these non-benzenoid rings, and the structural, electronic and magnetic characterization of the generated nanostructures by on-surface techniques such as SPM or XPS.**

For that purpose, a set of different synthetic strategies and approaches were developed in three specific objectives (three different sections):

- **Objective 1**

We intend the development of a synthetic strategy, combining in-solution chemistry and on-surface synthesis, to yield graphene nanostructures with saddle-shape curvature. For that purpose, we will incorporate higher-membered rings to the precursor structure, heptagonal or octagonal rings, to induce the saddle-shape curvature in the final GNRs and polymers. To achieve this, we will employ the in-solution synthetic methodologies previously developed within the research group for the synthesis of the molecular precursors and we will explore different on-surface-reaction conditions to yield the final nanomaterials.

- **Objective 2**

We propose the synthesis of a family of cyclopenta-ring-fused oligo(m-phenylene) macrocycles with varying sizes to explore how the curvature of the macrocycle changes relative to its size (hypothetically, from positive to negative curvature, passing through a zero curvature), and how this alteration in curvature impacts the macrocycle's properties. To accomplish this, we aim to develop a versatile methodology capable of synthesizing precursor molecules with different ring sizes combining in-solution chemistry with on-surface synthesis. Finally, we will characterize their structural, electronic and magnetic properties experimentally and theoretically.

- **Objective 3**

Finally, we aim to study a “novel” approach to induce curvature in graphene nanostructures through the interaction of localized unpaired electrons, located in 5-membered rings, with the surface underneath. For that purpose, we propose the on-surface synthesis of a curved pentaannulated-GNR which curvature originates from this radical-surface interaction.





## 3 RESULTS



The Results chapter delves into the structural, electronic, and magnetic characterization of the final synthesized graphene nanostructures, but also in the description of their synthesis, regarding the different steps carried out in combination of in-solution and on-surface methods. Additionally, some “unexpected” experimentally observed reaction rearrangements are in-depth studied to gain insights of the on-surface thermal stability of some of the non-benzenoid rings utilized.

A bottom-up approach was employed for the synthesis of all the materials, combining in-solution and on-surface synthetic, and characterization methods. For each synthesized material a comprehensive discussion will encompass the following aspects:

The in-solution synthesis strategy:

- We will elaborate on the in-solution synthesis of the precursor describing some of the key steps utilized in the synthetic strategy. The characterization of the precursors and the intermediates is further described in the Experimental Methods chapter by means of nuclear magnetic resonance (NMR), high-resolution mass spectrometry (HR-MS) and infrared spectroscopy (IR).

The on-surface synthesis:

- By means of STM, XPS and computational calculation we will address the study of the different phases at different temperatures before reaching the final nanomaterials. We will analyze the self-assembly phase after sublimating the precursors on top of metallic surfaces, and we will examine the intermediates products of the reactions.

The structural, electronic, and magnetic characterization of the final nanostructures:

- Structural high-resolution characterization using techniques such as nc-AFM, BR-STM or force spectroscopy with CO-functionalized tips will be employed.
- The electronic and/or magnetic properties will be examined through STS spectroscopy and dI/dV mapping, and they will be compared with computational results.

The study of the mechanism of reaction:

- For those unexpected rearrangements we will propose and/or calculate the reaction mechanisms by means of quantum and molecular methods QM/MM.

Bibliographic comparison:

- The obtained results, regarding synthesis and properties of the nanomaterials, will be compared and analyzed in relation to reported relevant literature.

This comprehensive approach aims to provide a thorough understanding of each nanomaterial, covering its synthesis, characterization at various stages, and a detailed examination of its final structural and functional properties.

### 3.1 Saddle-Shape Curvature into Graphene Nanostructures by the Incorporation of Higher-Membered Rings

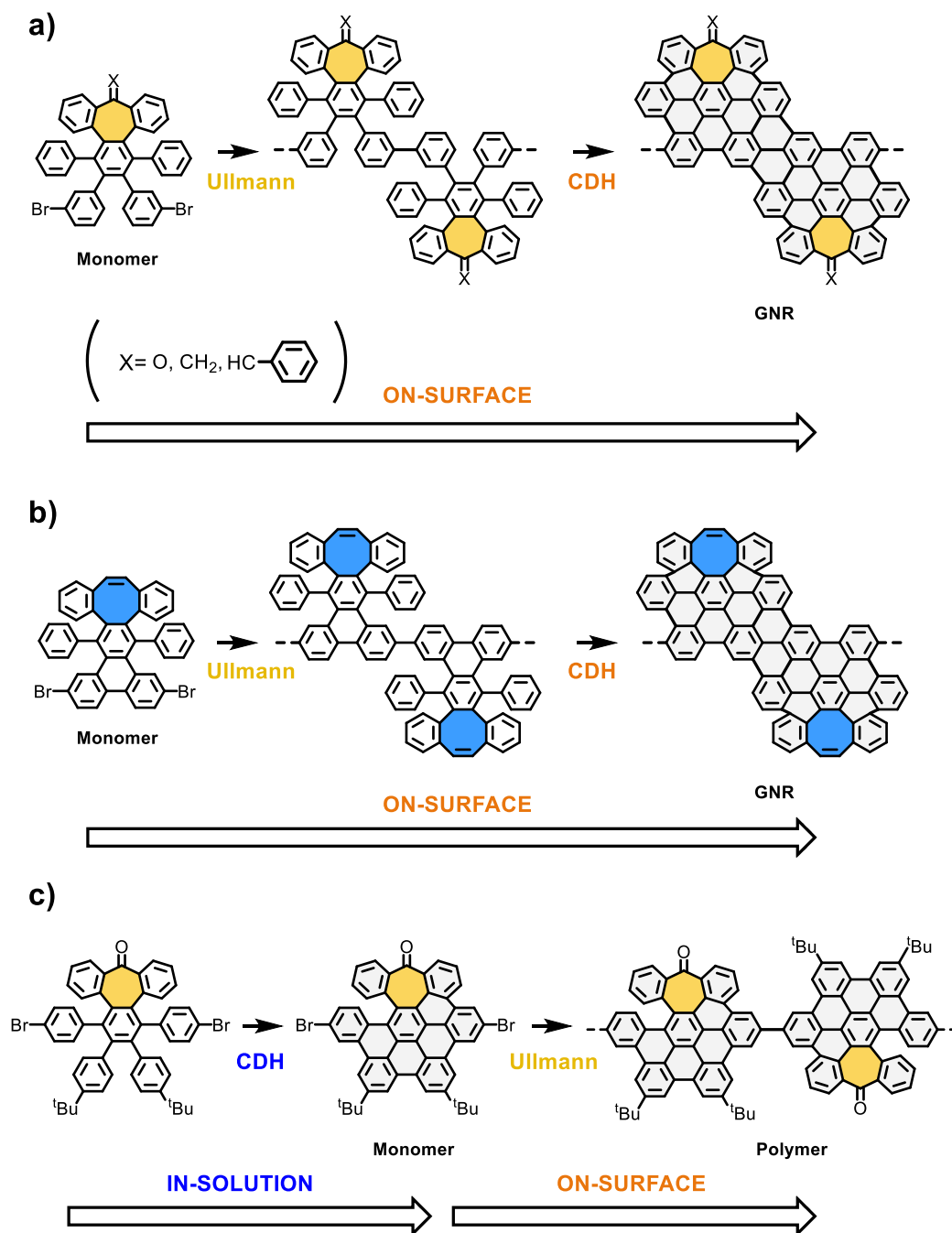
This section presents the outcomes of the on-surface synthesis and characterization towards saddle-shaped graphene nanostructures from precursors that already bear a higher-membered ring in its precursor structure (either seven or eight-membered rings). As stated in the Introduction chapter, the incorporation of a higher-membered ring in a hexagonal graphene nanostructure typically induces a saddle-shape curvature. This is mainly due to an imbalance of the internal angles of some of the carbons of the graphene nanoflake after the introduction of the higher-membered ring. In this regard, it is essential to have the synthetic selectivity to introduce the desired number of non-benzenoid rings at the required positions to modulate the geometry and electronic properties (the combination of non-benzenoid rings with different sizes may induce a flattening of the structure). In this sense, a bottom-up approach is required to abord this task with the enough selectivity.

The uniform methodology employed across all the synthesized materials in this section involved two key steps: first, the in-solution synthesis of the precursors containing the non-benzenoid ring (the non-benzenoid ring in the precursor was in-solution synthesized in this section); and second, the on-surface growth of the graphenic structures encompassing an Ullmann coupling reaction to enlarge the structure, and (only in some cases) a final cyclodehydrogenation reaction to fully conjugate the nanostructure.

In this regard, we followed two different synthetic approaches to induce the curvature in the structures. Firstly, non-cyclodehydrogenated precursors were used bearing the before commented higher-membered rings. In this regard, it was intended to produce the saddle-shape curvature in the final cyclodehydrogenation reaction on-surface after the structure enlargement through the Ullman coupling. **Scheme 9 a** and **b** show the utilized precursors bearing seven-membered rings and eight-membered rings respectively. Secondly, **Scheme 9 c** shows a second approach in the synthesis of saddle-shape graphene nanostructures that is based on the use of previously cyclodehydrogenated precursors (the saddle curvature is generated in solution), avoiding high temperatures for the on-surface synthesis and limiting the reaction on the surface to the Ullman coupling.

Next, the section is subdivided into other three subsections detailly explaining the results regarding to the three presented scenarios in **Scheme 9 a**, **b** and **c**. A brief summary ends each subsection with some conclusions and the main issues aborded.





Scheme 9. Synthetic strategies carried out in this section to yield saddle-shape graphene nanostructures.

### 3.1.1 Graphene Nanoribbons From Precursors Containing a Seven-Membered Ring

In this subsection, it is utilized the precursor **3.1.1-3Prec** (**Scheme 10**) bearing a cycloheptatrienone moiety (a seven-membered ring functionalized with a ketone group) to yield curved chevron-like GNRs after a hierarchical tandem of on-surface reactions (Ullman coupling and cyclodehydrogenation). The results of the sequential reaction were analyzed by means of XPS, STM and nc-AFM observing a novel rearrangement of the embedded tropone moiety into two different planar structures, contrary to what we expected (a curved GNR). In this regard we propose a reaction mechanism and we study the thermal stability of the 7-membered ring moiety on top of the Au(111) surface.

Subsequently, we derived **3.1.1-3Prec** into two different precursors (**3.1.1-8Prec** and **3.1.1-11Prec**, **Scheme 12**) with the aim of increasing the thermal stability of the seven-membered ring for synthesizing the aimed curved chevron-like GNRs. However, the inspection of the surfaces (in both cases) revealed dendritic products related with an unsuccessful synthesis.

#### *In-Solution synthesis and on-surface characterization of the r.t phase*<sup>158</sup>

**Scheme 10** shows the synthetic pathway to obtain the distorted chevron-like GNR **3.1.1-7** containing 7-membered rings. In this regard, precursor **3.1.1-3Prec** was designed to incorporate Br atoms at “meta” position, and a cycloheptatrienone moiety to induce the curvature in the structure. The ketone group (tropone moiety) was also incorporated in the cycloheptatrienone to see possible phenomena of self-assembly between GNRs due to hydrogen bond-like interactions among the carbonyl groups. In addition, this is also a useful moiety for further functionalization of the precursor enabling the synthesis of other derivatives as it will be seen below in this chapter.

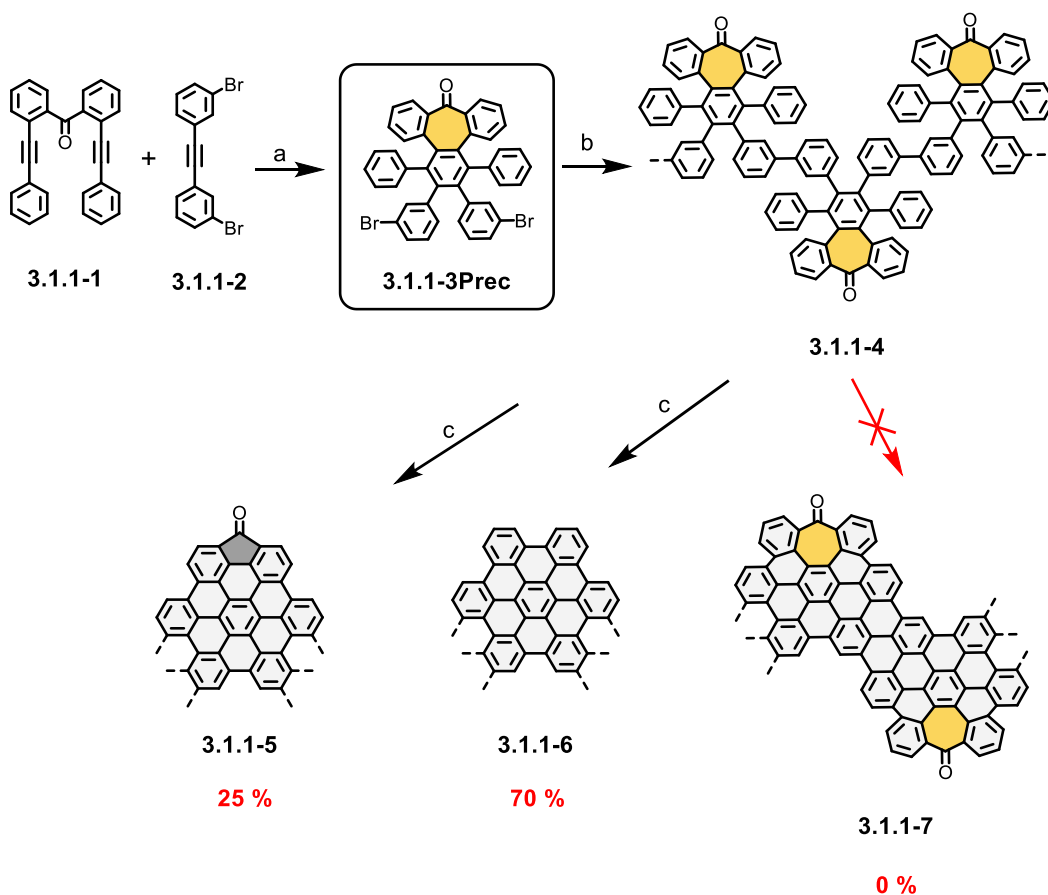
In-solution synthesis of **3.1.1-3Prec** was based on an already described strategy by our research group for the synthesis of distorted nanographenes incorporating heptagonal rings<sup>159</sup>. The key step of this strategy is a cobalt-mediated alkyne cyclotrimerization reaction. In a single step, the heptagonal ring and the polyphenylic backbone are selectively built incorporating substituents for future extensions or derivatizations (Br atoms in this case). In addition to the previously stated argument about the carbonyl group, it also useful during the synthesis because it hinders the formation of undesired 9,10-dihydroanthracenes<sup>160</sup> during the cyclotrimerization step. **3.1.1-3Prec** was soluble in most of the common organic solvents as methylene chloride, acetone, or chloroform, and it was characterized by means of nuclear magnetic resonance (NMR), high-resolution mass spectrometry (HR-MS) and infrared spectroscopy (IR).

<sup>158</sup> This work is a collaboration between MOREFUN group from the University of Granada, where the monomer was synthesized in solution; ESISNA group from CSIC of Madrid, where the on-surface growth of the nanostructures was studied, and Nanotech@Surfaces group from EMPA in Switzerland, where the high-resolution images with STM and nc-AFM were taken.

<sup>159</sup> I. R. Márquez, N. Fuentes, C. M. Cruz, V. Puente-Muñoz, L. Sotorrios, M. L. Marcos, D. Choquesillo-Lazarte, B. Biel, L. Crovetto, E. Gómez-Bengoa, M. T. González, R. Martín, J. M. Cuerva, A. G. Campaña, *Chem. Sci.* **2017**, *8*, 1068–1074.

<sup>160</sup> W. Baidossi, H. Schumann and J. Blum, *Tetrahedron*, **1996**, *52*, 8349–8364.

Subsequently, **3.1.1-3Prec** was deposited onto a Au(111) surface held at 200 °C to directly induce the cleavage of the C-Br bonds, initiating the aryl-aryl coupling. **Figure 31 a** represents a topography STM image of **3.1.1-4**, showing the well-known islands that oligomeric precursors of chevron-GNRs tend to do due to an attractive  $\pi$  -  $\pi$  interaction between external interdigitated phenyl rings<sup>161</sup>.



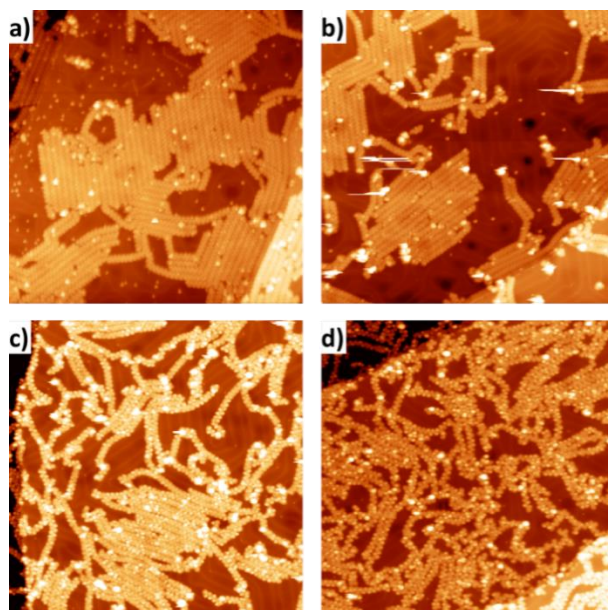
**Scheme 10.** Schematic representation of synthesis of monomer **3.1.1-3Prec** and the different reaction pathways toward the formation of tropone-GNR **a)**  $\text{CO}_2(\text{CO})_8$ , Toluene, 110 °C, 16 h, 51 %, **b)** Annealing at 200 °C on a Au(111) surface. **c)** Annealing at 400 °C on a Au(111) surface.

### Polymeric phase

**Figure 31 b** to **d** shows some cyclodehydrogenated intermediate states before the final cyclodehydrogenation temperature (350 °C). The before commented stacking, normally disappears upon the planarization of the oligomers into chevron GNRs after the

<sup>161</sup> J. Cai, P. Ruffieux, R. Jaafar, M. Bieri, T. Braun, S. Blankenburg, M. Muoth, A. P. Seitsonen, M. Saleh, X. Feng, K. Müllen, R. Fasel, *Nature* **2010**, *466*, 470–473.

cyclodehydrogenation reaction, due to steric repulsion between neighboring in-plane hydrogen atoms. But in our case, due to the attractive hydrogen-bonding like interaction mediated by the CO of the tropone, the chains should remain linked despite the possible steric repulsion induced by the hydrogen atoms in the planar chains. A similar behavior has been reported among N-doped chevron GNRs<sup>162</sup>. However, as can be seen in **Figure 31 c**, the chains start to disassembly when the annealing temperature is increased to 310 °C. In this sense, we deduce that molecular changes related to the ketone group in the 7-membered ring start to happen from this temperature before the final cyclodehydrogenation reaction.



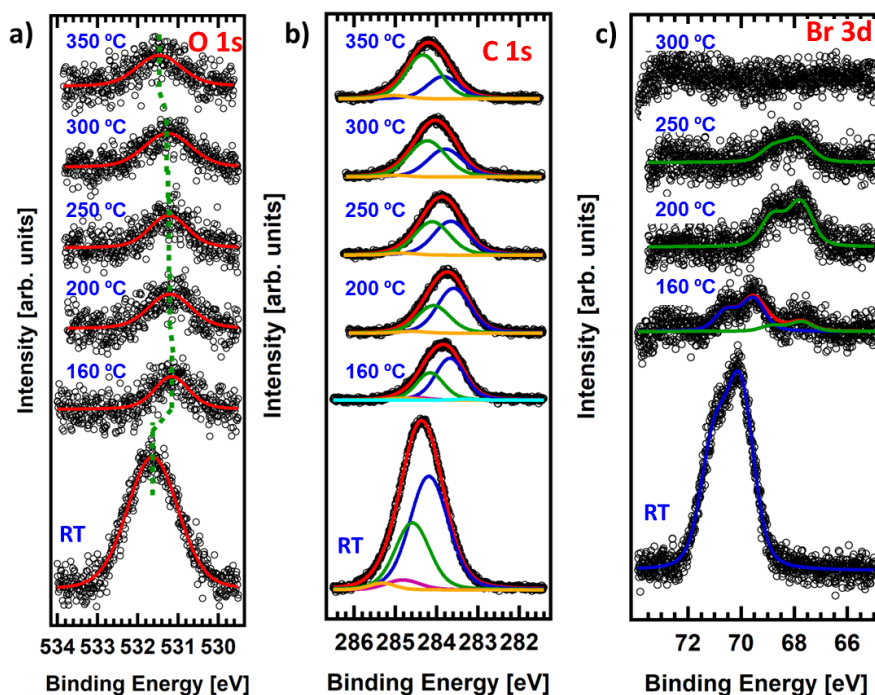
**Figure 31.** STM images of the thermal evolution of **3.1.1-4** on Au(111) after annealing at a) 200 °C, b) 250 °C, c) 310 °C, and d) 350 °C. STM parameters are as follows: Same size for every image 100 nm × 100 nm, (a) I = 30 pA, V = 1.0 V, (b) I = 20 pA, V = -1.2 V, (c) I = 20 pA, V = -1.0 V, (d) I = 20 pA, V = 1.0 V.

This hypothesis is supported by the analysis of the thermal evolution XPS core-level peaks of O 1s, C 1s and Br 3d in **Figure 32**. Regarding the O 1s core-level peak in **Figure 32 a**, a reference value for the binding energy (BE) of oxygen in the tropone unit is established through a multilayer deposition of **3.1.1-3** on the clean Au(111) surface at RT. This BE value corresponds to ketone groups (531.6 eV) described in the literature<sup>163</sup>, confirming that the molecule reaches the surface intact and discarding molecular decomposition in the crucible. Upon increasing the surface temperature to 160 °C, the O 1s core-level peak intensity significantly drops due to multilayer desorption. Simultaneously, there is a ~0.5 eV shift toward a lower BE, suggesting either a charge transfer from the surface to the molecules or an increased screening of the signal

<sup>162</sup> T. H. Vo, U. G. E. Perera, M. Shekhirev, M. Mehdi Pour, D. A. Kunkel, H. Lu, A. Gruverman, E. Sutter, M. Cotlet, D. Nykypanchuk, P. Zahl, A. Enders, A. Sinitskii, P. Sutter, *Nano Lett.*, **2015**, *15*, 5770–5777.

<sup>163</sup> F. Bebensee, K. Svane, C. Bombis, F. Masini, S. Klyatskaya, F. Besenbacher, M. Ruben, B. Hammer, T. Linderoth, *Chem. Commun.*, **2013**, *49*, 9308.

of the first monolayer<sup>164</sup>. Subsequent annealing steps at 200 °C, 250 °C, and 300 °C showed no significant modification in the energy position, indicating that the molecular structure of the tropone unit remains largely unchanged. These temperatures correspond to the formation of polymer **3.1.1-4** and the initial stages of CDH, suggesting that heptagonal rings remain unaltered during polymerization via surface-mediated Ullmann coupling. Annealing at 350 °C induces a 0.25 eV shift of the peak toward higher BE and an enlargement of the peak width, suggesting a progressive rearrangement of the CO unit in the structure.



**Figure 32.** a), b) and c) The thermal evolution of the O 1s, C 1s and Br 3d XPS core-level peak. The green line in a) shows the BE position of the peak maximum.

Regarding the thermal evolution of the C 1s core-level peaks in **Figure 32 b**, the XPS at RT exhibits four components associated with the four C species in **3.1.1-3Prec**: C–H (blue), C–C (green), C–Br (purple), and C=O (gold). Importantly, the area ratios align with the molecular stoichiometry. Upon annealing the system to 160 °C, two notable effects occur. Firstly, there is a discernible reduction in the total area of the C 1s signal due to multilayer desorption. Secondly, the C–Br signal decreases, accompanied by the emergence of a new component at 283.3 eV

<sup>164</sup> N. Ruiz del Árbol, I. Palacio, G. Otero-Irurueta, J. I. Martínez, P. L. de Andrés, O. Stetsovyh, M. Moro-Lagares, P. Mutombo, M. Svec, P. Jelínek, A. Cossaro, L. Floreano, G. J. Ellis, M. F. López, J. A. Martín-Gago, *Angew. Chem. Int. Ed.*, **2018**, *57*, 8582–8586.

(cyan curve), indicative of C atoms bound to metal atoms<sup>165</sup>. This suggests molecular dehalogenation starting at 160 °C, with some resulting C radicals being stabilized by the Au atoms on the surface, consistent with prior studies of GNRs on Au(111)<sup>166</sup>. As the temperature rises to 350 °C, a gradual conversion of the C–H signal to the C–C signal occurs, indicating the formation of new C–C bonds through surface-assisted cyclodehydrogenation, ultimately yielding the GNRs. Notably, the CO component is present at 350 °C.

Finally, the inspection of the Br 3d core-level peak's thermal evolution in **Figure 32 c** revealed the typical behavior for molecular precursors leading to GNRs on Au(111). At RT, the peak consists of a single component at 70.0 eV, expected for Br atoms attached to the molecule. Upon increasing the temperature to 160 °C, a new component at 67.7 eV appears, associated with Br atoms on the Au surface. This second component becomes the sole component at 200 °C, indicating complete dehalogenation of the molecules. Further temperature increases leads to a gradual decrease in this component until its complete disappearance at 300 °C due to Br desorption, in accordance with reported desorption temperatures<sup>167</sup>.

In summary, XPS and STM analyses are in reasonable agreement, supporting the conclusion that there is a modification of the tropone moiety likely occurring between 250 °C and 310 °C, with a preference toward the upper limit of 310 °C. There are no further thermal stability studies described for the tropone group on metal surfaces. Similar decarbonylation processes have been described for fluorene-based chevron GNRs<sup>169</sup> on Au but at higher temperatures, revealing a lower thermal stability of the tropone group with respect to the fluorone group.

### Cyclodehydrogenated phase

A temperature increase of the Au(111) sample to 350 °C promoted the final cyclodehydrogenation of the obtained nanostructures. In principle, it would be expected that after performing the sequential reactions, chevron-GNRs incorporating heptagonal rings should be formed. However, the before stated analysis of STM and XPS, and the inspection of high resolution nc-AFM and BR-STM images (**Figure 33**) revealed that **3.1.1-7** was not obtained. Conversely, as seen in the nc-AFM and BR-STM images in **Figure 33 a** and **b**, two other reaction products, a cyclopentadienone **3.1.1-5** and a pristine **3.1.1-6**, prevailed as indicated in the **Scheme 10**. In the lower part of the nc-AFM image, both the cyclopentadienone unit **3.1.1-5** and the pristine unit **3.1.1-6** can be distinguished. On the other hand, at the left top part of the image it can be seen an example of an unfinished rearrangement where the cyclopropenone is pointed out with a question mark. At the right top part, a defective structure can be also seen, pointed out with a question mark in the chemistry model panel (**Figure 33 c**).

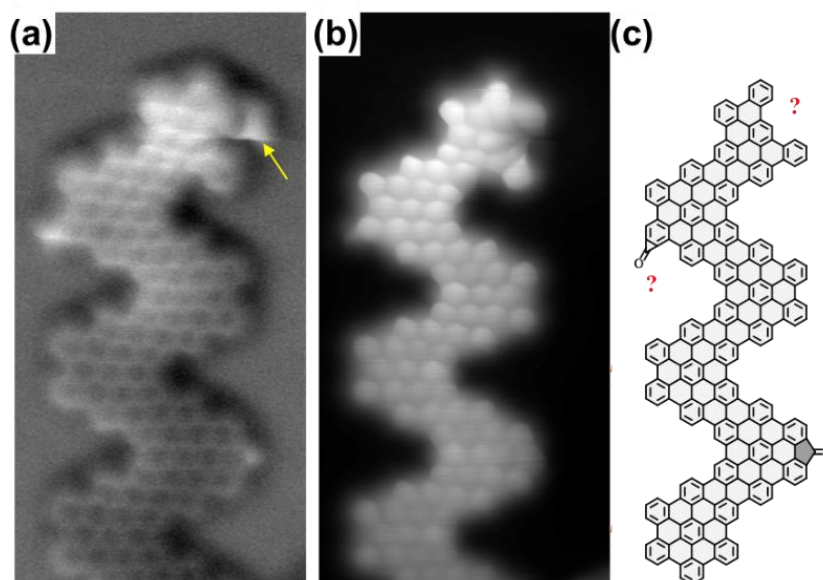
In this regard, we observed the formation of pristine chevron-GNRs **3.1.1-6** upon the detachment of a CO molecule (surface decarbonylation) with an estimated yield of ~ 70%. On

<sup>165</sup> K. A. Simonov, N. A. Vinogradov, A. S. Vinogradov, A. V. Generalov, E. M. Zagrebina, G. I. Svirskiy, A. A. Cafolla, T. Carpy, J. P. Cunniffe, T. Taketsugu, A. Lyalin, N. Märtensson, A. B. Preobrajenski, *ACS Nano*, **2015**, *9*, 8997–9011.

<sup>166</sup> M. Di Giovannantonio, O. Deniz, J. I. Urgel, R. Widmer, T. Dienel, S. Stolz, C. Sánchez-Sánchez, M. Muntwiler, T. Dumsclaff, R. Berger, A. Narita, X. Feng, K. Müllen, P. Ruffieux, R. Fasel, *ACS Nano*, **2018**, *12*, 74–81.

<sup>167</sup> C. Bronner, J. Björk, P. Tegeder, *J. Phys. Chem. C*, **2015**, *119*, 486–493.

the other hand, the formation of a cyclopentadienone unit **3.1.1-5**, in a fluorenone-GNR with an estimated yield of  $\sim 25\%$  was detected. Similar processes of intramolecular rearrangements and decarbonylation ring transformations have already been reported in the on-surface literature<sup>168, 169</sup> but not for heptagonal or higher-membered rings. Additionally, both pathways can be explained via a retro-Buchner-type reaction, that will be further explained below. The remaining 5% of the observed structures are associated with other species that cannot be clearly identified by means of nc-AFM or justified by the mechanisms proposed. We relate these structures to intramolecular CO rearrangements products or defective reaction products.



**Figure 33.** Synthesized chevron-GNRs on Au(111). **a)** Constant height frequency-shift nc-AFM image. **b)** Current image simultaneously obtained with a CO functionalized tip showing the most characteristic variations of the GNRs. **c)** A proposed chemical sketch of the GNR structure. Scanning parameters were as follows for (a) and (b): (6.5 nm 3 nm)  $V = 5$  mV.

### Rearrangement mechanism

The decarbonylation of benzannulated tropone under thermal conditions has been discussed in prior studies of chemistry in solution. Normally, these processes involve an electrocyclic ring closure and cheletropic extrusion of CO, resulting in the formation of the corresponding

<sup>168</sup> R. A. Durr, D. Haberer, Y.-L. Lee, R. Blackwell, A. M. Kalayjian, T. Marangoni, J. Ihm, S. G. Louie, F. R. Fischer, *J. Am. Chem. Soc.*, **2018**, *140*, 807–813.

<sup>169</sup> G. D. Nguyen, H.-Z. Tsai, A. A. Omrani, T. Marangoni, M. Wu, D. J. Rizzo, G. F. Rodgers, R. R. Cloke, R. A. Durr, Y. Sakai, F. Liou, A. S. Aikawa, J. R. Chelikowsky, S. G. Louie, F. R. Fischer, M. F. Crommie, *Nature Nanotech.*, **2017**, *12*, 1077–1082.

aromatic derivatives during pyrolysis<sup>170</sup>. A comparable sequence of reactions is proposed in the current scenario, as illustrated in **Scheme 11**.

In analogy with the well-known equilibrium between cycloheptatriene and norcaradiene<sup>171</sup>, the cycloheptatrienone moiety **I** would be in equilibrium with the norcaradienone intermediate **II** through electrocyclic ring closure. Following this, **II** can decompose via diradical **IV** or directly through a cheletropic extrusion of CO (transition from **II** to **III**), leading, in both instances, to the formation of a phenanthrene moiety **III** (resulting in **3.1.1-6**)<sup>170,172</sup>. Various mechanisms could elucidate the generation of norcaradienone **V**, either through intramolecular rearrangement via diradical **IV** or through a series of [1,5] sigmatropic shifts of the cyclopropanone subunit<sup>170,173</sup>. The ring opening/closure from norcaradienone **V** and subsequent dehydrogenation would give rise to the fluorenone unit in **VI** (similar to the case of **3.1.1-5**). It is noteworthy in this context that the pyrolysis of tropones described without surface interaction involves higher temperatures than those attained in our OSS case<sup>170</sup>. Hence, the role of the gold surface and the presence of Au adatoms in the reaction pathway should also be considered as in the retro-Buchner reaction mediated by Au(I) reported by Echavarren et al.<sup>174,175</sup>. In this scenario, cycloheptatrienes, in equilibrium with norcaradienes, may react with cationic Au(I) complexes to produce Au(I) carbenes and an aromatic system, aligning with the phenanthrene unit in the pristine GNR generated in our case. It's worth noting that the adatoms on the surface at elevated temperatures could function similarly to these complexes, given the demonstrated active role they play in catalyzing reactions<sup>176,177</sup>. Therefore, our findings can be explained by a retro-Buchner reaction involving a decarbonylation process forming a gold carbonyl. Thus, these results would represent the first example of an on-surface retro-Buchner-type reaction.

<sup>170</sup> G. Holzmann, G. Frenking, B. Steiner, *J. Chem. Soc., Perkin Trans.*, **1984**, 2, 1943.

<sup>171</sup> O. A. McNamara, A. R. Maguire, *Tetrahedron*, **2011**, 67, 9–40.

<sup>172</sup> R. West, K. Kusuda, V. N. M. Rao, *J. Am. Chem. Soc.*, **1971**, 93, 3627–3632.

<sup>173</sup> M. Kato, M. Mitsuda, T. Shibuya, K. Furuichi, *Bull. Chem. Soc. Jpn.*, **1991**, 64, 2081–2087.

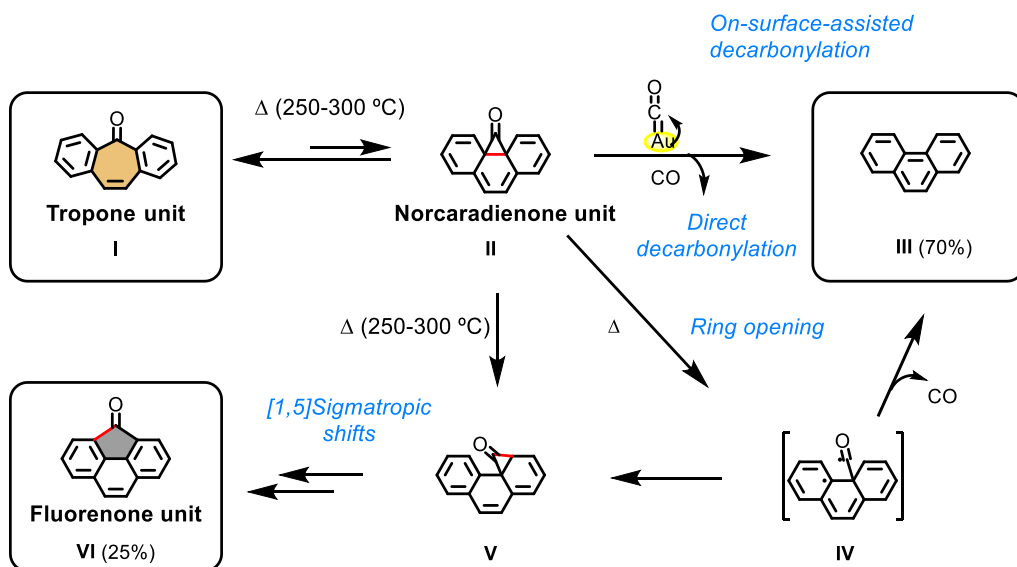
<sup>174</sup> M. Mato, B. Herlé, A. M. Echavarren, *Org. Lett.*, **2018**, 20, 4341–4345.

<sup>175</sup> M. Mato, C. García-Morales, A. M. Echavarren, *ChemCatChem*, **2019**, 11, 53–72.

<sup>176</sup> Q. Li, B. Yang, J. Björk, Q. Zhong, H. Ju, J. Zhang, N. Cao, Z. Shi, H. Zhang, D. Ebeling, A. Schirmeisen, J. Zhu, L. Chi, *J. Am. Chem. Soc.*, **2018**, 140, 6076–6082.

<sup>177</sup> Z. Zhang, D. F. Perepichka, R. Z. Khaliullin, *J. Phys. Chem. Lett.*, **2021**, 12, 11061–11069.





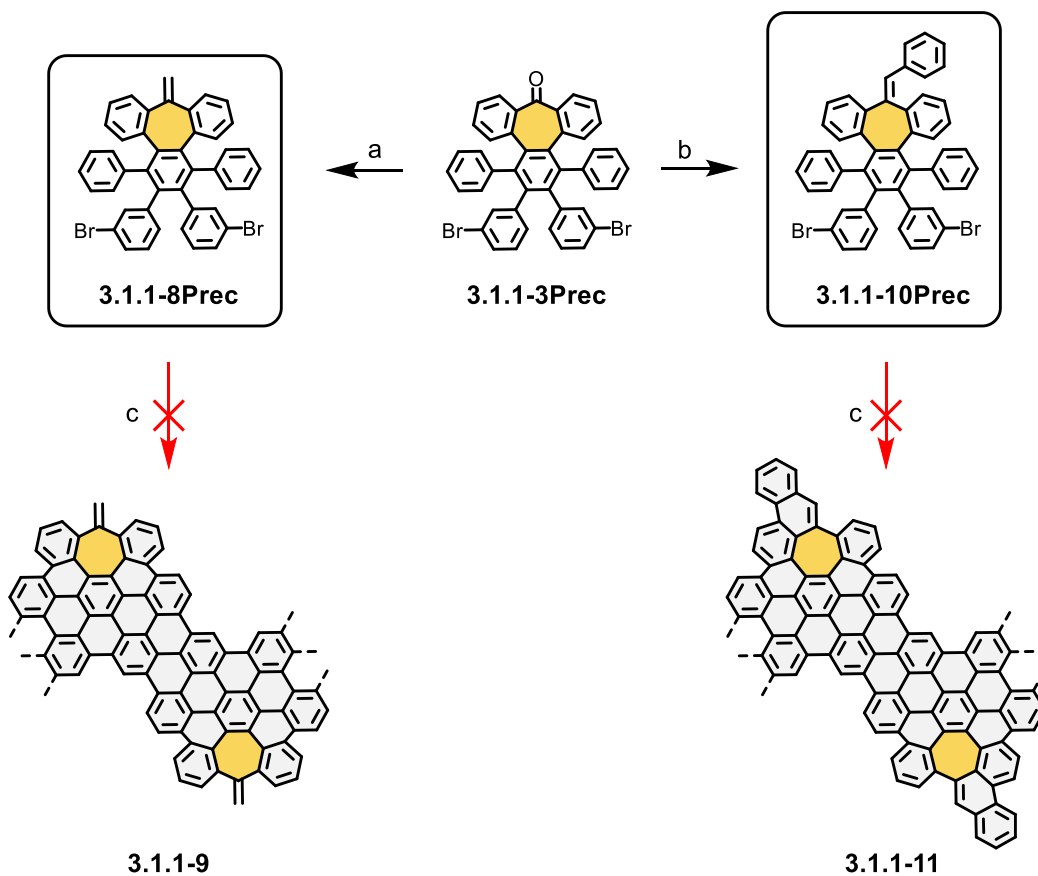
**Scheme 11.** A schematic representation of the proposed reaction pathways explaining the conversion of the troponone unit **I** (cycloheptatrienone, in purple) into a cyclopentadienone unit **VI** (yellow) or phenyl **III** (grey) units, including intermediate states.

### Troponone derivatized precursors<sup>178</sup>

In view of the last results in the growth of GNRs with the troponone moiety, two derivatizations were envisioned to yield an out-of-plane GNR. The aim was to preserve the general architecture of the monomer while derivatizing the troponone moiety to prevent the proposed on-surface retro–Buchner-type reaction. **Scheme 12** shows the new structures either functionalized with a methylene moiety, **3.1.1-8Prec**, or with a benzyl moiety **3.1.1-10Prec**; raising in both cases a fully  $sp^2$  conjugated final structure.

**3.1.1-8Prec** was yielded after Tebbe olefination in **3.1.1-3Prec**, 67% yield. On the other hand, **3.1.1-10Prec** was synthesized after performing two reactions from **3.1.1-3Prec**. First, an addition to the ketone moiety of the cycloheptatrienone ring with benzylmagnesium bromine, and second, an elimination reaction of the alcohol group in presence of thionyl chloride and pyridine to yield alkene **3.1.1-10Prec**, 64 % regarding both reactions. **3.1.1-8Prec** and **3.1.1-10Prec** were in-solution characterized by means of  $^1\text{H}$  NMR,  $^{13}\text{C}$  NMR and mass spectrometry.

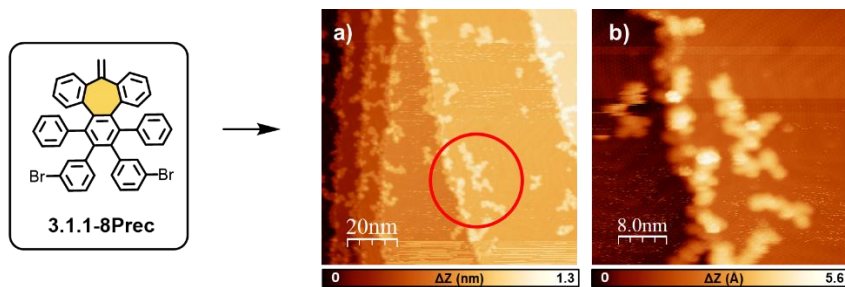
<sup>178</sup> This work is a collaboration between MOREFUN group from the University of Granada, where the precursors were synthesized; ESISNA group from CSIC of Madrid, where the growth of the nanostructures was studied and Nanosurf Lab from the Institute of Physics of the Czech Republic, where for **3.1.1-10Prec** high- resolution images with STM and nc-AFM were obtained.



**Scheme 12.** Schematic representation of the synthesis of monomers **3.1.1-8Prec** and **3.1.1-10Prec**, and the different reaction pathways toward the formation of derivatized cycloheptatriene GNRs. **a)** Tebbe reagent, THF, 0 °C, RT 67 %, **b)** 1) Benzylmagnesium bromide, THF, RT, 16 h, 2) Cl<sub>2</sub>SO, Py, RT, 2.5 h, 64% (both steps) **c)** Sequential annealing on a Au(111) surface, first 200 °C, then 350 °C for **3.1.1-8Prec**, 400 °C for **3.1.1-10Prec**.

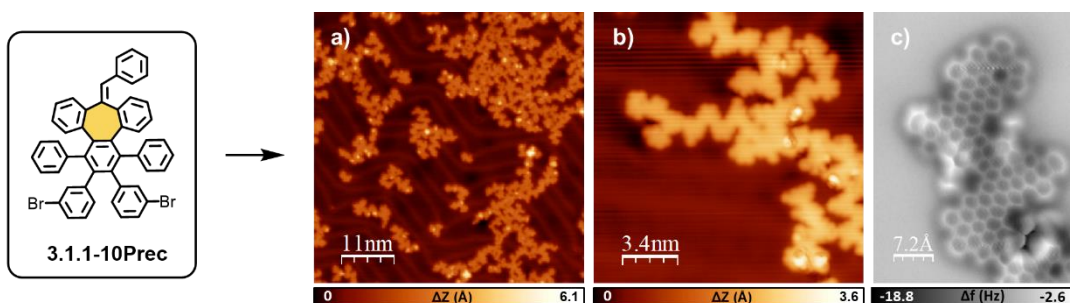
A common protocol for growing GNRs was employed with **3.1.1-8Prec**. First, the precursor was sublimated from a quartz crucible (at 230 °C) onto a Au(111) substrate held at 200 °C to induce the Ullmann coupling between monomers. Subsequently, the surface was further annealed until 350 °C to perform the final cyclodehydrogenation reaction.

**Figure 34 a** shows a topographic STM image after the last annealing step where irregular dendritic nanostructures were observed. In this regard, **Figure 34 b** reveals how the GNRs do not follow the axis of enlargement designed for the precursor. To rationalize these results, we assume an activation of the methylene-heptagonal moiety before or during the Ullmann coupling reaction. These activated heptagonal rings may couple with the created radicals during Ullmann reaction leading to irregular structures. Unluckily, we do not have further results of the phases at lower temperatures to prove this hypothesis (on-surface synthesis experiments are time-consuming and we decided not to expend more time in understanding this reaction). Due to the inhomogeneity of the dendrimers the proposal of a reaction mechanism for the rearrangements was also difficult.



**Figure 34.** On-surface synthesis of graphene dendritic nanostructures after sequentially annealing a Au(111) sample with **3.1.1-8Prec** first to 200 °C and second to 350 °C. **a)** Topographic constant-current STM image showing dendritic structure. **b)** Detail constant-current STM image. Scanning parameters were as follows: (a) 10 pA, -1.2 V; (b) 10 pA, -1.2 V.

Similar conclusions can be extracted in the experiment with **3.1.1-10Prec**. After following a similar protocol for the growth of GNRs (the molecules were evaporated from the crucible at 240 °C, and the Au(111) sample was annealed until 400 °C), the analysis of the topographic STM images in **Figure 35 b** and **c**, also revealed the formation of dendritic structures. Inspection of the nc-AFM images in **Figure 35 c** showed heterogeneous rearrangements of the 7-membered ring. The preservation of the heptagonal ring was scarce, and it was always surrounded by other defects (non-benzenoid rings) that lead the system to planarity. We did not study the phases at lower temperatures, and we did not propose a reaction mechanism for the rearrangements due to similar motifs as stated in **3.1.1-8Prec**.



**Figure 35.** On-surface synthesis of graphene dendritic nanostructures after sequentially annealing a Au(111) sample with **3.1.1-10Prec** first to 475 K and second to 675 K. **a)** Topographic constant-current STM image showing dendritic structure. **b)** Detail constant-current STM image. **c)** nc-AFM image with CO tip of a segment of graphene nanostructure. Scanning parameters were as follows: (a) 10 pA, -0.31 V; (b) 10 pA, -0.1 V, (c) 10 mV.

$^1\text{H}$  NMR spectroscopy was carried out before and after the UHV sublimation for both precursors showing identical spectra. Although it cannot be discarded that only the “broken molecules” from the crucible were sublimated it seems an improbable scenario. Therefore, we can “safely” discard the decomposition of the precursor before reaching the surface.

#### Summary

Using STM, nc-AFM, and XPS, we have demonstrated the unprecedented transformation of a cycloheptatrienone moiety embedded in a GNR into either a phenyl group or a cyclopentadienone unit during the cyclodehydrogenation step on Au(111) (the transformation takes place in the range of 250 °C to 310 °C). We propose that this rearrangement occurs through the detachment or rearrangement of the CO unit following a Retro-Buchner mechanism.

Two derivatives from the last monomer, methylene-cycloheptatriene-containing precursor **3.1.1-8Prec** and benzylic-cycloheptatriene-containing precursor **3.1.1-10Prec**, were tested for growing distorted GNRs on Au(111) substrate. With the use of STM and nc-AFM, dendritic structures were observed as the outcome of the reaction in both cases. Preactivation of the heptagonal moieties before or during polymerization step is suggested in view of the obtained results.

### 3.1.2 A Non-Benzenoid Graphene Nanoribbon from a Precursor Containing an Eight-Membered Ring

#### *Introduction*

This subsection delves into the results related with the synthesis of curved chevron-like GNRs using a new design of molecular monomer. In this regard, we expected that the modification from a seven-membered ring to an eight-membered ring would yield better results in the synthesis of these curved nanostructures.

The discussion in this subsection centers on the outcomes achieved using the monomer **3.1.2-Mono** (depicted in **Scheme 13**) that features an eight-membered ring cyclooctatetraene (COT). The analysis of the STM images after the thermal reactions to yield the curved GNR only showed planar products as result of the synthesis with an interesting non-benzenoid GNR as the major product of the reaction. Here, we present a detailed analysis of the reaction mechanism conducted by experimental STM images and computational calculations, which relates the configuration of the initial precursor (convex or concave) with the final outcomes of the reaction. Additionally, the electronic properties of the predominant product (the non-benzenoid GNR) are examined through STS spectroscopy and dI/dV mapping revealing interesting features.

#### *In-Solution synthesis and on-surface characterization of the r.t phase*<sup>179</sup>

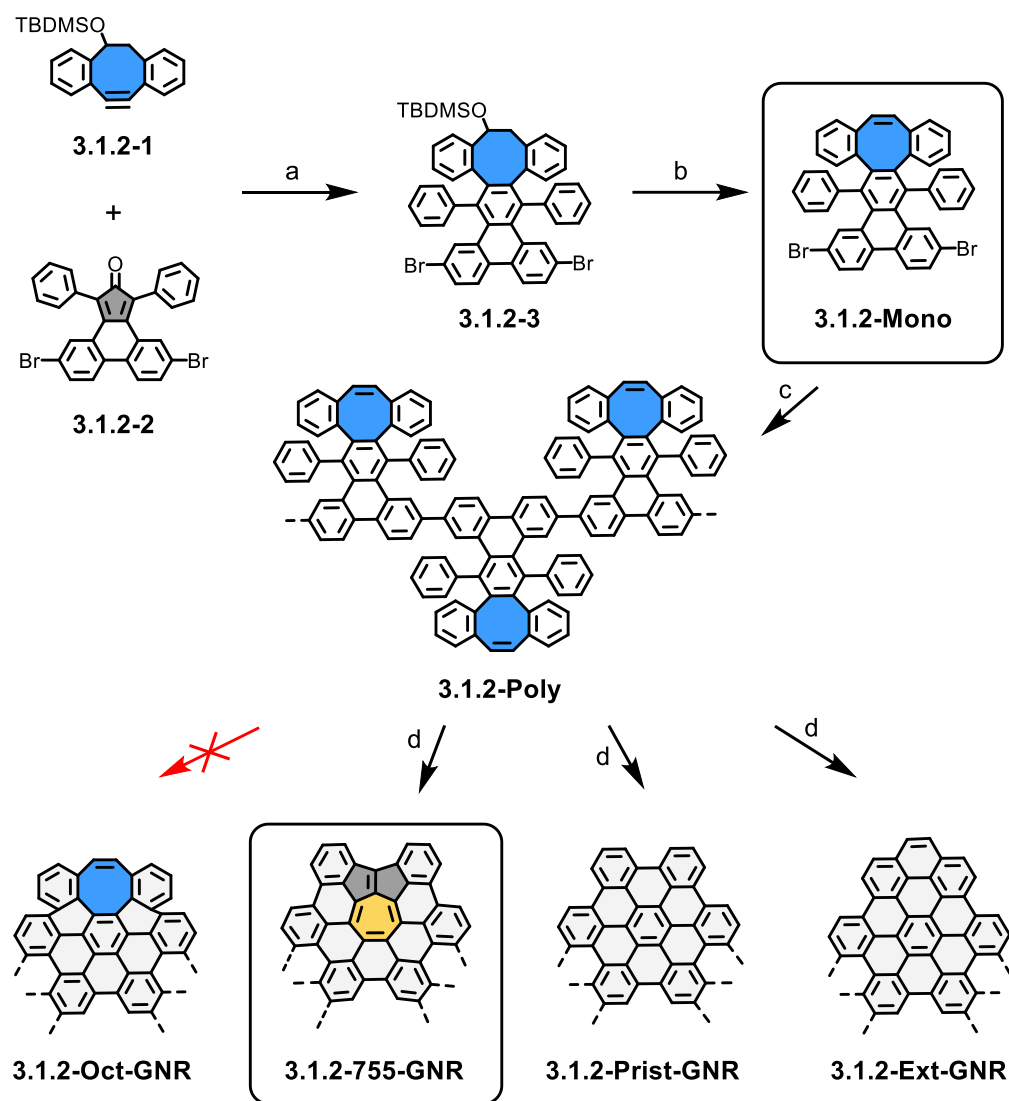
**3.1.2-Mono** was designed to incorporate Br atoms at the positions "meta", aiming to produce ribbons with chevron topology; and a COT moiety to induce the saddle distortion in the GNR, pushing it out of the plane. The in-solution synthesis of **3.1.2-Mono** followed an established strategy by our research group<sup>180</sup> based in a Diels-Alder reaction between a cyclooctyne **3.1.2-1** and cyclopentadienone **3.1.2-2**, yielding the precursor **3.1.2-Mono**.

Intermediate **3.1.2-3** was isolated as a mixture of diastereoisomers (91 % yield) in two pairs of enantiomers with a ~ 3:1 ratio. In this regard, the stereochemistry of **3.1.2-3** arises from the combination of the quaternary center at the top of the structure and the curvature of the octagonal ring. This curvature leads to two non-interconvertible convex-concave configurations, that will be explained below in the on-surface characterization. Subsequently, the alcohol group was deprotected with TBAF (93% yield), and a final elimination reaction with Burgess Reagent was conducted, resulting in product **3.1.2-Mono** (47% yield).

---

<sup>179</sup> This work is a collaboration between MOREFUN group from the University of Granada, where the monomer was synthesized; ESISNA group from CSIC of Madrid, where the growth of the nanostructures was experimentally studied and where computational calculations were done; and The Advanced Microscopy Laboratory from the University of Zaragoza, where high-resolution images and STS spectroscopies were taken.

<sup>180</sup> M. A. Medel, R. Tapia, V. Blanco, D. Miguel, S. P. Morcillo, A. G. Campaña, *Angew. Chem. Int. Ed.*, **2021**, *60*, 6094–6100.



**Scheme 13.** Schematic representation of the synthesis of COT-containing precursor, and the different products obtained in the synthesis of GNRs, the 42 % remaining yield are defective or very irregular products. **a)**  $\text{Ph}_2\text{O}$ , reflux, 2 h, 91 %; **b)** (I) TBAF, THF, rt, 1 h, 93 %; (II) Burgess Reagent, Toluene, 110 °C, 2 h, 47%; **c)** Annealing at 475 K on a Au(111) surface. **d)** Annealing at 625 K on a Au(111) surface.

**Figure 36 a** and **b** shows the result of the RT deposition of **3.1.2-Mono** onto a Au(111) surface, which yields the formation of three different molecular self-assemblies: elongated irregular chains with a bright backbone (see red circle), square-shaped linear aggregates (white circle) and rhomboidal-shaped clusters that arrange into chains or trimers (blue and green circles, respectively). Before entering into the analysis of the images, it is important to note that, although only one compound was detected under in-solution characterization of **3.1.2-Mono**, two different diastereomeric configurations, **3.1.2-Mono-Cc** (Cc refers to concave diastereomer, **Figure 36 c**) and **3.1.2-Mono-Cx** (Cx refers to concave diastereomer, **Figure 36**

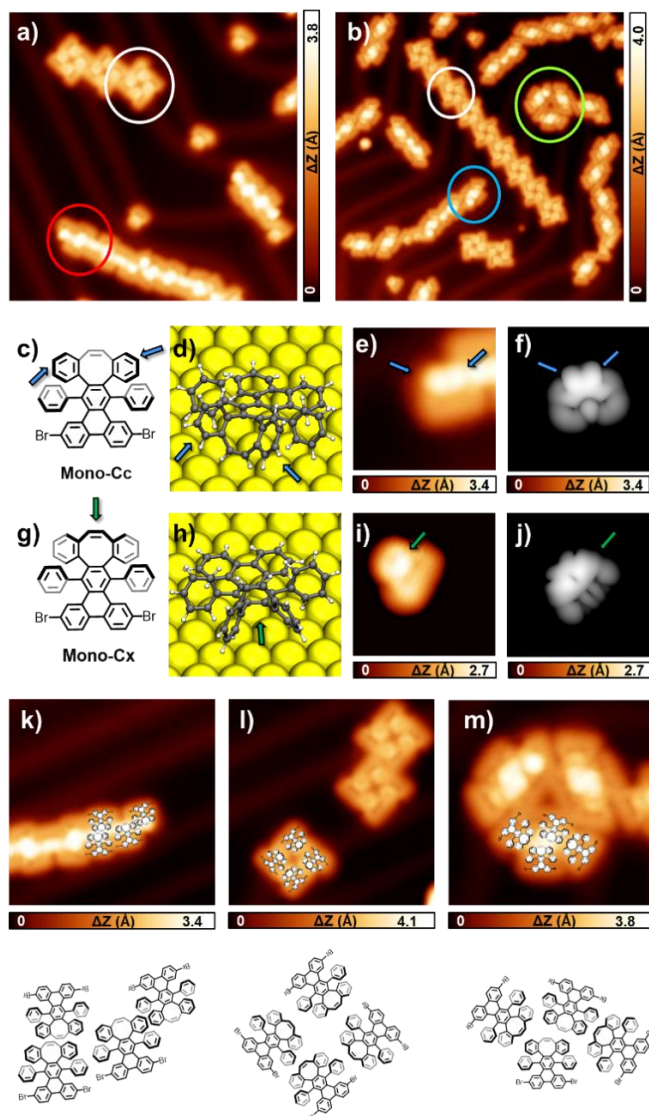
**g**), can be observed on the substrate due to a symmetry breakage induced by the surface relative to the curvature of the COT (see **Figure 36 d** and **Figure 36 h** for the **3.1.2-Mono-Cc** and **3.1.2-Mono-Cx** 3D DFT optimized configurations, respectively). The origin of such out-of-plane configurations can be explained in terms of aromaticity. In a planar conformation and following Hückel's rule<sup>181</sup>, the COT molecule has eight  $\pi$  electrons and is an antiaromatic molecule. To avoid this unfavorable scenario, it loses planarity adopting a boat conformation<sup>182</sup>, becoming a non-aromatic compound. This behavior is also observed in the COT-containing precursor **3.1.2-Mono**, whose COT ring escapes from planarity to avoid antiaromaticity and gives rise to the concave/convex configurations.

Interestingly, our high-resolution STM images allow us to unambiguously discern between both diastereomers, as the **3.1.2-Mono-Cc** is characterized by the presence of a double bright maximum at the narrower side (blue arrows in **Figure 36 e**), while **3.1.2-Mono-Cx** exhibits a single bright feature at the center (green arrow in **Figure 36 i**), as clearly corroborated by the STM simulations in **Figure 36 f** and **j**. Considering these aspects, we assign the elongated irregular chains to an alternating self-assembly of **3.1.2-Mono-Cc** stabilized by the  $\pi$ - $\pi$  stacking between neighboring dibenzo[a,e]cyclooctene moieties (**Figure 36 k**). On the other hand, square shape aggregates correspond to the self-assembly of four **3.1.2-Mono-Cx** molecules rotated by approximately  $90^\circ$  between each other in a chiral configuration (**Figure 36 l**). Finally, the triangular shape clusters are ascribed to the agglomeration of three tetramers each of them composed of two **3.1.2-Mono-Cc** and two **3.1.2-Mono-Cx** arranged in an alternating fashion, as depicted in **Figure 36 m**.

---

<sup>181</sup> E. Hückel, *Zeitschrift für Physik*, **1931**, 70, 204–286.

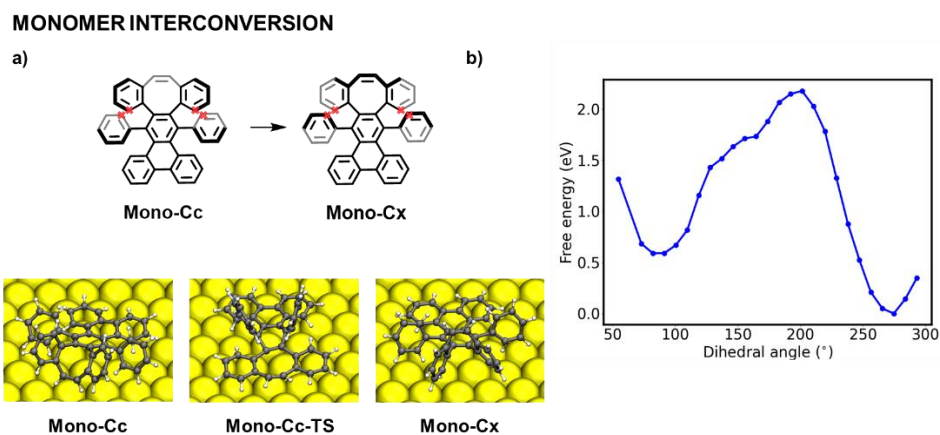
<sup>182</sup> H. S. Kaufman, I. Fankuchen, H. Mark, *Nature*, **1948**, 31, 165.



**Figure 36.** Characterization of the r.t. phase of **3.1.2-Mono** on Au(111). **a)** Topographic constant current STM image with 0.2 ML coverage. **b)** Topographic constant current STM image with 0.4 ML coverage. Red circle refers to **k)**, white circles refer to **l)**, green circle refers to **m)**. **c)** Chemical model of **3.1.2-Mono-Cc**, blue arrows depict the brightest features in **e)**. Bold lines represent out of plane bonds. **d)** Minimized DFT chemistry model of **3.1.2-Mono-Cc** on a Au(111) surface, blue arrows depict the brightest features in **e)**. **e)** Constant current STM image of **3.1.2-Mono-Cc**. **f)** Simulated constant current STM image of **3.1.2-Mono-Cc**. **g)** Chemical model of **3.1.2-Mono-Cx**, green arrow depicts the brightest feature in **i)**. Bold lines represent out of plane bonds. **h)** Minimized DFT chemistry model of **3.1.2-Mono-Cx** on a Au(111) surface, green arrow depicts the brightest features in **i)**. **i)** Constant current STM image of **3.1.2-Mono-Cx**. **j)** Simulated constant current STM image of **3.1.2-Mono-Cx**. **k)**, **l)**, **m)**, Constant-current detail STM images showing different diastereoselectivities of the self-assembly patterns with their respective chemical model below. **c)** and **d)** shows homodiastereoselectivity (concave and convex respectively) while **e)** shows a pattern based on the mixture of both diastereoisomers. Scanning parameters were as follows: **(a)** 21 nm × 21 nm, 50 pA, -1 V; **(b)** 30 nm × 30 nm, 50 pA, -1 V, **(e)** 3.5 nm × 3.5 nm, 50 pA, -0.05 V; **(i)** 3.5 nm × 3.5 nm, 10 pA, -0.01 V, **(k)** 10 nm × 10 nm, 50 pA, -0.94 V; **(l)** 10 nm × 10 nm, 50 pA, -0.94 V, **(m)** 7 nm × 7 nm, 50 pA, -1 V.



It is important to note that, according to our quantum and molecular mechanical (QM/MM) simulations<sup>183</sup>, convex and concave configurations in the monomeric phase do not interconvert between each other as the energy barrier for this process is relatively high (1.59 eV, see **Figure 37**). The steric repulsion between neighboring hydrogen atoms from the benzene rings attached to the central ring and those from the benzene rings attached to the COT moiety hinders the interconversion (see red crosses in **Figure 37 a**).

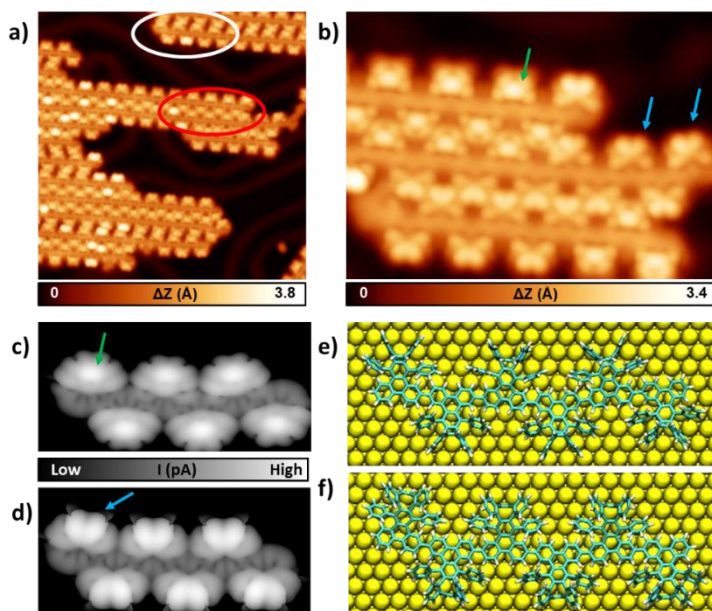


**Figure 37.** QM/MM simulations of the precursor interconversion from **3.1.2-Mono-Cc** to **3.1.2-Mono-Cx**. a) Chemical models (top) extracted from QM/MM simulations (bottom). b) Potential diagram of the process.

### Polymeric phase

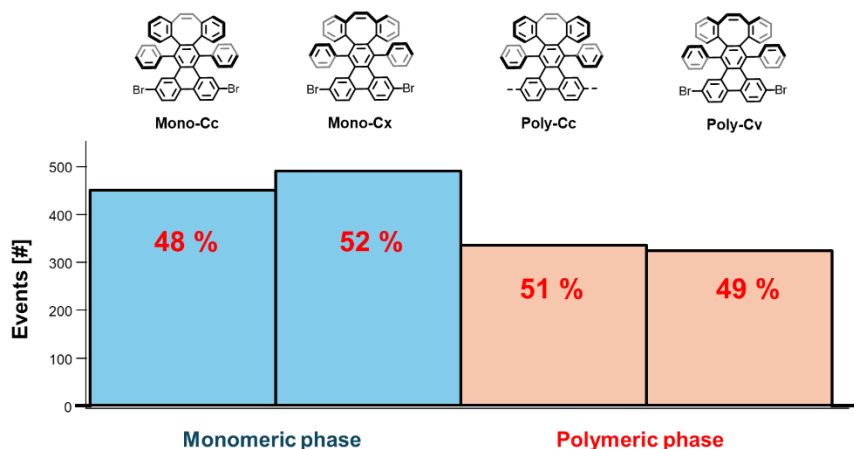
**Figure 38 a** shows an overview STM image of the Au(111) surface upon annealing at 475 K, where the formation of islands composed of molecular chains can be observed. Interestingly, we found two distinct types of interpolymeric interdigitation, illustrated by red and white circles. In this regard, the denser phase (red circle) has been previously documented in other chevron-like GNRs<sup>161</sup>, whereas the less densely packed phase (white circle) represents a novel observation for this type of GNR. A detailed analysis of diverse high-resolution STM images like the one presented in **Figure 38 b** sheds light on different interesting aspects. Firstly, the periodicity along the chains corresponds to 1.67 nm, in excellent agreement with the theoretical value (1.76 nm), and with the values reported for other chevron-like GNRs<sup>161</sup>. Secondly, the internal appearance observed in the monomeric phase at RT is preserved in the polymeric phase, thus allowing us to univocally assign them to the corresponding concave/convex configuration (see **Figure 38 c to f**).

<sup>183</sup> J. I. Mendieta-Moreno, R. C. Walker, J. P. Lewis, P. Gómez Puertas, J. Mendieta, J. Ortega, *J. Chem. Theory Comput.*, **2014**, *10*, 2185–2193.



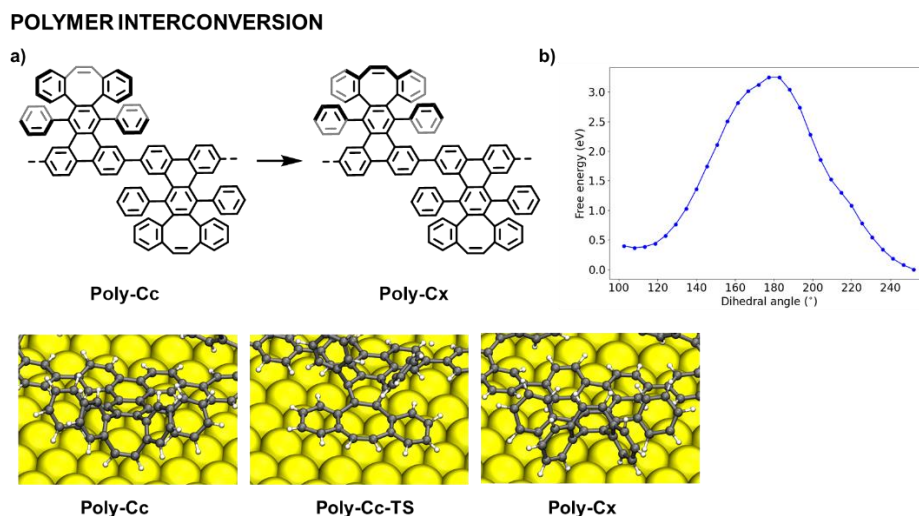
**Figure 38.** Polymer phase, 3.1.2-Poly, after Ullmann coupling at 200 °C on Au(111). **a)** Topographic constant current STM image showing different kinds of interdigitation between polymers. White circle shows long-like interdigitation, red circle depicts close-like interdigitation. **b)** Constant current detail STM image showing how curvature is preserved in monomers in a close-like interdigitation. Green arrow depicts convex monomers. Blue arrow depicts concave monomers. **c)** and **d)** Constant height STM image simulation of concave and convex polymer respectively. **e)** DFT minimized structure of convex polymer (top) on Au(111). **f)** DFT minimized structure of concave polymer on Au(111). Scanning parameters were as follows: (a) 25 nm × 25 nm, 0.1 nA, - 0.5 V, (b) 10 nm × 7.2 nm, 0.16 nA, - 0.05 V.

A statistical analysis on the number of concave/convex monomers in the polymeric phase corroborates that the interconversion barrier is high enough to avoid a configuration change even at 475 K, with approximately 50 % of the monomers in each configuration (**Figure 39**).



**Figure 39.** Statistical analysis of the abundance of each configuration at the monomeric phase and at the polymeric phase.

In fact, the interconversion barrier at the polymeric phase is even larger (2.81 vs 1.59 eV) than during the monomeric phase (**Figure 40**). The presence of both diastereoisomers along the polymer with low selectivity and their relative abundance will play a critical role in the atomic structure of the final GNRs, as it will be shown below.



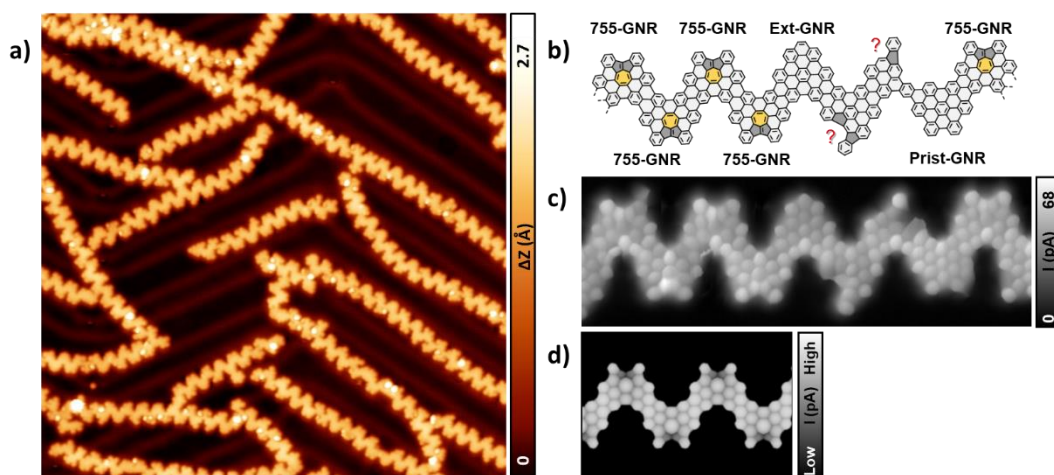
**Figure 40.** QM/MM simulations of the polymer interconversion from 3.1.2-Poly-Cc to 3.1.2-Poly-Cx. a) Chemical models (top) extracted from QM/MM simulations (bottom). b) Potential diagram of the process.

### Cyclodehydrogenated phase

To complete the formation of the GNRs through a surface-assisted cyclodehydrogenation (CDH) reaction, the system has been annealed to 675 K. **Figure 41 a** shows the resulting GNRs,

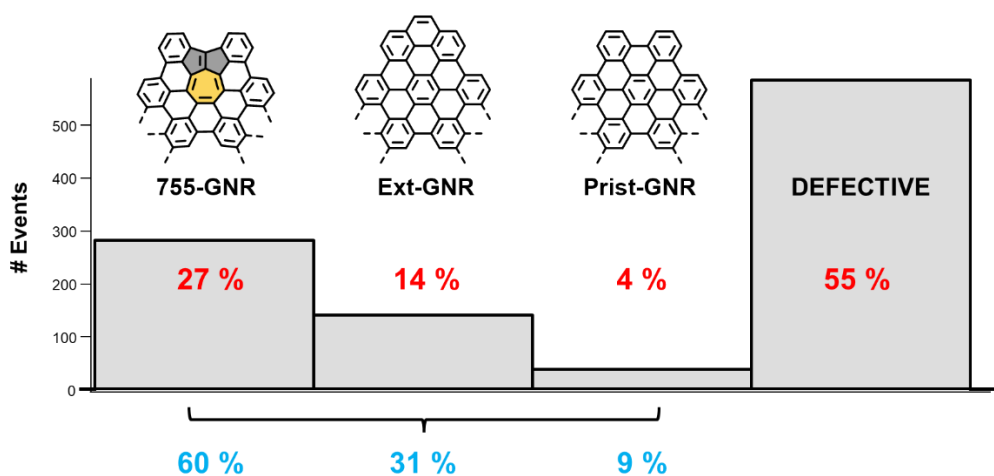
whose irregular appearance can be easily distinguished. This irregularity indicates a lack of selectivity in the final shape of the GNR and, consequently, the occurrence of intramolecular transformations. To determine the atomic structure of the final GNRs, bond-resolved STM (BR-STM) imaging with CO tips has been carried out. **Figure 41 b** and **c** present a GNR segment where the main precursor compositions can be easily identified. Apart from the defective products arising from the partial decomposition of the precursors during the CDH reaction (see red question marks in **Figure 41 b**), up to three well-defined products are obtained: a cyclopenta[c,d]azulene (755) moiety (**3.1.2-755-GNR**), isomer of **3.1.2-Oct-GNR**; a fully-hexagonal extended pristine chevron (**3.1.2-Ext-GNR**), isomer of **3.1.2-Oct-GNR** and **3.1.2-755-GNR**; and the pristine chevron (**3.1.2-Prist-GNR**), which implies the loss of two carbon atoms (see **Scheme 13**). Interestingly, the first main conclusion is that there is no evidence for the formation of **3.1.2-Oct-GNR**, i.e. the COT moiety does not survive to the CDH process, but it transforms into different products. This result is equivalent to the one observed in the last subsection for tropone moieties and suggests the low stability of high-membered rings at temperatures above 475 K on low interacting Au(111) surfaces and, most probably, on any other metallic surface. This instability can be understood if we consider the elevated energy cost and accumulated stress associated with having the distorted configuration of the fully cyclodehydrogenated COT moiety, preferring, therefore, to reconstruct itself into a planar configuration, with the corresponding energy gain of - 4.61 eV (as will be seen below).

**Figure 41 d** shows the simulated BR-STM image of a four-segment GNR with four consecutive cyclopenta[c,d]azulene (755) containing monomers for the direct comparison with the left part of the experimental GNR in **Figure 41 c**. It must be noted that this was the largest **3.1.2-755-GNR** segment that could be found, in agreement with its rather low yield (27 %).



**Figure 41.** Synthesized chevron-GNRs after annealing a Au(111) sample to 625 K. **a)** Topographic constant current STM image of GNRs. **b)** Chemistry model of the GNR segment in **c)**. **c)** Constant-height Bond-Resolved STM image. **d)** Constant-height STM simulation of **3.1.2-755** GNR. Scanning parameters were as follows: (a) 50 nm × 50 nm, 20 pA, - 0.03 V; (c) 8 nm × 2.6 nm, 5.2 mV.

Regarding the obtained products, our statistical analysis over  $\sim 1000$  monomers indicates that the majority case, discarding the defective products, is **3.1.2-755-GNR** (see **Figure 42**), which constitutes a completely novel motif in GNRs in particular, and a very rare one in graphene-based nanostructures in general, as seven-membered rings in graphenic structures typically appear together with a single pentagonal ring forming an azulene moiety<sup>184</sup>. Furthermore, to the best of our knowledge, this is the first report of this specific 755 configuration embedded in an extended structure on surfaces.



**Figure 42.** Distribution of the outcome of the reaction after annealing the Au sample until 320 °C. Numbers in red consider all the structures that form part of GNRs, numbers in blue only take into account non-defective species.

### Rearrangement mechanism

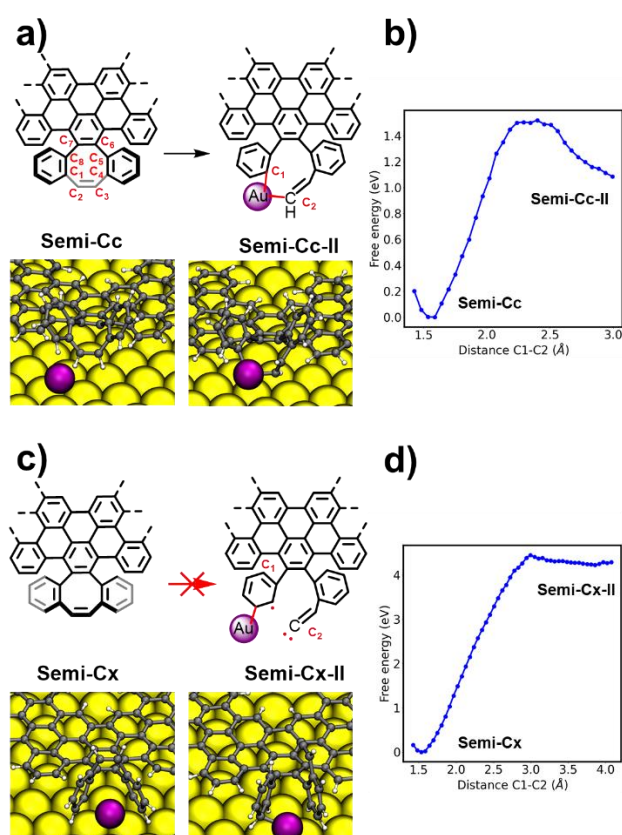
To gain insights of the rearrangement process, computational calculations were conducted to determine the reaction pathway from **3.1.2-Poly** to **3.1.2-755-GNR**, i.e. from the polymeric phase to the **3.1.2-755 GNR**. For this purpose, QM/ MM simulations<sup>185</sup> were employed to compute the free energy of the activation barriers for selected reaction steps. It is worthy to note that all our calculations have been carried out including a surface adatom as it has recurrently resulted in lower activation barriers (see **Figure A 1** in the annexes). Such an

<sup>184</sup> a) Q. Fan, D. Martin-Jimenez, D. Ebeling, C. K. Krug, L. Brechmann, C. Kohlmeyer, G. Hilt, W. Hieringer, A. Schirmeisen, J. M. Gottfried, *J. Am. Chem. Soc.*, **2019**, *141*, 17713–17720. b) T. G. Lohr, J. I. Urgel, K. Eimre, J. Liu, M. Di Giovannantonio, S. Mishra, R. Berger, P. Ruffieux, C. A. Pignedoli, R. Fasel, X. Feng, *J. Am. Chem. Soc.*, **2020**, *142*, 13565–13572.

<sup>185</sup> a) M. Telychko, J. Su, A. Gallardo, Y. Gu, J. I. Mendieta Moreno, D. Qi, A. Tadich, S. Song, P. Lyu, Z. Qiu, H. Fang, M. J. Koh, J. Wu, P. Jelinek, J. Lu, *Angew. Chem. Int. Ed.*, **2019**, *58*, 18591–18597. b) X. Liu, A. Matej, T. Kratky, J. I. Mendieta-Moreno, S. Günther, P. Mutombo, S. Decurtins, U. Aschauer, J. Repp, P. Jelinek, S. Liu, L. L. Patera, *Angew. Chem. Int. Ed.*, **2022**, *61*, e202112798.



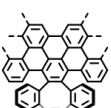
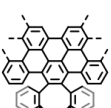
assumption is now well established in the field, with several results highlighting their critical role in surface-assisted reactions<sup>186</sup>. [refs].

**Figure 43 a** and **c** display the schematic representations of the partially cyclodehydrogenated **3.1.2-Semi-Cx** and **3.1.2-Semi-Cc** structures that have been used as the starting point for our computational study. The choice of these structures has a two-fold motivation: i) the experimental observation of the COT-755 rearrangement after the Ullmann coupling, i.e. during the cyclodehydrogenation step; and ii) the unfeasible rearrangement barriers obtained when starting directly from the polymeric phase **3.1.2-Poly**, without any prior partial CDH (see **Figure 44**, and annexes **Figure A 2**, **Figure A 3**). The scheme in panel **a** includes, for the sake of clarity, the labelling of the eight carbon atoms of the COT unit that will be involved in the reaction pathway.



**Figure 43.** Calculated first step (C1-C2 bond breakage) of the rearrangement for **3.1.2-Semi-Cc** and **3.1.2-Semi-Cx**. **a)** Chemical sketch (top) and 3D models extracted from QM/MM simulations (bottom) regarding the first step of the rearrangement for **3.1.2-Semi-Cc**. **b)** Potential energy diagram corresponding to **a)**. **c)** Chemical sketch (top) and 3D models extracted from QM/MM simulations (bottom) regarding the first step of the rearrangement for **3.1.2-Semi-Cx**. **d)** Potential energy diagram corresponding to **c)**.

<sup>186</sup> J. Björk, C. Sánchez-Sánchez, Q. Chen, C. A. Pignedoli, J. Rosen, P. Ruffieux, X. Feng, A. Narita, K. Müllen, R. Fasel, *Angew. Chem. Int. Ed.*, **2022**, *61*, e202212354.

	<b>C1-C2</b> (Adatom)	<b>C2-C3</b> (Adatom)	<b>C7-C8</b> (Adatom)	<b>C1-C2</b> (No Adatom)
 Poly-Cc	<b>2.14 eV</b>	<b>2.37 eV</b>	<b>3.97 eV</b>	-
 Poly-Cx	<b>6.00 eV</b>	<b>5.11 eV</b>	<b>2.46 eV</b>	-
 Semi-Cc	<b>1.52 eV</b>	<b>2.45 eV</b>	<b>4.75 eV</b>	<b>4.51 eV</b>
 Semi-Cx	<b>4.39 eV</b>	-	<b>2.47 eV</b>	-

**Figure 44.** Summary of the activation energies for the first step of the rearrangement regarding different initial products and conditions.

Attending to our experimental findings on the decomposition of the octagonal ring, the first step must be the rupture of such ring. In principle, this could proceed through the opening of any of the eight bonds in the COT unit. However, our theoretical results indicate that the energy barriers are not equal for all the bonds and, more interestingly, are highly dependent on the diastereomeric configuration (i.e. concavity vs convexity). Even more, as it will be shown below, only the concave configuration can yield the formation of **3.1.2-755-GNR**, thus being a specific reaction pathway.

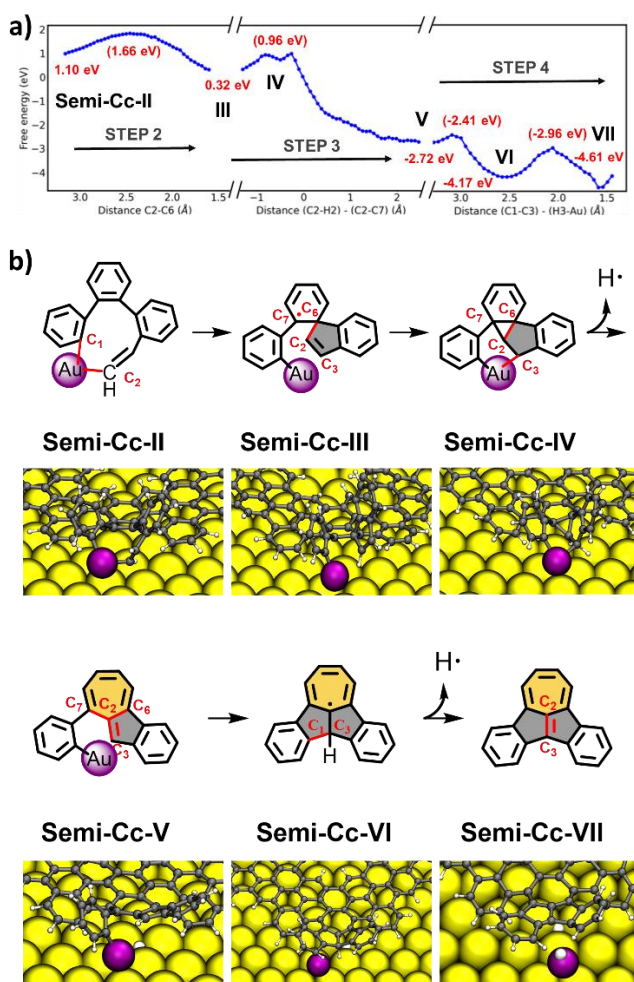
Among the eight bonds and the two diastereomeric configurations available, the rupture of the concave C<sub>1</sub>-C<sub>2</sub> bond via the insertion of the Au adatom presents the lowest activation barrier, 1.52 eV vs 4.39 eV for the convex configurations, (see **Figure 44** for the whole set of activation barriers, and see **Figure A 4** and **Figure A 5**, in the annexes, for further details on the transition states). This difference in energy can be ascribed to the curvature of each configuration that makes the C<sub>1</sub>-C<sub>2</sub> bond height relative to the surface to be 3.1 Å in **3.1.2-Semi-Cc** and 6.4 Å for **3.1.2-Semi-Cx** (note that the Au adatom is 2.3 Å above the surface), making the C<sub>1</sub>-C<sub>2</sub> bond inaccessible to the adatom. Furthermore, this step constitutes the rate-limiting step of the whole reaction.

**Figure 45** shows the subsequent steps of the rearrangement regarding the pathway from **3.1.2-Semi-Cc** to the final product **3.1.2-Semi-Cc-VII**. It must be noted that the chemical structures have been shortened in the figure for sake of clarity. At step 2 (see **Figure A 6** for details of the transition state, TS), a nucleophilic attack is carried out from **C<sub>2</sub>** to **C<sub>6</sub>** after the homolytic breakage of the **C<sub>2</sub>-Au** adatom bond. Intermediate **3.1.2-Semi-Cc-III**, based in a sHOMOo compound with an unpaired electron in **C<sub>7</sub>**, arises after overcoming a 0.56 eV activation barrier.

A gain of -3.04 eV in free energy takes place in step 3 after some rearrangements from the spiro **3.1.2-Semi-Cc-III** to the azulene intermediate **3.1.2-Semi-Cc-V**. First, from **3.1.2-Semi-Cc-III** to **3.1.2-Semi-Cc-IV**, a bond between **C<sub>2</sub>** and **C<sub>7</sub>** takes place, forming the cyclopropane intermediate **3.1.2-Semi-Cc-IV** while the radical formed in **C<sub>3</sub>** bonds to the Au adatom (**Figure A 7**). Next, from **3.1.2-Semi-Cc-IV** to **3.1.2-Semi-Cc-V** the loss of a hydrogen at **C<sub>2</sub>** and the homolytic breakage between **C<sub>3</sub>** and the Au adatom enables the formation of the double bond between **C<sub>2</sub>** and **C<sub>3</sub>** in the transition state **3.1.2-Semi-Cc-IV-TS**. Subsequently, and due to the norcaradiene–cycloheptatriene equilibrium,<sup>171</sup> intermediate **3.1.2-Semi-Cc-IV-TS** shifts into the azulene intermediate **3.1.2-Semi-Cc-V**.

Lastly, a cyclodehydrogenation reaction takes place in step 4 from **3.1.2-Semi-Cc-V** to **3.1.2-Semi-Cc-VII** (**Figure A 8**). After the cleavage of the bond between the Au adatom and **C<sub>1</sub>**, a bond between **C<sub>3</sub>** and **C<sub>1</sub>** is formed with the generation of an unpaired electron at **C<sub>2</sub>** in **3.1.2-Semi-Cc-VI**. The loss of a hydrogen in **C<sub>1</sub>** mediated by the Au adatom, and the double bond formation between **C<sub>3</sub>** and **C<sub>2</sub>**, enables the formation of the 755-containing intermediate **3.1.2-Semi-Cc-VII**. Two further cyclodehydrogenations from **3.1.2-Semi-Cc-VII** triggers the synthesis of the final **3.1.2-755-GNR**.

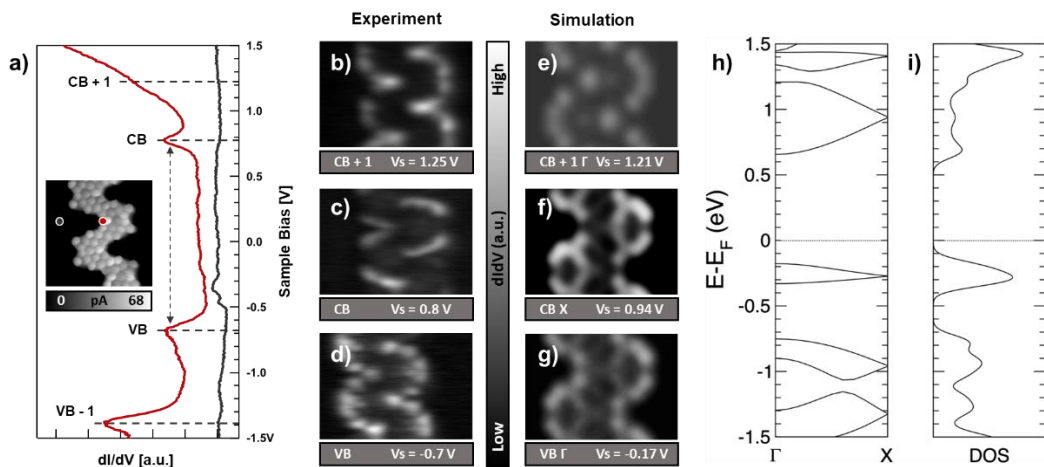




**Figure 45.** QM/MM simulations for steps 2, 3 and 4 of the rearrangement from **Semi-Cc-II**. **a)** Potential energy diagram. Activation barriers and reaction coordinates are depicted in the diagram. **b)** Chemical sketches and 3D models images extracted from QM/MM simulation. Chemical sketches are shortened for clarity.

### Electronic characterization

Once the synthesis of **3.1.2-755-GNR** and the rearrangement mechanism have been assessed, its local electronic structure on Au(111) was characterized by STS using a CO-functionalized tip. Red curve in **Figure 46 a** represents a differential conductance ( $dI/dV$ ) point spectrum recorded at the edge of the bay of **3.1.2-755-GNR** (see red spot in the inset STM image of **Figure 46 a**), showing peaks at  $-1.38$  eV,  $-0.66$  eV,  $0.77$  eV and  $1.5$  eV, all of them relative to the Fermi energy ( $V = 0$  V). The GNR valence band (VB) has been assigned to the  $-0.66$  eV peak and the peak at  $0.77$  eV has been identified as the conduction band (CB), resulting in the shortest bandgap for a purely carbon chevron GNR reported to date ( $1.43$  eV, see **Scheme A 1** and **Scheme A 2** in the annexes for other reported bandgaps of chevron-like GNRs).

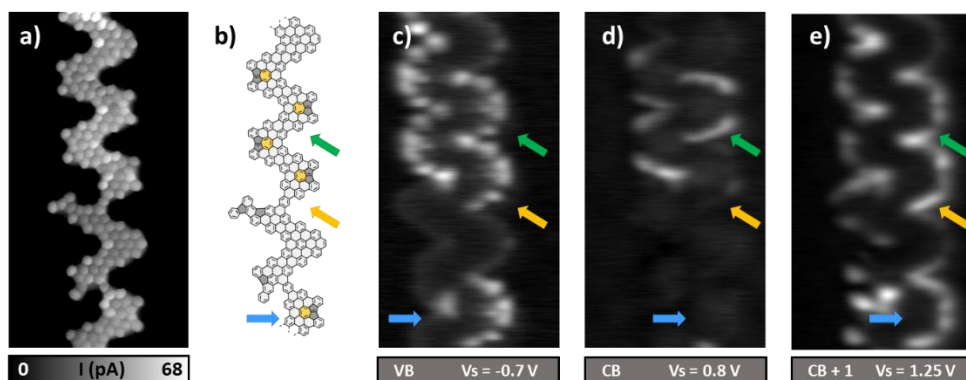


**Figure 46.** Electronic characterization of **755-GNR**. **a)** STS point spectra with CO tip, obtained at the color-coded positions in the BR STM image. Bandgap is calculated from the maxima of the VB to the CB, and is indicated with dashed lines. **b) to d)** Constant-height dI/dV maps at different bias values. **e) to g)** Calculated dI/dV maps at energies depicted. **h) and i)** Band diagram of and density of states of **755-GNR**. Scanning parameters were as follows: **(a)** BR STM image:  $3 \text{ nm} \times 3 \text{ nm}$ ,  $5.2 \text{ mV}$ . Point spectra:  $V_{\text{Mod}} = 20 \text{ mV}$ ; **(b)**  $4.32 \text{ nm} \times 3 \text{ nm}$ ,  $V_{\text{Mod}} = 20 \text{ mV}$ ; **(c)**  $4.32 \text{ nm} \times 3 \text{ nm}$ ,  $V_{\text{Mod}} = 20 \text{ mV}$  **(d)**  $4.32 \text{ nm} \times 3 \text{ nm}$ ,  $V_{\text{Mod}} = 20 \text{ mV}$ .

This value is further confirmed by the dI/dV maps recorded at these positions (see panels **b-d**), where the VB, CB and CB+1 can be discerned. It is worth mentioning that, while VB and CB+1 bands are homogeneously distributed along the whole GNR, independently on the exact nature of the units, and are similar to those reported for other chevron GNRs, the shape of the CB is characteristic of the 755 moiety. In fact, it can only be experimentally resolved in those 755 units that are fully embedded into other 755 units along the GNR (see **Figure 47** for the complete dI/dV map). Panels **e-g** in **Figure 46** show the simulated dI/dV maps for an infinite **3.1.2-755-GNR** (relaxed by DFT on gas phase)<sup>187</sup>, which are in qualitative good agreement with the experimental dI/dV maps. Additionally, **Figure 46 h** and **i** represent the band diagram of the **755-GNR** and its relative DOS.

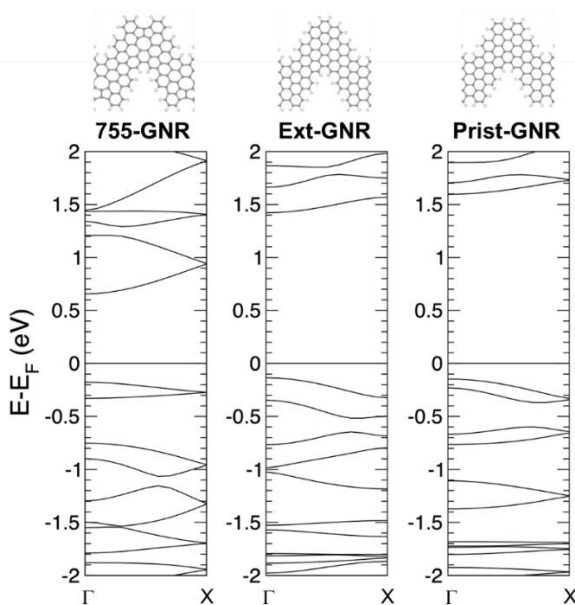
<sup>187</sup> Density functional theory (DFT) calculations were carried out using the all electron FHI-AIMS code2. For the description of the electronic structure of the freestanding unit cell, the hybrid exchange-correlation functional B3LYP3 + was employed in the calculations.

Theoretical dI/dV maps were calculated by the Probe Particle Scanning Tunneling Microscopy (PPSTM) code4 for a CO-like orbital tip, represented by a combination of PxPy (90%) and s-like wave character (10%) without tip relaxation.



**Figure 47.** Electronic characterization of a synthesized GNR by means of BR-STM and dI/dV mapping. **a)** Constant height bond resolved STM image. **b)** Chemical model showing the structure of the GNR in **a)**. **c) to e)** dI/dV maps at energies depicted below coinciding with the VB, the CB and the CB + 1. Scanning parameters were as follows: **(a)** 3 nm × 3 nm, 5.2 mV. Point spectra:  $V_{\text{Mod}} = 20$  mV; **(b)** 4.32 nm × 8 nm,  $V_{\text{Mod}} = 20$  mV; **(c)** 4.32 nm × 8 nm,  $V_{\text{Mod}} = 20$  mV **(d)** 4.32 nm × 8 nm,  $V_{\text{Mod}} = 20$  mV.

At this point, it is interesting to dig into the origin of the bandgap shortening in comparison with other chevron-like GNRs. **Figure 48** presents the computed band diagram for the three different products obtained: **3.1.2-755-GNR**, **3.1.2-Ext-GNR**, and **3.1.2-Prist-GNR**. While **3.1.2-Ext-GNR** presents a very similar band diagram to that of the **3.1.2-Prist-GNR** and other chevron-like GNRs, new bands emerge at the CB of **3.1.2-755-GNR**, which are the responsible for the bandgap shortening.



**Figure 48.** Calculated band diagrams for GNRs **3.1.2-755-GNR**, **3.1.2-Ext-GNR** and **3.1.2-Prist-GNR**.

#### Summary

Using STM and computational calculations, we have demonstrated the on-surface synthesis of a cyclopenta[c,d]azulene-containing chevron-like graphene nanoribbon **3.1.2-755-GNR** from a precursor bearing a COT ring **3.1.2-Mono**.

Due to the combination of symmetry breakage induced by the surface, and inherent curvature from the cyclooctatetraene ring in the monomer, the precursor presents two different configurations on the Au(111) substrate. Through quantum mechanical calculations we have elucidated a specific reaction mechanism, after Ullmann coupling, for the cyclooctatetraene - cyclopenta[c,d]azulene rearrangement involving one gold adatom. Only precursors with concave curvature triggers the on-surface activation barrier for the process.

Additionally, we have studied the electronic properties of the synthesized GNR through STS spectroscopy and dI/dV mapping. The introduction of the non-benzenoid cyclopenta[c,d]azulene moiety narrows the bandgap in comparison with other carbon chevron-like GNRs already described in literature.

### 3.1.3 Graphenic Polymers from Precursors Containing a Seven-Membered Ring

After the previous studies, where different cycloheptatriene and cyclooctatetraene moieties embedded in GNRs rearranged into planar compounds at CDH temperatures on Au(111), a new approach for the synthesis of curved graphene nanostructures on top of metallic surfaces is discussed in this subsection. This approach is based in the use of curved precursors already cyclodehydrogenated in solution. In this way, it is expected to circumvent the stability problems of the higher-membered rings on the Au(111) surface at high temperatures.

For that purpose, it is proposed the synthesis and characterization of the polymers **3.1.3-2Poly1** and **3.1.3-4Poly2** depicted in **Scheme 14**. On the one hand, the curvature of **3.1.3-2Poly1** arises from the inclusion of the cycloheptatrienone moiety, which induces a saddle-shape distortion in each of the monomers that encompasses the polymer. Alternatively, monomers in polymer **3.1.3-4Poly2** may show an even more distorted structure due to the combination of two sources of curvature, a [5]helicene and the cycloheptatrienone moiety, yielding an extended hepta[5]helicene (extended helicenes are those in which the helicene moiety is laterally “extended” in a conjugated  $\pi$  system<sup>188</sup>). In this regard, different oligomers and polymers have been reported in the literature illustrating the stability of [4]helicenes<sup>189</sup>, [6]helicenes<sup>190</sup>, and [7]helicenes<sup>191</sup> moieties at Ullmann coupling temperature on Au(111), which supports our hypothesis for this synthesis. Additionally, beyond the higher distortion and curvature of **3.1.3-4Poly2** due to the inclusion of the [5]helicene moiety, this group opens the door to intriguing chiral properties.

Finally, it is intended to compare both polymers (**3.1.3-2Poly1** and **3.1.3-4Poly2**) with the flat, fully hexagonal analogue polymer **3.1.3-6Poly3** (**Scheme 14**) already reported in the literature<sup>192</sup>. This enriched comparison between polymers will improve the toolbox in chemical reactivity of curved moieties on metallic substrates and the knowledge of the properties that curvature may induce in graphene nanostructures. Next, the obtained results to date related with precursor **3.1.3-3Prec2** are detailed (experiments with **3.1.3-1Prec1** are planned to be performed in future works).

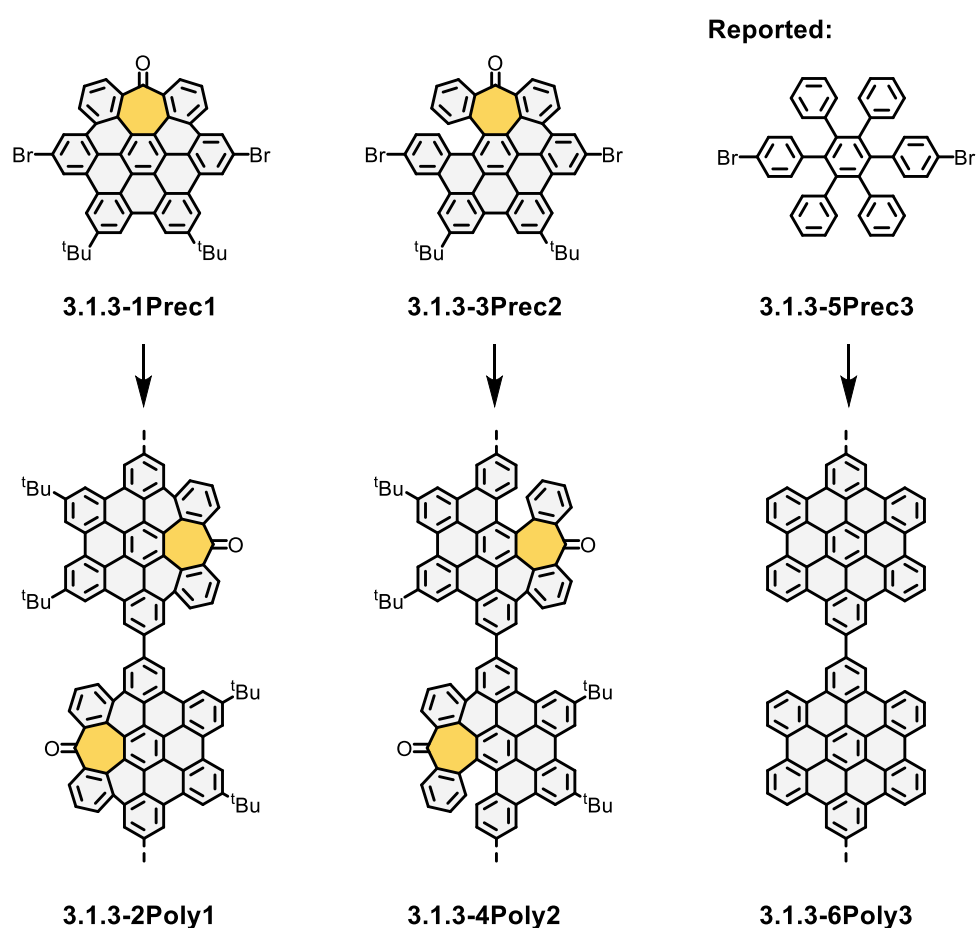
<sup>188</sup> **a)** F. Schlütter, T. Nishiuchi, V. Enkelmann, K. Müllen, *Angew. Chem., Int. Ed.*, **2014**, *53*, 1538. **b)** N. J. Schuster, D. W. Paley, S. Jockusch, F. Ng, M.L. Steigerwald, C. Nuckolls, *Angew. Chem., Int. Ed.*, **2016**, *55*, 13519. **c)** T. Fujikawa, Y. Segawa, K.J. Itami, *Org. Chem.*, **2017**, *82*, 7745.

<sup>189</sup> C. Wäckerlin, J. Li, A. Mairena, K. Martin, N. Avarvari, K.-H. Ernst, *Chem. Commun.*, **2016**, *52*, 12694–12697.

<sup>190</sup> J. Voigt, K. Martin, E. Neziri, M. Baljzović, C. Wäckerlin, N. Avarvari, K. Ernst, *Chemistry A European J.*, **2023**, *29*, e202300134.

<sup>191</sup> **a)** A. Mairena, C. Wäckerlin, M. Wienke, K. Grenader, A. Terfort, K.-H. Ernst, *J. Am. Chem. Soc.*, **2018**, *140*, 15186–15189. **b)** A. P. Solé, J. Klívar, M. Šámal, I. G. Stará, I. Starý, J. Mendieta-Moreno, K.-H. Ernst, P. Jelínek, O. Stetsovych, *Chem. Eur. J.*, **2024**, e202304127.

<sup>192</sup> H. Ooe, K. Ikeda, T. Yokoyama, *J. Phys. Chem. C*, **2023**, *127*, 7659–7665.



**Scheme 14.** Graphenic polymers related to this study. **3.1.3-4Poly2** was synthesized for the doctoral thesis while **3.1.3-2Poly1** will be addressed in the future.

*In-Solution synthesis and on-surface characterization of the r.t phase*<sup>193</sup>

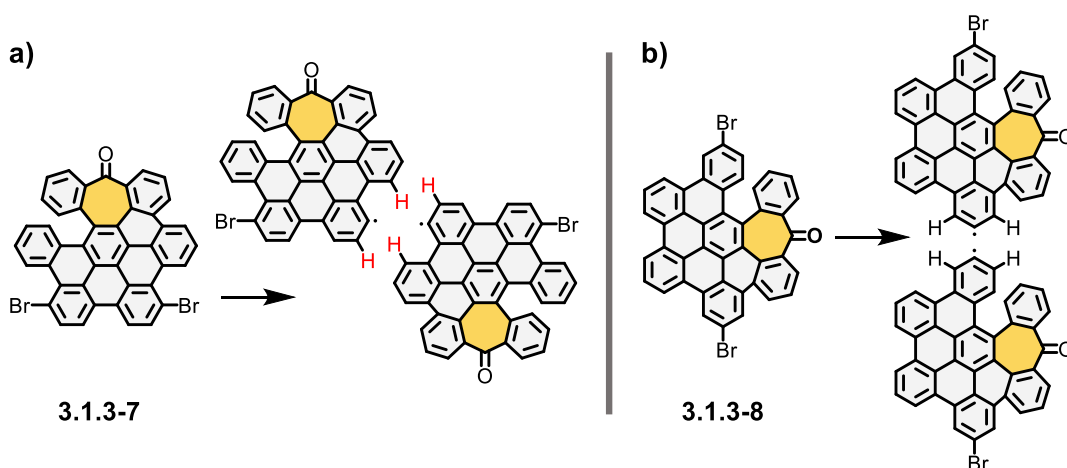
The chemical design of the monomer **3.1.3-3Prec2** is justified on several grounds. Firstly, a monomer previously cyclodehydrogenated in-solution was chosen for performing these experiments. This avoids high temperatures for the last cyclodehydrogenation step, where it has been seen that heptagonal and octagonal rings tend to rearrange to planarize. The aim is to preserve these non-benzenoid rings in the structure after reaching the temperature of the Ullmann coupling in Au(111).

Secondly, the inclusion of the tert-butyl groups is a requirement from the in-solution synthesis of the precursor. Although the synthesis without these groups was tested, suitable conditions to carry out the Scholl reaction were not found yet. Although it may seem a weakness for the surface characterization due to be a bulky group, these groups can be helpful in identifying the

<sup>193</sup> This work is a collaboration between MOREFUN group from the University of Granada, where the monomer was synthesized and ESISNA group from CSIC of Madrid, where the growth of the nanostructures was studied.

orientation of the monomer on the surface as it will be seen below. In addition, to the best of our knowledge, although there are some studies of molecules with tert-butyl groups on metallic surfaces<sup>194</sup>, this is the first study regarding their stability at high temperatures on Au(111). This is also a matter of interest to broaden the synthetic tools of the on-surface synthesis.

Third, the position of the bromine atoms in the structure is motivated by the interest in studying this polymer topology, which has been less developed in the OSS literature<sup>192</sup>. Furthermore, with cyclodehydrogenated monomers, as **3.1.3-7** in **Scheme 15 a**, the on-surface synthesis of chevron-type GNRs is not possible due to steric hindrance among hydrogens when two monomers approach in the Ullmann coupling (red hydrogens in **Scheme 15 a**). On the other hand, **Scheme 15 b** shows how for “para” structures, as **3.1.3-8**, there is less steric hindrance among near hydrogens.

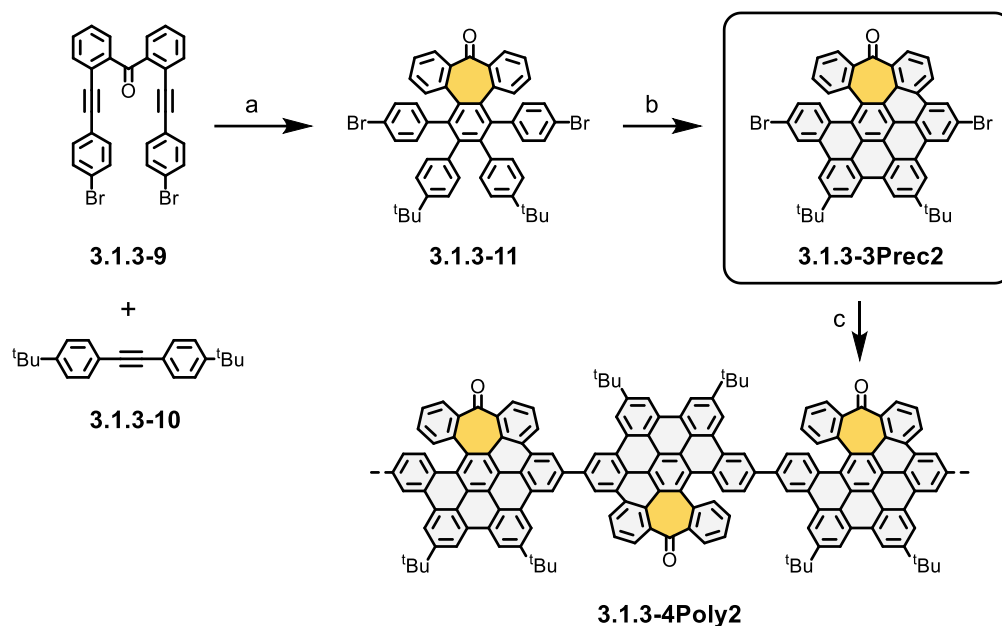


**Scheme 15.** Chemical models showing steric hindrance between monomers on-surface at Ullmann coupling depending on bromine position. **a)** Approximation between “meta isomers”. **b)** Approximation between “para isomers”.

In-solution synthesis of precursor **3.1.3-3Prec2** (**Scheme 16**) was carried out from polyphenilic **3.1.3-11**, that was already described by our research group<sup>195</sup>. Different conditions of the Scholl reaction (**3.1.3-11** to **3.1.3-3Prec2**) in presence of TfOH (Trifluoromethanesulfonic acid) and the oxidant DDQ (2,3-Dichloro-5,6-dicyano-1,4-benzoquinone) were tested until selectively achieving the hepta[5]helicene **3.1.3-3Prec2** (69 %) over the other cyclodehydrogenation products.

<sup>194</sup> **a)** K. Diller, A. Singha, M. Pivetta, C. Wäckerlin, R. Hellwig, A. Verdini, A. Cossaro, L. Floreano, E. Vélez-Fort, J. Dreiser, S. Rusponi, H. Brune, *RSC Adv.*, **2019**, *9*, 34421–34429. **b)** P. Tegeder, S. Hagen, F. Leyssner, M. V. Peters, S. Hecht, T. Klamroth, P. Saalfrank, M. Wolf, *Appl. Phys. A*, **2007**, *88*, 465–472. **c)** S. Hagen, F. Leyssner, D. Nandi, M. Wolf, P. Tegeder, *Chemical Physics Letters*, **2007**, *444*, 85–90. **d)** D. Heim, D. Écija, K. Seufert, W. Auwärter, C. Aurisicchio, C. Fabbro, D. Bonifazi, J. V. Barth, *J. Am. Chem. Soc.*, **2010**, *132*, 6783–6790.

<sup>195</sup> V. G. Jiménez, A. H. G. David, J. M. Cuerva, V. Blanco, A. G. Campaña, *Angew. Chem. Int. Ed.*, **2020**, *59*, 15124–15128.

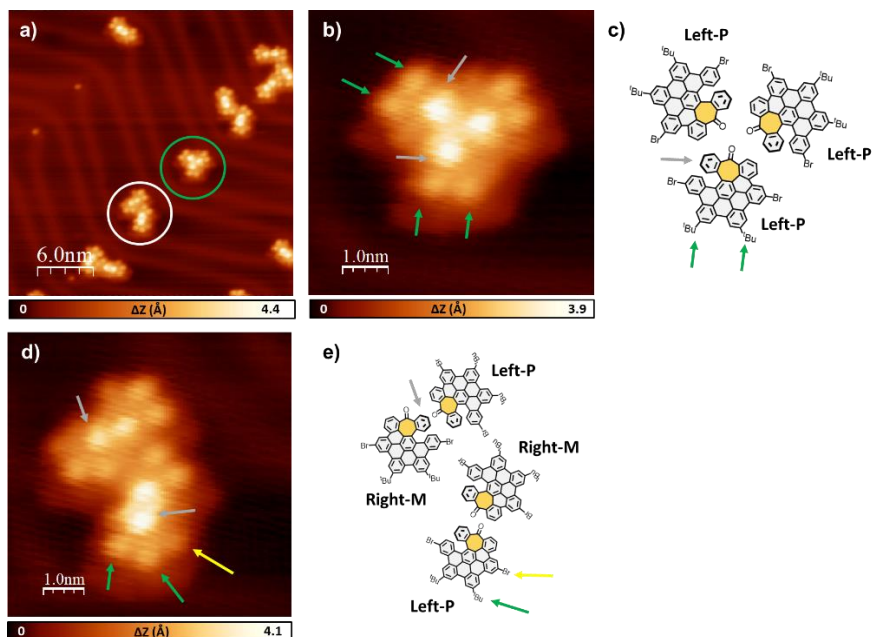


**Scheme 16.** Schematic representation of the synthetic strategy towards **3.1.3-4Poly2**. **a)**  $\text{CO}_2(\text{CO})_8$ , Toluene, 110 °C, 16 h, 56 %. **b)** DDQ, TFOH, DCM, 0 °C, 10 min, 69 %. **c)** Annealing at 475 K on a Au(111) surface.

Subsequently, **3.1.3-3Prec2** was sublimated from a crucible, under UHV conditions at 360 °C, onto a Au(111) surface held at r.t.. **Figure 49 a** represents a topography STM image showing the tendency of **3.1.3-3Prec2** to organize into clusters comprising two to four units in the kinks of the Au(111) reconstruction.

Constant current STM image in **Figure 49 b**, presents three precursors in a three-fold symmetry with a triangular arrangement. We attribute the brightest protrusion in these precursors, presented in the center of the structure (see the gray arrow in the STM image), to the hepta[5]helicene moiety; while the two features depicted with a green arrow to the tert-butyl moieties. In this regard, **Figure 49 c** presents a chemical model of the trimer structure composed by three units with P chirality, where the helicene moiety is oriented at the left part of the structure. The nomenclature P refers to the helicity of the helicene, that depends on the direction of the helicene (the rotating direction) starting from its higher ring. For clockwise directions the helicene it is called P, for anticlockwise M. We assume that the monomers in **Figure 49 c** are P because the bright protrusion corresponding to the helicene moiety is positioned at the molecule's center and not in the edge as it would be expected for M. Additionally, **Figure 49 d** and **e** show another detail STM image of a different arrange with its respective chemical model. This arrange showed precursors with helicenes both at the right part of the molecule and in the left part of the molecule presenting M and P enantiomers.

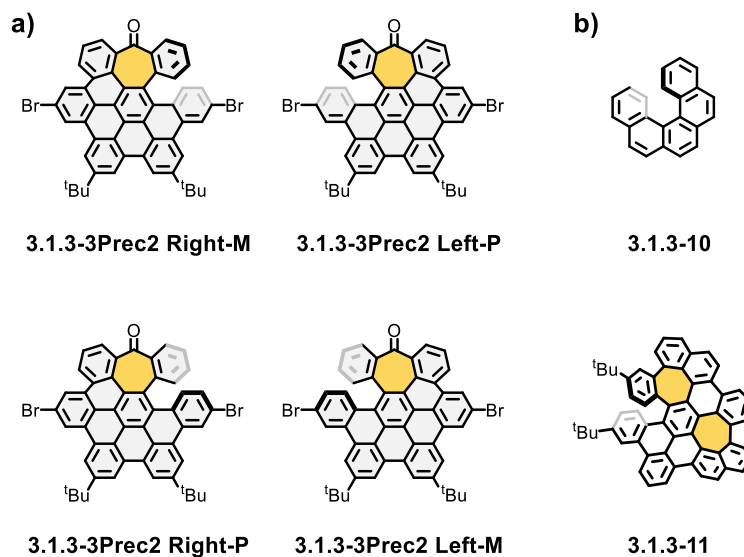




**Figure 49.** RT phase of **3.1.3-3Prec2** on Au(111). **a)** Topographic constant current STM image, below 0.1 ML coverage. Green circle depicts **b)**, white circle depicts **d)**. **b)** Detailed constant current STM image of a three-unit assembly. Gray arrow depicts hepta[5]helicene moiety, yellow arrow shows bromine atoms and green arrow depicts tert-butyl moiety. **c)** Chemical model referring to **b)** and showing stereoselectivities. **d)** Detailed constant current STM image of a four-unit assembly. **e)** Chemical model referring to **d)** and showing stereoselectivities. Scanning parameters: **(a)** 50 pA,  $-1.5$  V, **(b)** and **(d)** 50 pA,  $-1.5$  V.

Due to the symmetry breakage induced by the surface, four diastereoisomers should have been hypothetically observed regarding the side of the nanographene where the helicene falls on the surface (left or right) and the helicity of the helicene itself (M or P) as shown in **Scheme 17 a**. However, as stated before and after doing a further analysis, only **3.1.3-3Prec2 Right M** and **3.1.3-3Prec2 Left P** were identified on the surface, so it is assumed that **3.1.3-3Prec2** precursor is able to overcome the racemization barrier on surface (the four diastereoisomers had the same chances when falling into the surface). Only **3.1.3-3Prec2 Right-M** and **3.1.3-3Prec2 Left-P** are observed as these compounds maximize the Van der Waals interactions with the substrate, as opposed to their other diastereoisomers **3.1.3-3Prec2 Right-P** and **3.1.3-3Prec2 Left-M**. The thermal energy of the molecule itself on the surface at the r.t. deposition, or the released energy upon impact with the substrate after deposition justify the racemization. Examples of the conformational dependence of some molecules on surfaces due to the energy releasing upon deposition have been previously described in the literature<sup>196</sup>.

<sup>196</sup> L. Krumbein, K. Anggara, M. Stella, T. Michnowicz, H. Ochner, S. Abb, G. Rinke, A. Portz, M. Dürr, U. Schlickum, A. Baldwin, A. Floris, K. Kern, S. Rauschenbach, *Phys. Rev. Lett.*, **2021**, *126*, 056001.



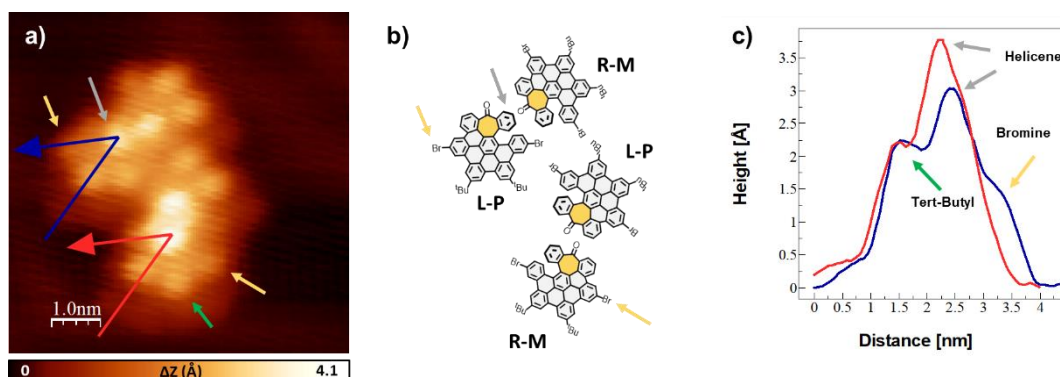
**Scheme 17.** [5]helicenes. **a)** Chemical models of the different possible **3.1.3-3Prec2** isomers on top of a surface. **b)** Reported [5]helicenes of interest from the literature.

In this regard, related compounds as the purely hexagonal [5]helicene **3.1.3-10** (**Scheme 17 b**), or the compound **3.1.3-11** that bears an heptagonal ring in the [5]helicene (**Scheme 17 b**), present an in-solution racemization barrier of 24.6 Kcal/mol<sup>197</sup> and 25.4 Kcal/mol<sup>198</sup> respectively (in solution these compounds may overcome these barriers after one day at r.t. due to thermal energy). Although the racemization barrier for the precursor **3.1.3-3Prec2** in-solution has not been measured to date, and the comparison between the in-solution and the on-surface environments is not straightforward, these reported activation energies support our hypothesis that the activation energy for the racemization of **3.1.3-3Prec2** on-surface should be low and could be overcome (only **3.1.3-3Prec2 Right-M** and **3.1.3-3Prec2 Left-P** are observed).

To gain more insights of the structure of **3.1.3-3Prec2**, we measured the apparent heights in **Figure 49 f**, revealing a dependence with its chemical environment. For the precursors at the bottom of the STM image in **Figure 49 d** (red profile) an approximate height of  $\sim 3.8$  Å is observed when helicenes interact facing each other. Conversely, precursor at the top part of **Figure 49 d** exhibit an apparent height of  $\sim 3$  Å. This nuanced behavior underscores how subtle changes in the interaction forces among **3.1.3-3Prec2** precursors can alter the conformation due to the inherent flexibility of the helicene moiety. In addition, **3.1.3-3Prec2** reveals two protrusions with an approximately  $\sim 1.7$  Å of apparent height on the sides of the structure (indicated by a yellow arrow), which we attribute to bromine atoms. Additionally, there are two protrusions at the bottom of the structures, measuring around  $\sim 2.3$  Å of apparent height (highlighted by a green arrow), assigned to the tert-butyl groups.

<sup>197</sup> C. Goedicke, H. Stegemeyer, *Tetrahedron Lett.*, **1970**, *12*, 937–940.

<sup>198</sup> Z. Qiu, S. Asako, Y. Hu, C. W. Ju, T. Liu, L. Rondin, D. Schollmeyer, J. S. Lauret, K. Müllen, A. Narita, *J. Am. Chem. Soc.*, **2020**, *142*, 14814–14819.

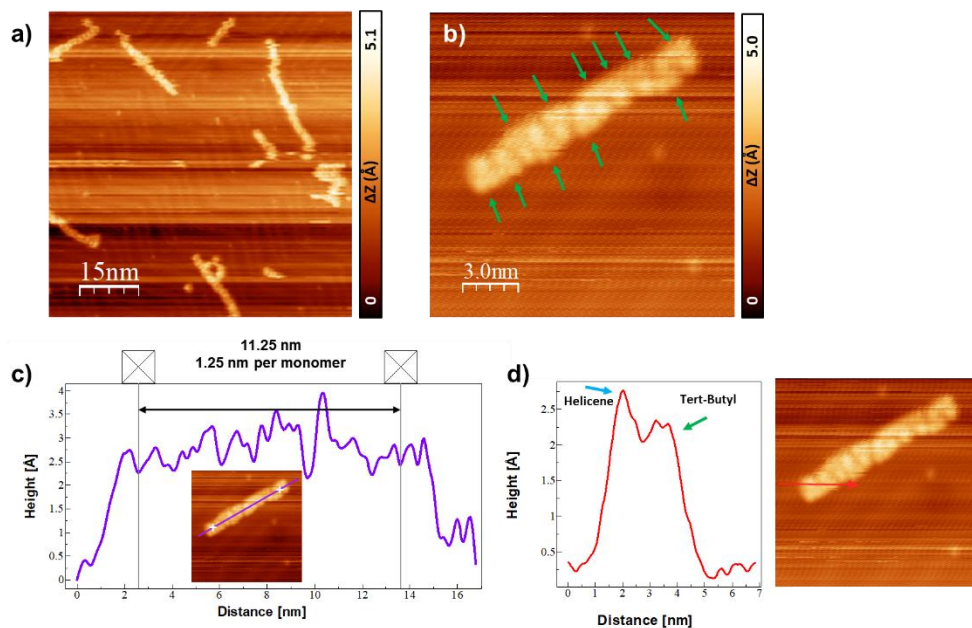


**Figure 50.** Measurement of the apparent heights of the different moieties of **3.1.3-3Prec2**. **a)** Detailed STM image of a four-unit assembly. Gray arrow depicts the hepta[5]helicene moiety, yellow arrow depicts bromine atoms and green arrow depicts the tert-butyl moieties. Big red a blue arrow depict where the apparent heights were measured in **c)**. **b)** Chemical models. **c)** Apparent height diagram. Scanning parameters were as follows: **(a)** 50 pA,  $-1.5$  V.

### Polymeric phase

Further annealing the substrate at  $200$  °C promoted the Ullmann coupling between monomers. **Figure 51 a** shows a topographic STM image where polymers with different lengths can be observed. Detailed inspection of a polymer in **Figure 51 b** enabled us to distinguish three distinct bright protrusions per monomer in the polymer, one associated with the hepta[5]helicene moiety and the other two with the tert-butyl groups, indicated in the image with a green arrow.

**Figure 51 c** illustrates the measurement of the experimental intermonomer distance,  $1.25$  nm, for the synthesized polymer. This value aligns closely with the reported  $1.29$  nm distance for purely hexagonal **3.1.3-6Poly3**<sup>192</sup>, validating the covalent nature of the synthesized polymer **3.1.3-4Poly2**. Notably, the structural variation between these polymers, specifically the inclusion of the hepta[5]helicene moiety, exerts only a minimal impact on the intermonomer distance.



**Figure 51.** Covalent polymers growth after annealing the Au(111) sample at 200 °C. **a)** Topographic constant current STM image. **b)** Detail constant current STM image of a polymer. Green arrow depicts tert-butyl positions. **c)** Length measurement in the polymer. **d)** Apparent height measurement in the polymer. Scanning parameters: (a) 50 pA, -1.5 V, (b) 50 pA, -1.5 V.

At low coverage, there is an absence of selectivity in the orientation of monomers within the polymer. Each monomer independently positions itself, without a discernible preference for the arrangement of tert-butyl groups on one side or the other of the polymer (green arrows in **Figure 51 b**). Due to the lack of resolution in the image, it is difficult to ascertain the chirality among monomers (right M, right P, left M, left P) at this stage. Future investigations with higher coverage and enhanced image resolution may reveal potential selectivities in this regard.

Finally, **Figure 51 d** provides the measurement of the apparent height through the hepta[5]helicene and tert-butyl moieties. The apparent height profile in **Figure 51 e** exhibits two maxima, a 2.9 Å peak corresponding to the hepta[5]helicene moiety and a 2.3 Å peak corresponding to the tert-butyl group. Therefore, the presumed stability of the hepta[5]helicene unit in the monomer at the Ullmann coupling temperature finds robust support in several compelling aspects. Firstly, the commented 2.9 Å protrusion aligns with the previously observed height (3.0 Å) during the self-assembly phase for helicenes that were not directly interacting with other helicenes moieties. Secondly, this protrusion exceeds the reported 1.8 Å height for the flat polymer **3.1.3-6Poly3** and the 2 Å height for planar graphene nanoribbons (GNRs)<sup>199</sup>, including chevron-like GNRs or armchair GNRs. Thirdly, in the subsection 3.1.1, the stability of the tropone moiety on Au(111) at the Ullmann coupling temperature was demonstrated.

<sup>199</sup> J. Cai, P. Ruffieux, R. Jaafar, M. Bieri, T. Braun, S. Blankenburg, M. Muoth, A. P. Seitsonen, M. Saleh, X. Feng, K. Müllen, R. Fasel, *Nature*, **2010**, *466*, 470–473.

Lastly, the literature offers additional instances illustrating the stability of [4]helicenes<sup>200</sup>, [6]helicenes<sup>201</sup>, and [7]helicenes<sup>202</sup> at Ullmann coupling temperature on Au(111).

Additionally, the stability of the tert-butyl groups in **3.1.3-4Poly2** is inferred based on the comparable height values observed in the r.t. phase. Specifically, the height remains constant at 2.3 Å in both the precursor and polymer phases. Since the tert-butyl moieties maintain a consistent chemical environment in both phases, the apparent height is expected to also remain unchanged.

### Summary

We have achieved an unprecedented synthesis of a distorted graphenic polymer on Au(111) featuring non-benzenoid extended hepta[5]helicenes. This synthesis demonstrates the stability of the hepta[5]helicene moiety at Ullmann coupling temperatures.

Utilizing STM image analysis, we have elucidated the conformational flexibility inherent in the helicene moiety. Our proposition suggests that the [5]helicene unit successfully surmounts the enantiomerization barrier at r.t. on Au(111). Additionally, the stability of the tert-butyl groups to Ullmann temperature has also been demonstrated through an apparent height analysis of STM images.

Achieving a complete understanding of **3.1.3-4poly2** necessitates future high-resolution characterization employing a functionalized CO tip, STS electronic characterization, and more studies at higher coverages. Further investigations are planned to delve into the polymer formation of **3.1.3-2Poly1** on Au(111) and conduct a comparative analysis between the two polymers.

---

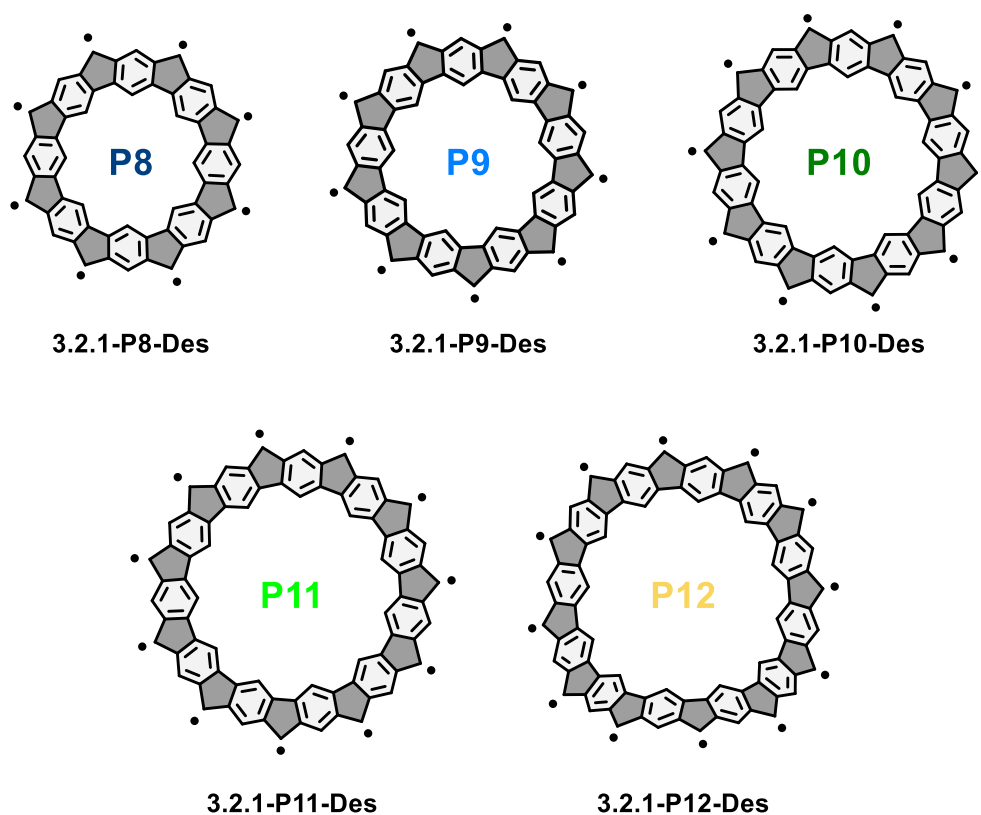
<sup>200</sup> C. Wäckerlin, J. Li, A. Mairena, K. Martin, N. Avarvari, K.-H. Ernst, *Chem. Commun.*, **2016**, 52, 12694–12697.

<sup>201</sup> J. Voigt, K. Martin, E. Neziri, M. Baljzović, C. Wäckerlin, N. Avarvari, K. Ernst, *Chemistry A European J.*, **2023**, 29, e202300134.

<sup>202</sup> A. Mairena, C. Wäckerlin, M. Wienke, K. Grenader, A. Terfort, K.-H. Ernst, *J. Am. Chem. Soc.*, **2018**, 140, 15186–15189.

### 3.2 Tuning the Structure, Curvature and Properties of a Cyclopenta-Ring-Fused Oligo(*m*-Phenylene) Macrocylic Family Through Structure Enlargement.

In this section, it is explored the synthesis and characterization of a family of cycloarenes, specifically, the cyclopenta-ring-fused oligo(*m*-phenylene) family, as depicted in **Scheme 18** (from **3.2.1-P8-Des** to **3.2.1-P12-Des**). Each macrocycle is composed by the same number of hexagonal rings, pentagonal rings, and radicals. For example, **3.2.1-P8-Des** has eight benzene rings, eight pentagonal rings and eight radicals (considering an open-shell scenario). In this regard, two main goals are intended for this section encompassing: (i) the study of the change of curvature presented by the macrocycles due to the enlargement of the structures; (ii) the study of the electronic and magnetic properties along the different sizes of macrocycles (the number of unpaired electrons and the conjugation of the structures will vary depending on the macrocycle size).



Scheme 18. Cyclopenta-ring-fused oligo(*m*-phenylene) macrocycles studied in this section.

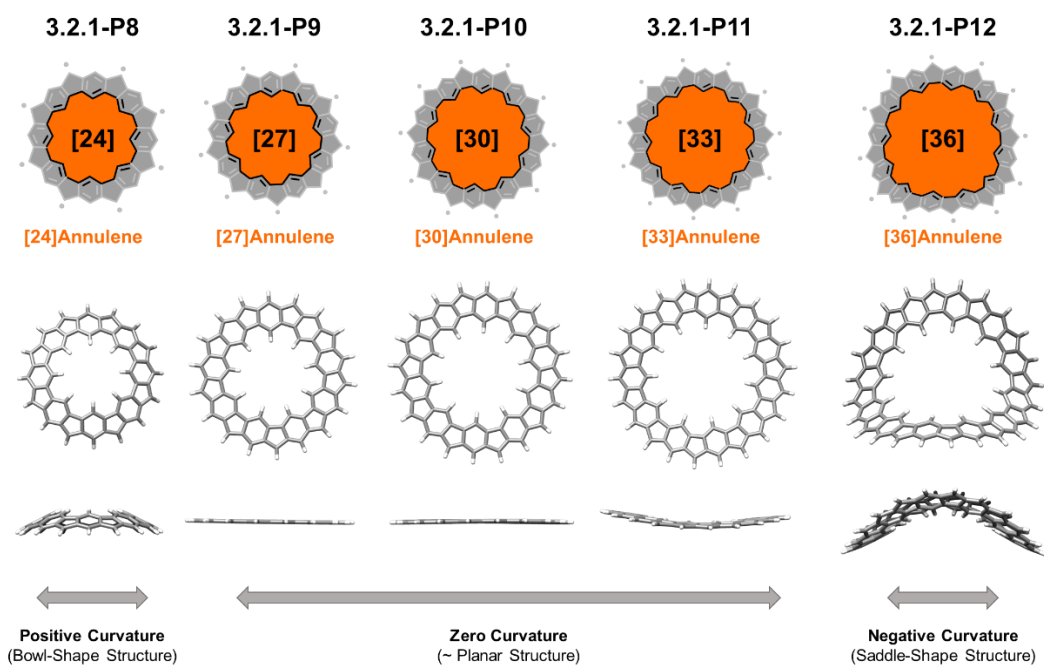
As it has been shown in the Curvature section of the Introduction chapter, the enlargement of a structure within a specific topology of cycloarene, tunes the curvature of the macrocycle. Different examples were regarded in that section, where the curvature changed from a bowl-shape, or positive curvature, to a saddle shape curvature, passing through planar structures. In this regard, we envision a positively curved structure for **3.2.1-P8-Des**, relatively flat structures as the size of the macrocycle grows (**3.2.1-P9-Des**, **3.2.1-P10-Des** and **3.2.1-P11-Des**), and a saddle-shape curvature for **3.2.1-P12-Des**. **Figure 52** presents this change in curvature along the enlargement of the structure with preliminary computational results obtained by a force field calculation with MMFF94s<sup>203</sup>.

In this respect, we approach the synthesis of these macrocycles (from **3.2.1-P8-Des** to **3.2.1-P12-Des**) by combining in-solution and on-surface methods. Although the surfaces generally tend to planarize the structures, we expect that the strain of the macrocycles is high enough to overcome this planarization effect of surfaces keeping the curvature related to their inner strain. The main advantage of synthesizing the final macrocycles on surface is that it enables their synthesis without the need of adding protecting groups to the highly reactive radical position. This is due thanks to the clean UHV environments where the experiments are conducted. In addition, this study expands the work already conducted by Liu et al.<sup>153</sup> with the synthesis of more sizes of macrocycles, **3.2.1-P9-Des**, **3.2.1-P11-Des** and **3.2.1-P12-Des**. A priori, the synthesis of these macrocycles in solution seems more challenging in the case of **3.2.1-P9-Des** and **3.2.1-P11-Des** due to their asymmetry.

This section begins with the presentation of the general synthetic approach followed to synthesize the different macrocycles. Following, we delve into five subsections encompassing the results of the five macrocycles (from **3.2.1-P8-Des** to **3.2.1-P12-Des**). Each subsection ends with a brief summary, including the main conclusions, and the main issues addressed for each macrocycle. Additionally, there are two general comparisons (electronic and structural) among macrocycles at the end of the subsection **3.2.4**, and at the end of the subsection **3.2.6**.

---

<sup>203</sup> T. A. Halgren, *J. Comput. Chem.*, **1996**, *17*, 490–519.



**Figure 52.** Curvature variation of the family of cyclopenta-ring-fused oligo(*m*-phenylene) macrocycles. Structures calculated by the force field MMFF94s.



### 3.2.1 Synthetic Strategy

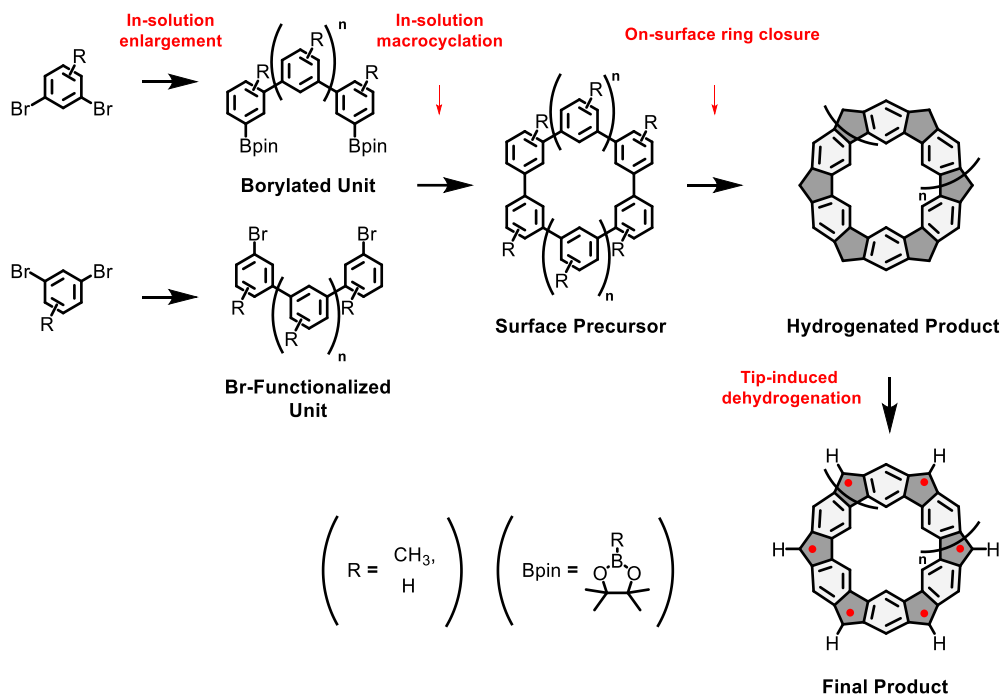
In the last years, the predominant approach to synthesize macrocycles on surfaces has involved the surface-assisted polymerization of tailored monomers<sup>204</sup>. Although this method facilitates the simultaneous synthesis of multiple products in a single reaction, allowing for a comparative analysis, it suffers from a lack of selectivity when aiming asymmetric products, or more sterically hindered products (generally, planar products are favored in the OSS). In addition, the monomer polymerization approach often yields very low quantities of the desired products (macrocycles) due to formation of oligomers (polymerization vs macrocyclization reactions).

Therefore, to selectively build the abovementioned macrocycles with the proper size (from **3.2.1-P8-Des** to **3.2.1-P12-Des**), a versatile synthetic strategy was designed combining in-solution chemistry with on-surface synthesis. As represented in **Scheme 19**, this strategy is based on the in-solution synthesis of the macrocyclic precursor and its subsequent deposition on the surface, thus avoiding unspecific on-surface polymerizations<sup>205</sup>. Our approach involves four key steps. Firstly, the in-solution synthesis of the tailored building blocks, for using them in the final in-solution macrocyclization reaction. For this purpose, commercially available synthons are enlarged through different Suzuki cross-coupling reactions until synthesizing the key borylated and brominated units (**Scheme 21**, **Scheme 22** and **Scheme 23**). The number of benzene rings and the functionalization of these units with methyl groups depends on the symmetry and size of the final macrocycle. Secondly, the in-solution macrocyclization of the borylated and the brominated building blocks through a Suzuki cross-coupling reaction. Thirdly, the on-surface oxidative ring closure reaction<sup>206</sup> on Au(111) (~ 310 °C). And finally, the final tip-induced dehydrogenation of the pentagonal rings to achieve the final product. The final size of the resulting macrocycles is selectively controlled in this bottom-up strategy.

<sup>204</sup> **a)** M. Chen, J. Shang, Y. Wang, K. Wu, J. Kuttner, G. Hilt, W. Hieringer, J. M. Gottfried, *ACS Nano*, **2017**, *11*, 134–143. **b)** E. Li, C.-K. Lyu, C. Chen, H. Xie, J. Zhang, J. W. Y. Lam, B. Z. Tang, N. Lin, *Commun Chem.*, **2022**, *5*, 174. **c)** F. Xiang, S. Maisel, S. Beniwal, V. Akhmetov, C. Ruppenstein, M. Devarajulu, A. Dörr, O. Papaianina, A. Göring, K. Y. Amsharov, S. Maier, *Nat. Chem.*, **2022**, *14*, 871–876. **d)** R. Yin, J. Wang, Z.-L. Qiu, J. Meng, H. Xu, Z. Wang, Y. Liang, X.-J. Zhao, C. Ma, Y.-Z. Tan, Q. Li, B. Wang, *J. Am. Chem. Soc.*, **2022**, *144*, 14798–14808. **e)** X. Zhu, Y. Liu, W. Pu, F.-Z. Liu, Z. Xue, Z. Sun, K. Yan, P. Yu, *ACS Nano*, **2022**, *16*, 10600–10607. **f)** U. Beser, M. Kastler, A. Maghsoumi, M. Wagner, C. Castiglioni, M. Tommasini, A. Narita, X. Feng, K. Müllen, *J. Am. Chem. Soc.*, **2016**, *138*, 4322–4325. **g)** Q. Fan, D. Martin-Jimenez, S. Werner, D. Ebeling, T. Koehler, T. Vollgraff, J. Sundermeyer, W. Hieringer, A. Schirmeisen, J. M. Gottfried, *J. Am. Chem. Soc.*, **2020**, *142*, 894–899.

<sup>205</sup> **a)** J. Su, W. Fan, P. Mutombo, X. Peng, S. Song, M. Ondráček, P. Golub, J. Brabec, L. Veis, M. Telychko, P. Jelínek, J. Wu, J. Lu, *Nano Lett.*, **2021**, *21*, 861–867. **b)** J. Hieulle, S. Castro, N. Friedrich, A. Vegliante, F. R. Lara, S. Sanz, D. Rey, M. Corso, T. Frederiksen, J. I. Pascual, D. Peña, *Angew. Chem. Int. Ed.*, **2021**, *60*, 25224–25229.

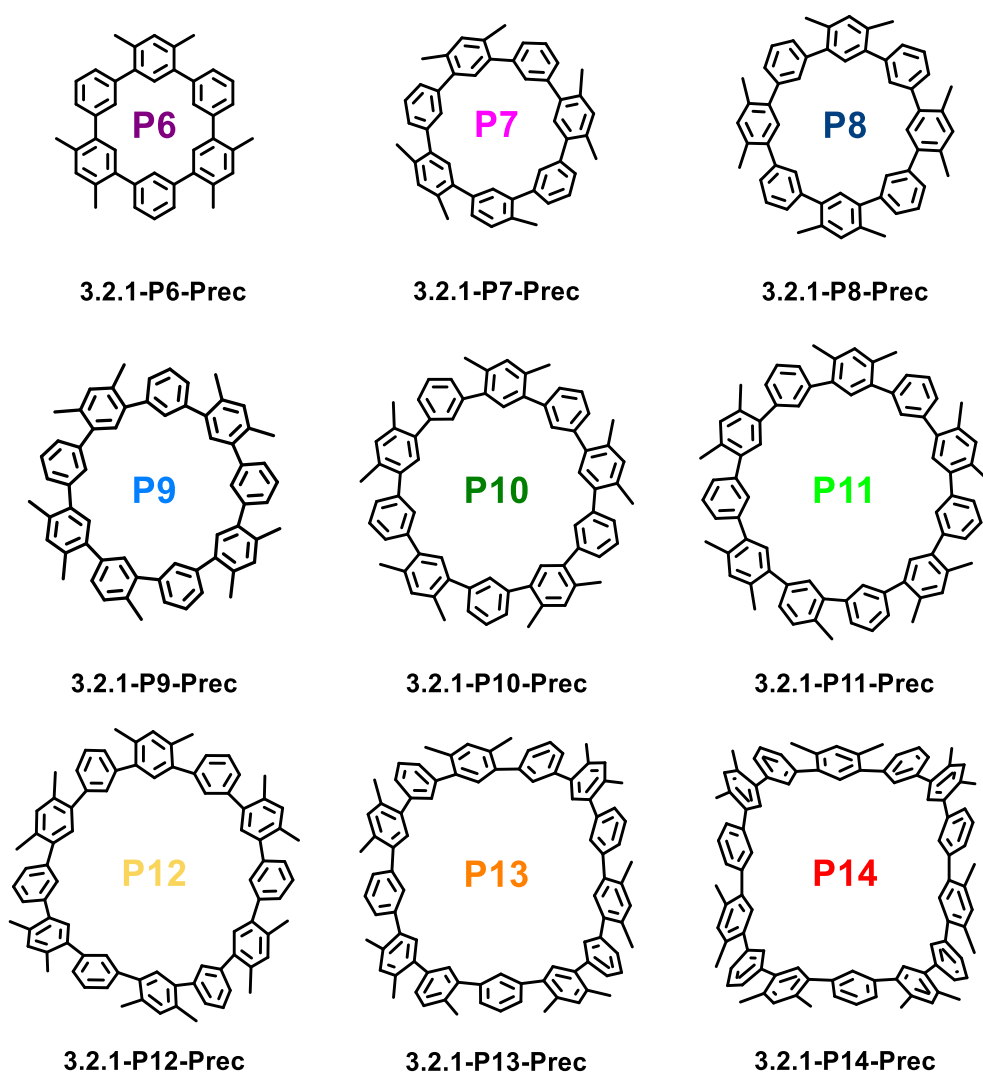
<sup>206</sup> **a)** M. Di Giovannantonio, K. Eimre, A. V. Yakutovich, Q. Chen, S. Mishra, J. I. Urgel, C. A. Pignedoli, P. Ruffieux, K. Müllen, A. Narita, R. Fasel, *J. Am. Chem. Soc.*, **2019**, *141*, 12346–12354. **b)** T. G. Lohr, J. I. Urgel, K. Eimre, J. Liu, M. Di Giovannantonio, S. Mishra, R. Berger, P. Ruffieux, C. A. Pignedoli, R. Fasel, X. Feng, *J. Am. Chem. Soc.*, **2020**, *142*, 13565–13572.



**Scheme 19.** General scheme of the synthetic approach utilized for the synthesis of the different cyclopenta-ring-fused oligo(*m*-phenylene) macrocycles.

Following this approach, macrocycles from **3.2.1-P6Prec** to **3.2.1-P14Prec** (**Scheme 20**) were prepared. Although macrocyclic precursors **3.2.1-P6Prec**, **3.2.1-P7Prec**, **3.2.1-P13Prec** and **3.2.1-P14Prec** were successfully synthesized and characterized by in-solution methods, it is beyond the scope of this doctoral thesis the on-surface synthesis and characterization of their corresponding cyclodehydrogenated final products. As commented before, our attention and efforts for the on-surface synthesis and characterization were focused on precursors from **3.2.1-P8Prec** to **3.2.1-P12Prec**.

The versatility of this synthetic route lies in its simplicity, as all the required precursors can be synthesized from three commercially-available synthons (**3.2.1-N1**, **3.2.1-M1** and **3.2.1-S1**). In this regard, every intermediate related to the synthesis of one macrocycle may be useful for the synthesis of another macrocycle, showcasing the versatility of the synthetic strategy. In addition, every reaction from the route is scalable, going from the milligrams to the gram scale, all the products were highly soluble in common organic solvents, easily purifiable by common organic methods and characterized by means of NMR, IR and HR-MS.

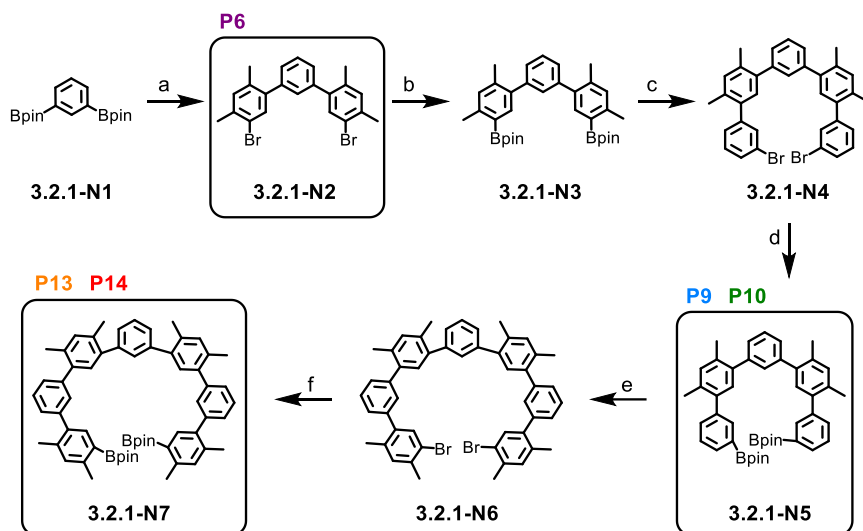


**Scheme 20.** In-solution synthesized macrocyclic precursors ranging sizes from **3.2.1-P6Prec** to **3.2.1-P14Prec**.

The final yields of the complete synthetic routes are: 20 % for **3.2.1-P6Prec**, 19 % for **3.2.1-P7Prec**, 14 % for **3.2.1-P8Prec**, 11 % for **3.2.1-P9Prec**, 15 % for **3.2.1-P10Prec**, 11 % for **3.2.1-P11Prec**, 11 % for **3.2.1-P12Prec**, 8 % for **3.2.1-P13Prec**, and 15 % for **3.2.1-P14Prec**.

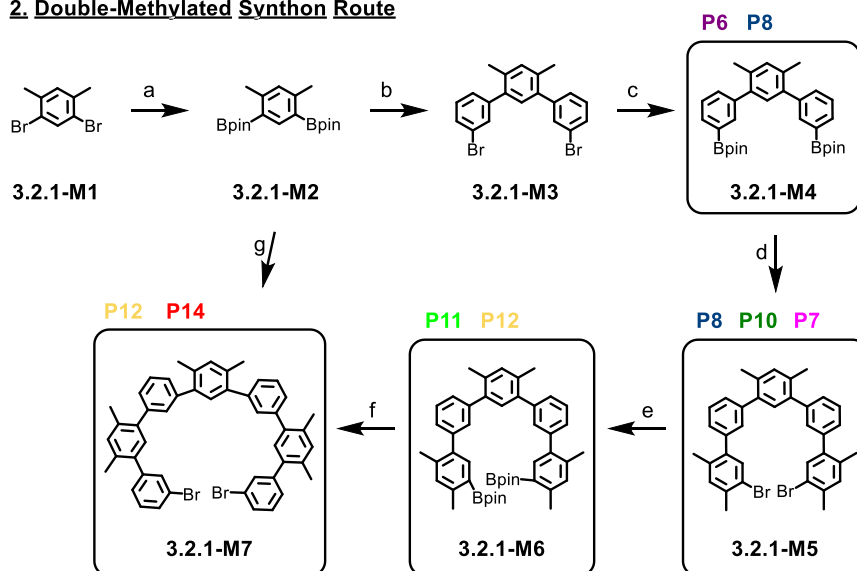
The building blocks used to synthesize each macrocycle are color coded along **Scheme 21**, **Scheme 22** and **Scheme 23** (on top of the respective structures). As previously commented, a Suzuki cross-coupling between the corresponding borylated and brominated units was conducted to synthesize the final macrocycle. For example, in the synthesis of **3.2.1-P9Prec**, the synthon **3.2.1-N5** from “Non-Methylated Synthon Route” in **Scheme 21**, and the synthon **3.2.1-S6** from “Single-Methylated Synthon Route” in **Scheme 23** were used, yielding the macrocycle **3.2.1-P9Prec** in 11 %.

## 1. Non-Methylated Synthon Route



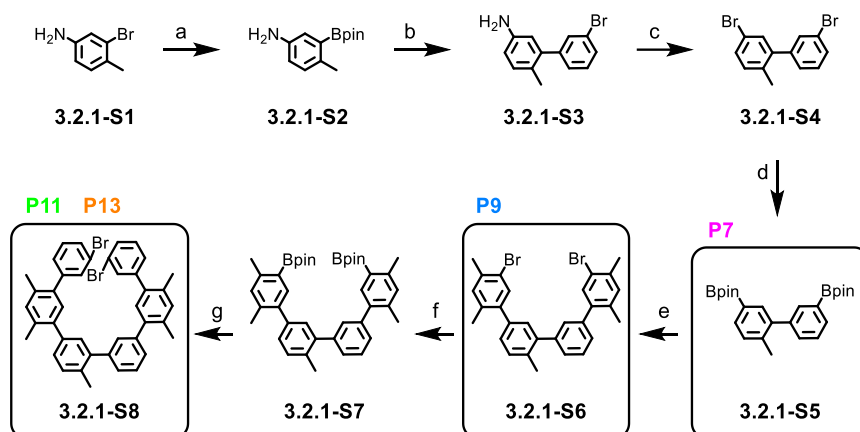
**Scheme 21.** a) 1,5-Dibromo-2,4-dimethylbenzene,  $K_2CO_3$ ,  $Pd(PPh_3)_4$ , DMF,  $H_2O$ ,  $80\text{ }^\circ\text{C}$ , 16 h, 46 %, b)  $B_2(pin)_2$ , AcOK,  $Pd(dppf)Cl_2$ , Dioxane,  $80\text{ }^\circ\text{C}$ , 16 h, 63 %, c) 1,3-Dibromo-benzene,  $K_2CO_3$ ,  $Pd(PPh_3)_4$ , DMF,  $H_2O$ ,  $80\text{ }^\circ\text{C}$ , 16 h, 50 %, d)  $B_2(pin)_2$ , AcOK,  $Pd(dppf)Cl_2$ , Dioxane,  $80\text{ }^\circ\text{C}$ , 16 h, 33 %, e) 1,5-Dibromo-2,4-dimethylbenzene,  $K_2CO_3$ ,  $Pd(PPh_3)_4$ , DMF,  $H_2O$ ,  $80\text{ }^\circ\text{C}$ , 16 h, 35 %, f)  $B_2(pin)_2$ , AcOK,  $Pd(dppf)Cl_2$ , Dioxane,  $80\text{ }^\circ\text{C}$ , 16 h, 55 %.

## 2. Double-Methylated Synthon Route



**Scheme 22.** a)  $B_2(pin)_2$ , AcOK,  $Pd(dppf)Cl_2$ , Dioxane,  $80\text{ }^\circ\text{C}$ , 16 h, 69 %, b) 1,3-Dibromobenzene,  $K_2CO_3$ ,  $Pd(PPh_3)_4$ , DMF,  $H_2O$ ,  $80\text{ }^\circ\text{C}$ , 16 h, 55 %, c)  $B_2(pin)_2$ , AcOK,  $Pd(dppf)Cl_2$ , Dioxane,  $80\text{ }^\circ\text{C}$ , 16 h, 58 %, d) 1,5-Dibromo-2,4-Dimethylbenzene,  $K_2CO_3$ ,  $Pd(PPh_3)_4$ , DMF,  $H_2O$ ,  $80\text{ }^\circ\text{C}$ , 16 h, 43 %, e)  $B_2(pin)_2$ , AcOK,  $Pd(dppf)Cl_2$ , Dioxane,  $80\text{ }^\circ\text{C}$ , 16 h, 46 %, f) 1,3-Dibromobenzene,  $K_2CO_3$ ,  $Pd(PPh_3)_4$ , DMF,  $H_2O$ ,  $80\text{ }^\circ\text{C}$ , 16 h, 39 %, g) 3.2.1-M3,  $K_2CO_3$ ,  $Pd(PPh_3)_4$ , DMF,  $H_2O$ ,  $80\text{ }^\circ\text{C}$ , 16 h, 33 %.

### 3. Single-Methylated Synthon Route



**Scheme 23.** **a)**  $\text{B}_2(\text{pin})_2$ , AcOK, Pd(dppf)Cl<sub>2</sub>, Dioxane, 80 °C, 16 h, 83%, **b)** 1,3-Dibromobenzene, K<sub>2</sub>CO<sub>3</sub>, Pd(PPh<sub>3</sub>)<sub>4</sub>, DMF, H<sub>2</sub>O, 80 °C, 16 h, 72 %, **c)** HBr, NaNO<sub>2</sub>, CuBr, MeCN, H<sub>2</sub>O, -30 °C to r.t., 24 h, 79 %, **d)**  $\text{B}_2(\text{pin})_2$ , AcOK, Pd(dppf)Cl<sub>2</sub>, Dioxane, 80 °C, 16 h, 82 %, **e)** 1,5-Dibromo-2,4-Dimethylbenzene, K<sub>2</sub>CO<sub>3</sub>, Pd(PPh<sub>3</sub>)<sub>4</sub>, DMF, H<sub>2</sub>O, 80 °C, 16 h, 51 %, **f)**  $\text{B}_2(\text{pin})_2$ , AcOK, Pd(dppf)Cl<sub>2</sub>, Dioxane, 80 °C, 16 h, 43 %, **g)** 1,3-Dibromobenzene, K<sub>2</sub>CO<sub>3</sub>, Pd(PPh<sub>3</sub>)<sub>4</sub>, DMF, H<sub>2</sub>O, 80 °C, 16 h, 45 %.

### 3.2.2 P8 Macrocycle

In this subsection, we will delve into the results of **3.2.1-P8-Des**, the first example of the family of cyclopenta-ring-fused oligo(*m*-phenylene) macrocycles, which bears eight pentagonal and hexagonal rings, and eight radicals. As previously commented, it is expected that this macrocycle will exhibit a positive curvature due to its in-solution reported analogue.

We will explore its on-surface synthesis, studying the phases at r.t. and after the thermal oxidative ring closure reaction, showing the different products obtained after the reaction. We will induce dehydrogenation reactions with the tip of the probe and the structure and curvature of **3.2.1-P8-Des** will be analyzed by means of constant height STM, nc-AFM, force spectroscopy<sup>207</sup> and DFT calculations. Finally, the electronic properties will be addressed by means of STS and dI/dV mapping.

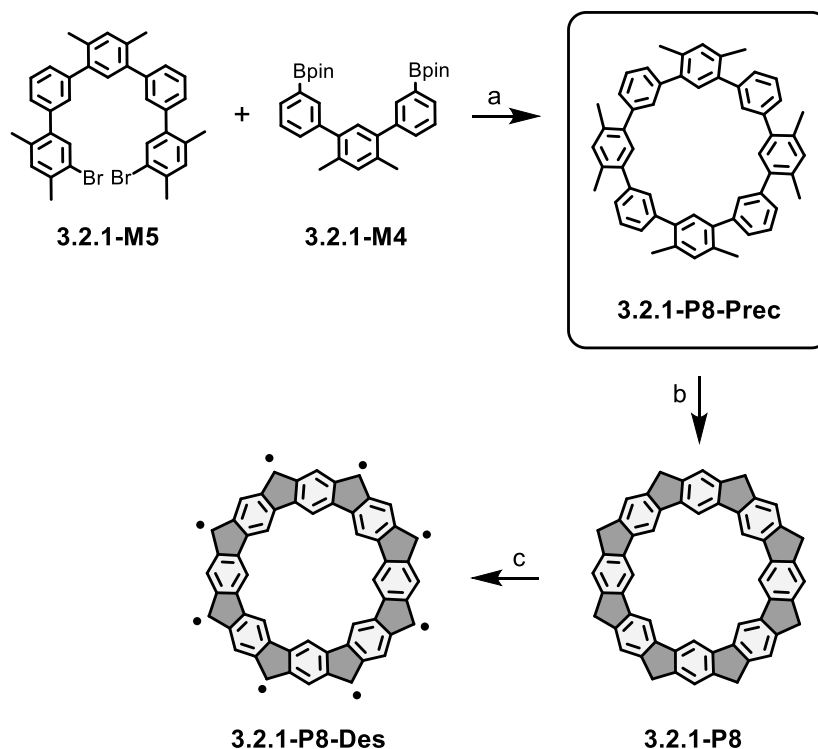
#### *In-Solution synthesis and on-surface characterization of the r.t phase*<sup>208</sup>

**3.2.1-P8-Prec** was in-solution synthesized and characterized (14 % yield) after conducting a Suzuki-Miyaura cross-coupling reaction between **3.2.1-M5** and **3.2.1-M4** (see **Scheme 24**). Subsequently, **3.2.1-P8-Prec** was sublimated from a tantalum pocket at 260 °C and deposited onto a clean Au(111) substrate held at r.t.

---

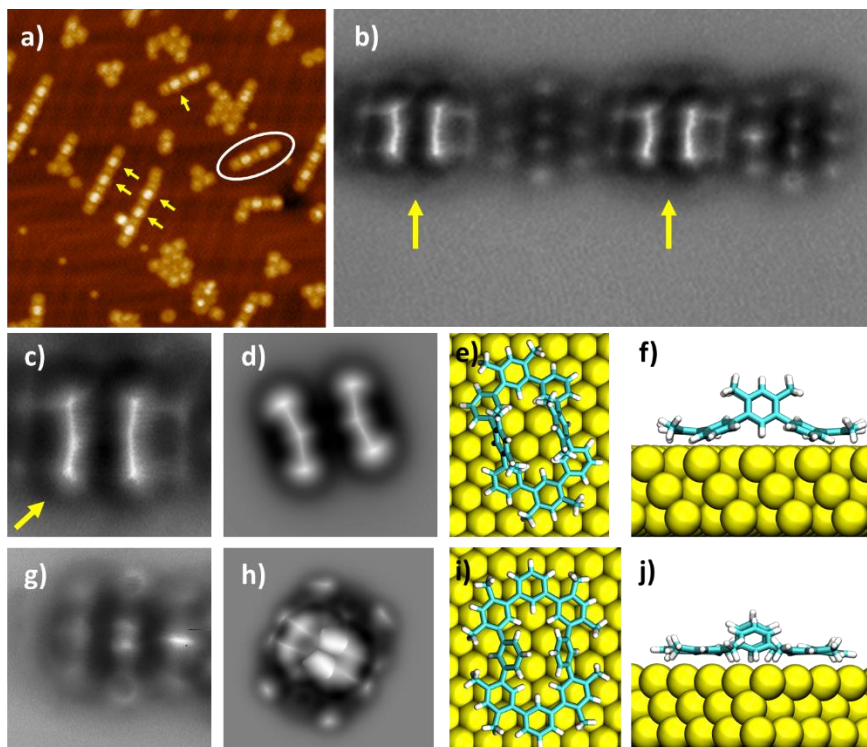
<sup>207</sup> **a)** Y. Sugimoto, P. Pou, M. Abe, P. Jelinek, R. Pérez, S. Morita, Ó. Custance, *Nature*, **2007**, *446*, 64–67. **b)** S. Kawai, A. S. Foster, T. Björkman, S. Nowakowska, J. Björk, F. F. Canova, L. H. Gade, T. A. Jung, E. Meyer, *Nat. Commun.*, **2016**, *7*, 11559. **c)** Z. Sun, M. P. Boneschanscher, I. Swart, D. Vanmaekelbergh, P. Liljeroth, *Phys. Rev. Lett.*, **2011**, *106*, 046104. **d)** M. A. Lantz, H. J. Hug, R. Hoffmann, P. J. A. Van Schendel, P. Kappenberger, S. Martin, A. Baratoff, H.-J. Güntherodt, *Science*, **2001**, *291*, 2580–2583.

<sup>208</sup> This work is a collaboration between the MOREFUN group from the University of Granada, where the monomer was synthesized; and the Nanosurf Lab from The Institute of Physics of the Czech Academy in Czech Republic, where the high-resolution STM and nc-AFM images, the STS spectroscopies and the computational calculations were conducted.



**Scheme 24.** Schematic representation of the synthetic strategy towards **3.2.1-P8-Des**. **a)**  $\text{Cs}_2\text{CO}_3$ ,  $\text{Pd}(\text{dppf})\text{Cl}_2$ , MeCN, Reflux, 24 h, 14 %. **b)** Sublimation onto a Au(111) surface and subsequent annealing at 310 °C. **c)** Tip induced dehydrogenations.

**Figure 53 a** shows a topographic STM image presenting different self-assembly patterns: islands, linear assemblies and individual molecules. An examination of these assemblies revealed two distinct conformations for **3.2.1-P8-Prec**. Notably, one of these conformations exhibits a greater apparent height compared to the other (bright monomers depicted with a yellow arrow in the STM image in **Figure 53 a**). Inspection of a linear assembly with nc-AFM in **Figure 53 b** (depicted with a white ellipse in **Figure 53 a**) revealed insights of these two different conformations of **3.2.1-P8-Prec**. On the one hand, **Figure 53 c, d, e** and **f** (experimental nc-AFM image, simulated nc-AFM image, top and side views of the DFT minimized chemical structure, respectively) detail the conformer (**3.2.1-P8-Prec-Con1**) with higher apparent height. **3.2.1-P8-Prec-Con1** presents two of the four methylated benzene rings facing to each other almost parallel between them in an almost perpendicular orientation with respect to the surface. On the other hand, **Figure 53 g, h, i** and **j**, show the second conformation (**3.2.1-P8-Prec-Con2**), where the central non-methylated benzene rings are less tilted in comparison with **3.2.1-P8-Prec-Con1**, presenting a lower height.



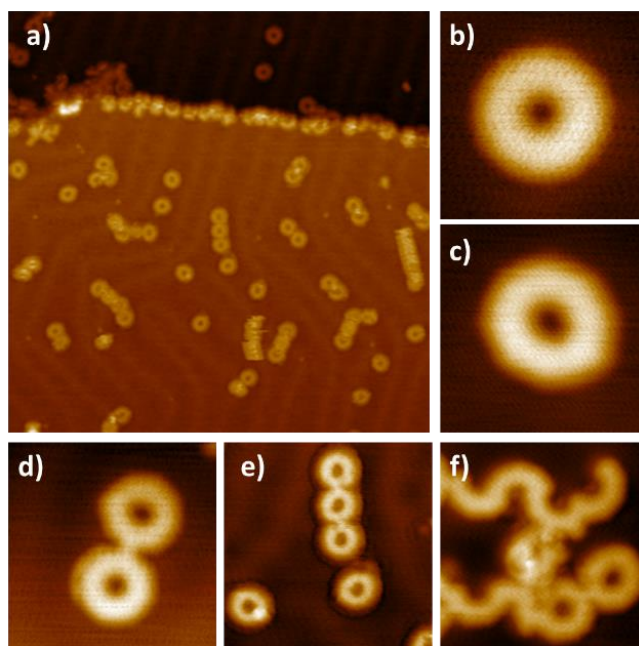
**Figure 53.** R.t. phases of **3.2.1-P8-Prec** on Au(111). **a)** Topographic constant current STM image. Yellow arrows depict one of the conformations of **3.2.1-P8-Prec** (**3.2.1-P8-Prec-Confl1**). White ellipse shows the self-assembly magnified in **b)**. **b)** Nc-AFM image showing the two different conformations of **3.2.1-P8-Prec**. **c)** Nc-AFM detailed image of **3.2.1-P8-Prec-Confl1**. **d)** Nc-AFM image simulation of **3.2.1-P8-Prec-Confl1**. **e)** and **f)** DFT minimized structure of **3.2.1-P8-Prec-Confl1** on the Au(111) lattice. **g)** Nc-AFM detailed image of **3.2.1-P8-Prec-Confl2**. **h)** Nc-AFM image simulation of **3.2.1-P8-Prec-Confl2**. **i)** and **j)** DFT minimized structure of **3.2.1-P8-Prec-Confl2** on the Au(111) lattice. Scanning parameters were as follows: **(a)** 50 nm × 50 nm, 10 pA, 50 mV, **(b)** 8 nm × 4 nm, 2 mV, **(c)** 1.7 nm × 1.7 nm, 2 mV, **(g)** 2 nm × 2 nm, 2 mV.

### Ring closure reaction

Further annealing of the sample for 10 minutes at 310 °C triggered the ring closure reaction between the methyl moieties and the benzene rings. **Figure 54 a** shows a topographic STM image where different molecular topologies can be observed encompassing: perfect symmetric round **3.2.1-P8** molecules (8 % yield after the analysis of 2000 species<sup>209</sup>, **Figure 54 b**), asymmetric **3.2.1-P8** molecules (**Figure 54 c**), and some side products like dimers (**Figure 54 d**), trimers (**Figure 54 e**) and other defective species as the opened macrocycles in **Figure 54 f**. We ascribe the synthesis of the observed oligomers to an inter coupling reaction between different macrocycles as a consequence of the activation of the methyl groups.

<sup>209</sup> This yield is calculated among all the cyclodehydrogenated macrocycles (those individual and forming oligomers, pristine and defected) in the terraces after annealing the sample at 310 °C. Same for subsequent subsections regarding all the synthesized macrocycles.





**Figure 54.** **3.2.1-P8** and side products obtained after annealing the Au(111) sample at 310 °C for 10 minutes. **a)** Topographic constant current STM image. **b)** Constant current detailed STM image of **3.2.1-P8**. **c)** STM image of an asymmetric **3.2.1-P8**. **d)** STM image of a **3.2.1-P8** dimer. **e)** STM image of a **3.2.1-P8** trimer. **f)** STM image of a defective polymer. Scanning parameters were as follows: **(a)** 50 nm × 50 nm, 10 pA, 50 mV, **(b)** 3 nm × 3 nm, 10 pA, 50 mV, **(c)** 3 nm × 3 nm, 10 pA, 50 mV, **(d)** 5 nm × 5 nm, 10 pA, 50 mV, **(e)** 10 nm × 10 nm, 10 pA, 50 mV, **(f)** 6 nm × 6 nm, 10 pA, 50 mV.

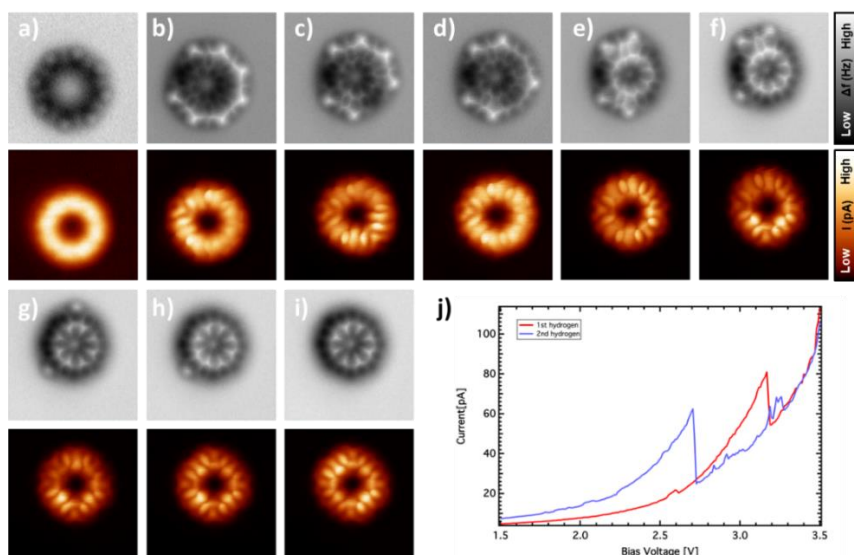
Regarding the round perfect **3.2.1-P8**, constant height STM and nc-AFM images in **Figure 55 a** showed a fully hydrogenated symmetric **3.2.1-P8** with eight bright lobes related to the out-of-plane CH<sub>2</sub> moieties of the pentagonal rings. Resolution of the pentagonal and hexagonal rings of the macrocycle in the nc-AFM image from **Figure 55 a** was not possible due to a positive bowl curvature of **3.2.1-P8**. Additionally, approaching the tip resulted in a displacement of the molecule, disabling a better resolution.

No signs of thermal dehydrogenation (radical CH· moiety at the apex of the pentagonal rings) were found at this temperature. Therefore, tip-induced dehydrogenations with a CO tip were employed to sequentially cleave single hydrogens in a controlled manner. **Figure 55** shows the complete series of dehydrogenations starting from a fully hydrogenated molecule (**Figure 55 a**) and yielding a fully dehydrogenated molecule (**Figure 55 i**). Every cleaving step was recorded, obtaining nc-AFM and constant height STM images simultaneously. The dehydrogenation procedure was based on the injection of inelastic electrons through a bias ramp while locating the tip on top of the pentagonal ring until observing a sudden jump in the current channel. **Figure 55 j** shows the first and second events of dehydrogenation of **3.2.1-P8**. Afterward, an nc-AFM image was recorded to see the produced changes in the molecule. Typically, biases ranged from 2.7 to 3.5 eV to carry out the dehydrogenations.

After the first hydrogen cleavage, the molecule showed less mobility on top of the surface. This enabled us to further approach the tip, improving the image resolution. From **Figure 55 b** to

**Figure 55 d**, almost all the hexagonal and pentagonal rings were visible in the nc-AFM images, showing an “almost flat” conformation in these intermediates. We relate the observed dark depressions at some pentagonal rings (in the nc-AFM images) to a strong interaction of the radical with the surface. This radical-surface interaction bends the pentagonal ring towards the surface creating the black depression in the image, while releasing, at the same time, the inner strain of the molecule and planarizing the other parts of the structure<sup>210</sup>.

The sequential removal of hydrogen atoms triggered the loss of the resolution from the pentagonal and hexagonal rings in the AFM images due to a curved conformation of **3.2.1-P8** that adopts a truncated-cone shape (bowl curvature). As stated before, this curvature is not only specific of our on-surface study. Liu et al.<sup>153</sup> also observed this curvature in the X-Ray diffraction analysis of their analogue molecule. Liu et al. described a plausible theoretical activation barrier for the curvature inversion (convex-concave), however, no signs of this inversion were observed neither during the tip-induced dehydrogenations nor upon performing bias ramps on **3.2.1-P8-Des**. Although theoretical calculations have not been accounted yet for this dynamics of **3.2.1-P8-Des** on top of the Au(111) surface, we ascribe this observed higher stability of the convex conformation to the higher contact surface of the convex conformation with the Au(111) substrate in comparison with the concave conformation (higher amount of Van der Waals interactions).



**Figure 55.** Site-selective **3.2.1-P8** molecule dehydrogenation by the SPM probe after applying a bias ramp. **a)** to **i)** Changes in molecule after sequential dehydrogenations. Top: nc-AFM image, bottom: constant current STM image simultaneously obtained with a CO functionalized tip. **j)** Current vs bias plot of two dehydrogenation events. Every image was acquired with the same scanning parameters (**a)** to **(i)**: 3 nm × 3 nm, 5 mV.

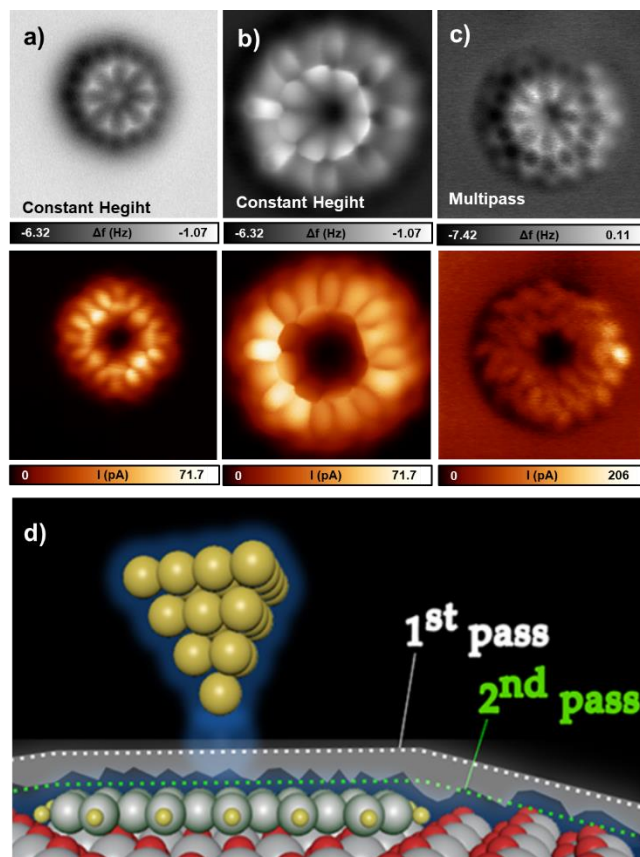
<sup>210</sup> M. Di Giovannantonio, K. Eimre, A. V. Yakutovich, Q. Chen, S. Mishra, J. I. Urgel, C. A. Pignedoli, P. Ruffieux, K. Müllen, A. Narita, R. Fasel, *J. Am. Chem. Soc.*, **2019**, *141*, 12346–12354.

After the whole tip-induced dehydrogenation sequence, the successful synthesis of **3.2.1-P8-Des** was assumed as no bright protrusions remained in the structure as evidenced by the nc-AFM image (**Figure 56 a**). In order to obtain a better molecular resolution, the tip was further approached in **Figure 56 b** (-62 pm with respect to **Figure 56 a**), enabling the visualization of the hexagonal rings of the structure. To further improve the molecular structure, the multipass technique<sup>211</sup> was performed, obtaining the nc-AFM and the STM images in **Figure 56 c**, where the pentagonal and hexagonal rings were observed.

The so-called multipass technique is a powerful tool to visualize curved molecules with nc-AFM. **Figure 56 d** shows a summary of how this technique works. Firstly, it is utilized the frequency shift as a closed feedback loop for a first line scan of the molecule. A  $\Delta f$  value for the topographic set point is settled, aligning with a probe-surface separation regime where the atomic interaction responsible for contrast is minimally detected, and the Van der Waals forces prevails (white line in **Figure 56 d**). Secondly, the second line scan is executed in an open feedback loop, utilizing the topography recorded in the first line scan. During this process a constant offset distance is applied, progressively bringing the probe closer to the surface for a better resolution in the image (green line in **Figure 56 d**).

---

<sup>211</sup> C. Moreno, O. Stetsovych, T. K. Shimizu, O. Custance, *Nano Lett.*, **2015**, *15*, 2257–2262.

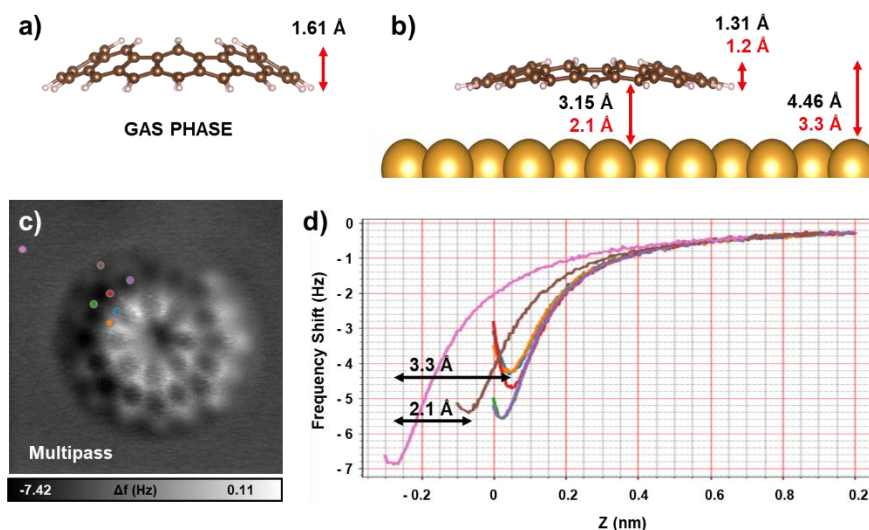


**Figure 56.** 3.2.1-P8-Des structural characterization. **a) & b)** Nc-AFM (top) and constant current STM images (bottom) at different heights (b at -62 pm in respect to a). Nc-AFM and STM were simultaneously acquired. **c)** Nc-AFM and constant current STM images obtained by multipass technique. **d)** Methodology for acquiring multipass images. Image adapted with permission<sup>211</sup>. Copyright 2015, American Chemical Society. Scanning parameters were as follows: (a): 3 nm  $\times$  3 nm, 5 mV, (b): 1.9 nm  $\times$  1.9 nm, 2 mV, (c): 3 nm  $\times$  3 nm, 5 mV.

### Adsorption analysis

In order to gain more insights into the structure of **3.2.1-P8-Des** and its adsorption configuration, DFT calculations in gas phase, DFT + vdW calculations on Au(111) and force spectroscopy measurements were performed. **Figure 57 a** depicts the chemical structure of **3.2.1-P8-Des** in gas phase, which exhibits an internal molecular height of 1.61 Å. On the other hand, **3.2.1-P8-Des** on top of a Au slab (**Figure 57 b**) yielded a height value of 1.31 Å. This height difference is ascribed to a slight planarization of the molecule due to the Van der Waals interactions with the surface. The height of the molecule with respect to the surface was also calculated from the computational simulations (3.15 Å) and compared with the experimentally obtained values from the z-spectroscopy (**Figure 57 d**). The values are included in **Figure 57 b**, where black values correspond to theoretical calculations and red ones to the experimental z-spectroscopy. In this regard, a good agreement in the height of the molecule (1.3 Å vs 1.2 Å) was obtained between the experiment and the theory, supporting the curvature of the molecule. On the other hand, the same agreement was not achieved in the height of the molecule with

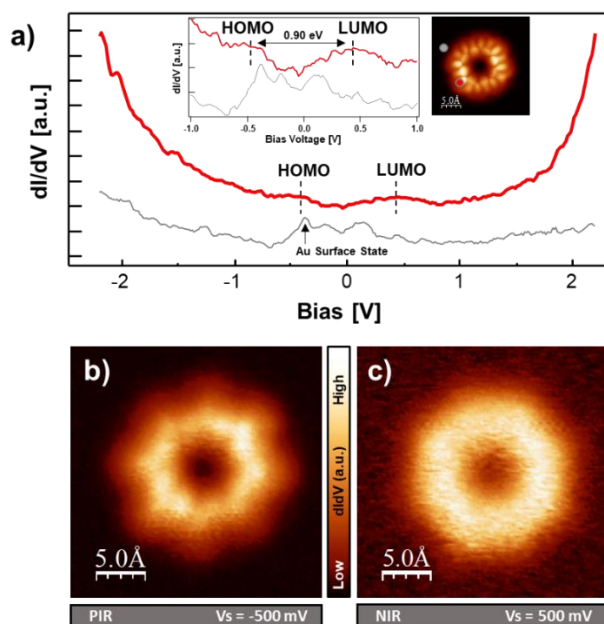
respect to the surface. We assume that this high difference (50 %) can be related to a strong interaction of the radicals with the surface, reducing the molecule-surface distance. In this sense, the DFT + vdW method might be underestimating the interaction of the free radicals from **3.2.1-P8-Des** with the surface.



**Figure 57.** Adsorption characterization of **3.2.1-P8-Des** on Au(111). **a)** **3.2.1-P8-Des** chemical structure in gas phase after minimization by DFT. **b)** **3.2.1-P8-Des** chemical structure adsorbed on Au(111) after minimization by QM/MM. Black/red distances refer to calculated/experimental values from d). **c)** Reference nc-AFM image where force spectroscopies were conducted. **d)** Force spectroscopy curves. Scanning and spectrum parameters were as follows: (c) 3 nm × 3 nm, 5 mV, (d) 2 mV.

### Electronic characterization

Moreover, **Figure 58** shows the electronic characterization of **3.2.1-P8-Des** by means of STS point spectroscopy and dI/dV mapping with a CO functionalized tip. The STS point spectroscopy (**Figure 58 a**) shows broad peaks at -0.44 eV and 0.46 eV, which can be related with the HOMO and LUMO states, respectively (the HOMO-LUMO gap is 0.90 eV). The highly intense states observed below -2 V and beyond 2 V can be related to the HOMO - 1 and the LUMO + 1 states of the molecule. In this regard, dI/dV mapping was also utilized (**Figure 58 b** and c) to characterize the LDOS of the HOMO and LUMO states. Firstly, the HOMO state, measured at -500 mV, presented a 2-fold symmetric structure (in a similar fashion to the CHSTM image in the inset of **Figure 58 a**). On the other hand, the measurement of the LUMO state, obtained at 500 mV, shows a fully symmetric state in the macrocycle.



**Figure 58.** Electronic characterization of **3.2.1-P8-Des** on Au(111). **a)** STS point spectra. Spectra acquisition points are color coded in the constant height STM image in the inset. **b)**  $dI/dV$  map of the HOMO state acquired at -500 mV. **c)**  $dI/dV$  map of the LUMO state acquired at 500 mV. Scanning and spectra parameters were as follows: (a):  $V_{Mod} = 10$  mV (spectra), 5 mV (constant height STM image), (b)  $V_{Mod} = 10$  mV, (c)  $V_{Mod} = 10$  mV.

Finally, it is worthy commenting about the ground state of the synthesized **3.2.1-P8-Des**. In the case of the in-solution reported analogue molecule, Liu et al.<sup>153</sup> described a singlet open shell ground state. This molecule exhibited global aromaticity, encompassing two independent triplet ring currents whose total sum was a singlet, matching with their experimental magnetic characterization. The Baird's<sup>212</sup> rule justified the aromatic character of these two triplet ring currents. In our on-surface scenario, the ground state described by Liu et al. might not be valid due to the change of geometry of **3.2.1-P8-Des** in solution vs on the surface (Van der Waals interactions with the surface), and due to the possible strong interactions of the radicals with the Au(111) (there is low adsorption height of the molecule, shown in **Figure 57**). Therefore, further calculations are required for obtaining the electronic ground state of **3.2.1-P8-Des**.

### Summary

**3.2.1-P8-Des** was successfully synthesized, including the in-solution synthesis and characterization of the precursor, the study of the r.t. phase after the precursor sublimation, the analysis of the Au(111) sample after the ring closure reaction and the final tip-induced dehydrogenation.

Final **3.2.1-P8-Des** exhibited a positively curved structure (bowl) that was characterized by means of nc-AFM, CH-STM and multipass nc-AFM. Electronic characterization of **3.2.1-P8-Des** revealed peaks corresponding to the HOMO and LUMO with a 0.9 eV HOMO-LUMO

<sup>212</sup> N. C. Baird, *J. Am. Chem. Soc.*, **1972**, *94*, 4941–4948.

gap. Z-Spectroscopy, DFT and QM/MM calculations provided valuable insights into the adsorption characteristics of the curved **3.2.1-P8-Des** on the Au(111) surface, indicating a possible symmetric interaction between the surface and the molecule (discrepancy in height between theoretical and experimental values).

Further calculations will be conducted to accurately determine the electronic ground state and the magnetic properties (ACID and NICS), which could involve DFT spin restricted and higher calculation methods with different electronic multiplicities and symmetries.

### 3.2.3 P9 Macrocycle

The following subsection deals with the next example in the family of macrocycles, **3.2.1-P9-Des**. As a first hypothesis, we expected a planar geometry for **3.2.1-P9-Des**, due to a better matching of the angles and bond lengths to those expected for  $sp^2$  carbons in five- and six-membered rings. Beyond its structure and geometry, the odd number of  $\pi$  radicals in **3.2.1-P9-Des** makes it an interesting compound to study its electronic properties and its magnetic phenomena. To the best of our knowledge, this is the first synthesis described towards **3.2.1-P9-Des**, as its synthesis has remained elusive for the in-solution methods.

Next, we will delve into the experimental details of its on-surface synthesis and characterization, accompanied by different high-level quantum chemistry calculations, including DFT, CASSCF(11,10), CASSCF(10,10)+NEVPT2 or DMRG in order to fully understand the ground state of the molecule and its exotic aromatic and magnetic structure.

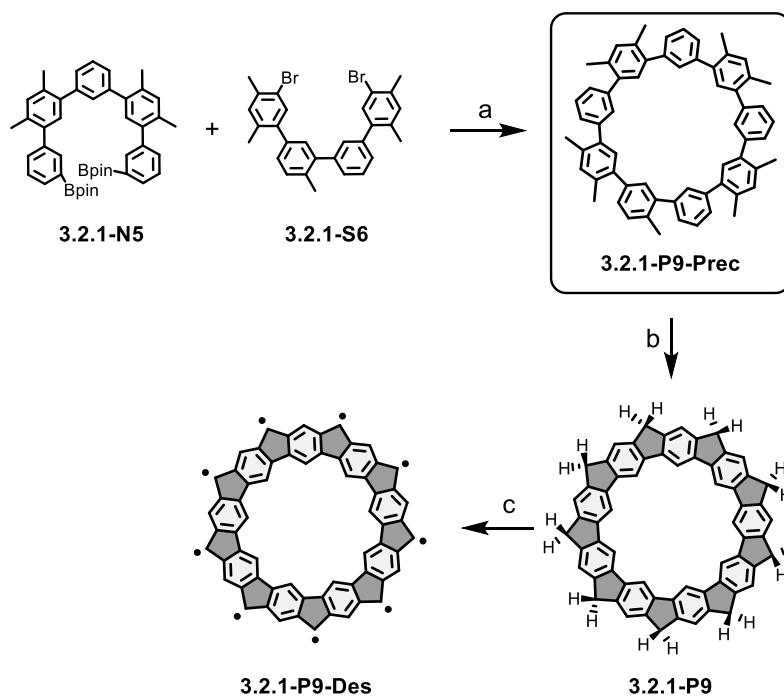
#### *In-Solution synthesis and on-surface characterization of the r.t phase*<sup>213</sup>

**Scheme 25** shows the successful in-solution synthesis of the precursor **3.2.1-P9-Prec**, 11 % yield, after the final macrocyclization reaction. Subsequently, it was sublimed from a tantalum pocket (260 °C) on a pristine Au(111) surface held at r.t. Topography STM image in **Figure 59 a** shows some linear arrangements and some clusters of **3.2.1-P9-Prec**, where the precursor has an oval shape with two bright protrusions per molecule in the center of the macrocycle. Although the conformation of all the **3.2.1-P9-Prec** was very similar, no repetitive self-assembled clusters were found.

---

<sup>213</sup> This work is a collaboration between the MOREFUN group from the University of Granada, where the monomer was synthesized; and the Nanosurf Lab from The Institute of Physics of the Czech Academy in Czech Republic, where the high-resolution STM and nc-AFM images, the STS spectroscopies and the computational calculations were conducted.

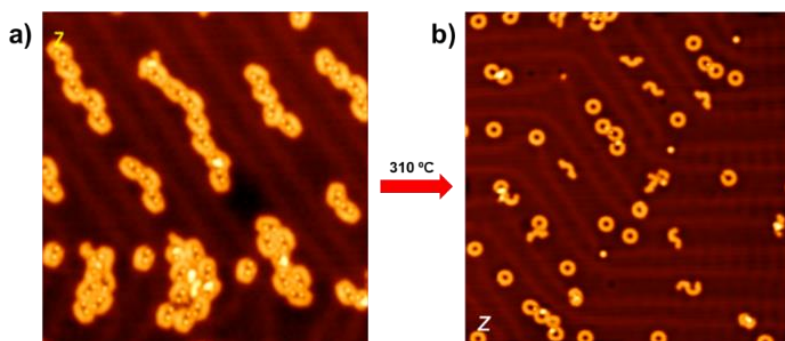




**Scheme 25.** Schematic representation of the synthetic strategy towards **3.2.1-P9-Des**. **a)**  $\text{Cs}_2\text{CO}_3$ ,  $\text{Pd}(\text{dppf})\text{Cl}_2$ , MeCN, Reflux, 24 h, 11 %. **b)** Sublimation on a Au(111) surface and subsequent annealing at 310 °C. **c)** Tip-induced dehydrogenations.

### Ring closure reaction

Subsequent annealing at 310 °C led to the formation of **3.2.1-P9** (3 % yield after the analysis of 1000 species). **Figure 59 b** shows an overview topography STM image acquired after the thermal annealing, revealing the circular shape of **3.2.1-P9**, predominantly found at the fcc regions of the herringbone reconstruction of the Au(111) substrate (as expected). Some other side products were found as oligomers or defective molecules (in a similar fashion as described for **3.2.1-P8**).

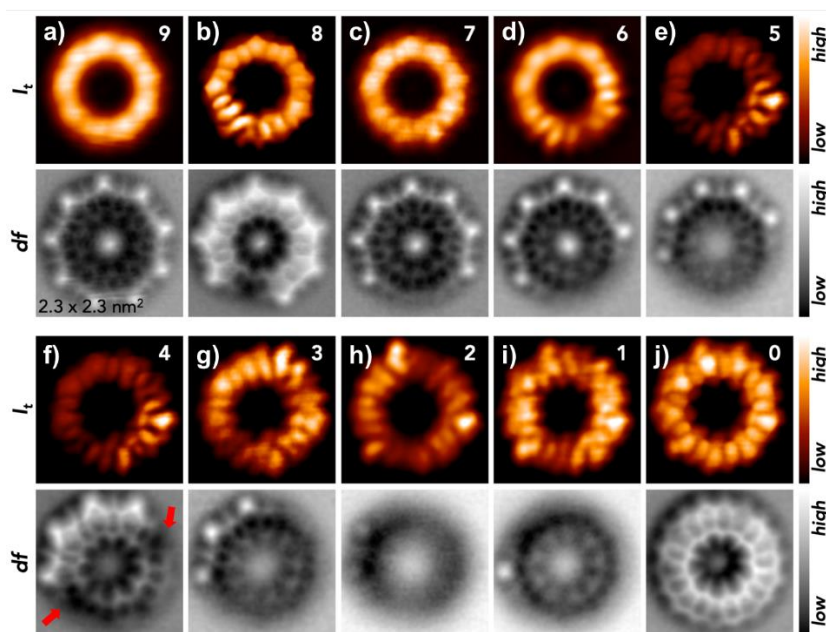


**Figure 59.** On-surface synthesis of **3.2.1-P9** molecule on Au(111) surface. **a)** Constant current STM image of **3.2.1-P9-Prec** at r.t.. **b)** Constant current STM image of **3.2.1-P9** after annealing the Au (111) sample at 310 °C. Some oligomers and some defective molecules were also found. Scanning parameters were as follows: (a) 30 nm x 30 nm, 10 pA, 50 mV, (b) 50 nm x 50 nm, 10 pA, 50 mV.

**Figure 60 a** represents high-resolution constant height STM and nc-AFM images of **3.2.1-P9** revealing its inner structure, including five and six-membered rings, and nine bright protrusions corresponding to the CH<sub>2</sub> moieties in the five-membered rings. This observation confirms the oxidative ring closure reaction of the nine methyl groups affording the formation of nine five-membered rings.

#### Tip-induced dehydrogenations

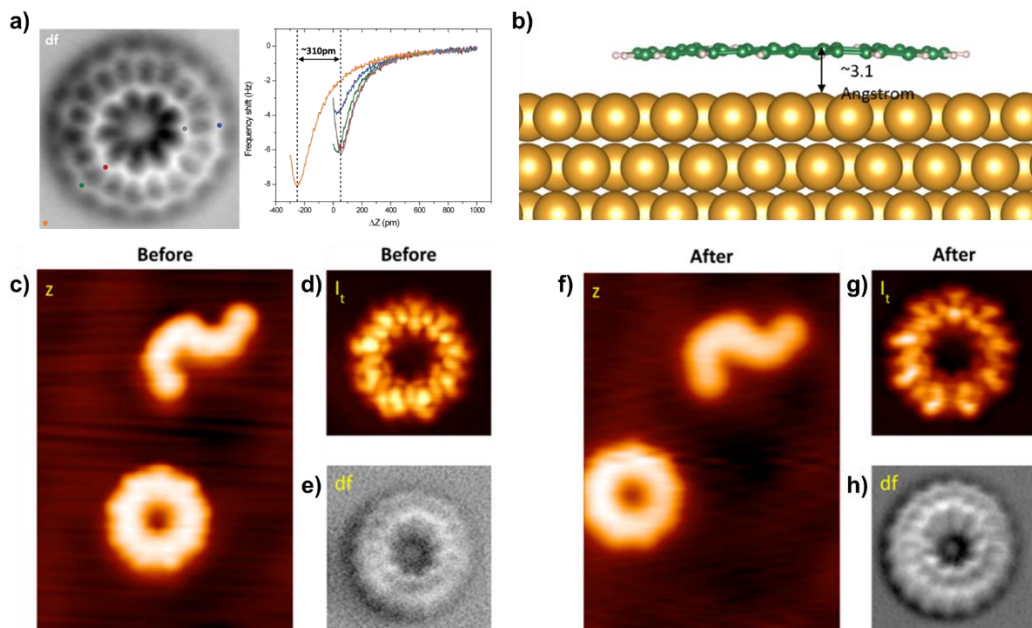
In the next step, we employed tip-induced manipulation to sequentially remove the extra nine hydrogens (**Figure 60**), giving rise to the formation of the final product **3.2.1-P9-Des** (**Figure 60 j**). High-resolution AFM images show that at some stages of the dehydrogenation, some dehydrogenated 5-membered rings are significantly deformed due to the strong interaction of the pentagonal apex carbon atom with the metal surface (e.g. red arrows in **Figure 60 f**). Interestingly, after the complete dehydrogenation of all the pentagonal rings, the molecule becomes planar. This indicates that the formation of **3.2.1-P9-Des** macrocycle stabilizes the sp<sup>2</sup> configuration.



**Figure 60.** Site-selective **3.2.1-P9** dehydrogenation by SPM probe after applying a bias ramp. The number of hydrogens that remains in the molecule is depicted in the top right part of the image. Top: constant current STM image; bottom: nc-AFM image simultaneously acquired. Every image was obtained with the same scanning parameters:  $2.3 \text{ nm} \times 2.3 \text{ nm}$ , 3 mV.

### Adsorption analysis

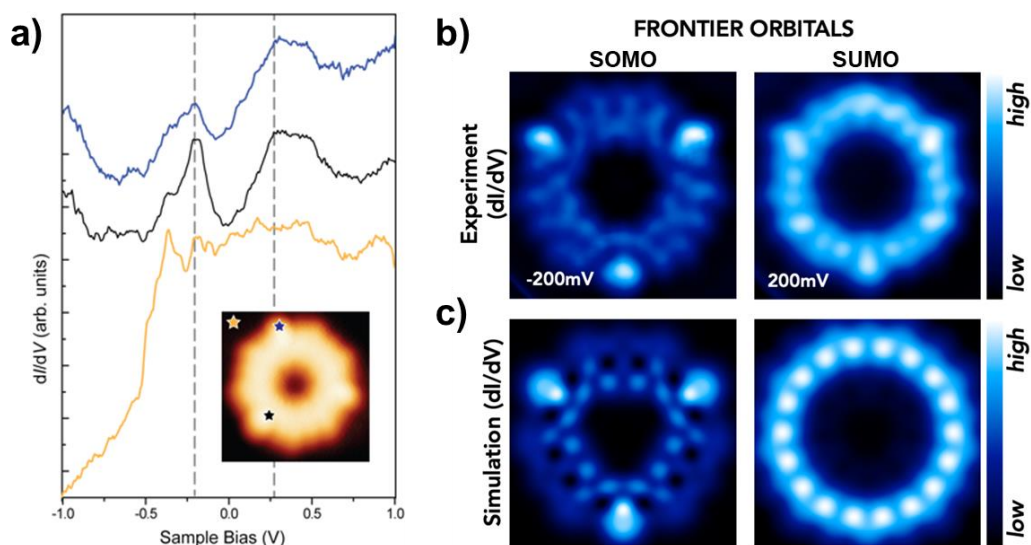
The planar conformation of the **3.2.1-P9-Des** is further demonstrated by force spectroscopy acquired over different positions on the outer and inner rings of the molecule (**Figure 61 a**). Moreover, the difference between the minima of the  $df(z)$  curve acquired on bare Au(111) surface and **3.2.1-P9-Des** shows that the adsorption height of the molecule is  $\sim 300 \text{ pm}$  above the surface, which matches well with a calculated adsorption height of  $310 \text{ pm}$  obtained from the total energy DFT + vDW calculations (**Figure 61 b**). In opposite with what we observed with **3.2.1-P8-Des** (adsorption height was  $\sim 210 \text{ pm}$  above the surface), the adsorption height of **3.2.1-P9-Des** indicates a relatively weak interaction with the Au(111) surface. This scenario is further confirmed by the lateral manipulation of **3.2.1-P9-Des** that did not alternate its chemical structure as shown in **Figure 61 c to h**.



**Figure 61.** Characterization of the weak substrate-3.2.1-P9-Des interaction. **a)** Nc-AFM image and force spectroscopy. Surface-molecule distance is depicted in the force spectroscopy. Acquiring points for force spectroscopy are depicted in the nc-AFM image. **b)** Chemical model of 3.2.1-P9-Des on a Au(111) slab, minimized by DFT + vdW. The molecule-surface distance is indicated. Carbon atoms are shown green, hydrogen atoms white and gold atoms yellow. **c)** Constant current STM image of the initial position of the 3.2.1-P9-Des. **d) & e)** Constant height STM and nc-AFM of 3.2.1-P9-Des before the lateral manipulation, respectively. **f)** Constant current STM image of the final position of the 3.2.1-P9-Des. **g) & h)** Constant height STM and nc-AFM of 3.2.1-P9-Des after the lateral manipulation, respectively. Scanning parameter were as follows: **(a)** 2.3 nm × 2.3 nm, 3 mV (nc-AFM image), 2 mV (curves), **(c)** 5 nm × 7 nm, 10 pA, 50 mV, **(d)** 2.5 nm × 2.5 nm, 2 mV, **(e)** 2.5 nm × 2.5 nm, 2 mV, **(f)** 5 nm × 7 nm, 10 pA, 50 mV, **(g)** 2.5 nm × 2.5 nm, 2 mV, **(h)** 2.3 nm × 2.3 nm, 2 mV.

### Electronic characterization

To characterize the electronic structure of 3.2.1-P9-Des, STS was conducted and compared with many-body quantum chemistry calculations. **Figure 62 a** represents the point spectra STS data acquired on 3.2.1-P9-Des and on Au(111), revealing a relatively small gap ( $\sim 480$  mV) determined by two resonant states located -200 and 280 mV, respectively. Constant height  $dI/dV$  map acquired at -200 mV shows a characteristic 3-fold symmetric state appearing on top of the non-adjacent five-membered rings (**Figure 62 b** (SOMO)). On the other hand, the  $dI/dV$  map acquired at +200 mV shows a more uniform circular contrast over 3.2.1-P9-Des macrocycle, as shown in **Figure 62 b** (SUMO).



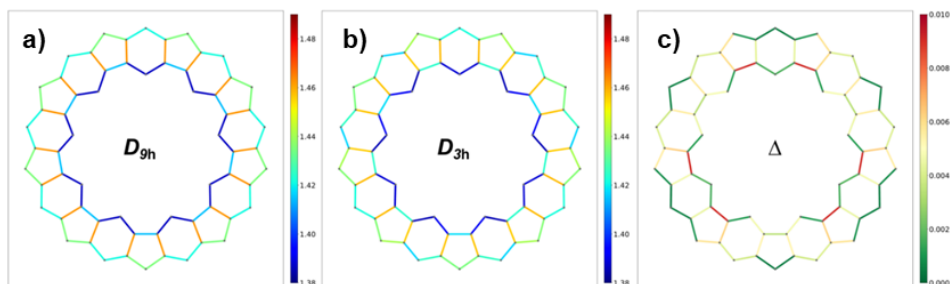
**Figure 62.** Electronic characterization of **3.2.1-P9-Des**. **a)**  $dI/dV$  point spectra of **3.2.1-P9-Des**. Dashed lines depict the SOMO-SUMO gap. The spectra were acquired at positions depicted in the constant current STM image of **3.2.1-P9-Des**. **b)**  $dI/dV$  maps of **3.2.1-P9-Des** at -200 mV and 200 mV bias voltages. **c)** simulated  $dI/dV$  maps of the HOMO and LUMO states. Scanning and spectra parameters were as follows: **(a)**  $2.3 \text{ nm} \times 2.3 \text{ nm}$ , 10 pA, 50 mV (STM image),  $V_{\text{Mod}} = 20 \text{ mV}$  (spectra). **(b)**  $2.3 \text{ nm} \times 2.3 \text{ nm}$ ,  $V_{\text{Mod}} = 20 \text{ mV}$  (SOMO and SUMO).

To understand the obtained experimental  $dI/dV$  maps, and to gain more insights into the electronic ground state of the system, total energy DFT and different high-level quantum chemistry calculations, including CASSCF(11,10), CASSCF(10,10)+NEVPT2 and DMRG, were performed. These multi-configurational methods can serve as a better approach than spin-unrestricted DFT when dealing with systems with strongly correlated electrons<sup>214</sup> as is the case of **3.2.1-P9-Des**.

Firstly, using spin-unrestricted DFT calculations in the gas phase with TPSS exchange-correlation functional<sup>215</sup>, we optimized the molecular geometry of **3.2.1-P9-Des** imposing  $D_{9h}$  and  $D_{3h}$  symmetries. At this DFT level, the two symmetries are energetically similar, only being the  $D_{9h}$  geometry 18 meV lower in energy than the  $D_{3h}$  symmetry. **Figure 63** displays the bond lengths of the optimized structures (**Figure 63 a** and **Figure 63 b**) and their differences (**Figure 63 c**), revealing the presence of an annulene within annulene (AWA) structure with bond length alternation within the inner and outer carbon rings interconnected by single C-C bonds.

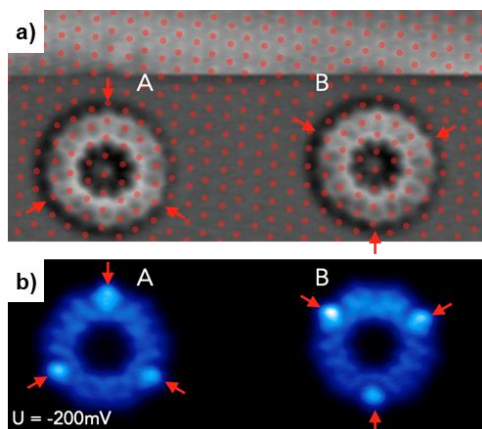
<sup>214</sup> D. Casanova, M. Head-Gordon, *Phys. Chem. Chem. Phys.*, **2009**, *11*, 9779.

<sup>215</sup> J. Tao, J. P. Perdew, V. N. Staroverov, G. E. Scuseria, *Phys. Rev. Lett.*, **2003**, *91*, 146401.



**Figure 63.** Bond-length graphs analyzing two geometries and the difference between them. All distances are in Å.

To understand which is the role of the surface in the final geometry of **3.2.1-P9-Des**, we carried out spin-polarized total energy DFT PBE<sup>216</sup> calculations with dispersion corrections<sup>217</sup> including the Au(111) substrate. These calculations showed how the **3.2.1-P9-Des** macrocycle adopted a planar configuration at approximately 320 pm above the surface (good agreement with the experimental and theoretical values depicted in **Figure 61 b**), revealing a weak dispersion interaction with the underlying substrate. Importantly, we found that the weak interaction with the surface stabilizes the  $D_{3h}$  structure, matching with the high symmetry axis of the Au(111) surface. This adsorption position also matches with the experimentally observed registry of **3.2.1-P9-Des** with the underlying Au(111) substrate shown in **Figure 64 a**. This observation points toward a symmetry reduction of **3.2.1-P9-Des** to the  $D_{3h}$  geometry due to the weak interaction with the substrate, orienting **3.2.1-P9-Des** along the Au(111) surface. **Figure 64 b** shows the alignment of the 3-fold symmetry of the LUMO state with the Au(111) substrate.

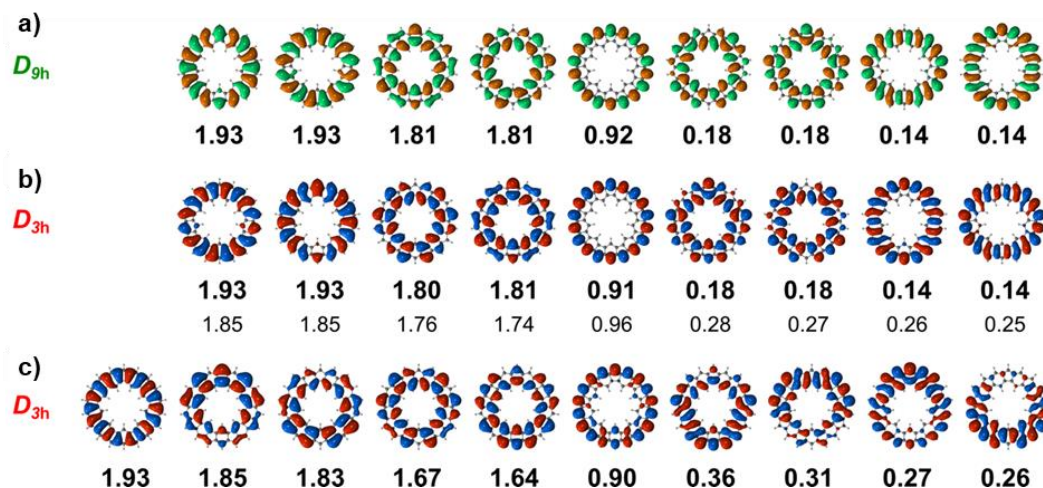


**Figure 64.** Register with the Au(111) substrate of two **3.2.1-P9-Des** molecules. **a)** Nc-AFM image obtained with a CO tip. The image is overlaid with a mesh of red dots that denotes the positions of the Au(111) atoms. The red arrows denote the positions of the visible bright protrusions of the dI/dV image in **b)**. **b)** The dI/dV map of the same molecules in **a)** obtained at -200 mV with a CO tip. Scanning parameters were as follows: **a)** 1 mV; **b)**  $V_{\text{Mod}} = 20$  mV.

<sup>216</sup> J. P. Perdew, K. Burke, M. Ernzerhof, *Phys. Rev. Lett.*, **1996**, 77, 3865–3868.

<sup>217</sup> A. Tkatchenko, M. Scheffler, *Phys. Rev. Lett.*, **2009**, 102, 073005.

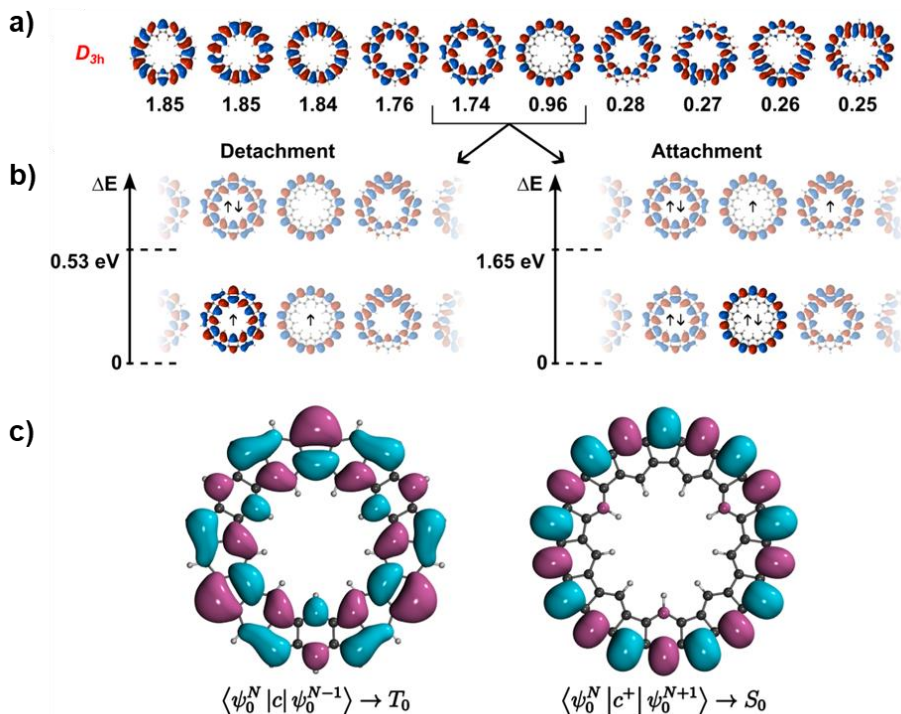
To get more insight into the electronic structure of **3.2.1-P9-Des**, we then carried out many-body calculations using the  $D_{9h}$  and the  $D_{3h}$  geometries. For both cases, we found that the ground state was a doublet, and the natural orbitals (NOs) were practically unchanged between the two symmetries. For different methods, the NOs and their occupation numbers in active spaces are shown in **Figure 65**. Guided by the before-commented experimental evidence of the three-fold symmetry and the spin-polarized total energy DFT PBE calculations with dispersion corrections, we will further focus solely on the electronic structure of the  $D_{3h}$  geometry.



**Figure 65.** Sets of natural orbitals. a) Calculations from NEVPT2/CASSCF(9,9). The ground state is a doublet. b) Calculations from NEVPT2/CASSCF(9,9). The ground state is doublet. The second row of occupation numbers is from DMRG(63,63) calculations. Ordering of NOs is based on the DMRG occupations. c) MRCIS(11,10) natural orbitals. The ground state is doublet.

In order to link the computational calculations to the experimental evidence and prove the validity of the doublet  $D_{3h}$  ground state,  $dI/dV$  maps were calculated. In this sense, STS measurements and  $dI/dV$  mapping correspond to the attachment/detachment of an electron for bias voltage polarities corresponding to empty/occupied states, respectively. Therefore, the observable  $dI/dV$  maps correspond to the many-body electronic transition from neutral  $N$  to charged  $N\pm 1$  states. To simulate these processes correctly, including reorganization of the electronic structures in charged  $N+1$  states, we adopted the concept of Dyson orbitals<sup>218</sup> representing electron (de)attachment  $\langle \psi_o^{N\pm 1} | \hat{c}^{(+)} | \psi_o^N \rangle$  processes that can be directly comparable to  $dI/dV$  maps of frontier orbitals, even for strongly correlated molecules. To obtain Dyson orbitals, shown in **Figure 66**, we calculated the charged  $N\pm 1$  ground states  $\psi_o^{N\pm 1}$ . According to NEVPT2/CASSCF(8,9) for  $N-1$ , and NEVPT2/CASSCF(10,9) for  $N+1$ , the energetically more favorable ground states for the charged states are triplet and singlet, respectively, see **Figure 66 b**.

<sup>218</sup> D. G. Truhlar, P. C. Hiberty, S. Shaik, M. S. Gordon, D. Danovich, *Angew. Chem. Int. Ed.*, **2019**, *131*, 12460–12466.



**Figure 66.** a) CASSCF(9,9) natural orbitals of doublet ground state of **3.2.1-P9-Des** in  $D_{3h}$  symmetry.

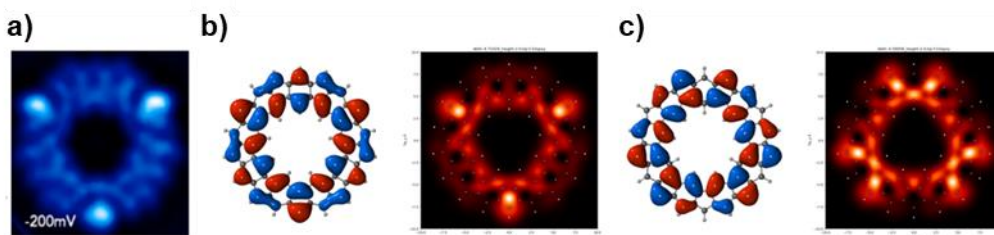
Occupation numbers and order are from full- $\pi$  DMRG calculations. b) Configurations in  $N\pm 1$  states in natural orbital basis corresponding to Dyson orbitals of electron transfers to  $N\pm 1$  states. Energy scales illustrate the lowest singlet and triplet states. Electron detachment and attachment lead to triplet and singlet ground states, respectively.

Natural orbitals that do not change occupancy are translucent, highlighting their absence in the Dyson orbital picture. c) CASSCF calculated Dyson orbitals from neutral doublet to the charged states.

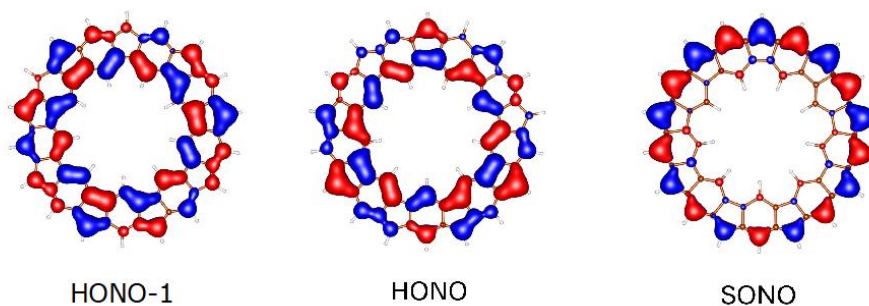
In the case of the electron detachment, although the resulting first Dyson orbital exhibits a very similar three-fold symmetry to that of the HONO (**Figure 67 c**) it fails in reproducing the correct spatial contrast from the experimental dI/dV map at negative voltage (**Figure 67 a**). In this regard, only the second Dyson orbital exhibits the correct three-fold symmetry, as the HONO-1, and the proper spatial contrast when simulating the dI/dV map. As seen in **Figure 67 b**, the use of this orbital perfectly matches with the experimental dI/dV map. To understand this inconsistency, we carried out full- $\pi$  DMRG(63,63) calculations, including all the  $\pi$  orbitals in the active space. The analysis of the occupation numbers shows a good agreement between methods (**Figure 65**), supporting the choice of the active space for CASSCF and MRCIS calculations (**Figure 65 b** and **c**). Moreover, the DMRG orbital ordering swaps the HONO and HONO-1 orbitals compared to CASSCF (see **Figure 68**). This detail is central to the Dyson orbital calculations. Although the difference in the occupation numbers of these two orbitals is minimal, their swapping is manifested in dI/dV, *vide infra*. In summary, **Figure 62 b** and **c** show the excellent agreement between experimental and theoretical dI/dV maps. This



agreement strongly supports the presence of the doublet ground state in reduced three-fold symmetry.



**Figure 67.** a) Experimental dI/dV map at bias voltage -200 mV. b) Natural orbital and corresponding dI/dV map of SONO-2 from CASSCF. c) Natural orbital and corresponding dI/dV map of SONO-1 from CASSCF.



**Figure 68.** Singly occupied natural orbital (SONO) and two lower-lying ones (HONO, HONO-1) calculated at the DMRG(63,63)/def2-SVP level.

It is worth noting that according to the quantum chemistry calculations, the SOMO level is strongly delocalized over the outer ring in the whole macrocycle (see red arrow in **f**). We assume, that this strong delocalization of the unpaired electron prevents a strong interaction with the underlying surface as has been experimentally assessed in **Figure 61**. In contrast, as reported in the literature, highly localized carbon-centered radicals, e.g. truxene<sup>219</sup>, indeno[1,2-*a*]fluorene<sup>220</sup> or those presented in partially hydrogenated **3.2.1-P9** (**Figure 59**), placed in five-membered rings tended to form covalent bonds even with low reactive metals such as gold.

<sup>219</sup> S. Mishra, S. Fatayer, S. Fernández, K. Kaiser, D. Peña, L. Gross, *ACS Nano*, **2022**, *16*, 3264–3271.

<sup>220</sup> S. Mishra, M. Vilas-Varela, L.-A. Lieske, R. Ortiz, S. Fatayer, I. Rončević, F. Albrecht, T. Frederiksen, D. Peña, L. Gross, *Nat. Chem.*, **2024**, DOI [10.1038/s41557-023-01431-7](https://doi.org/10.1038/s41557-023-01431-7).

### Aromatic–magnetic characterization

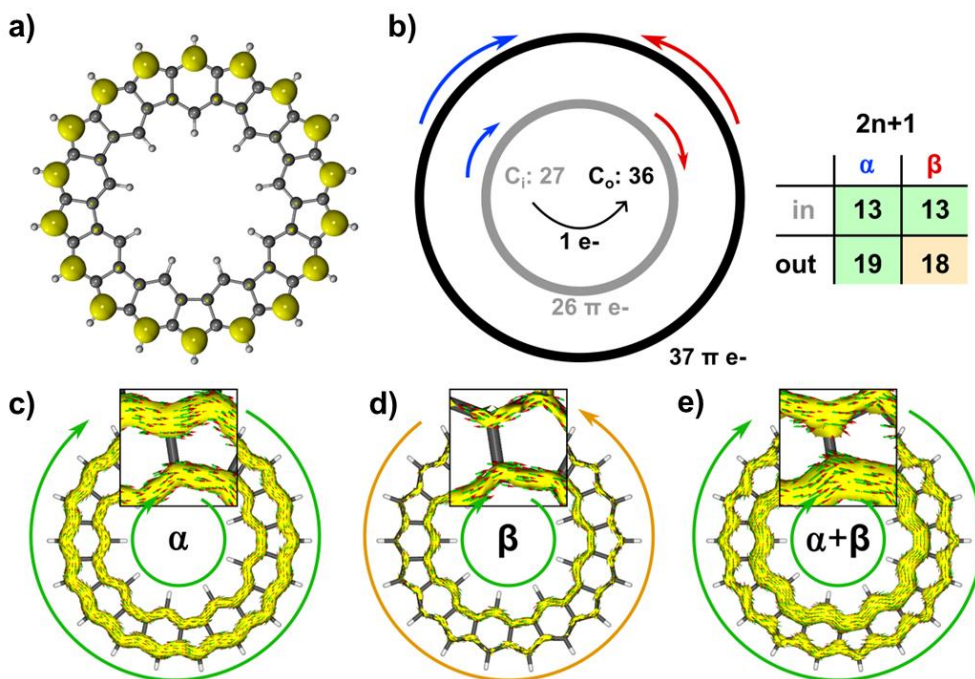
Finally, it is worth commenting on the aromatic  $\pi$ -circuits of **3.2.1-P9-Des**. As a macrocycle with an odd number of  $\pi$ -electrons and an annulene within annulene structure (AWA<sup>221</sup>), **3.2.1-P9-Des** offers a rich playground for aromaticity rules. A simple Hückel  $4n+2$  rule<sup>181</sup> predicts the nonaromatic nature of the macrocycle as a whole and the nonaromatic and antiaromatic nature of the inner and outer rings, respectively (27 and 36  $\pi$ -electrons, respectively). By looking at the calculated unpaired densities (**Figure 69 a**), it is evident that the unpaired electron is located on the outer rim, resulting from a charge transfer from the inner to the outer ring. This leads to a change in aromaticity on individual rings, rendering the inside aromatic with 26 electrons and the outside nonaromatic with 37 electrons. If we continue a step further and consider the  $2n+1$  aromaticity rule by Mandado and work by Fowler and colleagues<sup>222</sup> (for annulenes, odd number ( $2n + 1$ ) of  $\alpha$  or  $\beta$  electrons are aromatic while an even number ( $2n$ ) of  $\alpha$  or  $\beta$  electrons are antiaromatic), we separate the  $\pi$  electrons into spin channels on individual AWA rings. The result is illustrated in **Figure 69 b**, which leads to three aromatic and one antiaromatic contribution. Finally, the inner ring is predicted to be fully aromatic, with 13  $\pi$ -electrons in each spin channel. Conversely, the outer ring bears 19 alpha and 18 beta electrons, demonstrating competition between induced ring currents.

We then calculated the anisotropy of the current-induced density (ACID<sup>223</sup>) plots for individual spins and their total plot on the D3h doublet ground state. These calculations were obtained from the DFT solutions as they were not readily available from CASSCF simulations (we qualitatively confirmed that the orbitals in both CASSCF and DFT were qualitatively the same). In the spin-dependent  $\pi$ -ACID plots (**Figure 69 c, d**), there are two conrotating diatropic ring currents in spin alpha. In contrast, spin beta contains diatropic inner and weak paratropic outer ring currents. These results support the discussed decomposition of aromaticity. **Figure 69 e** shows the total  $\pi$ -ACID, revealing the overall appearance of two conrotating diatropic rings and the global aromaticity of **3.2.1-P9-Des**.

<sup>221</sup> **a)** M. Piccardo, A. Soncini, P. W. Fowler, G. Monaco, R. Zanasi, *Phys. Chem. Chem. Phys.*, **2020**, *22*, 5476–5486. **b)** J. Aihara, *RSC Adv.*, **2014**, *4*, 7256. **c)** H. Miyoshi, R. Sugiura, R. Kishi, S. N. Spisak, Z. Wei, A. Muranaka, M. Uchiyama, N. Kobayashi, S. Chatterjee, Y. Ie, I. Hisaki, M. A. Petrukhina, T. Nishinaga, M. Nakano, Y. Tobe, *Angew. Chem. Int. Ed.*, **2022**, *61*, e202115316.

<sup>222</sup> M. Mandado, A. M. Graña, I. Pérez-Juste., *J. Chem. Phys.*, **2008**, *129*, 164114.

<sup>223</sup> D. Geuenich, K. Hess, F. Köhler, R. Herges, *Chem. Rev.*, **2005**, *105*, 3758–3772.



**Figure 69.** a) Unpaired electron density from CASSCF(9,9). b) Schematic diagram of the decomposition of **3.2.1-P9-Des** into annulenes and spin channels. Number of carbons in inner and outer rings is 27 and 36, respectively, although charge transfer leads to numbers of  $\pi$ -electrons to be 26 and 37, respectively. The table on the right decomposes these  $\pi$ -electrons into both spins. Mandado's  $2n+1$  then leads to three diatropic and one paratropic ring currents. c)  $\pi$ -ACID plot of alpha-spin orbitals with both rings being diatropic. d)  $\pi$ -ACID plot of beta-spin orbitals, with inner ring showing diatropic, and outer paratropic ring currents. e) Total  $\pi$ -ACID of **3.2.1-P9-Des**. All four components of the ring current result in the plotted picture.

### Summary

We have on-surface synthesized **3.2.1-P9-Des** with an odd number of  $\pi$ -electrons on the Au(111) surface. A combination of ab initio methods and experimental measurements sheds light on the complicated description of the electronic structure of **3.2.1-P9-Des** that showed a weak interaction with the underlying surface, enabling the system to reduce the symmetry.

We identify the polyradicaloid doublet ground state with strongly delocalized SOMO orbital. This polyradicaloid doublet with  $D_{3h}$  symmetry exhibits two diatropic ring currents in an AWA system after a charge transfer between the concentric rings, establishing the global aromatic character of **3.2.1-P9-Des**. We argue that the global aromatic character is responsible for the substantial reduction of the polyradical character of the **3.2.1-P9-Des** macrocycle.

### 3.2.4 P10 Macrocycle

Next, this subsection shows the experimental results and the discussion on the synthesis and characterization of the macrocycle **3.2.1-P10-Des**. Although a flat geometry was expected for **3.2.1-P10-Des**, due to previous in-solution experimental work<sup>153</sup>, we found that **3.2.1-P10-Des** got tilted or curved on the surface due to strong interactions of localized radical electrons with the surface underneath. In this regard, we characterized the different isomers observed as a consequence of the interaction with the surface. Of special interest in comparison to P8 and P9 was the observation of an endo-isomer formed upon the ring-closure reaction where one of the methylated benzene rings conducted the reaction towards the inner pore of the macrocycle.

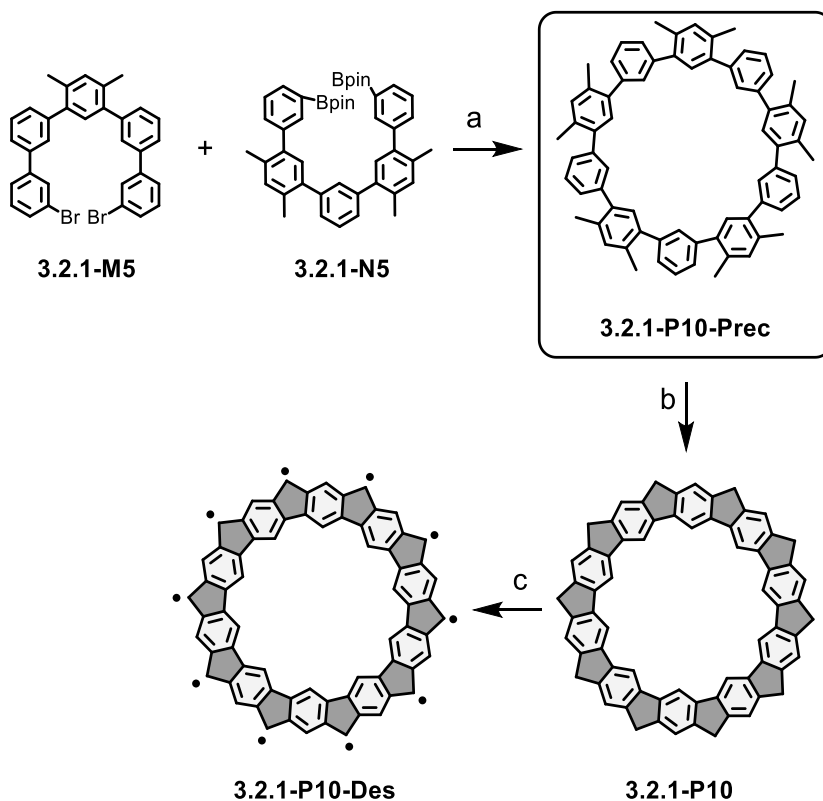
At the end of the subsection, a comparison of the structural and electronic properties among the three on-surface synthesized macrocycles and the two in-solution synthesized **3.2.1-P8-Des** and **3.2.1-P10-Des** homologues is depicted.

#### *In-Solution synthesis and on-surface characterization of the r.t phase*<sup>224</sup>

Precursor **3.2.1-P10-Prec** was successfully synthesized and characterized in-solution after a cross-coupling reaction between **3.2.1-M5** and **3.2.1-N5** synthons in 15 % yield (**Scheme 18**). Subsequently, the precursor **3.2.1-P10-Prec** was deposited on top of a clean Au(111) substrate held at r.t.. The molecules were sublimated at 310 °C from a tantalum pocket. The STM image in **Figure 70 a** showed aleatory self-assembly patterns, which we relate to a higher conformational freedom of **3.2.1-P10-Prec** due to its higher size in comparison with **3.2.1-P8-Prec** or **3.2.1-P9-Prec**.

---

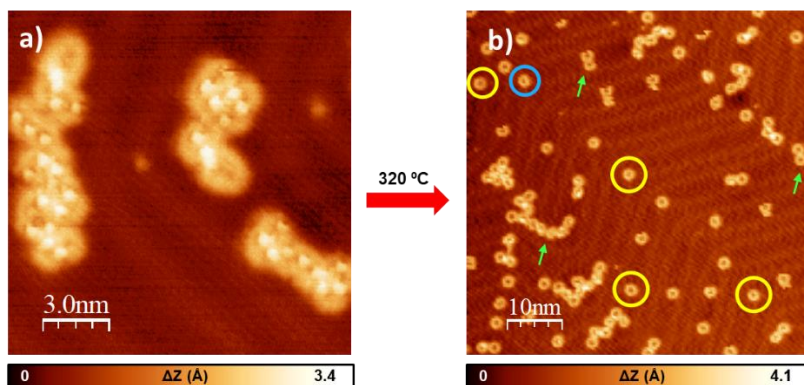
<sup>224</sup> This work is a collaboration between the MOREFUN group from the University of Granada, where the monomer was synthesized, and the Nanosurf Lab from The Institute of Physics of the Czech Academy in Czech Republic, where the high-resolution STM and nc-AFM images, the STS spectroscopies and the computational calculations were conducted.



**Scheme 26.** Schematic representation of the synthetic strategy towards **3.2.1-P10-Des**. **a)**  $\text{Cs}_2\text{CO}_3$ ,  $\text{Pd}(\text{dppf})\text{Cl}_2$ , MeCN, Reflux, 24 h, 15 %. **b)** Sublimation on a Au(111) surface and subsequent annealing at 320 °C. **c)** Tip induced dehydrogenations.

### Ring closure reaction

Further annealing of the sample at 320 °C for ten minutes enabled the oxidative ring closure reaction to synthesize **3.2.1-P10**. As highlighted with yellow circles in **Figure 70 b**, perfect round molecules were observed mainly localized at the fcc region of the herringbone reconstruction of the Au(111) (2 % yield for **3.2.1-P10** after the analysis of ~ 1000 molecules). On the other hand, some side products, depicted with green arrows in **Figure 70 b**, were also observed, attributed to clusters, polymers, dimers or defective molecules. Additionally, depicted with a blue circle, an endo-isomer of **3.2.1-P10** (**3.2.1-P10-Endo1**) was observed (it will be detailedly analysed after).



**Figure 70.** On-surface synthesis of **3.2.1-P10** molecules on the Au(111) surface. **a)** Constant current STM detailed image of the **3.2.1-P10-Prec** at the r.t. phase. **b)** Constant current topographic STM image after annealing the Au (111) sample at 320 °C. Yellow circles depict the **3.2.1-P10**, blue circle depicts the **3.2.1-P10-Endo1** molecule and the green arrows depict oligomers or defective molecules. Scanning parameters were as follows: (a) 10 pA, 50 mV, (b) 10 pA, 211 mV.

**Figure 71** shows the analysis of **3.2.1-P10** by means of nc-AFM and constant current STM before and after the tip-induced dehydrogenations. Regarding the nc-AFM image in **Figure 71 b** and the STM image in **Figure 71 c**, **3.2.1-P10** is observed as a fully symmetric structure. Ten bright lobes were observed in the nc-AFM, corresponding to the out-of-plane CH<sub>2</sub> moieties from the pentagonal rings.

#### *Tip-induced dehydrogenations and adsorption analysis*

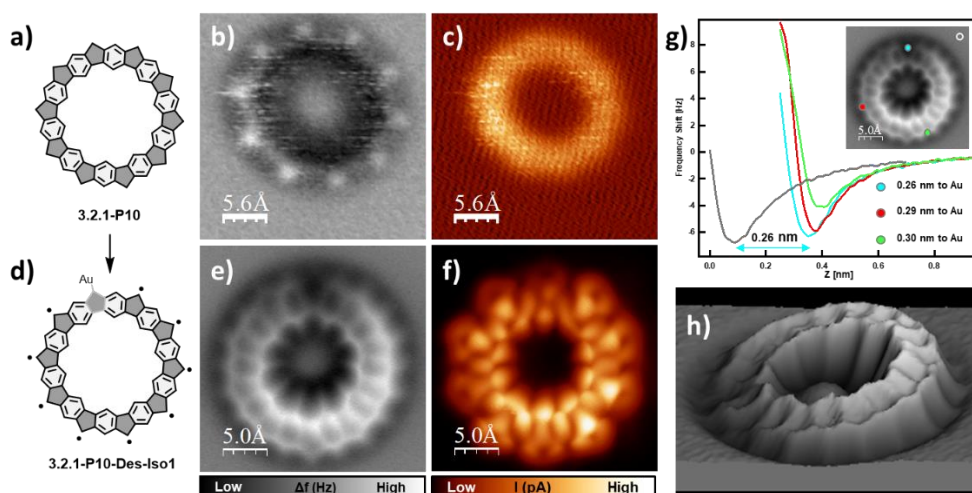
Sequential tip-induced dehydrogenation on top of the CH<sub>2</sub> moieties was carried out to cleave the hydrogens from the pentagonal positions (see **3.2.1-P8 Macrocycle** subsection for more details of this process). The full tip-induced dehydrogenation sequence can be found in **Figure A 10** in the annexes. **Figure 71 e** and **f** confirmed the structure of **3.2.1-P10-Des** while showing a localized distortion in the structure, as can be seen in the top part of the nc-AFM image at one of the five-membered rings. The change in the frequency shift between the top and the bottom parts of the structure revealed the tilted structure of **3.2.1-P10-Des** on top of the Au(111) substrate, better evidenced (in a qualitative way) in the 3D representation in **Figure 40 h**. This tilted adsorption geometry was corroborated by Z-spectroscopy, revealing a 0.4 Å difference between the highest and the lowest part of the molecule in **Figure 71 g**, with an approximately 2 ° tilt relative to the plane of the surface. We relate this phenomenon (the tilt of the structure) to a strong interaction of a localized radical with the substrate. The pentagonal ring approaches the surface and the radical hybridizes with the surface creating a Au-C bond<sup>225</sup>, with the elimination of the π unpaired electron and the inducement of a tilt in the molecular geometry on the Au(111). In this sense, we assume a planar adsorption geometry for the molecule with a slight tilt with respect to the plane of the surface. However, theoretical calculations of the AFM images are needed to compare with the experimental data to confirm this geometry on top of the Au(111) surface. In this regard, the X-Ray diffraction pattern in the

<sup>225</sup> C. Zhao, Q. Huang, L. Valenta, K. Eimre, L. Yang, A. V. Yakutovich, W. Xu, J. Ma, X. Feng, M. Juriček, R. Fasel, P. Ruffieux, C. A. Pignedoli, *Phys. Rev. Lett.*, **2024**, *132*, 046201.

previous reported in-solution work<sup>153</sup> also described a flat geometry for the homologous macrocycle of **3.2.1-P10-Des**.

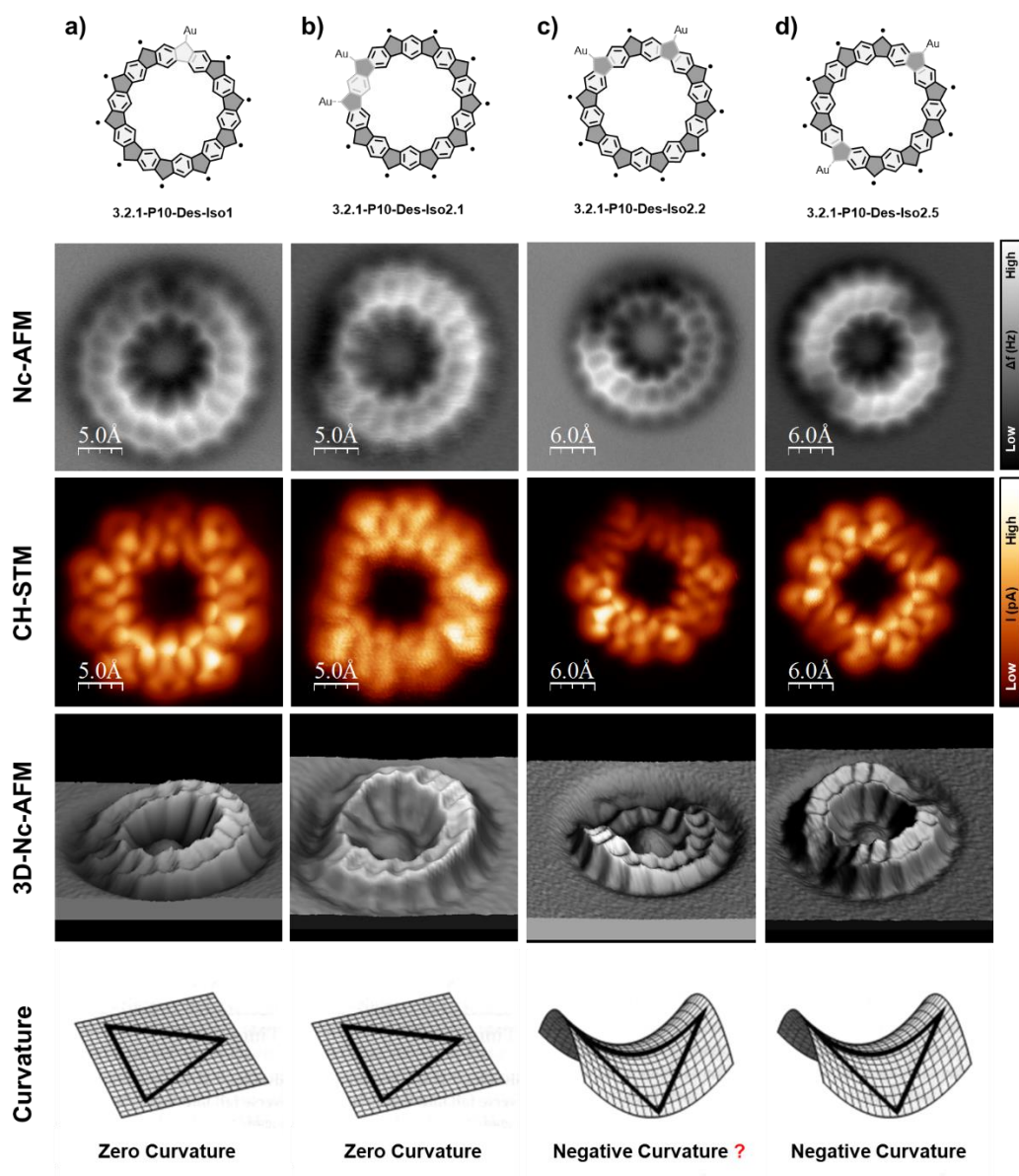
In principle, the electronic structure of **3.2.1-P10-Des** results in a magnetically active molecule due to its odd number of radicals. Considering its highest open-shell scenario **3.2.1-P10-Des** would present nine unpaired electrons, conversely, considering the highest close-shell scenario, **3.2.1-P10-Des** would have one unpaired electron.

The reason for which this strong interaction with the surface is observed in **3.2.1-P10-Des** but not in **3.2.1-P9-Des** or **3.2.1-P8-Des** still remains unclear for us. We ascribe the lower energy required to couple a radical with the surface in **3.2.1-P10-Des**, in comparison with **3.2.1-P8-Des** or **3.2.1-P9-Des**, to a lower strain of the P10 structure due to its bigger size (subtle changes in bond lengths and angles that carbons exhibit after the enlargement of the structure). Because of this lower strain, **3.2.1-P10-Des** become more flexible and hence, it can interact more easily with the surface.



**Figure 71.** **3.2.1-P10** and **3.2.1-P10-Des** structural characterization. **a)** **3.2.1-P10** chemical model. **b)** and **c)** Nc-AFM and constant height STM images, respectively, of **3.2.1-P10**. **d)** **3.2.1-P10-Des-Iso1** chemical model. **e)** and **f)** Nc-AFM and constant height STM images, respectively, of **3.2.1-P10-Des-Iso1**. **g)** Force spectroscopy on **3.2.1-P10-Des-Iso1**. Acquiring spectra points are color coded and depicted in the nc-AFM image in the inset. **h)** 3D representation of the nc-AFM image from **e)**. Scanning and spectra parameters were as follows: **(b)** 2 mV, **(c)** 2 mV, **(e)** 2 mV, **(f)** 2 mV, **(g)** 2 mV (curves), 2 mV (inset image), **(h)** 2 mV.

After performing the tip-induced dehydrogenation reactions in different **3.2.1-P10** molecules, other isomers derived from **3.2.1-P10-Des** were observed depending on the number and the position of the five-membered rings that “strongly” interacted with the surface. **Figure 72** shows the four isomers observed on the surface after the dehydrogenation process (as commented before, we assume the “strong interactions” in each position where a five-membered ring presents a dark depression in the nc-AFM images).



**Figure 72.** Structural characterization of the different isomers of **3.2.1-P10-Des**. **a)** In order: chemical model, nc-AFM, constant height, 3D-nc-AFM and type of curvature of **3.2.1-P10-Des-Iso1**. **b)** Same for **3.2.1-P10-Des-Iso2.1**. **c)** Same for **3.2.1-P10-Des-Iso2.2**. **d)** Same for **3.2.1-P10-Des-Iso2.5**. Scanning parameters were as follows: (a) 2 mV, (b) 2 mV, (c) 2 mV, (d) 2 mV.

At this point it is noteworthy to create a notation that depends on the interactions of the molecules with the surface for referring to the different observed isomers. In “iso2.X” the first number refers to number of interactions that the macrocycle has with the surface while the second number refers to the number of six-membered rings in the shortest pathway separating the two pentagonal rings that couple with the surface. Therefore, beyond the already commented **3.2.1-P10-Des-Iso1**, the other three observed isomers present two strong



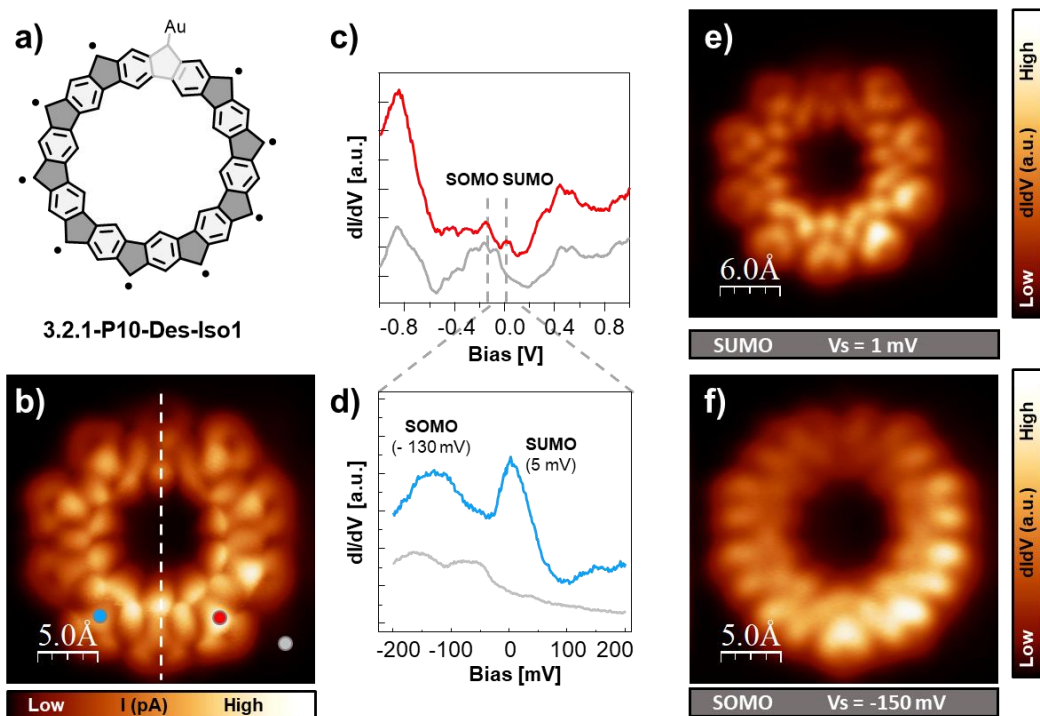
interactions with the surface differently located depending on the isomer. **3.2.1-P10-Des-Iso2.1** in **Figure 72 b**, **3.2.1-P10-Des-Iso2.2** in **Figure 72 c** and **3.2.1-P10-Des-Iso2.5** in **Figure 72 d**. All of them, in theory, have eight  $\pi$  unpaired radicals. In this regard, a magnetically active electronic state can not be directly stated for them as their ground state could be close-shell.

Interestingly, in terms of curvature, **3.2.1-P10-Des-Iso1** and **3.2.1-P10-Des-Iso2.1** present a geometry based on a tilted plane (a slope) relative to the underlying surface, as can be seen in the 3D-nc-AFM images in **Figure 72 a** and **b** (it is worthy to remember that the 3D nc-AFM images help with the qualitative understanding of the geometry on top of the surface but they are not a real picture of their adsorption geometries). In this sense, the zero curvature, already reported for the in-solution homologue of **3.2.1-P10-Des**, is preserved in these two isomers. Conversely, **3.2.1-P10-Des-Iso2.5** shows a very interesting saddle-shape geometry (negative curvature) as depicted in the 3D nc-AFM image from **Figure 72 d**. To the best of our knowledge, this is the first report of an on-surface synthesized graphene nanostructure presenting a saddle-shape curvature. Lastly, **3.2.1-P10-Des-Iso2.2** shows an irregular curvature that we also relate to a saddle-shape-like structure. Noteworthy, for **3.2.1-P10-Des-Iso2.2** and **3.2.1-P10-Des-Iso2.5**, it is assumed that the curvature is induced by the interaction of the radicals with the substrate and not to an inner strain of the molecule.

A reliable statistical analysis regarding the four isomers was not possible. Conducting single-molecule experiments is challenging and time-consuming, making it difficult to gather sufficiently large statistical datasets in a reasonable time. However, it is noteworthy that we observed, after the dehydrogenation reactions, isomers **3.2.1-P10-Des-Iso1** and **3.2.1-P10-Des-Iso2.5** more frequently, which we relate to a higher stability compared to the other isomers.

### Electronic characterization

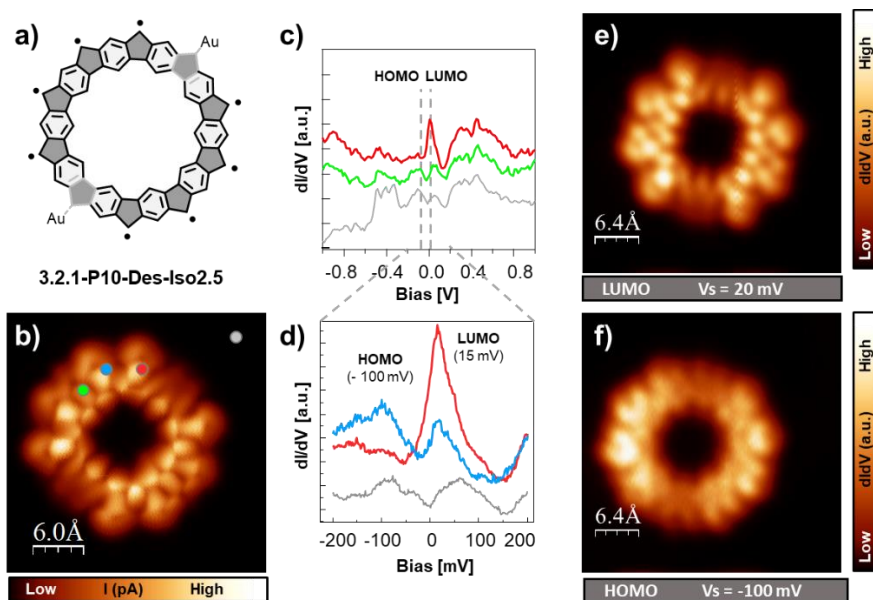
Consequently, an electronic characterization by means of STS and dI/dV mapping was conducted on them (on **3.2.1-P10-Des-Iso1** and on **3.2.1-P10-Des-Iso2.5**). **Figure 73** shows the electronic characterization of **3.2.1-P10-Des-Iso1**. STS with CO tip was conducted to gain insights of the LDOS in **Figure 73 c** and **d**, showing the SOMO and the SUMO at  $-130$  mV and  $5$  mV respectively, and with a  $\sim 0.14$  eV gap (remember that **3.2.1-P10-Des-Iso1** should have at least one unpaired electron if we discard processes of charge transfer with the substrate). Additionally, dI/dV mapping was performed to obtain the spatial distribution of these states. Different conclusions can be obtained regarding these dI/dV maps. Firstly, as it can be seen in the intensity of the LDOS in both HOMO and LUMO, it decreases where the pentagonal rings “strongly” interact with the Au surface. We can envision two main reasons to explain this phenomenon. On the one hand, it can be due to a real absence of the LDOS in the molecule in the part that is interacting with the surface. On the other hand, it can be associated to experimental factors like a lower intensity due to the lower height of the molecule in that part. Further computational calculations are needed to solve this question. Secondly, the SOMO dI/dV map reveals a qualitatively higher LDOS in the outer ring of the **3.2.1-P10-Des-Iso1** structure. This suggests that the radical predominantly locates in the outer ring, similar to the observation made with **3.2.1-P9-Des**.



**Figure 73.** Electronic characterization of **3.2.1-P10-Des-Iso1**. **a)** Chemical model of **3.2.1-P10-Des-Iso1**. **b)** Constant current STM image. **c)** and **d)**  $dI/dV$  point spectra. Positions where spectra were acquired are color depicted in **b)**. **e)** and **f)**  $dI/dV$  maps at 1 mV and -150 mV showing SUMO and SOMO respectively. Scanning and spectra parameters were as follows: **(b)** 2 mV, **(c)**  $V_{\text{Mod}} = 10$  mV, **(d)**  $V_{\text{Mod}} = 10$  mV, **(e)**  $V_{\text{Mod}} = 10$  mV, **(f)**  $V_{\text{Mod}} = 10$  mV.

The same procedure was performed for **3.2.1-P10-Des-Iso2.5**, as can be seen in **Figure 74**. In this case, the STS in **Figure 74 c** and **d** also showed a low HOMO-LUMO gap,  $\sim 0.12$  eV, with states located at  $-100$  mV and  $15$  mV. Similar conclusions can be gathered from the  $dI/dV$  maps. Firstly, the LDOS decreases where there is a strong interaction of a pentagonal ring with the surface. Secondly, the LDOS for **3.2.1-P10-Des-Iso2.5** is symmetrical regarding the mirror plane that contains both strong interactions with the surface. In addition, and same as with **3.2.1-P10-Des-Iso1**, the LDOS is strongest at the outer ring of the macrocycle for the HOMO.

If we compare both isomers electronically, although in theory **3.2.1-P10-Des-Iso1** should have an unpaired electron while **3.2.1-P10-Des-Iso2.5** should not (naively, it may seem a huge difference electronically) there is only a tiny shortening of the HOMO-LUMO gap (0.12 eV vs 0.14) for the “doubly interacting” **3.2.1-P10-Des-Iso2.5** macrocycle, and a displacement of this states to lower energies in the case of **3.2.1-P10-Des-Iso1**. Interestingly, the features of the HOMO and LUMO states resemble (similar shape/topology of the states) between both macrocycles if we do not consider those parts of the molecule where the pentagonal rings strongly interact with the surface.

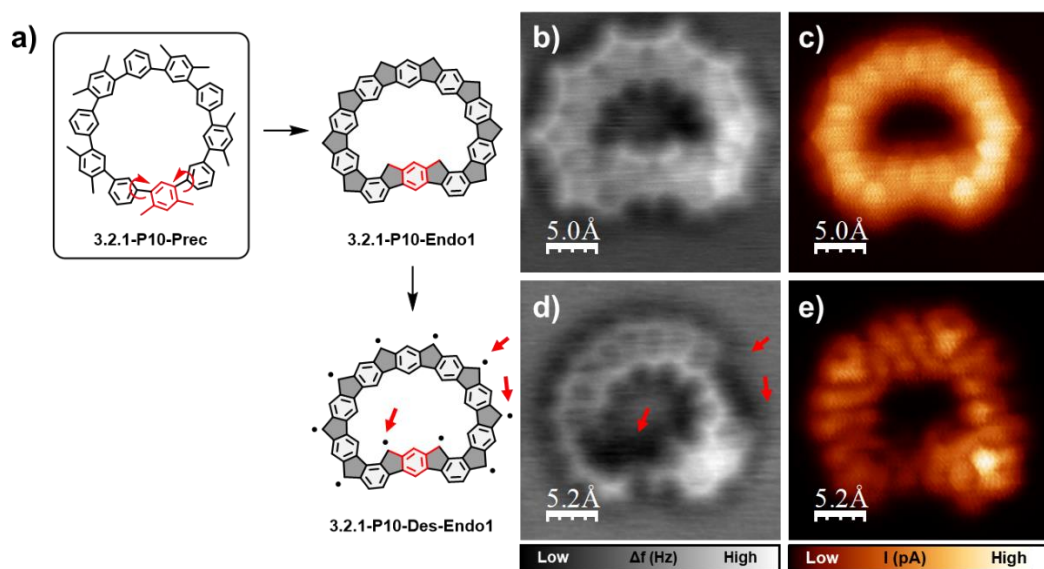


**Figure 74.** Electronic characterization of **3.2.1-P10-Des-Iso2.5**. **a)** Chemical model of **3.2.1-P10-Des-Iso2.5**. **b)** Constant current STM image. **c)** and **d)** dI/dV point spectra. Position where spectra were acquired are color depicted in **b)**. **e)** and **f)** dI/dV maps at 20 mV and -100 mV showing LUMO and HOMO resonances, respectively. dI/dV maps are slightly rotated anticlockwise with respect to image **b)**. Scanning and spectra parameters were as follows: **(b)** 2 mV, **(c)**  $V_{\text{Mod}} = 10$  mV, **(d)**  $V_{\text{Mod}} = 10$  mV, **(e)**  $V_{\text{Mod}} = 10$  mV, **(f)**  $V_{\text{Mod}} = 10$  mV.

### The endo product

Finally, **Figure 75** shows an endo isomer of **3.2.1-P10**. **3.2.1-P10-Endo1** is the result of the rotation of one of the methylated benzene rings towards the inner pore of the macrocycle, as shown in **Figure 75 a**. The enlargement of the structure from **3.2.1-P8-Des** to **3.2.1-P10-Des** also increases the inner pore size of the macrocycle allowing other possible conformations of the precursor where the methylated benzene ring can be tilted towards the pore. This new “allowed” conformations may give rise to “new” endo products during the oxidative ring closure reactions (as will be seen in the following subsections).

**3.2.1-P10-Endo1** was characterized by means of nc-AFM and BR-STM in **Figure 75 b** and **c**, showing a flat geometry in which we were able to resolve the pentagonal and hexagonal rings. **Figure 75 d** and **e** show the final dehydrogenated **3.2.1-P10-Des-Endo1** structure after performing the tip-induced reactions on **3.2.1-P10-Endo1**. Pronounced interactions with the substrate were also observed for **3.2.1-P10-Des-Endo1** as evidenced by the dark depressions highlighted with red arrows in the nc-AFM of **Figure 75 d**. Notably, the structure depicted in this figure displayed three “strong” interactions with the surface, which in principle results in a seven  $\pi$  unpaired electrons structure. Hence, this molecular entity, due to its off-balanced radical account, should emerge as a magnetically active molecule because at least, one electron will be always unpaired.



**Figure 75.** On-surface characterization of **3.2.1-P10-Endo1** and **3.2.1-P10-Des-Endo1**. **a)** Scheme of the formation of **3.2.1-P10-Endo1** through the rotation of two bonds of **3.2.1-P10-Prec**, and the subsequent synthesis of **3.2.1-P10-Des-Endo1** carried on with tip-induced dehydrogenations. Red arrows depict pentagonal positions with a strong interaction with the surface regarding image **d)** and **e)**. **b)** and **c)** nc-AFM and constant height STM images regarding **3.2.1-P10-Endo1**. **d)** and **e)** nc-AFM and constant height STM images of **3.2.1-P10-Des-Endo1**. Scanning parameters were as follows (**b)** 2 mV, (**c)** 2 mV, (**d)** 2 mV, (**e)** 2 mV.

### Summary

Annealing **3.2.1-P10-Prec** onto a clean Au(111) substrate facilitated the successful oxidative ring closure reaction yielding **3.2.1-P10** molecules. Subsequent tip-induced dehydrogenation lead to **3.2.1-P10-Des** that presented localized distortions attributed to strong interactions with the substrate, leading to tilted, relative to the surface, or curved structures. Different isomers depending on the number of interactions with the substrate and the position of them in the macrocycle were found, being the most common **3.2.1-P10-Des-Iso1** (with zero curvature) and **3.2.1-P10-Des-Iso2.5** (with negative curvature).

By means of STS and dI/dV mapping **3.2.1-P10-Des-Iso1** and **3.2.1-P10-Des-Iso2.5** were electronically characterized, showcasing the dependence of the LDOS with the surface interaction and the curvature of the macrocycles.

Additionally, compound **3.2.1-P10-Endo1** was also synthesized as an endo isomer of **3.2.1-P10** due to the rotation of one methylated benzene ring during the ring closure reaction. Tip-induced dehydrogenations were successfully carried out yielding **3.2.1-P10-Endo1-Des**.

### Comparison among macrocycles

**Figure 76** shows a comparison among the properties of the different on-surface synthesized cyclopenta-ring-fused oligo(*m*-phenylene) macrocycles with their previously reported in-solution synthesized homologues. A straightforward comparison cannot be done among the in-

solution and the on-surface macrocycles because: first, the reported macrocycles were prepared with mesityl groups at the five-membered rings to protect the unpaired electrons, and secondly, the surface does not normally play an innocent role in the geometry, and in the electronic properties of the molecules<sup>226</sup>. However, some conclusions can be drawn after the analysis of the macrocycles. First, regarding the geometry of the on-surface synthesized macrocycles, we have observed different size-dependent geometries for the macrocycles. **3.2.1-P8-Des** presented a positively curved geometry (truncated cone), **3.2.1-P9-Des** was planar, and **3.2.1-P10-Des** showed different isomers that ranged from tilted planar structures to saddle-shaped geometries. Structurally, our results match well with the in-solution results regarding **3.2.1-P8-Des**, which also presented a curved structure as shown in the structure obtained from the X-ray diffraction analysis in **Figure 76**. On the other hand, the X-ray pattern of the in-solution **3.2.1-P10-Des** homologue presents a completely planar structure that matched well with the tilted geometries assumed for some of the **3.2.1-P10-Des** isomers, but not with those that presented the saddle shape curvature.

After magnetically characterizing **3.2.1-P8-Des** and **3.2.1-P10-Des** by means of NMR, EPR (electron paramagnetic resonance) or SQUIDS measurements (superconducting quantum interference device); and computationally, through DFT and RAS-SF/6-31G(d), Liu et al.<sup>153</sup> reported open-shell ground states for **3.2.1-P8-Des** and **3.2.1-P10-Des**, exhibiting singlet and triplet multiplicities, respectively. On the other hand, **3.2.1-P9-Des** was on-surface electronically (STS and dI/dV mapping) and computationally (DFT, CASSCF(11,10), CASSCF(10,10)+NEVPT2 or DMRG) characterized yielding a doublet ground state with a single unpaired electron.




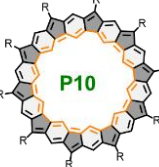
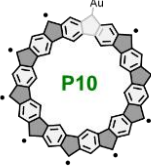
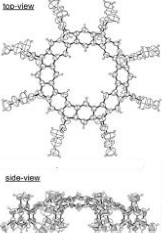
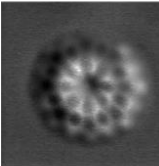
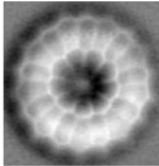
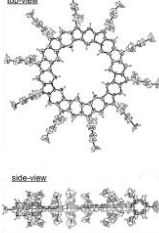
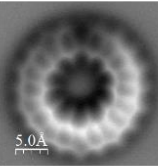
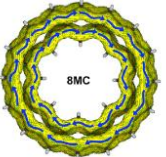
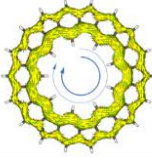
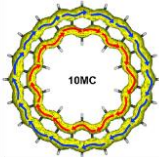
It is not straightforward to compare in-solution electrochemical bandgaps with the on-surface obtained bandgaps, as commented before. However, there is an independent general tendency to narrow the HOMO-LUMO gap upon increasing the macrocycle size both in solution and on surface. This is expected due to a higher delocalization of the electrons in larger structures, as it happens, for example, in graphene-based nanostructures<sup>227</sup>. For the in-solution homologues, **3.2.1-P8-Des** presents an electrochemical HOMO-LUMO gap of 0.55 eV while **3.2.1-P10-Des** homologue exhibited a 0.12 eV to 0.14 eV electrochemical bandgap. On the other hand, for the on-surface macrocycles there is a narrowing from 0.9 eV in **3.2.1-P8-Des** to 0.12-0.14 eV in **3.2.1-P10-Des** (with an intermediate HOMO-LUMO gap of 0.48 eV for **3.2.1-P9-Des**).

In terms of aromaticity, in-solution **3.2.1-P8-Des** analogue, **3.2.1-P10-Des** analogue and on-surface **3.2.1-P9-Des** presented an AWA system after the calculated magnetic-analysis by ACID. For the three molecules, both ring currents were diamagnetic (clockwise direction) exhibiting an aromatic character. Huckel's and Baird's rule for aromaticity were useful to describe the aromatic system of in-solution analogues **3.2.1-P8-Des** and **3.2.1-P10-Des**, while Huckel's and Mandado's were used in the case of **3.2.1-P9-Des** due to its paramagnetic nature. Further computational calculations are being conducted to shed light into the aromaticity of the adsorbed structure **3.2.1-P8-Des** and the different isomers of **3.2.1-P10-Des**.

<sup>226</sup> J. B. Neaton, M. S. Hybertsen, S. G. Louie, *Phys. Rev. Lett.*, **2006**, *97*, 216405.

<sup>227</sup> V. S. Iyer, M. Wehmeier, J. D. Brand, M. A. Keegstra, K. Müllen, *Angewandte Chemie Int. Ed.*, **1997**, *36*, 1604–1607.

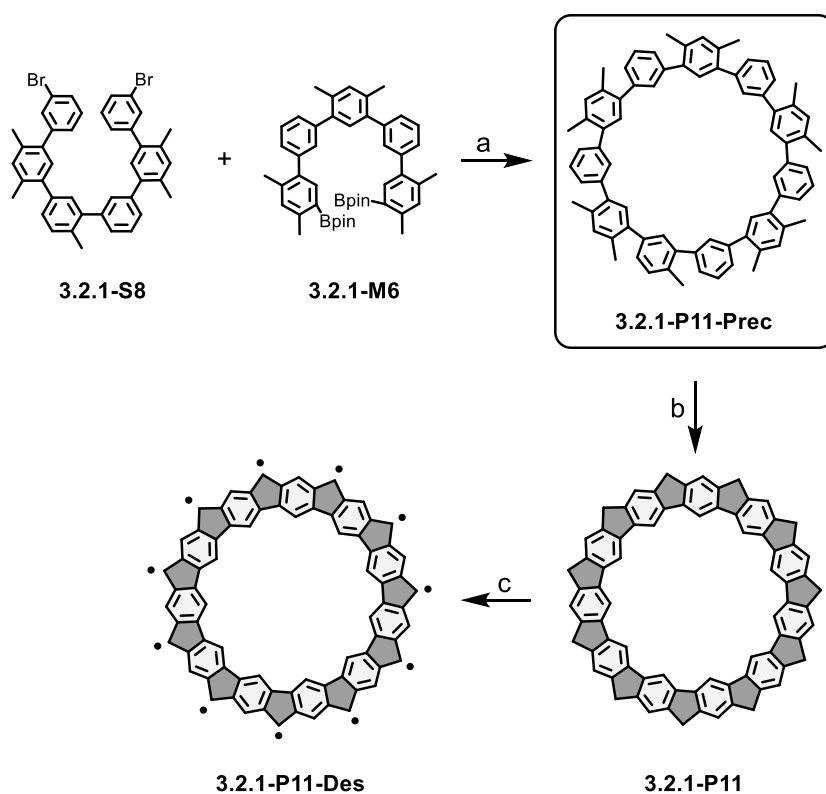
Finally, despite the different macrocycle coverages on the surface potentially impacting these results, a decrease in the reaction yields is observed as the ring size increases (from 8% in **3.2.1-P8-Des** to 2% in **3.2.1-P10-Des**). Although still, there is room for the improvement of the reaction yields by the systematic study of different reaction conditions (hot evaporation, different annealing times and temperatures for the ring closure reaction, different substrates...), we can ascribe this tendency to: (i) the bigger amount of ring closures to be performed from **3.2.1-P8-Des** to **3.2.1-P10-Des**, (ii) the higher planarity of the structures, enhancing intercoupling reactions between the macrocycles, and (iii), the bigger amount of secondary products, namely endo-products, upon the enlargement of the structure.

	IN-SOLUTION	ON-SURFACE	ON-SURFACE	IN-SOLUTION	ON-SURFACE
<b>Chemical Model</b>					
<b>Nc-AFM/ X-Ray Diff.</b>					
<b>Ground State</b>	Singlet	?	Doublet	Triplet	?
<b>Homo – Lumo Gap (Optical)</b>	< 0.5 eV	-	-	< 0.5 eV	-
<b>Homo – Lumo Gap (Electrochemical)</b>	0.55 eV	-	-	0.12 eV	-
<b>Homo – Lumo Gap (On-Surface)</b>	-	0.90 eV	0.48 eV	-	0.14 eV (3.2.2-P10-Des-Iso1) 0.12 eV (3.2.2-P10-Des-Iso2.4)
<b>Global Aromaticity</b>		?			?
<b>On-Surface Yield</b>	-	8 %	3 %	-	2 %

**Figure 76.** Comparison of the properties of the different cyclopenta-ring-fused oligo(*m*-phenylene) macrocycles, either reported in solution or synthesized on a surface (in this thesis). X-Ray Diffraction, Ground State, HOMO – LUMO Gap (Optical), HOMO – LUMO Gap (Electrochemical) and Global Aromaticity of in-solution described 3.2.1-P8-Des and 3.2.1-P10-Des homologues were reported by Liu et al.<sup>153</sup> R = Mesityl protecting group.

### 3.2.5 P11 Macrocycle

In this subsection, we explore the reaction outcomes of **3.2.1-P11-Prec** after its thermally-induced ring closure reaction on a Au(111) substrate. Additionally, we investigate its dehydrogenated final products resulting from tip-induced reactions. Examination after the ring closure reveals a mixture of planar endo-products, where one or two methylated benzene rings reacted toward the inner pore of the macrocycle, contrarily to expected **3.2.1-P11** (**Scheme 27**). STM and nc-AFM further unveiled strong interactions of localized unpaired electrons with the surface in these endo-products after the final tip-induced dehydrogenation reactions, akin to observations in the previous subsection with **3.2.1-P10-Des**.

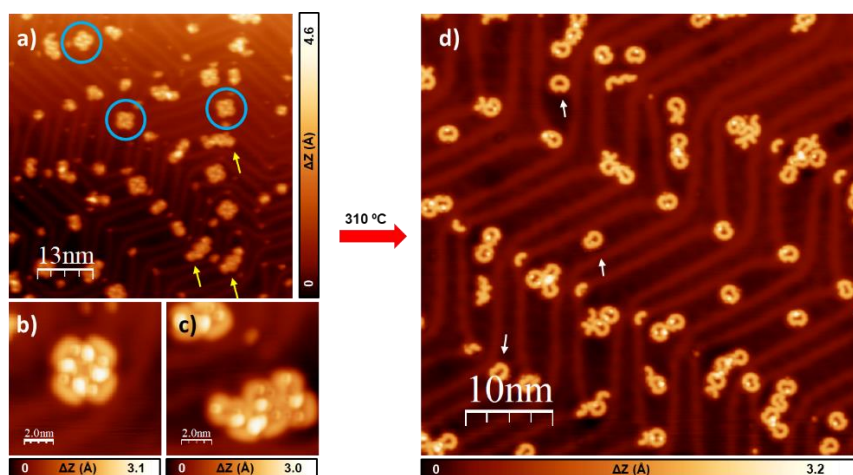


**Scheme 27.** Schematic representation of the synthetic strategy towards **3.2.1-P11-Des**. **a)**  $\text{Cs}_2\text{CO}_3$ ,  $\text{Pd}(\text{dppf})\text{Cl}_2$ , MeCN, Reflux, 24 h, 11 %. **b)** Sublimation on a Au(111) surface and subsequent annealing at 310 °C. **c)** Tip-induced dehydrogenations.



*In-Solution synthesis and on-surface characterization of the r.t phase*<sup>228</sup>

**3.2.1-P11-Prec** was successfully synthesized and characterized after the Suzuki coupling reaction between **3.2.1-S8** and **3.2.1-M6** (11 % yield). The initial step of the on-surface synthesis involved the deposition of **3.2.1-P11-Prec** onto a pristine Au(111) substrate maintained at r.t. (the sublimation of the molecules was performed at 340 °C from a tantalum pocket). Analysis via constant current STM (**Figure 77 a**) revealed a self-assembled arrangement, depicted with a blue circle, and some irregular arrangements, depicted with yellow arrows.



**Figure 77.** On-surface synthesis of **3.2.1-P11** molecule on Au(111) surface. **a)** Constant current topographic STM image of the r.t. phase of **3.2.1-P11-Prec**. Blue circles depict the self-assembly pattern in **b)**. Yellow arrows indicate similar assemblies as those shown in **c)**. **b) & c)** Constant current detailed STM images of two different arrangements of **3.2.1-P11-Prec**. **d)** Constant current topographic STM image of the Au(111) sample after annealing at 310 °C for 10 minutes. White arrows depict **3.2.1-P11** endo products. Scanning parameters were as follows: (a) 10 pA, 101 mV, (b) 10 pA, 101 mV, (c) 10 pA, 101 mV, (d) 10 pA, 101 mV.

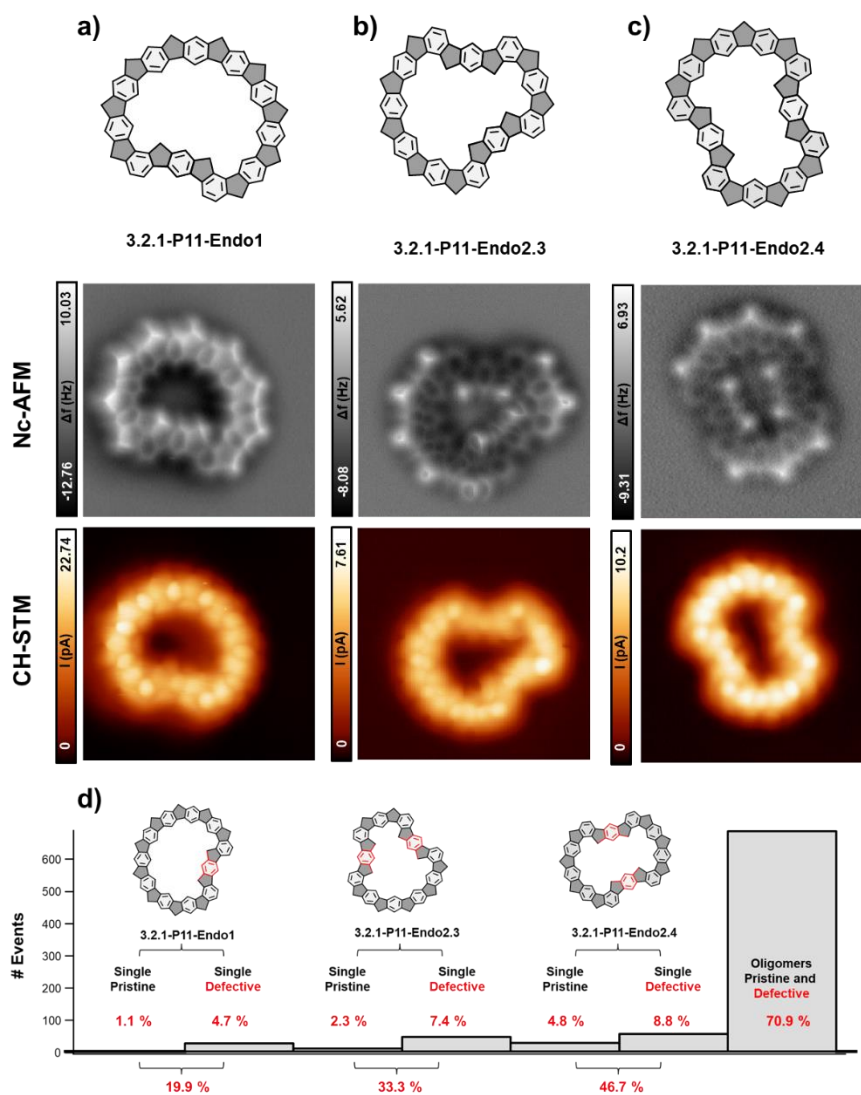
**Figure 77 b** presents a detailed STM image of a four-unit self-assembly arrangement with a propeller-shaped fashion. The four molecules comprising the arrangement have the same conformation, however, the high complexity of the precursor complicates the proposal of a hypothesis regarding the orientation of the precursor within the arrangement on top of the surface. Furthermore, **Figure 77 c** shows another arrangement of **3.2.1-P11-Prec** wherein the molecules adopt a different conformation compared with the one observed in the propeller-shaped fashion of **Figure 77 b**. This variation in conformation can be attributed to a higher conformational freedom due to the larger size of **3.2.1-P11-Prec** precursor relative to previous precursors **3.2.1-P8-Prec** or **3.2.1-P9-Prec**.

<sup>228</sup> This work is a collaboration between the MOREFUN group from the University of Granada, where the monomer was synthesized, and the Nanosurf Lab from The Institute of Physics of the Czech Academy in Czech Republic, where the high-resolution STM and nc-AFM images, the STS spectroscopies and the computational calculations were conducted.

### Ring closure reaction

Subsequent sample annealing at 310 °C facilitated the oxidative ring closure reaction of the precursors. However, inspection of the topographic STM image in **Figure 77 d** revealed no signs of circular **3.2.1-P11** macrocycles. Instead, some related endo products (not perfectly round macrocycles) were mainly found on the fcc region of the Au(111) herringbone reconstruction (depicted with white arrows in **Figure 77 d**). Additionally, various side products were observed including intermolecular couplings forming either clusters or oligomers, partially reacted molecules and some not macrocyclic (opened) fragments of **3.2.1-P11**.

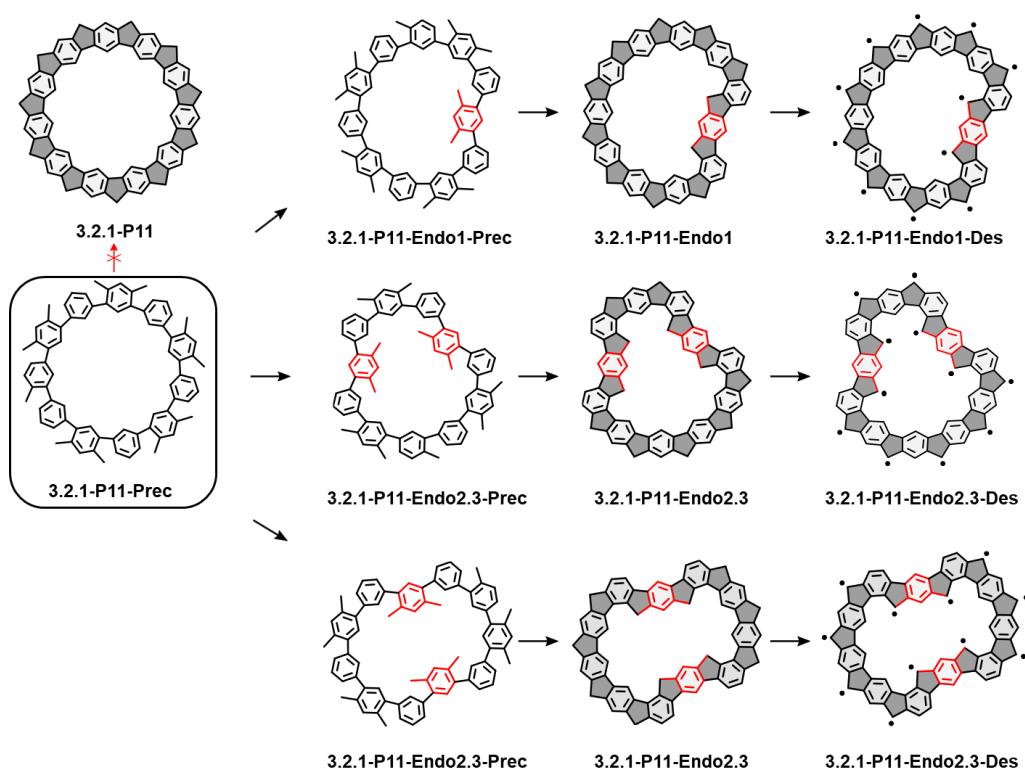
**Figure 78** shows the inspection of the abovementioned “endo-products” by means of high resolution nc-AFM and constant height STM revealing three different species: **3.2.1-P11-Endo1** (**Figure 78 a**), **3.2.1-P11-Endo2.3** (**Figure 78 b**) and **3.2.1-P11-Endo2.4** (**Figure 78 c**). All these topologies presented a flat structure (without considering the CH<sub>2</sub> moieties) and eleven bright protrusions in the nc-AFM images, the latter related to the out-of-plane CH<sub>2</sub> moieties located at the apex of the pentagonal rings. A nomenclature of the endo products is elaborated for this doctoral thesis, and it is only valid for the family of cyclopenta-ring-fused oligo(*m*-phenylene) macrocycles. Please do not get confused with the before presented nomenclature with the different **3.2.1-P10-Iso** that referred to the interactions with the surface. For the endo-compounds, the first number after the word “endo” refers to the number of benzene rings that carried out the cyclodehydrogenation reaction towards the inner pore of the macrocycle. The second number alludes to the number of benzene rings that separates both through the shortest path (in case of more benzene rings towards the inner pore, more numbers should be added).



**Figure 78.** Structural characterization of the obtained endo products and statistical analysis of the outcomes of the on-surface reaction. **a)**, **b)** and **c)** Schematic model, nc-AFM and constant height STM images simultaneously obtained of **3.2.1-P11-Endo1**, **3.2.1-P11-Endo2.3** and **3.2.1-P11-Endo2.4**, respectively. **d)** Statistical analysis of the outcomes of the reaction carried out with more than 1000 molecules. Yields under the histogram do not consider the “oligomers pristine and defective” bar at the right. Scanning parameters were as follows **(a)** 2 mV, 3 nm  $\times$  3 nm, **(b)** 2 mV, 3 nm  $\times$  3 nm, **(c)** 2 mV, 3 nm  $\times$  3 nm.

A statistical analysis was carried out over more than 1000 molecules in **Figure 78 d** to evaluate the outcomes of the ring closure reaction in the synthesis of the different endo products. In this regard, **3.2.1-P11-Endo1** was synthesized in  $\sim 1\%$  yield, **3.2.1-P11-Endo2.3** in  $\sim 2\%$  and **3.2.1-P11-Endo2.4** in  $\sim 5\%$ . Just at the right of each endo topology column (“single pristine”), there is another column named “single defective” that refers to individual defective macrocycles of each topology. We assume most of these “defective” macrocycles as either intermediate steps between the precursor and the product after the ring closure reaction or molecules that lost one

or more methyl groups. Finally, the most populated bar with a 71 % corresponds to clusters and oligomers with perfect and defective monomers. As shown in **Scheme 28**, we ascribe the formation of these endo topologies to the rotation of one or two of the doubly methylated benzene rings towards the inner side of the macrocycle pore before the total ring closure reaction.



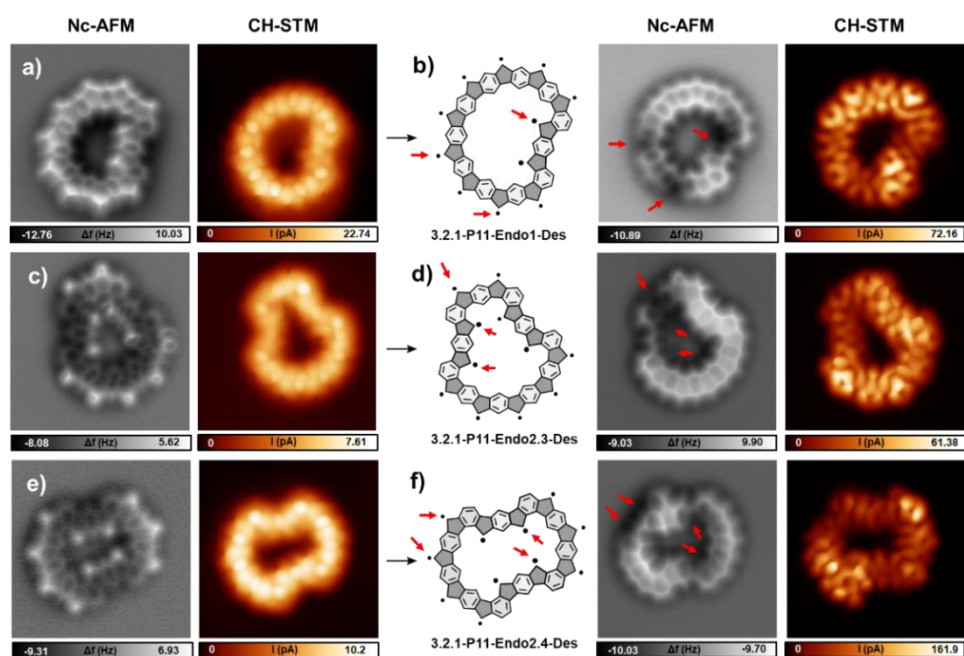
**Scheme 28.** Outcome of the oxidative ring closure of **3.2.1-P11-Prec** on Au(111) at 310 °C, and post tip-induced dehydrogenation of the endo isomers.

Here, the intriguing issue is the absence of **3.2.1-P11** macrocycles although the synthesis of the circular topology for **3.2.1-P8**, **3.2.1-P9** and **3.2.1-P10** was successful. In this sense, we assume that during the cyclodehydrogenation reaction, the intermediates with one or two methylated benzene rings oriented towards the inner pore of the macrocycle are energetically more favorable than those intermediates where all the methylated benzene rings are oriented outwards the macrocycle. In this sense, we hypothesize that this process is kinetically driven as our first predictions for the circular **3.2.1-P11** molecule also yielded an almost planar structure (**Figure 52**). That is, Van der Waals interactions due to planarization of the structure may not significantly stabilize the endo isomers more than the circular topology. Computational calculations are necessary to fully understand this issue.

The reason why this phenomenon (synthesis of the endo-products) does not occur in **3.2.1-P8** or in **3.2.1-P9** may be motivated by the smaller pore sizes in comparison with the higher pores of **3.2.1-P10** or **3.2.1-P11**. Those intermediates with the methylated benzene rings towards the inner pore in **3.2.1-P8** and **3.2.1-P9** might not be stable due to higher steric interactions.

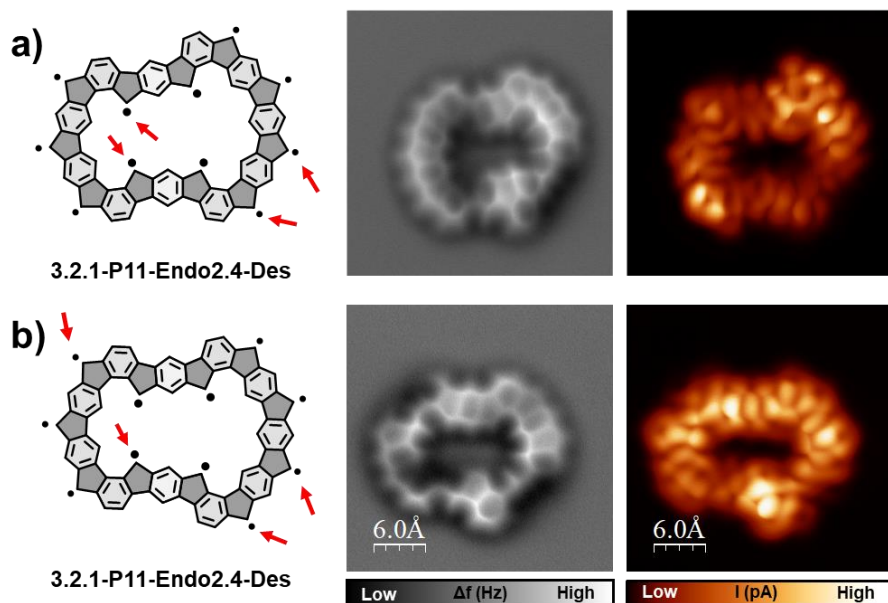
#### Tip-induced dehydrogenations

Tip-induced dehydrogenations were performed in **3.2.1-P11-Endo1**, **3.2.1-P11-Endo2.3** and **3.2.1-P11-Endo2.4**. Figures regarding the sequential removal of hydrogens can be found in the annexes: **Figure A 11**, **Figure A 12** and **Figure A 13**, respectively. As seen in the previous subsection for **3.2.1-P10-Des**, pronounced interactions of some of the pentagonal rings with the substrate after the hydrogen removals were exhibited for all the endo P11 products, as evidenced by the dark depressions highlighted with red arrows in the nc-AFM images presented in **Figure 79**. Notably, structures **3.2.1-P11-Endo1-Des** and **3.2.1-P11-Endo2.3-Des** depicted in **Figure 79 a** and **c**, respectively, displayed three interactions with the surface, resulting in eight free radicals delocalized within the molecular framework. In this regard it is not possible to state a magnetically active state for these isomers as a close-shell for all of them should be taken into account. Further theoretical calculations are required to gain more insights in this issue. On the other hand, **3.2.1-P11-Endo2.4-Des** in **Figure 79 e** showed four interactions with the surface with seven free  $\pi$  radicals. This molecular entity, due to its off-balanced radical count, should emerge as a magnetically active molecule. Future STS experiments are planned to get insights on the electronic properties of these entities.



**Figure 79.** Tip-induced dehydrogenation of 3.2.1-P11-Prec endo-isomers. a) nc-AFM image and simultaneously obtained constant height STM image of 3.2.1-P11-Endo1. b) Chemical model, nc-AFM image and simultaneously obtained constant height STM image of 3.2.1-P11-Endo1-Des. c) 3.2.1-P11-Endo 2.2. d) 3.2.1-P11-Endo 2.2-Des. e) 3.2.1-P11-Endo2.4. f) 3.2.1-P11-Endo2.4-Des. Scanning parameters were as follows: (a) to (f) 2 mV, 3 nm  $\times$  3 nm.

Finally, and similarly to 3.2.1-P10-Des, 3.2.1-P11-Endo2.4-Des also shows different isomers depending on the number and position of pentagonal rings that interact with the surface. **Figure 80** shows two examples of 3.2.1-P11-Endo2.4-Des isomers with the same number of pentagonal radicals interacting with the surface but at different locations. As commented before, further experiments are needed to explore the most stable isomers in terms of the interactions with the surface for each of the endo products already characterized.



**Figure 80.** Structural characterization of different isomers of **3.2.1-P11-Endo2.4-Des**. Every isomer **a)** and **b)** is characterized by its respective nc-AFM and constant height STM images simultaneously obtained. Red arrows depict the pentagonal rings involved in a strong interaction with the surface. Scanning parameters were as follows: (a) 2 mV (nc-AFM & STM), (b) 3 nm × 3 nm, 2 mV (nc-AFM & STM).

### Summary

After the sublimation of **3.2.1-P11-Prec** on Au(111) and its subsequent annealing at 310 °C, no **3.2.1-P11** macrocycles were observed. Instead, various endo products were detected, including **3.2.1-P11-Endo1**, **3.2.1-P11-Endo2.3**, and **3.2.1-P11-Endo2.4**. They were characterized by means of nc-AFM and CH-STM. A statistical analysis indicated that the reaction yield varies for these endo products, with **3.2.1-P11-Endo2.4** being the most prevalent.

Tip-induced dehydrogenation reactions were performed on the endo products, resulting in structures such as **3.2.1-P11-Endo1-Des**, **3.2.1-P11-Endo2.3-Des** and **3.2.1-P11-Endo2.4-Des**, exhibiting interactions with the substrate. Different isomers were observed for the endo-products depending on the number and position of pentagonal rings interacting with the surface, highlighting the importance of surface interactions in determining the stability and electronic properties of the molecules. Further studies are needed to fully understand the reaction mechanisms and electronic properties of these molecules.

### 3.2.6 P12 Macrocycle

In this subsection, we explore the results related to the outcomes of the ring closure reaction of **3.2.1-P12-Prec** on Au(111). Our expectations to synthesize the circular **3.2.1-P12** were low after the results obtained in the previous subsection with **3.2.1-P11-Prec**, which did not yield the circular **3.2.1-P11**. In this regard, the bigger the inner pore of the macrocycle is, the more possibilities the structure has to stabilize an intermediate where a double methylated benzene

ring is oriented towards the inner pore during the ring closure reactions (less steric hindrance). In this regard, we were interested in the characterization of the different expected planar endo-products related to the change in the macrocycle size from **3.2.1-P11** to **3.2.1-P12**. By means of STM and nc-AFM, we characterized these products, and subsequently, tip-induced reactions were conducted on them. The final products showed strong interactions with the surface as stated before for previous macrocycles.

At the end of the subsection, a final scheme is depicted, as a summary, with the outcomes of the ring closure reaction of all the macrocyclic precursor utilized (from **3.2.1-P8-Prec** to **3.2.1-P12-Prec**) to synthesize the cyclopenta-ring-fused oligo(*m*-phenylene) macrocycles.

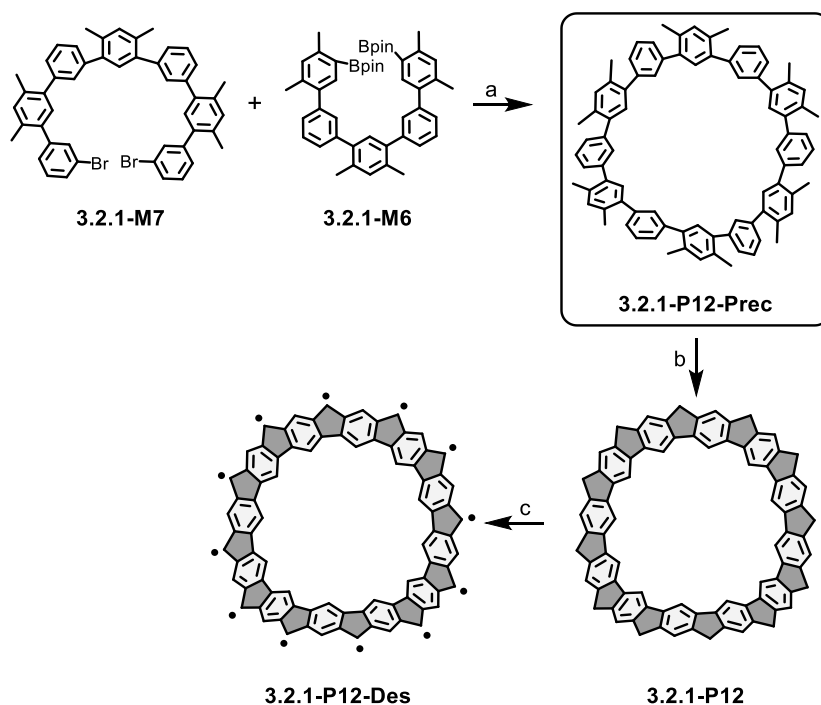
*In-Solution synthesis and on-surface characterization of the r.t phase*<sup>229</sup>

**3.2.1-P12-Prec** was yielded (11 %) after the final macrocyclization reaction between **3.2.1-M7** and **3.2.1-M6** (see **Scheme 29**). The synthesis towards **3.2.1-P12** commenced with the deposition of **3.2.1-P12-Prec** onto a clean Au(111) substrate maintained at r.t. using a tantalum pocket at 360 °C. Inspection of the STM images in **Figure 81 a, b, and c** did not reveal a well-defined self-assembly pattern of **3.2.1-P12-Prec**. Each molecule appeared in a different shape in STM, underscoring the great conformational freedom of **3.2.1-P12-Prec** and making challenging the assignment of a specific conformation. However, all of them had an oval shape with bright features in the inner pore of the ring.

---

<sup>229</sup> This work is a collaboration between the MOREFUN group from the University of Granada, where the monomer was synthesized, and the Nanosurf Lab from The Institute of Physics of the Czech Academy in Czech Republic, where the high-resolution STM and nc-AFM images, the STS spectroscopies and the computational calculations were conducted.

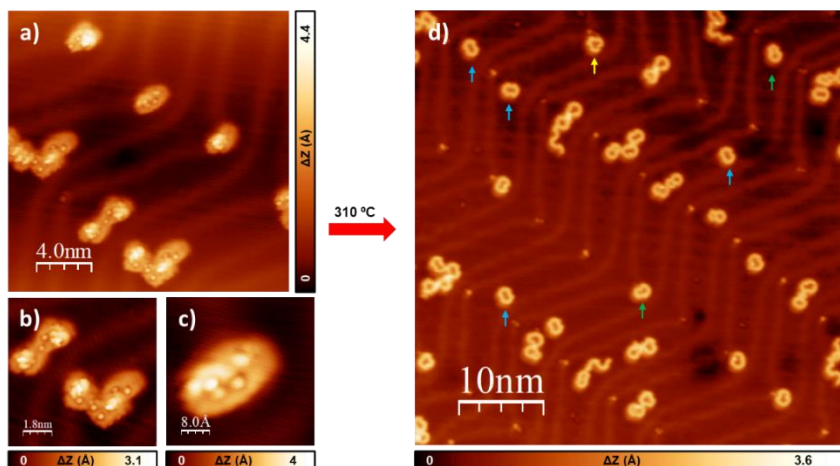




**Scheme 29.** Schematic representation of the synthetic strategy towards **3.2.1-P12-Des**. **a)**  $\text{Cs}_2\text{CO}_3$ ,  $\text{Pd}(\text{dppf})\text{Cl}_2$ , MeCN, Reflux, 24 h, 11 %. **b)** Sublimation on a Au(111) surface and subsequent annealing at 320 °C. **c)** Tip-induced dehydrogenations.

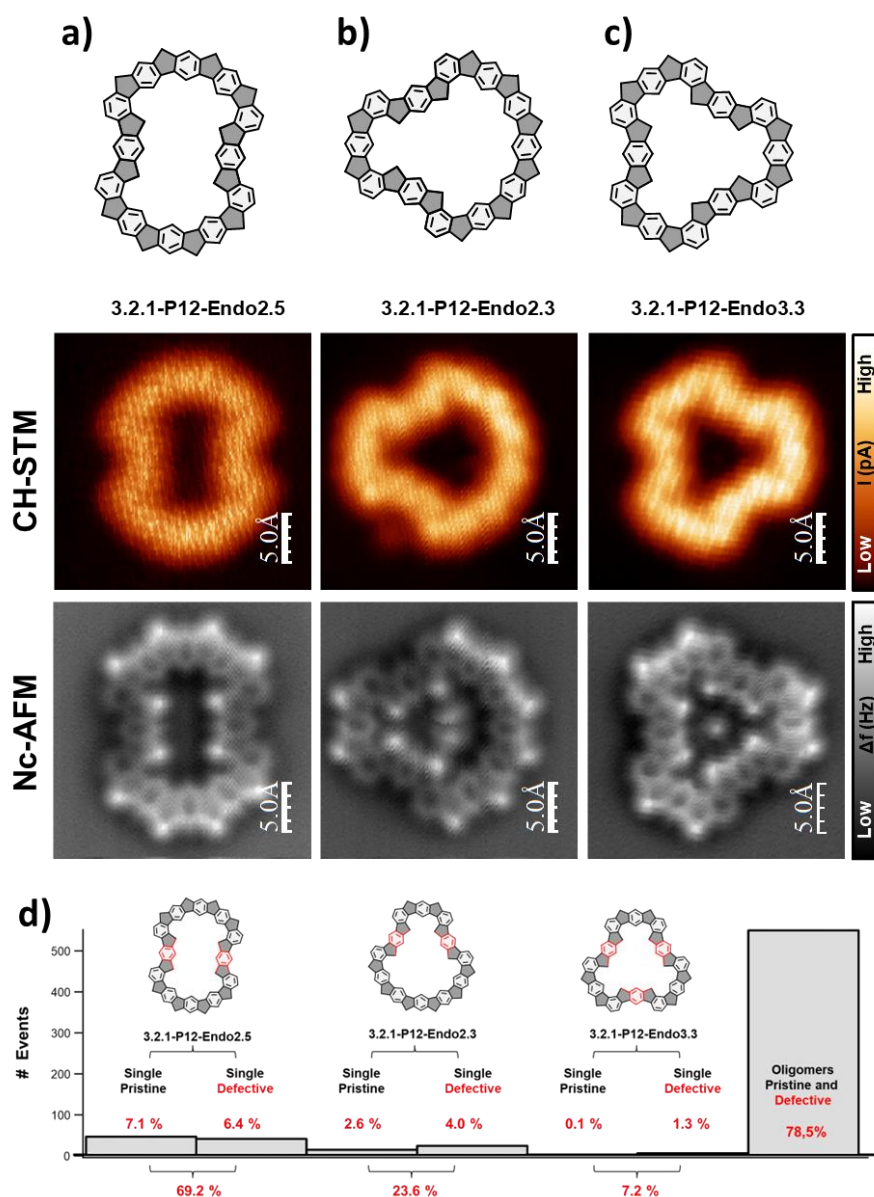
### Ring closure reaction

Subsequent annealing of the sample at 320 °C facilitated the oxidative ring closure reaction of the precursors. Examination of the topographic STM image in **Figure 81 d** revealed no indications of **3.2.1-P12** macrocycles, likewise in the previous subsection with **3.2.1-P11**. Instead, related endo products (macrocycles not perfectly round) were found, predominantly at the fcc region of the herringbone reconstruction of the Au(111), as depicted by green, blue and yellow arrows (different types of endo-products) in **Figure 81 d**. Additionally, various side products were observed with similar topologies as previously stated for the other macrocycles (cluster, oligomers, defective molecules, not fully reacted molecules...).



**Figure 81.** On-surface synthesis of **3.2.1-P12** molecule on Au(111) surface. **a)** Constant current topographic STM image of **3.2.1-P12-Prec**, r.t. phase. **b)** & **c)** Constant current detailed STM images. **d)** Constant current topographic STM image of cyclodehydrogenated **3.2.1-P12**. Scanning parameters were as follows: (a) 10 pA, 101 mV, (b) 10 pA, 101 mV, (c) 10 pA, 101 mV, (d) 10 pA, 101 mV.

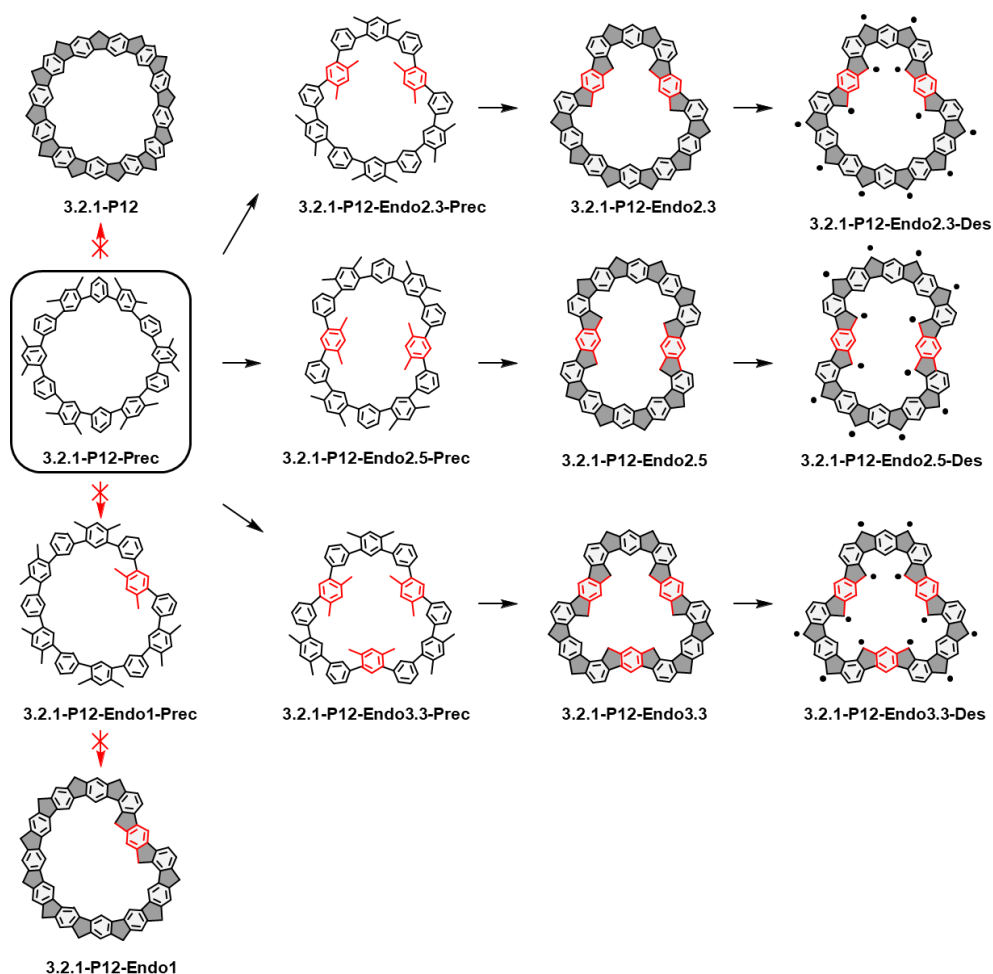
**Figure 82** presents a detailed analysis of the previously mentioned "endo-products" by high-resolution nc-AFM and constant height STM, as well as a statistical analysis of the outcomes of the reaction. In this case, the topology of the observed endo products varied again in comparison with those observed in previous **3.2.1-P10** and **3.2.1-P11**, as expected given its larger size (more degrees of freedom). It was observed **3.2.1-P12-Endo2.3** in **Figure 82 a**, **3.2.1-P12-Endo2.5** in **Figure 82 b** and **3.2.1-P12-Endo3.3** in **Figure 82 c**. All these structures exhibited a flat conformation (excluding the CH<sub>2</sub> moieties) with twelve bright protrusions in the nc-AFM images, corresponding to the out-of-plane CH<sub>2</sub> moieties situated at the apex of the pentagonal rings. In this regard, a statistical analysis, depicted in **Figure 82 d**, was conducted over more than 1000 molecules to assess the outcomes of the ring closure reaction. The synthesis yielded approximately 7 % of **3.2.1-P12-Endo2.5**, ~ 3% of **3.2.1-P12-Endo2.3**, and ~ 0.1% of **3.2.1-P12-Endo3.3** (only one case of a non-defective **3.2.1-P12-Endo3.3** molecule was found on the small scanned region of the single crystal). As state in the previous subsection, the column "single defective", at the right side of "single pristine" in **Figure 82 d**, is mainly integrated by partially reacted molecules or by molecules that lost at least one of the methyl moieties. Finally, the most prevalent category, constituting 79%, comprises clusters and oligomers formed by perfect and/or defective monomers.



**Figure 82.** Structural characterization (nc-AFM and constant height STM images simultaneously obtained) of the formed endo products after annealing the sample at 320 °C. **a)** Nc-AFM and constant height STM images of **3.2.1-P12-Endo2.5**. **b)** Nc-AFM and constant height STM images of **3.2.1-P12-Endo2.3**. **c)** Nc-AFM and constant height STM images of **3.2.1-P12-Endo3.3**. **d)** Statistical analysis of the outcomes from the on-surface ring closure reaction of **3.2.1-P12-Prec** on Au(111) at 320 °C. Scanning parameters were as follows (a) 2 mV, (b) 2 mV, (c) 2 mV.

**Scheme 30** shows which methylated benzene rings rotated towards the inner side of the pore, yielding the observed endo products. In the case of **3.2.1-P12-Iso2.3** and **3.2.1-P12-Iso2.5**, two methylated benzene rings rotated, while three of them did in **3.2.1-P12-Iso3.3**. We assume that the low yield of **3.2.1-P12-Iso3.3** (0.1 %) might be related to a higher strain of the intermediate

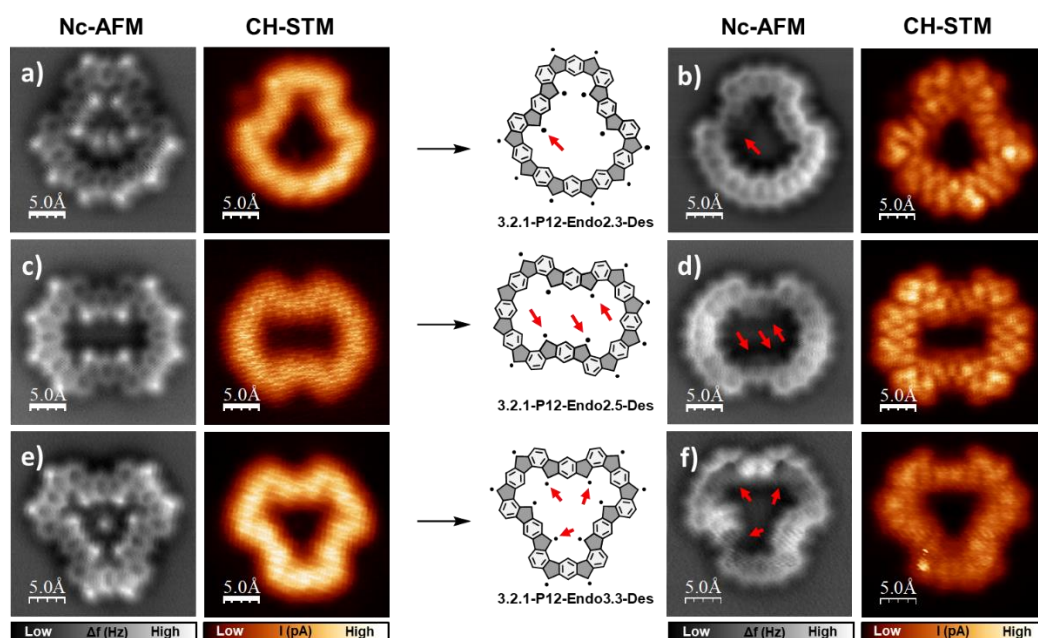
during the ring closure reaction (bigger steric hindrance between the methylated benzene rings in the inner pore). Further calculations, QM/MM, would help with the understanding in these yield differences between the macrocycles. The absence of **3.2.1-P12** and **3.2.1-P12-Endo1** macrocycles should be motivated by similar arguments as commented in the previous subsection (**3.2.5 P11 Macrocyclic**), where some intermediates with methylated benzene rings facing the inner side of the pore during the ring closure reaction should be energetically more favorable than **3.2.1-P12**. Additionally, preliminary calculations show that **3.2.1-P12** and **3.2.1-P12'-Endo1** are not planar molecules and, hence, they may result thermodynamically less favorable than the endo-products **3.2.1-P12-Iso2.3**, **3.2.1-P12-Iso2.5** and **3.2.1-P12-Iso3.3**.



**Scheme 30.** Outcome of the oxidative ring closure reaction of **3.2.1-P12-Prec** on Au(111) at 320 °C, and post tip-induced dehydrogenation of the **3.2.1-P12**endo isomers.

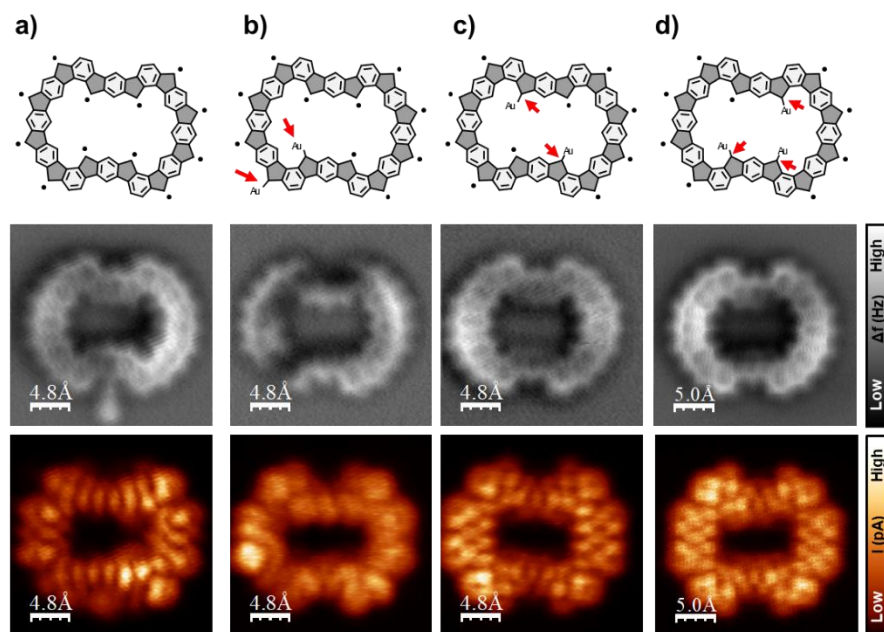
### Tip-induced dehydrogenations

Tip-induced dehydrogenations were performed in **3.2.1-P12-Endo2.3**, **3.2.1-P12-Endo2.5** and **3.2.1-P11-Endo3.3**. Figures regarding the sequential removal of hydrogens can be found in the annexes: **Figure A 14**, **Figure A 15** and **Figure A 16**. As seen in the previous subsections, pronounced interactions of some of the pentagonal rings with the substrate after (and during) the hydrogen removals were exhibited for all the P12 endo products, as evidenced by the dark depressions highlighted with red arrows in the nc-AFM images presented in **Figure 83**.



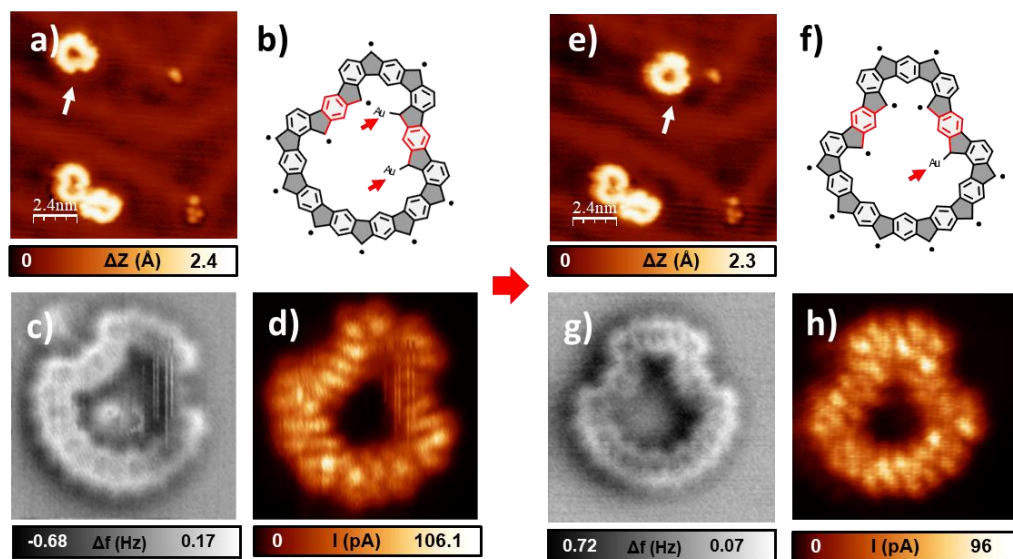
**Figure 83.** Tip-induced dehydrogenation of **3.2.1-P12** endo-isomers. **a)** Nc-AFM image and simultaneously obtained constant height STM image of **3.2.1-P12-Endo2.3**. **b)** **3.2.1-P12-Endo2.3-Des** **c)** **3.2.1-P12-Endo2.5** **d)** **3.2.1-P12-Endo2.5-Des**. **e)** **3.2.1-P12-Endo3.3**. Scanning parameters were as follows: **(a)** 2 mV, 2.5 nm × 2.5 nm; **(b)** 2 mV, 2.5 nm × 2.5 nm; **(c)** 2 mV, 2.5 nm × 2.5 nm; **(d)** 2 mV, 2.5 nm × 2.5 nm; **(e)** 2 mV, 2.5 nm × 2.5 nm; **(f)** 2 mV, 2.5 nm × 2.5 nm.

**3.2.1-P12-Endo2.5-Des** was further analyzed as it was the endo product synthesized in higher yield (~ 7%). Tip-induced dehydrogenations were performed in different **3.2.1-P12-Endo2.5** molecules. **Figure 84** shows different **3.2.1-P12-Endo2.5-Des** isomers depending on the number of interactions with the surface, exhibiting zero, two or three couplings with it; and with different distribution in the inner and on the outer ring of the macrocycle. Due to the huge number of possibilities regarding the number of isomers, the time required to perform the experiments, and the lack of a clear repetitive isomer, complicated a proper statistical analysis on the pentagonal interactions with the surface.



**Figure 84.** Structural characterization of different **3.2.1-P12-Endo2.5-Des** isomers. Every isomer is characterized by means of simultaneously obtained nc-AFM and constant height STM images. Scanning parameter were as follows: (a) 2 mV, (b) 2 mV, (c) 2 mV, (d) 2 mV.

Finally, a last experiment was performed to show the dependence of these isomers with their adsorption site on the Au(111) substrate. It is expected that depending on the registry of the radicals with the surface, they may couple or not with it (the coupling is more favorable on a top Au(111) position than on a bridge or a hollow positions, as already described in the literature<sup>220</sup>). **Figure 85** shows a manipulation event where a **3.2.1-P12-Endo2.3-Des** was moved (white arrows in **Figure 85 a** and **e**) with the subsequent change in the chemical structure as evidenced by the variation in the dark depressions in the nc-AFM images, (two pentagonal rings in **Figure 85 c** and one pentagonal ring in **Figure 85 g** as depicted with red arrows in their respective chemical models). In this sense, it can be assumed that the final geometry of the macrocycles is influenced by their adsorption site due to the interactions of the radicals located in the five-membered rings with the gold underneath.



**Figure 85.** Tip-induced manipulation of a **3.2.1-P12-Endo2.3-Des** macrocycle. **a)** Topographic constant current STM image before the manipulation event. **b)** Chemical model of **3.2.1-P12-Endo2.3-Des** depicting the pentagonal rings that are coupled to the surface. **c)** nc-AFM initial state image of **3.2.1-P12-Endo2.3-Des**. **d)** Simultaneously obtained constant height STM image. **e)** Topographic constant current STM image after the manipulation event. **f)** Chemical model of **3.2.1-P12-Endo2.3-Des** depicting the pentagonal rings that are coupled with the surface. **g)** nc-AFM final state image of **3.2.1-P12-Endo2.3-Des**. **h)** Simultaneously obtained constant height STM image. Scanning parameters were as follows: (a) 10 pA, 101 mV, (c) & (d) 2.4 nm × 2.4 nm, 2 mV, (e) 10 pA, 101 mV, (g) & (h) 2.4 nm × 2.4 nm, 2 mV.

### Summary

In summary, the oxidative ring closure reaction of **3.2.1-P12-Prec** on Au(111) mainly yielded endo products with varied topologies encompassing **3.2.1-P12-Endo2.3**, **3.2.1-P12-Endo2.5** and **3.2.1-P12-Endo3.3**, and failed to produce the circular **3.2.1-P12** macrocycle. Statistical analysis of the outcomes of the reaction revealed that the most prevalent endo-product was **3.2.1-P12-Endo2.5** with a ~ 7% yield, followed by **3.2.1-P12-Endo2.3** in ~ 3 % yield. On the other hand, **3.2.1-P12-Endo3.3** was difficult to find on the surface (it was only observed once).

Tip-induced dehydrogenations showed pronounced interactions between unpaired electrons localized at the five-membered rings of the endo-products with the substrate, yielding different curved isomers depending on the number of interactions and the position of them. Further experiments, i.e. manipulating a **3.2.1-P12-Endo2.3** macrocycle, demonstrated the dependence of these isomers with their chemisorption position on the substrate. Future experiments and calculations characterizing the electronic properties of the macrocycles are required to understand the ground state of these compounds.

### Summary of the synthesized macrocycles

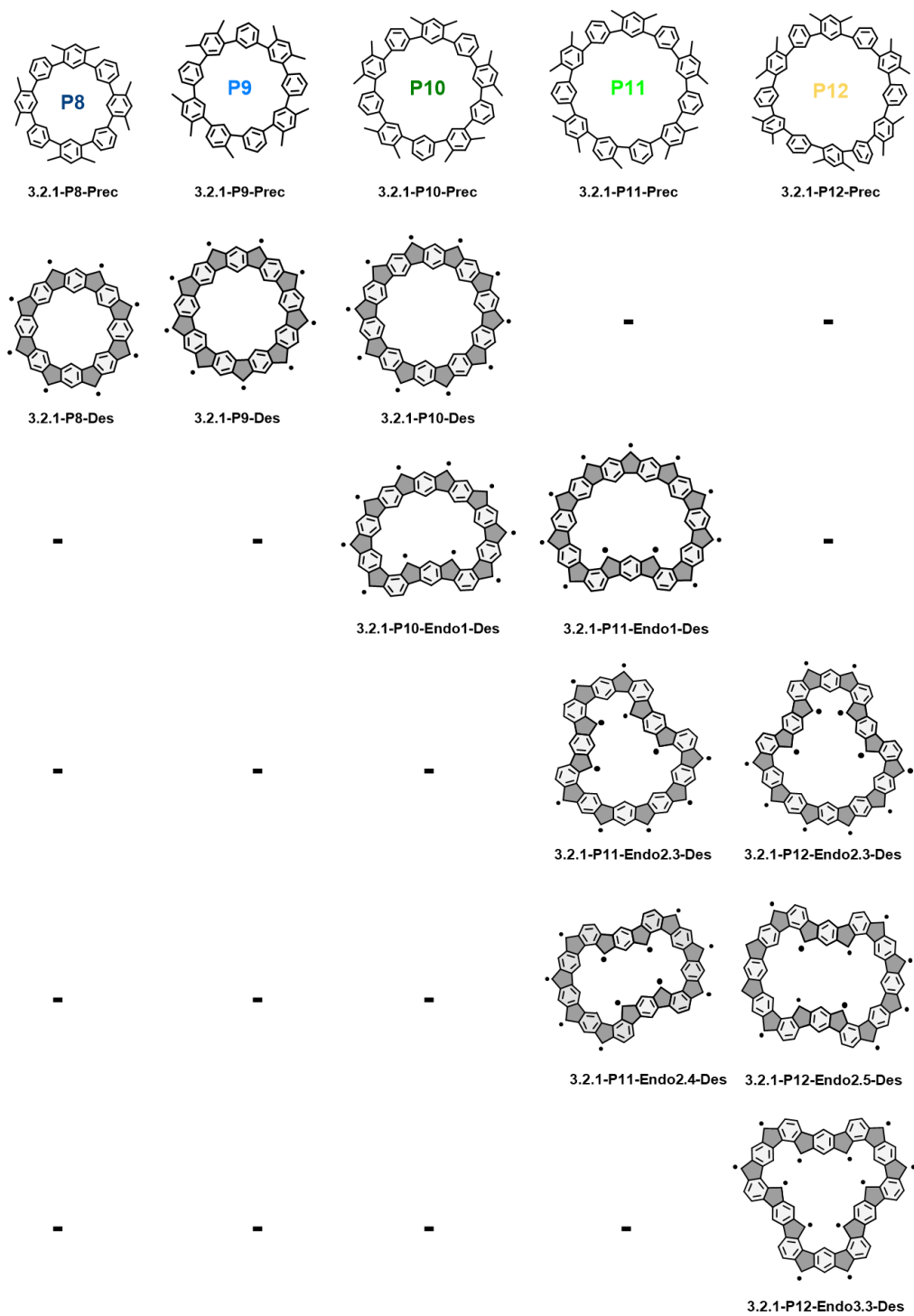
As a summary, **Scheme 31** shows the on-surface synthesis on Au(111) of the different macrocycles obtained from **3.2.1-P8-Prec** to **3.2.1-P12-Prec**. As it can be seen, round macrocyclic products were only obtained for **3.2.1-P8**, **3.2.1-P9** and **3.2.1-P10** after the thermal ring closure reaction. **3.2.1-P8** performed a positive (bowl) curvature (due to inner structural strain) before and after performing the tip-induced dehydrogenations on the CH<sub>2</sub> moieties. On the other hand, **3.2.1-P9** showcased a flat conformation before and after the final dehydrogenations, and finally, although **3.2.1-P10** showed a flat conformation after the thermal ring closure reaction, it became curved after the tip-induced dehydrogenations due to localized interactions of some of their pentagonal rings with the underlying Au(111) surface. The interaction of the pentagonal rings with the surface was also observed in the products obtained from **3.2.1-P11-Prec** and **3.2.1-P12-Prec**.

Above the “P10 size”, some “endo products” started to be synthesized after the ring closure reaction. We ascribe the major stability of these higher size endo products to their higher planarity (endo products would have presented a large curvature for **3.2.1-P8-Prec** and **3.2.1-P9-Prec**). In this regard, the more planar they are, the more van der Waals interactions with the surface they have, enhancing certain reaction pathways during the ring closure reaction. In this sense, “endo1 macrocycles” were synthesized for **3.2.1-P10-Prec** and **3.2.1-P11-Prec**, “endo2.X macrocycles” were synthesized for **3.2.1-P11-Prec** and **3.2.1-P12-Prec**, and an “endo3.1 macrocycle” was synthesized for **3.2.1-P12-Prec** (see



**3.2.5** P11 for the endo nomenclature).

Future experiments will be conducted with the already in-solution prepared precursors: **3.2.1-P6-Prec**, **3.2.1-P7-Prec**, **3.2.1-P13-Prec** and **3.2.1-P14-Prec** macrocycles presented in the **3.2.1** subsection. In this regard, it is expected that **3.2.1-P6-Prec** and **3.2.1-P7-Prec** will present an even higher curved structure with a truncated cone geometry (positive curvature) after their ring-closure reactions. Additionally, the final macrocycle from **3.2.1-P7-Prec** may present a magnetically active ground state due to its odd number of unpaired electrons. Conversely, we mainly expect more endo products for the higher **3.2.1-P13-Prec** and **3.2.1-P14-Prec**, increasing the yield for the “endo3.X macrocycle” topology in these bigger precursors. Exciting new topologies and properties may arise from these precursors, but this is a target for future experiments.



Scheme 31. Summary of the on-surface synthesis from 3.2.1-P8-Des to 3.2.1-P12-Des.

### 3.3 A Cyclopentaannulated Chevron-Like Graphene Nanoribbon Composed of Nanodomains

Finally, beyond the generation of curvature due to the steric hindrance between rings or substituents,<sup>230</sup> as occurring in helicenes or twistacenes, or to the inner structural strain induced by lattice defects<sup>114</sup>, as in nanographenes containing seven-membered ring<sup>231</sup> or in the cyclopenta-ring-fused oligo(*m*-phenylene) macrocycles, this section focuses on an alternative approach based on the interaction of localized radicals (from the graphenic nanostructures) with the underlying surface on which they are adsorbed.

This study was inspired by the previously observed evidence of how some localized radical electrons in **3.2.1-P10-Des**, **3.2.1-P11-Des** and **3.2.1-P12-Des** attached to the surface, and how this behavior curved their structures in an unexpected fashion (considering the steric interactions and inner strain factors, the compounds should not possess that curvature without the interaction with the surface). Interestingly, other structures have already been reported exhibiting similar interactions with the surface, as truxene<sup>219</sup>, the clar's goblet, triangulene<sup>232</sup>, or the indeno[1,2-*a*]fluorene<sup>220</sup>. Therefore, we considered to use this phenomenon to induce curvature by design in other graphenic nanostructures bearing radicals at the pentagonal rings.

For that purpose, a new chevron-like GNR **3.3-GNR (Scheme 32)** was designed with pentagonal rings at the sides of the structure to be partially dehydrogenated (with the tip of the probe) to induce their interaction with the surface, and with a suitable monomer size to couple with the surface with a subsequent wrinkle of the structure (it is needed a wider monomer, ~ 1.15 nm from 5-membered ring to 5-membered ring, in comparison to the atomic spacing where the pentagonal rings attach to the surface, ~ 0.95 nm). In this regard, Monomer **3.3-Mono** was designed to incorporate Br atoms at “meta” positions to achieve graphene nanoribbons with chevron topology, and methyl moieties to give rise to the pentagonal rings and the extra hexagonal ring in the top part of **3.3-GNR** (the non-benzenoid rings are on-surface synthesized contrary to the section 3.1 where non-benzenoid rings were already included in the in-solution synthesis).

Although other GNRs bearing non-benzenoid rings have already been synthesized on surfaces<sup>233</sup>, in this section we report on the first example of an on-surface synthesized curved GNR. In this regard, we will describe the in-solution synthesis of the precursor and the sequential steps of the on-surface synthesis (r.t. phase, Ullmann coupling, cyclodehydrogenation and ring closure reaction), analyzing the different intermediates obtained by means of STM and

<sup>230</sup> M. Rickhaus, M. Mayor, M. Jurićek, *Chem. Soc. Rev.*, **2016**, *45*, 1542–1556.

<sup>231</sup> **a)** Chaolumen, I. A. Stepek, K. E. Yamada, H. Ito, K. Itami, *Angew. Chem. Int. Ed.*, **2021**, *60*, 23508. **b)** I. R. Márquez, S. Castro-Fernández, A. Millán, A. G. Campaña, *Chem. Com-mun.*, **2018**, *54*, 6705. **c)** S. H. Pun, Q. Miao, *Acc. Chem. Res.*, **2018**, *51*, 1630.

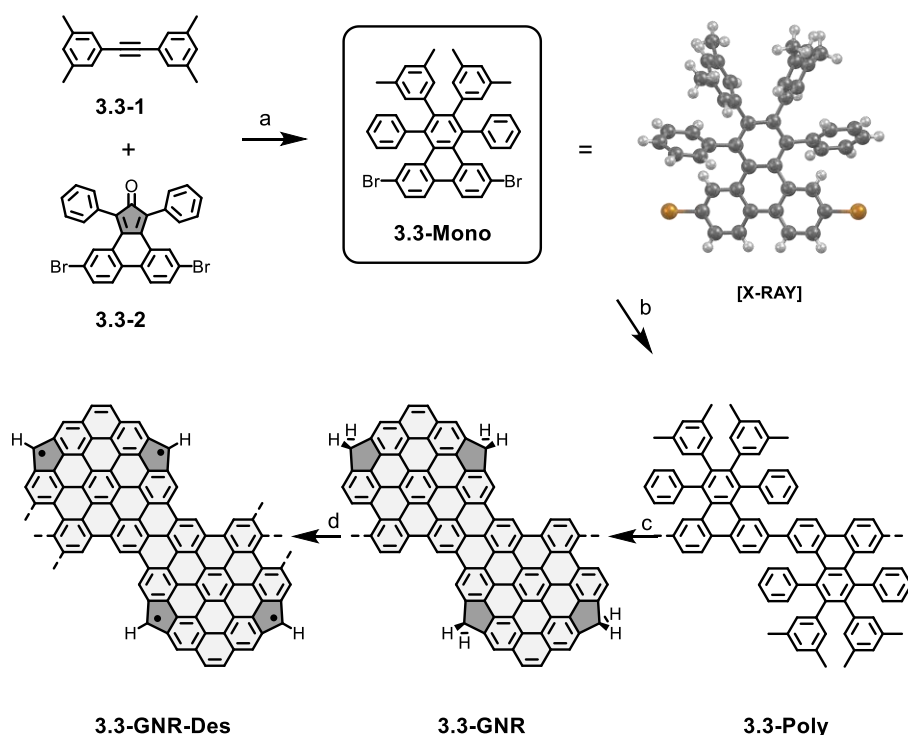
<sup>232</sup> C. Zhao, Q. Huang, L. Valenta, K. Eimre, L. Yang, A. V. Yakutovich, W. Xu, J. Ma, X. Feng, M. Jurićek, R. Fasel, P. Ruffieux, C. A. Pignedoli, *Phys. Rev. Lett.*, **2024**, *132*, 046201.

<sup>233</sup> **a)** M. Liu, M. Liu, L. She, Z. Zha, J. Pan, S. Li, T. Li, Y. He, Z. Cai, J. Wang, Y. Zheng, X. Qiu, D. Zhong, *Nat. Commun.*, **2017**, *8*, 14924. **b)** Q. Fan, L. Yan, M. W. Tripp, S. R. Kachel, M. Chen, A. S. Foster, U. Koert, P. Liljeroth, J. M. Gottfried, *Science*, **2021**, *372*, 852-856.

nc-AFM. We will delve into the characterization of the registry with the surface by nc-AFM imaging, including manipulation experiments to modify it. Finally, the magnetic and the electronic properties are inspected, remarking the influence of the curvature in the GNR and in the hybridization with the substrate.

*In-Solution synthesis and on-surface characterization of the r.t phase*<sup>234</sup>

The in-solution synthesis of **3.3-Mono** was successfully achieved through a Diels Alder reaction between alkyne **3.3-1** and cyclopentadienone **3.3-2**. **3.3-Mono**. The final product was characterized by means of <sup>1</sup>H NMR and <sup>13</sup>C NMR, HR-MS, IR and x-ray diffraction (**Scheme 32**).



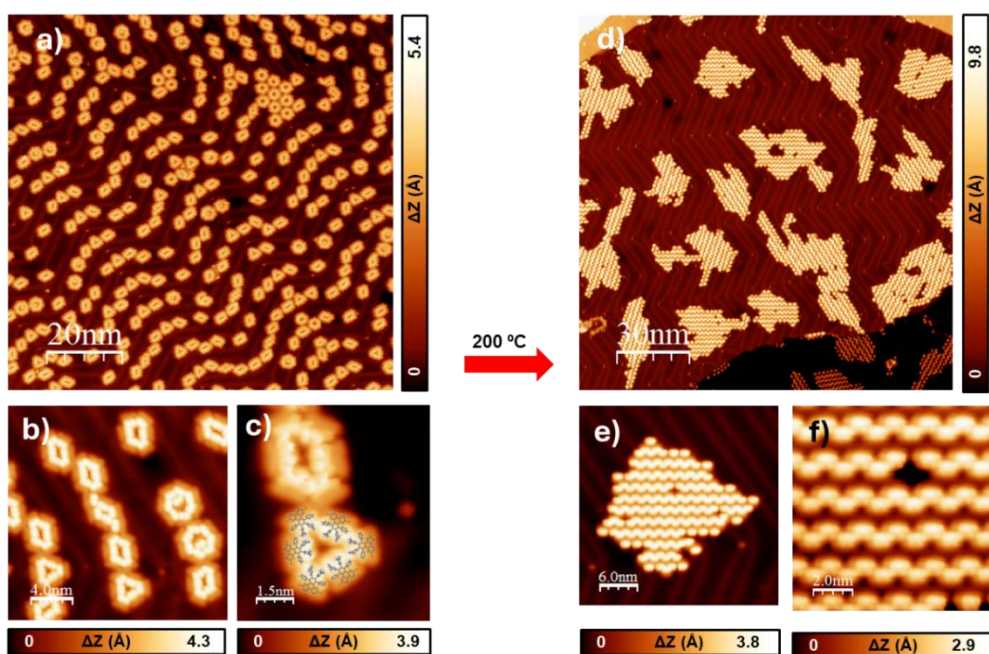
**Scheme 32.** Schematic representation of the in-solution synthesis of monomer **3.3-Mono** and the on-surface synthesis of GNR **3.2.1-5**. a) Ph<sub>2</sub>O, reflux, 2 h, 85 %, b) Annealing at 475 K on a Au(111) surface. c) Annealing at 675 K on a Au(111) surface.

<sup>234</sup> This work is a collaboration between MOREFUN group from the University of Granada, where the monomer was synthesized, the ESISNA group from ICMM-CSIC, where the growth of the nanostructures was studied, the Advanced Microscopy Laboratory from the University of Zaragoza, and the Nanosurf Lab from the Institute of Physics of the Czech Academy of Science in Czech Republic, where the high-resolution STM and nc-AFM images and STS spectra were taken.

**Figure 86 a** presents a STM image of the r.t. phase of **3.3-Mono**. The precursor was sublimated from a crucible at 225 °C onto a Au(111) surface held at r.t. For a coverage of  $\sim 0.3$  monolayers, **Figure 86 b** shows the different self-assembly patterns of **3.3-Mono**. The precursor arranges into small clusters of 6-7 units that followed the Au(111) surface reconstruction and that had different topologies as triangles, rectangles, rhomboids... As depicted in **Figure 86 c**, monomers tended to arrange in the clusters orienting the methylated benzene rings of **3.3-Mono** towards the inner pore of the cluster, to maximize the  $\pi - \pi$  interactions.

### Polymeric phase

Further annealing of the sample at 200 °C triggered the Ullman coupling reaction yielding the polymer **3.3-Poly**, as shown in **Figure 86 d**. **Figure 86 e** and **f** show how all the monomers in the **3.3-Poly** polymers have the same appearance (no unexpected reactions are happening), and how they agglomerate into islands due to an attractive  $\pi - \pi$  interaction between the external interdigitated phenyl rings, as common for chevron-like GNRs<sup>161</sup>.



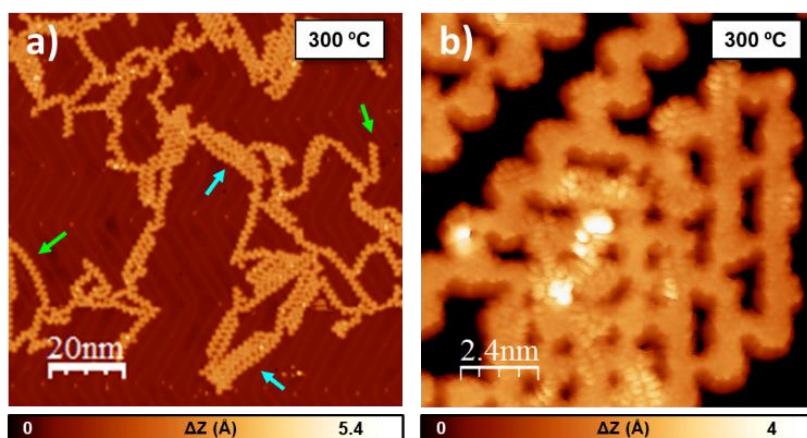
**Figure 86.** R.t. and polymer phase in the on-surface synthesis of **3.3-GNR-Des** on Au(111). **a**), **b**) & **c**) Topographic and detailed constant current STM images of **3.3-Mono** in the r.t. phase. **d**), **e**) & **f**) Topographic and detailed constant current STM images of **3.3-Poly** after polymerization. Scanning parameters were as follows: (a) 50 pA, -200 mV, (b) -100 mV, 31.6 pA, (c) -100 mV, 31.6 pA, (d) 30 pA, 1 V, (e) 30 pA, 1 V, (f) 30 pA, 1 V.

### Cyclodehydrogenation and ring closure reaction

A subsequent annealing step was conducted at 300 °C to induce cyclodehydrogenation and ring closure reactions in **3.3-Poly**. Topographic STM image in **Figure 87 a** shows two kinds of

topologies after this step: a “porous graphene”, as depicted with blue arrows, and some GNRs segments highlighted with green arrows.

High resolution STM image from **Figure 87 b** shows the “porous graphene” that presents an inhomogeneous porosity and several defects. We speculate that this porosity is due to a competition between the intra-ring closure reaction and the interchain covalent coupling involving the methyl moieties. The irregularity in the porosity can be attributed to the several fashions in which the four methyl groups of one monomer may couple with other positions of another GNR. Further analysis of the “porous graphene” was not conducted due to the lack of reproducibility in these porous patterns.



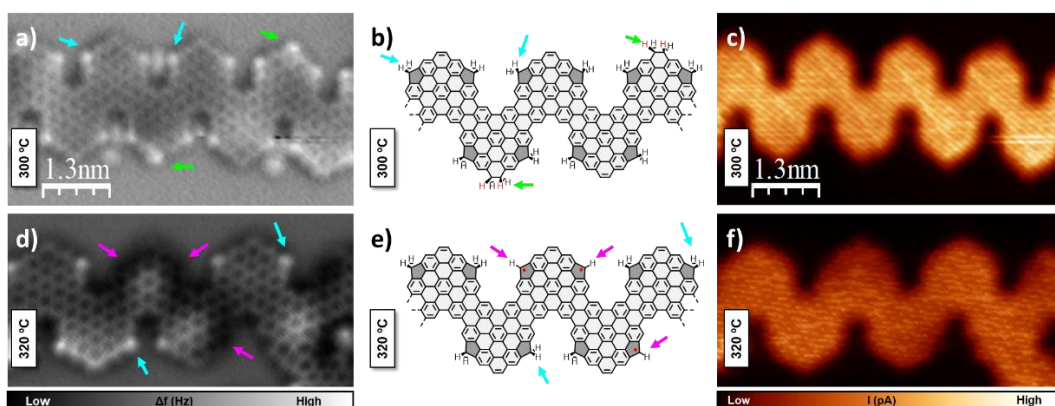
**Figure 87.** Cyclodehydrogenated 3.3-GNR phase after annealing the Au(111) at 300 °C. **a)** Topographic constant current STM image of the 3.3-GNR phase. **b)** Detailed constant current STM image of the “porous graphene”. Scanning parameters were as follows: (a) 51.3 pA, 1.07 V, (b) 5 mV, 60 pA.

“Pristine” GNRs segments of 3.3-GNR were inspected in **Figure 88**. It is worthwhile to mention that we were not able to find an isolated GNR, always presenting at least one bond to another GNR. Hence, we can assume similar energy barriers between the intra-ring oxidative closure and the interchain covalent coupling mentioned before.

Nc-AFM image from **Figure 88 a** shows a GNR with a flat backbone, bright protrusions at the sides of each monomer (see blue arrows), and bright protrusions at the top part of some monomers (see green arrows). We relate these features to the hydrogens pointing up from the  $sp^3$  carbons of the pentagonal rings (blue arrow) and the hexagonal rings (green arrow). We consider the top hexagonal rings (those with a bright protrusion) doubly hydrogenated as depicted in **Figure 88 b** since a monohydrogenated hexagonal ring would have an unpaired radical that should have been measured either through a Kondo resonance in the CH STM image from **Figure 88 c**, or through a dark depression in the nc-AFM image from **Figure 88 a** due to a strong interaction with the surface.

An additional annealing step at 320 °C was conducted to further thermally dehydrogenate the structure. In this case, **Figure 88 d** shows an intermediate state between 3.3-GNR and 3.3-

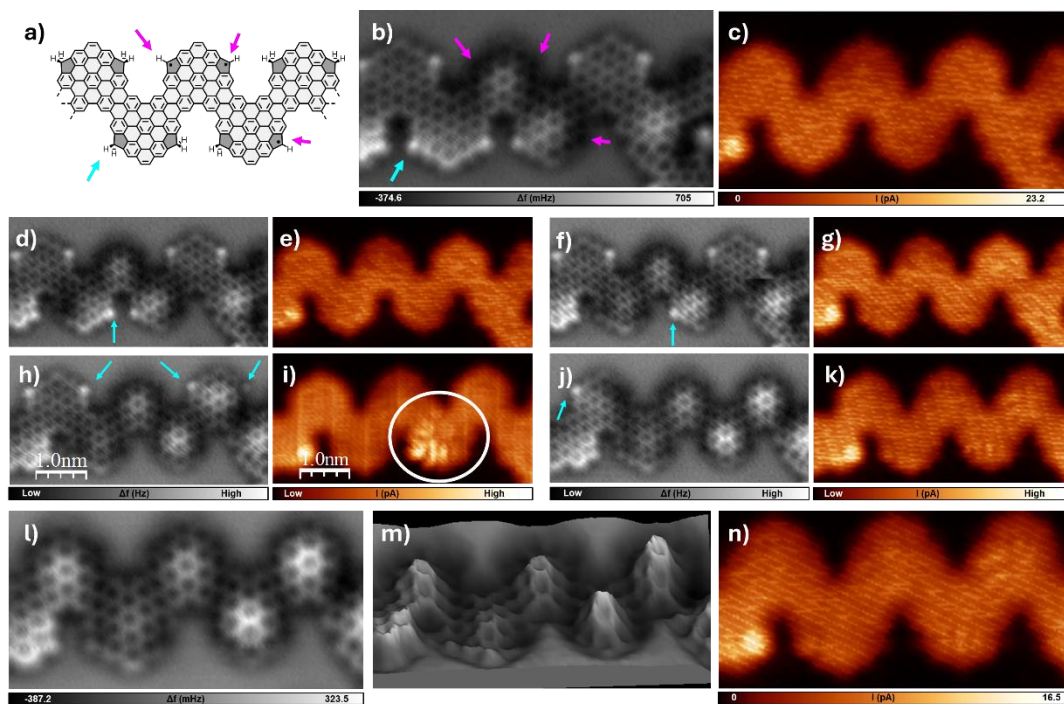
**GNR-Des** where every hexagonal ring was dehydrogenated (no bright protrusions are seen anymore) and where some of the pentagonal rings were already dehydrogenated, resulting in a dark depression in the surface (pink arrow). Therefore, we can assume that more energy is required to dehydrogenate the pentagonal rings of **3.3-GNR** than the hexagonal moieties of **3.3-GNR**.



**Figure 88.** High resolution images of **3.3-GNR** at different temperatures and different dehydrogenation stages. **a)**, **b)** and **c)** nc-AFM image, chemical model and CH-STM image, respectively, of a GNR after annealing the sample at 300 °C. Blue/green arrows depict not dehydrogenated pentagonal/hexagonal rings. **d)**, **e)** and **f)** nc-AFM image, chemical model and CH-STM image, respectively, of a GNR after annealing the sample at 320 °C. Blue/pink arrows depict not dehydrogenated/dehydrogenated pentagonal rings. Scanning parameters were as follows: **(a)** and **(c)** 5 mV, **(d)** and **(f)** 3 nm × 3 nm, 5 mV.

### Tip-induced dehydrogenations

Tip-induced dehydrogenations were employed to sequentially remove extra hydrogens from **3.3-GNR**, giving rise to the formation of the final **3.3-GNR-Des**. Following this procedure, hydrogens from all the pentagonal units were sequentially removed, as can be seen in the nc-AFM images with its respective constant height STM images in **Figure 89 a** to **n** (some intermediates of the dehydrogenation process are avoided to preserve conciseness in the figure). Nc-AFM image in **Figure 89 i** shows an indicative difference in the frequency shift values between the central part of some monomers of the **3.3-GNR-Des** GNR and their peripheric parts (where the pentagonal rings are located). In this regard, we can understand **3.3-GNR-Des** as a GNR that comprises “nanodomes” per unit monomer with positive bowl curvatures, as shown in the qualitative 3D model of the nc-AFM image in **Figure 89 m**.



**Figure 89.** Site-selective **3.3-GNR** dehydrogenation by the SPM probe tip. Tip-induced dehydrogenations were performed in the GNR phase formed at 320 °C. **a), b)** and **c)** Chemical model, nc-AFM image and simultaneously obtained constant height STM image of the initial state. Blue/pink arrows depict hydrogenated/dehydrogenated positions. **d) to k)** Sequential changes in the GNR after tip-induced dehydrogenations. **l), m)** and **n)** Final state.

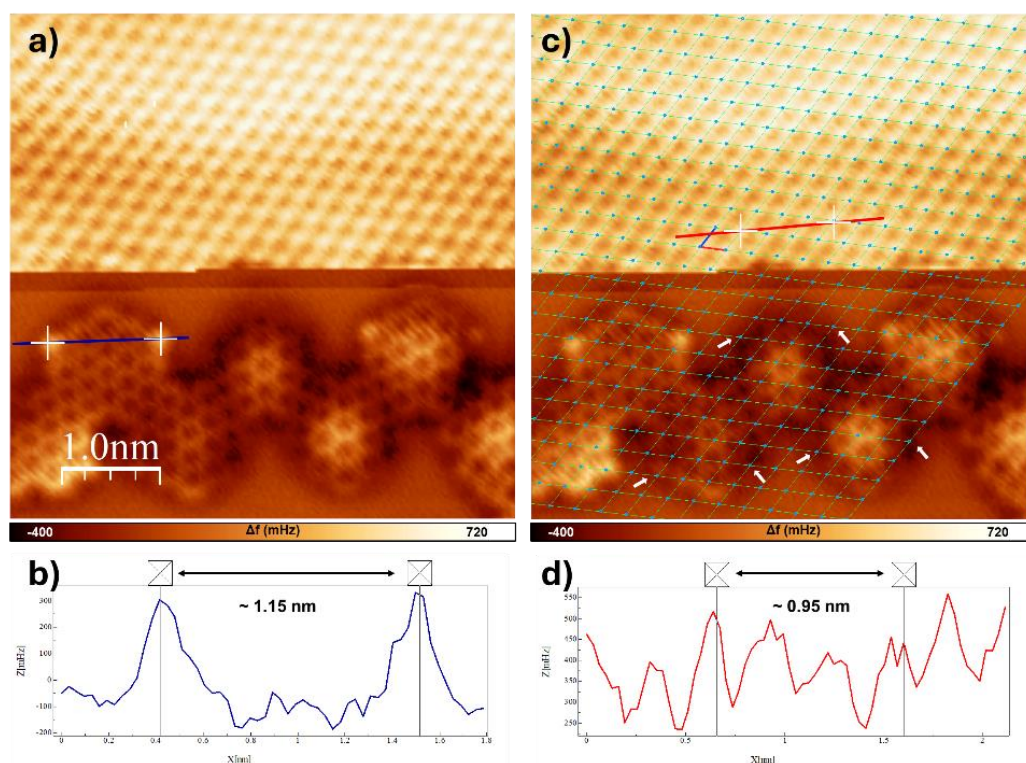
Nc-AFM image, its respective 3D model (showing the “nanodome” structure per monomer, and the simultaneously obtained constant height STM image. Every image was acquired with same scanning parameters (**a)** to **(n)**): 3 nm × 3 nm, 5 mV.

### Adsorption analysis

To have a better understanding of the GNR curvature and its registry with the surface, a nc-AFM image of a semidehydrogenated **3.3-GNR-Des** with atomic resolution of the Au(111) lattice was obtained. The acquisition of the image was conducted as follows: first (in the same image), scanning the Au lattice in constant height mode with a fixed height (close approach); and second, scanning the ribbon in constant height mode with a different height (the height of the tip was shifted manually during the image acquisition).

Tracing a profile (**Figure 90 b)** in the nc-AFM image in **Figure 90 a)** a distance between contiguous hydrogenated positions of 1.15 nm was obtained. Additionally, to tentatively assigned the interaction sites between the dehydrogenated C atoms and the underlying Au surface, an artificial lattice simulating the Au(111) atomic positions was superimposed in **Figure 90 c)**. The coupling positions are indicated in the nc-AFM image with white arrows, resulting in a distance ~ 0.95 nm from one position of the Au lattice to the other (see diagram in **Figure 90 d)**.





**Figure 90.** Registry with the Au(111) substrate of a semydehydrogenated GNR. **a)** and **c)** nc-AFM images without and with (respectively) the drawn lattice. **b)** and **d)** distance diagrams obtained in **a)** and **c)**, respectively. Scanning parameter: **(a)** and **(c)** 1 mV.

Therefore, we can ascribe the origin of the before mentioned distortion of the structure to the interaction of the localized radicals in the pentagonal rings with the surface underneath. It is already known in the literature that this interaction is maximized when the radical is located on a top position of the Au(111) lattice. Hence, we assume that the **3.3-GNR-Des** adapts its structure (wrinkles) to the lattice distances to augment the interaction, curving its structure with a resulting depression of the lateral parts and an elevation of its central region.

### Magnetic characterization

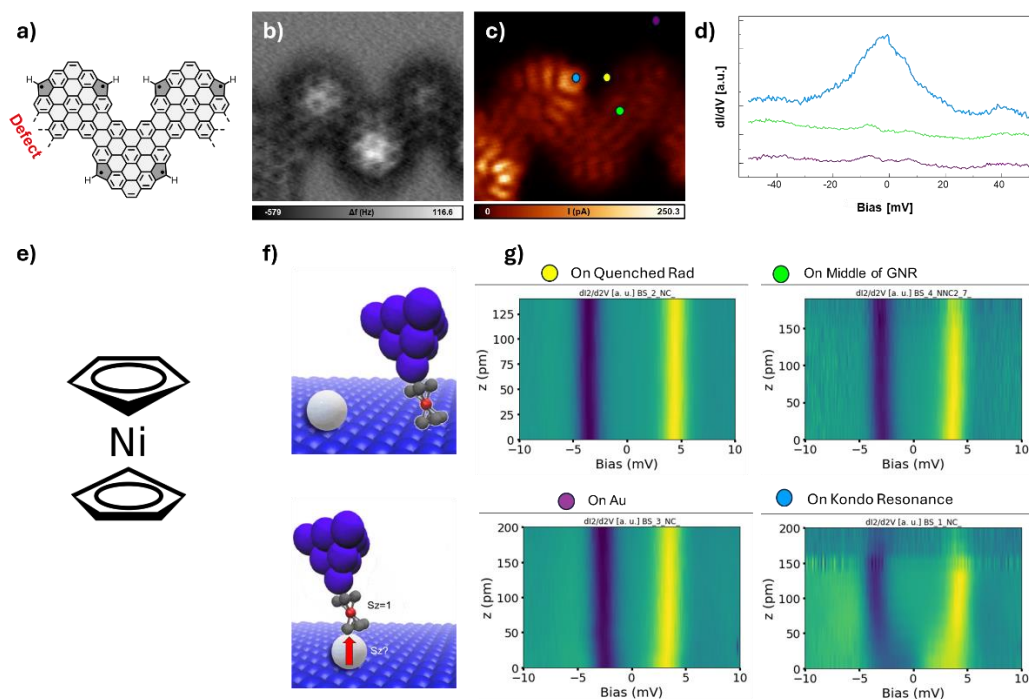
During the tip-induced dehydrogenation processes in **Figure 89**, new states near zero bias emerged in the constant height STM channel, as can be seen in the white circle in **Figure 89 d**. In order to characterize these resonances, STS with a functionalized CO tip was performed. This analysis was carried out in a GNR composed by three consecutive pristine units of **3.3-GNR-Des** and a defective unit on the left side of the ribbon, **Figure 91 a**. As can be seen in the point spectra from **Figure 91 d**, a state emerges at zero bias related with an unpaired electron mainly localized in a five-membered ring in the structure (blue curve in the STS). Other positions of the ribbon, as other five-membered rings or other benzene rings in the GNR backbone did not show any resonance at zero bias (green curve in the STS).

These “zero bias” states may relate to magnetic Kondo resonances due to  $\pi$  radicals. While, in principle, all radicals should strongly interact with the surface quenching its magnetic signature (for the **3.3-GNR-Des**), some of them might not have the appropriate top position geometry on the Au sample, thus presenting a magnetic response. To analyze the magnetic character of these states, STS at different heights with a nickelocene ( $\text{NiCp}_2$ ) tip were performed.  $\text{NiCp}_2$  is a magnetic molecule with  $S_z=1$  and magnetic anisotropy of  $\sim 4\text{meV}$ . These properties make them a potential single-molecule magnetic sensor when attached to a STM probe<sup>235</sup>. Recorded STS spectra with the  $\text{NiCp}_2$  tip at different heights (within a reasonable height range) should remain constant (regarding the energy, the intensity of the signal may obviously change) when there is no magnetic impurity in the approaching point underneath. On the other hand, when the tip approaches a magnetic impurity, spectra at close distances may shift compared to spectra at long distances due to the magnetic exchange coupling  $J(z)$  between the  $\text{NiCp}_2$  tip and the magnetic impurity below.

As can be seen in **Figure 91 g**  $\text{NiCp}_2$  STS remains constant at different heights when it is performed on the middle of the chain (green dot), on top of a pentagonal ring that does not exhibit a zero-bias state (yellow dot), or on top of the Au(111) substrate (purple dot). This result qualitatively indicates that none of these positions in the ribbon or in the substrate have a magnetic character. On the other hand, when the  $\text{NiCp}_2$  STS is performed on top of the pentagonal ring with the Kondo resonance (blue position in **Figure 91 b**), the STS at short distances narrowed, indicating a magnetic exchange coupling with that position of the GNR and proving the magnetic character of that zero-bias signal.

---

<sup>235</sup> **a)** G. Czap, P. J. Wagner, F. Xue, L. Gu, J. Li, J. Yao, R. Wu, W. Ho, *Science*, **2019**, *364*, 670–673. **b)** M. Ormaza, N. Bachellier, M. N. Faraggi, B. Verlhac, P. Abufager, P. Ohresser, L. Joly, M. Romeo, F. Scheurer, M.-L. Bocquet, N. Lorente, L. Limot, *Nano Lett.*, **2017**, *17*, 1877–1882. **c)** B. Verlhac, N. Bachellier, L. Garnier, M. Ormaza, P. Abufager, R. Robles, M.-L. Bocquet, M. Ternes, N. Lorente, L. Limot, *Science*, **2019**, *366*, 623–627.



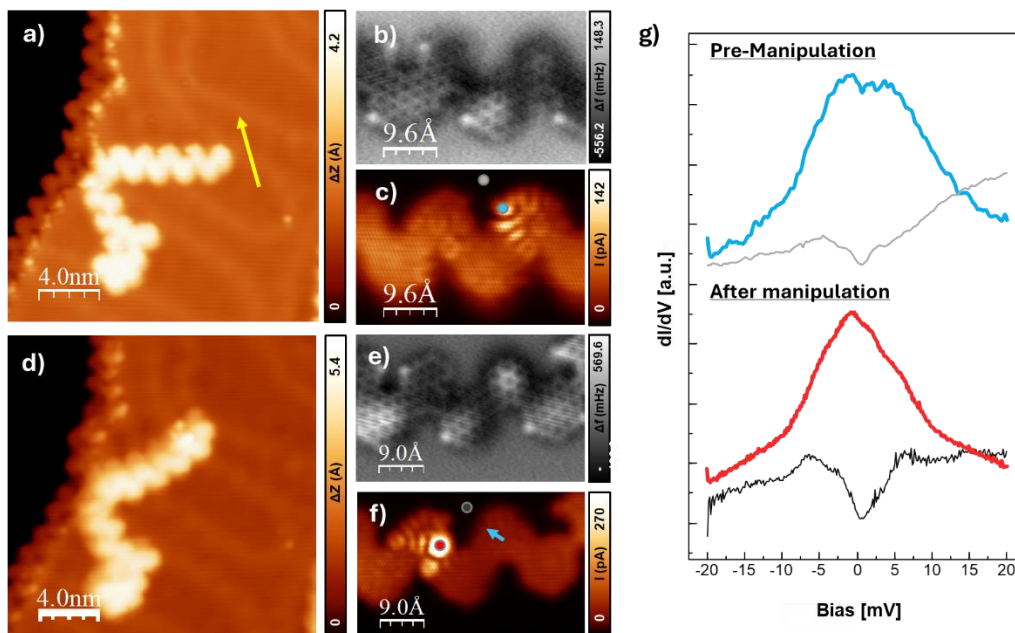
**Figure 91.** Magnetic characterization a 3,3-GNR-Des. **a)** Chemical model of the analyzed GNR. **b) & c)** nc-AFM image and constant height STM image simultaneously obtained. **d)**  $dI/dV$  point spectra with CO tip. **e)** Chemical structure of the nickelocene molecule. **f)** Schematics of the process of measuring the magnetic response with a Nickelocene tip. **g)** STS spectra at different heights and different positions on the GNR with a nickelocene tip. Y axis is the second derivative of the current  $d^2I/d^2V$ . Positions where the spectra were acquired are color code at figure b). Scanning and spectra parameters were as follows: **(b)**  $3 \text{ nm} \times 2.7 \text{ nm}$ , 4 mV, **(c)**  $3 \text{ nm} \times 2.7 \text{ nm}$ , 4 mV, **(d)**  $V_{\text{Mod}} = 1 \text{ mV}$ , **(g)**  $V_{\text{Mod}} = 1 \text{ mV}$ .

### Manipulation experiment

To have a better understanding and get insights into the dependence of the interactions of the pentagonal rings with the substrate, an experiment manipulating a GNR was performed. As can be seen in **Figure 92 c**, a zero-bias state associated to a Kondo resonance appeared during the dehydrogenation process of a GNR, as denoted in the point spectrum from **Figure 92 g** (blue curve).

The manipulation event was performed at constant height mode. Compared with the GNR (in the  $z$  axis), the tip was located closer to the surface and then moved across de GNR. Saturation in the current channel was observed denoting a strong interaction with the GNR. Retracting the tip from the surface left the interaction with the GNR. The GNR was then manipulated, changing its position on the substrate, and the GNR was rescanned after the displacement event (**Figure 92 d**). In the nc-AFM image taken at the new position (**Figure 92 e**) it is observed how the hydrogenated and dehydrogenated pentagonal rings remained intact after the manipulation event, but regarding the constant height STM images (**Figure 92 c** and **f**) the scenario changed. The Kondo resonance from the initial state disappeared, as can be seen in **Figure 92 g** (blue arrow), while a new Kondo resonance at a different defective position emerged (red curve in

**Figure 92 g).** This experiment underpins how the difference in position where the **3.3-GNR-Des** is chemisorbed modulates the structure of the ribbon and the magnetic response.

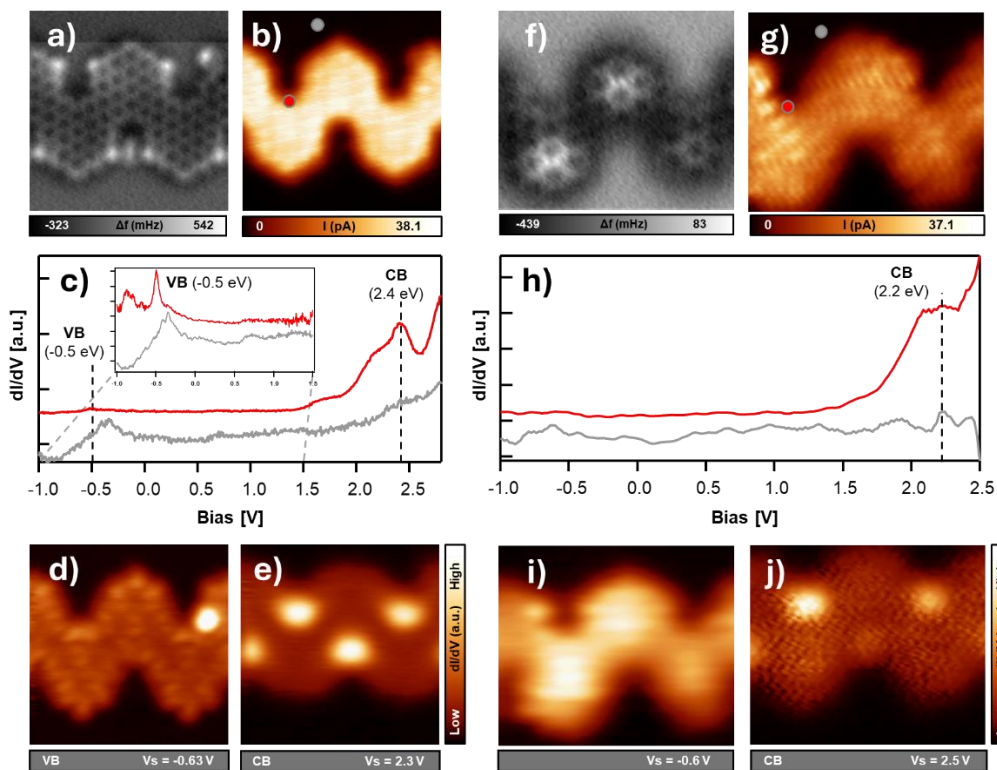


**Figure 92.** Manipulation of a GNR. **a)** Topographic constant current STM image at the initial state (IS). **b)** nc-AFM detailed image of the GNR at the IS. **c)** Simultaneously obtained constant height STM image at the IS. **d)** Topographic constant current STM image at the final state (FS). **e)** nc-AFM detailed image of the chain at the FS. **f)** Simultaneously obtained constant height STM image at the FS. Scanning parameters were as follows: **(a)** 51 mV, 10 pA, **(b)** 6 mV **(c)** 6 mV, **(d)** 10 pA, 51 mV, **(e)** 6 mV, **(f)** 6 mV, **(g)**  $V_{\text{Mod}} = 1$  mV.

### Electronic characterization

**Figure 93** illustrates the study of the electronic properties of both hydrogenated **3.3-GNR** and dehydrogenated **3.3-GNR-Des** GNRs. This analysis was conducted utilizing STS point spectra and  $dI/dV$  mapping techniques employing CO-functionalized tips.

On the one hand, nc-AFM and CH-STM images in **Figure 93 a** and **b** show the studied “hydrogenated” **3.3-GNR** ribbon. The  $dI/dV$  point spectrum from **Figure 93 c**, recorded at the edge of the bay of the ribbon (**Figure 93 b**), presents peaks at  $-0.5$  eV, associated to the VB, and at  $2.4$  eV, related to the CB, resulting in a  $\sim 2.9$  eV bandgap. The inset in **Figure 93 c** clearly shows the VB that is hardly visible when the full spectrum is recorded, due to a huge difference in intensity between the VB and the CB. The  $dI/dV$  maps from **Figure 93 d** and **e**, recorded at  $-0.63$  eV and  $2.3$  eV, respectively, show how the VB mostly distributes along the border of the ribbon, while the CB is intensively located at the bays.



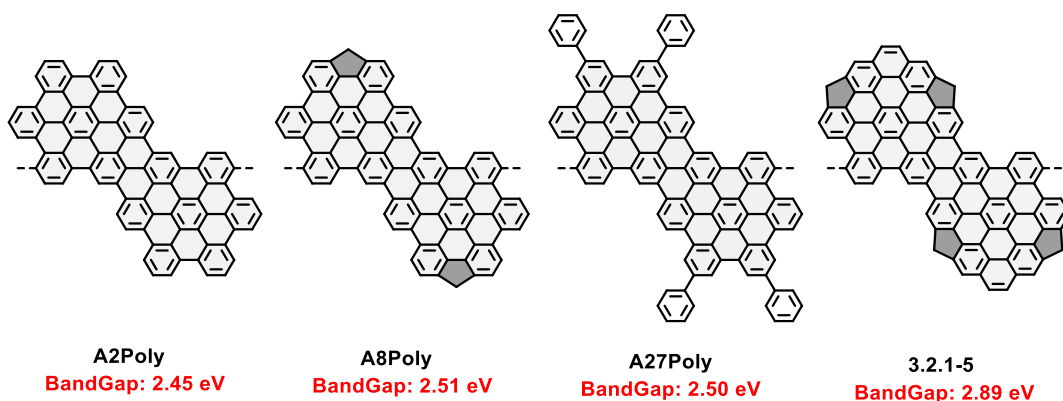
**Figure 93.** Electronic characterization of **3.3-GNR** and **3.3-GNR-Des** on Au(111) with a CO tip. **a**) & **b**) nc-AFM and simultaneously obtained constant height STM images of **3.3-GNR**. **c**) STS point spectra obtained at depicted position in **b**) (color coded). Dashed lines indicate valence and conduction bands. **d**) & **e**) Constant height dI/dV maps of **3.3-GNR** at - 0.63 and 2.3 eV respectively. **f**) & **g**) nc-AFM and simultaneously obtained constant height STM images of **3.3-GNR-Des**. **h**) STS point spectra obtained at depicted position in **g**) (color coded). Dashed line indicates the valence band. **i**) & **j**) Constant height dI/dV maps of **3.3-GNR-Des** at - 0.6 and at 2.5 eV respectively. Scanning parameters were as follows: (**a**) & (**b**) 2.9 nm  $\times$  2.9 nm, 4 mV, (**c**)  $V_{\text{Mod}} = 20$  mV, (**d**) & (**e**) 2.9 nm  $\times$  2.9 nm,  $V_{\text{Mod}} = 10$  mV; (**f**) & (**g**) 3 nm  $\times$  2.5 nm, 5 mV; (**h**)  $V_{\text{Mod}} = 10$  mV; (**i**) & (**j**) 3 nm  $\times$  2.5 nm,  $V_{\text{Mod}} = 10$  mV.

On the other hand, the point spectrum of **3.3-GNR-Des** in **Figure 93 h** only presents a signal related to the CB at 2.2 eV, while a clear state related with the VB is missing. dI/dV mapping was performed to try to determine the VB (**Figure 93 i** and **j**), which turned out to be located at - 0.6 V, while the CB appeared at 2.5 V, presenting a similar pattern as that already seen for the CB in **3.3-GNR**. We assume that the irregular intensity presented in **Figure 93 j** for the CB is related to the irregularities in curvature of the structure.

In this regard, we relate the absence of the VB in **3.3-GNR-Des** to the hybridization of the GNR with the underlying surface due to the coupling between the pentagonal rings and the surface. On the other hand, we consider two plausible reasons for the CB displacement ( $\sim 0.2$  eV) from the **3.3-GNR** to the **3.3-GNR-Des**: (i) the hybridization with the surface; (ii) the emerged curvature in **3.3-GNR-Des** (curvature may modify the overlapping between orbitals and hence may modify the electronic properties of the GNR).

Finally, **Scheme 3** presents a comparison of the electronic bandgap of **3.3-GNR** with some chevron-like ribbons reported in the literature (for additional examples, refer to **Scheme A 1** and **Scheme A 2**). Notably, among all the reported chevron-like topologies, **3.3-GNR** demonstrates the highest bandgap value. Additionally, the inclusion of non-conjugated rings in the GNR, as observed in **A8Poly** GNR and **A27Poly**, results in elevated bandgap values (2.51 eV and 2.50 eV, respectively) compared to the pristine chevron-like GNR **A2Poly**. This suggests that incorporating non-conjugated rings to the backbone in the structure may offer a viable strategy for modulating and widening the bandgap in chevron-like GNRs.

Future deeper studies regarding calculations of the electronic bands for **3.3-GNR-Des** and **3.3-GNR** are needed for a better understanding of the role of the inclusion of pentagonal rings in the structures, its hybridization with the substrate when they are dehydrogenated and the role of the curvature in shifting the electronic properties. The examples of **3.3-GNR-Des** and **3.3-GNR** serve as illustrations of how the incorporation of non-benzenoid rings and the inducement of curvature can effectively tune the electronic bandgap in graphene nanostructures.



Scheme 33. Related GNRs to 3.2.1-5 and its relative experimentally obtained bandgaps on Au(111).

### Summary

The on-surface synthesis of GNRs from **3.3-Mono** on Au(111) was successfully accomplished. This involved successive Ullmann coupling, cyclodehydrogenation, and ring closure reactions to yield **3.3-Poly** and **3.3-GNR**. Further tip-induced dehydrogenation steps resulted in the formation of GNRs **3.3-GNR-Des**, characterized by the curvature of the monomeric units into nanodomes and positive bowl curvatures.

Zero-bias states related to magnetic Kondo resonances were characterized using CO and NiCp<sub>2</sub> tips, indicating the presence of  $\pi$  radicals in the GNRs. Manipulation experiments demonstrated the modulation of the GNR structure and magnetic response by changing its position on the substrate, highlighting the influence of the chemisorption sites on the GNR properties and structure.

---

STS and  $dI/dV$  mapping revealed differences in the electronic properties of hydrogenated GNR **3.3-GNR** and dehydrogenated **3.3-GNR-Des**, that we ascribe to: (i) a hybridization between GNRs and the substrate due to a strong interaction via the pentagonal rings, (ii) to the curvature of the structure. Comparison with other reported GNRs indicated that the inclusion of rings not conjugated to the backbone of the GNR, can effectively modulate and widen the bandgap, offering potential for tuning the electronic properties. And on the other hand, coupling the GNR to the surface or curving it also modifies the electronic properties.

Further computational studies are needed to completely understand the electronic band structures of **3.3-GNR-Des** and **3.3-GNR** and to elucidate the role of pentagonal rings, the curvature and their hybridization with the substrate in tuning GNR properties.





## 4 EXPERIMENTAL METHODS

“



This chapter provides relevant information about the methodologies employed throughout the experimental work of this doctoral thesis, and about the fundamental aspects of the techniques utilized. Given the extensive range of techniques employed due to the combination of in-solution and on-surface methodologies, a detailed description of each is beyond the scope of this thesis. Therefore, this chapter will focus on the explanation of the primary protocols used for the in-solution synthesis of precursors and their characterization, as well as on the qualitative illustration of the OSS methodologies,

For readers interested in organic synthesis, refer to the first section on in-solution methodologies. This section provides general information on the techniques used, detailed descriptions of the synthesis and characterization of the compounds, extensive information on the X-ray diffraction structures, and the NMR spectra of all new compounds synthesized in this doctoral thesis. On the other hand, if your interest lies in the surface sciences, I invite you to explore the second section. Here, you will find a description of the main UHV system used, the protocols for sample preparation, and an overview of the primary characterization techniques employed (STM, AFM, and XPS). But if your curiosity is broad enough, please feel free to explore both sections for an in-depth understanding of the experimental work conducted in this doctoral thesis.

## 4.1 In-Solution Synthesis and Characterization

In this section, we will detail the procedures employed to synthesize and characterize the precursors utilized in this thesis. We will provide a description of the performed methodologies to set the chemical reactions, followed by thorough characterization using NMR spectroscopy, HR-MS, IR, and X-Ray diffraction (in those cases where suitable crystals were obtained). Additionally, representative NMR spectra of the prepared compounds will be presented. It's worth noting that all experiments related to the in-solution synthesis of customized precursors, as well as their subsequent characterization, were mainly conducted at the Nanographout laboratory of the University of Granada, Spain.

### 4.2.1 General Information

**Reagents and solvents:** All chemicals labeled as reagents and solvents were purchased from commercial suppliers and utilized without additional purification, unless explicitly mentioned. Anhydrous tetrahydrofuran (THF) was obtained through fresh distillation over Na/benzophenone and subsequently cooled down to r. t. under an argon atmosphere.

**Chromatography:** Flash column chromatography employed Silica gel 60 (230-400 mesh, Scharlab, Spain) as the stationary phase. Thin layer chromatography was conducted on aluminum sheets coated with silica gel and a fluorescent UV254 indicator (obtained from Sigma-Aldrich). The TLC plates were examined under UV light at wavelengths of 254 nm or 365 nm and, if necessary, stained with phosphomolybdic acid (5% ethanol solution).

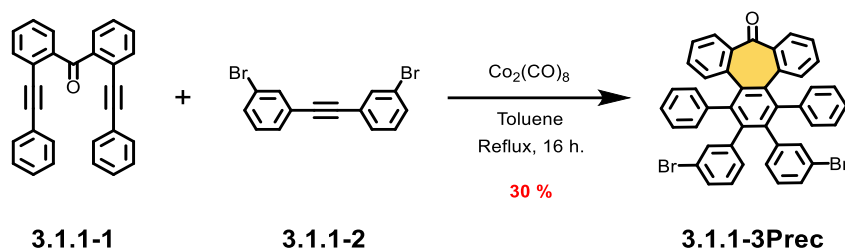
**Nuclear Magnetic Resonance Spectroscopy:** All  $^1\text{H}$  and  $^{13}\text{C}$  NMR spectra were recorded using Bruker Avance Neo spectrometers (400 MHz, 500 MHz, and 600 MHz) at a constant temperature of 298 K. Chemical shifts are presented in ppm and referenced to the residual solvent. Coupling constants (J) are expressed in Hertz (Hz). Multiplicities are denoted as follows: s = singlet, br s = broad singlet, d = doublet, t = triplet, m = multiplet, dd = doublet of doublets, td = triplet of doublets, ddd = doublet of doublet of doublets, dt = doublet of triplets. Proton assignment was carried out through 2D NMR experiments such as COSY, HSQC, and HMBC, where applicable. The assignment of  $^{13}\text{C}$  NMR multiplicities was achieved using DEPT techniques.

**Mass Spectrometry:** High-resolution mass spectrometry measurements were conducted on: i) a Waters XEVO GL-XS QToF mass spectrometer equipped with an electrospray ionization source coupled to a time-of-flight spectrometer as the detection system (ESI-ToF), ii) a Bruker ULTRAFLEX III spectrometer equipped with a matrix-assisted laser desorption ionization source coupled with a time-of-flight spectrometer as detection system (MALDI-ToF), iii) a Bruker MAXIS II spectrometer with an atmospheric pressure chemical ionization coupled to a time-of-flight spectrometer (APCI), and iv) on a Waters GCT mass spectrometer equipped with an electron impact (EI) source of ionization coupled to a time-of-flight spectrometer and the detection system connected to a Bruker 436-GC gas chromatography system (GC-EI).

**Infrared Spectroscopy:** Spectra were recorded on a Perkin Elmer Spectrum Two IR spectrometer using attenuated total reflection (ATR) of the solid compound. The spectral range covered 4000-450  $\text{cm}^{-1}$ .

#### 4.2.2 Synthesis and Characterization of the Prepared Compounds

##### Compound 3.1.1-3Prec



In a 100 mL round bottom flask, a degassed mixture of dialkyne<sup>236</sup> **3.1.1-1** (230 mg, 0.60 mmol) and  $\text{Co}_2(\text{CO})_8$  (267 mg, 0.78 mmol) in toluene (8 mL) was stirred at 110 °C during 30 min. Then, a degassed solution of the 1,2-bis(3-bromophenyl)ethyne<sup>237</sup> **3.1.1-2** (302 mg, 0.9 mmol) in toluene (2 mL) was added dropwise during 30 min. The reaction was allowed to stir during 16 h at 110 °C under an argon atmosphere. Afterwards, the mixture was cooled down to r.t. and the solvent was removed under reduced pressure. The residue was adsorbed on silica gel and purified firstly by column chromatography ( $\text{SiO}_2$ , Hexane/ $\text{CH}_2\text{Cl}_2$ : 7/3) and then by preparative TLC ( $\text{SiO}_2$ , Hexane/ $\text{CH}_2\text{Cl}_2$ : 7/3) to give the corresponding compound **3.1.1-3Prec** (130 mg, 30%) as a white solid mixture of two atropisomers (55:45).

<sup>1</sup>H NMR (500 MHz,  $\text{CDCl}_3$ ):  $\delta$  = 7.56 (*major isomer*, t,  $J$  = 1.7 Hz, 1H), 7.50 (*minor isomer*, t,  $J$  = 1.7 Hz, 1H), 7.41 (dd,  $J$  = 7.6, 1.1 Hz, 2H), 7.31 – 7.24 (m, 1H), 7.17 – 7.08 (m, 3H), 7.04 (tt,  $J$  = 7.6, 1.9 Hz, 1H), 7.01 – 6.95 (m, 3H), 6.95 – 6.88 (m, 2H), 6.87 – 6.77 (m, 4H), 6.64 – 6.53 (m, 2H), 6.51 – 6.44 (m, 2H), 6.36 (*minor isomer*, dt,  $J$  = 7.7, 1.3 Hz, 1H), 6.30 (*major isomer*, dt,  $J$  = 7.7, 1.3 Hz, 1H).

<sup>13</sup>C NMR (126 MHz,  $\text{CDCl}_3$ ):  $\delta$  = 200.2 (C), 200.0 (C), 146.0 (C), 141.87 (C), 141.85 (C), 141.8 (C), 141.6 (C), 141.5 (C), 141.4 (C), 141.3 (C), 140.98 (C), 140.96 (C), 140.93 (C), 140.05 (C), 140.02 (C), 140.0 (C), 135.97 (C), 135.96 (C), 135.95 (C), 134.5 (CH), 134.34 (C), 134.33 (C), 134.32 (C), 134.3(CH), 133.4 (CH), 133.2 (CH), 133.0 (CH), 132.99 (CH), 132.97 (CH), 132.4 (CH), 132.11 (CH), 132.08 (CH), 130.43 (CH), 130.41 (CH), 130.1 (CH), 130.0 (CH), 129.0 (CH), 128.9 (CH), 128.86 (CH), 128.73 (CH), 128.71 (CH), 128.66 (CH), 128.63 (CH), 128.59 (CH), 128.57 (CH), 127.8 (CH), 127.7 (CH), 127.5 (CH), 127.49 (CH), 127.4 (CH), 127.38 (CH),

<sup>236</sup> I. R. Márquez, N. Fuentes, C. M. Cruz, V. Puente-Muñoz, L. Sotorrios, M. L. Marcos, D. Choquesillo-Lazarte, B. Biel, L. Crovetto, E. Gómez-Bengoa, M. T. González, R. Martín, J. M. Cuerva and A. G. Campaña, *Chem. Sci.*, **2017**, *8*, 1068–1074.

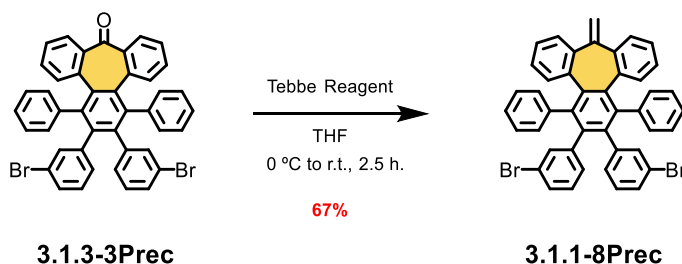
<sup>237</sup> M. J. Mio, L. C. Kopel, J. B. Braun, T. L. Gadzikwa, K. L. Hull, R. G. Brisbois, C. J. Markworth and P. A. Grieco, *Org. Lett.*, **2002**, *4*, 3199–3202.

127.3 (CH), 126.9 (CH), 126.8 (CH), 126.7 (CH), 126.67 (CH), 126.0 (CH), 125.8 (CH), 124.4 (CH), 124.34 (CH), 124.30 (CH), 121.2 (C), 121.1 (C), 120.6 (C), 120.4 (C).

**HR-MS** (ESI-TOF):  $m/z$  calcd for  $C_{43}H_{27}Br_2O[M+H]^+$ : 717.0429; found: 717.0419.

**IR** (ATR): 1684, 1593, 1561, 1292, 1215, 748, 727, 716, 667, 638  $cm^{-1}$ .

### Compound 3.1.1-8Prec

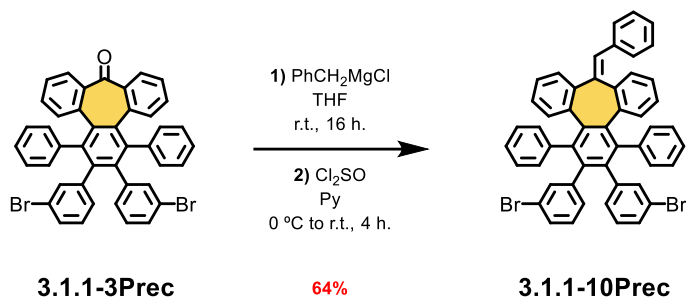


In a 100 mL round bottom flask, 0.5 mL (0.22 mmol) of 0.5M Tebbe's reagent solution in toluene was added dropwise at 0 °C to a solution of **3.1.1-3Prec** (120 mg, 0.17 mmol) in dry THF (8 mL). The mixture was allowed to stir at r.t. for 2.5 hours. Afterwards, the crude was quenched with water, extracted with DCM and washed with water and brine. The organic layer was dried over anhydrous  $Na_2SO_4$  and the solvent was removed under reduced pressure. The residue was adsorbed on silica gel and purified by column chromatography ( $SiO_2$ , Hexane/ $CH_2Cl_2$ : 8/2) to give a white solid corresponding to a mixture of two atropisomers (100:60) of compound **3.1.1-8Prec** (80 mg, 67%).

**$^1H$  NMR** (500 MHz,  $CD_2Cl_2$ ):  $\delta$  7.60 (*major isomer*, s, 1H), 7.54 (*major isomer*, s, 1H), 7.36 (*major isomer*, d,  $J = 7.0$  Hz, 1H), 7.33 (*major isomer*, d,  $J = 7.4$  Hz, 1H), 7.28 (*minor isomer*, d,  $J = 7.7$  Hz, 0H), 7.18 (m, 8H), 7.01 (m, 13H), 6.98 – 6.85 (m, 11H), 6.84 (*major isomer*, t,  $J = 7.5$  Hz, 2H), 6.67 (m, 8H), 6.58 (*major isomer*, d,  $J = 7.8$  Hz, 1H), 6.52 (*major isomer*, t,  $J = 8.0$  Hz, 4H), 6.46 (*minor isomer*, d,  $J = 7.9$  Hz, 0H), 6.43 (*major isomer*, d,  $J = 7.7$  Hz, 1H), 6.38 (*major isomer*, d,  $J = 7.7$  Hz, 1H), 5.55 (s, 4H).

**$^{13}C$  NMR** (126 MHz,  $CD_2Cl_2$ ):  $\delta$  151.83 (C), 151.74 (C), 151.65 (C), 148.15 (C), 148.11 (C), 148.10 (C), 148.06 (C), 143.13 (C), 143.08 (C), 143.06 (C), 141.30 (C), 141.28 (C), 141.22 (C), 141.17 (C), 140.40 (C), 140.37 (C), 140.34 (C), 138.56 (C), 138.53 (C), 135.41 (C), 135.17 (C), 135.03 (CH), 134.00 (CH), 133.83 (CH), 133.24 (CH), 133.21 (CH), 133.18 (CH), 133.12 (CH), 133.07 (CH), 133.03 (CH), 132.99 (CH), 131.21 (CH), 131.16 (CH), 131.12 (CH), 129.70 (CH), 129.57 (CH), 129.22 (CH), 129.19 (CH), 129.15 (CH), 129.12 (CH), 129.00 (CH), 128.93 (CH), 128.41 (CH), 127.69 (CH), 127.67 (CH), 127.65 (CH), 127.58 (CH), 127.46 (CH), 127.25 (CH), 127.18 (CH), 127.14 (CH), 126.27 (CH), 126.17 (CH), 126.08 (CH), 126.04 (CH), 126.02 (CH), 126.00 (CH), 125.99 (CH), 125.96 (CH), 125.93 (CH), 121.34 (C), 121.30 (C), 121.07 (C), 120.97 (C), 112.65 ( $CH_2$ ), 112.62 ( $CH_2$ ), 112.59 ( $CH_2$ ).

**HR-MS** (APCI):  $m/z$  calcd for  $C_{44}H_{29}Br_2[M+H]^+$ : 717.0615 found: 717.0598.

**Compound 3.1.1-10Prec**

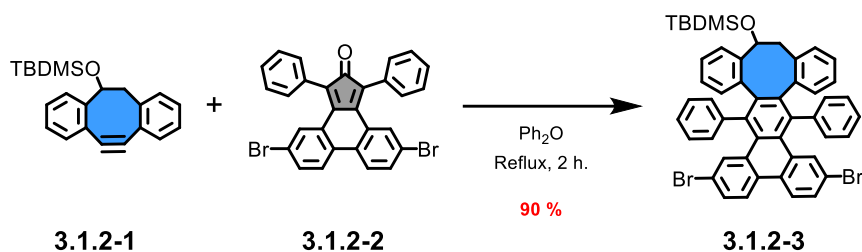
In a 100 mL round bottom flask, 2.4 mL (2.8 mmol) of 1M benzylmagnesium chloride solution in THF were added dropwise at r.t. to a degassed solution of **3.1.1-3Prec** (200 mg, 0.28 mmol) in THF. The mixture was stirred at r.t. during 16 hours. Then, the reaction was quenched adding water dropwise, and the crude was diluted with CH<sub>2</sub>Cl<sub>2</sub> and extracted with 1M HCl (x2) and brine. The organic layer was dried (Na<sub>2</sub>SO<sub>4</sub>), filtered, evaporated in a 100 ml round flask and used in the next step without further purification.

4 mL of pyridine were added to the last mixture and it was degassed. Then, 0.04 mL (0.49 mmol) of thionyl chloride were added at 0 °C. The mixture was allowed to stir at r.t. for 4 hours. The reaction was quenched adding water dropwise and the crude was diluted with CH<sub>2</sub>Cl<sub>2</sub> and extracted with 1M HCl 10% (x2) and brine. The organic layer was dried (Na<sub>2</sub>SO<sub>4</sub>), filtered, and evaporated under reduced pressure. The residue was adsorbed on silica gel and purified by column chromatography (SiO<sub>2</sub>, Hexane/CH<sub>2</sub>Cl<sub>2</sub>: 85/15) affording **3.1.1-10Prec** (140 mg, 64%) as a white solid.

**<sup>1</sup>H NMR** (300 MHz, CDCl<sub>3</sub>): δ 7.69 – 7.43 (m, 3H), 7.31 (m, 4H), 7.22 – 6.20 (m, 25H).

**HR-MS** (MALDI): m/z calcd for C<sub>43</sub>H<sub>27</sub>Br<sub>2</sub>ONa [M+Na]<sup>+</sup>: 793.0929; found: 793.0948.

## Compound 3.1.2-3



In a Schlenk tube, alkyne **3.1.2-1**<sup>238</sup> (100 mg, 0.299 mmol) and cyclopentadienone **3.1.2-2**<sup>239</sup> (182 mg, 0.299 mmol) were dissolved in diphenyl ether (2 mL) and bubbled with Ar. The reaction mixture was refluxed over 2 h in a sand bath. The crude was allowed to cool down to r.t., diluted with hexane (2 mL) and introduced in the column to be purified by column flash chromatography on silica gel (SiO<sub>2</sub>, Hexane/CH<sub>2</sub>Cl<sub>2</sub> 9:1) affording **3.1.2-3** as a white solid (228 mg, 90%) mixture of two diastereomers in 3:1 proportion. The major diastereomer was isolated through some re-precipitations with MeOH/DCM (10/1) before characterization.

**<sup>1</sup>H NMR** (400 MHz, CD<sub>2</sub>Cl<sub>2</sub>): δ 8.29 (s, 1H), 8.27 (s, 1H), 7.94 (d, *J* = 2.0 Hz, 1H), 7.81 (d, *J* = 2.0 Hz, 1H), 7.54 (t, *J* = 2.0 Hz, 1H), 7.52 (t, *J* = 2.0 Hz, 1H), 7.33 – 7.06 (m, 10H), 6.99 (td, *J* = 7.5, 1.5 Hz, 1H), 6.95 – 6.75 (m, 5H), 6.66 (ddd, *J* = 7.5, 5.9, 2.8 Hz, 1H), 6.52 – 6.43 (m, 1H), 4.97 (dd, *J* = 9.2, 4.6 Hz, 1H), 3.64 (dd, *J* = 14.6, 9.3 Hz, 1H), 2.80 (dd, *J* = 14.6, 4.6 Hz, 1H), 0.92 (s, 9H), -0.03 (s, 3H), -0.21 (s, 3H).

**<sup>13</sup>C NMR** (101 MHz, CD<sub>2</sub>Cl<sub>2</sub>): δ 143.5 (C), 143.4 (C), 142.7 (C), 142.4 (C), 142.3 (C), 140.8 (C), 140.1 (C), 137.6 (C), 137.35 (C), 137.34 (C), 133.6 (CH), 133.5 (CH), 132.8 (C), 132.6 (C), 131.3 (CH), 131.2 (C), 130.8 (C), 130.5 (CH), 130.33 (C), 130.32 (CH), 130.27 (C), 130.26 (CH), 128.9 (CH), 127.6 (CH), 127.5 (CH), 127.4 (CH), 126.9 (CH), 125.5 (CH), 125.3 (CH), 125.0 (CH), 124.0 (CH), 120.5 (C), 120.3 (C), 72.1 (CH), 48.2 (CH<sub>2</sub>), 26.4 (CH<sub>3</sub>) 26.2 (CH<sub>3</sub>), 18.5 (C). (Some <sup>13</sup>C signals were not observed due to overlapping processes).

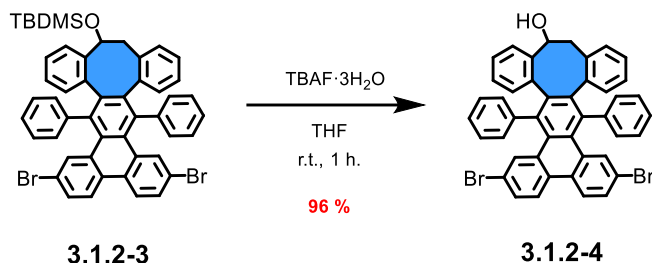
**HR-MS** (ESI-TOF): *m/z* calcd for C<sub>50</sub>H<sub>42</sub>ONaSiBr<sub>2</sub> [M+Na]<sup>+</sup>: 869.1255, found: 869.1281.

**IR** (ATR): 3060, 3026, 2953, 2927, 2855, 1735, 1597, 1471, 1253, 1070, 835, 758, 700 cm<sup>-1</sup>.

<sup>238</sup> S. C. Kornmayer, F. Rominger, R. Gleiter, *Synthesis*, **2009**, 15, 2547-2552.

<sup>239</sup> T. H. Vo, M. Shekhirev, D. A. Kunkel, F. Orange, M. J. F. Guinel, A. Enders, A. Sinitskii, *Chem. Commun.*, **2014**, 50, 4172-4174.



**Compound 3.1.2-4**

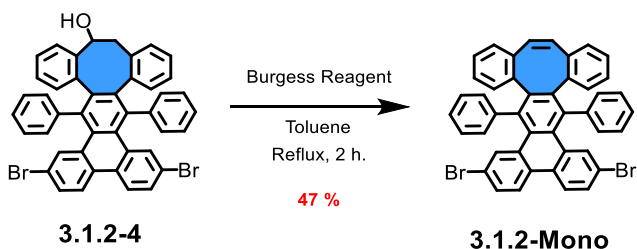
In a round bottom flask, TBAF·3H<sub>2</sub>O (167 mg, 0.53 mmol) was added to a solution of **3.1.2-3** (180 mg, 0.21 mmol) in THF (8 mL) at r.t. and the mixture was then stirred for 1 h. The solvent was evaporated and the crude was diluted with CH<sub>2</sub>Cl<sub>2</sub> and extracted with H<sub>2</sub>O. The organic layer was dried (Na<sub>2</sub>SO<sub>4</sub>), filtered and evaporated at reduced pressure. Purification by flash column chromatography (SiO<sub>2</sub>, hexane/AcOEt 9/1) afforded compound **3.1.2-4** as a white solid (150 mg, 96 %).

**<sup>1</sup>H NMR** (400 MHz, CD<sub>2</sub>Cl<sub>2</sub>): δ 8.28 (d, *J* = 2.5 Hz, 1H), 8.26 (d, *J* = 2.5 Hz, 1H), 7.91 (d, *J* = 2.0 Hz, 1H), 7.82 (d, *J* = 2.1 Hz, 1H), 7.54 (d, *J* = 1.9 Hz, 1H), 7.52 (d, *J* = 2.0 Hz, 1H), 7.35 – 6.97 (m, 11H), 6.92 – 6.77 (m, 5H), 6.69 (dt, *J* = 7.6, 4.3 Hz, 1H), 6.53 (d, *J* = 7.4 Hz, 1H), 5.10 (ddd, *J* = 9.3, 5.6, 3.5 Hz, 1H), 3.71 (dd, *J* = 14.7, 9.3 Hz, 1H), 2.73 (dd, *J* = 14.8, 5.6 Hz, 1H), 2.06 (d, *J* = 3.7 Hz, 1H).

**<sup>13</sup>C NMR** (101 MHz, CD<sub>2</sub>Cl<sub>2</sub>): δ 143.3 (C), 143.2 (C), 142.7 (C), 142.5 (C), 141.8 (C), 140.6 (C), 139.8 (C), 137.9 (C), 137.7 (C), 137.6 (C), 133.6 (CH), 133.4 (CH), 132.63 (C), 132.57 (C), 131.14 (C), 131.07 (CH), 130.94 (C), 130.93 (CH), 130.34 (C), 130.32 (CH), 130.27 (CH), 128.9 (CH), 127.6 (CH), 127.5 (CH), 127.1 (CH), 125.8 (CH), 125.6 (CH), 125.0 (CH), 122.8 (CH), 120.5 (C), 120.3 (C), 71.4 (CH), 46.6 (CH<sub>2</sub>). (Some <sup>13</sup>C signals were not observed due to overlapping processes).

**HR-MS** (ESI-TOF): *m/z* calcd for C<sub>44</sub>H<sub>28</sub>ONaBr<sub>2</sub> [M+Na]<sup>+</sup>: 753.0405, found: 753.0399.

**IR** (ATR): 3577, 3414, 3057, 3016, 2932, 1590, 1492, 1442, 1386, 1263, 1093, 999, 801 cm<sup>-1</sup>.

**Compound 3.1.2-Mono**

In a Schlenk tube, **3.1.2-4** (90 mg, 0.123 mmol) and Burgess Reagent (44 mg, 0.184 mmol) were dissolved in toluene (6 mL) and bubbled with Ar. The reaction mixture was refluxed over 2h.

Once cooled down to r.t., the solvent was removed under reduced pressure and the crude was diluted with DCM and washed with brine. The organic layer was dried over anhydrous  $\text{Na}_2\text{SO}_4$ , and the solvent was removed under reduced pressure. The crude was purified by column chromatography ( $\text{SiO}_2$ , Hexane/DCM 9:1) and **3.1.2-Monoc** was obtained (41 mg, 47 %) as a white solid.

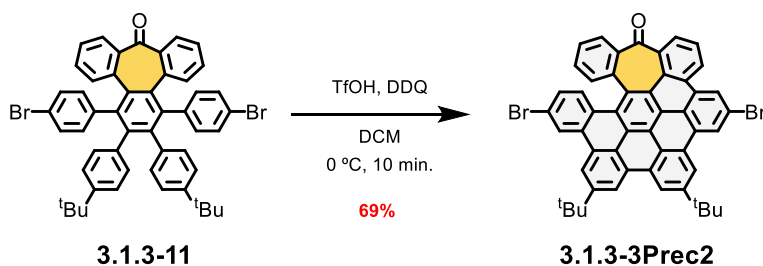
**$^1\text{H NMR}$**  (500 MHz,  $\text{CDCl}_3$ ):  $\delta$  8.18 (d,  $J = 8.7$  Hz, 2H), 7.72 (d,  $J = 2.0$  Hz, 2H), 7.47 (dd,  $J = 8.7, 2.0$  Hz, 2H), 7.22 – 7.08 (m, 8H), 6.92 (s, 2H), 6.91 – 6.89 (m, 4H), 6.77 – 6.60 (m, 4H).

**$^{13}\text{C NMR}$**  (126 MHz,  $\text{CDCl}_3$ ):  $\delta$  142.24 (C), 142.17 (C), 140.0 (C), 138.1 (C), 137.7 (C), 133.41 (CH), 133.40 (CH), 132.1 (C), 130.7 (CH), 130.0 (C), 129.80 (C), 129.75 (CH), 128.3 (CH), 126.8 (CH), 126.2 (CH), 126.1 (CH), 125.6 (CH), 124.0 (CH), 119.6 (C).

**HR-MS** (ESI-TOF):  $m/z$  calcd for  $\text{C}_{44}\text{H}_{26}\text{Br}_2\text{K}$   $[\text{M}+\text{K}]^+$ : 753.0023, found: 753.0024.

**IR** (ATR): 2922, 2847, 1737, 1725, 1443, 1374, 1224, 1052  $\text{cm}^{-1}$ .

### Compound 3.1.3-3Prec2



Compound **3.1.3-11** was prepared as previously reported in literature<sup>240</sup>. **3.1.3-11** (51 mg, 0.06 mmol) and DDQ (62 mg, 0.27 mmol) were added to a round bottom flask and dissolved in anhydrous  $\text{CH}_2\text{Cl}_2$  (2 mL) under an Ar atmosphere. Once the mixture was cooled to 0 °C, trifluoroacetic acid (0.097 mL) was added and the mixture was stirred at 0 °C for 10 min. The resulting solution was diluted with  $\text{CH}_2\text{Cl}_2$  (4 mL) and silica gel was added. The solvent was removed under vacuum and the crude was purified by flash column chromatography ( $\text{SiO}_2$ ,  $\text{CH}_2\text{Cl}_2$ /Hexane 6:4) affording **3.1.3-3Prec2** (35 mg, 69%) as a yellow solid.

**$^1\text{H NMR}$**  (500 MHz,  $\text{CD}_2\text{Cl}_2$ ):  $\delta$  9.25 (s, 1H), 9.22 (s, 1H), 9.16 (s, 1H), 9.07 (s, 1H), 8.92 (s, 1H), 8.90 (s, 1H), 8.87 (s, 1H), 8.84 (d,  $J = 8.1$  Hz, 1H), 8.12 (d,  $J = 7.4$  Hz, 1H), 7.87 (d,  $J = 7.8$  Hz, 1H), 7.82 (t,  $J = 7.6$ , 1H), 7.55 (d,  $J = 8.9$  Hz, 1H), 7.49 (t,  $J = 7.5$  Hz, 1H), 7.27 (d,  $J = 8.9$  Hz, 1H), 7.13 (d,  $J = 7.5$  Hz, 1H), 6.58 (d,  $J = 7.8$  Hz, 1H), 1.78 (s, 9H), 1.77 (s, 9H).

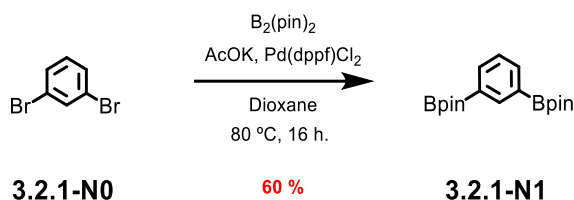
**$^{13}\text{C NMR}$**  (126 MHz,  $\text{CD}_2\text{Cl}_2$ ):  $\delta$  199.6 (C), 151.0 (C), 150.7 (C), 143.3 (C), 142.5 (C), 139.4 (C), 135.3 (CH), 134.1 (C), 133.6 (CH), 132.7 (C), 132.3 (C), 131.42 (CH), 131.36 (C), 130.8 (C), 130.7 (C), 130.6 (C), 130.4 (C), 130.1 (C), 129.7 (C), 129.6 (CH), 129.5 (CH), 129.14 (CH), 129.10 (C), 128.9 (CH), 128.7 (C), 128.4 (CH), 127.3 (C), 126.8 (CH), 126.1 (CH), 125.4 (CH), 125.0

<sup>240</sup> V. G. Jiménez, A. H. G. David, J. M. Cuerva, V. Blanco, A. G. Campaña, *Angew. Chem. Int. Ed.*, **2020**, *59*, 15124-15128.

(CH), 124.3 (C), 123.6 (C), 123.5 (C), 122.7 (C), 122.5 (C), 122.42 (C), 122.38 (C), 122.0 (C), 120.9 (CH), 120.7 (CH), 120.4 (CH), 119.7 (CH), 36.28 (C), 36.26 (C), 32.17 (CH<sub>3</sub>), 32.15 (CH<sub>3</sub>).

**HR-MS** (MALDI):  $m/z$  calcd for C<sub>51</sub>H<sub>34</sub>Br<sub>2</sub>O<sub>1</sub> [M]<sup>+</sup>: 822.0957, found 822.0981.

### Compound 3.2.1-N1



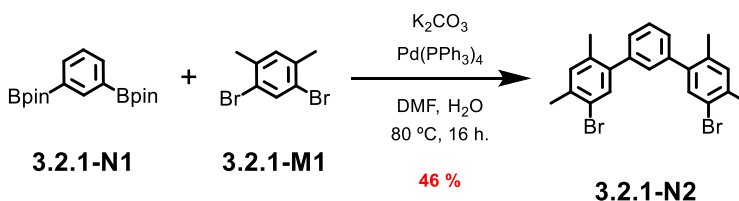
1,3-Dibromobenzene **3.2.1-N0** (8 g, 33.91 mmol), Pd(dppf)Cl<sub>2</sub> (620 mg, 0.85 mmol), Bis(pinacolato)diboron (21.53 g, 84.78 mmol) and AcOK (19.97 g, 203.46 mmol) were placed into a 250 mL round bottom flask under an Ar atmosphere. The solids were suspended in degassed dioxane (90 mL) and the reaction mixture was heated at 80 °C for 16 h. Once cooled down to r.t., the solvent was removed under reduced pressure and the crude was diluted with EtOAc and washed with brine. The organic layer was dried over anhydrous Na<sub>2</sub>SO<sub>4</sub> and the solvent was removed under reduced pressure. The crude was purified by column chromatography (SiO<sub>2</sub>, Hexane/EtOAc 98:2) giving **3.2.1-N1** (6.72 g, 60 %) as a white solid.

<sup>1</sup>H NMR (500 MHz, CDCl<sub>3</sub>): δ = 8.28 (s, 1H), 7.90 (dd,  $J = 7.4, 1.4$  Hz, 2H), 7.37 (t,  $J = 7.4$  Hz, 1H), 1.34 (s, 24H).

<sup>13</sup>C NMR (126 MHz, CDCl<sub>3</sub>): δ = 141.4 (CH), 137.8 (CH), 127.2 (CH), 83.9 (C), 25.0 (CH<sub>3</sub>). (The signal for the carbon nuclei bonded to the boron nuclei was not observed due to the quadrupolar relaxation induced by the boron nuclei).

Spectral data agree with those previously reported<sup>241</sup>.

### Compound 3.2.1-N2



Compound **3.2.1-N1** (1.1 g, 3.33 mmol), **3.2.1-M1** 1,5-Dibromo-2,4-dimethylbenzene (3.08 g, 11.67 mmol), Pd(PPh<sub>3</sub>)<sub>4</sub> (385 mg, 0.33 mmol) and K<sub>2</sub>CO<sub>3</sub> (2.30 g, 16.67 mmol) were placed into a 500 mL round bottom flask under an Ar atmosphere. The solids were dissolved in a degassed mixture of DMF (133 mL) and distilled water (7 mL) and the reaction mixture was heated at 80

<sup>241</sup> S. H. Fu, M. Higuchi, D. G. Kurth, *Org. Lett.*, **2007**, *9*, 559–562.

°C for 16 h. The resulting mixture was diluted with CH<sub>2</sub>Cl<sub>2</sub> and washed with water and brine. The organic layer was dried over anhydrous Na<sub>2</sub>SO<sub>4</sub> and the solvent was evaporated under reduced pressure. The crude was purified by column chromatography (SiO<sub>2</sub>, Hexane) giving **3.2.1-N2** (683 mg, 46%) as a white foam.

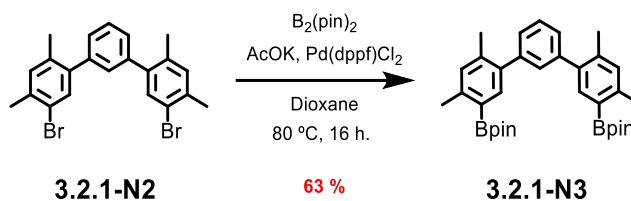
**<sup>1</sup>H NMR** (500 MHz, CDCl<sub>3</sub>): δ = 7.50 – 7.43 (m, 3H), 7.29 (dd, *J* = 8.0, 1.6 Hz, 2H), 7.23 (t, *J* = 1.8 Hz, 1H), 7.17 (s, 2H), 2.43 (s, 6H), 2.25 (s, 6H).

**<sup>13</sup>C NMR** (126 MHz, CDCl<sub>3</sub>): δ = 141.1 (C), 140.5 (C), 136.8 (C), 134.6 (C), 133.3 (CH), 132.9 (CH), 130.0 (CH), 128.2 (CH), 128.0 (CH), 121.8 (C), 22.5 (CH<sub>3</sub>), 20.1 (CH<sub>3</sub>).

**HR-MS** (APCI): *m/z* calcd. for C<sub>22</sub>H<sub>21</sub>Br<sub>2</sub> [M+H]<sup>+</sup>: 444.9985, found: 444.9981.

**IR** (ATR): 2920, 1467, 1382, 1030, 882, 712 cm<sup>-1</sup>.

### Compound 3.2.1-N3



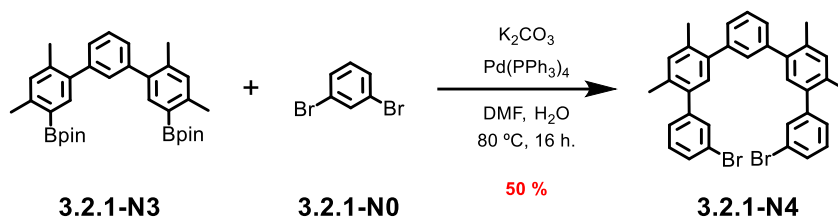
Compound **3.2.1-N2** (2.2 g, 4.95 mmol), Pd(dppf)Cl<sub>2</sub> (181 mg, 0.25 mmol), Bis(pinacolato)diboron (3.14 g, 12.38 mmol) and AcOK (2.92 g, 29.7 mmol) were placed into a 250 mL round bottom flask under an Ar atmosphere. The solids were suspended in degassed dioxane (25 mL) and the reaction mixture was heated at 80 °C for 16 h. Once cooled down to r.t., the solvent was removed under reduced pressure and the crude was diluted with EtOAc and washed with brine. The organic layer was dried over anhydrous Na<sub>2</sub>SO<sub>4</sub> and the solvent was removed under reduced pressure. The crude was purified by column chromatography (SiO<sub>2</sub>, Hexane/EtOAc 98:2) giving **3.2.1-N3** (1.69 g, 63 %) as a white solid.

**<sup>1</sup>H NMR** (500 MHz, CDCl<sub>3</sub>): δ 7.73 (s, 2H), 7.49 – 7.40 (m, 1H), δ 7.35 – 7.30 (m, 3H), 7.14 (s, 2H), 2.59 (s, 6H), 2.34 (s, 6H), 1.36 (s, 24H).

**<sup>13</sup>C NMR** (126 MHz, CDCl<sub>3</sub>): δ 144.0 (C), 141.6 (C), 138.7 (C), 138.3 (C), 137.7 (CH), 132.1 (CH), 130.5 (CH), 127.7 (CH), 127.7 (CH), 83.4 (C), 25.0 (CH<sub>3</sub>), 21.9 (CH<sub>3</sub>), 20.7 (CH<sub>3</sub>). (The signal for the carbon nuclei bonded to the boron nuclei was not observed due to the quadrupolar relaxation induced by the boron nuclei).

**HR-MS** (ESI-TOF): *m/z* calcd. for C<sub>34</sub>H<sub>44</sub>B<sub>2</sub>O<sub>4</sub>Na [M+Na]<sup>+</sup>: 561.3335, found: 561.3341.

**IR** (ATR): 2977, 1604, 1372, 1332, 1142, 859, 738 cm<sup>-1</sup>.

**Compound 3.2.1-N4**

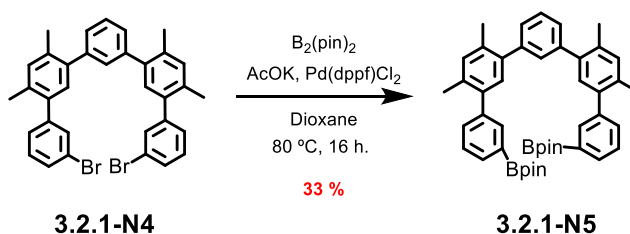
Compound **3.2.1-N3** (1.64 g, 3.14 mmol), **3.2.1-N0** 1,3-Dibromobenzene (2.59 g, 10.99 mmol), Pd(PPh<sub>3</sub>)<sub>4</sub> (0.36 g, 0.31 mmol) and K<sub>2</sub>CO<sub>3</sub> (2.17 g, 15.7 mmol) were placed into a 250 mL round bottom flask under an Ar atmosphere. The solids were dissolved in a degassed mixture of DMF (125 mL) and distilled water (6.5 mL) and the reaction mixture was heated at 80 °C for 16 h. The resulting mixture was diluted with CH<sub>2</sub>Cl<sub>2</sub> and washed with water and brine. The organic layer was dried over anhydrous Na<sub>2</sub>SO<sub>4</sub> and the solvent was evaporated under reduced pressure. The crude was purified by column chromatography (SiO<sub>2</sub>, Hexane/DCM 95:5) giving **3.2.1-N4** (0.93 g, 50%) as a white foam.

<sup>1</sup>H NMR (500 MHz, CD<sub>2</sub>Cl<sub>2</sub>): δ 7.52 (m, 2H), 7.50 – 7.42 (m, 3H), 7.35 – 7.25 (m, 7H), 7.21 (s, 2H), 7.13 (s, 2H), 2.33 (s, 6H), 2.28 (s, 6H).

<sup>13</sup>C NMR (126 MHz, CD<sub>2</sub>Cl<sub>2</sub>): δ 144.4 (C), 141.9 (C), 140.0 (C), 138.5 (C), 135.4 (C), 134.7 (C), 133.1 (CH), 132.7 (CH), 131.6 (CH), 130.7 (CH), 130.2 (CH), 130.2 (CH), 128.7 (CH), 128.5 (CH), 128.7 (CH), 122.6 (C), 20.5 (CH<sub>3</sub>), 20.2 (CH<sub>3</sub>).

HR-MS (APCI) m/z calcd. for C<sub>34</sub>H<sub>29</sub>Br<sub>2</sub> [M+H]<sup>+</sup>: 597.0613, found: 597.0629.

IR (ATR): 2860, 1593, 1558, 1467, 1264, 783, 700 cm<sup>-1</sup>.

**Compound 3.2.1-N5**

Compound **3.2.1-N4** (0.88 g, 1.47 mmol), Pd(dppf)Cl<sub>2</sub> (54 mg, 0.073 mmol), Bis(pinacolato)diboron (0.93 g, 3.67 mmol) and AcOK (0.86 g, 8.80 mmol) were placed into a 250 mL round bottom flask under an Ar atmosphere. The solids were suspended in degassed dioxane (10 mL) and the reaction mixture was heated at 80 °C for 16 h. Once cooled down to r.t., the solvent was removed under reduced pressure and the crude was diluted with DCM and washed with brine. The organic layer was dried over anhydrous Na<sub>2</sub>SO<sub>4</sub> and the solvent was removed under reduced pressure. The crude was purified by column chromatography (SiO<sub>2</sub>, Hexane/DCM 75:25) giving **3.2.1-N5** (335 mg, 33 %) as a white solid.

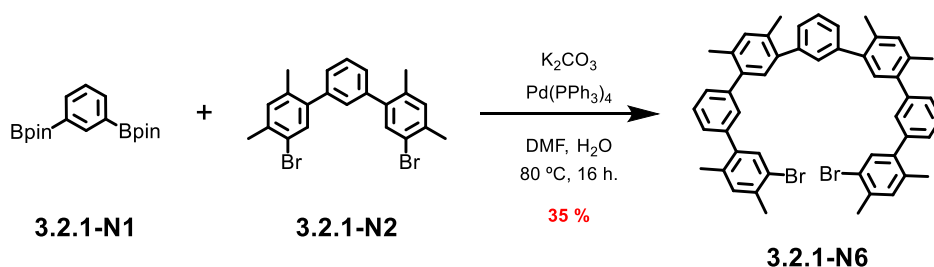
**$^1\text{H}$  NMR** (500 MHz,  $\text{CDCl}_3$ ):  $\delta$  7.82 (d,  $J = 2.1$  Hz, 2H), 7.79 (dd,  $J = 7.2, 1.4$  Hz, 2H), 7.50 – 7.39 (m, 5H), 7.38 (d,  $J = 1.9$  Hz, 1H), 7.35 – 7.32 (m, 2H), 7.20 (dd,  $J = 6.0, 1.8$  Hz, 4H), 2.36 (d,  $J = 1.8$  Hz, 6H), 2.31 (d,  $J = 1.8$  Hz, 6H), 1.36 (s, 12H), 1.35 (s, 12H).

**$^{13}\text{C}$  NMR** (126 MHz,  $\text{CDCl}_3$ ):  $\delta$  141.5 (C), 141.1 (C), 139.6 (C), 139.4 (C), 135.7 (CH), 134.3 (C), 134.2 (C), 132.4 (CH), 133.2 (CH), 132.3 (CH), 131.5 (CH), 130.4 (CH), 127.9 (CH), 127.8 (CH), 127.5 (CH), 83.9 (C), 25.0 ( $\text{CH}_3$ ), 20.3 ( $\text{CH}_3$ ), 20.2 ( $\text{CH}_3$ ). (The signal for the carbon nuclei bonded to the boron nuclei was not observed due to the quadrupolar relaxation induced by the boron nuclei).

**HR-MS** (ESI-TOF):  $m/z$  calcd. for  $\text{C}_{46}\text{H}_{52}\text{B}_2\text{O}_4\text{Na}$   $[\text{M}+\text{Na}]^+$ : 713.3964, found: 713.3958.

**IR** (ATR): 2978, 1602, 1354, 1143, 860, 711  $\text{cm}^{-1}$ .

### Compound 3.2.1-N6



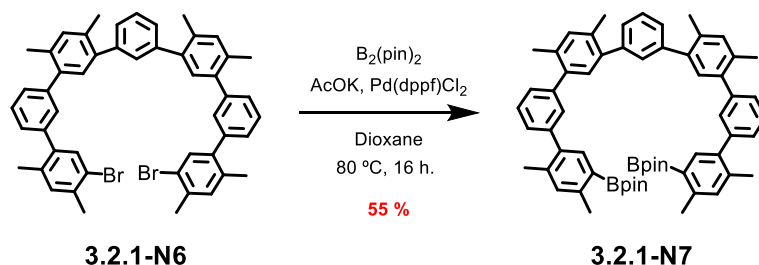
Compound **3.2.1-N1** (0.56 g, 1.7 mmol), **3.2.1-N2** (2.62 g, 5.9 mmol),  $\text{Pd(PPh}_3)_4$  (0.19 g, 0.17 mmol) and  $\text{K}_2\text{CO}_3$  (1.17 g, 8.4 mmol) were placed into a 250 mL round bottom flask under an Ar atmosphere. The solids were dissolved in a degassed mixture of DMF (67 mL) and distilled water (3.5 mL) and the reaction mixture was heated at 80 °C for 16 h. The resulting mixture was diluted with  $\text{CH}_2\text{Cl}_2$  and washed with water and brine. The organic layer was dried over anhydrous  $\text{Na}_2\text{SO}_4$  and the solvent was evaporated under reduced pressure. The crude was purified by column chromatography ( $\text{SiO}_2$ , Hexane/DCM 93:7) giving **3.2.1-N6** (478 mg, 35%) as a white foam. **3.2.1-N2** (1.05 g, 2.36 mmol, 40%) was recovered from the chromatography purification.

**$^1\text{H}$  NMR** (400 MHz, Methylene Chloride- $d_2$ ):  $\delta$  7.47 – 7.41 (m, 5H), 7.36 – 7.31 (m, 5H), 7.28 (t,  $J = 1.8$  Hz, 2H), 7.25 (d,  $J = 7.6$  Hz, 2H), 7.21 (s, 2H), 7.19 (s, 2H), 7.15 (s, 2H), 2.38 (s, 6H), 2.33 (s, 6H), 2.33 (s, 6H), 2.21 (s, 6H).

**$^{13}\text{C}$  NMR** (101 MHz,  $\text{CD}_2\text{Cl}_2$ ):  $\delta$  142.1 (C), 142.0 (C), 141.8 (C), 140.8 (C), 140.0 (C), 139.8 (C), 137.1 (C), 135.3 (C), 134.9 (C), 134.8 (C), 133.6 (CH), 133.3 (CH), 133.0 (CH), 131.8 (CH), 130.8 (CH), 130.8 (CH), 128.6 (CH), 128.5 (CH), 128.4 (CH), 128.2 (CH), 128.0 (CH), 122.1 (C), 22.7 ( $\text{CH}_3$ ), 20.5 ( $\text{CH}_3$ ), 20.4 ( $\text{CH}_3$ ), 20.3 ( $\text{CH}_3$ ).

**HR-MS** (ESI-TOF):  $m/z$  calcd. for  $\text{C}_{50}\text{H}_{44}\text{Br}_2\text{Na}$   $[\text{M}+\text{Na}]^+$ : 827.1693, found: 827.1708.

**IR** (ATR): 2919, 1599, 1468, 1434, 1022, 882, 712  $\text{cm}^{-1}$ .

**Compound 3.2.1-N7**

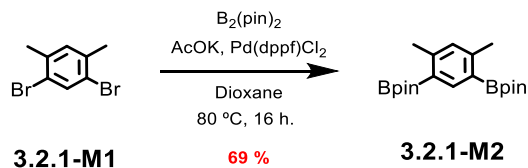
Compound **3.2.1-N6** (363 mg, 0.45 mmol), Pd(dppf)Cl<sub>2</sub> (17 mg, 0.023 mmol), Bis(pinacolato)diboron (286 mg, 1.13 mmol) and AcOK (267 mg, 2.71 mmol) were placed into a 250 mL round bottom flask under an Ar atmosphere. The solids were suspended in degassed dioxane (5 mL) and the reaction mixture was heated at 80 °C for 16 h. Once cooled down to r.t., the solvent was removed under reduced pressure and the crude was diluted with EtOAc and washed with brine. The organic layer was dried over anhydrous Na<sub>2</sub>SO<sub>4</sub> and the solvent was removed under reduced pressure. The crude was purified by column chromatography (SiO<sub>2</sub>, Hexane/DCM 6:4) giving **3.2.1-N7** (223 mg, 55 %) as a white solid.

**<sup>1</sup>H NMR** (500 MHz, CD<sub>2</sub>Cl<sub>2</sub>): δ 7.61 (s, 2H), 7.45 (m, 3H), 7.38 (m, 1H), 7.36 – 7.26 (m, 8H), 7.22 (s, 4H), 7.10 (s, 2H), 2.53 (s, 6H), 2.35 (s, 12H), 2.28 (s, 6H), 1.32 (s, 24H).

**<sup>13</sup>C NMR** (126 MHz, CD<sub>2</sub>Cl<sub>2</sub>): δ 144.4 (C), 142.2 (C), 142.0 (C), 141.9 (C), 140.01 (C), 139.99 (C), 139.0 (C), 138.7 (C), 138.0 (CH), 134.8 (C), 134.8 (C), 133.0 (CH), 132.4 (CH), 131.8 (CH), 130.8 (CH), 128.4 (CH), 128.4 (CH), 128.2 (CH), 128.1 (CH), 83.9 (C), 25.3 (CH<sub>3</sub>), 22.1 (CH<sub>3</sub>), 20.9 (CH<sub>3</sub>), 20.48 (CH<sub>3</sub>), 20.46 (CH<sub>3</sub>). (The signal for the carbon nuclei bonded to the boron nuclei was not observed due to the quadrupolar relaxation induced by the boron nuclei. Some CH signals were not observed due to overlapping processes).

**HR-MS** (ESI-TOF): *m/z* calcd. for C<sub>62</sub>H<sub>68</sub>B<sub>2</sub>O<sub>4</sub>Na [M+Na]<sup>+</sup>: 921.5220, found: 921.5250.

**IR** (ATR): 2967, 1602, 1371, 1331, 1141, 859, 713 cm<sup>-1</sup>.

**Compound 3.2.1-M2**

Compound **3.2.1-M1** (5 g, 18.94 mmol), Pd(dppf)Cl<sub>2</sub> (347 mg, 0.47 mmol), Bis(pinacolato)diboron (12.03 g, 47.36 mmol) and AcOK (11.15 g, 113.65 mmol) were placed into a 250 mL round bottom flask under an Ar atmosphere. The solids were suspended in

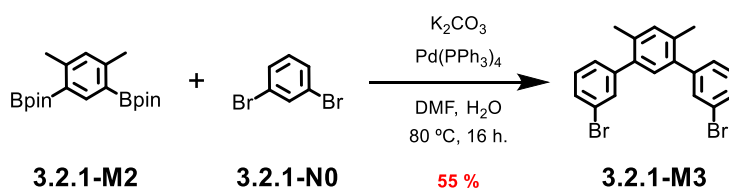
degassed dioxane (60 mL) and the reaction mixture was heated at 80 °C for 16 h. Once cooled to r.t., the solvent was removed under reduced pressure and the crude was diluted with EtOAc and washed with brine. The organic layer was dried over anhydrous Na<sub>2</sub>SO<sub>4</sub> and the solvent was removed under reduced pressure. The crude was purified by column chromatography (SiO<sub>2</sub>, Hexane/EtOAc 98:2) giving **3.2.1-M2** (4.7 g, 69 %) as a white solid.

**<sup>1</sup>H NMR** (500 MHz, CDCl<sub>3</sub>): δ = 8.12 (s, 1H), 6.98 (s, 1H), 2.50 (s, 6H), 1.34 (s, 24H).

**<sup>13</sup>C NMR** (126 MHz, CDCl<sub>3</sub>): δ = 147.8 (C), 143.7 (CH), 131.6 (CH), 83.2 (C), 24.9 (CH<sub>3</sub>), 22.4 (CH<sub>3</sub>). (The signal for the carbon nuclei bonded to the boron nuclei was not observed due to the quadrupolar relaxation induced by the boron nuclei).

Spectral data agree with those previously reported<sup>242</sup>.

### Compound 3.2.1-M3



Compound **3.2.1-M2** (226 mg, 0.8 mmol), **3.2.1-N0** (660 mg, 2.8 mmol), Pd(PPh<sub>3</sub>)<sub>4</sub> (92 mg, 0.08 mmol) and K<sub>2</sub>CO<sub>3</sub> (551 mg, 4 mmol) were placed into a 100 mL round bottom flask under an Ar atmosphere. The solids were dissolved in a degassed mixture of DMF (32 mL) and distilled water (2 mL) and the reaction mixture was heated at 80 °C for 16 h. The resulting mixture was diluted with CH<sub>2</sub>Cl<sub>2</sub> and washed with water and brine. The organic layer was dried over anhydrous Na<sub>2</sub>SO<sub>4</sub> and the solvent was evaporated under reduced pressure. The crude was purified by column chromatography (SiO<sub>2</sub>, Hexane) giving **3.2.1-M3** (186 mg, 55%) as a white foam.

**<sup>1</sup>H NMR** (500 MHz, CDCl<sub>3</sub>): δ = 7.50 (t, *J* = 1.4 Hz, 2H), 7.49 – 7.43 (m, 2H), 7.32 – 7.24 (m, 4H), 7.19 (s, 1H), 7.07 (s, 1H), 2.30 (s, 6H).

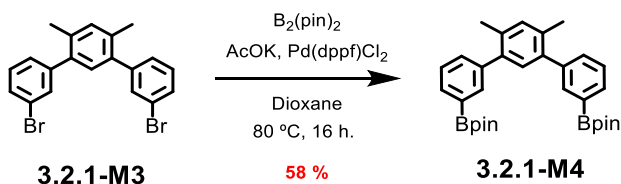
**<sup>13</sup>C NMR** (126 MHz, CDCl<sub>3</sub>): δ = 143.6 (C), 138.3 (C), 134.8 (C), 132.8 (C), 132.3 (CH), 131.01 (C), 130.01 (CH), 129.8 (CH), 128.1 (CH), 122.4 (C), 20.1 (CH<sub>3</sub>).

**HR-MS** (ESI-TOF): *m/z* calcd. for C<sub>20</sub>H<sub>16</sub>Br<sub>2</sub> [M]<sup>+</sup>: 415.9599, found: 415.9585.

**IR** (ATR): 2917, 1592, 1557, 1464, 1072, 880, 783, 696 cm<sup>-1</sup>.

<sup>242</sup> Y. D. Yang, H. Y. Gong, *Chem. Commun.*, **2019**, 55, 3701–3704.



**Compound 3.2.1-M4**

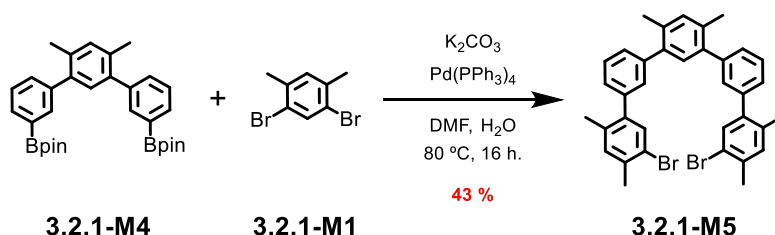
Compound **3.2.1-M3** (1.24 g, 2.98 mmol), Pd(dppf)Cl<sub>2</sub> (109 mg, 0.15 mmol), Bis(pinacolato)diboron (1.89 g, 7.45 mmol) and AcOK (1.76 g, 17.88 mmol) were placed into a 250 mL round bottom flask under an Ar atmosphere. The solids were suspended in degassed dioxane (16 mL) and the reaction mixture was heated at 80 °C for 16 h. Once cooled down to r.t., the solvent was removed under reduced pressure and the crude was diluted with DCM and washed with brine. The organic layer was dried over anhydrous Na<sub>2</sub>SO<sub>4</sub> and the solvent was removed under reduced pressure. The crude was purified by column chromatography (SiO<sub>2</sub>, Hexane/DCM 8:2) giving **3.2.1-M4** (0.88 g, 58 %) as a white solid.

<sup>1</sup>H NMR (500 MHz, CDCl<sub>3</sub>): δ 7.80 (s, 2H), 7.77 (dt, *J* = 7.2, 1.4 Hz, 2H), 7.46 (dt, *J* = 7.6, 1.7 Hz, 2H), 7.41 (t, *J* = 7.4 Hz, 2H), 7.16 (s, 1H), 7.15 (s, 1H), 2.29 (s, 6H), 1.34 (s, 26H).

<sup>13</sup>C NMR (126 MHz, CDCl<sub>3</sub>): δ = 141.2 (C), 139.5 (C), 135.8 (CH), 134.2 (C), 133.2 (CH), 132.30 (CH), 132.28 (CH), 131.5 (CH), 127.5 (CH), 83.9 (C), 25.0 (CH<sub>3</sub>), 20.2 (CH<sub>3</sub>). (The signal for the carbon nuclei bonded to the boron nuclei was not observed due to the quadrupolar relaxation induced by the boron nuclei).

HR-MS (ESI-TOF): *m/z* calcd. for C<sub>32</sub>H<sub>40</sub>O<sub>4</sub>B<sub>2</sub> [M + Na]<sup>+</sup>: 533.3021, found: 533.3029.

IR (ATR): 2977, 1411, 1355, 1314, 1143, 863, 712 cm<sup>-1</sup>.

**Compound 3.2.1-M5**

Compound **3.2.1-M4** (0.95 g, 1.86 mmol), **3.2.1-M1** 1,5-Dibromo-2,4-dimethylbenzene (1.72 mg, 6.51 mmol), Pd(PPh<sub>3</sub>)<sub>4</sub> (0.22 g, 0.19 mmol) and K<sub>2</sub>CO<sub>3</sub> (1.29 g, 9.31 mmol) were placed into a 250 mL round bottom flask under an Ar atmosphere. The solids were dissolved in a degassed mixture of DMF (75 mL) and distilled water (4 mL) and the reaction mixture was heated at 80 °C for 16 h. The resulting mixture was diluted with CH<sub>2</sub>Cl<sub>2</sub> and washed with water and brine. The organic layer was dried over anhydrous Na<sub>2</sub>SO<sub>4</sub> and the solvent was evaporated

under reduced pressure. The crude was purified by column chromatography (SiO<sub>2</sub>, Hexane/DCM 95/5) giving **3.2.1-M5** (440 mg, 43%) as a white foam.

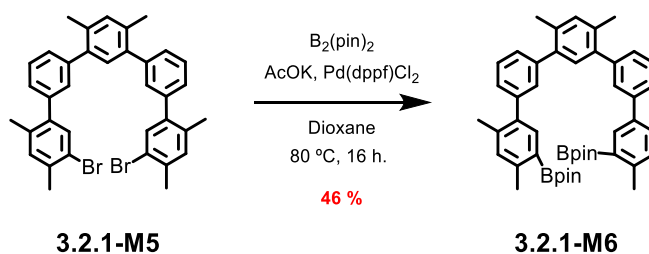
<sup>1</sup>H NMR (500 MHz, Chloroform-*d*): δ 7.55 – 7.46 (m, 1H), 7.41 (d, *J* = 7.7 Hz, 0H), 7.37 (s, 0H), 7.34 – 7.27 (m, 1H), 7.19 (s, 0H), 2.46 (s, 1H), 2.42 (s, 1H), 2.29 (s, 1H).

<sup>13</sup>C NMR (126 MHz, CDCl<sub>3</sub>): δ 141.6 (C), 141.3 (C), 140.4 (C), 139.4 (C), 136.6 (C), 134.6 (C), 134.5 (C), 133.3 (CH), 132.8 (CH), 132.7 (CH), 131.5 (CH), 130.2 (CH), 128.2 (CH), 128.1 (CH), 127.6 (CH), 121.8 (C), 22.5 (CH<sub>3</sub>), 20.3 (CH<sub>3</sub>), 20.1 (CH<sub>3</sub>).

HR-MS (APCI): *m/z* calcd. for C<sub>36</sub>H<sub>32</sub>Br<sub>2</sub> [H]<sup>+</sup>: 625.0926, found: 625.0934.

IR (ATR): 2952, 2920, 1600, 1468, 1030, 882, 713 cm<sup>-1</sup>.

### Compound 3.2.1-M6



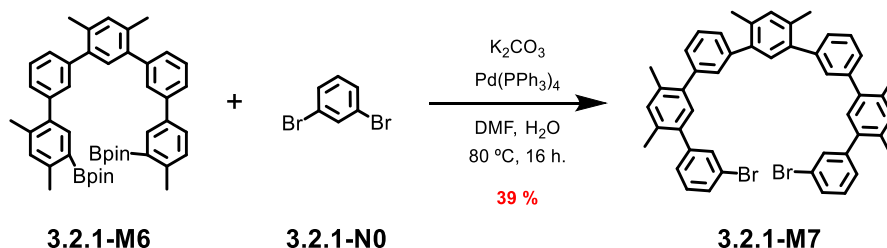
Compound **3.2.1-M5** (465 mg, 0.75 mmol), Pd(dppf)Cl<sub>2</sub> (27 mg, 0.04 mmol), Bis(pinacolato)diboron (476 mg, 1.88 mmol) and AcOK (442 mg, 4.5 mmol) were placed into a 250 mL round bottom flask under an Ar atmosphere. The solids were suspended in degassed dioxane (8 mL) and the reaction mixture was heated at 80 °C for 16 h. Once cooled down to r.t., the solvent was removed under reduced pressure and the crude was diluted with DCM and washed with brine. The organic layer was dried over anhydrous Na<sub>2</sub>SO<sub>4</sub> and the solvent was removed under reduced pressure. The crude was purified by column chromatography (SiO<sub>2</sub>, Hexane/EtOAc 9:1) giving **3.2.1-M6** (246 mg, 46 %) as a white solid.

<sup>1</sup>H NMR (500 MHz, Methylene Chloride-*d*<sub>2</sub>): δ 7.61 (s, 2H), 7.45 (t, *J* = 7.5 Hz, 2H), 7.36 – 7.25 (m, 6H), 7.22 (s, 2H), 7.10 (s, 2H), 2.53 (s, 6H), 2.35 (s, 6H), 2.29 (s, 6H), 1.32 (s, 24H).

<sup>13</sup>C NMR (126 MHz, CD<sub>2</sub>Cl<sub>2</sub>): δ 144.39 (C), 142.24 (C), 141.93 (C), 140.03 (C), 138.97 (C), 138.68 (C), 137.97 (CH), 134.83 (C), 133.01 (CH), 132.40 (CH), 131.84 (CH), 130.79 (CH), 128.36 (CH), 128.23 (CH), 128.11 (CH), 83.93 (C), 25.25 (CH<sub>3</sub>), 22.04 (CH<sub>3</sub>), 20.91 (CH<sub>3</sub>), 20.45 (CH<sub>3</sub>). (The signal for the carbon nuclei bonded to the boron nuclei was not observed due to the quadrupolar relaxation induced by the boron nuclei).

HR-MS (ESI-TOF): *m/z* calcd. for C<sub>48</sub>H<sub>56</sub>B<sub>2</sub>O<sub>4</sub>Na [M+Na]<sup>+</sup>: 741.4278, found: 741.4298.

IR (ATR): 2976, 1604, 1372, 1333, 1144, 1065, 859, 738 cm<sup>-1</sup>.

**Compound 3.2.1-M7**

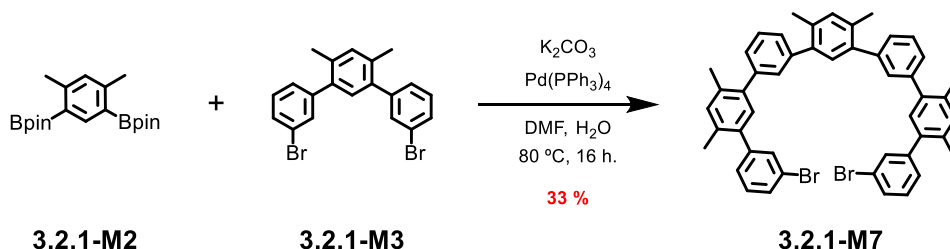
Compound **3.2.1-M6** (178 mg, 0.25 mmol), **3.2.1-N0** 1,3-Dibromobenzene (204 mg, 0.87 mmol),  $\text{Pd}(\text{PPh}_3)_4$  (29 mg, 0.03 mmol) and  $\text{K}_2\text{CO}_3$  (171 mg, 1.23 mmol) were placed into a 250 mL round bottom flask under an Ar atmosphere. The solids were dissolved in a degassed mixture of DMF (10 mL) and distilled water (0.5 mL) and the reaction mixture was heated at 80 °C for 16 h. The resulting mixture was diluted with  $\text{CH}_2\text{Cl}_2$  and washed with water and brine. The organic layer was dried over anhydrous  $\text{Na}_2\text{SO}_4$  and the solvent was evaporated under reduced pressure. The crude was purified by column chromatography ( $\text{SiO}_2$ , Hexane/DCM 92.5:7.5) giving **3.2.1-M7** (75 mg, 39%) as a white foam.

$^1\text{H NMR}$  (400 MHz, Chloroform-*d*):  $\delta$  7.53 (t,  $J = 1.8$  Hz, 2H), 7.51 – 7.42 (m, 4H), 7.40 – 7.26 (m, 10H), 7.24 (d,  $J = 3.1$  Hz, 2H), 7.22 (s, 2H), 7.16 (s, 2H), 2.38 (s, 6H), 2.36 (s, 6H), 2.32 (s, 6H).

$^{13}\text{C NMR}$  (101 MHz,  $\text{CDCl}_3$ ):  $\delta$  143.8 (C), 141.5 (C), 141.3 (C), 139.7 (C), 139.5 (C), 138.1 (C), 135.0 (C), 134.4 (C), 134.2 (C), 132.7 (CH), 132.6 (CH), 132.4 (CH), 131.6 (CH), 131.3 (CH), 130.3 (CH), 129.9 (CH), 129.7 (C), 128.1 (CH), 128.00 (CH), 127.9 (CH), 127.8 (CH), 122.3 (C), 20.3 ( $\text{CH}_3$ ), 20.1 ( $\text{CH}_3$ ). Some  $^{13}\text{C}$  signals were not observed due to overlapping processes.

**HR-MS** (APCI):  $m/z$  calcd. for  $\text{C}_{48}\text{H}_{41}\text{Br}_2$   $[\text{M}+\text{H}]^+$ : 777.1533, found: 777.1555.

**IR** (ATR): 2921, 1559, 1468, 891, 713  $\text{cm}^{-1}$ .

**Compound 3.2.1-M7**

Compound **3.2.1-M2** (120 mg, 0.34 mmol), **3.2.1-M3** (488 mg, 1.17 mmol),  $\text{Pd}(\text{PPh}_3)_4$  (39 mg, 0.03 mmol) and  $\text{K}_2\text{CO}_3$  (232 mg, 1.68 mmol) were placed into a 50 mL round bottom flask under an Ar atmosphere. The solids were dissolved in a degassed mixture of DMF (8.5 mL) and distilled water (0.6 mL) and the reaction mixture was heated at 80 °C for 16 h. The resulting

mixture was diluted with  $\text{CH}_2\text{Cl}_2$  and washed with water and brine. The organic layer was dried over anhydrous  $\text{Na}_2\text{SO}_4$  and the solvent was evaporated under reduced pressure. The crude was purified by column chromatography ( $\text{SiO}_2$ , Hexane/DCM 92.5:7.5) giving **3.2.1-M7** (90 mg, 33%) as a white foam.

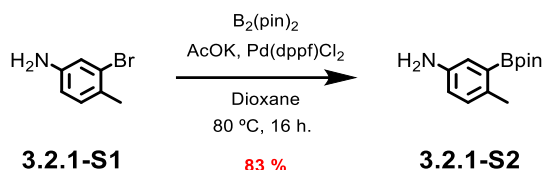
**$^1\text{H}$  NMR** (400 MHz, Chloroform-*d*):  $\delta$  7.53 (t,  $J = 1.8$  Hz, 2H), 7.51 – 7.42 (m, 4H), 7.40 – 7.26 (m, 10H), 7.24 (d,  $J = 3.1$  Hz, 2H), 7.22 (s, 2H), 7.16 (s, 2H), 2.38 (s, 6H), 2.36 (s, 6H), 2.32 (s, 6H).

**$^{13}\text{C}$  NMR** (101 MHz,  $\text{CDCl}_3$ ):  $\delta$  143.8 (C), 141.5 (C), 141.3 (C), 139.7 (C), 139.5 (C), 138.1 (C), 135.0 (C), 134.4 (C), 134.2 (C), 132.7 (CH), 132.6 (CH), 132.4 (CH), 131.6 (CH), 131.3 (CH), 130.3 (CH), 129.9 (CH), 129.7 (C), 128.1 (CH), 128.00 (CH), 127.9 (CH), 127.8 (CH), 122.3 (C), 20.3 ( $\text{CH}_3$ ), 20.1 ( $\text{CH}_3$ ). Some  $^{13}\text{C}$  signals were not observed due to overlapping processes.

**HR-MS** (APCI):  $m/z$  calcd. for  $\text{C}_{48}\text{H}_{41}\text{Br}_2$   $[\text{M}+\text{H}]^+$ : 777.1533, found: 777.1555.

**IR** (ATR): 2921, 1559, 1468, 891, 713  $\text{cm}^{-1}$ .

### Compound 3.2.1-S2



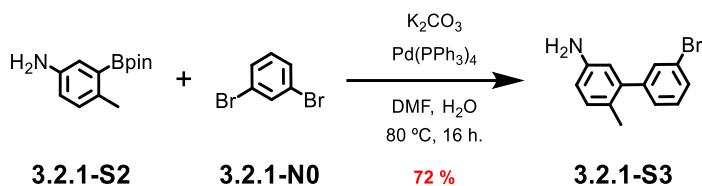
**3.2.1-S1** 3-bromo-4-methylaniline (6.22 g, 33.43 mmol),  $\text{Pd}(\text{dppf})\text{Cl}_2$  (489 mg, 0.67 mmol), Bis(pinacolato)diboron (10.61 g, 41.79 mmol) and AcOK (9.84 g, 100.29 mmol) were placed into a 250 mL round bottom flask under Ar atmosphere. The solids were suspended in degassed dioxane (90 mL) and the reaction mixture was heated 80 °C for 16 h. Once cooled to r.t., the solvent was removed under reduced pressure and the crude was dissolved with  $\text{CH}_2\text{Cl}_2$  and washed with brine. The organic layer was dried over anhydrous  $\text{Na}_2\text{SO}_4$  and the solvent removed under reduced pressure. The crude was purified by column chromatography ( $\text{SiO}_2$ , Hexane/AcOEt 92.5:7.5) giving **3.2.1-S2** (6.5 g, 83%) as a white powder.

**$^1\text{H}$  NMR** (500 MHz,  $\text{CDCl}_3$ ):  $\delta$  7.12 (d,  $J = 2.7$  Hz, 1H), 6.97 (d,  $J = 8.0$  Hz, 1H), 6.68 (dd,  $J = 8.1, 2.7$  Hz, 1H), 3.50 (s, 2H), 2.42 (s, 3H), 1.34 (s, 12H).

**$^{13}\text{C}$  NMR** (126 MHz,  $\text{CDCl}_3$ ):  $\delta$  143.3 (C), 135.0 (C), 130.8 (CH), 122.6 (CH), 118.0 (CH), 83.5 (C), 25.0 ( $\text{CH}_3$ ), 21.3 ( $\text{CH}_3$ ). (A signal for the carbon nuclei bonded to the boron nuclei was not observed due to the quadrupolar relaxation induced by the boron nuclei).

Spectral data agree with those previously reported<sup>243</sup>.

<sup>243</sup> E. F. DiMauro, J. Newcomb, J. J. Nunes, J. E. Bemis, C. Boucher, J. L. Buchanan, W. H. Buckner, V. J. Cee, L. Chai, H. L. Deak, et al., *J. Med. Chem.*, **2006**, *49*, 5671–5686.

**Compound 3.2.1-S3**

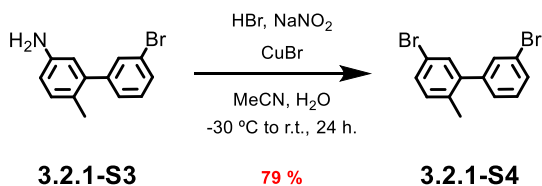
Compound **3.2.1-S2** (4 g, 17.16 mmol), **3.2.1-N0** 1,3-Dibromobenzene (6.07 g, 25.74 mmol),  $\text{Pd}(\text{PPh}_3)_4$  (500 mg, 0.43 mmol) and  $\text{K}_2\text{CO}_3$  (7.11 g, 51.48 mmol) were placed into a 250 mL round bottom flask under Ar atmosphere. The solids were dissolved in a degassed mixture of DMF (48 mL) and distilled water (4mL) and the reaction mixture was heated 80 °C for 16 h. The resulting mixture was diluted with  $\text{CH}_2\text{Cl}_2$  and washed with water and brine. The organic layer was dried over anhydrous  $\text{Na}_2\text{SO}_4$  and the solvent was evaporated under reduced pressure. The crude was purified by column chromatography ( $\text{SiO}_2$ , Hexane/AcOEt 92:8) giving **3.2.1-S3** (3.23g, 72%) as a white foam.

$^1\text{H NMR}$  (500 MHz,  $\text{CD}_2\text{Cl}_2$ ):  $\delta$  7.52 – 7.38 (m, 2H), 7.32 – 7.21 (m, 2H), 7.03 (d,  $J = 8.1$  Hz, 1H), 6.61 (dd,  $J = 8.1, 2.6$  Hz, 1H), 6.53 (d,  $J = 2.7$  Hz, 1H), 3.64 (s, 2H), 2.12 (s, 3H).

$^{13}\text{C NMR}$  (126 MHz,  $\text{CD}_2\text{Cl}_2$ ):  $\delta$  145.2 (C), 145.0 (C), 141.6 (C), 132.5 (CH), 131.7 (CH), 130.2 (CH), 130.2 (CH), 128.4 (CH), 125.2 (C), 122.5 (C), 116.7 (CH), 115.1 (CH), 19.6 ( $\text{CH}_3$ ).

**HR-MS** (ESI-TOF):  $m/z$  calcd. for  $\text{C}_{13}\text{H}_{13}\text{Br}_2\text{N}$   $[\text{M}+\text{H}]^+$ : 262.0231, found: 262.0229.

**IR** (ATR): 3448, 3366, 2922, 1619, 1556, 1503, 1472, 1317, 1224, 1139, 1073, 1035, 996, 866, 787, 696  $\text{cm}^{-1}$ .

**Compound 3.2.1-S4**

Amine **3.2.1-S3** (5.57 g, 21.25 mmol) was dissolved in  $\text{CH}_3\text{CN}$  (35 mL) and cooled down to  $-30^\circ\text{C}$ . First, a solution of HBr 48% (8.8 ml, 45.61mmol) was added slowly and then a solution of  $\text{NaNO}_2$  (1.16 g, 23.37 mmol) in water (9.3 mL) was added dropwise. The mixture was stirred for 30 minutes.  $\text{CuBr}$  (4.57 g, 31.87 mmol) was added, and the mixture was stirred over night at r.t.. After that, the reaction was quenched by slow addition of ice water and sodium carbonate until neutralization. The resulting mixture was diluted with  $\text{CH}_2\text{Cl}_2$  and washed with brine. The organic layer was dried over anhydrous  $\text{Na}_2\text{SO}_4$  and the solvent was evaporated under reduced pressure. The crude was purified by column chromatography ( $\text{SiO}_2$ , Hexane/AcOEt 99:1) giving **3.2.1-S4** (5.48 g, 79%) as a white foam.

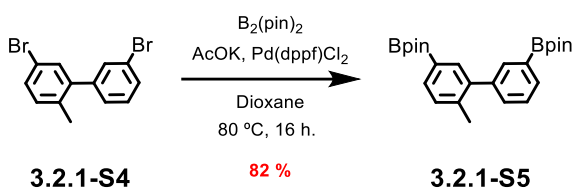
**$^1\text{H}$  NMR** (500 MHz,  $\text{CD}_2\text{Cl}_2$ ):  $\delta$  7.52 (ddd,  $J = 7.9, 2.0, 1.1$  Hz, 1H), 7.47 (t,  $J = 1.8$  Hz, 1H), 7.40 (dd,  $J = 8.1, 2.2$  Hz, 1H), 7.36 (d,  $J = 2.2$  Hz, 1H), 7.32 (t,  $J = 7.8$  Hz, 1H), 7.25 (dt,  $J = 7.7, 1.4$  Hz, 1H), 7.16 (d,  $J = 8.0$  Hz, 1H), 2.20 (s, 3H).

**$^{13}\text{C}$  NMR** (126 MHz,  $\text{CD}_2\text{Cl}_2$ ):  $\delta$  143.2 (C), 142.9 (C), 135.1 (C), 132.7 (CH), 132.6 (CH), 132.5 (CH), 131.1 (CH), 130.9 (CH), 130.4 (CH), 128.4 (CH), 122.7 (C), 119.7 (C), 20.2 ( $\text{CH}_3$ ).

**HR-MS** (GC-EI):  $m/z$  calcd. for  $\text{C}_{13}\text{H}_{10}\text{Br}_2$   $[\text{M}]^+$ : 325.9129, found: 325.9128.

**IR** (ATR): 2923, 1587, 1554, 1463, 1030, 879, 809, 785  $\text{cm}^{-1}$ .

### Compound 3.2.1-S5



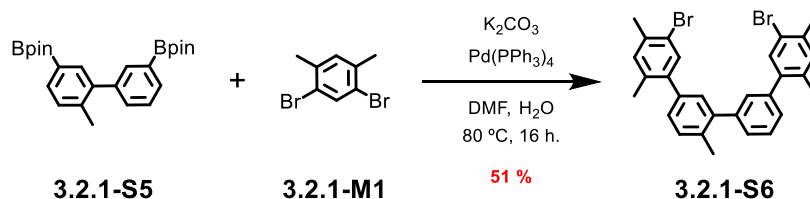
Compound **3.2.1-S4** (5.48 g, 16.81 mmol),  $\text{Pd(dppf)Cl}_2$  (307 mg, 0.42 mmol), Bis(pinacolato)diboron (10.67 g, 42.03 mmol) and AcOK (9.9 g, 100.85 mmol) were placed into a 250 mL round bottom flask under an Ar atmosphere. The solids were suspended in degassed dioxane (45 mL) and the reaction mixture was heated 80 °C for 16 h. Once cooled to r.t., the solvent was removed under reduced pressure and the crude was dissolved with  $\text{CH}_2\text{Cl}_2$  and washed with brine. The organic layer was dried over anhydrous  $\text{Na}_2\text{SO}_4$  and the solvent removed under reduced pressure. The crude was purified by column chromatography ( $\text{SiO}_2$ , Hexane/AcOEt 97:3) giving **3.2.1-S5** (5.8 g, 82%) as a white foam.

**$^1\text{H}$  NMR** (500 MHz,  $\text{CD}_2\text{Cl}_2$ ):  $\delta$  7.78 – 7.73 (m, 1H), 7.73 (s, 1H), 7.65 (d,  $J = 7.5$  Hz, 1H), 7.61 (s, 1H), 7.43 (m, 2H), 7.30 (d,  $J = 7.6$  Hz, 1H), 2.29 (s, 3H), 1.36 (s, 12H), 1.34 (s, 12H).

**$^{13}\text{C}$  NMR** (126 MHz,  $\text{CD}_2\text{Cl}_2$ ):  $\delta$  141.9 (C), 141.8 (C), 139.3 (C), 136.8 (CH), 136.0 (CH), 134.1 (CH), 133.6 (CH), 132.6 (CH), 130.3 (CH), 127.9 (CH), 84.4 (C), 84.3 (C), 25.3 ( $\text{CH}_3$ ), 25.3 ( $\text{CH}_3$ ), 21.1 ( $\text{CH}_3$ ). (Two signals for the carbon nuclei bonded to the boron nuclei were not observed due to the quadrupolar relaxation induced by the boron nuclei).

**HR-MS** (ESI-TOF):  $m/z$  calcd. for  $\text{C}_{25}\text{H}_{34}\text{Br}_2\text{O}_4\text{Na}$   $[\text{M}+\text{Na}]^+$ : 443.2550, found: 443.2557.

**IR** (ATR): 2978, 1607, 1354, 1313, 1145,  $\text{cm}^{-1}$ .

**Compound 3.2.1-S6**

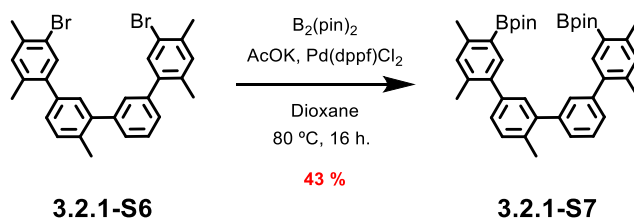
Compound **3.2.1-S5** (400 mg, 0.95 mmol), 1,5-Dibromo-2,4-dimethylbenzene (880 mg, 3.33 mmol),  $Pd(PPh_3)_4$  (110 mg, 0.095 mmol) and  $K_2CO_3$  (658 mg, 4.76 mmol) were placed into a 250 mL round bottom flask under an Ar atmosphere. The solids were dissolved in a degassed mixture of DMF (40 mL) and distilled water (2mL) and the reaction mixture was heated  $80\text{ }^\circ\text{C}$  for 16 h. The resulting mixture was diluted with  $CH_2Cl_2$  and washed with water and brine. The organic layer was dried over anhydrous  $Na_2SO_4$  and the solvent was evaporated under reduced pressure. The crude was purified by column chromatography ( $SiO_2$ , Hexane/DCM 95:5) giving **3.2.1-S6** (258 mg, 51%) as a white foam.

$^1H$  NMR (500 MHz,  $CDCl_3$ ):  $\delta$  7.50 – 7.42 (m, 3H), 7.37 – 7.27 (m, 4H), 7.21 (m, 2H), 7.15 (s, 1H), 7.14 (s, 1H), 2.41 (s, 3H), 2.40 (s, 3H), 2.37 (s, 3H), 2.25 (s, 6H).

$^{13}C$  NMR (126 MHz,  $CDCl_3$ ):  $\delta$  141.6 (C), 141.5 (C), 141.1 (C), 140.9 (C), 140.3 (C), 138.1 (C), 136.6 (C), 136.4 (C), 134.5 (C), 134.5 (C), 134.2 (C), 133.2 (CH), 133.2 (CH), 132.7 (CH), 132.7 (CH), 130.5 (CH), 130.3 (CH), 130.0 (CH), 128.1 (CH), 128.0 (CH), 127.7 (CH), 121.7 (C), 121.7 (C), 22.4 ( $CH_3$ ), 22.4 ( $CH_3$ ), 20.3 ( $CH_3$ ), 19.99 ( $CH_3$ ), 19.96 ( $CH_3$ ). (Some  $^{13}C$  signals were not observed due to overlapping processes).

HR-MS (GC-ED):  $m/z$  calcd. for  $C_{29}H_{26}Br_2$   $[M]^+$ : 534.0383, found: 534.0391.

IR (ATR): 2920, 1599, 1469, 1381, 1026, 882, 713, 560  $cm^{-1}$ .

**Compound 3.2.1-S7**

Compound **3.2.1-S6** (1.91 g, 3.56 mmol),  $Pd(dppf)Cl_2$  (131 mg, 0.18 mmol), Bis(pinacolato)diboron (2.26 g, 8.89 mmol) and AcOK (2.09 g, 21.34 mmol) were placed into a 250 mL round bottom flask under an Ar atmosphere. The solids were suspended in degassed dioxane (25 mL) and the reaction mixture was heated  $80\text{ }^\circ\text{C}$  for 16 h. Once cooled to r.t., the solvent was removed under reduced pressure and the crude was diluted with DCM and washed with brine. The organic layer was dried over anhydrous  $Na_2SO_4$  and the solvent was removed

under reduced pressure. The crude was purified by column chromatography (SiO<sub>2</sub>, Hexane/DCM 8:2) giving **3.2.1-S7** (0.96 g, 43 %) as a white solid.

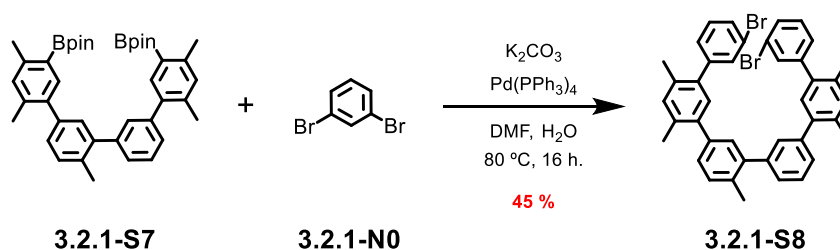
**<sup>1</sup>H NMR** (500 MHz, CD<sub>2</sub>Cl<sub>2</sub>): δ 7.64 (d, J = 2.5 Hz, 1H), 7.61 (d, J = 2.6 Hz, 1H), 7.48 (t, J = 7.6 Hz, 1H), 7.39 – 7.27 (m, 4H), 7.26 – 7.17 (m, 2H), 7.12 (s, 1H), 7.10 (s, 1H), 2.55 (s, 3H), 2.53 (s, 3H), 2.38 (s, 3H), 2.31 (s, 3H), 2.30 (s, 3H), 1.33 (m, 24H).

**<sup>13</sup>C NMR** (126 MHz, CD<sub>2</sub>Cl<sub>2</sub>): δ 144.4 (C), 144.3 (C), 142.3 (C), 142.23 (C), 142.15 (C), 140.0 (C), 139.0 (C), 138.8 (C), 138.7 (C), 138.0 (CH), 134.3 (C), 132.44 (CH), 132.42 (CH), 131.2 (CH), 130.8 (CH), 130.6 (CH), 128.7 (CH), 128.43 (CH), 128.37 (CH), 128.1 (CH), 83.95 (C), 83.92 (C), 25.3 (CH<sub>3</sub>), 22.1 (CH<sub>3</sub>), 20.9 (CH<sub>3</sub>), 20.6 (CH<sub>3</sub>). (A signal for the carbon nuclei bonded to the boron nuclei was not observed due to the quadrupolar relaxation induced by the boron nuclei). (Some <sup>13</sup>C signals were not observed due to overlapping processes).

**HR-MS** (ESI-TOF): m/z calcd. for C<sub>41</sub>H<sub>50</sub>B<sub>2</sub>O<sub>4</sub>Na [M+Na]<sup>+</sup>: 651.3806, found: 651.3813.

**IR** (ATR): 2976, 1604, 1371, 1333, 1144, 1064, 861, 715 cm<sup>-1</sup>.

### Compound 3.2.1-S8



Compound **3.2.1-S7** (550 mg, 0.88 mmol), 1,3-Dibromobenzene **3.2.1-N0** (723 mg, 3.06 mmol), Pd(PPh<sub>3</sub>)<sub>4</sub> (101 mg, 0.09 mmol) and K<sub>2</sub>CO<sub>3</sub> (605 mg, 4.38 mmol) were placed into a 250 mL round bottom flask under Ar atmosphere. The solids were dissolved in a degassed mixture of DMF (35 mL) and distilled water (1.8 mL) and the reaction mixture was heated 80 °C for 16 h. The resulting mixture was diluted with CH<sub>2</sub>Cl<sub>2</sub> and washed with water and brine. The organic layer was dried over anhydrous Na<sub>2</sub>SO<sub>4</sub> and the solvent was evaporated under reduced pressure. The crude was purified by column chromatography (SiO<sub>2</sub>, Hexane/DCM 95:5) giving **3.2.1-S8** (273 mg, 45%) as a white foam.

**<sup>1</sup>H NMR** (500 MHz, CD<sub>2</sub>Cl<sub>2</sub>) δ 7.52 (m, 2H), 7.51 – 7.44 (m, 3H), 7.39 – 7.24 (m, 10H), 7.22 (s, 1H), 7.20 (s, 1H), 7.15 (s, 1H), 7.13 (s, 1H), 2.37 (s, 3H), 2.35 (s, 3H), 2.35 (s, 3H), 2.29 (s, 3H), 2.28 (s, 3H).

**<sup>13</sup>C NMR** (126 MHz, CD<sub>2</sub>Cl<sub>2</sub>) δ 144.43 (C), 144.39 (C), 142.23 (C), 142.16 (C), 141.8 (C), 140.0 (C), 139.8 (C), 139.5 (C), 138.52 (C), 138.51 (C), 135.39 (C), 135.38 (C), 134.7 (C), 134.52 (C), 134.51 (C), 133.1 (CH), 132.8 (CH), 131.6 (CH), 131.2 (CH), 130.71 (CH), 130.68 (CH), 130.23 (CH), 130.22 (CH), 130.20 (CH), 128.70 (CH), 128.65 (CH), 128.5 (CH), 128.33 (CH), 128.28 (CH), 122.59 (CH), 122.58 (C), 20.6 (CH<sub>3</sub>), 20.52 (CH<sub>3</sub>), 20.50 (CH<sub>3</sub>), 20.3 (CH<sub>3</sub>), 20.2 (CH<sub>3</sub>)

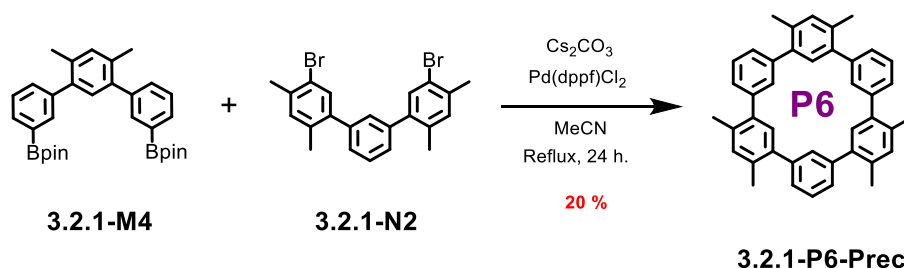


(In theory there should be 17 aromatic (C) carbon peaks but only 16 were observed and 19 aromatic (CH) carbon peaks but only 15 were observed; presumably some peaks have merged together.).

**HR-MS** (ESI-TOF):  $m/z$  calcd. for  $C_{41}H_{34}Br_2Na$   $[M+Na]^+$ : 709.0909, found: 709.0931.

**IR** (ATR): 2926, 1592, 1558, 1467, 1263, 1072, 885, 788, 730  $cm^{-1}$ .

**Compound 3.2.1-P6-Prec**



Compound **3.2.1-N2** (130 mg, 0.29 mmol), compound **3.2.1-M4** (150 mg, 0.29 mmol) Pd(dppf)Cl<sub>2</sub> (43 mg, 0.06 mmol) and Cs<sub>2</sub>CO<sub>3</sub> (4.72 g, 14.5 mmol) were placed into a 250 mL two-neck round-bottom flask under an Ar atmosphere. The solids were dissolved in dry acetonitrile (186 mL) and the reaction mixture was refluxed for 24 h. Once cooled to r.t., the mixture was filtrated and the solvent was removed under reduced pressure. The crude was dissolved in CH<sub>2</sub>Cl<sub>2</sub> and washed once with water and twice with brine. The organic layer was dried over anhydrous Na<sub>2</sub>SO<sub>4</sub> and the solvent removed under reduced pressure. The crude was purified by column chromatography (SiO<sub>2</sub>, Hexane/DCM 85:15) giving **3.2.1-6-Prec** (31 mg, 20%) as a white solid.

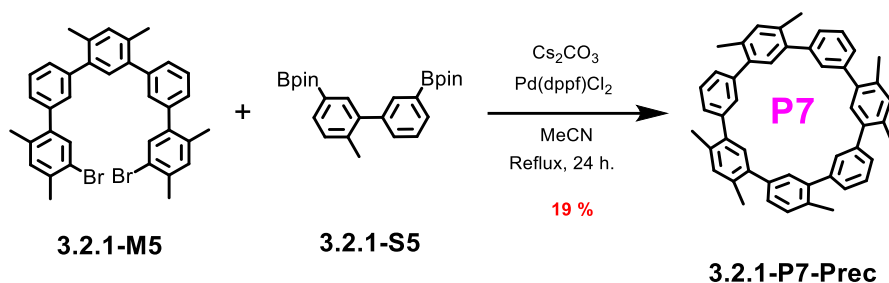
**<sup>1</sup>H NMR** (500 MHz, [D<sub>4</sub>]-*o*-DCB):  $\delta$  = 7.58 – 7.39 (m, 12H), 7.28 (s, 3H), 7.07 (s, 3H), 2.41 (s, 18H).

**<sup>13</sup>C NMR** (126 MHz, [D<sub>4</sub>]-*o*-DCB):  $\delta$  = 142.4 (C), 139.5 (C), 134.0 (C), 133.3 (CH), 133.2 (CH), 131.7 (CH), 127.8 (CH), 126.9 (CH), 20.3 (CH<sub>3</sub>).

**HR-MS** (ESI-TOF):  $m/z$  calcd. for  $C_{42}H_{36}$   $[M + Na]^+$ : 563.2715, found: 563.2734.

**IR** (ATR): 3021, 2921, 1727, 1599, 1505, 1385, 1266, 1033, 889, 799, 711  $cm^{-1}$ .

## Compound 3.2.1-P7-Prec



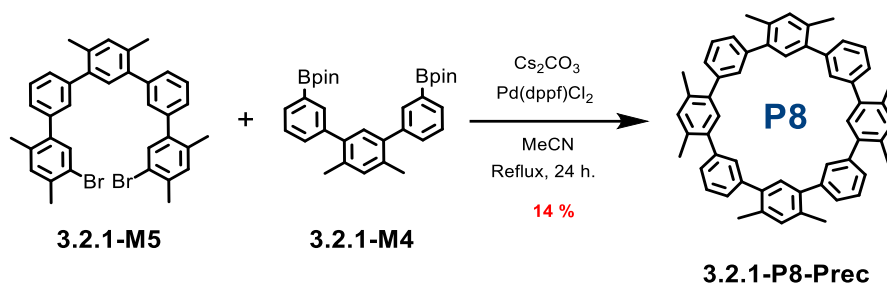
Compound **3.2.1-M5** (120 mg, 0.192 mmol), compound **3.2.1-S5** (80.7 mg, 0.192 mmol) Pd(dppf)Cl<sub>2</sub> (28.1 mg, 0.028 mmol) and Cs<sub>2</sub>CO<sub>3</sub> (313.1 g, 9.608 mmol) were placed into a 250 mL two-neck round-bottom flask under an Ar atmosphere. The solids were dissolved in dry acetonitrile (180 mL) and the reaction mixture was refluxed for 24 h. Once cooled to r.t., the mixture was filtrated and the solvent was removed under reduced pressure. The crude was dissolved in CH<sub>2</sub>Cl<sub>2</sub> and washed once with water and twice with brine. The organic layer was dried over anhydrous Na<sub>2</sub>SO<sub>4</sub> and the solvent removed under reduced pressure. The crude was purified by column chromatography (SiO<sub>2</sub>, Hexane/DCM 85:15) giving **3.2.1-P7-Prec** (23 mg, 19%) as a white solid.

**<sup>1</sup>H NMR** (500 MHz, CD<sub>2</sub>Cl<sub>2</sub>) δ 7.69 – 6.78 (m, 21H), 2.38 (m, 21H).

**<sup>13</sup>C NMR** (126 MHz, CD<sub>2</sub>Cl<sub>2</sub>) δ 142.24 (C), 142.15 (C), 142.0 (C), 141.9 (C), 141.8 (C), 141.7 (C), 139.44 (C), 139.35 (C), 139.3 (C), 139.13 (C), 139.11 (C), 138.9 (C), 138.74 (C), 138.72 (C), 134.2 (C), 134.12 (C), 134.10 (C), 134.06 (C), 134.0 (C), 133.8 (C), 132.53 (CH), 132.48 (CH), 131.89 (CH), 131.85 (CH), 131.81 (CH), 131.1 (CH), 130.2 (CH), 130.14 (CH), 130.09 (CH), 129.6 (CH), 128.0 (CH), 127.7 (CH), 127.6 (CH), 127.54 (CH), 127.51 (CH), 127.45 (CH), 127.2 (CH), 127.1 (CH), 127.03 (CH), 126.96 (CH), 20.0 (CH<sub>3</sub>), 19.91 (CH<sub>3</sub>), 19.89 (CH<sub>3</sub>), 19.8 (CH<sub>3</sub>). (Some <sup>13</sup>C signals were not observed due to overlapping processes).

**HR-MS** (MALDI-TOF): m/z calcd. for C<sub>49</sub>H<sub>42</sub> [M]<sup>+</sup>: 630.3279, found: 630.3281.

**IR** (ATR): 2920, 1800, 1599, 1481, 1264, 891, 800, 712 cm<sup>-1</sup>.

**Compound 3.2.1-P8-Prec**

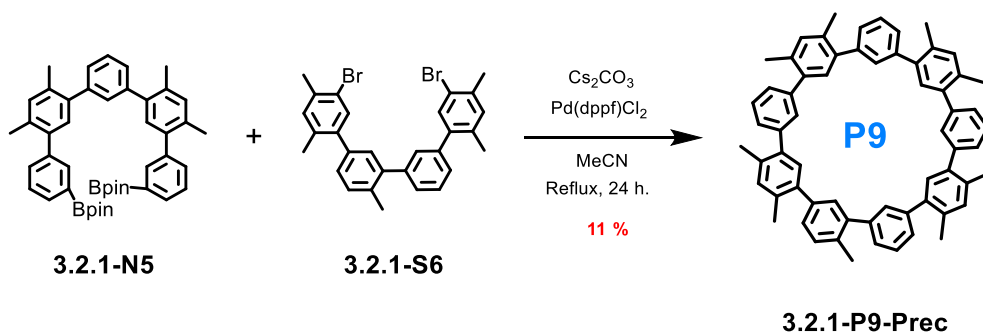
Compound **3.2.1-M5** (192 mg, 0.31 mmol), compound **3.2.1-M4** (157 mg, 0.31 mmol) Pd(dppf)Cl<sub>2</sub> (45 mg, 0.06 mmol) and Cs<sub>2</sub>CO<sub>3</sub> (5.05 g, 15.5 mmol) were placed into a 250 mL two-neck round-bottom flask under an Ar atmosphere. The solids were dissolved in dry acetonitrile (190 mL) and the reaction mixture was refluxed for 24 h. Once cooled to r.t., the mixture was filtrated and the solvent was removed under reduced pressure. The crude was dissolved in CH<sub>2</sub>Cl<sub>2</sub> and washed once with water and twice with brine. The organic layer was dried over anhydrous Na<sub>2</sub>SO<sub>4</sub> and the solvent removed under reduced pressure. The crude was purified by column chromatography (SiO<sub>2</sub>, Hexane/DCM 85:15) giving **3.2.1-P8-Prec** (31 mg, 14%) as a white solid.

<sup>1</sup>H NMR (500 MHz, CDCl<sub>3</sub>): δ: 7.42 – 7.31 (m, 16H), 7.22 (s, 4H), 7.18 (m, 4H), 2.37 (d, J = 2.4 Hz, 24H).

<sup>13</sup>C NMR (126 MHz, CDCl<sub>3</sub>): δ: 141.9 (C), 139.6 (C), 134.3 (C), 132.5 (CH), 132.2 (CH), 131.1 (CH), 127.6 (CH), 127.1 (CH), 20.1 (CH<sub>3</sub>).

HR-MS (ESI-TOF): m/z calcd. for C<sub>56</sub>H<sub>48</sub> [M+Na]<sup>+</sup>: 743.3654, found: 743.3673.

IR (ATR): 2951, 2922, 2855, 1600, 1472, 1263, 800, 713 cm<sup>-1</sup>.

**Compound 3.2.1-P9-Prec**

Compound **3.2.1-S6** (150 mg, 0.22 mmol), compound **3.2.1-N5** (118 mg, 0.22 mmol) Pd(dppf)Cl<sub>2</sub> (33 mg, 0.44 mmol) and Cs<sub>2</sub>CO<sub>3</sub> (3.62 g, 11.12 mmol) were placed into a 250 mL two-neck round-bottom flask under an Ar atmosphere. The solids were dissolved in dry

acetonitrile (130 mL) and the reaction mixture was refluxed for 24 h. Once cooled to r.t., the mixture was filtrated and the solvent was removed under reduced pressure. The crude was dissolved in  $\text{CH}_2\text{Cl}_2$  and washed once with water and twice with brine. The organic layer was dried over anhydrous  $\text{Na}_2\text{SO}_4$  and the solvent removed under reduced pressure. The crude was purified by column chromatography ( $\text{SiO}_2$ , Hexane/DCM 85:15) giving **3.2.1-P9-Prec** (26 mg, 11%) as a white solid.

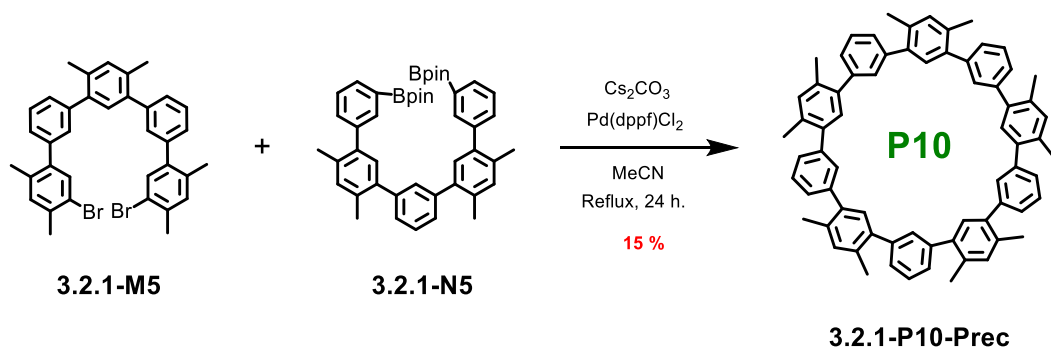
$^1\text{H NMR}$  (500 MHz,  $\text{CD}_2\text{Cl}_2$ )  $\delta$ : 7.41 (m,  $J = 7.3, 4.7$  Hz, 4H), 7.34 – 7.21 (m, 14H), 7.22 – 7.15 (m, 5H), 7.13 – 7.07 (m, 4H), 2.38 – 2.19 (m, 27H).

$^{13}\text{C NMR}$  (126 MHz,  $\text{CD}_2\text{Cl}_2$ )  $\delta$ : 142.4 (C), 142.4 (C), 142.2 (C), 142.19 (C), 142.19 (C), 142.15 (C), 142.10 (C), 140.0 (C), 139.9 (C), 139.92 (C), 139.91 (C), 139.88 (C), 139.84 (C), 139.65 (C), 139.61 (C), 134.78 (C), 134.72 (C), 134.70 (C), 134.6 (C), 134.4 (C), 132.84 (CH), 132.82 (CH), 132.80 (CH), 131.66 (CH), 131.64 (CH), 131.0 (CH), 130.59 (CH), 130.57 (CH), 130.53 (CH), 130.3 (CH), 128.7 (CH), 128.3 (CH), 128.15 (CH), 128.09 (CH), 128.07 (CH), 128.02 (CH), 20.49 ( $\text{CH}_3$ ), 20.44 ( $\text{CH}_3$ ), 20.40 ( $\text{CH}_3$ ), 20.38 ( $\text{CH}_3$ ), 20.34 ( $\text{CH}_3$ ). (Some  $^{13}\text{C}$  signals were not observed due to overlapping processes).

**HR-MS** (ESI-TOF):  $m/z$  calcd. for  $\text{C}_{63}\text{H}_{54}$   $[\text{M}+\text{K}]^+$ : 849.3862, found: 849.3867.

**IR** (ATR): 3012, 2950, 2921, 1601, 1476, 1447, 1265, 893, 801, 738, 713  $\text{cm}^{-1}$ .

### Compound 3.2.1-P10-Prec



Compound **3.2.1-M5** (170 mg, 0.27 mmol), compound **3.2.1-N5** (184 mg, 0.27 mmol)  $\text{Pd}(\text{dppf})\text{Cl}_2$  (40 mg, 0.05 mmol) and  $\text{Cs}_2\text{CO}_3$  (4.44 g, 13.61 mmol) were placed into a 250 mL two-neck round-bottom flask under an Ar atmosphere. The solids were dissolved in dry acetonitrile (160 mL) and the reaction mixture was refluxed for 24 h. Once cooled to r.t., the mixture was filtrated and the solvent was removed under reduced pressure. The crude was dissolved in  $\text{CH}_2\text{Cl}_2$  and washed once with water and twice with brine. The organic layer was dried over anhydrous  $\text{Na}_2\text{SO}_4$  and the solvent removed under reduced pressure. The crude was purified by column chromatography ( $\text{SiO}_2$ , Hexane/DCM 85:15) giving **3.2.1-P10-Prec** (37 mg, 15%) as a white solid.

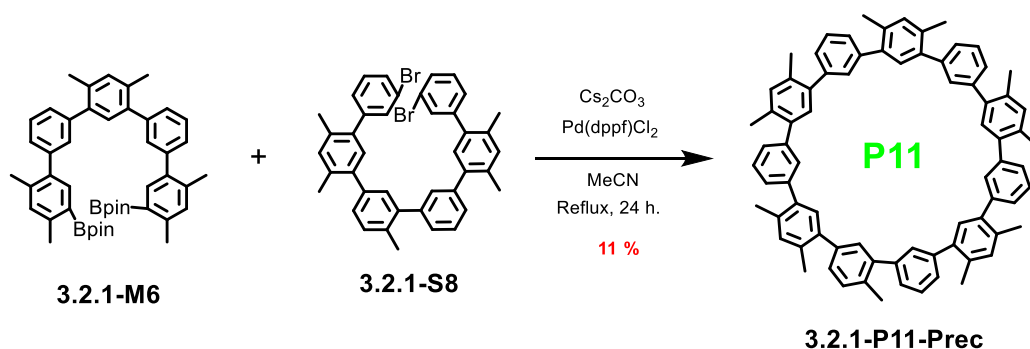
**<sup>1</sup>H NMR** (500 MHz, CDCl<sub>3</sub>) δ 7.49 – 7.38 (m, 5H), 7.37 – 7.27 (m, 15H), 7.22 (s, 5H), 7.17 – 7.10 (m, 5H), 2.35 (s, 30H).

**<sup>13</sup>C NMR** (126 MHz, CDCl<sub>3</sub>) δ 142.1 (C), 140.0 (C), 134.8 (C), 132.9 (CH), 131.7 (CH), 130.7 (CH), 128.21 (CH), 128.16 (CH), 20.5 (CH<sub>3</sub>).

**HR-MS** (ESI-TOF): *m/z* calcd. for C<sub>70</sub>H<sub>60</sub> [M+Na]<sup>+</sup>: 923.4593, found: 923.4610.

**IR** (ATR): 3011, 2950, 2920, 1600, 1474, 1448, 1265, 893, 813, 737, 711 cm<sup>-1</sup>.

### Compound 3.2.1-P11-Prec



Compound **3.2.1-M6** (167 mg, 0.23 mmol), compound **3.2.1-S8** (160 mg, 0.23 mmol) Pd(dppf)Cl<sub>2</sub> (34 mg, 0.05 mmol) and Cs<sub>2</sub>CO<sub>3</sub> (3.62 g, 11.64 mmol) were placed into a 250 mL two-neck round-bottom flask under an Ar atmosphere. The solids were dissolved in dry acetonitrile (140 mL) and the reaction mixture was refluxed for 24 h. Once cooled to r.t., the mixture was filtered and the solvent was removed under reduced pressure. The crude was dissolved in CH<sub>2</sub>Cl<sub>2</sub> and washed once with water and twice with brine. The organic layer was dried over anhydrous Na<sub>2</sub>SO<sub>4</sub> and the solvent removed under reduced pressure. The crude was purified by column chromatography (SiO<sub>2</sub>, Hexane/DCM 85:15) giving **3.2.1-P11-Prec** (26 mg, 11%) as a white solid.

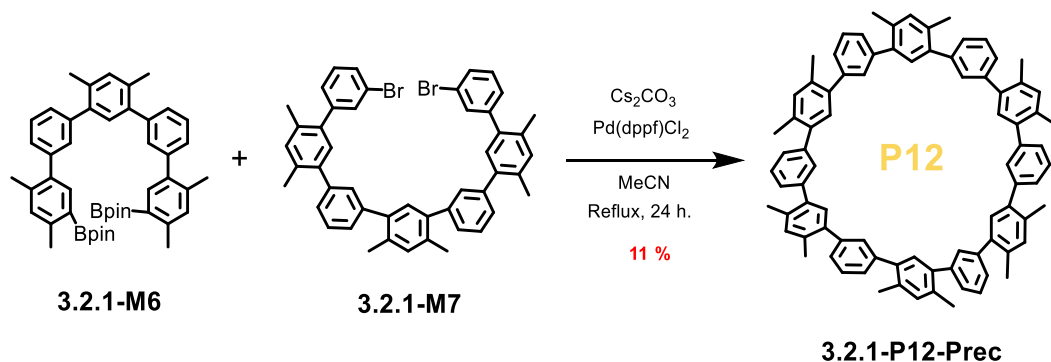
**<sup>1</sup>H NMR** (500 MHz, CD<sub>2</sub>Cl<sub>2</sub>) δ: 7.53 – 7.20 (m, 23H), 7.21 – 7.14 (m, 6H), 7.10 (dd, *J* = 2.6, 1.4 Hz, 4H), 2.37 – 2.21 (m, 33H).

**<sup>13</sup>C NMR** (126 MHz, CD<sub>2</sub>Cl<sub>2</sub>) δ: 142.23 (C), 142.02 (C), 142.01 (C), 141.97 (C), 141.96 (C), 141.93 (C), 139.91 (C), 139.90 (C), 139.88 (C), 139.85 (C), 139.65 (C), 139.61 (C), 134.80 (C), 134.78 (C), 134.75 (C), 134.72 (C), 134.59 (C), 134.31 (C), 132.95 (CH), 132.94 (CH), 132.92 (CH), 131.77 (CH), 131.76 (CH), 131.74 (CH), 131.20 (CH), 130.73 (CH), 130.46 (CH), 129.82 (CH), 128.65 (CH), 128.58 (CH), 128.38 (CH), 128.31 (CH), 128.29 (CH), 128.26 (CH), 128.22 (CH), 128.20 (CH), 128.19 (CH), 128.14 (CH), 20.57 (CH<sub>3</sub>), 20.55 (CH<sub>3</sub>), 20.43 (CH<sub>3</sub>), 20.43 (CH<sub>3</sub>), 20.43 (CH<sub>3</sub>), 20.42 (CH<sub>3</sub>), 20.40 (CH<sub>3</sub>). (Some <sup>13</sup>C signals were not observed due to overlapping processes).

**HR-MS** (ESI-TOF): *m/z* calcd. for C<sub>77</sub>H<sub>66</sub> [M + Na]<sup>+</sup>: 1013.5062, found: 1013.5082.

**IR** (ATR): 3021, 2921, 2159, 1955, 1605, 1473, 893, 712  $\text{cm}^{-1}$ .

**Compound 3.2.1-P12-Prec**



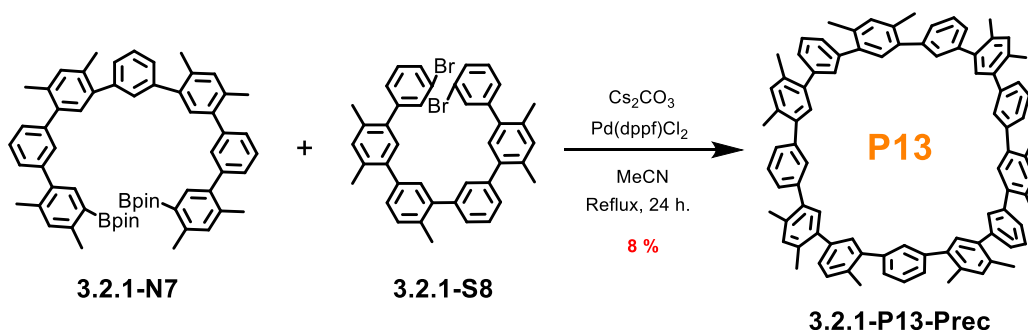
Compound **3.2.1-M6** (54 mg, 0.075 mmol), compound **3.2.1-M7** (58 mg, 0.075 mmol)  $\text{Pd}(\text{dppf})\text{Cl}_2$  (11 mg, 0.015 mmol) and  $\text{Cs}_2\text{CO}_3$  (1.22 g, 3.76 mmol) were placed into a 250 mL two-neck round-bottom flask under an Ar atmosphere. The solids were dissolved in dry acetonitrile (46 mL) and the reaction mixture was refluxed for 24 h. Once cooled to r.t., the mixture was filtrated and the solvent was removed under reduced pressure. The crude was dissolved in  $\text{CH}_2\text{Cl}_2$  and washed once with water and twice with brine. The organic layer was dried over anhydrous  $\text{Na}_2\text{SO}_4$  and the solvent removed under reduced pressure. The crude was purified by column chromatography ( $\text{SiO}_2$ , Hexane/DCM 85:15) giving **3.2.1-P12-Prec** (8 mg, 11%) as a white solid.

**$^1\text{H}$  NMR** (400 MHz,  $\text{CD}_2\text{Cl}_2$ )  $\delta$  7.43 – 7.38 (m, 6H), 7.32 – 7.27 (m, 18H), 7.17 (s, 6H), 7.13 (s, 6H), 2.30 (s, 36H).

**$^{13}\text{C}$  NMR** (101 MHz,  $\text{CD}_2\text{Cl}_2$ )  $\delta$  142.0 (C), 139.9 (C), 134.8 (C), 133.0 (CH), 131.8 (CH), 130.8 (CH), 128.22 (CH), 128.18 (CH), 20.4 ( $\text{CH}_3$ ).

**HR-MS** (ESI-TOF):  $m/z$  calcd. for  $\text{C}_{84}\text{H}_{72}\text{Na}[\text{M}+\text{Na}]^+$ : 1103.5532, found: 1103.5520.

**IR** (ATR): 2922, 1600, 1472, 892, 798, 712  $\text{cm}^{-1}$ .

**Compound 3.2.1-P13-Prec**

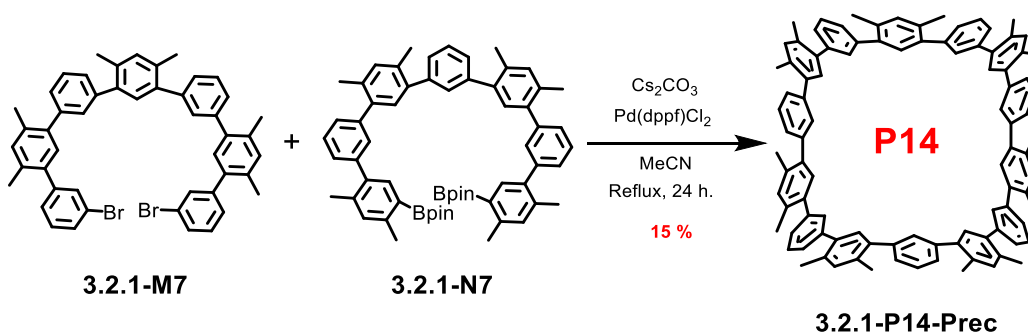
Compound **3.2.1-N7** (111 mg, 0.12 mmol), compound **3.2.1-S8** (85 mg, 0.12 mmol) Pd(dppf)Cl<sub>2</sub> (18 mg, 0.02 mmol) and Cs<sub>2</sub>CO<sub>3</sub> (2.02 g, 6.20 mmol) were placed into a 250 mL two-neck round-bottom flask under an Ar atmosphere. The solids were dissolved in dry acetonitrile (73 mL) and the reaction mixture was refluxed for 24 h. Once cooled to r.t., the mixture was filtrated and the solvent was removed under reduced pressure. The crude was dissolved in CH<sub>2</sub>Cl<sub>2</sub> and washed once with water and twice with brine. The organic layer was dried over anhydrous Na<sub>2</sub>SO<sub>4</sub> and the solvent removed under reduced pressure. The crude was purified by column chromatography (SiO<sub>2</sub>, Hexane/DCM 85:15) giving **3.2.1-P3-Prec** (11 mg, 8%) as a white solid.

**<sup>1</sup>H NMR** (400 MHz, CD<sub>2</sub>Cl<sub>2</sub>): δ 7.46 – 7.21 (m, 27H), 7.19 – 7.12 (m, 12H), 2.36 – 2.25 (m, 39H).

**<sup>13</sup>C NMR** (101 MHz, CD<sub>2</sub>Cl<sub>2</sub>): δ 142.04 (C), 142.03 (C), 142.00 (C), 139.93 (C), 139.91 (C), 134.76 (C), 133.00 (CH), 132.97 (CH), 131.82 (CH), 130.77 (CH), 128.25 (CH), 128.18 (CH), 20.5 (CH<sub>3</sub>), 20.4 (CH<sub>3</sub>). (Some <sup>13</sup>C signals were not observed due to overlapping processes).

**HR-MS** (ESI-TOF): m/z calcd. for C<sub>91</sub>H<sub>78</sub>Na [M+Na]<sup>+</sup>: 1193.6001, found: 1193.6028.

**IR** (ATR): 2921, 1599, 1472, 1264, 1033, 892, 712 cm<sup>-1</sup>.

**Compound 3.2.1-P14-Prec**

Compound **3.2.1-M7** (96 mg, 0.12 mmol), compound **3.2.1-N7** (111 mg, 0.12 mmol) Pd(dppf)Cl<sub>2</sub> (18 mg, 0.03 mmol) and Cs<sub>2</sub>CO<sub>3</sub> (2.02 g, 6.20 mmol) were placed into a 250 mL two-neck round-bottom flask under an Ar atmosphere. The solids were dissolved in dry acetonitrile (73 mL) and the reaction mixture was refluxed for 24 h. Once cooled to r.t., the mixture was filtrated and the solvent was removed under reduced pressure. The crude was dissolved in CH<sub>2</sub>Cl<sub>2</sub> and washed once with water and twice with brine. The organic layer was dried over anhydrous Na<sub>2</sub>SO<sub>4</sub> and the solvent removed under reduced pressure. The crude was purified by column chromatography (SiO<sub>2</sub>, Hexane/DCM 80:20) giving **3.2.1-P14-Prec** (24 mg, 15%) as a white solid.

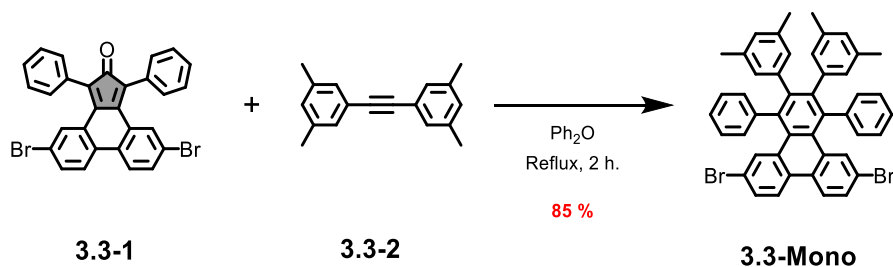
<sup>1</sup>H NMR (500 MHz, CD<sub>2</sub>Cl<sub>2</sub>) δ 7.38 (t, *J* = 7.4 Hz, 7H), 7.32 – 7.24 (m, 21H), 7.16 (s, 7H), 7.14 (s, 7H), 2.29 (s, 42H).

<sup>13</sup>C NMR (126 MHz, CD<sub>2</sub>Cl<sub>2</sub>) δ 142.0 (C), 139.9 (C), 134.8 (C), 132.9 (CH), 131.8 (CH), 130.7 (CH), 128.3 (CH), 128.2 (CH), 20.4 (CH<sub>3</sub>).

HR-MS (ESI-TOF): *m/z* calcd. for C<sub>98</sub>H<sub>84</sub>Na [M+Na]<sup>+</sup>: 1284.6505, found: 1284.6533.

IR (ATR): 2921, 1599, 1471, 893, 712 cm<sup>-1</sup>.

### Compound 3.3-Mono



Compounds **3.3-2239** and **3.3-1244** were prepared according to already described procedures. In a Schlenk tube, **3.3-1** (71 mg, 0.304 mmol) and **3.3-2** (165 mg, 0.304 mmol) were dissolved in diphenyl ether (1.2 mL) and bubbled with Ar. The reaction mixture was refluxed over 2 h in a sand bath. The crude was allowed to cool to r.t., diluted with hexane (2 mL) and introduced in the column washing with hexane to be purified by column flash chromatography on silica gel (SiO<sub>2</sub>, Hexane/CH<sub>2</sub>Cl<sub>2</sub> 9:1) affording **3.3-Mono** (191 mg, 85%) as a white solid.

<sup>1</sup>H NMR (500 MHz, CD<sub>2</sub>Cl<sub>2</sub>): δ 8.24 (d, *J* = 8.7 Hz, 2H), 7.69 (d, *J* = 2.0 Hz, 2H), 7.49 (dd, *J* = 8.6, 2.0 Hz, 2H), 7.24 – 7.13 (m, 6H), 7.09 (m, 4H), 6.56 (s, 2H), 6.33 (s, 4H), 1.98 (s, 12H).

<sup>13</sup>C NMR (126 MHz, CD<sub>2</sub>Cl<sub>2</sub>): δ 142.8 (C), 142.5 (C), 140.1 (C), 137.9 (C), 136.3 (C), 133.2 (CH), 133.0 (C), 132.4 (CH), 130.5 (C), 130.1 (C), 129.9 (CH), 128.6 (CH), 127.2 (CH), 127.2 (CH), 125.1 (CH), 120.5 (C), 21.2 (CH<sub>3</sub>). (Some <sup>13</sup>C signals were not observed due to overlapping processes).

<sup>244</sup> Z. Guo, J. Zhang, J. Zhang, M. Xie, *Org. Lett.*, **2022**, *24*, 7784–7789.



**HR-MS** (MALDI):  $m/z$  calcd for  $C_{46}H_{34}Br_2 [M]^+$ : 744.1022, found 744.1023.

**IR** (ATR): 3023, 2917, 1600, 1470, 1094, 1000, 854, 798.

#### 4.2.1 X-Ray Diffraction Structure

X-ray diffraction-quality single crystals of compound **3.3-Mono** were obtained by vapor diffusion of acetonitrile into a chloroform solution of **3.3-Mono**. The X-ray diffraction measurement was carried out on a Bruker D8 Venture diffractometer with a Photon III detector using Mo  $K\alpha$  radiation. SHELXT<sup>245</sup> was used to solve the structure, which was then refined applying the full-matrix least-squares against  $F^2$  procedure with SHELX 2018<sup>246</sup> using the WinGX32<sup>247</sup> software. During the refinement, hydrogen atoms were placed in idealized positions ( $U_{eq}(H) = 1.2U_{eq}(C)$  or  $U_{eq}(H) = 1.5U_{eq}(C)$ ) and were allowed to ride on their parent atoms.

Some disorder was found in one of the  $CHCl_3$  molecules. The C and one of the Cl atoms were found to be disordered in two positions. This disorder was modelled using the PART instruction. The SADI restraint was also applied.

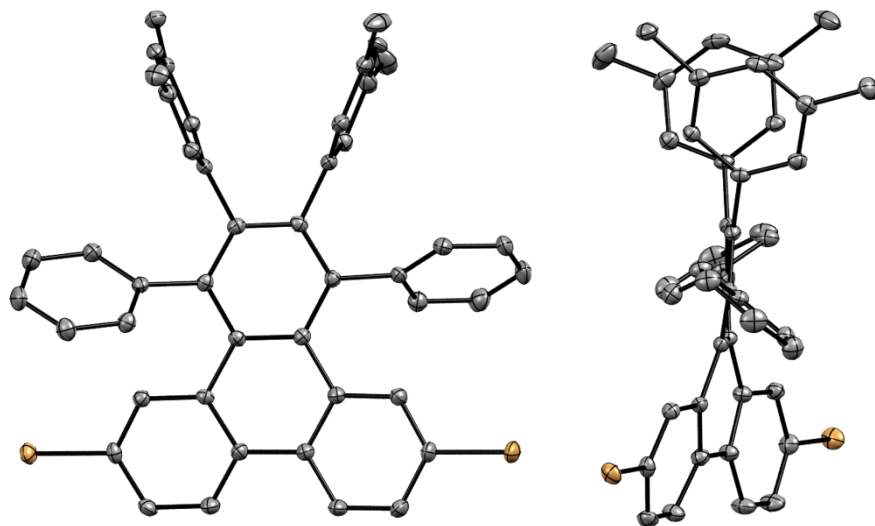
Summary of the X-ray diffraction measurement and refinement data:

Chemical formula,  $C_{46}H_{34}Br_2 \cdot CHCl_3$ ;  $M_r$ , 865.90; crystal size [ $mm^3$ ],  $0.358 \times 0.103 \times 0.051$ ; temperature, 293 K; wavelength [ $\text{\AA}$ ], 0.71073 (Mo  $K\alpha$ ), crystal system, monoclinic; space group,  $-P 21/c$ ;  $a$  [ $\text{\AA}$ ], 22.799(11);  $b$  [ $\text{\AA}$ ], 8.130(4);  $c$  [ $\text{\AA}$ ], 43.865(2);  $a$  [ $^\circ$ ], 90;  $\beta$  [ $^\circ$ ], 104.998;  $\gamma$  [ $^\circ$ ], 90;  $V$  [ $\text{\AA}^3$ ], 7853.8(7);  $Z$ , 8;  $\rho_{calcd}$  [ $Mg\ m^{-3}$ ], 1.465;  $\mu$  [ $mm^{-1}$ ], 2.302;  $F(000)$ , 3504.0;  $\theta$  range [ $^\circ$ ], 1.849 to 28.449;  $hkl$  ranges,  $-30/30$ ,  $-10/10$ ,  $-58/58$ ; reflections collected, 119263; independent reflections, 19730;  $R_{int}$ , 0.0346; completeness to  $\theta = 25.242^\circ$ , 100%; refinement method; full-matrix least-squares on  $F^2$ ; Final R indices [ $I > 2\sigma(I)$ ],  $R_1 = 0.0352$ ,  $wR_2 = 0.0717$ ; R indices (all data),  $R_1 = 0.0438$ ,  $wR_2 = 0.0754$ ; goodness-of-fit on  $F^2$ , 1.062.

<sup>245</sup> G. M. Sheldrick, *Acta Crystallogr. A Found Adv.*, **2015**, *71*, 3–8.

<sup>246</sup> G. M. Sheldrick, *Acta Cryst. A Found Crystallogr.*, **2008**, *64*, 112–122.

<sup>247</sup> L. J. Farrugia, *J. Appl. Cryst.*, **2012**, *45*, 849–854.



**Figure 94.** ORTEP-type<sup>248</sup> drawing of the structure of compound **3.3-Mono**, showing the thermal ellipsoids at 50% probability. H atoms have been omitted for clarity.

---

<sup>248</sup> O. V. Dolomanov, L. J. Bourhis, R. J. Gildea, J. A. K. Howard, H. Puschmann, *J. Appl Cryst.*, **2009**, *42*, 339–341.

## 4.2.1 Representative NMR of the Prepared Compounds

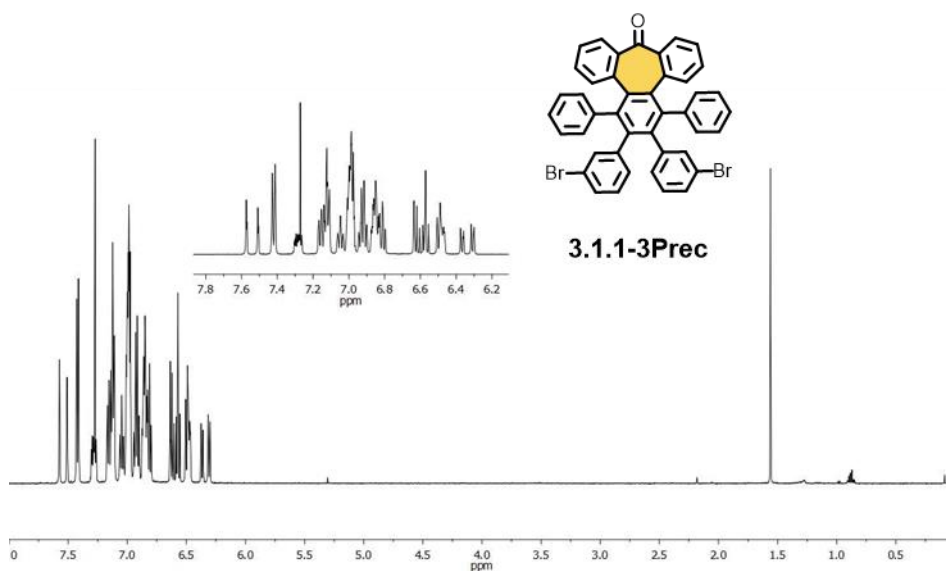


Figure 95.  $^1\text{H}$  NMR (500 MHz,  $\text{CDCl}_3$ ) spectrum of compound 3.1.1-3Prec.

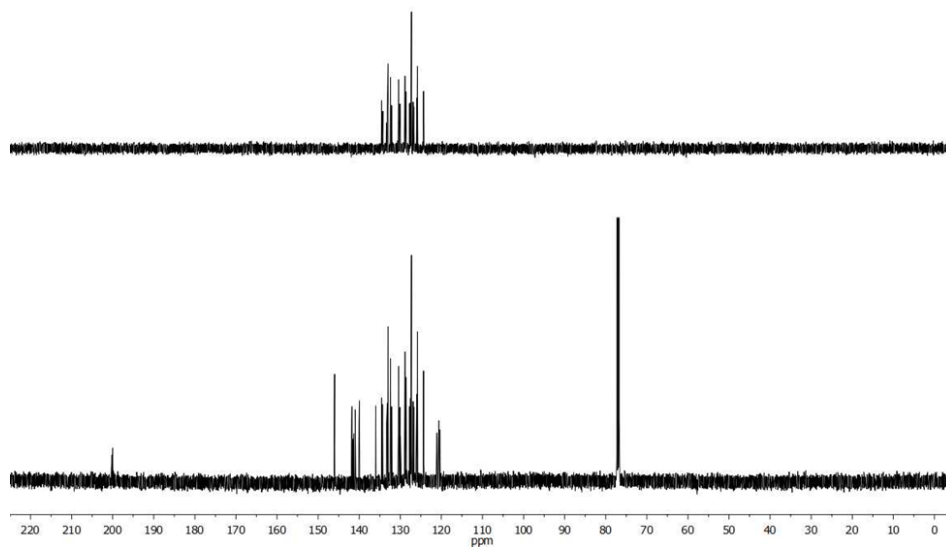


Figure 96. DEPT-135 NMR (126 MHz,  $\text{CDCl}_3$ ) (top) and  $^{13}\text{C}$  NMR (126 MHz,  $\text{CDCl}_3$ ) (bottom) spectra of compound 3.1.1-3Prec.



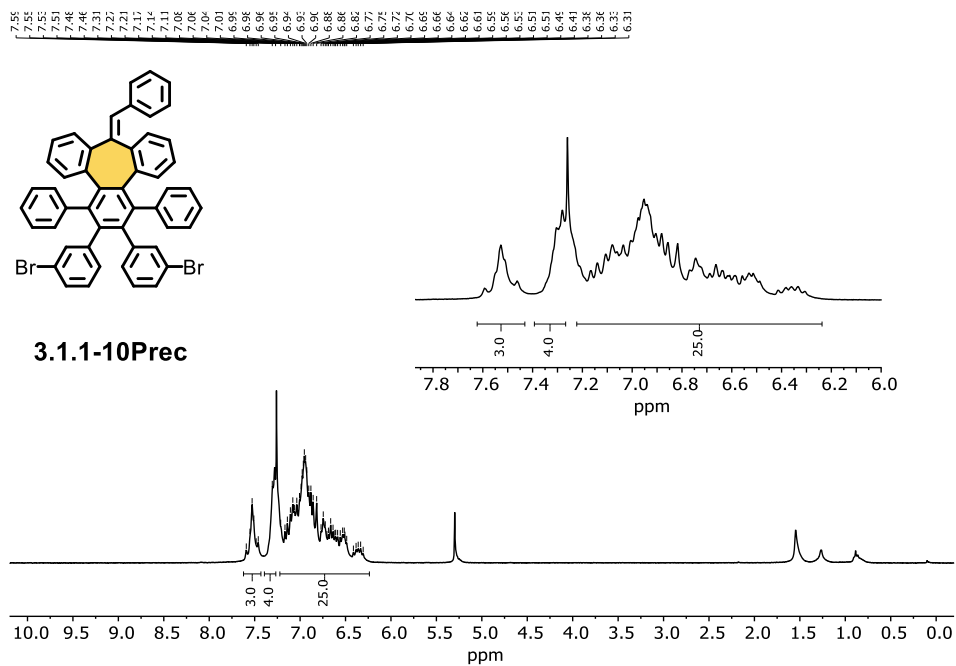


Figure 99.  $^1\text{H NMR}$  (300 MHz,  $\text{CDCl}_3$ ) spectrum of compound **3.1.1-10Prec**.



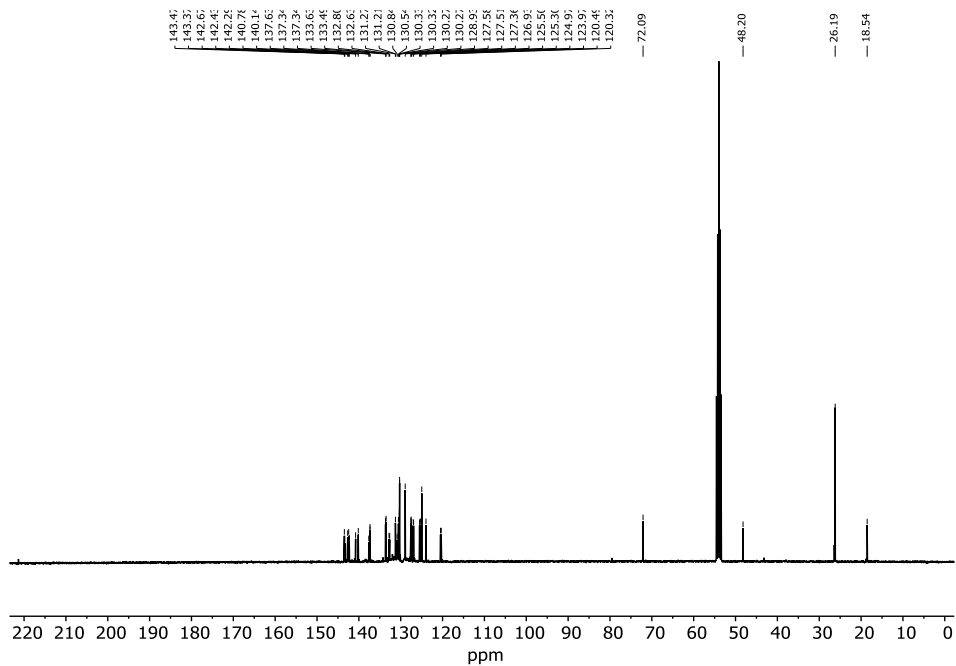
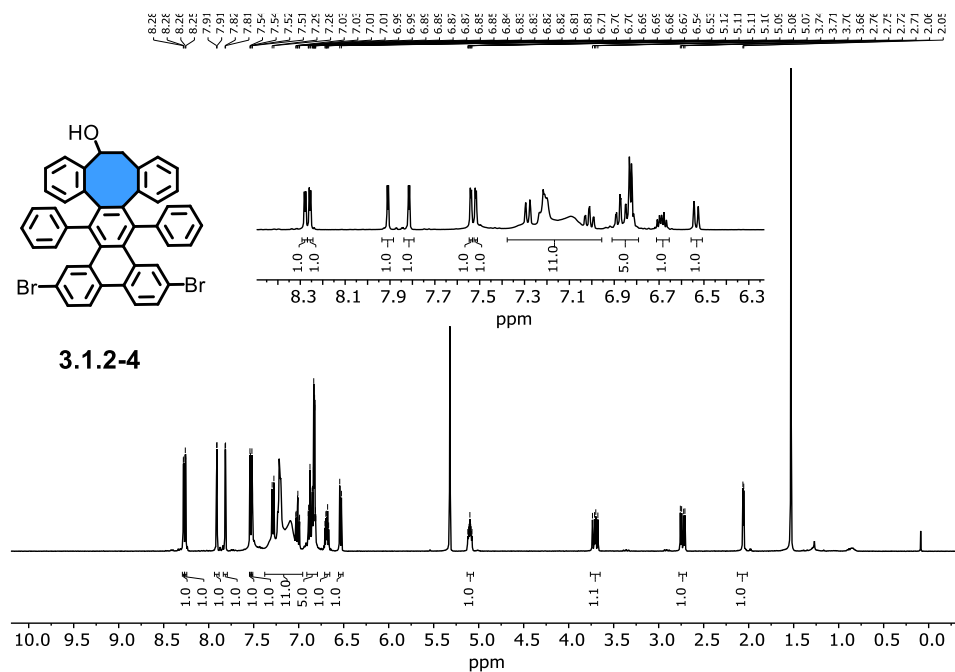
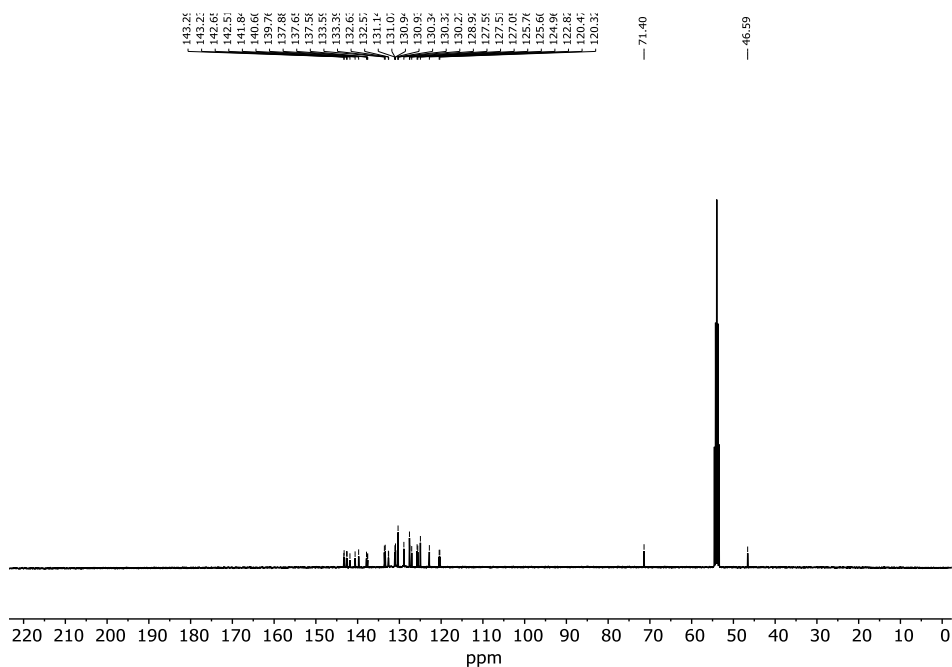
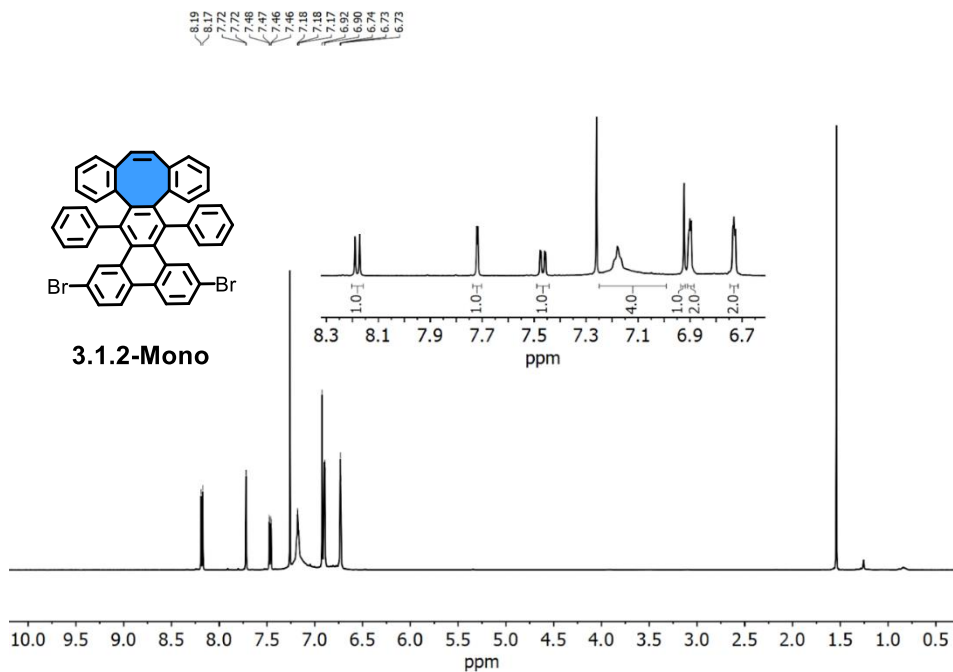
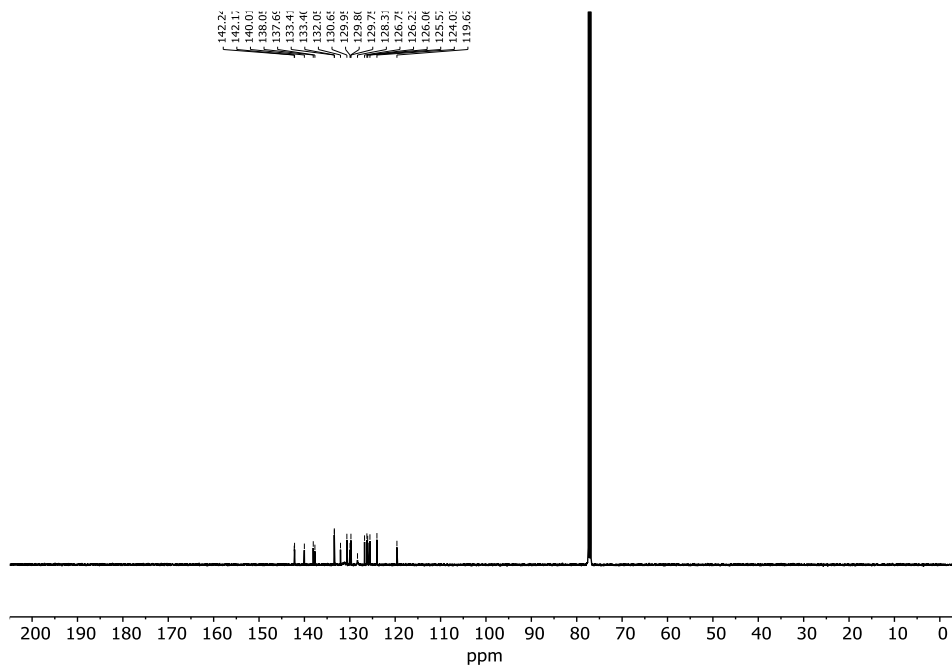


Figure 102.  $^{13}\text{C}$  NMR (101 MHz,  $\text{CD}_2\text{Cl}_2$ ) spectrum of the major isomer of compound 3.1.2-3.

Figure 103. <sup>1</sup>H NMR (400 MHz, CD<sub>2</sub>Cl<sub>2</sub>) spectrum of compound 3.1.2-4.Figure 104. <sup>13</sup>C NMR (126 MHz, CD<sub>2</sub>Cl<sub>2</sub>) spectrum of compound 3.1.2-4.



Figure 105.  $^1\text{H NMR}$  (500 MHz,  $\text{CDCl}_3$ ) spectrum of compound **3.1.2-Mono**.Figure 106.  $^{13}\text{C NMR}$  (126 MHz,  $\text{CDCl}_3$ ) spectrum of compound **3.1.2-Mono**.

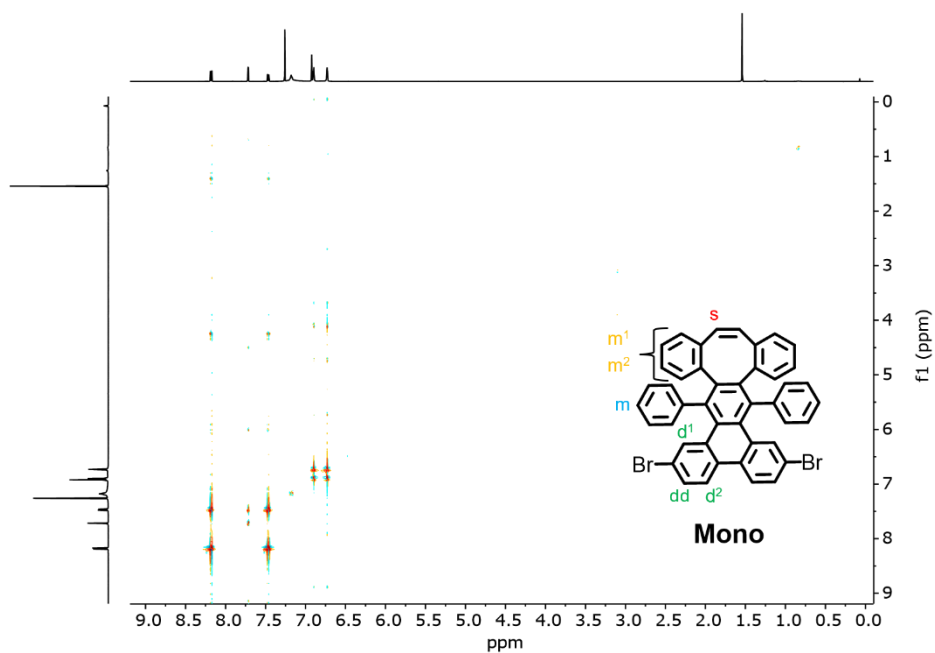


Figure 107. COSY NMR (500 and 500 MHz, CDCl<sub>3</sub>) spectrum of compound 3.1.2-Mono.

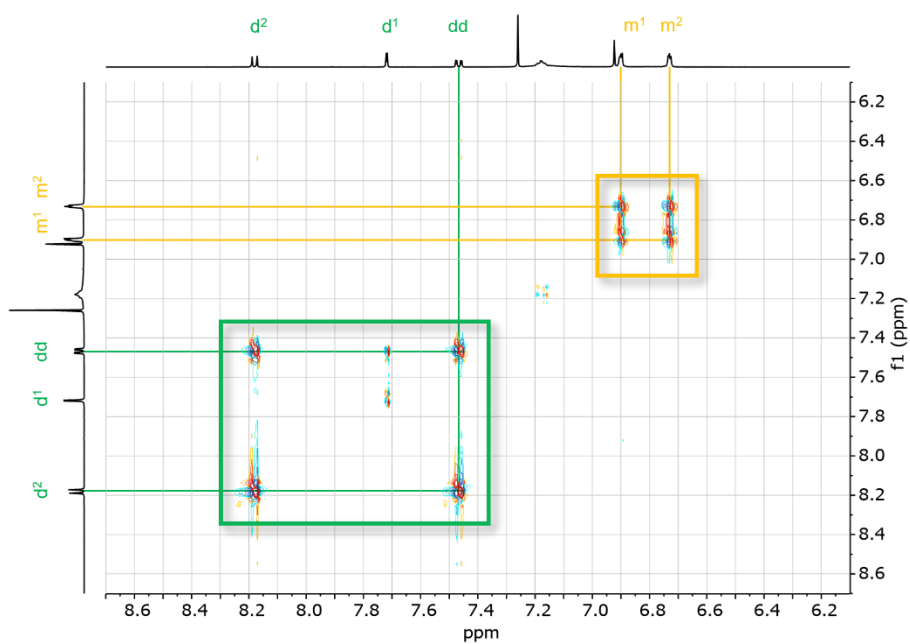


Figure 108. Partial COSY NMR (500 and 500 MHz, CDCl<sub>3</sub>) spectrum of compound 3.1.2-Mono.

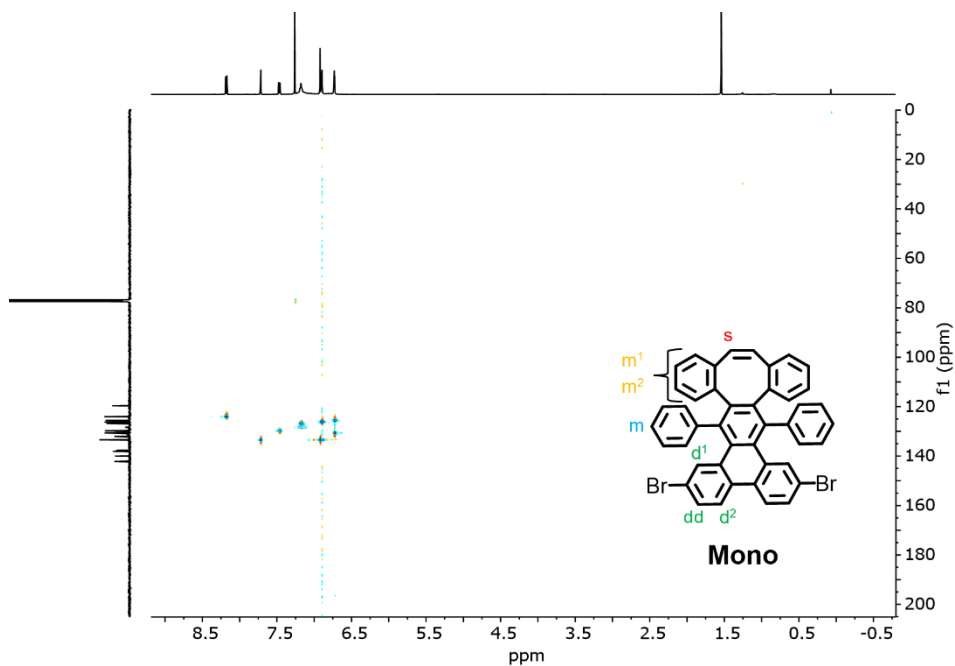


Figure 109. HSQC NMR (500 and 126 MHz,  $\text{CDCl}_3$ ) spectrum of compound 3.1.2-Mono.

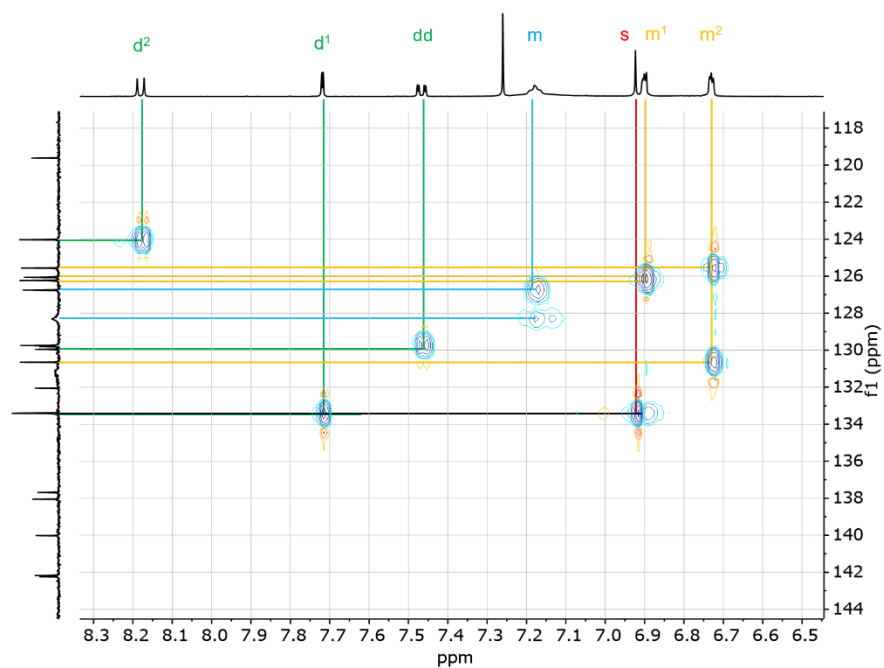


Figure 110. Partial HSQC NMR (500 and 126 MHz,  $\text{CDCl}_3$ ) spectrum of compound 3.1.2-Mono.

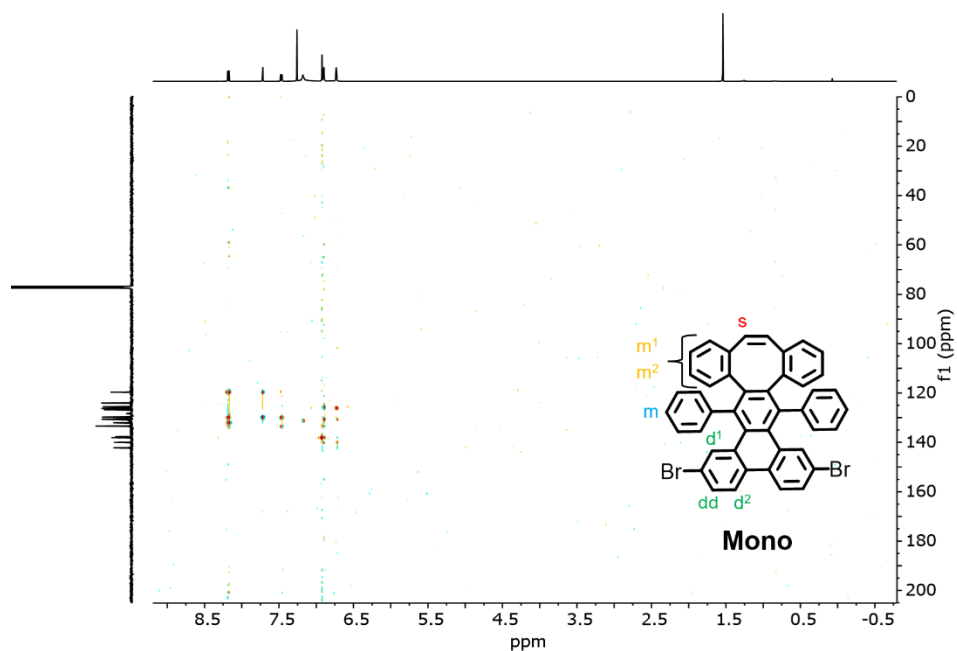


Figure 111. HMBC NMR (500 and 126 MHz, CDCl<sub>3</sub>) spectrum of compound 3.1.2-Mono.

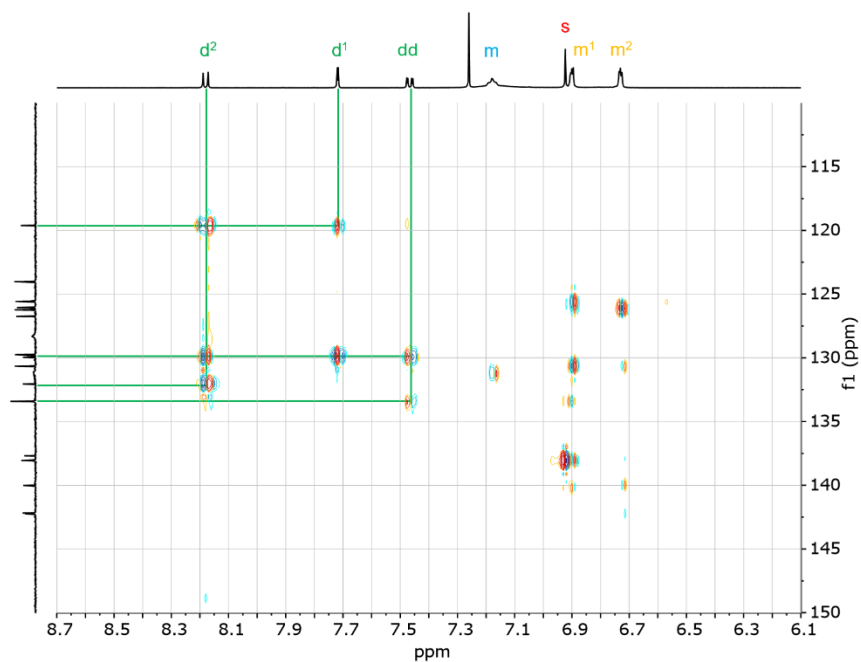


Figure 112. Partial HMBC NMR (500 and 126 MHz, CDCl<sub>3</sub>) spectrum of compound 3.1.2-Mono.



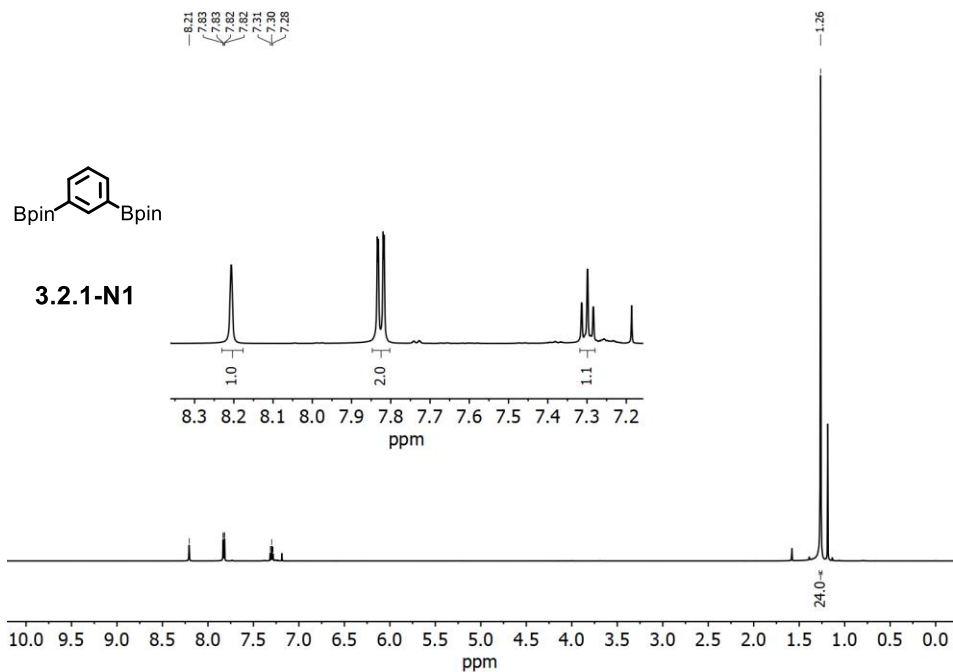


Figure 115.  $^1\text{H}$  NMR (500 MHz,  $\text{CDCl}_3$ ) spectrum of compound 3.2.1-N1.

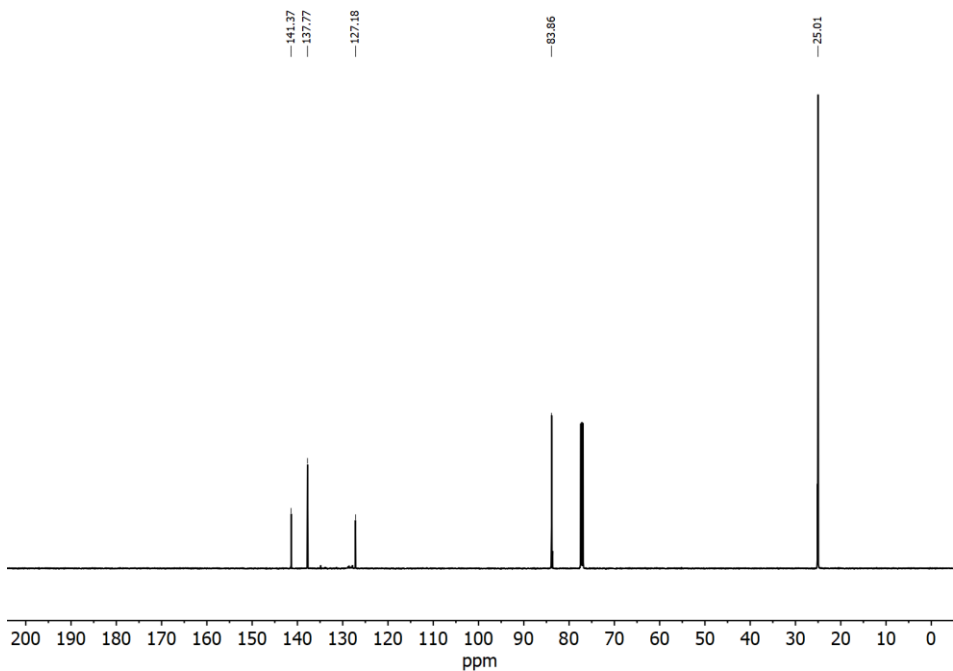


Figure 116.  $^{13}\text{C}$  NMR (126 MHz,  $\text{CDCl}_3$ ) spectrum of compound 3.2.1-N1.

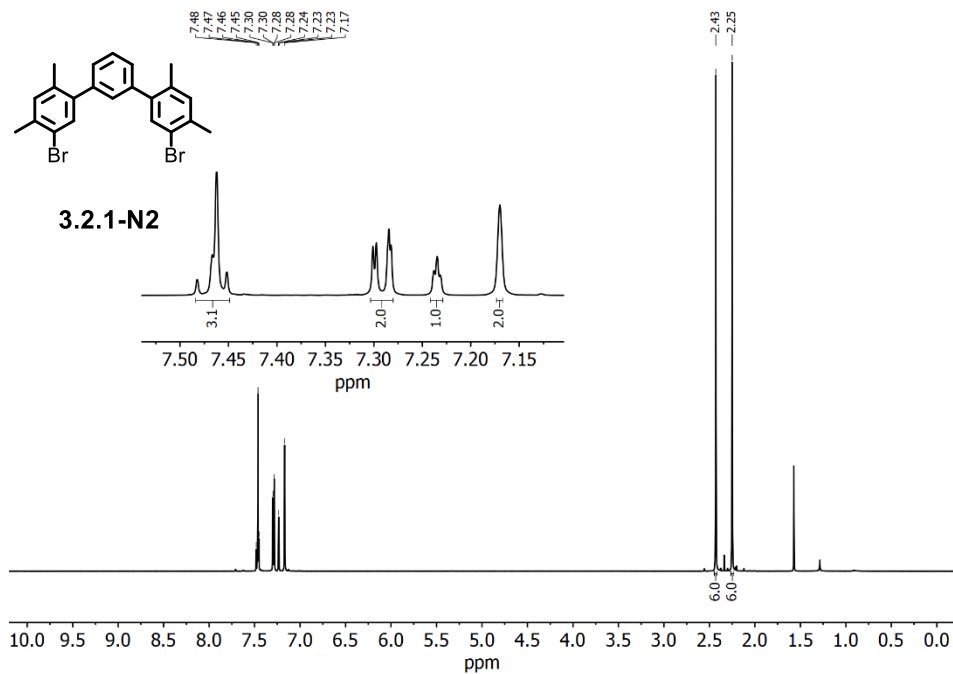


Figure 117. <sup>1</sup>H NMR (500 MHz, CDCl<sub>3</sub>) spectrum of compound 3.2.1-N2.

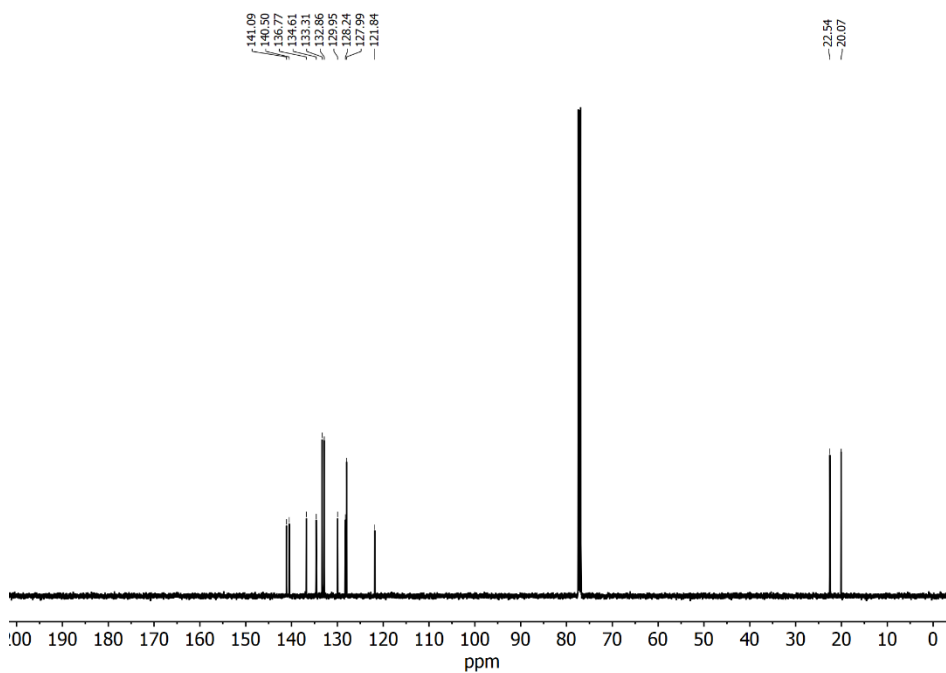


Figure 118. <sup>13</sup>C NMR (126 MHz, CDCl<sub>3</sub>) spectrum of compound 3.2.1-N2.

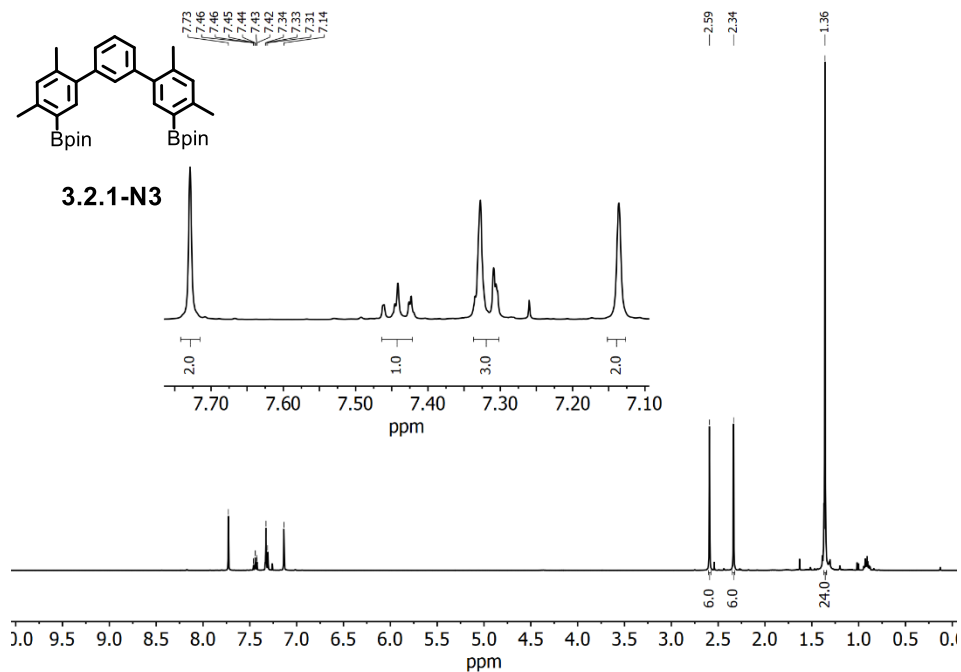


Figure 119. <sup>1</sup>H NMR (500 MHz, CDCl<sub>3</sub>) spectrum of compound 3.2.1-N3.

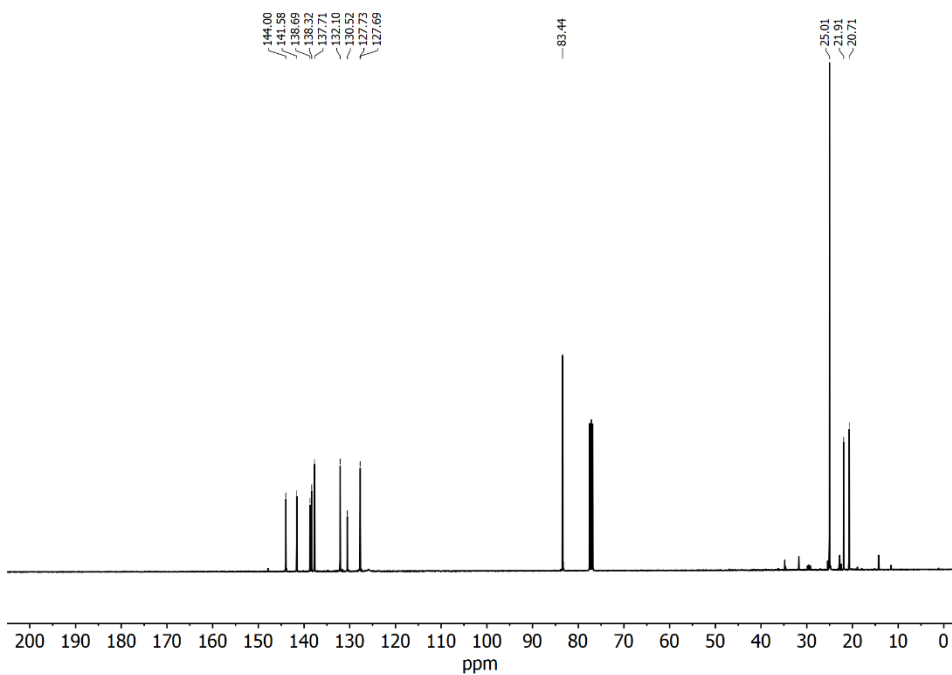
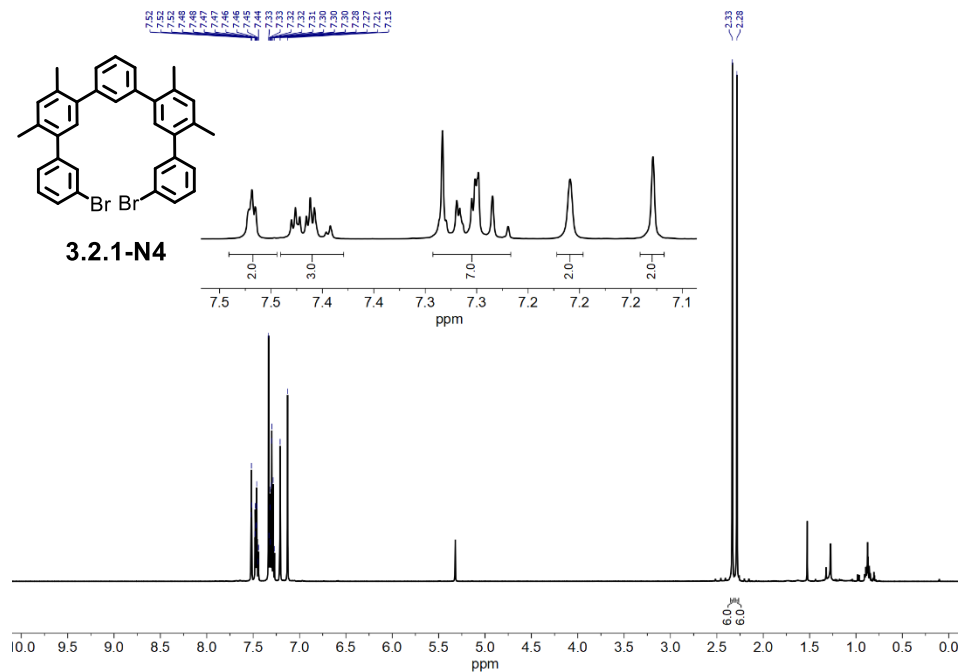
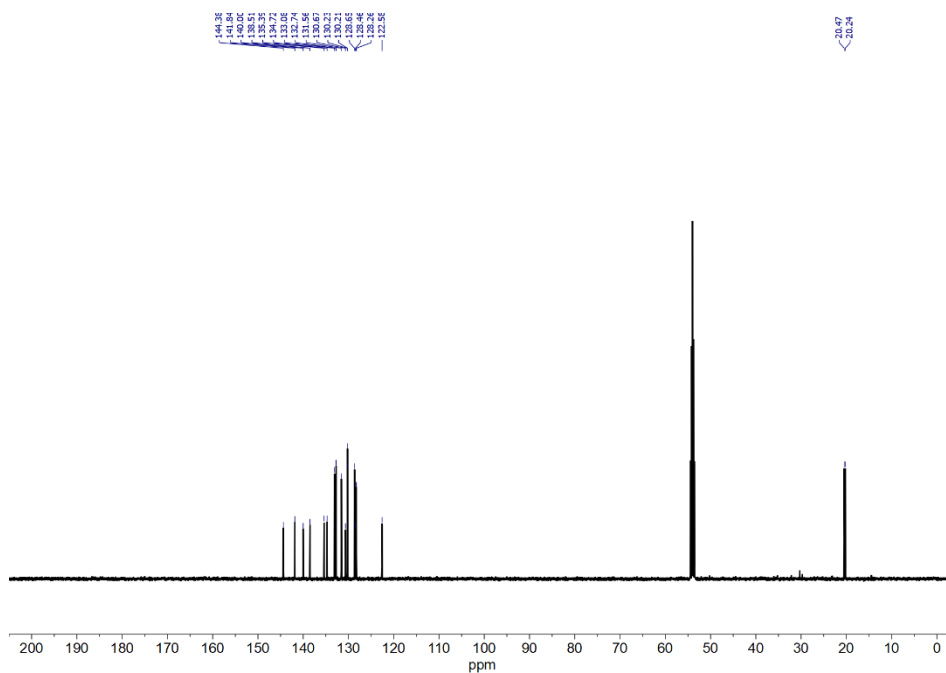
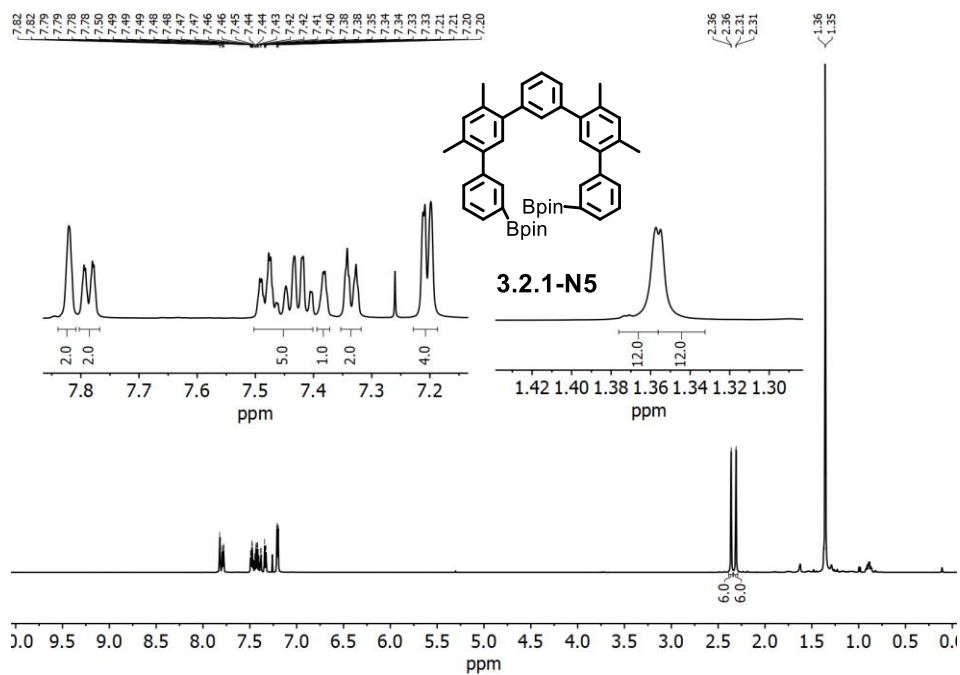
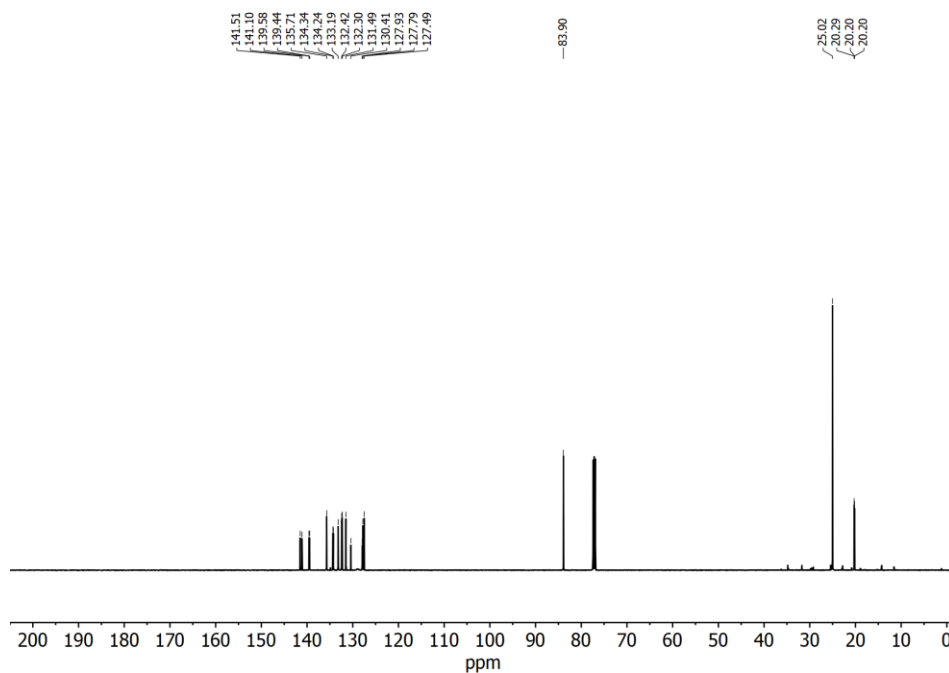
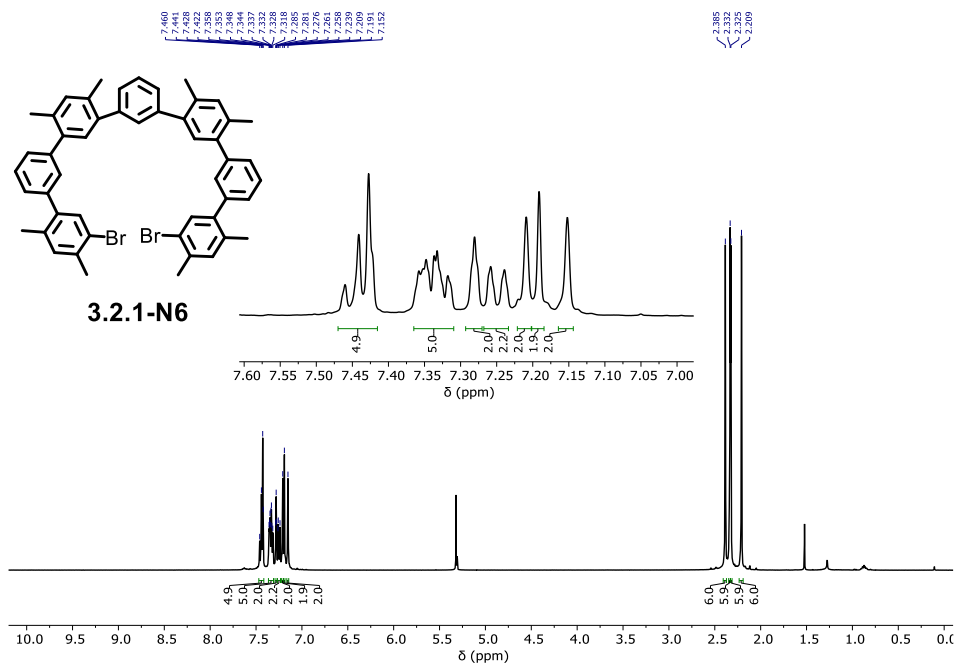
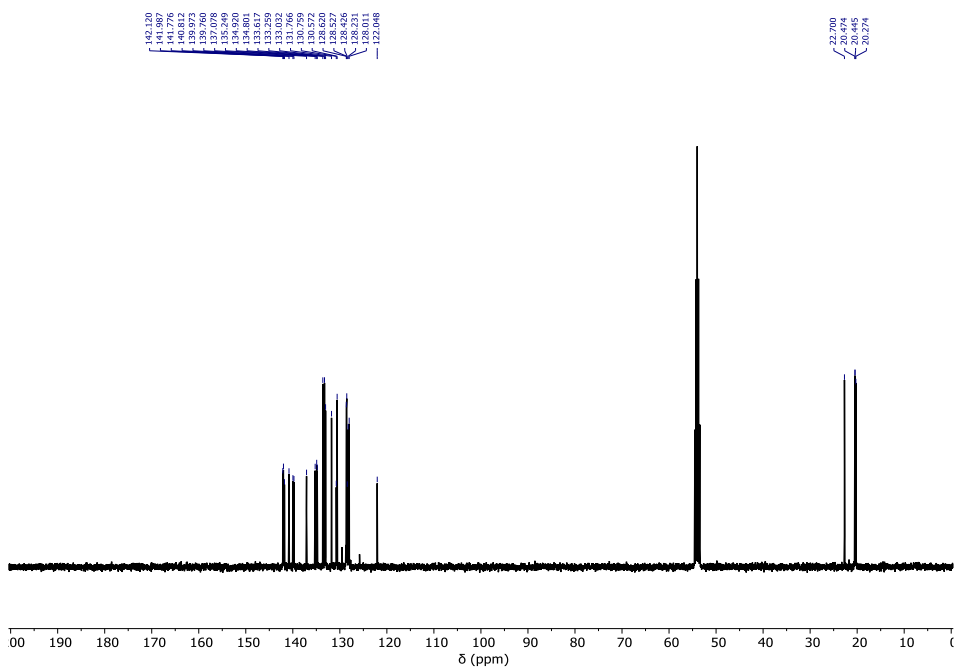


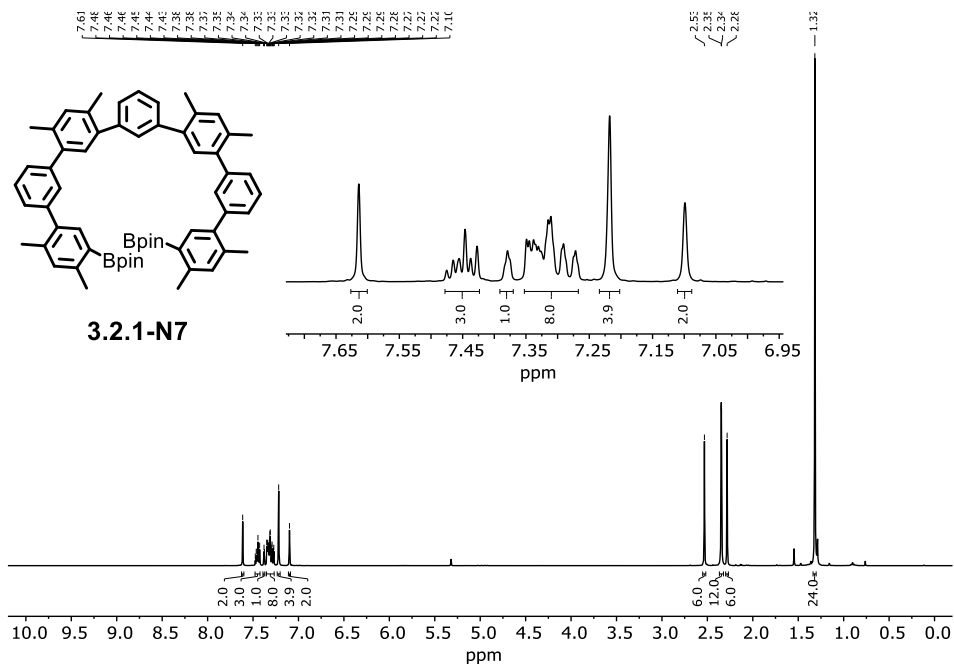
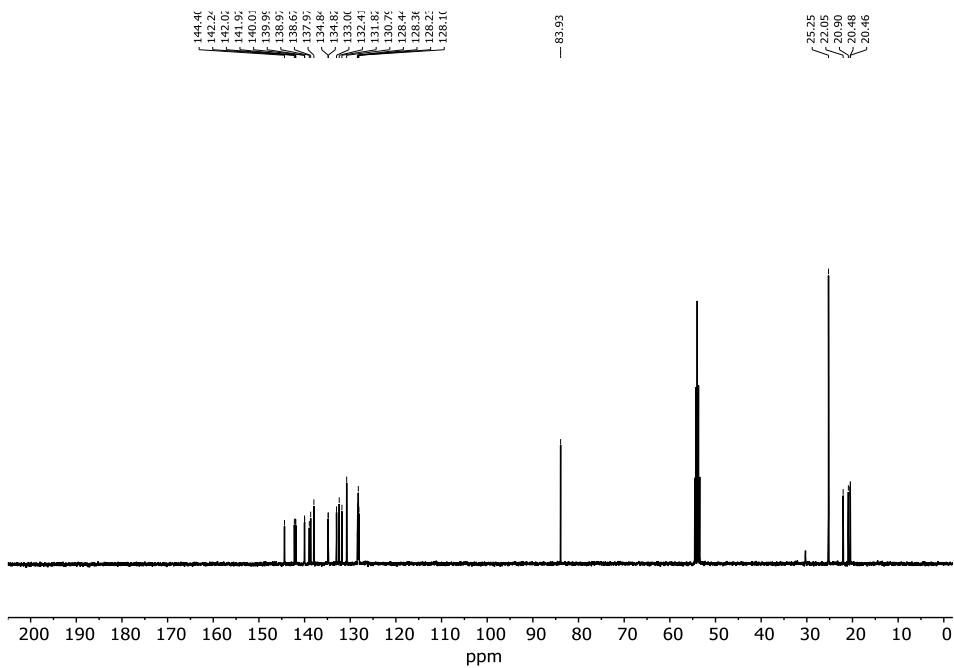
Figure 120. <sup>13</sup>C NMR (500 MHz, CDCl<sub>3</sub>) spectrum of compound 3.2.1-N3.



Figure 121. <sup>1</sup>H NMR (500 MHz, CD<sub>2</sub>Cl<sub>2</sub>) spectrum of compound 3.2.1-N4.Figure 122. <sup>13</sup>C NMR (126 MHz, CD<sub>2</sub>Cl<sub>2</sub>) spectrum of compound 3.2.1-N4.

Figure 123. <sup>1</sup>H NMR (500 MHz, CDCl<sub>3</sub>) spectrum of compound 3.2.1-N5.Figure 124. <sup>13</sup>C NMR (126 MHz, CDCl<sub>3</sub>) spectrum of compound 3.2.1-N5.

Figure 125.  $^1\text{H NMR}$  (500 MHz,  $\text{CD}_2\text{Cl}_2$ ) spectrum of compound 3.2.1-N6.Figure 126.  $^{13}\text{C NMR}$  (126 MHz,  $\text{CD}_2\text{Cl}_2$ ) spectrum of compound 3.2.1-N6.

Figure 127. <sup>1</sup>H NMR (500 MHz, CD<sub>2</sub>Cl<sub>2</sub>) spectrum of compound **3.2.1-N7**.Figure 128. <sup>13</sup>C NMR (126 MHz, CD<sub>2</sub>Cl<sub>2</sub>) spectrum of compound **3.2.1-N7**.

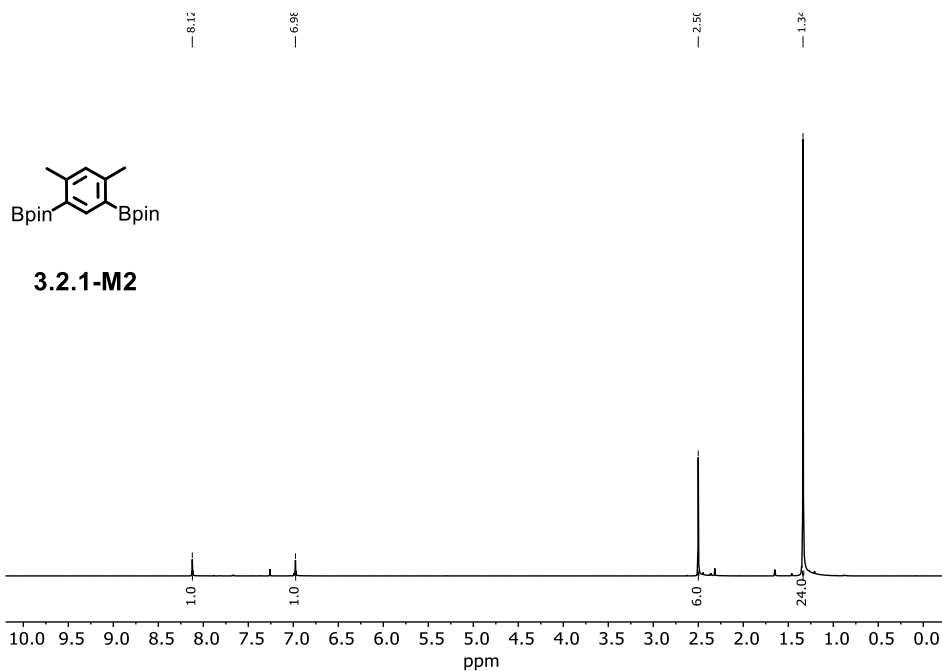


Figure 129. <sup>1</sup>H NMR (500 MHz, CDCl<sub>3</sub>) spectrum of compound 3.2.1-M2.

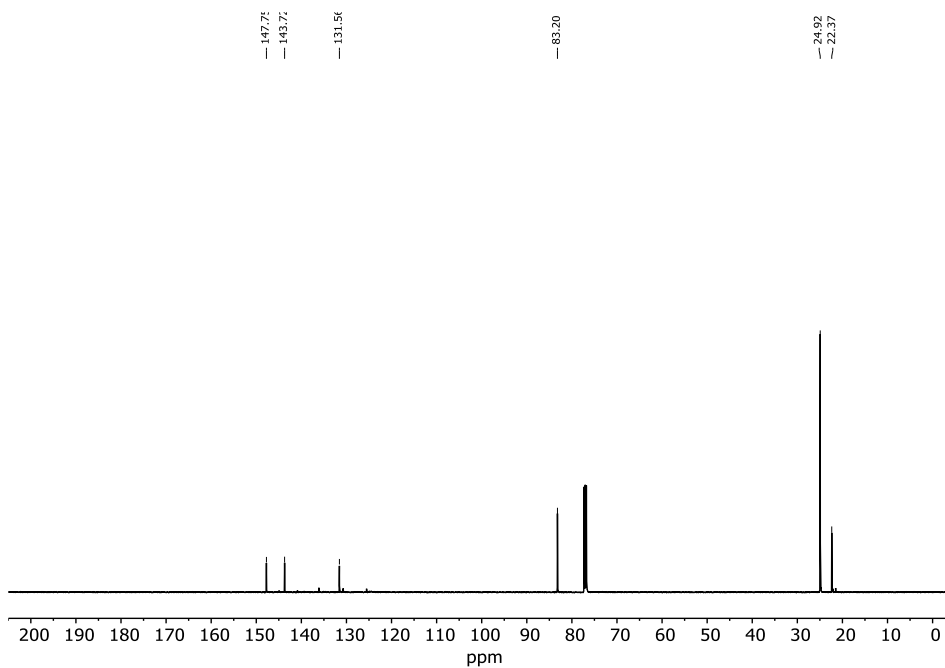


Figure 130. <sup>13</sup>C NMR (126 MHz, CDCl<sub>3</sub>) spectrum of compound 3.2.1-M2.

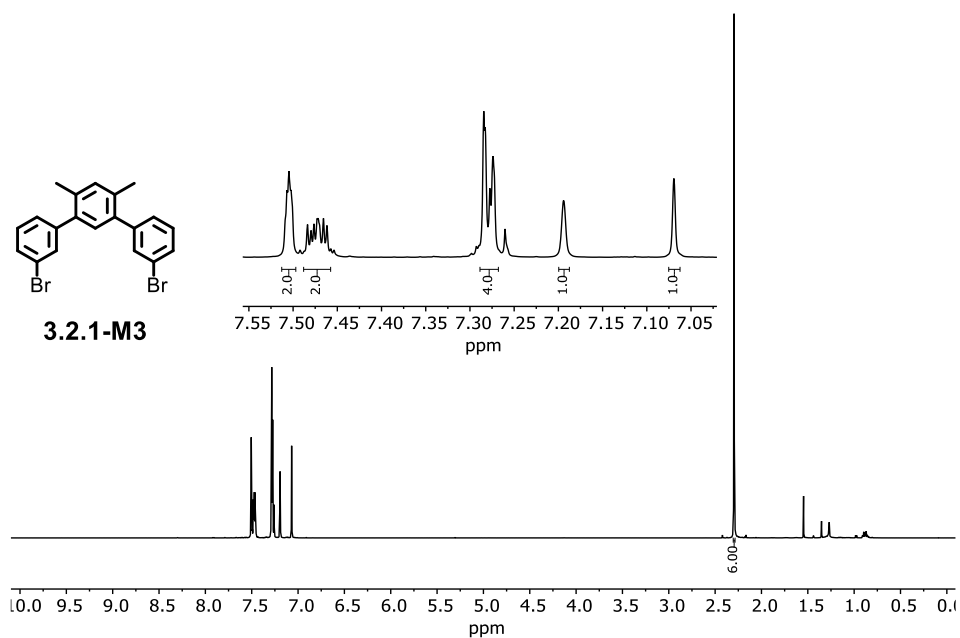


Figure 131.  $^1\text{H NMR}$  (500 MHz,  $\text{CDCl}_3$ ) spectrum of compound **3.2.1-M3**.

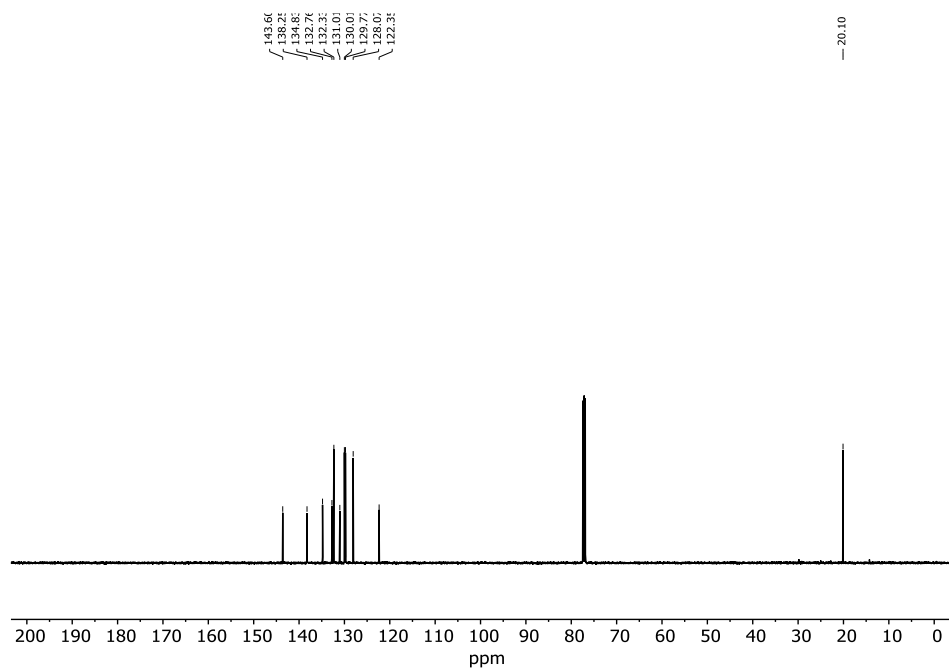
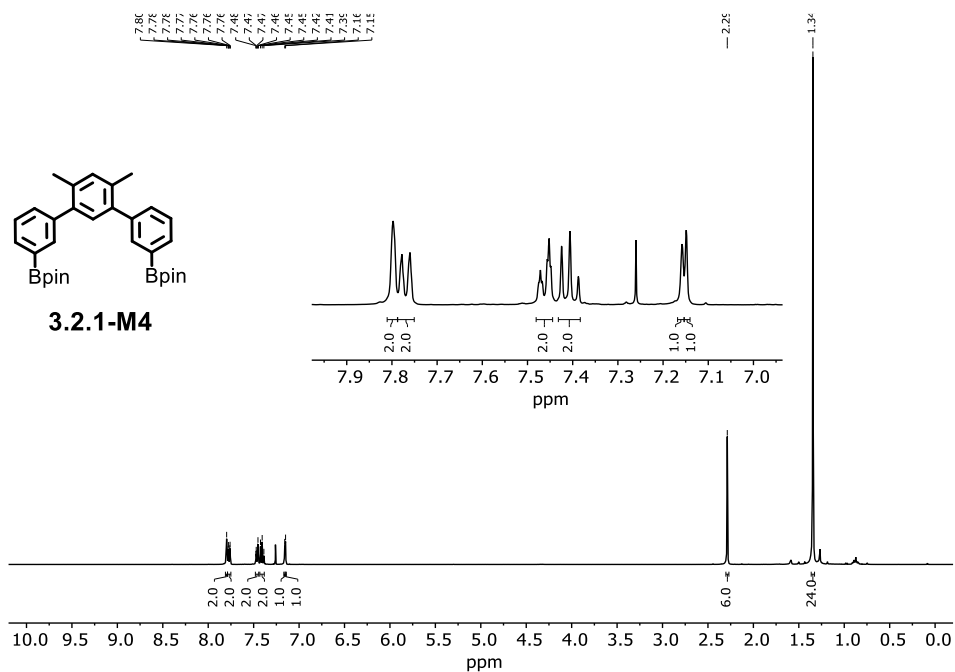
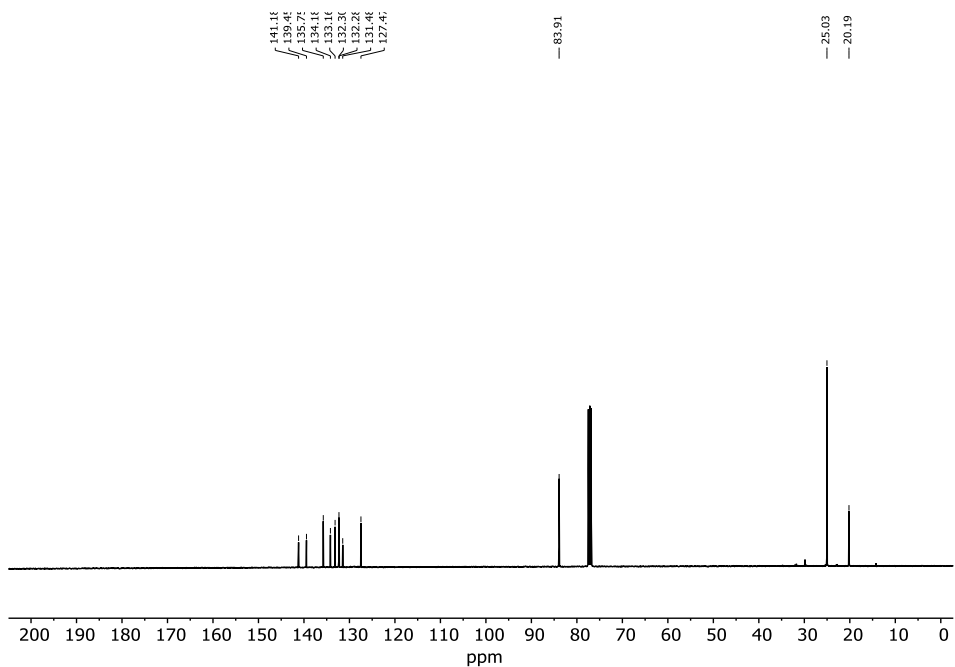


Figure 132.  $^{13}\text{C NMR}$  (126 MHz,  $\text{CDCl}_3$ ) spectrum of compound **3.2.1-M3**.

Figure 133.  $^1\text{H}$  NMR (500 MHz,  $\text{CDCl}_3$ ) spectrum of compound 3.2.1-M4.Figure 134.  $^{13}\text{C}$  NMR (126 MHz,  $\text{CDCl}_3$ ) spectrum of compound 3.2.1-M4.





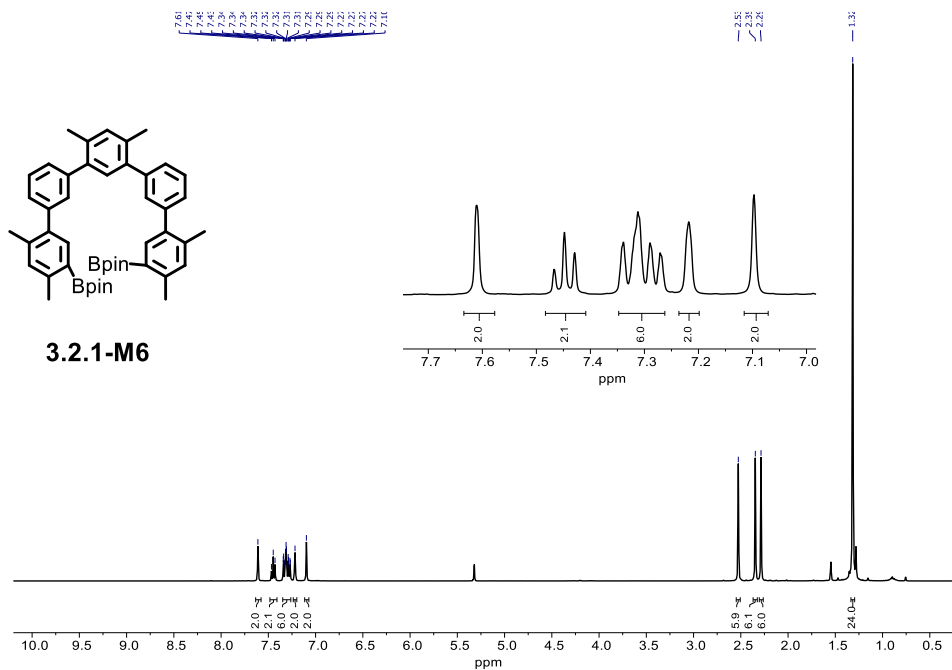


Figure 137.  $^1\text{H}$  NMR (500 MHz,  $\text{CD}_2\text{Cl}_2$ ) spectrum of compound **3.2.1-M6**.

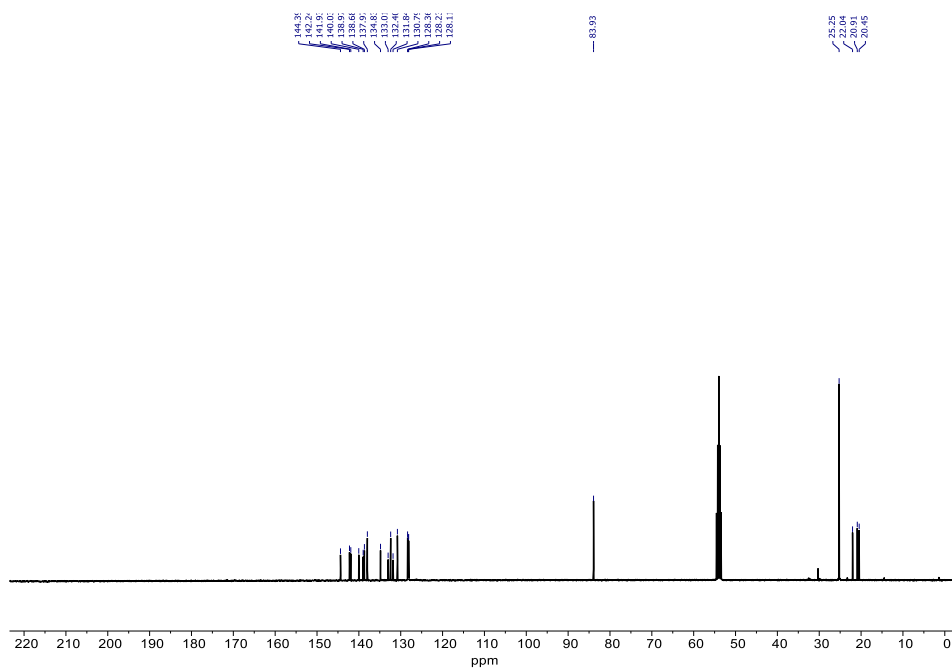
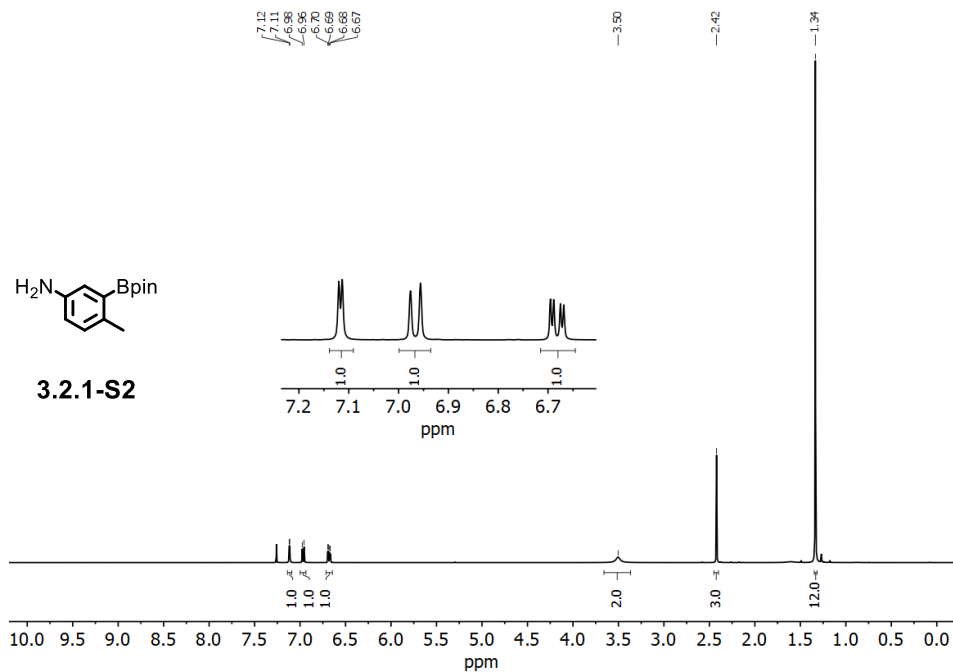
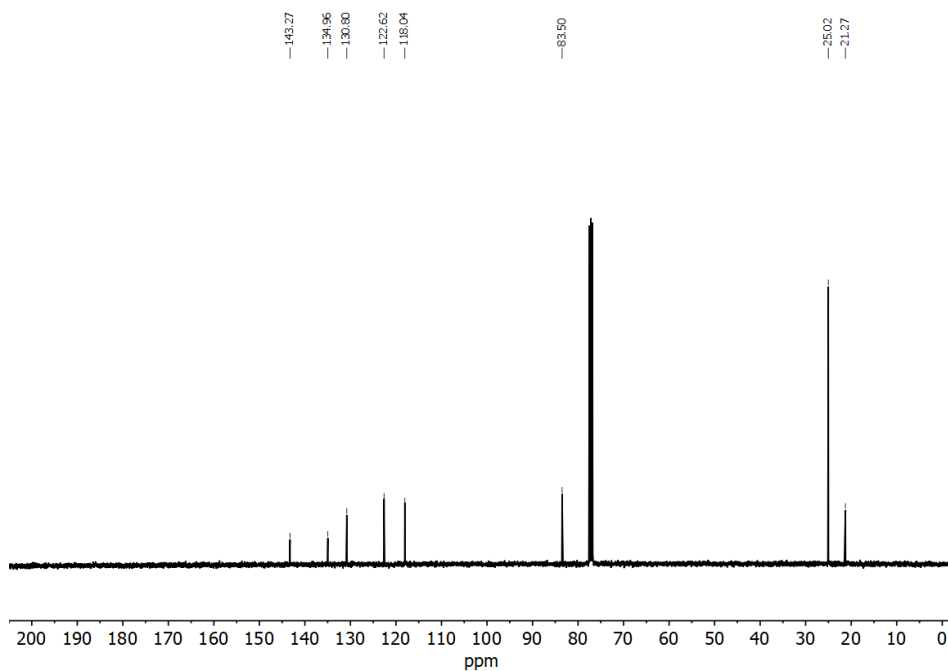
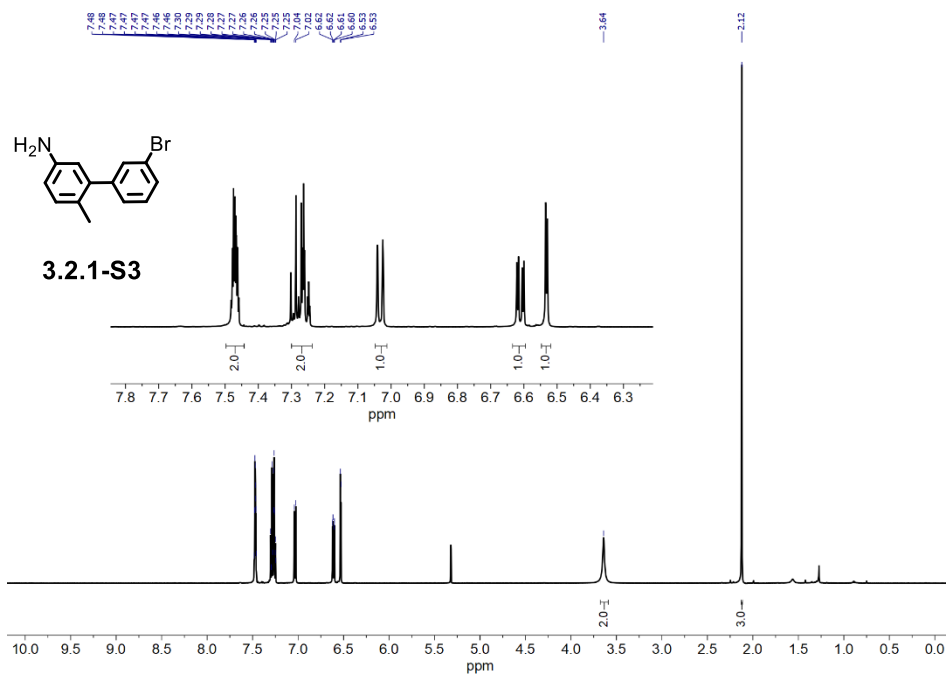
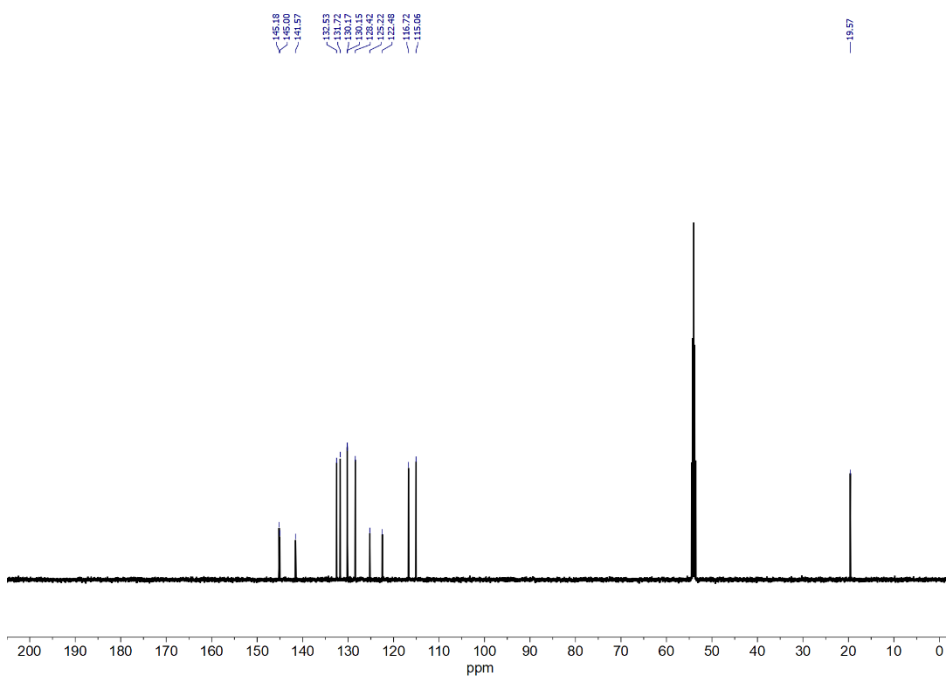


Figure 138.  $^{13}\text{C}$  NMR (126 MHz,  $\text{CD}_2\text{Cl}_2$ ) spectrum of compound **3.2.1-M6**.



Figure 141.  $^1\text{H NMR}$  (500 MHz,  $\text{CDCl}_3$ ) spectrum of compound 3.2.1-S2.Figure 142.  $^{13}\text{C NMR}$  (126 MHz,  $\text{CDCl}_3$ ) spectrum of compound 3.2.1-S2.

Figure 143. <sup>1</sup>H NMR (500 MHz, CD<sub>2</sub>Cl<sub>2</sub>) spectrum of compound 3.2.1-S3.Figure 144. <sup>13</sup>C NMR (500 MHz, CD<sub>2</sub>Cl<sub>2</sub>) spectrum of compound 3.2.1-S3.

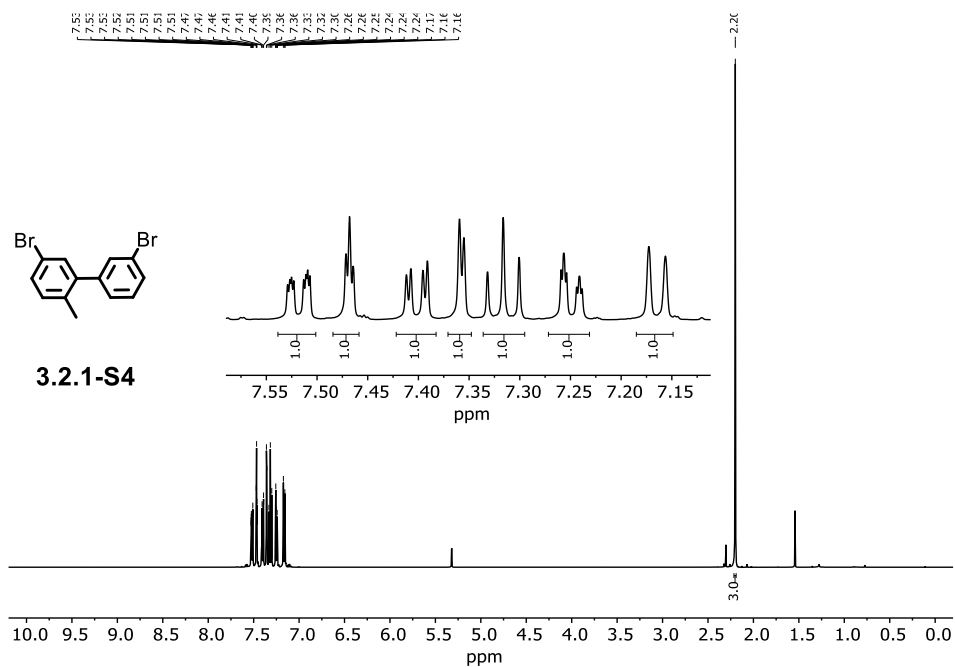


Figure 145.  $^1\text{H}$  NMR (500 MHz,  $\text{CD}_2\text{Cl}_2$ ) spectrum of compound 3.2.1-S4.

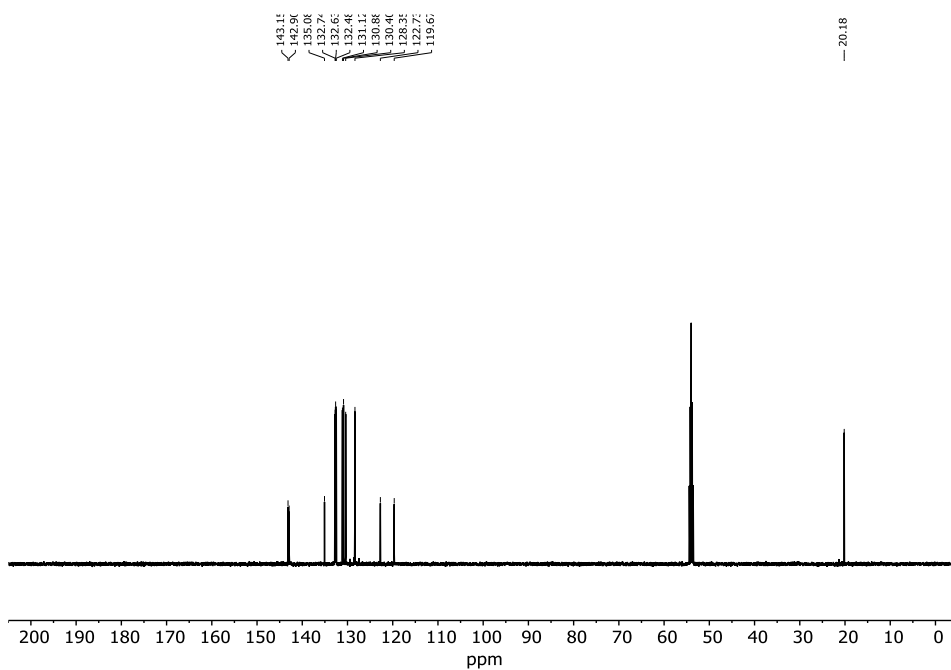
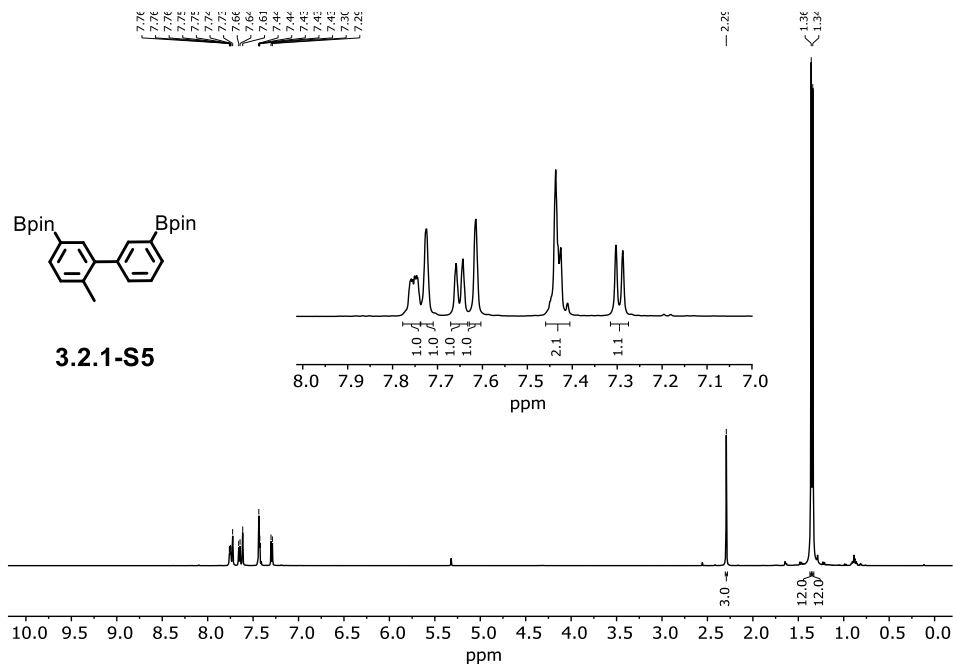
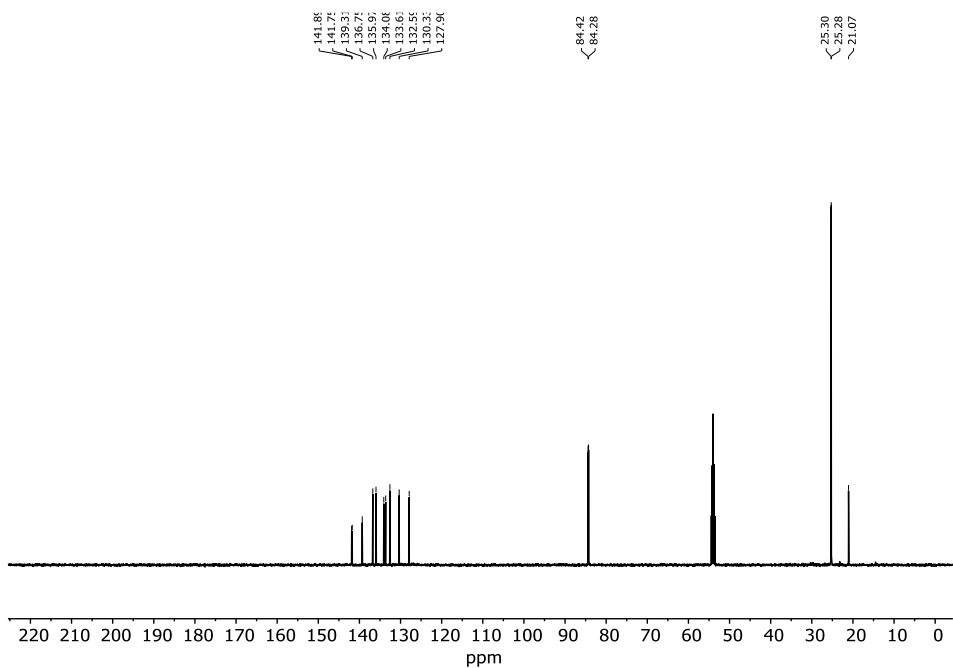
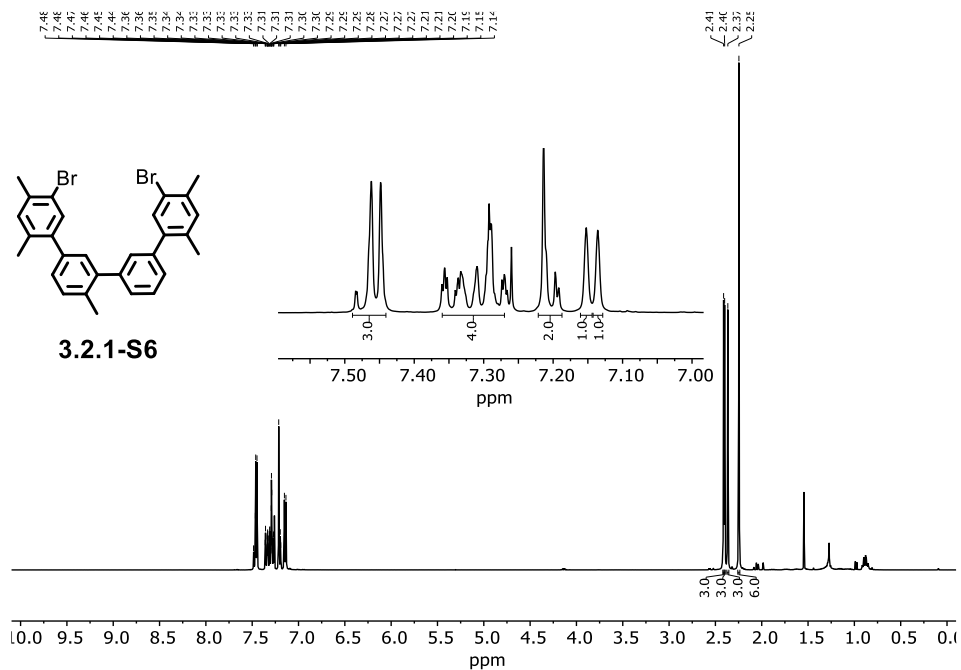
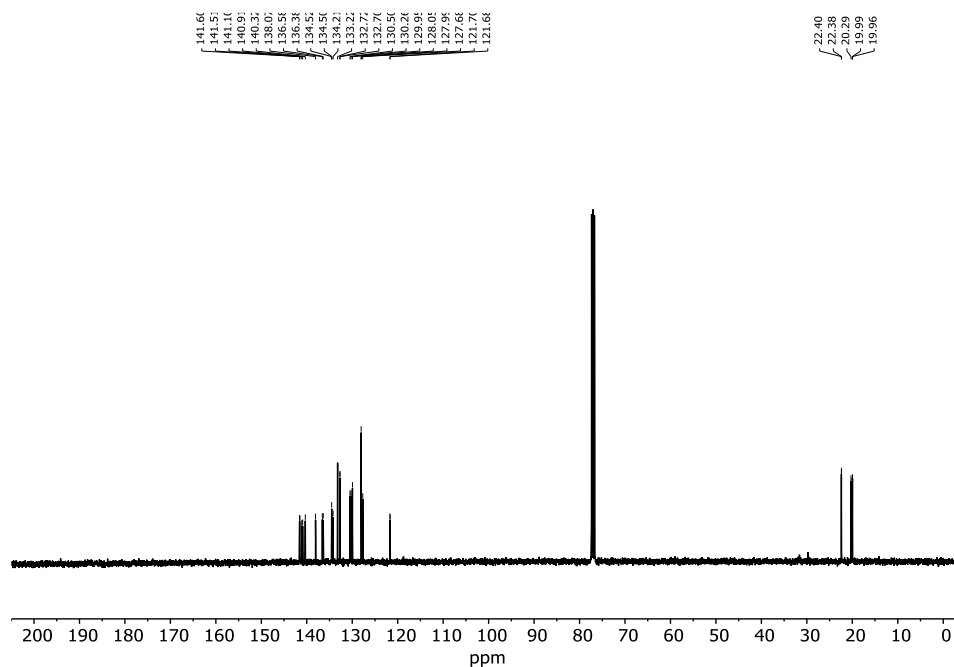
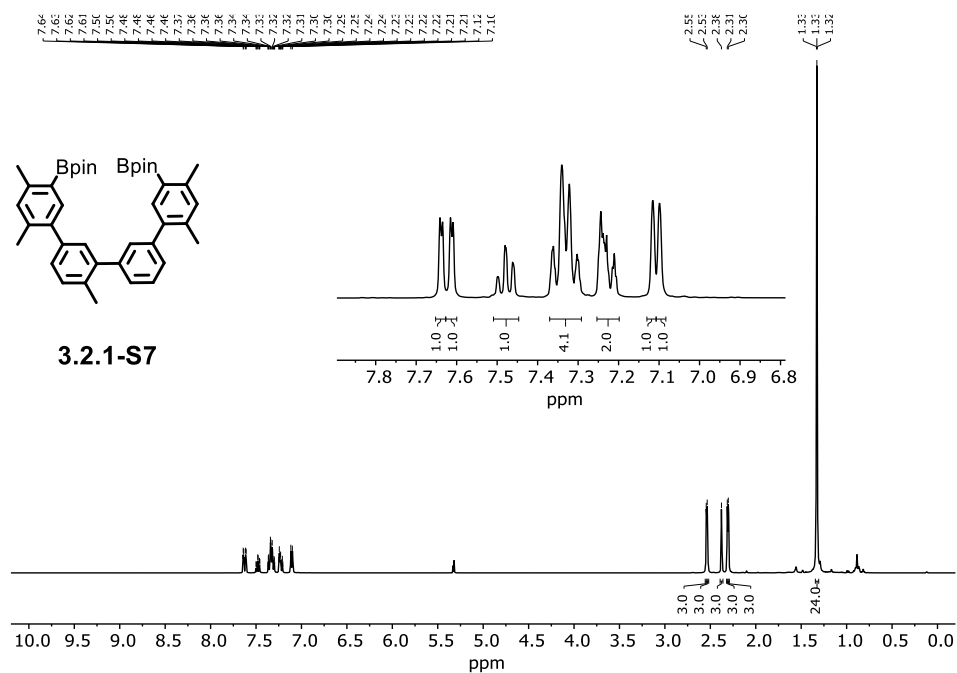
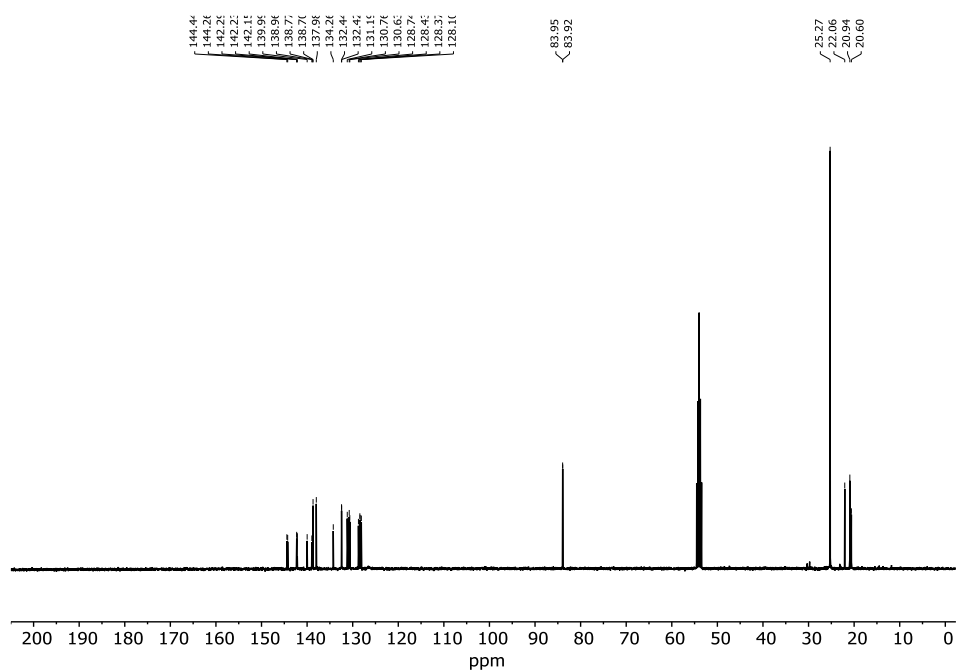


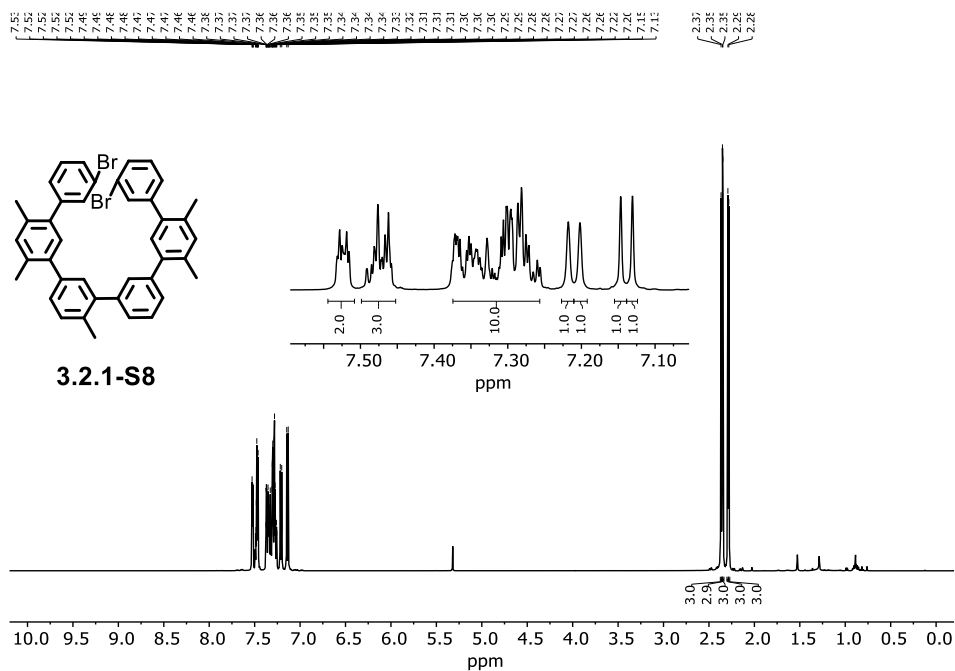
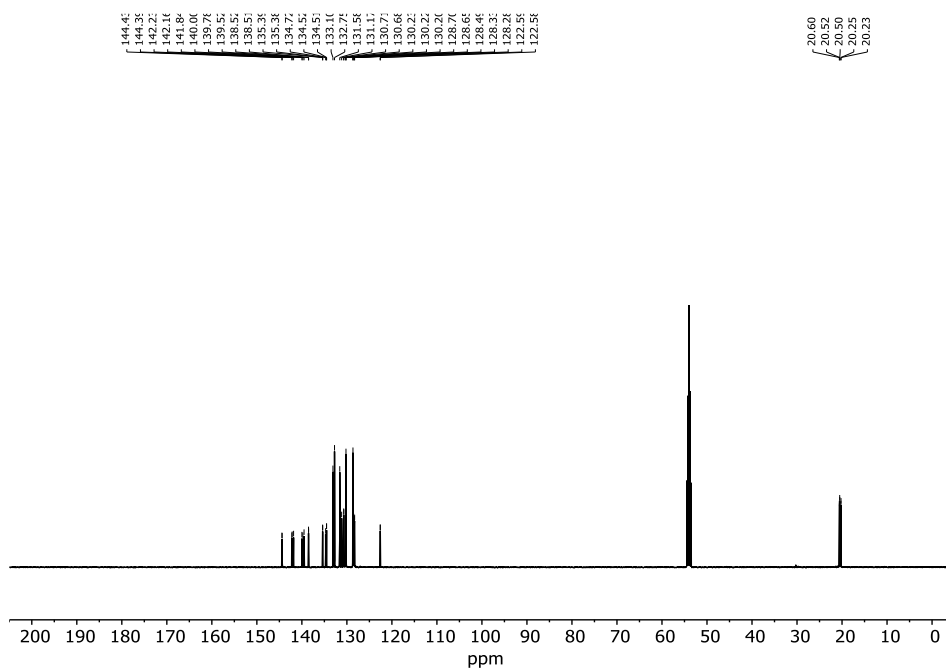
Figure 146.  $^{13}\text{C}$  NMR (126 MHz,  $\text{CD}_2\text{Cl}_2$ ) spectrum of compound 3.2.1-S4.

Figure 147. <sup>1</sup>H NMR (500 MHz, CD<sub>2</sub>Cl<sub>2</sub>) spectrum of compound 3.2.1-S5.Figure 148. <sup>13</sup>C NMR (126 MHz, CD<sub>2</sub>Cl<sub>2</sub>) spectrum of compound 3.2.1-S5.

Figure 149. <sup>1</sup>H NMR (500 MHz, CDCl<sub>3</sub>) spectrum of compound 3.2.1-S6.Figure 150. <sup>13</sup>C NMR (126 MHz, CDCl<sub>3</sub>) spectrum of compound 3.2.1-S6.

Figure 151. <sup>1</sup>H NMR (500 MHz, CD<sub>2</sub>Cl<sub>2</sub>) spectrum of compound 3.2.1-S7.Figure 152. <sup>13</sup>C NMR (126 MHz, CD<sub>2</sub>Cl<sub>2</sub>) spectrum of compound 3.2.1-S7.



Figure 153. <sup>1</sup>H NMR (500 MHz, CD<sub>2</sub>Cl<sub>2</sub>) spectrum of compound 3.2.1-S8.Figure 154. <sup>13</sup>C NMR (126 MHz, CD<sub>2</sub>Cl<sub>2</sub>) spectrum of compound 3.2.1-S8.

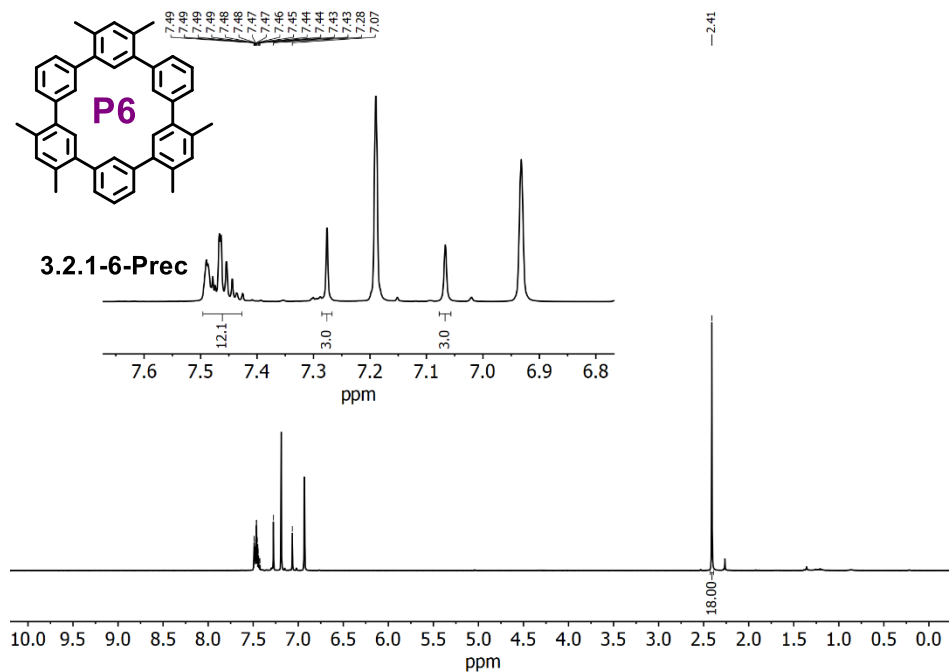


Figure 155.  $^1\text{H}$  NMR (500 MHz,  $[\text{D}_4]-o\text{-DCB}$ ) spectrum of compound **3.2.1-6-Prec**.

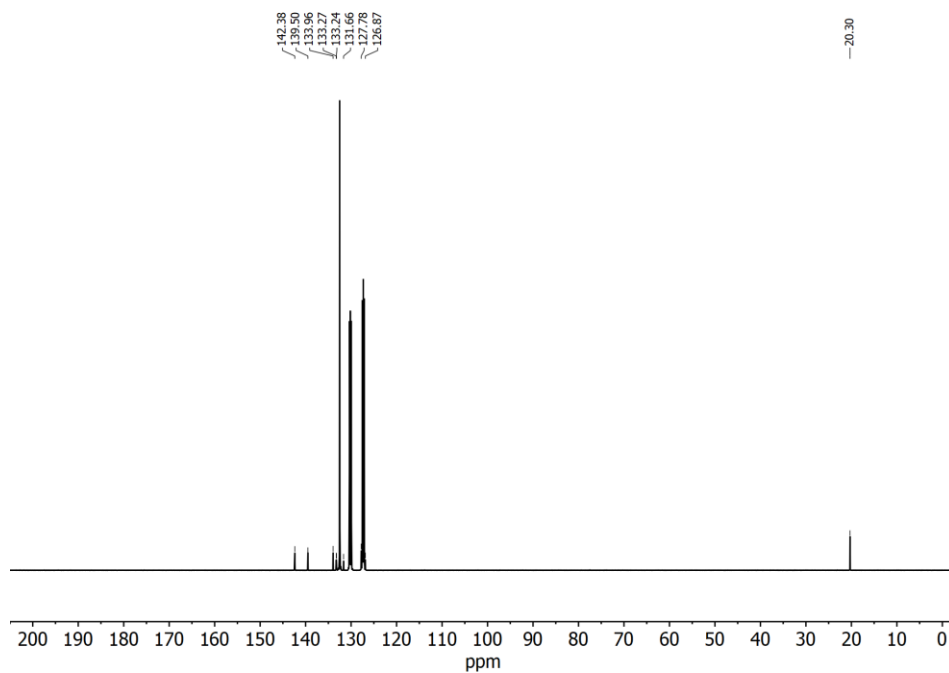


Figure 156.  $^{13}\text{C}$  NMR (126 MHz,  $[\text{D}_4]-o\text{-DCB}$ ) spectrum of compound **3.2.1-6-Prec**.

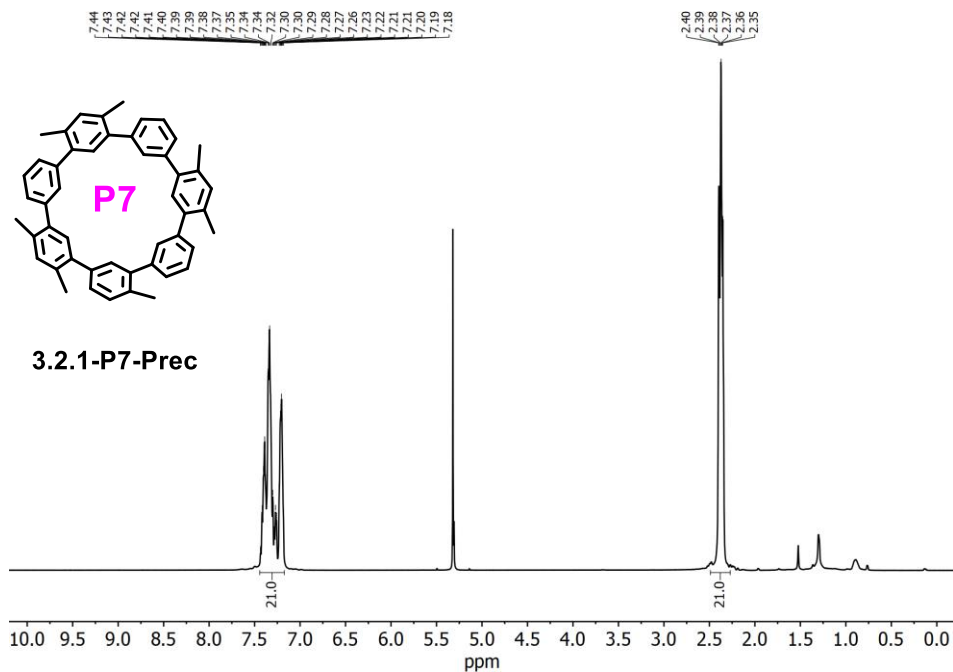


Figure 157. <sup>1</sup>H NMR (500 MHz, CD<sub>2</sub>Cl<sub>2</sub>) spectrum of compound 3.2.1-P7-Prec.

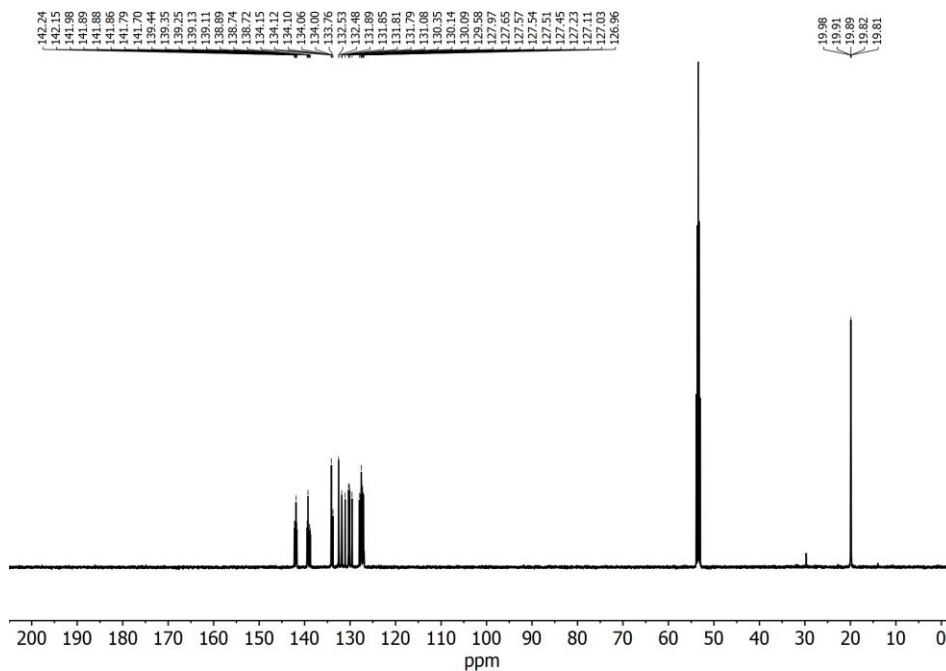


Figure 158. <sup>13</sup>C NMR (126 MHz, CD<sub>2</sub>Cl<sub>2</sub>) spectrum of compound 3.2.1-P7-Prec.

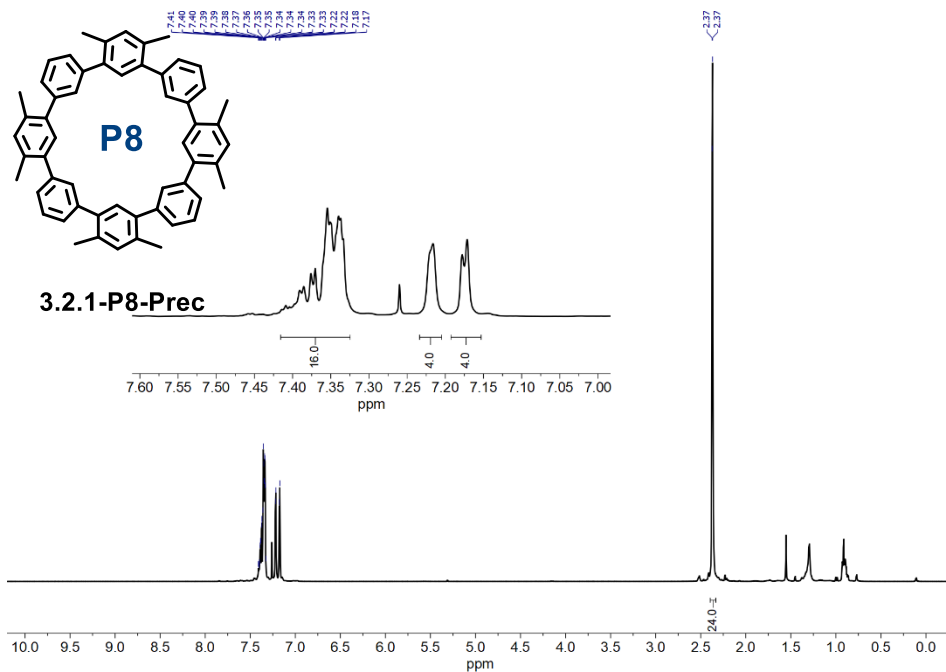


Figure 159.  $^1\text{H}$  NMR (500 MHz,  $\text{CDCl}_3$ ) spectrum of compound **3.2.1-P8-Prec**.

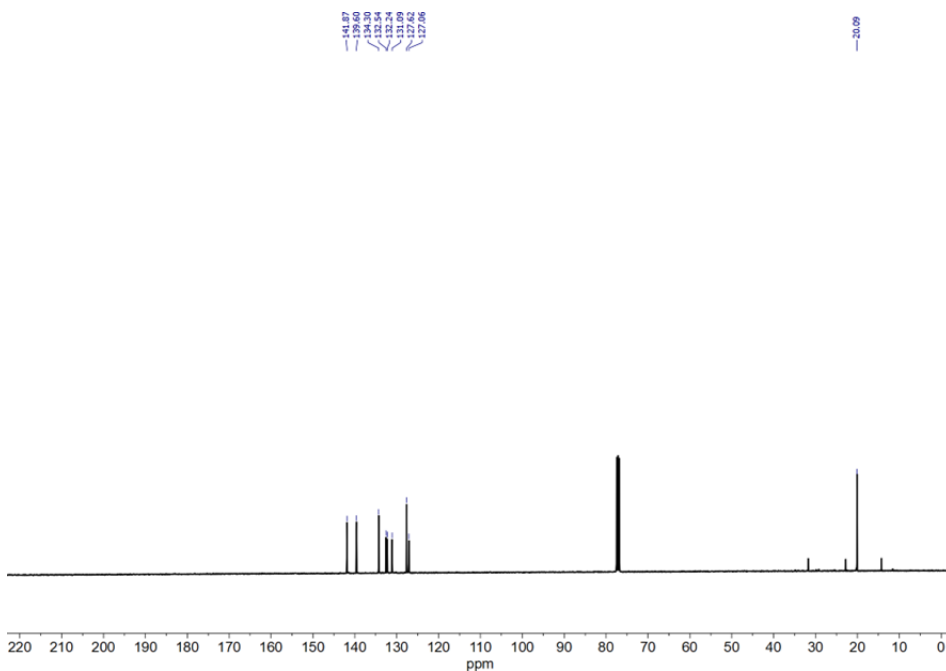


Figure 160.  $^{13}\text{C}$  NMR (126 MHz,  $\text{CDCl}_3$ ) spectrum of compound **3.2.1-P8-Prec**.

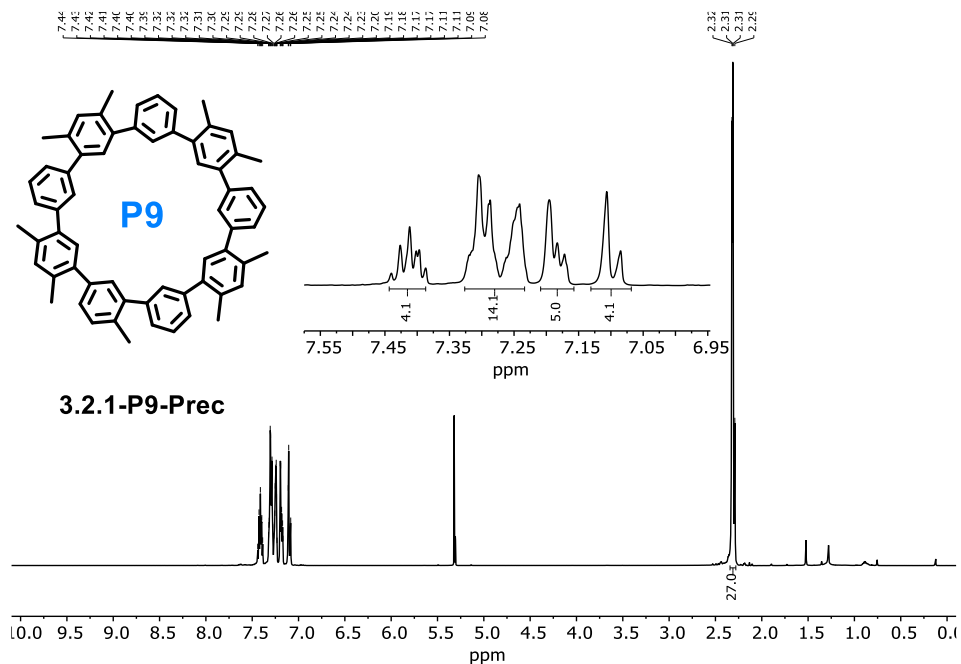


Figure 161. <sup>1</sup>H NMR (500 MHz, CD<sub>2</sub>Cl<sub>2</sub>) spectrum of compound **3.2.1-P9-Prec**.

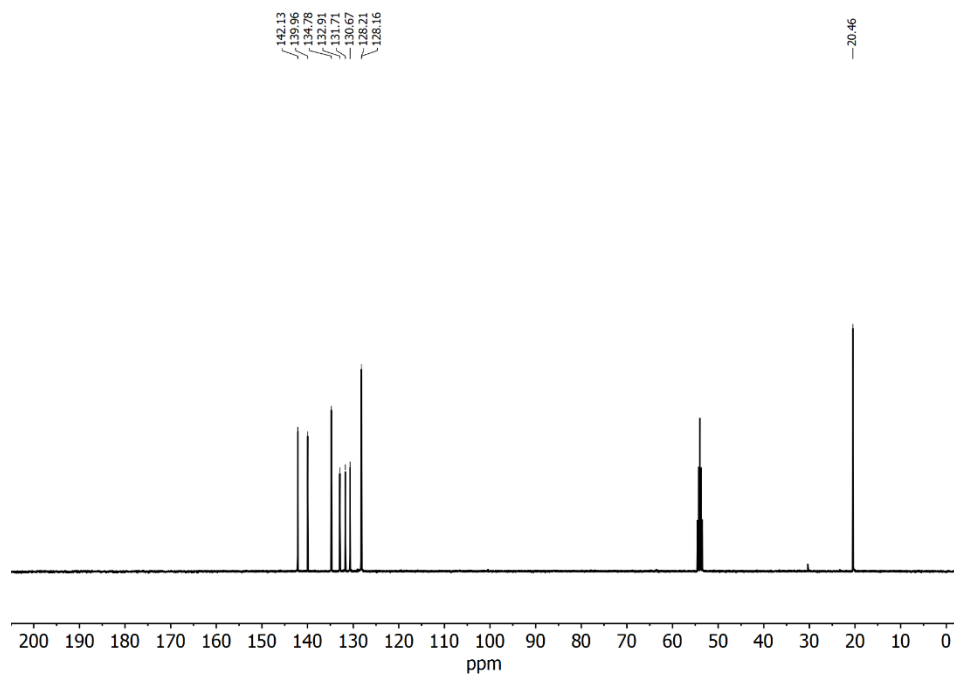


Figure 162. <sup>13</sup>C NMR (126 MHz, CD<sub>2</sub>Cl<sub>2</sub>) spectrum of compound **3.2.1-P9-Prec**.

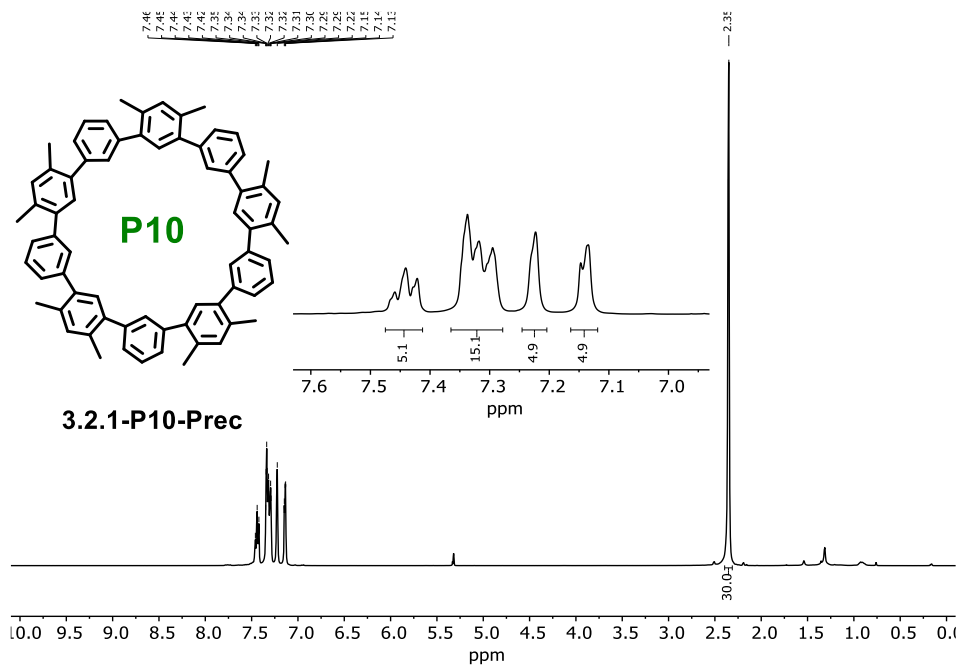


Figure 163.  $^1\text{H}$  NMR (500 MHz,  $\text{CD}_2\text{Cl}_2$ ) spectrum of compound 3.2.1-P10-Prec.

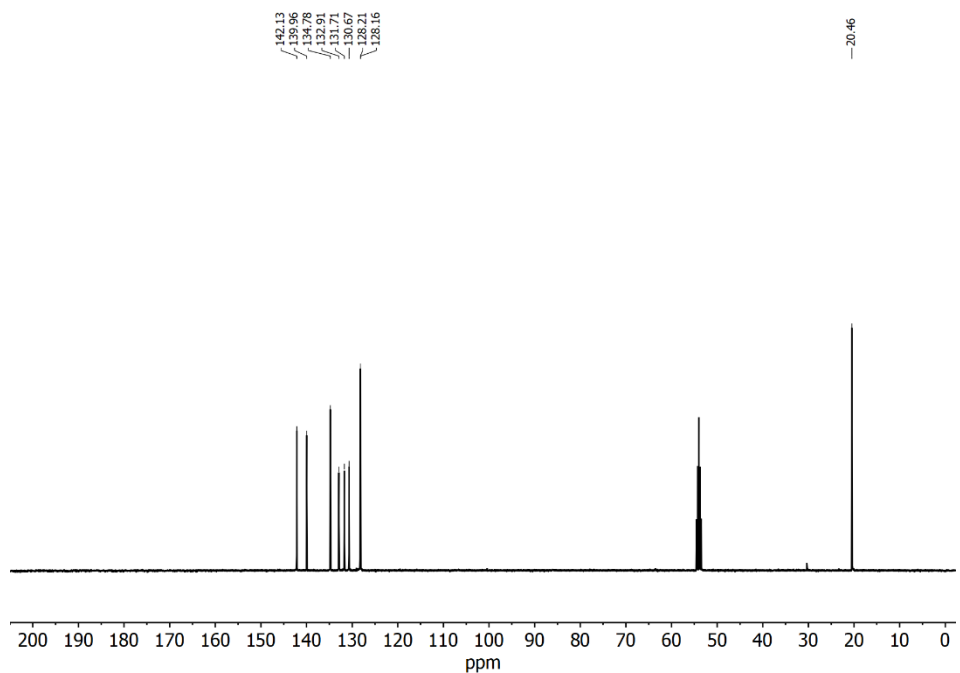
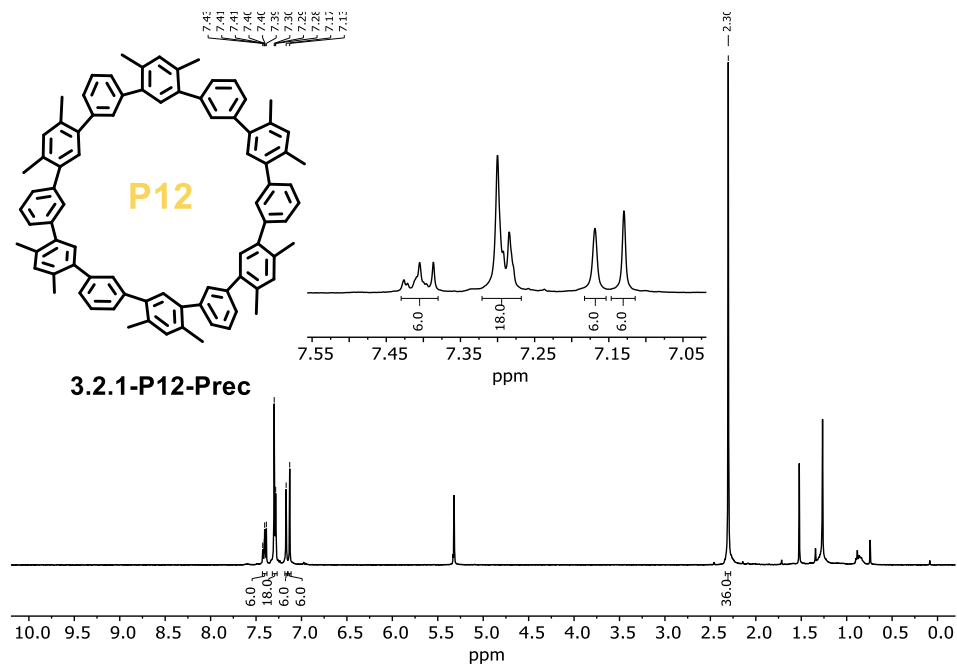
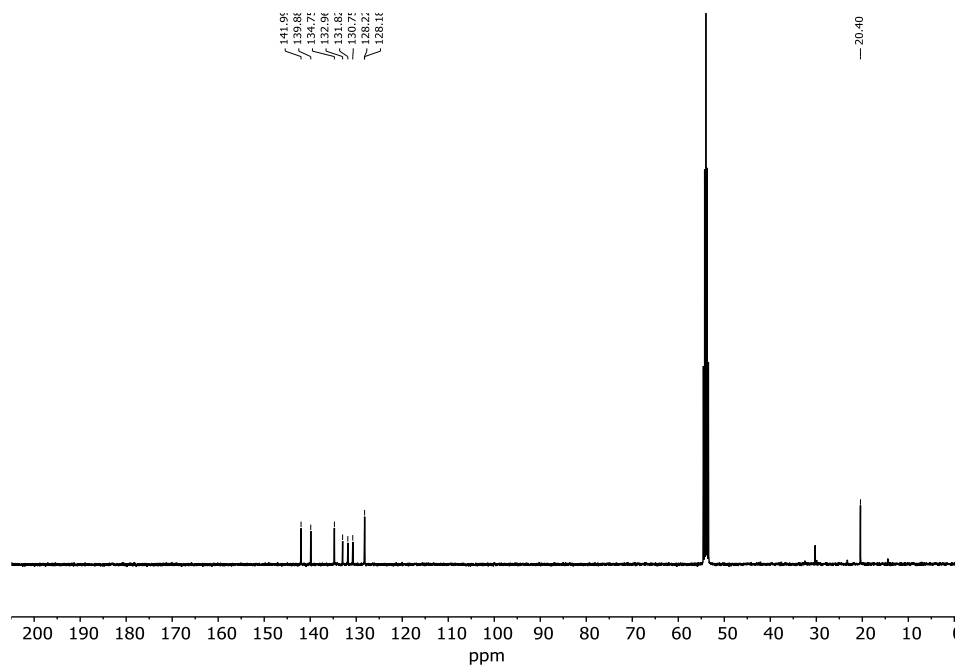
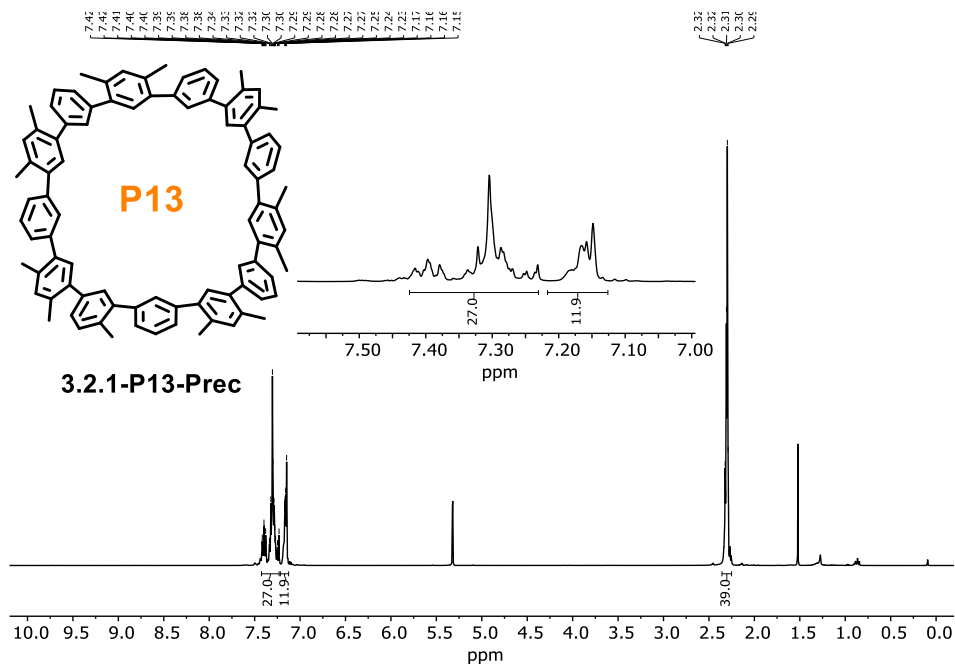
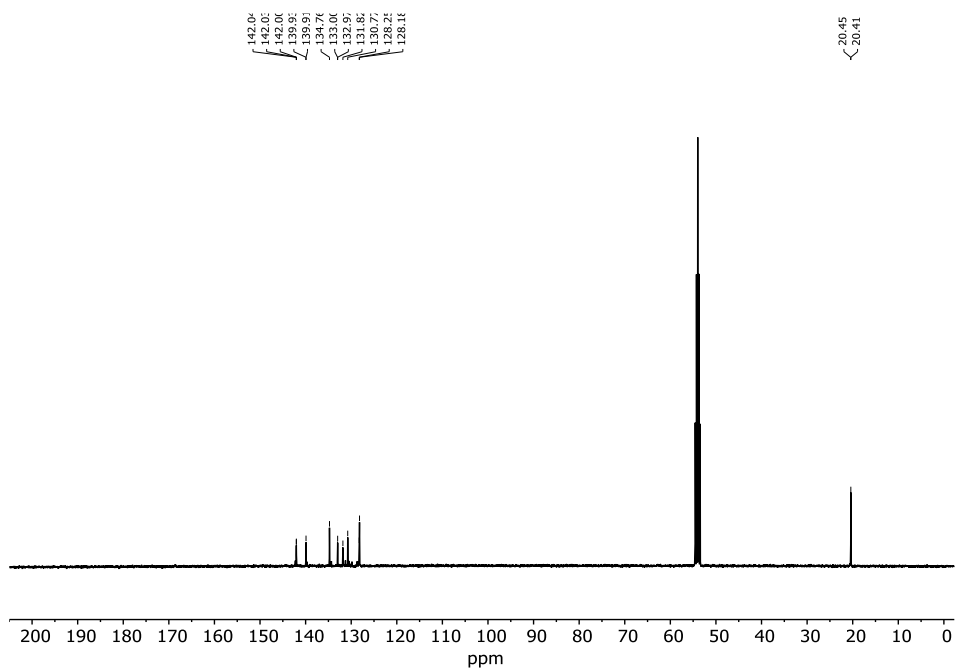


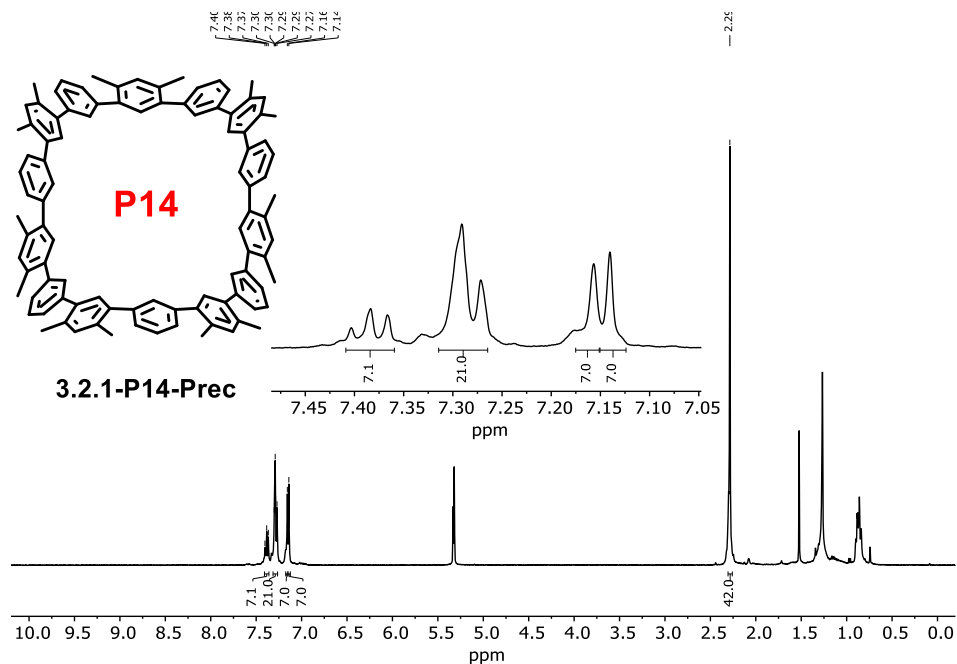
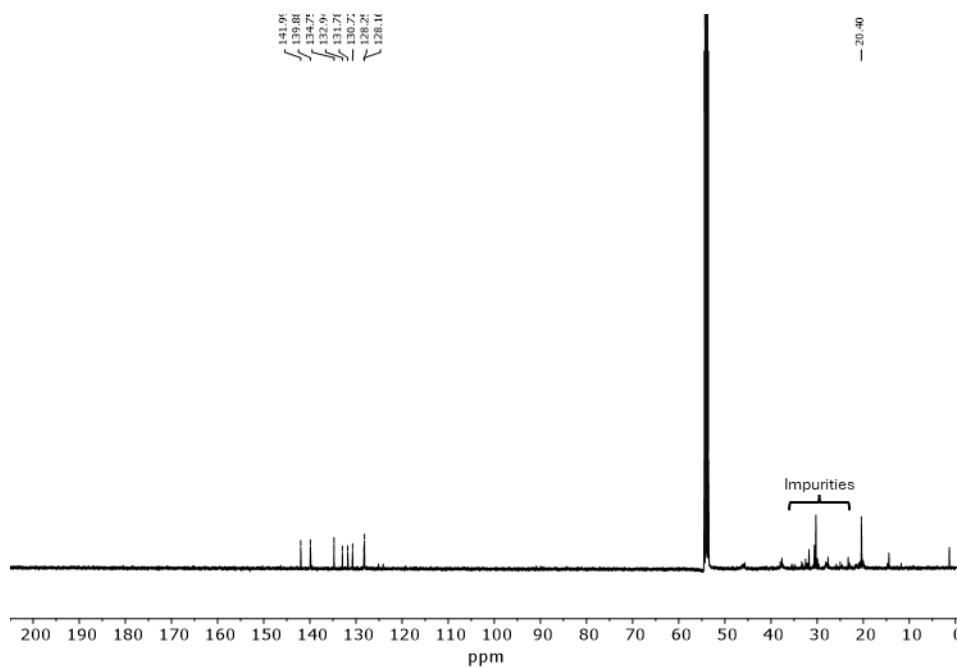
Figure 164.  $^{13}\text{C}$  NMR (126 MHz,  $\text{CD}_2\text{Cl}_2$ ) spectrum of compound 3.2.1-P11-Prec.

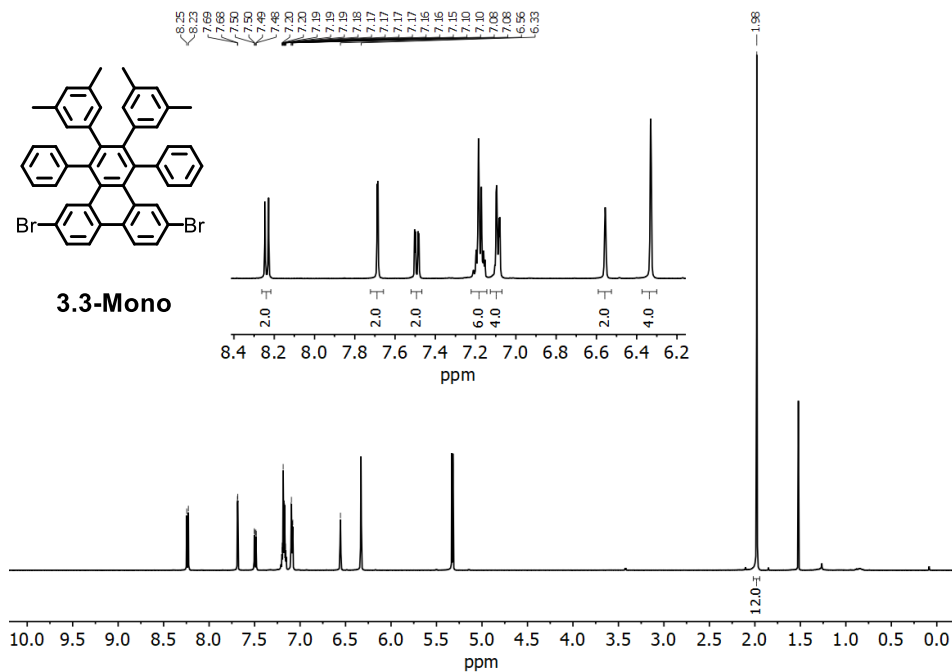
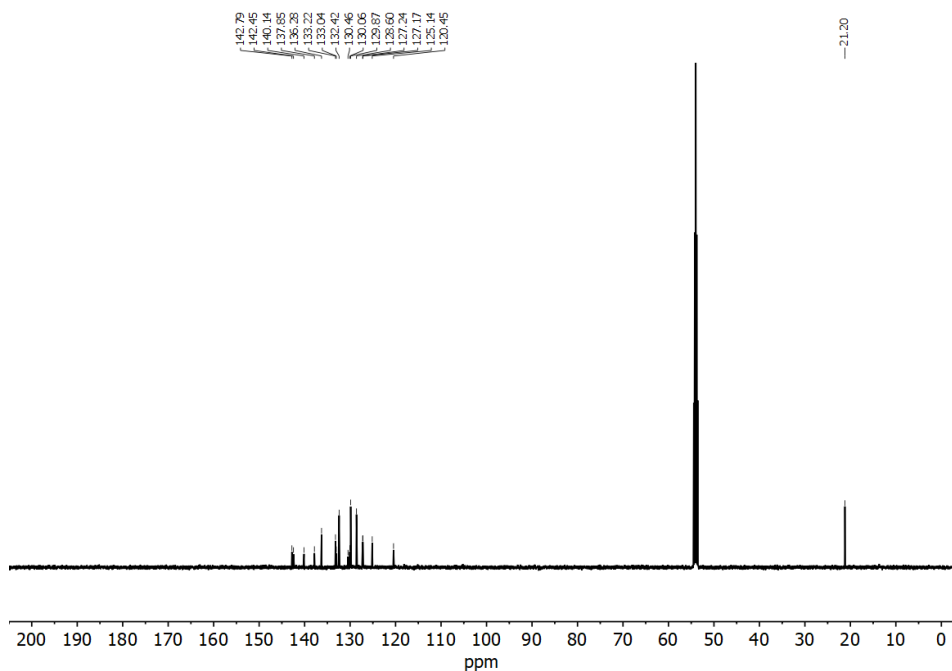


Figure 167. <sup>1</sup>H NMR (400 MHz, CD<sub>2</sub>Cl<sub>2</sub>) spectrum of compound 3.2.1-P12-Prec.Figure 168. <sup>13</sup>C NMR (101 MHz, CD<sub>2</sub>Cl<sub>2</sub>) spectrum of compound 3.2.1-P12-Prec.



Figure 169.  $^1\text{H}$  NMR (400 MHz,  $\text{CD}_2\text{Cl}_2$ ) spectrum of compound 3.2.1-P13-Prec.Figure 170.  $^{13}\text{C}$  NMR (101 MHz,  $\text{CD}_2\text{Cl}_2$ ) spectrum of compound 3.2.1-P13-Prec.

Figure 171.  $^1\text{H}$  NMR (500 MHz,  $\text{CD}_2\text{Cl}_2$ ) spectrum of compound **3.2.1-P14-Prec**.Figure 172.  $^{13}\text{C}$  NMR (126 MHz,  $\text{CD}_2\text{Cl}_2$ ) spectrum of compound **3.2.1-P14-Prec**.

Figure 173.  $^1\text{H NMR}$  (500 MHz,  $\text{CD}_2\text{Cl}_2$ ) spectrum of compound 3.3-Mono.Figure 174.  $^{13}\text{C NMR}$  (126 MHz,  $\text{CD}_2\text{Cl}_2$ ) spectrum of compound 3.3-Mono.

## 4.2 On-Surface Synthesis Methods and Characterization Techniques

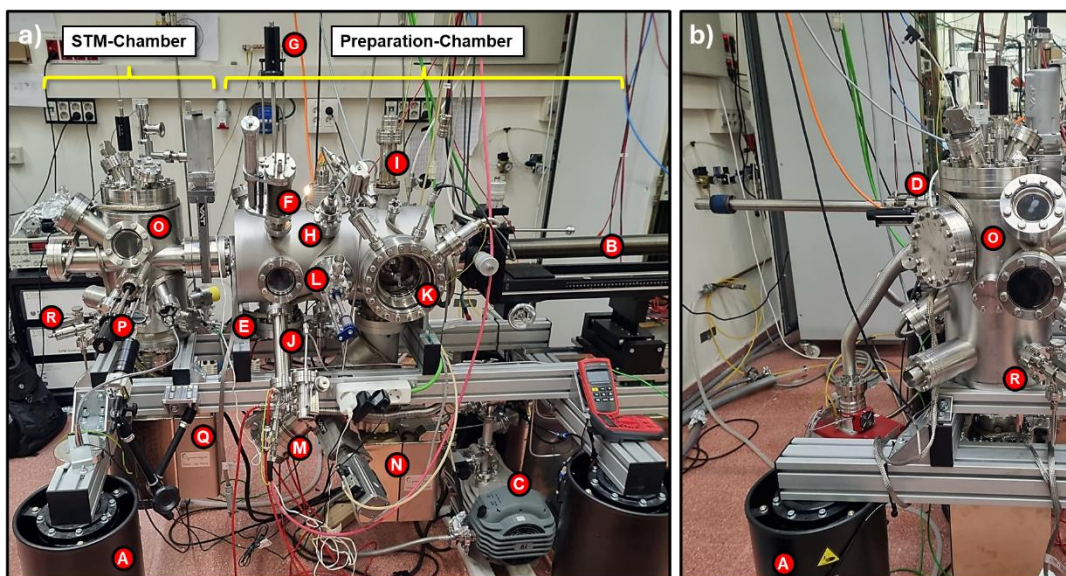
In this thesis, the synthesis and characterization of the final graphene nanostructures were carried out by on-surface methods. Essentially, the procedure was based on: Firstly, sublimation of the molecular precursors onto a metallic surface, specifically Au(111); secondly, annealing the Au(111) sample, taking advantage of its catalytic properties to induce chemical reactions in the precursors; and finally, characterizing the nanostructures structurally, electronically and magnetically through different techniques such as STM, nc-AFM, STS or XPS. Additionally, in some cases, the STM tip was utilized to manipulate and induce chemical modifications on the final structures. Both synthesis and characterization were performed under UHV conditions, typically at pressures around  $1 \cdot 10^{-10}$  mbar. STM, nc-AFM and STS characterization were carried out at cryogenic temperatures around 4 K, while XPS spectroscopy was performed at r.t.

In this section, we will examine the experimental setup utilized for conducting the experiments, the methodologies employed to prepared the desired substrates, and we will delve in the fundamental principles underlying the characterization techniques employed.

### 4.2.1 Experimental Set-Up

Some of the results related with the on-surface synthesis and characterization presented in this thesis are a collaborative work between the ESISNA Group, at the ICMM-CSIC in Madrid, and other research groups: the Nanosurf Group at the Institute of Physics of the Czech Republic in Prague, Czech Republic; the Nanotech@Surfaces Group at EMPA in Zurich, Switzerland; and the Advanced Microscopy Laboratory at the University of Zaragoza, Spain. In the Results chapter, there is a description of the specific contributions made by each group to the respective projects. Delving in the experimental set-up of each machine that helped with the presented results is out of the scope of this thesis, hence, we will only focus in the set-up of the machine from the ESISNA Group: “Nautilus”.

As it can be seen in **Figure 175**, “Nautilus” is equipped with two main chambers, the preparation chamber, on the right, and the STM chamber, left-sided in the figure. The whole system is isolated from external mechanical noises with a set of 4 pneumatic legs (**A**), (see nomenclature in **Figure 175**), and UHV pressures (around  $1 \cdot 10^{-10}$  mbar) are routinely achieved in both chambers thanks to a set of pumps that maintains the reduced pressure.



**Figure 175.** Front and side view pictures of “Nautilus”. The various components comprising “Nautilus” are labeled with letters corresponding to descriptions in the main text.

Regarding the preparation chamber, it is integrated by the following equipment:

- The main manipulator (**B**) (VAB Vakuum). It allows the movement of the samples within the different “stages” of the preparation chamber, and also, it enables the movement from the preparation chamber to the STM chamber (and vice versa). It also allows annealing resistively the samples until  $\sim 600$  °C (the temperature is controlled with a thermocouple) and cooling them down to  $-173$  °C thanks to a cooling set-up composed of a capillary coil through which it is possible to flow LN<sub>2</sub>.
- A scroll pump (**C**) (Agilent).
- The fast entry lock (**D**). It allows the fast entry of new samples and molecular crucibles into the preparation chamber thanks to a previous vacuum stage ( $1 \cdot 10^{-7}$  mbar). It is equipped with a turbomolecular pump (80 l/s Pfeiffer) that is connected to the main scroll pump (**C**).
- The six-fold evaporator (**E**), (Mantis GmbH). It allows storing up to 6 different crucibles under the UHV and, the simultaneous deposition of three of them through the shutter.
- A quartz crystal microbalance, QCM, (**F**) for determining the evaporation rate of the molecular precursors.
- A wobble stick (**G**), to manipulate crucibles from the main manipulator (**B**) to the six-fold evaporator (**E**).
- An ion gun (**H**), (IQE-11/35, SPECS). It enables the preparation of clean samples through the sputtering process. A leak valve for the introduction of Ar<sub>2</sub> gas is placed next to it.
- A quadrupole mass spectrometer QMS (**I**), (Prisma, Pfeiffer).

- A hydrogen cracker (**J**) for experiments requiring atomic hydrogen.
- A low-energy electron diffractometer LEED, (**K**), (Spectaleed OMICRON).
- Electron-beam heating stage (**L**), (Ferrovac GmbH), it allows heating samples at high temperatures,  $> 1000$  °C.
- Turbomolecular Pump (**M**) (300 l/s, Agilent).
- Ionic Pump (**N**) (150 l/s, Gamma Vacuum, TiTan).

On the other hand, the equipment regarding the STM chamber:

- The STM (**O**) (STREAM, Sigma Surface-Science). Enables the characterization of surfaces at variable temperatures: r.t., 78 K with the use of LN<sub>2</sub> and 8 K with LHe.
- A wobble stick, (**P**), to manipulate samples from the main manipulator (**B**) to the sample's parking, or to the STM head.
- An ionic pump (**Q**) (150 l/s, Gamma Vacuum, TiTan).
- A leak valve (**R**) for the introduction of CO gas.

### 4.2.2 Sample Preparation Methods

All the experiments were carried out on clean Au(111) samples that underwent standard cleaning procedures to prepare atomically-clean well-defined surfaces. Subsequently, molecular precursors were sublimated either from quartz crucibles or homemade tantalum pockets, while the evaporation rate was determined using a QCM.

#### Sputtering and Annealing

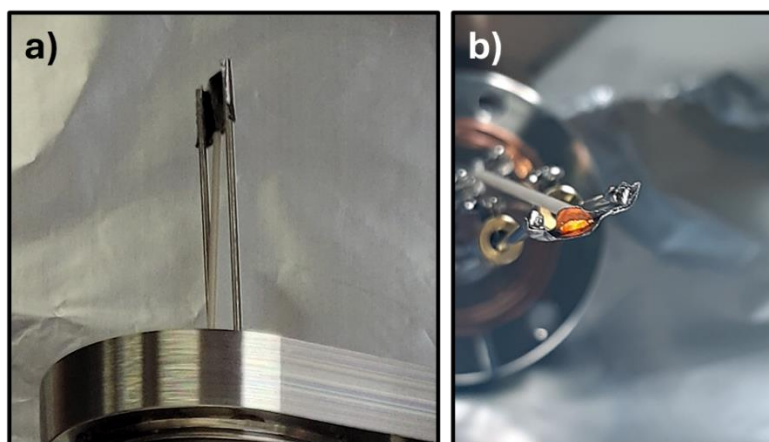
The cleaning procedure conducted for the Au(111) samples consists in two main steps: sputtering and annealing. During sputtering, the sample is bombarded with ionized atoms of Argon causing the removal of tens to hundreds of nanometers of material. In this regard, Ar gas is introduced into the ionization gas (the preparation chamber reaches pressures of approximately  $P \approx 10^{-6}$  mbar) and then, the sample is aligned with the sputter gun, which is activated with an electric potential of 1 kV for 15 minutes. The impact of the ions on the sample generates currents of  $I \approx 10$   $\mu$ A, which is monitored with a multimeter placed in series between the sample and ground. The sputtering process creates roughness on the surface.

The second stage involves heating the sample at around half of its melting point, approximately 450°C in Au(111), for 10 minutes. This step promotes the mobility of metallic atoms, facilitating the formation of a new flat and homogeneous surface. Heating is achieved using a resistive heating element connected to a power supply in the manipulator (**B**).

#### Evaporators

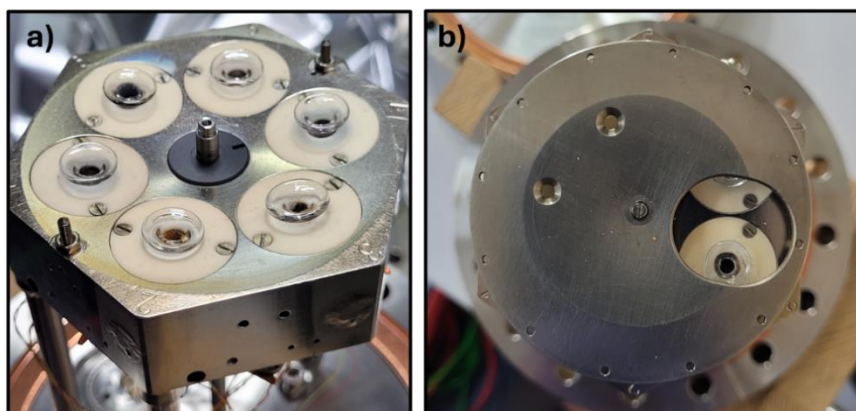
Sublimating molecules onto metallic surfaces is a common preparation in this thesis. It was accomplished either heating homemade tantalum pockets in an external evaporator, or quartz crucibles in a six-fold evaporator (both with the powder of the molecular precursors inside).

**Figure 176** shows a handmade tantalum pocket evaporator. The molecular precursor is placed inside the pocket and the system is heated externally. The temperature was measured through a K-type thermocouple (alumel/chromel) spot-welded directly onto the tantalum pocket. In addition to be an economical method, this approach is useful when it is necessary to change the evaporator to a different chamber for a new experiment.



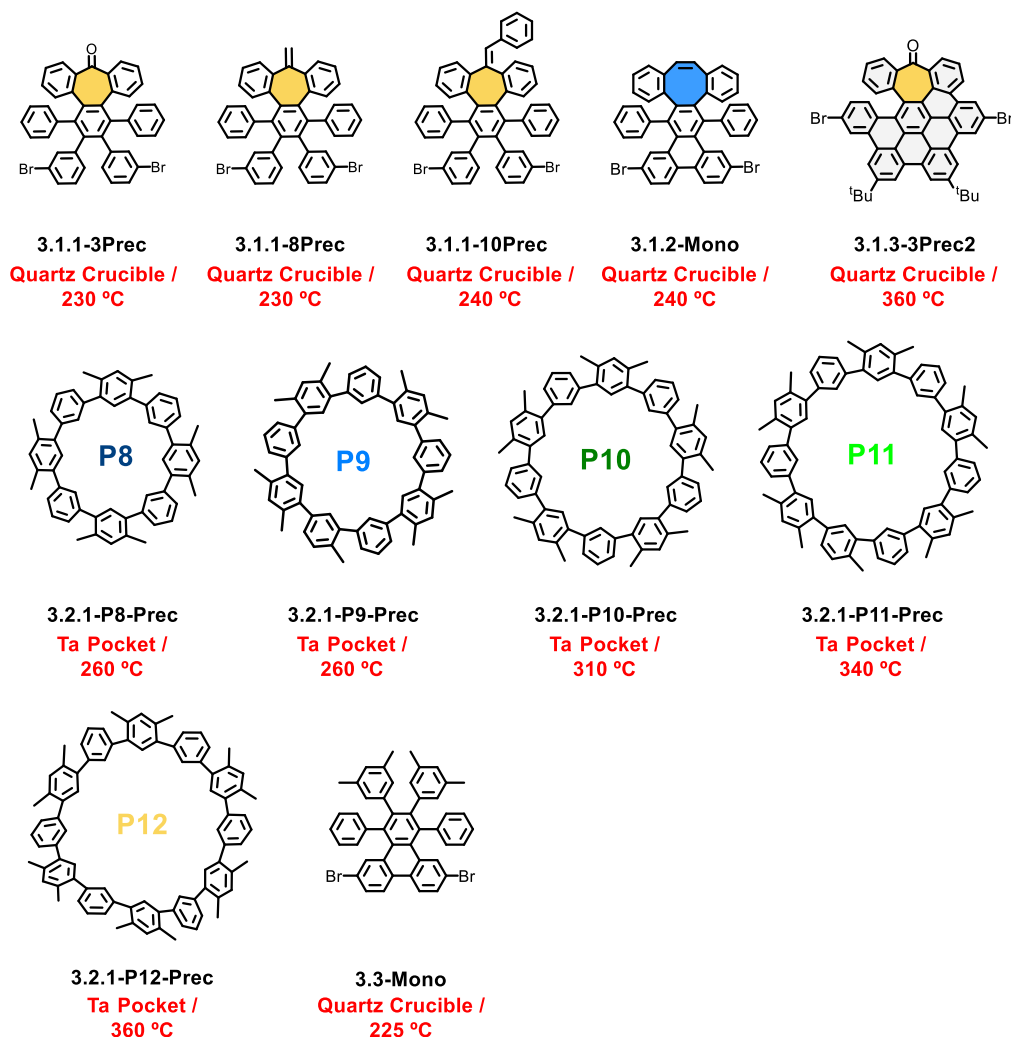
**Figure 176.** Tantalum pocket evaporator.

Regarding the quartz crucibles, they were heated in a six-fold evaporator, as can be seen in **Figure 177**. This instrument allows holding six different molecules inside the UHV and enables the deposition from three of them simultaneously through the three holes in the top shielding (**Figure 177 b**). The six-fold evaporator offers a rapid, efficient and reproducible alternative to the external evaporators, omitting the baking stage required in external evaporators to reach low pressures.



**Figure 177.** Six-Fold evaporator with quartz crucibles.

In this regard, **Scheme 34** presents a summary of the molecules that were used in this doctoral thesis, with their respective sublimation temperatures and with the method of evaporation (quartz crucible or tantalum pocket) depicted for each case.



**Scheme 34.** Utilized molecules in this doctoral thesis with their respective sublimation temperatures.

### Quartz Crystal Microbalance

QCM is a highly sensitive technique used to measure small changes in mass. It is used in this thesis to determine the evaporation rate of the molecular precursors before their adsorption on the sample.

It is based on the piezoelectric properties of quartz crystals and consists in a thin crystal oscillator made from Au-coated quartz that resonates when an alternating voltage is applied.



When matter is deposited on the crystal, its resonance frequency shifts, being detected by the system (piezoelectricity) and converting the signal into mass or layers.

In the late 1950s<sup>249</sup>, Sauerbrey demonstrated that the frequency change ( $\Delta f$ ) of an oscillating quartz crystal could be linearly correlated with its mass change ( $\Delta m$ ) using the following equation (Sauerbrey equation):

$$\Delta m = \frac{-C * \Delta f}{n} \quad (4.1.1)$$

where  $n$  is the overtone number and  $C$  is a constant that depends on the property of the crystal used. For example, a 5 MHz AT-cut quartz crystal<sup>250</sup> at r.t. typically exhibits a constant  $C$  value of approximately 17.7 ng/(cm<sup>2</sup>·Hz). This means that an increase in mass of 17.7 ng/cm<sup>2</sup> deposited onto a 5 MHz quartz crystal leads to a frequency change of 1 Hz. Given the precision to measure the frequency of a 5 MHz quartz crystal within 0.01 Hz in vacuum<sup>251</sup>, QCM enables precise measurement of masses at the nanogram scale, thereby facilitating the detection of subtle changes in evaporation rates<sup>252</sup>.

This equation is only valid under three conditions: (i) the added mass is small compared to the mass of the crystal itself, (ii) the added mass is rigidly adsorbed, and (iii) the mass is evenly distributed over the active area of the crystal.

#### 4.2.3 Scanning Tunneling Microscopy and Spectroscopy

Once the sample was prepared, the main technique employed to get insights of the structural and electronic information of the substrate was the Scanning Tunneling Microscopy (STM). STM is a technique widely used in nanotechnology and surface science, among other scientific fields, to study surfaces at the atomic scale. It operates by scanning a sharpened metal tip on a conductive surface placed in close proximity, typically within a distance of a few angstroms, while applying a bias voltage among both.

The remarkable success of the STM stems from the intrinsic characteristics of the tunneling current (the measured property in STM). Its exponential dependence with the tip-sample distance, coupled with its direct relationship with the density of states enables the atomic resolution when imaging surfaces and molecules, and additionally, the exploration of their electronic properties. This achievement owes much to the technology based in piezoelectric, which allows the movement of the tip (the probe) with an extraordinary sensitivity in the picometer range. The development of the STM in 1981 by Gerd Binnig and Heinrich Rohrer<sup>253</sup>,

<sup>249</sup> G. Sauerbrey, *Zeitschrift für Physik*, **1959**, 155, 206–222.

<sup>250</sup> F. Lack, G. Willard, I. Fair, *Bell System Technical Journal*, **1934**, 13, 453–463.

<sup>251</sup> A.W. Czanderna, R. Vasofsky, *Prog. Surf. Sci.*, **1979**, 9, 45–82.

<sup>252</sup> A. W. Warner, C. D. Stockbridge, *Journal of Applied Physics*, **1963**, 34, 437–438.

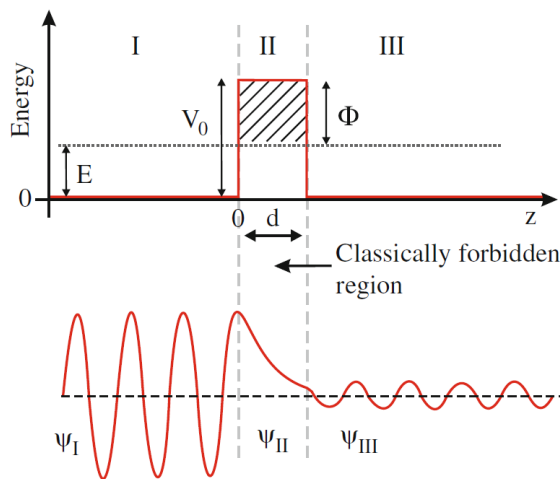
<sup>253</sup> G. Binnig, H. Rohrer, C. Gerber, E. Weibel, *Physical Review Letters*, **1982**, 49, 57–61.

researchers at IBM Zurich Research Laboratory in Switzerland, led to their prestigious recognition with the Nobel Prize in Physics in 1986.

Working Principle of the STM

The principle that governs the operation of the STM is the quantum tunneling, a phenomenon derived from the quantum mechanics and based on the non-zero probability of electrons to pass through a potential barrier (tunneling) that they classically would not overcome. In the STM context, this barrier corresponds to the vacuum gap between the metallic tip and the surface. An experimental manifestation appears when applying a bias voltage ( $V$ ) between both when in close proximity. Under these conditions, electrons can tunnel through the vacuum, leading to the generation of a detectable current (the tunneling current), typically in the order of pA to nA.

**Figure 178** shows a simple model of the tunneling process for a single electron in a 1D barrier. A square potential barrier  $V(z)$  of height  $V_0$  is considered above the bottom of the potential ( $V = 0$ ) in the region between  $z = 0$  and  $z = d$ .  $E$  is the energy of the electron tunneling through the barrier.



**Figure 178.** Schematics of a tunneling process showing the three different regions for a 1D barrier. Reproduced with permission from Springer Nature<sup>254</sup>.

<sup>254</sup> B. Voigtländer, *Scanning Probe Microscopy: Atomic Force Microscopy and Scanning Tunneling Microscopy*, Springer Berlin Heidelberg, Berlin, Heidelberg, 2015.

The Schrödinger time-independent equation within the 1D case can be written as:

$$\frac{\hbar^2}{2m} \frac{\partial^2}{\partial z^2} \psi(z) = [V(z) - E] \psi(z) \quad (4.1.2)$$

If we insert the expression of a right traveling plane wave,  $\psi = e^{ikz}$ , into equation (4.1.2), this results in:

$$-\frac{\hbar^2}{2m} k^2 = V(z) - E \quad (4.1.3)$$

where k:

$$k = \sqrt{\frac{2m}{\hbar^2} [E - V(z)]} \quad (4.1.4)$$

The presented 1D model in **Figure 178** encompasses three different regions (I, II and III) with different energies (I = III but II > I). In regions I and III, outside the barrier,  $V = 0$  and the solution has the form of an oscillating wave for a free electron:

$$k = \sqrt{\frac{2m}{\hbar^2} E}, \psi_{free} = e^{ikz} \quad (4.1.5)$$

On the other hand, in region II, inside the barrier,  $V = V_0$  and  $E - V_0 < 0$ . Thus, k is imaginary and therefore, if we define  $k = i\kappa$ , the real variable results as:

$$k = \sqrt{\frac{2m}{\hbar^2} [V_0 - E]}, \psi_{barrier} = e^{-\kappa z} \quad (4.1.6)$$

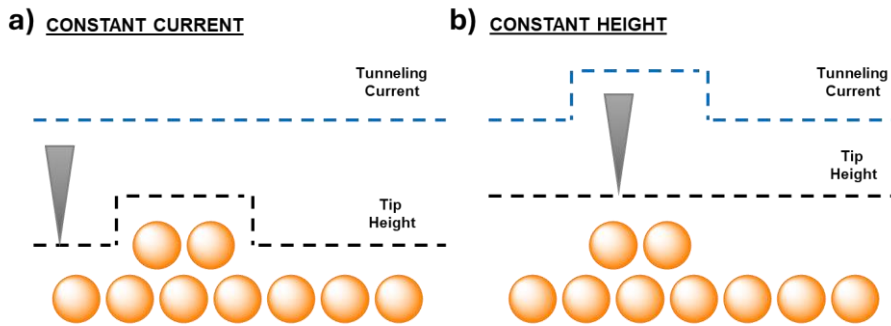
This is not an oscillating solution as found for the regions I and III (in which the potential vanishes), but an exponentially decaying (real) wave function that is generally found for regions in which the potential is larger than the particle energy. This behavior is represented in **Figure 178** at the bottom panel.

The tunneling current presents atomic resolution due to this stated exponential dependence of the electron wavefunction within the barrier (the tip-sample distance), decreasing rapidly as the tip is retracted from the surface. For example, experimentally, in a clean vacuum tunneling junction, the tunneling current approximately decreases by a factor of 10 when the tip-sample distances increase by 0.1 nm. This characteristic grants the STM an exceptional lateral and vertical resolution, enabling detection of changes in object height as small as 10 picometer.

In this regard, another crucial progress that facilitated the development of the STM was the technology based in piezoelectric materials. By applying a voltage, these materials allowed for precise movement of the tip on the picometer scale, being compatible with the highly sensitive tunneling current. In a typical STM setup, a piezoelectric scanner element, typically a tubular piezo made of lead zirconate titanate, is utilized. This element comprises four metallic surface electrodes, governing the movement along the  $\pm X$  and  $\pm Y$  axes, with an additional electrode controlling movement along the  $Z$  axis for tip extension and retraction.

### Measurement modes

**Figure 179** shows the two main STM operation modes known as constant current and constant height. In constant current mode, a feedback loop continuously monitors the tunneling current between the tip and the sample, comparing it to a preset current setpoint. Any discrepancy between the measured current and the set current generates a signal, utilized as input for a Proportional-Integral Controller (PI) within a Digital Signal Processor (DSP). This controller calculates an output signal  $\Delta z$ , representing topographical variations, to compensate the discrepancies in current. The initial digital signal is then converted to an analog signal via a digital-analog converter (DAC). A High-Voltage Amplifier is also needed before applying to the  $Z$  electrode of the piezoelectric tube for precise movement, closing the feedback loop. **Figure 179 a** shows the profiles that typically are obtained in this mode where the current is kept constant while the tip height is tracked scanning the  $XY$  plane.



**Figure 179.** Schematics of the two main modes of scanning in STM, constant current mode and constant height mode.

On the other hand, the constant height mode (**Figure 179 b**) keeps the feedback loop open, and the measured signal is the tunneling current during XY plane scanning. Constant height mode enables faster scanning speeds, as the system is independent of the feedback response, and normally, higher image resolutions. However, it's important to note that operating in constant height mode increases the risk of sample damage, as the lack of feedback increases the potential for collision with the sample.

Finally, it is noteworthy to remark that both modes do not offer an accurate depiction of the height or shape of objects since the tunneling current, upon which the images are based, correlates with the local density of states (LDOS) of both the tip and probed object, as it will be discussed below. Consequently, the resulting images heavily relies on the applied bias voltage during the acquisition.

### The Tunneling Current

As it has been shown before, the wave function of the tunneling of electrons through a potential barrier depends exponentially on the size of the barrier. This behavior can be expressed by a transmission coefficient ( $T$ ) that quantifies the probability of finding an electron at the initial ( $z = 0$ ) or final ( $z = d$ ) positions of the tunneling barrier, being useful to understand the relation between tunneling current and density of states, as it will be shown below. The expression for  $T$  is given by:

$$T = \frac{\psi(d)^2}{\psi(0)^2} \propto e^{-2\kappa d} \quad (4.1.7)$$

Initial efforts to formulate a general expression for the tunneling current arose in the 1950s and 1960s, notably pioneered by Bardeen in the study of superconductors<sup>255</sup> and early transistors.

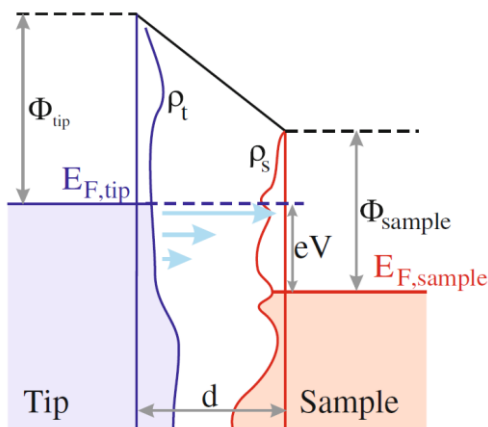
<sup>255</sup> J. Bardeen, *Physical Review Letters*, **1961**, *6*, 57–59.

Building upon this work, Tersoff and Hamman<sup>256</sup> (1983) derived an approximation for the tunneling current (see **Eq. (4.1.8)**) directly related to the density of states of both the tip ( $\rho_t$ ) and sample ( $\rho_s$ ):

$$I = \frac{4\pi e}{\hbar} \int_0^V \rho_t(E_F - V + \epsilon) \rho_s(E_F + \epsilon) T(d, \epsilon, V) d \quad (4.1.8)$$

Here,  $T(d, \epsilon, V)$  denotes the transmission factor of the current between tip and sample states,  $d$  represents the tip-sample distance,  $V$  stands for the bias voltage, and  $\epsilon$  denotes the energy relative to the sample's Fermi level.

At absolute zero temperature, electronic states below the Fermi levels of both tip and sample are occupied, aligning their levels when no bias voltage is applied. However, applying a bias voltage ( $V$ ) induces a relative displacement of their Fermi levels ( $\Delta E_F = V$ ). Consequently, electrons from occupied states in the tip can tunnel through the vacuum to unoccupied states in the sample, or vice versa depending on the bias polarity. This key feature, depicted in **Eq. (4.1.8)** and in **Figure 180** illustrates the fundamental relationship between tunneling current and density of states, enabling the measurement of the electronic properties of the sample.



**Figure 180.** Tunneling junction energy level diagram. The applied bias shifts the Fermi level by  $eV$ . Reproduced with permission of Springer Nature<sup>254</sup>.

### Scanning Tunneling Spectroscopy

The measured tunneling current is the contribution of all the occupied states tunneling from the tip to the surface (from  $E_F$  to  $V$  assuming a positive sample bias). However, if we

<sup>256</sup> a) J. Tersoff, D. R. Hamann, *Physical Review Letters*, **1983**, 50, 1998-2001. b) J. Tersoff, D. R. Hamann, *Physical Review B*, **1985**, 31, 805-813.

differentiate the expression for the tunneling current (eq. (4.1.8)) with respect to the bias, the main contribution to the current change for that specific energy is the density of states of the sample,  $\rho_s(\epsilon)$ :

$$\left. \frac{dI}{dV} \right|_{eV_{Bias}} \approx \frac{4\pi e^2}{\hbar} \rho_t(0) \rho_s(eV_{Bias}) |T(eV_{Bias}, V, d)| \quad (4.1.9)$$

This expression can be simplified assuming a constant transmission coefficient ( $T$ ) and tip density of states,  $\rho_t$ :

$$\frac{dI}{dV} \approx \rho_s(eV) \quad (4.1.10)$$

As commented, this  $dI/dV$  is proportional to the local density of states (LDOS) of the sample, facilitating being sensitive to various quantities that depend on the occupation state and the energy levels as: magnetic properties<sup>257</sup>, topological states<sup>258</sup> or material's bandgap<sup>259</sup>.

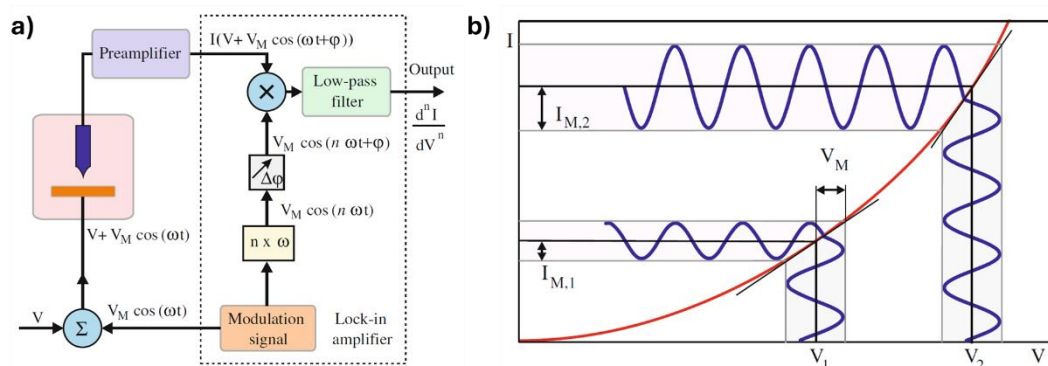
Experimental realization of the LDOS signal measurement can be done by numerical differentiation of the STM current. However, for a less noisy and more accurate measurement, a lock-in setup is commonly utilized as illustrated in **Figure 181 a**. In this setup, an AC reference signal with known frequency and phases (the modulation signal:  $V_M \cos \omega t$ ), is added to the applied DC bias voltage  $E_V$ . This allows the lock-in to discern the responses of the differential conductance. Only the contribution of the output signal that has the same frequency as the reference is deconvoluted. The uncorrelated phases are filtered out by the low-pass filter allowing us to measure the LDOS ( $dI/dV$ ) of the sample, at a specific energy and ranging different biases with great precision.

**Figure 181 b** shows the graphic representation of the measurement of the first derivative ( $dI/dV$ ) of the red I-V curve. Different factors may affect to the measurement of this property. Although the same modulation around values  $V_1$  and  $V_2$  are applied (blue line), the measured amplitude of the resulting modulated tunneling current is proportional to the slope of the I-V curve ( $dI/dV$ ) at  $V_1$  and  $V_2$ , respectively. Bigger oscillations ( $V_{Mod}$ ) imply better signal to noise ratios but reduces energy resolution, as can also be understood from **Figure 181 b**. A lower signal-to-noise can be compensated with higher tunneling currents, for the cost of risking the tip-sample junction integrity; or by increasing the acquisition time at expenses of a more time-consuming measurement.

<sup>257</sup> S. Song, J. Su, M. Telychko, J. Li, G. Li, Y. Li, C. Su, J. Wu, J. Lu, *Chem. Soc. Rev.*, **2021**, *50*, 3238–3262.

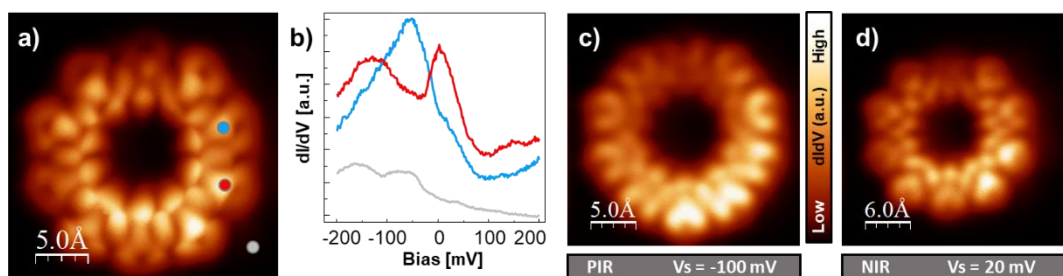
<sup>258</sup> D. J. Rizzo, G. Veber, T. Cao, C. Bronner, T. Chen, F. Zhao, H. Rodriguez, S. G. Louie, M. F. Crommie, F. R. Fischer, *Nature*, **2018**, *560*, 204–208.

<sup>259</sup> L. Talirz, P. Ruffieux, R. Fasel, *Advanced Materials*, **2016**, *28*, 6222–6231.



**Figure 181.** a) Experimental lock-in setup utilized for obtaining the  $dI/dV$  signal. Reproduced with permission of Springer Nature<sup>254</sup>. b) Graphic representation of the measurement of the first derivative of the I-V curve.

A combination of STS and surface scanning is also possible and useful to obtain the distribution of the LDOS at a certain energy with high spatial resolution. This technique is called  $dI/dV$  mapping, and the procedure, again, consists of scanning the area applying a DC bias  $E_V$ , and a constant AC modulation while monitoring the  $dI/dV$  to get a quantitative picture of the LDOS. **Figure 182** illustrates the electronic characterization of a molecule used in this thesis including a constant height STM image, a  $dI/dV$  point spectrum, and two  $dI/dV$  maps at selected energies.



**Figure 182.** Electronic characterization of 3.2.1-P10-Des-Con1 Molecule. a) Constant height STM image. b) Point spectra with color-coded location in a). c) and d)  $dI/dV$  maps for HOMO and LUMO with energies depicted in the bottom bar. Scanning parameters were as follows: (a) 2 mV; (b) Point spectra:  $V_{Mod} = 2$  mV; (c)  $V_{Mod} = 2$  mV; (d)  $V_{Mod} = 2$  mV.

#### 4.2.4 Atomic Force Microscopy

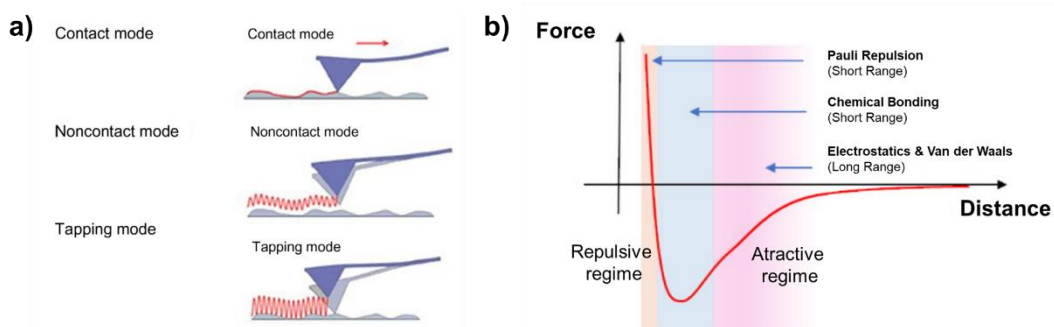
Despite the significant success that marked the development of the STM within the scientific community, its capabilities remained limited to conductive tips and samples. Motivated by this, Binnig et al. envisioned a new microscope based on a different property, the forces between the tip and the sample. In 1985, they pioneered the development of the Atomic Force Microscope (AFM)<sup>260</sup>.

<sup>260</sup> G. Binnig, C. F. Quate, and C. Gerber, *Physical Review Letters*, **1986**, 56, 930–933.



In this regard, a tip is attached to a cantilever and scanned over a surface while amplitude ( $A$ ) and frequency ( $f$ ) are measured, reflecting the tip-sample interactions. This tip-cantilever system can be understood and modeled as a simple harmonic oscillator with parameters like resonance frequency ( $f_0$ ), stiffness ( $k$ ), and quality factor ( $Q$ ). Therefore, measured amplitudes and frequencies can be related to the interactions (forces) between the tip and the sample.

In this thesis, we have employed a specific AFM mode known as non-contact AFM (nc-AFM). In this mode, the tip oscillates with an external actuator and approaches the surface without making physical contact, maintaining a distance where no permanent deformation occurs to either the tip or the sample, **Figure 183 a**. This distance typically ranges from a few angstroms to one nanometer, where the probe can sense short-range forces (e.g., Pauli repulsion or chemical bonding) and long-range forces (e.g., van der Waals or electrostatics), as described by the Lennard-Jones potential, **Figure 183 b**.



**Figure 183.** a) AFM general modes. b) Lennard Jones potential diagram showing different attractive and repulsive regimes and some of the interactions involved. a) was modified with Reproduced with permission of Elsevier<sup>261</sup>.

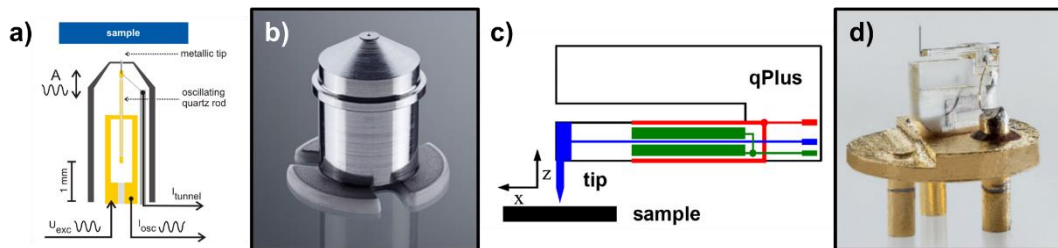
Nc-AFM sensors typically exhibit higher stiffness (approximately 40 N/m) and resonant frequencies compared to cantilevers used in other AFM modes. This increased stiffness is necessary to prevent the probe from snapping into contact due to the sensing of short-range interactions<sup>262</sup>, such as Pauli repulsion. SPM tips can be mounted onto these sensors to facilitate simultaneous nc-AFM and STM measurements. Among the most commonly used sensors for this purpose are the qPlus<sup>263</sup> and the Kolibri<sup>264</sup>. In the case of the Kolibri sensor, the oscillation occurs in the longitudinal axis with a resonant frequency of approximately 1 MHz<sup>264</sup>, see **Figure 184 a** and **b**. Conversely, the qPlus sensor (illustrated in **Figure 184 c** and **d**), the quartz resonator is mounted in a tuning fork-shaped where the tip is glued, presenting a resonant frequency of approximately 30 kHz. Both sensors were used in this thesis for obtaining the nc-AFM images.

<sup>261</sup> R. Asmatulu, W. S. Khan, in *Synthesis and Applications of Electrospun Nanofibers*, Elsevier, **2019**, pp. 257–281.

<sup>262</sup> F. J. Giessibl, *Phys. Rev. B*, **1997**, *56*, 16010–16015.

<sup>263</sup> Franz J Giessibl. *Principles and applications of the qplus sensor*, Springer, **2009**, pp. 121–142.

<sup>264</sup> a) F. J. Giessibl, F. Pielmeier, T. Eguchi, T. An, Y. Hasegawa. *Physical Review B*, **2011**, *84*, 125409. b) S. Torbrügge, O. Schaff, J. Rychen, *Journal of Vacuum Science & Technology B*, **2010**, *28*, C4E12-C4E20.



**Figure 184.** Kolibri sensor in a) and b) (schematics and real image), and q-plus sensor in c) and d) (schematics and real image).

A feedback loop monitors changes in amplitude ( $A$ ) or frequency ( $f$ ) of the sensor relative to a defined setpoint due to tip-sample interactions, with two main modes for signal control and monitoring: amplitude modulation (AM-AFM)<sup>260</sup> and frequency modulation (FM-AFM). In amplitude-modulation (AM-AFM) mode, the sensor is driven with a fixed initial frequency. While scanning the surface, the sensor’s resonant frequency changes, due to tip-sample interactions, but in this mode, the sensor is always driven to the fixed initial frequency, recording the corresponding decreases or increases in oscillation amplitude as the experimental signal. However, AM-AFM faces limitations when measuring at the atomic scale, particularly in UHV conditions, where altered sensor’s mechanical properties increase the quality factor ( $Q$ ), reducing operational bandwidth. The recovery time for amplitude using stiff sensors in UHV, such as the qPlus sensor or the kolibri in AM-AFM mode, can be too slow for typical acquisition times<sup>265</sup>.

On the other hand, Frequency Modulation Atomic Force Microscopy (FM-AFM), introduced in 1991<sup>265</sup>, consistently drives the sensor to its frequency resonance ( $f_0$ ) while simultaneously maintaining a constant amplitude ( $A$ ) and a phase difference of  $\pi/2$  (known as the resonance condition). Typically, the measured experimental parameter is the frequency shift ( $\Delta f$ ), representing the disparity between a reference resonance frequency (e. g. the resonance frequency when the tip is absence of interactions with the sample, far regime) and the resonance frequency at each point on the sample. FM-AFM signals are managed and adjusted through a feedback phase-locked-loop<sup>266</sup> for both frequency and amplitude precise analysis of tip-sample interactions.

Eq. (4.1.11) shows the relationship between the frequency of oscillation and the averaged forces present ( $F_{ts}$ ) between tip and sample in a full oscillation,

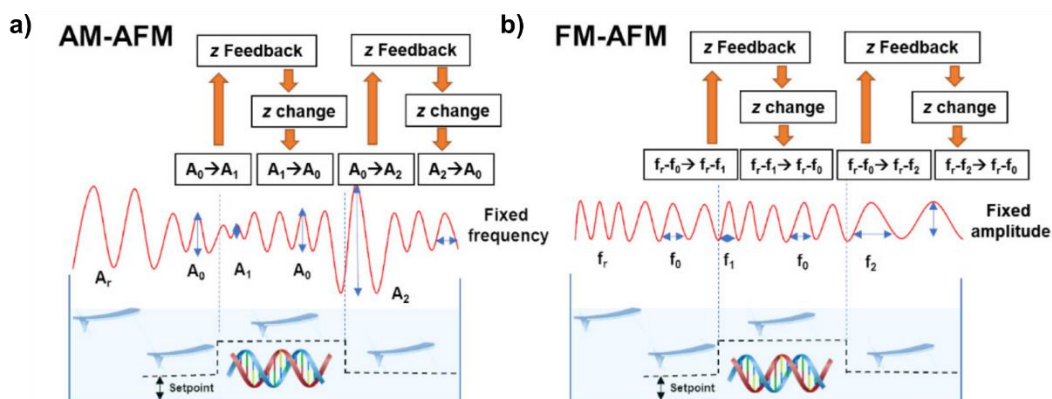
$$\Delta f = f - f_0 - \frac{f_0}{k_0 A^2} (AF_{ts}(t) \cos(2\pi f_0 t)) \tag{4.1.11}$$

<sup>265</sup> T. R. Albrecht, P. Grütter, D. Horne, and D. Rugar, *Journal of Applied Physics*, **1991**, 69, 668–673.

<sup>266</sup> L. Nony, A. Baratoff, D. Schär, O. Pfeiffer, A. Wetzel, E. Meyer, *Phys. Rev. B*, **2006**, 74, 235439.

The presence of non-conservative forces between tip and sample changes the amplitude of the oscillation and the energy needed to drive again the sensor to a constant amplitude will be the excitation or dissipation channel. Experimentally, the amplitude, phase, dissipation, and frequency shift contain all the information on the interaction of the tip with the sample, and it is possible to deduce a relationship between the frequency of oscillation and the averaged forces present between the tip and the sample in a full oscillation.

Finally, it is noteworthy commenting that both AM-AFM and FM-AFM modes can be conducted either in constant height mode; or in the other hand in the constant amplitude or in the constant frequency modes, as shown in **Figure 185**. Although the constant height FM-AFM mode was primarily utilized in this thesis, we employed the constant frequency mode to conduct the multipass technique for analyzing an out-of-plane molecule. Further details regarding this technique were provided in the Results chapter.



**Figure 185.** Schemas showing the operation of the Constant Amplitude AM-AFM mode and of the Constant frequency Shift FM-AFM mode. Reproduced with permission of MDPI<sup>267</sup>.

#### 4.2.5 Atomic-Molecular Manipulation

Besides characterizing surfaces, the SPM has demonstrated to be a powerful tool to manipulate the atomic scale since Eigler and Schweizer's groundbreaking work in 1990<sup>268</sup>, where they arranged the IBM letters on a Ni(110) surface by manipulating (sliding) Xenon atoms with the STM tip (**Figure 186**). Artificial structures as quantum corrals<sup>269</sup> and Lieb lattices<sup>270</sup> or single molecule reactions<sup>271</sup> have proven the scientific potential of molecular and atomic manipulation.

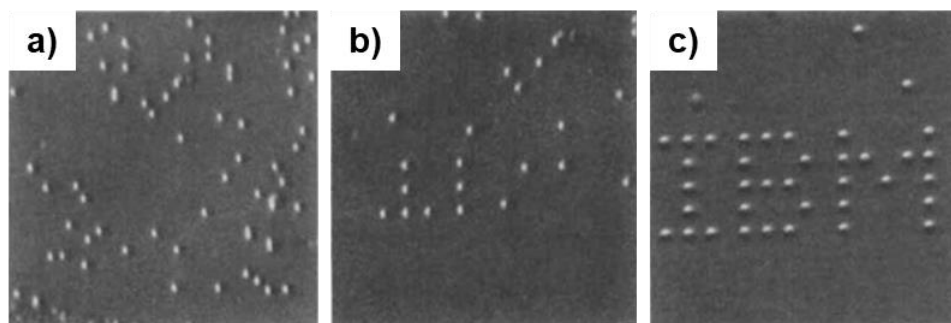
<sup>267</sup> E. Lipiec, K. Sofińska, S. Seweryn, N. Wilkosz, M. Szymonski, *Molecules*, **2021**, *26*, 6476.

<sup>268</sup> D. M. Eigler, E. K. Schweizer, *Nature*, **1990**, *344*, 524–526.

<sup>269</sup> M. F. Crommie, C. P. Lutz, D. M. Eigler, *Science*, **1993**, *262*, 218–220.

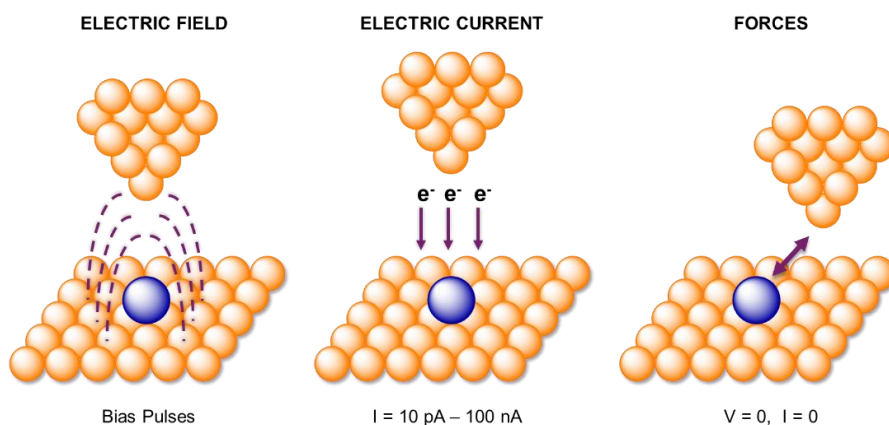
<sup>270</sup> M. R. Slot, T. S. Gardenier, P. H. Jacobse, G. C. P. van Miert, S. N. Kempkes, S. J. M. Zevenhuizen, C. M. Smith, D. Vanmaekelbergh, I. Swart, *Nature Physics*, **2017**, *13*, 672–676.

<sup>271</sup> a) S.-W. Hla, L. Bartels, G. Meyer, K.-H. Rieder, *Phys. Rev. Lett.* **2000**, *85*, 2777–2780. b) F. Albrecht, S. Fatayer, I. Pozo, I. Tavernelli, J. Repp, D. Peña, L. Gross, *Science* **2022**, *377*, 298–301.



**Figure 186.** Sequence of STM images showing the manipulation of xenon atoms on a nickel (110) surface during the construction of the IBM pattern. Reproduced with permission from Nature Publishing Group<sup>268</sup>.

Understanding the tip-sample interactions occurring within the tunneling junction of the STM is essential to manipulate the matter at the atomic level. **Figure 187** shows the main tip-sample interactions<sup>272</sup> encompassing: the electrical field between them, the electron tunneling current and the forces between the tip and the surface. Specific modifications to the position of the atom or molecule, or the inducement of chemical reactions in them, can be performed by utilizing one or a combination of these interactions.



**Figure 187.** Interactions of a STM tunneling junction that may participate in a manipulation event.

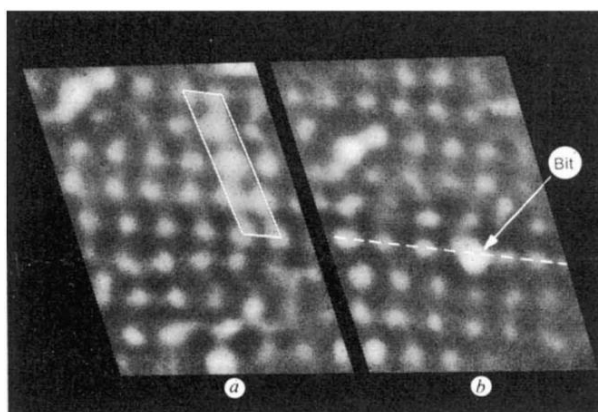
### Electric Field

Although the molecule or atom may move during this process (and in the process of injection of electrons, see below), we will only focus on the tip-induced reactions. When the STM tip is brought into proximity with the surface and a bias voltage is applied, an electric field of

<sup>272</sup> C. Wang, L. Chi, A. Ciesielski, P. Samorì, *Angew. Chem. Int. Ed.*, **2019**, *58*, 18758–18775.

approximately  $100 \text{ V cm}^{-1}$  can be generated<sup>273</sup>, being sufficient to break interatomic covalent bonds. This electric field exhibits a circular gradient over the surface, and because the strength of this electric field is greatest at the tip's apex, it becomes possible to manipulate surfaces with true atomic accuracy.

In this regard, Swartzentruber and colleagues achieved a milestone by demonstrating the creation of an atomic-scale "bit" through the removal of a single Ge atom from a Ge(111)- $2 \times 8$  surface<sup>274</sup>. The defect-free region chosen for atom manipulation was imaged with atomic resolution under a scanning bias voltage of approximately 1 V. By increasing the tip-to-surface bias to around 4 V, successful dissociation of covalent Ge-Ge bonds was initiated. This was subsequently followed by retracting the tip from the surface by approximately  $1 \text{ \AA}$  and reducing the bias voltage back to 1 V to continue imaging the surface, see **Figure 188**.



**Figure 188.** STM images of a manipulation performed by electric field in a reconstructed (111) germanium surface ( $50 \times 65 \text{ \AA}$ ). **a)** The surface before modification. A single unit cell of the  $c$ -( $2 \times 8$ ) reconstruction is highlighted. **b)** The same region after the surface modification. Reproduced with permission from Nature Publishing Group<sup>274</sup>.

### Injection of Electrons

An alternative approach to break bonds and induce reactions in atoms or molecules is the injection of electrons from the tip to the sample. Depending on the energy, the electron injection can be categorized in two approaches: field emission and inelastic tunneling.

In the field emission process, the STM tip serves as an electron emission gun. High-energy electrons (typically above 3 eV) can be emitted when the bias voltage exceeds the work function of the tip, which is approximately 4.5 V for tungsten, for instance. To prevent an excessively large tunneling current, the separation between the tip and the surface must be increased above  $10 \text{ \AA}$ . Consequently, field emission manipulations lack of bond selectivity affecting significantly

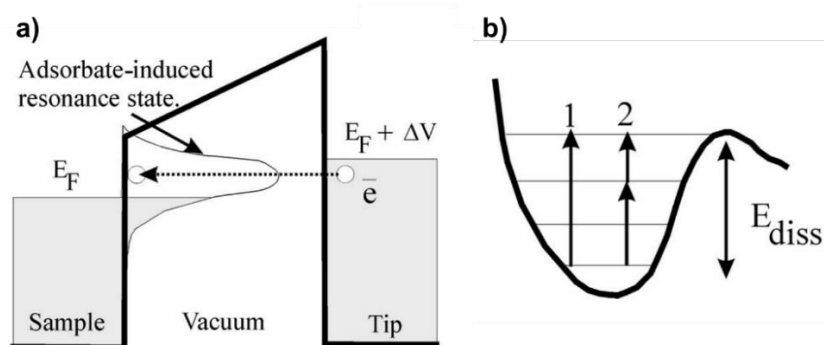
<sup>273</sup> H. D. Beckey, *J. Mass Spectrom. Ion Phys.*, **1969**, 2, 500-502.

<sup>274</sup> R. S. Becker, J. A. Golovchenko, B. S. Swartzentruber, *Nature*, **1987**, 325, 419–421.

large areas (approximately  $100 \text{ \AA}^2$ ). In this regard, at the early 1990s, Avouris and coworkers<sup>275</sup> demonstrated the dissociation of  $\text{B}_{10}\text{H}_{14}$  and  $\text{O}_2$  molecules on  $\text{Si}[111]$  using field emission electrons (high STM biases  $\geq 4 \text{ V}$  and  $\geq 6 \text{ V}$ , respectively).

On the other hand, chemical transformations can also be conducted with inelastic tunneling electrons when operating with small tip-to-surface distances (less than  $1 \text{ nm}$ ) and low bias voltages. The tunneling electrons can transfer energy to the molecule by means of a temporary electron attachment to the molecule in an “adsorbate-induced resonance state”<sup>276</sup>, **Figure 189 a**. The dissociation of the molecule occurs when the transferred energy from the temporary electron to the molecule surpasses the dissociation barrier.

**Figure 189 b** depicts the two main processes for Inelastic Electron Tunneling (IET)<sup>277</sup>, regarded as single electron excitation (1 in **Figure 189 b**), and multiple electrons excitations (2 in **Figure 189 b**). In a single excitation process, the energy transferred from a lone tunneling electron is adequate to break the molecular bond. Conversely, in multiple excitations, numerous electrons participate in the bond-breaking process. When an electron transfers energy to the molecule, it prompts excitation at an upper energy level, subsequently raising the excited energy level through energy transfers by other electrons. The dissociation of the molecule occurs when this cumulative energy surpasses the dissociation barrier.



**Figure 189.** Inducing reactions through inelastic tunneling electrons. Reproduced with permission from Annual Reviews<sup>278</sup>

Inelastic tunneling enables the selective targeting of a single bond due to the short distances and low biases used. Moreover, the number of tunneling electrons can be adjusted to control the reaction rate and pathway, thereby achieving localized and controllable bond dissociations. On this subject, different tip-induced reactions have been described in the literature, finding as

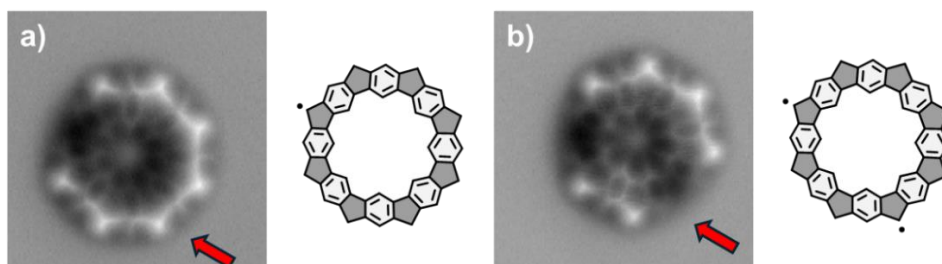
<sup>275</sup> a) G. Dujardin, R. Walkup, P. Avouris, *Science*, **1992**, *255*, 1232–1234. b) R. Martel, P. Avouris, I. W. Lyo, *Science*, **1996**, *272*, 385–88.

<sup>276</sup> a) S. W. Hla, L. Bartels, G. Meyer, K. H. Rieder, *Phys. Rev. Lett.*, **2000**, *85*, 2777–80. b) L. J. Lauhon, W. Ho, *Phys. Rev. Lett.*, **2000**, *84*, 1527–30.

<sup>277</sup> B. C. Stipe, M. A. Rezaei, W. Ho, S. Gao, M. Persson, B. I. Lundqvist, *Phys. Rev. Lett.*, **1997**, *78*, 4410–13.

<sup>278</sup> S. W. Hla, K. H. Rieder, *Annu. Rev. Phys. Chem.*, **2003**, *54*, 307–330.

examples: skeletal rearrangements<sup>279</sup>, the Bergman cyclization<sup>280</sup>, debrominations<sup>281</sup> or C-H activations<sup>282</sup>. In this thesis, we have mainly manipulated molecules through inelastic tunneling electrons to activate hydrogens from  $sp^3$  pentagonal rings to create radicals at those positions (C-H activation), **Figure 190**.



**Figure 190.** Tip-induced activation of a  $sp^3$  pentagonal ring performed in this thesis through the injection of inelastic electrons.

### Force Manipulation

Lastly, it is also possible to manipulate atoms and molecules through the tip-sample interaction forces. These manipulations are typically conducted at close distances and with low biases and currents<sup>278</sup>. Although force manipulations may induce transformations, as reported isomerization<sup>283</sup> or tautomerization<sup>284</sup>, in this work we employed this kind of manipulation to displace molecular nanostructures in the substrate.

Depending on the displacement direction of the molecule or atom (either perpendicular or parallel to the surface), we can categorize the manipulation technique as either vertical or lateral manipulation. In a vertical manipulation, the molecule is picked up by the tip, which may improve the imaging quality. This vertical manipulation is routinely performed to pick up CO molecules to conduct high resolution STM and nc-AFM images<sup>285</sup>.

On the other hand, during the lateral atomic manipulation, the molecule is moved along the surface without losing the contact. Three distinct manipulation modes have been investigated: (i) the pulling mode, utilized when the final tip apex atom is positioned "after" the adsorbate (in

<sup>279</sup> N. Pavlíček, P. Gawel, D. R. Kohn, Z. Majzik, Y. Xiong, G. Meyer, H. L. Anderson, L. Gross, *Nature Chem.*, **2018**, *10*, 853–858.

<sup>280</sup> B. Schuler, S. Fatayer, F. Mohn, N. Moll, N. Pavlíček, G. Meyer, D. Peña, L. Gross, *Nature Chem.*, **2016**, *8*, 220–224.

<sup>281</sup> **a)** S. Kawai, O. Krejčí, T. Nishiuchi, K. Sahara, T. Kodama, R. Pawlak, E. Meyer, T. Kubo, A. S. Foster, *Sci. Adv.*, **2020**, *6*, 8913. **b)** Q. Zhong, A. Ihle, S. Ahles, H. A. Wegner, A. Schirmeisen, D. Ebeling, *Nat. Chem.*, **2021**, *13*, 1133–1139.

<sup>282</sup> C. Zhao, Q. Huang, L. Valenta, K. Eimre, L. Yang, A. V. Yakutovich, W. Xu, J. Ma, X. Feng, M. Juriček, R. Fasel, P. Ruffieux, C. A. Pignedoli, *Phys. Rev. Lett.*, **2024**, *132*, 046201.

<sup>283</sup> A. Ishii, A. Shiotari, Y. Sugimoto, *Chem. Sci.*, **2021**, *12*, 13301–13306.

<sup>284</sup> J. N. Ladenthin, T. Frederiksen, M. Persson, J. C. Sharp, S. Gawinkowski, J. Waluk, T. Kumagai, *Nature Chem.*, **2016**, *8*, 935–940.

<sup>285</sup> L. Gross, F. Mohn, N. Moll, P. Liljeroth, and G. Meyer, *Science*, **2009**, *325*, 1110–1114.

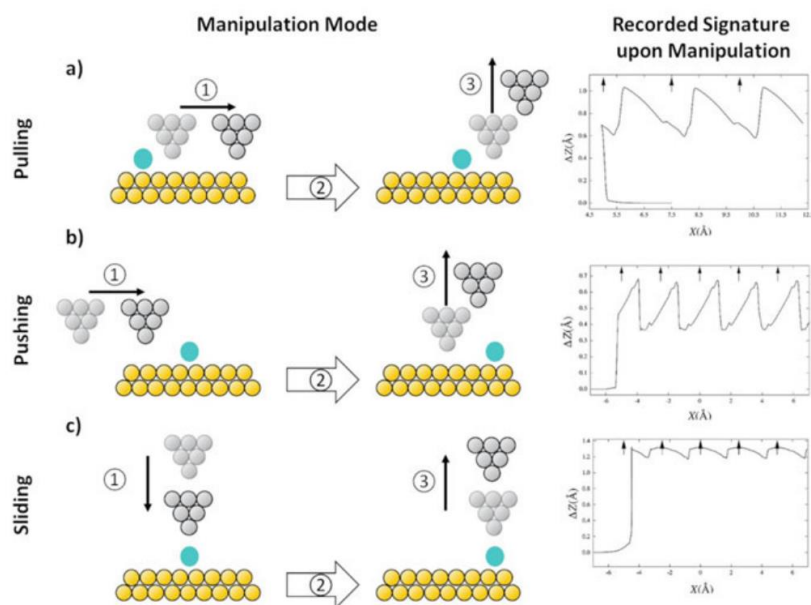
the direction of manipulation) and the molecular entity is displaced by attractive forces, (ii) the pushing mode, employed when the apex is positioned "before" the adsorbate (in the direction of manipulation) and repulsive forces are used, and (iii) the sliding mode, when the tip is positioned "on top" of the adsorbate creating an attractive potential energy trap between the tip apex and the adsorbate, (**Figure 191**). To ensure precise manipulation and avoid a blind process, changes in the tunneling current ( $I(t)$ ), in constant height mode, or changes in the tip height ( $\Delta z$ ), in constant current mode, can be monitored during the manipulation sequence.

In the manipulation sequence of a single atom adsorbate in constant current mode, the pulling mode is characterized by two primary features: first, as the tip apex moves laterally away from the atom, the  $\Delta z$  signal shows a gradual decrease (the tip approaches to the surface to keep the current constant because the adsorbate is further) followed by a sudden increase due to the shift of the atom to its next stable position on the surface (**Figure 191 a**).

Conversely, the pushing mode exhibits a reverse sawtooth profile of the  $\Delta z$  signal in comparison with the pulling mode. The  $\Delta z$  signal increases (the tip retracts from the surface) due to the repulsive interaction with the adsorbate when moving the tip towards it. When this interaction is stronger than the adsorption energy, the adsorbate moves to the next stable position on the surface and the  $\Delta z$  signal decreases (the tip approaches to the surface to keep the current constant because the adsorbate is far) (**Figure 191 b**).

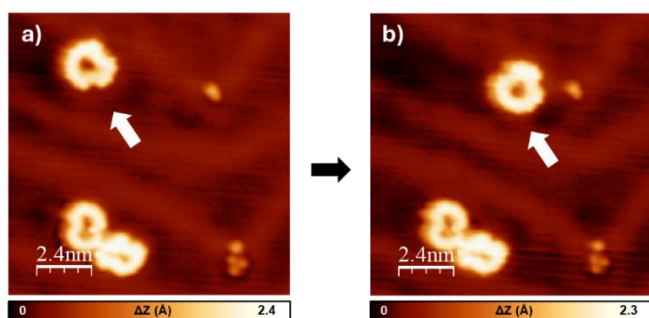
Finally, in the sliding mode, a minimal variation in the  $\Delta z$  signal occurs when the atom is laterally displaced on the surface. Similar interpretations of manipulation signals can be derived for constant-height mode manipulation of a single atom regarding the tunneling current (**Figure 191 c**).





**Figure 191.** Manipulation modes by force interactions in constant current mode. Reproduced with permission from Springer Link<sup>286</sup>.

The lower surface mobility of large molecules makes difficult their manipulation and the reported experimental evidences show a better success rate in constant height mode with the pushing mode<sup>287</sup>. Lateral atomic manipulations performed in this thesis have been conducted in constant height mode.



**Figure 192.** Lateral movement of a molecule on Au(111) performed in this thesis.

<sup>286</sup> F. Moresco, C. Joachim, Eds., *Single Molecule Mechanics on a Surface: Gears, Motors and Nanocars*, Springer International Publishing, Cham, **2023**.

<sup>287</sup> a) L. Gross, F. Moresco, P. Ruffieux, A. Gourdon, C. Joachim, K. H. Rieder, *Physical Review B*, **2005**, *71*, 165428.

b) J. Mielke, S. Selvanathan, M. Peters, J. Schwarz, S. Hecht, L. Grill, *Journal of Physics: Condensed Matter*, **2012**, *24*, 394013.

### 4.2.6 Tip Functionalization & High-Resolution Images

After understanding the basics on SPM and the different approaches to manipulate the sample, it is important to comment on the role of functionalizing tips and its impact in the measurements.

The spatial conformation and valence orbitals of the atoms or molecules at the probes affect the sensitivity of the measurements, finding crucial differences depending on the tip's wave function. Several theoretical studies have delved into this topic<sup>288</sup>. In this regard, Tersoff and Hamann demonstrated that, for s-wave tip states, STM images approximately resemble the local density of states determined by the modulus squared of the sample wave functions at the Fermi energy. In contrast, for p-wave tip states, STM images are anticipated to reveal spatial derivatives of sample wave functions reflected in sharper features in the STM images, as described by Chen's derivative rule<sup>289</sup>.

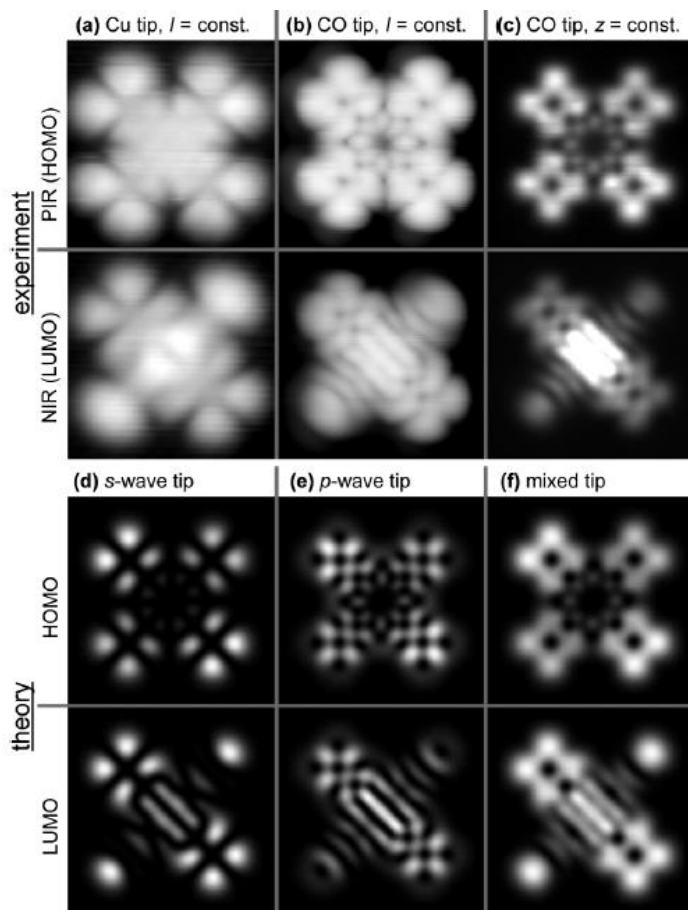
In relation, Persson and coworkers<sup>290</sup> analyzed the frontier molecular orbitals of a Naphthalocyanine molecule with a CO tip, showing an increased lateral resolution compared with those of the bare tip (Cu tip), **Figure 193 a, b and c**. Additionally, they performed calculations using a Tersoff - Hamann approach demonstrating contributions of p-wave tip states to those images obtained with the CO tip, as can be seen in **Figure 193 d, e and f**.

---

<sup>288</sup> J. Tersoff, D. R. Hamann, *Phys. Rev. B*, **1985**, *31*, 805.

<sup>289</sup> **a)** C. J. Chen, *J. Vac. Sci. Technol. A*, **1988**, *6*, 319. **b)** C. J. Chen, *Phys. Rev. B*, **1990**, *42*, 8841.

<sup>290</sup> L. Gross, N. Moll, F. Mohn, A. Curioni, G. Meyer, F. Hanke, M. Persson, *Phys. Rev. Lett.*, **2011**, *107*, 086101.

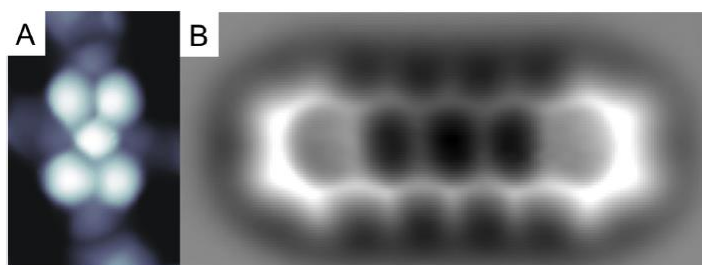


**Figure 193.** Naphthalocyanine on NaCl (2ML) on Cu(111) measured using a Cu tip and a Co tip. HOMO is measured at  $V = -1.65$  V while LUMO at  $V = 0.60$  V. Calculated images are obtained at  $z_0 = 5.0$  Å of the HOMO and LUMO with a *s*-wave tip a *p*-wave tip and with a mixed tip. Reproduced with permission of<sup>290</sup>

On the other hand, the increased resolution in STM images is not only enhanced by the selection rules governing the tunneling process (as seen before), but also by the lateral bending of the molecule on the tip while scanning the sample. In this regard, Temirov and coworkers, in 2008<sup>291</sup>, resolved the hexagonal pattern of a perylenetetracarboxylic dianhydride molecule, PTCDA, thanks to a STM tip functionalized with hydrogen (**Figure 194 a**). Shortly after, Leo Gross and his team got a similar result on nc-AFM measurements of pentacene using a CO molecule attached to a tip<sup>292</sup> (**Figure 194 b**).

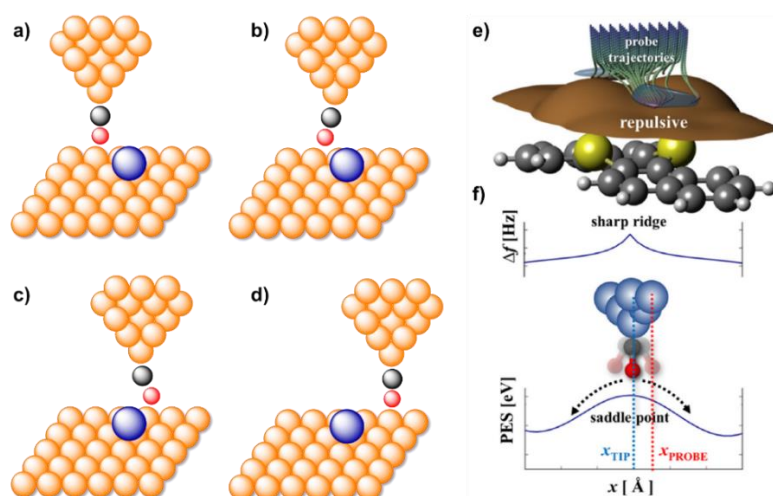
<sup>291</sup> R. Temirov, S. Soubatch, O. Neucheva, A. C. Lassise, F. S. Tautz, *New Journal of Physics*, **2008**, *10*, 053012.

<sup>292</sup> L. Gross, F. Mohn, N. Moll, P. Liljeroth, G. Meyer, *Science*, **2009**, *325*, 1110–1114.



**Figure 194.** High resolution STM and nc-AFM images of molecules obtained with functionalized tips. **a)** Experimental constant height HR-STM  $dI/dV$  figure of PTCDA on Au(111) obtained with H-tip at  $V_{\text{bias}} = -1.6$  V. Reproduced with permission of IOP Publishing Ltd<sup>291</sup>. **(b)** Constant height frequency shift nc AFM image of a pentacene molecule on a Cu(111) surface acquired with a CO-tip. Reprinted with permission from AAAS<sup>292</sup>.

The appearance of sharply resolved structural resolution in **Figure 194**, is due to strong lateral relaxations of the probe particle attached to the metallic tip apex. **Figure 195 a to d** schematically shows the idea of the lateral relaxation of the probe particle. In addition, **Figure 195 e** shows the trajectories that exhibits the probe particle at close distances while scanning the dibenzo[a,h]thianthrene (DBTH) molecule. These probe trajectories (relaxations) follow the potential energy basins (attractive regions) due to the Pauli repulsion (where the maximum electronic density is located). **Figure 195 f** shows the produced sharp edge in the frequency shift signal (top) coinciding with the borders of neighboring basins (bottom curve of the potential energy surface (PES)). These sharp edges cause the enhanced resolution in the SPM images.

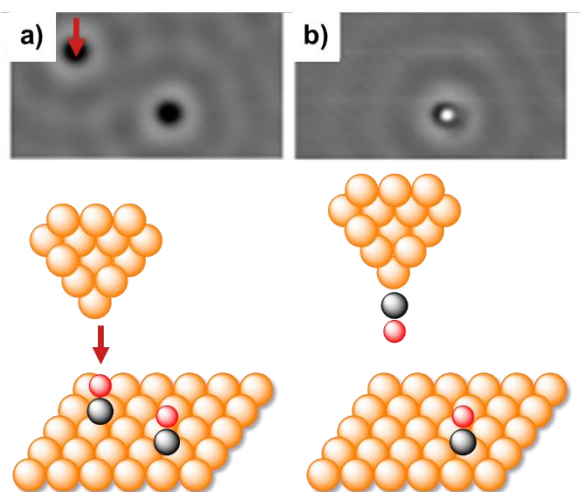


**Figure 195.** Lateral bending of the probe particle while scanning a surface. **a) to d)** Simple schematics showing the relaxation of the probe particle. **e)** Probe trajectories and basins regions while scanning a DBTH molecule. **f)** Appearance of the sharp edge in the frequency shift due to convex shape of the potential energy surface (PES). **e)** and **f)** Reproduced with permission of Top Science<sup>293</sup>

<sup>293</sup> P. Jelínek, *J. Phys.: Condens. Matter*, **2017**, *29*, 343002.

In this thesis, we have mainly employed CO as probe particles to obtain high resolution images. In this regard, after deposition of the molecules of interest on the surface, the SPM chamber was exposed to a CO atmosphere (controlling the pressure with a leak valve typically to  $\sim 10^{-8}$  mBar) and, subsequently, a CO molecule was picked-up to scan the surface.

The typical procedure that we followed to pick a CO began preparing a clean metal tip by controlled indentation into the metal surface. Afterwards, two different protocols were conducted to pick the CO molecule. On the one hand, we scanned the surface in constant current mode at  $\sim 110$  mV and 300 pA until observing an improvement in the image resolution, indicating the decoration of the tip. An alternative way to realize that the CO tip was achieved was the characteristic contrast change when scanning other CO molecules, switching from a “depression” contrast **Figure 196 a**, to a characteristic “sombbrero” shape during conventional STM<sup>294</sup>, **Figure 196 b**.



**Figure 196.** Change in contrast when decorating the tip with a CO molecule. The red arrow depicts the CO molecule picked up. In the schemes, the black sphere represents the carbon atom and the red sphere depicts the oxygen atom. STM images were adapted with permission from The American Association for the Advancement of Science<sup>294</sup>.

On the other hand, the CO molecule was also picked up through a “vertical manipulation” in constant height mode. In this procedure, we located the tip on top of a CO molecule with typical parameters of 100 mV and 100 pA until a drastic jump in the tunneling current was observed.

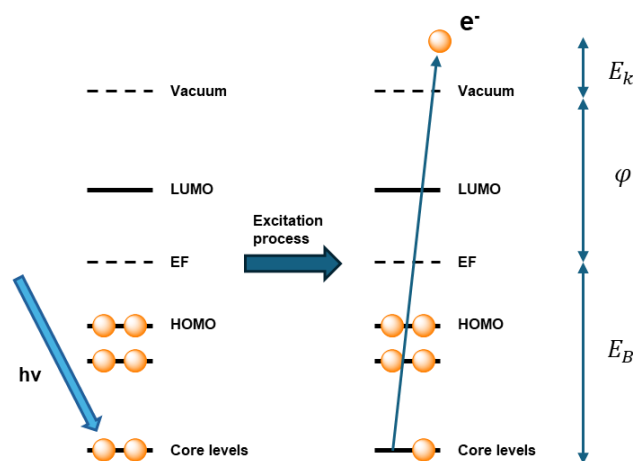
<sup>294</sup> L. Gross, F. Mohn, N. Moll, P. Liljeroth and G. Meyer, *Science*, **2009**, 325, 1110–1114.

### 4.2.7 Photoemission Spectroscopy

Lastly, in this thesis, X-rays photoemission spectroscopy (XPS) was conducted to obtain chemical information after performing some on-surface reactions. In a more general way, photoemission spectroscopy is a technique based on the photoelectric effect, where electrons are emitted from a solid due to their excitation by light. This effect was discovered by Heinrich Hertz<sup>295</sup> and Wilhelm Hallwachs<sup>296</sup> in 1887 and explained by Einstein in 1905<sup>297</sup>. In this technique, a sample is irradiated with X-rays. The atoms of the sample absorb the radiation getting excited and releasing electrons. These ejected electrons have a kinetic energy determined by a formula that relates the energy of the absorbed photon, the binding energy of the emitted electron, and the work function of the sample:

$$E_{kin} = h\nu - E_B - \varphi \quad (4.1.12)$$

where  $E_{kin}$  is the kinetic energy of the emitted electron,  $h\nu$  is the photon energy,  $E_B$  is the binding energy of the emitted electron and  $\varphi$  is the sample work function. **Figure 197** shows a scheme of the process.



**Figure 197.** Schematics of the XPS physical principle.

The kinetic energy of the emitted electron is measured as a function of the photoelectron intensity (the number of photoelectrons detected at the analyzer). This kinetic energy is then converted into binding energy through the relation (4.1.12), which provides information about the energy levels of the atoms in the sample and their chemical surroundings<sup>298</sup>. Several factors influence the measured photoelectron intensity as: the photoionization cross-section of the

<sup>295</sup> H. Hertz, *Annalen der Physik und Chemie*, **1887**, 267, 983–1000.

<sup>296</sup> W. Hallwachs, *Annalen der Physik und Chemie*, **1888**, 269, 301–312.

<sup>297</sup> A. Einstein, *Annalen der Physik*, **1905**, 322, 132–148.

<sup>298</sup> D. Briggs and M.P. Seah, *Practical Surface Analysis*, Vol.1, New York: Ed. Wiley, **1990**.

element, the mean free path of the photoelectrons and the distribution of the atomic species on the substrate. This relationship is given by:

$$I = \frac{J_I \sigma_A (h\nu_I) L_A^Z(Y_e, h\nu_I) \Omega_d}{\cos \theta_I} \frac{1}{4\pi} \int_0^d N(x) e^{-\frac{x}{\lambda \cos \theta_d}} dx \quad (4.1.13)$$

where  $J_I$  is the number of incident photons,  $\sigma_A$  is the photoionization cross-section of element A,  $L_A^Z$  is the emission asymmetry factor,  $\Omega_d$  is the detection solid angle,  $d$  is the distance from the surface to the bulk along we integrate the emitters density,  $N(x)$  is the emitters density (atomic density of the surface),  $x$  is the position,  $\theta$  is the incident or detection angle depending on the suffix and  $\lambda$  is the photoelectron mean free path. The suffix  $d$  refers to the detection while the suffix  $I$  is relative to the incident beam.

The measurement of the kinetic energy of the photoelectrons (photoelectron intensity) is performed in UHV conditions, and in a hemispherical electron analyzer for energy filtering, and an electron multiplier like a channeltron or a channelplate as a collector. Depending on the energy of the radiation, different sources are used, like standard X-Ray guns sources with a double anode of Mg ( $K_\alpha$ ,  $h\nu=1253.6$  eV) and Al ( $K_\beta$ ,  $h\nu=1486.6$  eV) for X-Rays. Additionally, synchrotron radiation can also be used as an illumination source exhibiting higher energy binding resolutions compared with a common laboratory setup<sup>299</sup>, meV in the synchrotron vs 0.1 to 0.7 eV resolutions in laboratories.

<sup>299</sup> G. Margaritondo, *Introduction to Synchrotron Radiation*, Oxford: Oxford University Press, 1988.





## 5 CONCLUSIONS



Based on the obtained results after the experimental work carried out during this thesis, we can draw the following conclusions:

- **Relative to objective 1**

- We have experimentally studied the thermal rearrangement on Au(111) of a cycloheptatrienone (seven-membered ring) moiety, embedded in a chevron-like GNR, into either a phenyl or a cyclopentadienone group through an unprecedented Retro-Buchner reaction. The stability of the cycloheptatrienone was guaranteed on Au(111) until  $\sim 310$  °C by means of STM and XPS.

- We have assessed the synthesis of a GNR containing non-benzenoid cyclopenta[c,d]azulene moieties on Au(111). The rearrangement mechanism of the dibenzo[a,e]cyclooctene moiety into the cyclopenta[c,d]azulene moiety was studied by means of STM and theoretical simulations (QM/MM) showing a remarkably specificity regarding the initial diastereomeric configuration related to the convexity-concavity of the eight-membered ring. This study manifests the new possibilities that the on-surface synthesis may offer due to the 2D environments where the reactions take place where the breakage of symmetry induced by the substrates play a role. The non-benzenoid synthesized GNR narrowed the electronic bandgap in comparison with other reported chevron-like GNRs, converting it into a good candidate for optoelectronic applications.

- We have successfully synthesized a graphene polymer containing extended saddle-shaped hepta[5]helicene moieties within each monomer. This study probes the feasibility of using precursors already cyclodehydrogenated in solution to avoid high temperatures related with cyclodehydrogenation steps in the on-surface synthesis of graphene nanostructures. This strategy opens the pave for the fabrication of more intricate and curved graphenic nanostructures.

- **Relative to objective 2**

- We have demonstrated the versatility of an in-solution synthetic strategy developed for the preparation of molecular precursors (from a 6-units to a 14-units precursor) towards differently sized cyclopenta-ring-fused oligo(*m*-phenylene) macrocycles.

- We have on-surface synthesized and electronically characterized a family of cyclopenta-ring-fused oligo(*m*-phenylene) macrocycles bearing eight, nine and ten units. Among them, the eight-unit macrocycle performed a positive curvature due to an inner strain of the structure, exhibiting a  $\sim 0.9$  eV HOMO-LUMO gap on Au(111). Alternatively, the nine-unit macrocycle showed a flat configuration with a magnetically active doublet ground state, and an exotic annulene-within-annulene structure with two concentric aromatic ring currents. Finally, the ten-unit macrocycle showed radical-surface interactions with either planar structures, with a tilt relative to the surface, or saddle-shaped curved structures. These different structures exhibited a very

short HOMO-LUMO gaps (from  $\sim 0.12$  eV to  $\sim 0.14$  eV). In this regard, the synthesized family of macrocycles present promising properties for future applications in optoelectronics and or spintronics.

- We have successfully synthesized a family of endo-products related to the cyclopenta-ring-fused oligo(*m*-phenylene) macrocycles bearing ten, eleven and twelve units. Different endo-isomers were structurally characterized by means of nc-AFM and STM, presenting, in its majority, a curved structure due to the strong radical-surface interactions. Further studies need to be conducted to unravel the possible intriguing electronic and magnetic properties of these compounds.

- **Relative to objective 3**

- We have successfully prepared a chevron-like GNR presenting local positive curvature in form of “nanodomes” proving that the strategy to induce curvature in graphene nanostructure through the radical-surface interaction is viable. The inspection of the electronic properties showed how the curvature induced by the interaction modified the bandgap shifting the CB in comparison with its flat and hydrogenated counterpart. This work proves how electronic properties can be tailored through the combination of interactions with the surface and curvature in the graphene nanostructures.

- **General conclusion**

As a general conclusion, it can be drawn that although graphene nanostructures tend to planarize on top of metallic surfaces, maximizing the Van der Waals interactions with them, there is still room for the on-surface synthesis of curved graphene nanostructures through some of the synthetic methodologies explored in this thesis: the utilization of already curved precursors without the employment of high temperatures in the on-surface reactions, the use of properly sized precursors to induce the curvature due to inner strain of the structures, or the use of radical-surface interactions to curve the structures.

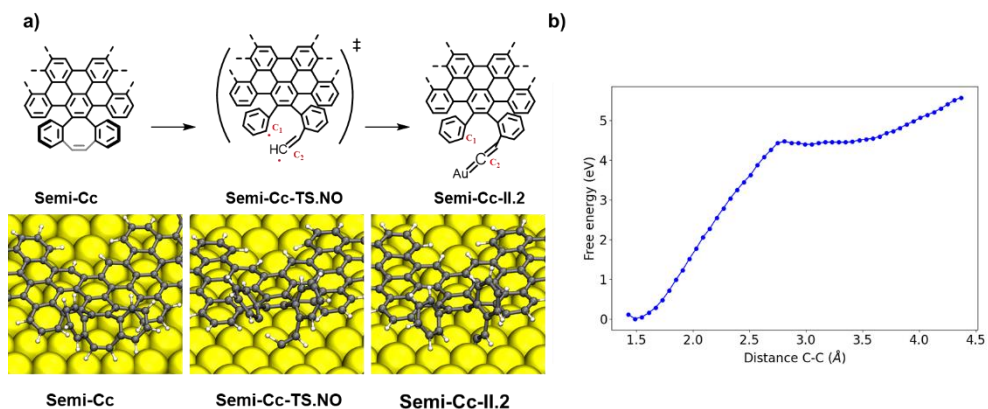




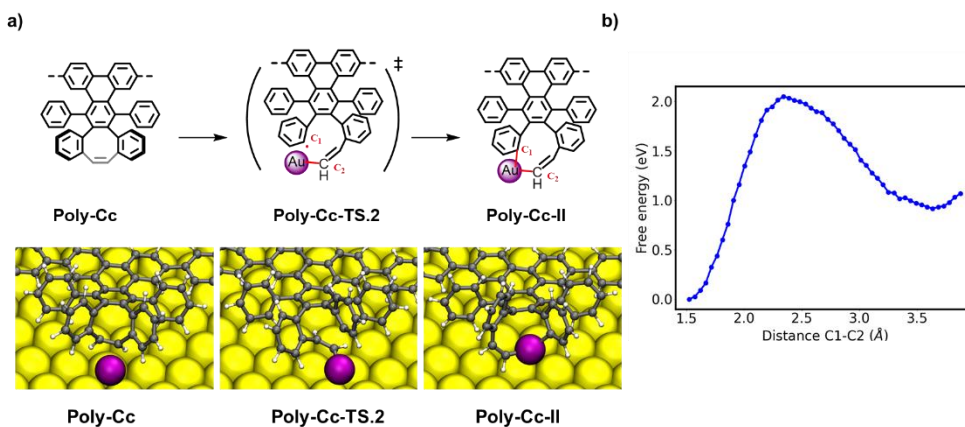
6 ANNEXES





QM/MM calculations**STEP 1 – Semi-Cc to Semi-Cc-II, NO Au ADATOM**

**Figure A 1.** QM/MM simulations for Step 1 of the rearrangement from **3.1.2-Semi-Cc** to **3.1.2-Semi-Cc-II.2** without the presence of the Au adatom. **a)** Chemical models (top) were extracted from the QM/MM simulations (bottom). **b)** Free energy diagram for the process.

**STEP 1 – Poly-Cc to Poly-Cc-II (C1-C2)**

**Figure A 2.** QM/MM simulations of the first step of the rearrangement for the polymer **3.1.2-Poly-Cc** regarding the C1-C2 bond breakage. **a)** Chemical models (top) extracted from QM/MM simulations (bottom). **b)** Free energy diagram of the process.

## STEP 1 – Poly-Cc to Poly-Cc-II.2 (C2-C3)

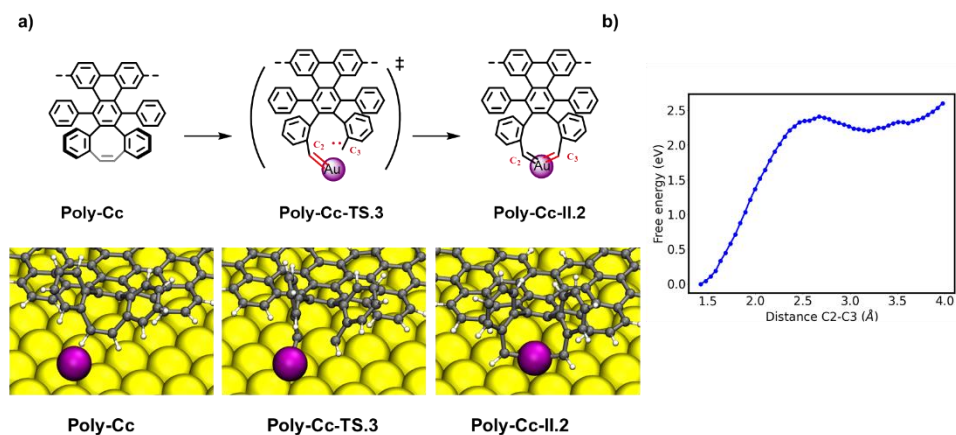


Figure A 3. QM/MM simulations of the first step of the rearrangement for the polymer 3.1.2-Poly-Cc regarding the C2-C3 bond breakage. a) Chemical models (top) extracted from QM/MM simulations (bottom). b) Free energy of the process.

## STEP 1 – Semi-Cx to Semi-Cx-II

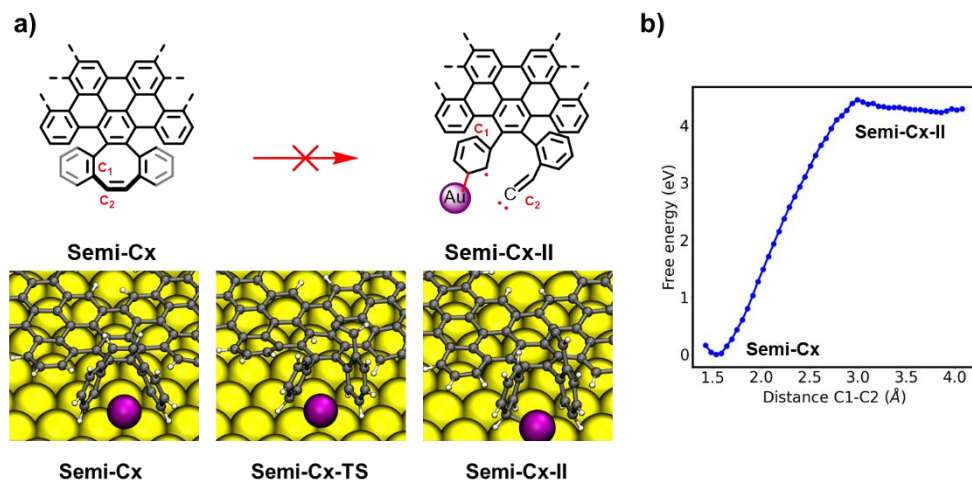


Figure A 4. QM/MM simulations for Step 1 of the rearrangement from 3.1.2-Semi-Cx to 3.1.2-Semi-Cx-II. a) Chemical models (top) were extracted from the QM/MM simulations (bottom). b) Free energy diagram for the process.

## STEP 1 - Semi-Cc to Semi-Cc-II

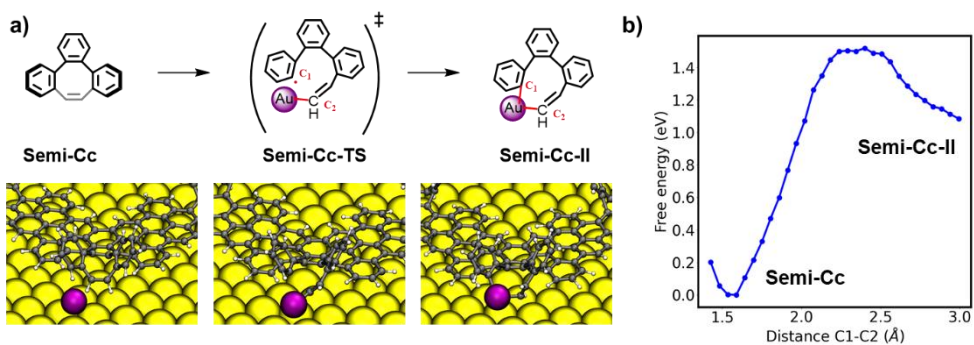


Figure A 5. QM/MM simulations for the first step of the rearrangement from 3.1.2-Semi-Cc to 3.1.2-Semi-Cc-II. Chemical models (shortened for clarity) are extracted from the QM/MM simulations. **b)** Free energy diagram of the process.

## STEP 2

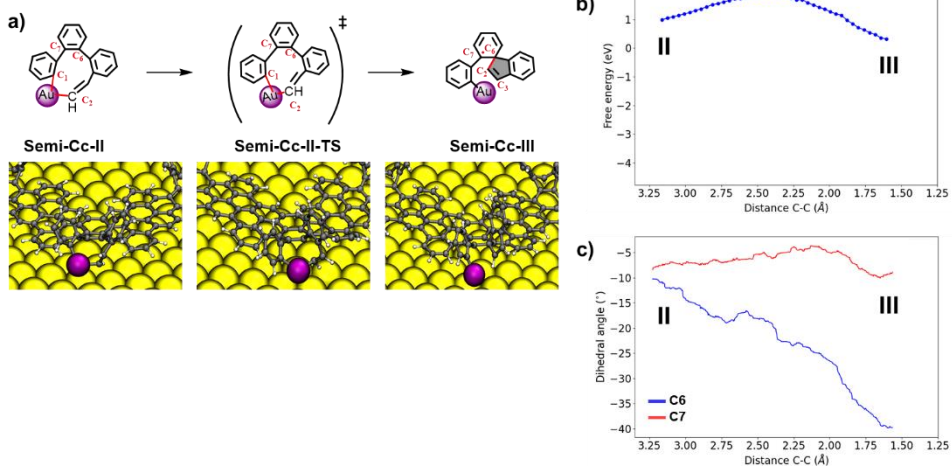
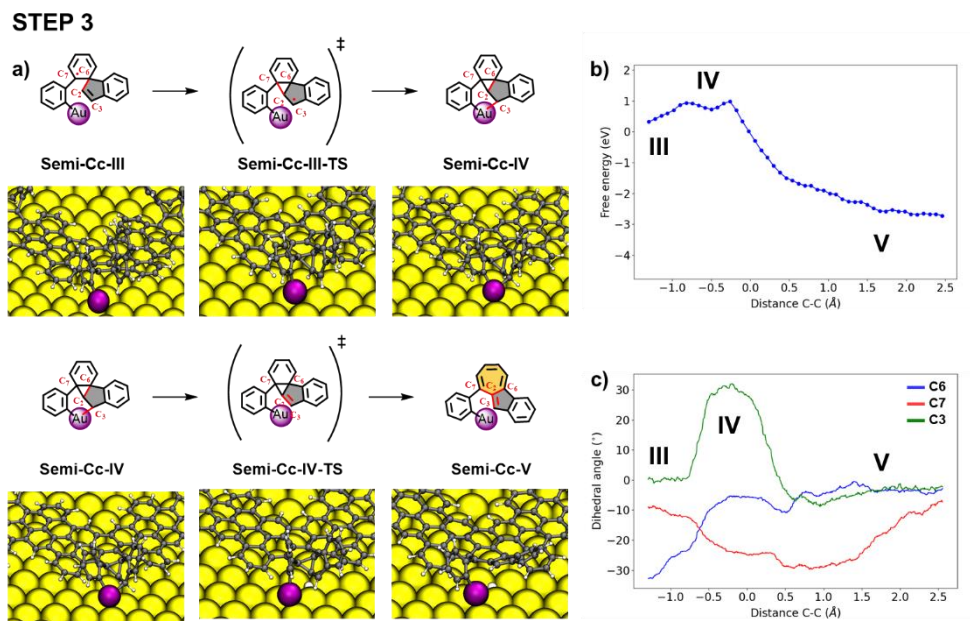
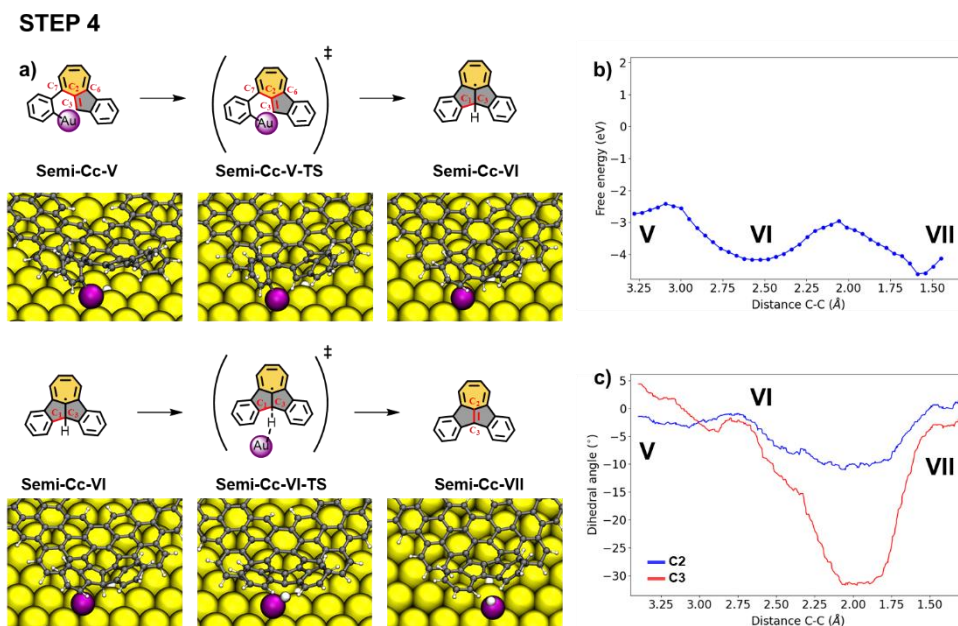


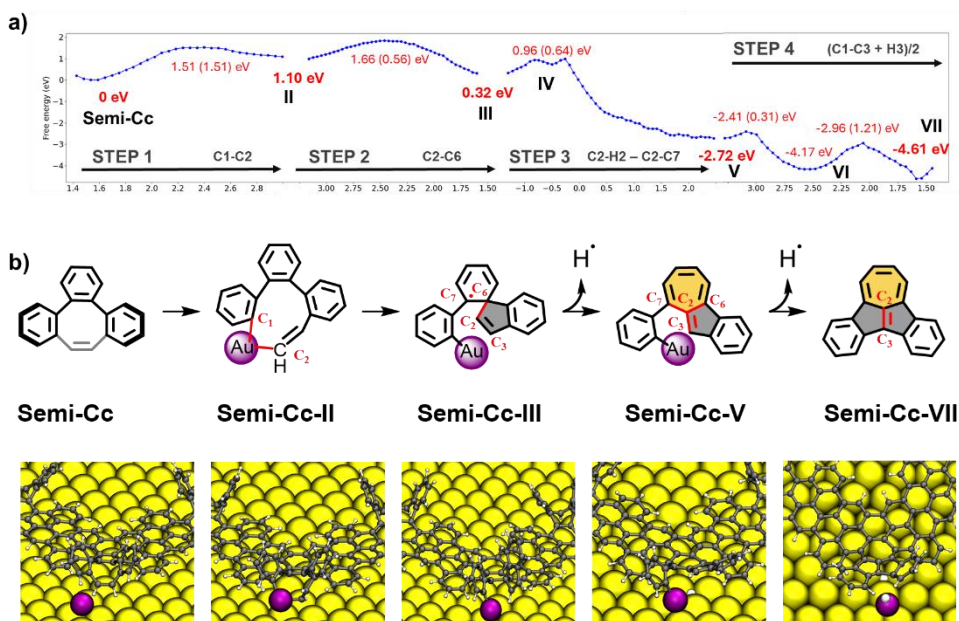
Figure A 6. QM/MM simulations for the second step of the rearrangement from 3.1.2-Semi-Cc-II to 3.1.2-Semi-Cc-III. Chemical models (shortened for clarity) are extracted from the QM/MM simulations. **b)** Free energy diagram of the process. **c)** Selected dihedral angles shift for carbons **C6** (blue curve) and **C7** (red curve).



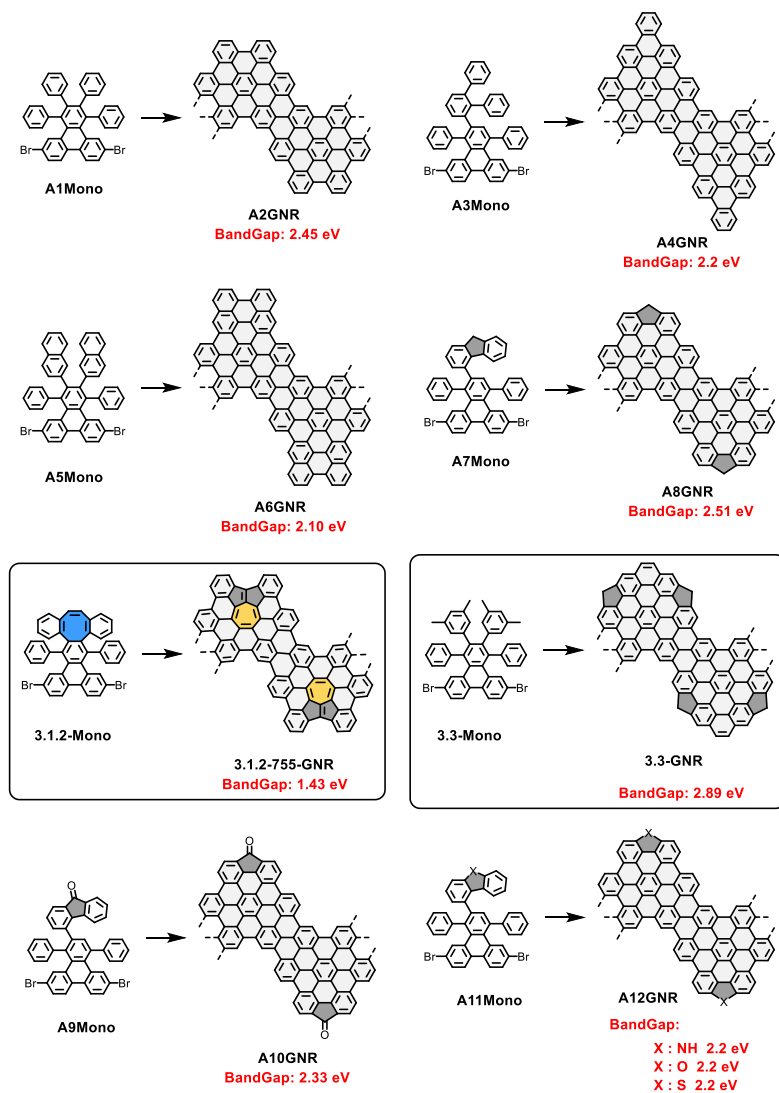
**Figure A 7.** QM/MM simulations for the third step of the rearrangement from 3.1.2-Semi-Cc-III to 3.1.2-Semi-Cc-V. Chemical models (shortened for clarity) are extracted from the QM/MM simulations. **b)** Free energy diagram of the process. **c)** Selected dihedral angles shift for carbons C6 (blue curve) and C7 (red curve) and C3 (green curve).



**Figure A 8.** QM/MM simulations for the final step of the rearrangement from 3.1.2-Semi-Cc-V to 3.1.2-Semi-Cc-VII. Chemical models (shortened for clarity) are extracted from the QM/MM simulations. **b)** Free energy diagram of the process. **c)** Selected dihedral angles shift for carbons C2 (blue curve) and C3 (red curve).



**Figure A 9.** Summary of the rearrangement mechanism from 3.1.2-Semi-Cc into 3.1.2-Semi-Cc-VII. **a)** Free energy diagram for the process (divided into four main steps). Atoms involved in the reaction coordinate are depicted in each step. **b)** Chemical models (top) were extracted from the QM/MM simulations (bottom). Chemical models are shortened for clarity.

Reported chevron-like GNRs

**Scheme A 1.** Reported chevron-like GNRs on Au(111) surface. Bandgap and ribbon synthesis: **A2GNR**<sup>300</sup>, **A4GNR**<sup>301</sup>, **A6GNR**<sup>300</sup>, **A8GNR**<sup>302</sup> Bandgap graphically extracted, **A10GNR**<sup>303</sup>, **A12GNR**<sup>304</sup>.

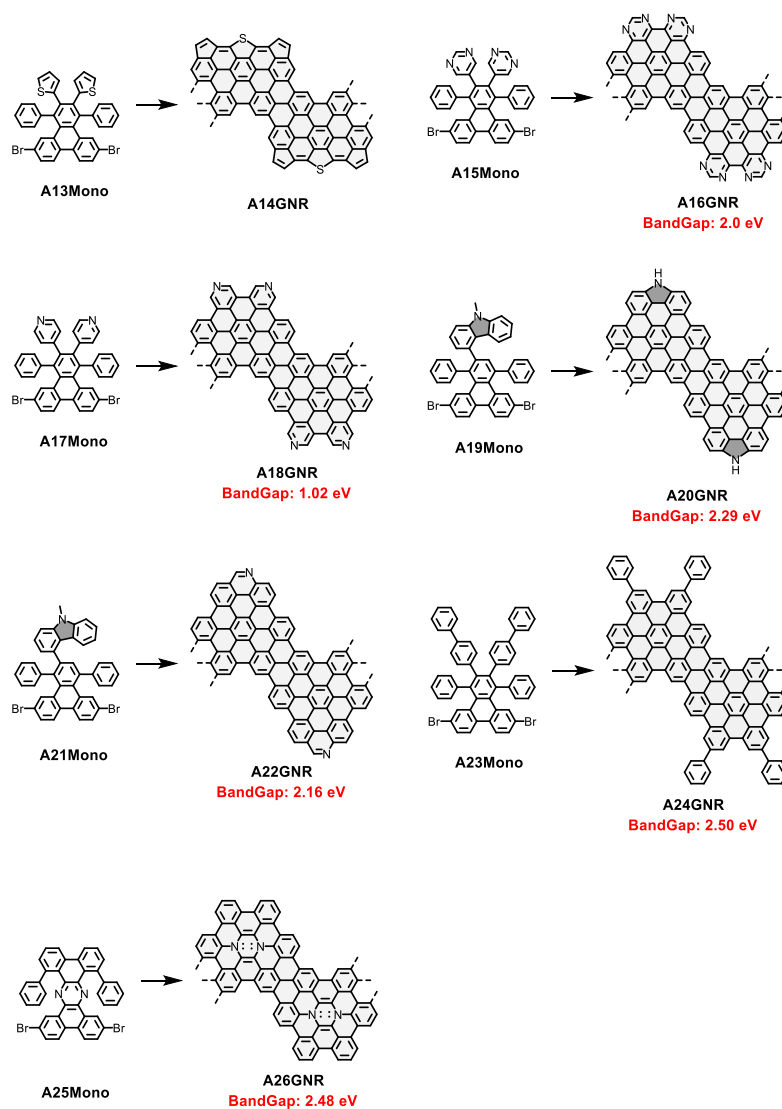
<sup>300</sup> C. Bronner, R. A. Durr, D. J. Rizzo, Y.-L. Lee, T. Marangoni, A. M. Kalayjian, H. Rodriguez, W. Zhao, S. G. Louie, F. R. Fischer, M. F. Crommie, *ACS Nano*, **2018**, *12*, 2193–2200.

<sup>301</sup> J. D. Teeter, P. Zahl, M. Mehdi Pour, P. S. Costa, A. Enders, A. Sinitskii, *ChemPhysChem*, **2019**, *20*, 2281–2285.

<sup>302</sup> P. H. Jacobse, R. D. McCurdy, J. Jiang, D. J. Rizzo, G. Veber, P. Butler, R. Zuzak, S. G. Louie, F. R. Fischer, M. F. Crommie, *J. Am. Chem. Soc.*, **2020**, *142*, 13507–13514.

<sup>303</sup> G. D. Nguyen, H.-Z. Tsai, A. A. Omrani, T. Marangoni, M. Wu, D. J. Rizzo, G. F. Rodgers, R. R. Cloke, R. A. Durr, Y. Sakai, F. Liou, A. S. Aikawa, J. R. Chelikowsky, S. G. Louie, F. R. Fischer, M. F. Crommie, *Nature Nanotech.*, **2017**, *12*, 1077–1082.

<sup>304</sup> R. A. Durr, D. Haberer, Y.-L. Lee, R. Blackwell, A. M. Kalayjian, T. Marangoni, J. Ihm, S. G. Louie, F. R. Fischer, *J. Am. Chem. Soc.* **2018**, *140*, 807–813.



**Scheme A 2.** Reported chevron-like GNRs on Au(111) surface. Bandgap and ribbon synthesis: **A14Poly**<sup>305</sup>, **A16Poly**<sup>306</sup>, **A18Poly**<sup>307</sup>, **A20Poly**<sup>308</sup> (the bandgap was graphically extracted), **A22Poly**<sup>308</sup>, **A24Poly**<sup>309</sup> (the bandgap was graphically extracted), **A26Poly**<sup>310</sup> (the bandgap was graphically extracted).

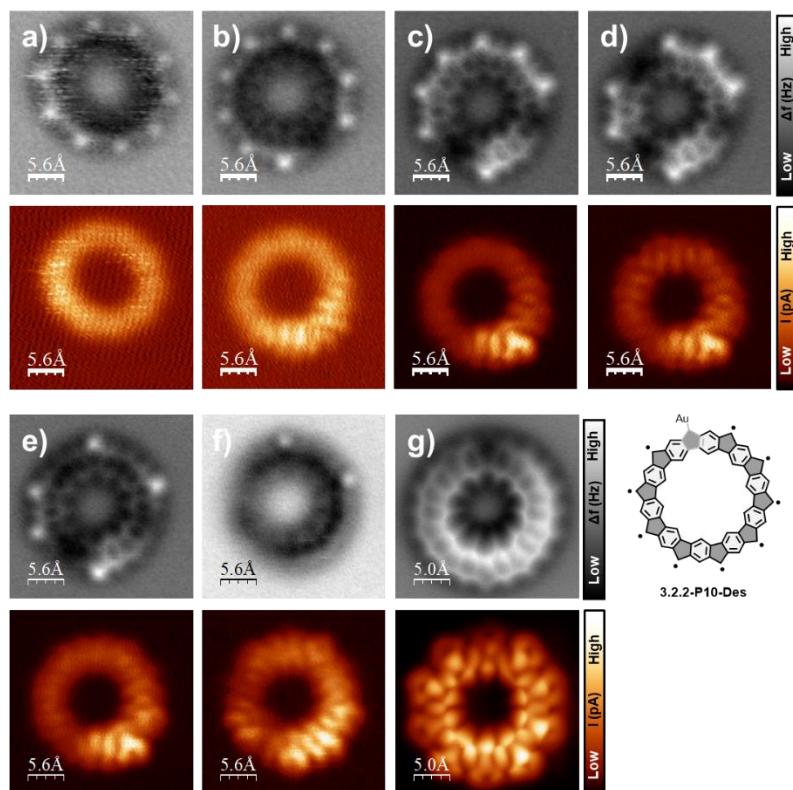
<sup>305</sup> Y. Cao, J. Qi, Y.-F. Zhang, L. Huang, Q. Zheng, X. Lin, Z. Cheng, Y.-Y. Zhang, X. Feng, S. Du, S. T. Pantelides, H.-J. Gao, *Nano Res.*, **2018**, *11*, 6190–6196.

<sup>306</sup> J. Cai, C. A. Pignedoli, L. Talirz, P. Ruffieux, H. Söde, L. Liang, V. Meunier, R. Berger, R. Li, X. Feng, K. Müllen, R. Fasel, *Nature Nanotech.*, **2014**, *9*, 896–900.

<sup>307</sup> Y. Zhang, Y. Zhang, G. Li, J. Lu, X. Lin, S. Du, R. Berger, X. Feng, K. Müllen, H.-J. Gao, *Applied Physics Letters*, **2014**, *105*, 023101.

<sup>308</sup> D. J. Rizzo, M. Wu, H.-Z. Tsai, T. Marangoni, R. A. Durr, A. A. Omrani, F. Liou, C. Bronner, T. Joshi, G. D. Nguyen, G. F. Rodgers, W.-W. Choi, J. H. Jørgensen, F. R. Fischer, S. G. Louie, M. F. Crommie, *Nano Lett.*, **2019**, *19*, 3221–3228.

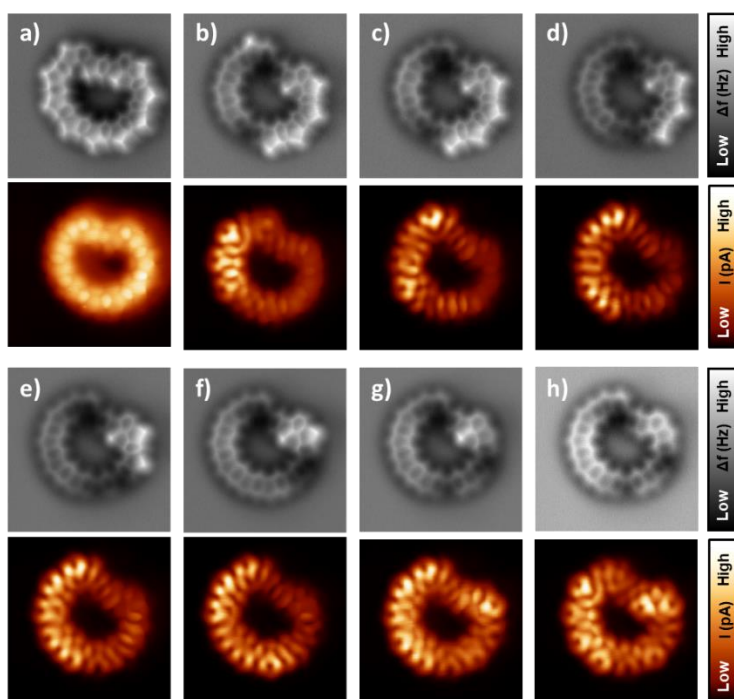
<sup>309</sup> M. Shekhirev, P. Zahl, A. Sinitskii, *ACS Nano*, **2018**, *12*, 8662–8669.

Tip-induced dehydrogenations

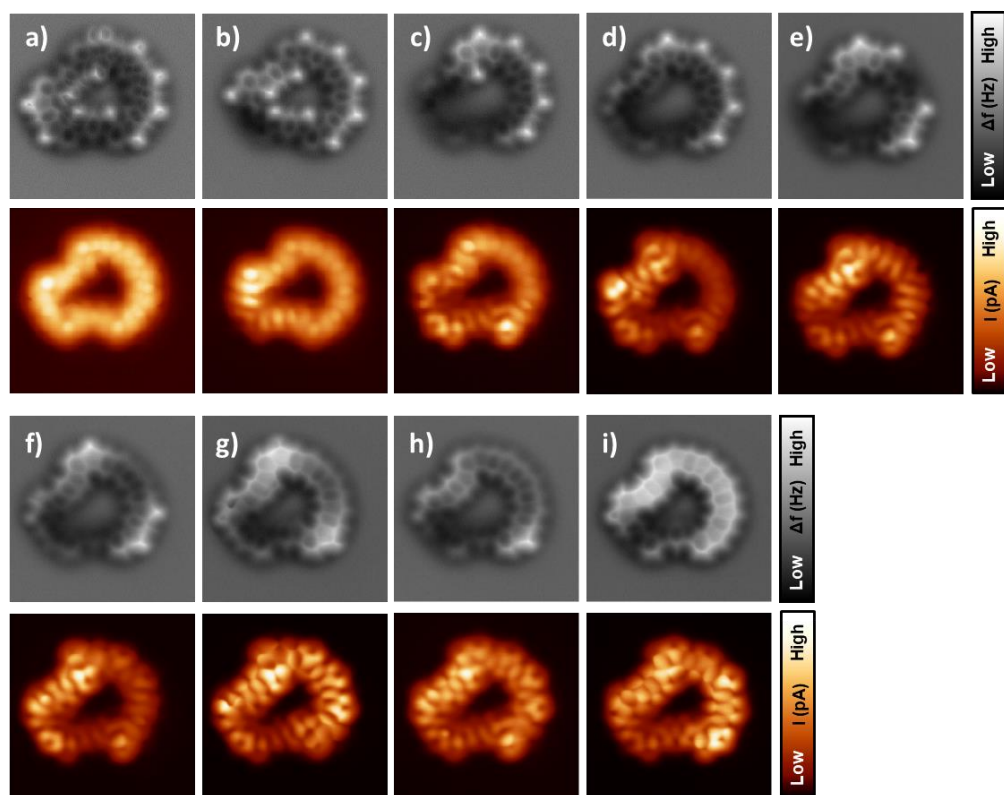
**Figure A 10.** Site-selective 3.2.1-P10 molecule dehydrogenation by SPM probe to applied bias. **a) to g)** Shows molecular changes after sequential dehydrogenations. Top, nc-AFM image; bottom, constant current STM image simultaneously obtained, CO functionalized tip. Every image was acquired with same scanning parameters (**a)** to (**g**):  $3 \text{ nm} \times 3 \text{ nm}$ , 2 mV.

<sup>310</sup> E. C. H. Wen, P. H. Jacobse, J. Jiang, Z. Wang, R. D. McCurdy, S. G. Louie, M. F. Crommie, F. R. Fischer, *J. Am. Chem. Soc.*, **2022**, *144*, 13696–13703.

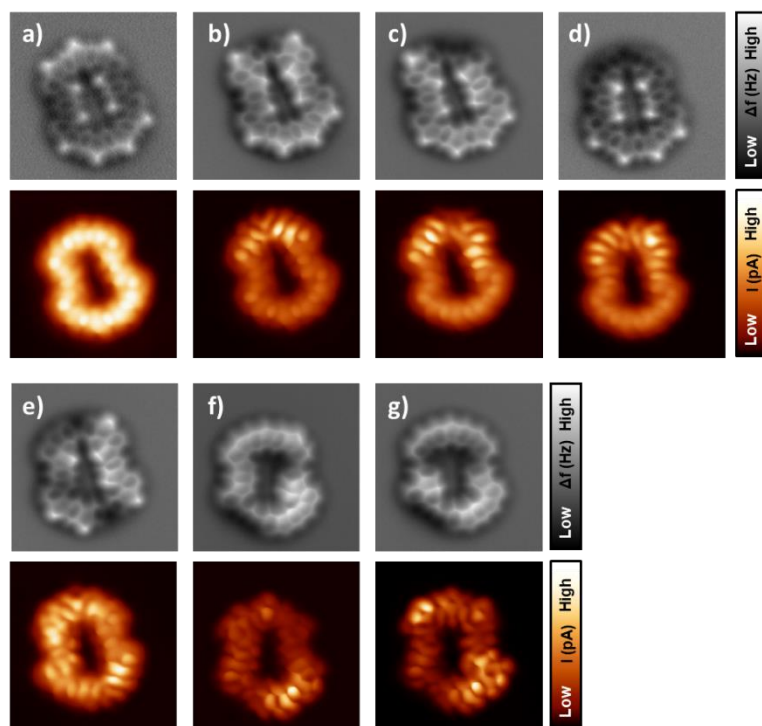




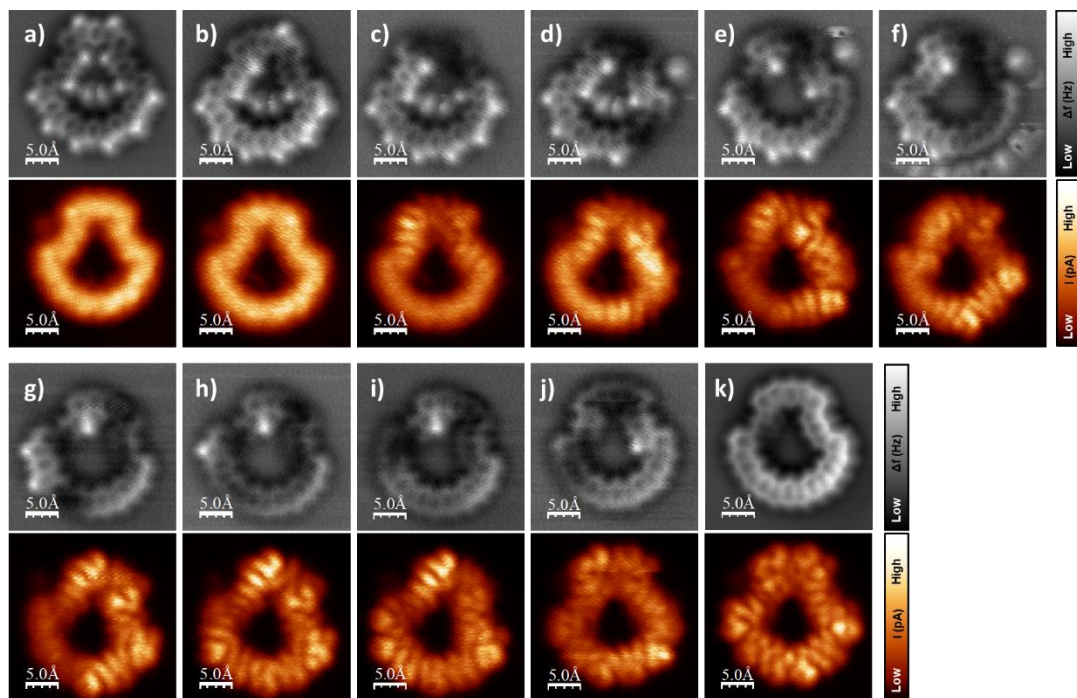
**Figure A 11.** Site-selective **3.2.1-P11-Endo1** molecule dehydrogenation by SPM probe to applied bias. **a) to h)** Shows molecular changes after sequential dehydrogenations. Top, nc-AFM image; bottom, constant current STM image simultaneously obtained, CO functionalized tip. Every image was acquired with same scanning parameters **(a) to (i)**:  $3 \text{ nm} \times 3 \text{ nm}$ ,  $2 \text{ mV}$ .



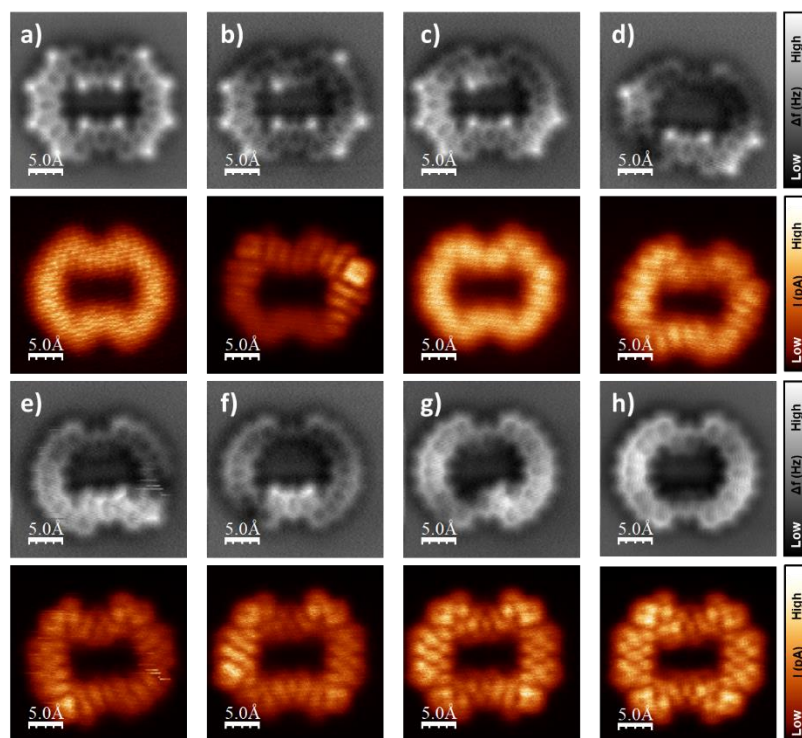
**Figure A 12.** Site-selective 3.2.1-P11-Endo2.3 molecule dehydrogenation by SPM probe to applied bias. **a) to h)** Shows molecular changes after sequential dehydrogenations. Top, nc-AFM image; bottom, constant current STM image simultaneously obtained, CO functionalized tip. Every image was acquired with same scanning parameters (**a) to (i)**:  $3 \text{ nm} \times 3 \text{ nm}$ , 2 mV.



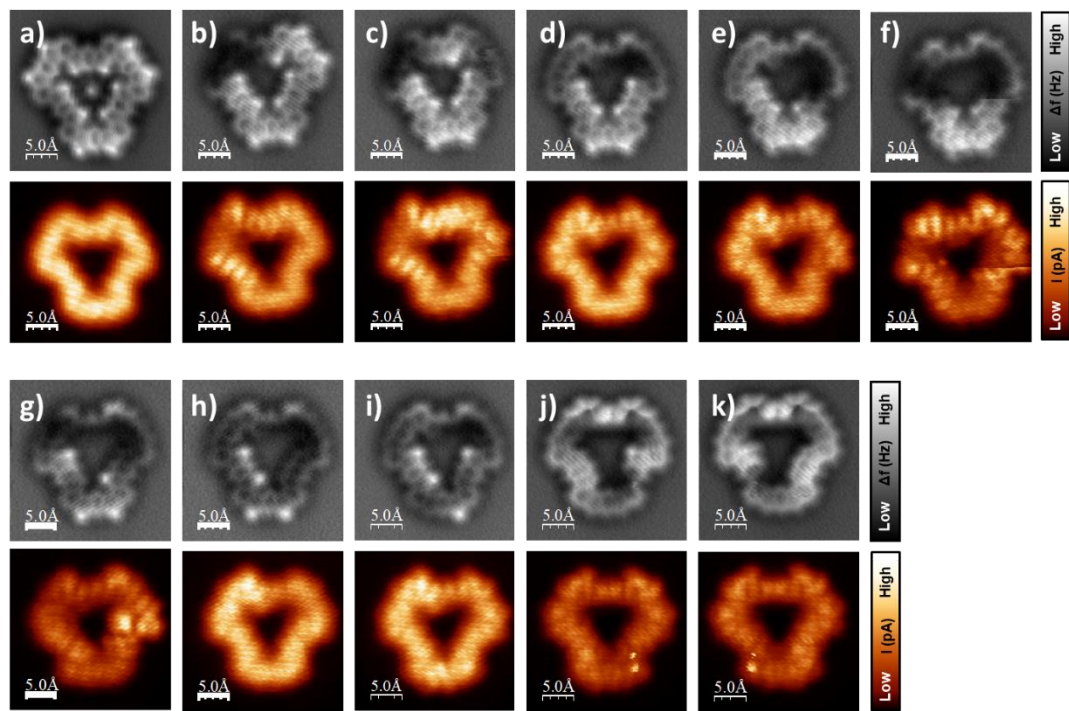
**Figure A 13.** Site-selective **3.2.1-P11-Endo2.4** molecule dehydrogenation by SPM probe to applied bias. **a) to h)** Shows molecular changes after sequential dehydrogenations. Top, nc-AFM image; bottom, constant current STM image simultaneously obtained, CO functionalized tip. Every image was acquired with same scanning parameters **(a) to (i)**:  $3 \text{ nm} \times 3 \text{ nm}$ , 2 mV.



**Figure A 14.** Site-selective 3.2.1-P12-Endo2.3 molecule dehydrogenation by SPM probe to applied bias. **a) to k)** Shows molecular changes after sequential dehydrogenations. Top, nc-AFM image; bottom, constant current STM image simultaneously obtained, CO functionalized tip. Every image was acquired with same scanning parameters (a) to (k): 2 mV.



**Figure A 15.** Site-selective 3.2.1-P12-Endo2.5 molecule dehydrogenation by SPM probe to applied bias. **a) to h)** Shows molecular changes after sequential dehydrogenations. Top, nc-AFM image; bottom, constant current STM image simultaneously obtained, CO functionalized tip. Every image was acquired with same scanning parameters (**a)** to (**h)**): 2 mV.



**Figure A 16.** Site-selective 3.2.1-P12-Endo3.3 molecule dehydrogenation by SPM probe to applied bias. **a) to k)** Shows molecular changes after sequential dehydrogenations. Top, nc-AFM image; bottom, constant current STM image simultaneously obtained, CO functionalized tip. Every image was acquired with same scanning parameters **(a) to (k):** 2 mV.

List of publications

- "On-Surface Thermal Stability of a Graphenic Structure Incorporating a Tropone Moiety", I. R. Márquez, N. Ruíz del Árbol, J. I. Urgel, F. Villalobos, R. Fasel, M. F. López, J. M. Cuerva, J. A. Martín-Gago, A. G. Campaña, C. Sánchez-Sánchez, *Nanomaterials*, **2022**, *12*, 488.
- "On-surface synthesis of non-benzenoid conjugated polymers by selective atomic rearrangement of ethynylarenes", A. Jiménez-Martín, † F. Villalobos, † B. Mallada, S. Edalatmanesh, A. Matěj, J. M. Cuerva, P. Jelínek, A. G. Campaña, B. de la Torre. *Chem. Sci.*, **2023**, *14*, 1403-1412.

This article is part of the themed collection of the journal *Chemical Science*: **Emerging Frontiers in Aromaticity**.

- "Single-molecule identification of the isomers of a lipidic antibody activator", B. Mallada, † F. Villalobos, † B. Donoso, R. Casares, G. Longhi, J. I. Mendieta-Moreno, A. Jimenez-Martín, A. Häidour, R. Seepersaud, L. Rajagopal, B. de la Torre, A. Millán, J. M. Cuerva, *J. Phys. Chem. Lett.*, **2024**, *15*, 6935–6942.
- "Globally Aromatic Odd-Electron  $\pi$ -Magnetic Macrocyclic", F. Villalobos, † J. Berger, † A. Matěj, † R. Nieman, A. Sánchez-Grande, D. Soler, A. Pinar Solé, H. Lischka, M. Matoušek, J. Brabec, L. Veis, A. Millan, C. Sánchez-Sánchez, A. G. Campaña, J. M. Cuerva, and P. Jelínek, *submitted to Chem*, **2024**.
- "Diastereomeric Configuration Drives an On-Surface Specific Rearrangement into Low Bandgap Non-Benzenoid Graphene Nanoribbons", F. Villalobos, † J. I. Mendieta-Moreno, † J. Lobo-Checa, S. P. Morcillo, J. I. Martínez, J. María Gómez-Fernández, P. L. de Andres, J. A. Martín-Gago, J. M. Cuerva, A. G. Campaña, C. Sánchez-Sánchez, *submitted to J. Am. Chem. Soc.*, **2024**.

A preprint version of the article can be found in: [10.26434/chemrxiv-2024-lrl41](https://doi.org/10.26434/chemrxiv-2024-lrl41)

Cite this: *Chem. Sci.*, 2023, 14, 1403

All publication charges for this article have been paid for by the Royal Society of Chemistry

## On-surface synthesis of non-benzenoid conjugated polymers by selective atomic rearrangement of ethynylarenes†

Alejandro Jiménez-Martin,<sup>1</sup> Federico Villalobos,<sup>1</sup> Benjamin Mallada,<sup>1,2</sup> Shayan Edalatmanesh,<sup>3,4</sup> Adam Matěj,<sup>5</sup> Juan M. Cuerva,<sup>6</sup> Pavel Jelinek,<sup>7</sup> Araceli G. Campaña<sup>8</sup> and Bruno de la Torre<sup>9\*</sup>

Here, we report a new on-surface synthetic strategy to precisely introduce five-membered units into conjugated polymers from specifically designed precursor molecules that give rise to low-bandgap fulvalene-bridged bisanthene polymers. The selective formation of non-benzenoid units is finely controlled by the annealing parameters, which govern the initiation of atomic rearrangements that efficiently transform previously formed diethynyl bridges into fulvalene moieties. The atomically precise structures and electronic properties have been unmistakably characterized by STM, nc-AFM, and STS and the results are supported by DFT theoretical calculations. Interestingly, the fulvalene-bridged bisanthene polymers exhibit experimental narrow frontier electronic gaps of 1.2 eV on Au(111) with fully conjugated units. This on-surface synthetic strategy can potentially be extended to other conjugated polymers to tune their optoelectronic properties by integrating five-membered rings at precise sites.

Received 23rd August 2022  
Accepted 19th December 2022

DOI: 10.1039/d2sc04722e

rsc.li/chemical-science

### Introduction

The ability to control their characteristics with rational chemical synthesis has made conjugated polymers excellent candidates for technological applications such as light emitting devices, solar cells, organic field-effect transistors, photocatalysts and biosensors.<sup>1,2</sup> These semiconductors and synthetic metals have been generated from a wide range of organic precursors comprising heterocyclic compounds as well as non-benzenoid polycyclic hydrocarbons.<sup>3</sup> The successful synthesis of these non-benzenoid compounds has recently provided profound insights into the electronic properties of antiaromatic and/or open-shell systems.<sup>4–9</sup> For example, these antiaromatic compounds have demonstrated higher charge carrier mobility

than their aromatic counterparts,<sup>10</sup> although the interpretation of these properties is still unclear.<sup>11,12</sup> Unfortunately, conventional wet synthesis of conjugated polymers containing non-benzenoid compounds is difficult in the case of unstable final compounds due to their inherent low solubility, high intrinsic reactivity and the occurrence of undesirable structural defects<sup>13</sup> that prevent complete control of the molecular structure.

On-surface synthesis<sup>14,15</sup> under ultra-high vacuum (UHV) conditions is a promising strategy for synthesizing non-benzenoid compounds. This approach has proven to be ideal for fabricating (macro)molecular architectures with atomic precision and tailored electronic properties.<sup>16</sup> The rational design of precursor molecules and the stabilization offered by single-crystal substrates allow the engineering of specific products, enabling the fine-tuning of their structural and electronic properties,<sup>15</sup> the fabrication of intrinsically reactive molecular structures<sup>17–19</sup> and the investigation of rearrangement reactions<sup>18–23</sup> of particular interest for non-benzenoid  $\pi$ -extended nanostructures.<sup>24</sup> It therefore provides unique opportunities to address the scientific challenge of fabricating well-defined conjugated polymers incorporating non-benzenoid components, with the goal of designing chemically robust, low bandgap polymers. Nevertheless, there are only a few reports discussing the on-surface formation of non-benzenoid moieties,<sup>18,25–29</sup> sometimes in conjugated polymers.<sup>8,21,30–35</sup> Most of them have utilized strategies based on oxidative ring closure,<sup>8,36</sup> bond rotation<sup>37</sup> or the use of molecular precursors with embedded 5-membered rings.<sup>38,39</sup> Therefore, it is highly desirable to provide new strategies that allow the controlled

\*Regional Centre of Advanced Technologies and Materials, Czech Advanced Technology and Research Institute (CATRI), Palacký University Olomouc, Olomouc 783 71, Czech Republic. E-mail: bruno.de@upol.cz

<sup>†</sup>Faculty of Nuclear Sciences and Physical Engineering, Czech Technical University in Prague, Břehova 7, Prague 1 15 19, Czech Republic

<sup>‡</sup>Departamento de Química Orgánica, Universidad de Granada (UGR), Unidad de Excelencia de Química UEQ, C. U. Puentenueva, Granada 18071, Spain. E-mail: araceli@ugr.es

<sup>§</sup>Department of Physical Chemistry, Faculty of Science, Palacký University, Olomouc 78371, Czech Republic

<sup>¶</sup>Institute of Physics, Czech Academy of Sciences, Prague 162 00, Czech Republic

† Electronic supplementary information (ESI) available: Methods, Fig. S1 to S8, synthesis of the material, NMR spectra, MS spectra, single crystal X-ray crystallography, references. See DOI: <https://doi.org/10.1039/d2sc04722e>

‡ These authors contributed equally to this work.



formation and detailed analysis of such non-benzenoid molecules.

Here, we exploited the atomic rearrangement of ethynylarene to cyclopenta-fused polycyclic aromatic hydrocarbons, to give rise to low bandgap fulvalene-bridged bisanthrene polymers on an atomically flat Au(111) surface. To this end, we synthesized 9,10-bis(trimethylsilyl)ethynylanthracene and 10,10'-bis(trimethylsilyl)ethynyl-9,9'-bianthracene as precursors (**1** and **4** in Fig. 1, respectively). Each of them was intentionally designed with a dual purpose: (i) to form one-dimensional diethynyl-bridged polymers after homo-coupling of terminal alkynes (Glaser-like coupling) on the surface;<sup>40</sup> and (ii) to favor the selective atomic rearrangement of the linker giving rise to non-benzenoid units.<sup>41</sup> Furthermore, endowing precursors **1** and **4** with trimethylsilyl (TMS) groups allows chemical protection of the compounds and the *in situ* deprotection of such terminal alkynes on-surface under UHV conditions. This strategy offers an alternative to the use of unstable or highly-reactive monomers.<sup>42–44</sup> Using scanning tunneling microscopy and spectroscopy (STM and STS), in combination with non-contact atomic force microscopy (nc-AFM) and density functional theory (DFT) calculations, we analyzed the chemical structure and electronic properties of the reaction products. Importantly, overall, we reveal the successful formation of fulvalene-bridged bisanthrene conjugated polymers that exhibit a low bandgap of a measurable value of 1.2 eV.

## Results and discussion

Fig. 1 shows the chemical structure of the precursor molecules **1** and **4**, which we have used in this study. **1** and **4** were synthesized in solution from commercially available 9,10-dibromoanthracene and 10,10'-dibromo-9,9'-bianthracene, respectively, *via* double Sonogashira coupling with trimethylsilylacetylene (see ESI† for details of the synthesis). The corresponding unprotected terminal alkynes 9,10-diethynylanthracene and 10,10'-diethynyl-9,9'-bianthracene

were also synthesized in solution by treatment of **1** and **4** with tetrabutylammonium fluoride. However, we observed that these compounds tend to react or decompose under ambient conditions. Besides, thermo gravimetric analysis (TGA) shows a gradual decomposition of protected **4** at temperatures above the evaporation threshold (Fig. S1†). For this reason, we decided to keep the trimethylsilyl protecting groups and perform *in situ* deprotection prior to the on-surface polymerization.

Sublimation of **1** under UHV conditions on clean Au(111) maintained at room temperature gives rise to self-assembled molecular islands of anthracene units with their remaining TMS groups, as depicted by the STM and nc-AFM images (Fig. 2a, inset) and in perfect agreement with previous reports on Ag(111).<sup>45</sup> The STM images after sample annealing at 225 °C (*cf.* Fig. 2b) reveal that polymerization of **1** has been triggered, leading to the formation of one-dimensional molecular structures on the surface. In the close-up nc-AFM image recorded with a functionalized CO-tip (Fig. 2c), polymer units were resolved. These consist of anthracene units coupled by diethynyl motifs, confirming the formation of **2**. The two triple bonds are unambiguously distinguishable as bright dots, which is consistent with recent observations on synthesized ethynylene-bridged anthracene polymers<sup>46</sup> and poly(*p*-phenylene ethynylene) molecular wires on Au(111).<sup>47</sup> Interestingly, compared to the reported ethynylene-bridges, diethynyl units increase the electronic bandgap from 1.5 eV<sup>46</sup> to approximately 1.9 eV (see Fig. S2†). In addition, intramolecular rearrangement of **2** is frequently observed, and a significant number of five-membered rings are found in the linkers, giving rise to structure **3**, as shown in Fig. 2c, right. From the STM/AFM images, we inferred that residual hydrogen from the environment chemically passivates the alkynes at the termini of the polymers. The fact that these non-benzenoid units are consistently found in the linkers indicates that they all originated by arrangement of the ethynylene moiety. Indeed, it is clear that along the bridged unit, the 5-membered ring can be found to be coupled to an ethynylene segment, as can be inferred by the presence of the

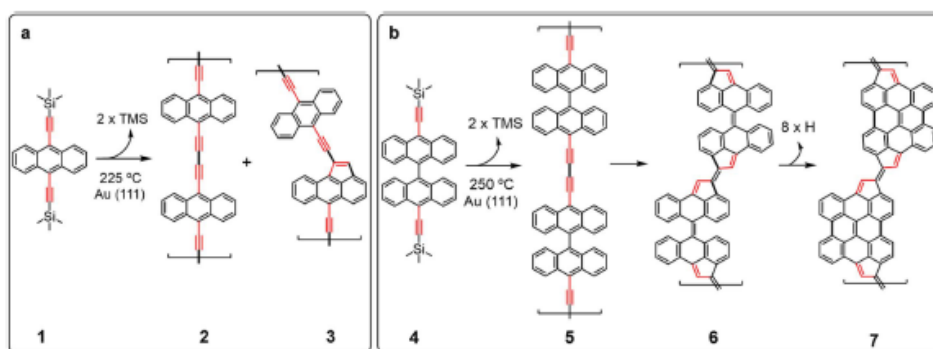


Fig. 1 Scheme of the reaction sequence of (a) anthracene and (b) bianthracene based precursors after being deposited on Au(111) and annealed up to 225 °C and 250 °C, respectively, to produce conjugated polymers incorporating non-benzenoid units.

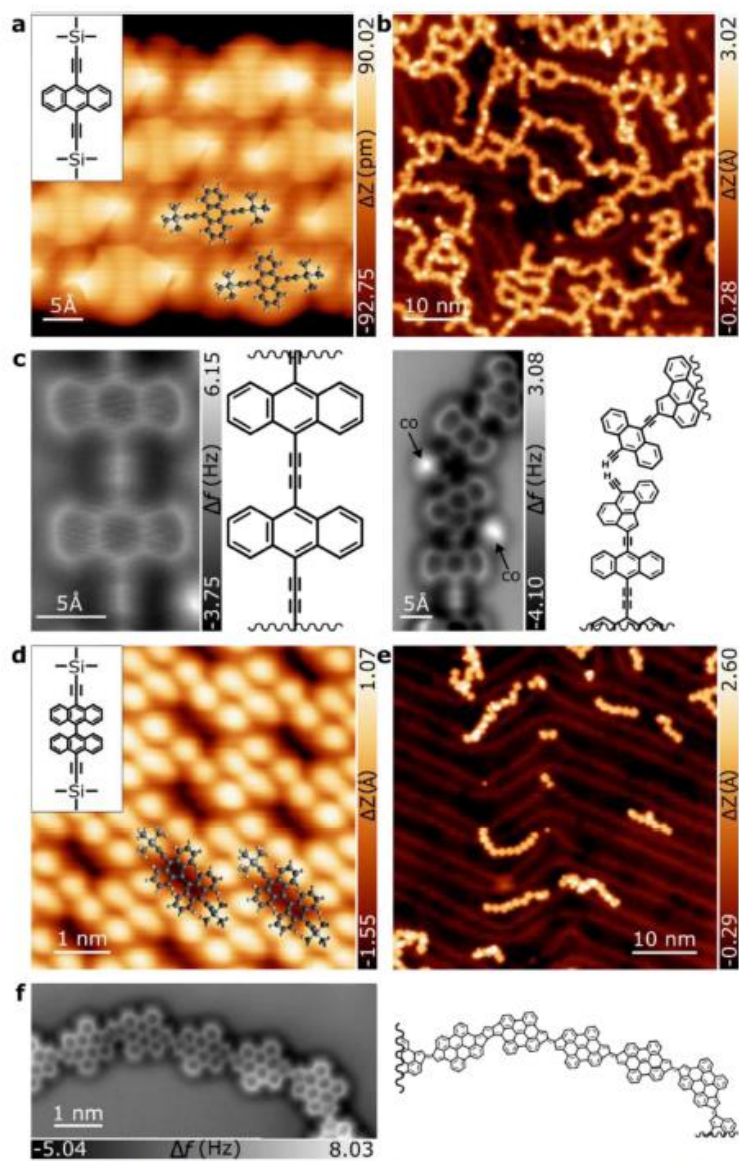


Fig. 2 On-surface synthesis of fulvalene-bonded bisanthrene polymers. (a) STM topographic overview with a superimposed model of precursor (1) (top left inset) upon deposition at RT on Au(111) (0.05 V, 0.01 nA). (b) STM topographic overview after thermal annealing at 225 °C (0.1 V, 0.01 nA). (c) nc-AFM detailed images of the one-dimensional molecular structures of (b) including their respective model. The images show the presence of diethynyl bonds and ethynyl-pentagon joints. (d) STM topographic overview with a model of precursor (4) (top left inset) after deposition at RT on Au(111) (-2 V, 0.05 nA). (e) STM topographic overview of the sample after annealing at 250 °C (0.1 mV, 0.02 nA). (f) High-resolution nc-AFM image of a fulvalene-bridged bisanthrene polymer and the corresponding model of the polymer.

triple bond in the nc-AFM images (*cf.* Fig. 2c, right). Thus, the linear anthracene-diethynyl-anthracene backbone reacts to form five-membered rings by thermally induced ethynylarene rearrangement to cyclopenta fused anthracene, as previously described.<sup>48</sup> This finding suggests not only the possibility of tuning the polymer bandgap by introducing the diethylene linker, but a mechanism for inducing the formation of five-membered rings by selective atomic rearrangement.

To strengthen our hypothesis and investigate the generality of the ethynylarene rearrangement to cyclopenta fused polycyclic aromatic hydrocarbons, we synthesized compound **4** (Fig. 1) and studied its polymerization reaction on the Au(111) surface with the aim of obtaining low bandgap conjugated polymers. Pleasingly, *in situ* alkyne deprotection and Glaser-like coupling on the Au(111) surface leading to bisanthene-based conjugated polymers also worked with **4**, albeit at higher temperatures (see Fig. S3†). Similarly, STM images of islands formed by bianthracene **4** display bright rounded features due to the bulky TMS protecting groups (Fig. 2d). A first step of annealing **4** on Au(111) to  $T = 250^\circ\text{C}$  for 30 minutes triggers the polymerization of **4** leading to the formation of one-dimensional molecular structures on the surface (*cf.* Fig. 2e). The chains have an average length of 9.6 nm (see Fig. S3†) and are composed of straight and zig-zag segments, which can be found in *cis*- or *trans*-configurations depending on the bonding between monomers (see Fig. S4† for more details). They do not exhibit protrusions, indicating successful planarization of the units. nc-AFM imaging with a functionalized CO-tip<sup>49</sup> was used to reveal the chemical structure of the polymer. Its skeleton was unambiguously resolved (Fig. 2f), confirming that it is composed of a sequence of bisanthene monomers with fused fulvalene bridges (**7**). Notably, the reaction is highly selective and only minority concomitant defects are detected for submonolayer coverage. The calculated bond dissociation energy (BDE) of the reaction-participant radical positions for anthracene (**2**), bianthracene (**5**), and bisanthene polymers in the gas phase (Fig. S5†) shows that the dissociation required to initiate the cyclo-pentafused rearrangement yields significantly different values for anthracene and bianthracene polymers. The formation of pentagon moieties is less energetically favorable for anthracene polymers in the gas phase by  $5.2\text{ kcal mol}^{-1}$ , indicating selective initiation of the atomic rearrangement.

The absence of 1,3-butadiyne traces suggests that they all converted to fulvalene bridges. In principle, the rearrangement of ethynylarene to cyclopenta fused polycyclic aromatic hydrocarbons may proceed through any of the five distinct sequences of elementary reactions that differ in the temporal order of ring closure and hydrogen migration/transfer. Our findings provide no direct evidence of a preference for any temporal order but taking into account the capability of gold surfaces to activate aromatic CH bonds,<sup>50</sup> the generation of an aryl radical followed by 5-*endo-dig* radical cyclization<sup>51</sup> and subsequent passivation of the generated radical seems to be the most simple and plausible mechanism considering the reported thermal rearrangement of ethynylarenes in solution (*cf.* Fig. 3a).

It is notable that the proposed mechanism at the surface may involve the activity of individual gold adatoms<sup>22,23</sup> to passivate

the emerging radicals, which may ultimately stabilize with residual hydrogen, highlighting the catalytic role of single atoms at the surface (see Fig. 3b). Unfortunately, no intermediate structures (**5** and **6** in Fig. 1) could be identified to support a rearrangement mechanism. Importantly, all of our efforts to generate diethynylene-bridged bisanthene polymers by lowering the reaction temperature on the Au(111) substrates failed, clearly confirming that the formation of the five-membered rings is highly efficient (see Fig. S3†). We also tested the possibility of growing Glaser polymers (**1** and **4**) on Ag(111). However, the surface showed low reactivity for such coupling. This is probably due to the strong molecule-substrate interaction, leading to low molecular diffusion, which is a prerequisite for efficient on-surface chemistry.

Next, we examined the structural and electronic properties of the fulvalene-bridged bisanthene polymer **7**, including the dominant resonance shape. In this regard, the rule of Glidewell and Lloyd<sup>52</sup> provides a conceptual picture for predicting the resonance form in polycyclic aromatic hydrocarbons incorporating non-benzenoid units. According to this rule, a resonance structure with the smallest  $4n + 2$  groups, avoiding the formation of the smallest  $4n$  groups, represents the most stable form or the one that contributes most to the resonance. Locally, the fulvalene bridge can exhibit two types of resonance forms, *i.e.*, the C-C bond connecting two pentagons can be single or double. From this hypothesis, at least two distinct resonance forms can be conceived, as illustrated in Fig. 4a. Application of Glidewell and Lloyd's rule shows that the structure associated with a double bond linker (blue color in Fig. 4a) should be the most stable, since the other option (red color in Fig. 4a) would imply the formation of four groups with  $4\pi$ -electrons in the bisanthene moiety, which should be avoided according to the rule. Interestingly, the system stabilizes four Clar's sextets on the bisanthene unit (depicted in blue in Fig. 4a), the maximum number. To investigate this hypothesis, we performed bond order discrimination using nc-AFM with a CO-tip.<sup>53</sup> High-resolution nc-AFM images of the fulvalene-bridged polymers (see Fig. 4b) show different bond lengths within the bisanthene unit, whose statistically average value is shown in the left panel of Fig. 4c (see Fig. S6† for details). The bond length analysis was qualitatively confirmed by DFT calculations (right panel of Fig. 4c). The analysis revealed that the variation of the bond distance in the polymer matches the  $\pi$ -resonance predicted by Glidewell and Lloyd's rule, further corroborating its validity on surfaces.

Although aromaticity is well understood for benzenoid compounds, the application of these concepts to non-benzenoid systems is not trivial. A better understanding of their "aromatic character" may lead to fruitful theoretical proposals and to the synthesis of novel non-benzenoid conjugated compounds on surfaces. In addition, the aromatic character of a given compound determines the relationship between its constituents and its chemical reactivity or electron delocalization energy.<sup>54</sup> Therefore, it is interesting to analyze the degree of aromaticity and antiaromaticity of the bisanthene-fulvalene polymer. The left panel of Fig. 4d shows the calculated nucleus-independent chemical shift (NICS)<sup>55</sup> of a bisanthene-

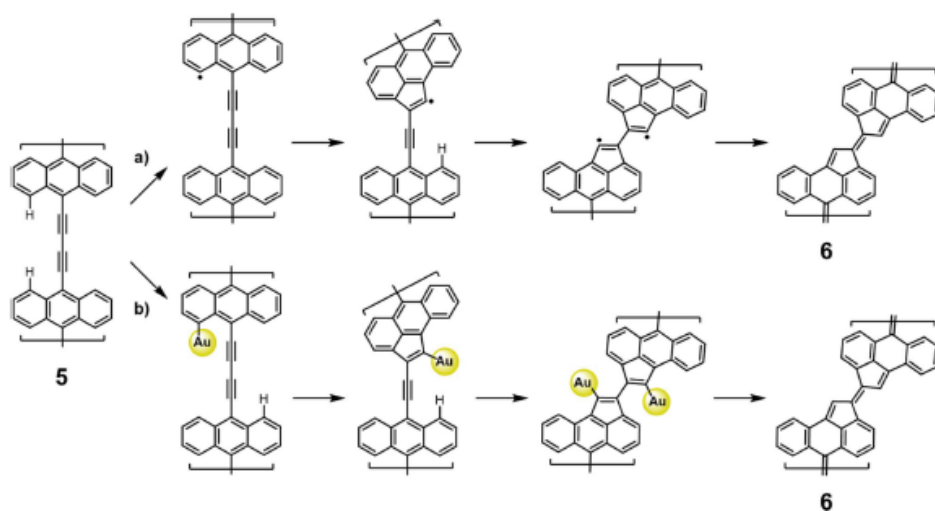


Fig. 3 Proposed reaction mechanism giving rise to fulvalene units. (a) Traditional, and (b) on-surface proposed ethynylarene rearrangement to cyclopenta fused polycyclic aromatic hydrocarbons. An initial hydrogen abstraction is followed by oxidative ring closure and  $\pi$ -electron reconfiguration, while individual gold atoms may stabilize transient radicals.

fulvene dimer passivated by  $H_2$  at the edges to induce the double bond character of the C-C bond connecting two pentagons. Thus, the structure is closed shell since the potential radicals are quenched, at least for the dimer. NICS analysis revealed that the four benzenoid rings at the bisanthrene links are clearly aromatic, while the central six-membered ring possesses values close to zero, typical of non-aromaticity, thus reproducing well the bond length analysis and corroborating

the resonance form discussed above. On the other hand, in the pentagons of the fulvalene segment, we find positive values for the shielding tensor component ( $-\sigma_{zz}$ ), which may indicate antiaromaticity. Qualitatively, however, those values are close to zero, which may indicate that the pentagons do not participate in the  $\pi$ -conjugation of the system. The deviation of conjugation pathway from zig-zag edge near the fulvalene rings effectively prolongs the conjugation path from 22 to 26 electrons,

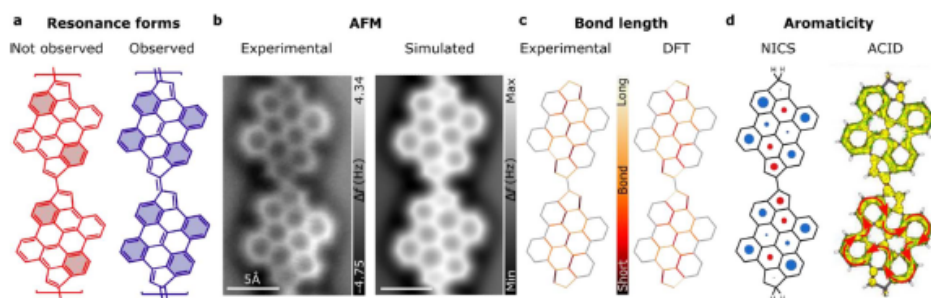


Fig. 4 Resonance and bond analysis of fulvalene-linked polymers. (a) Proposed resonance structures of bisanthrene-fulvalene polymers. In blue (red) are the observed (not-observed) resonance forms of the fulvalene-based polymers on the surface (Clar's sextets are highlighted). (b) Experimental (left) and simulated (right) nc-AFM images of fulvalene-bridged one-dimensional structures. (c) Experimental (left) and DFT (right) bond length analysis for a bisanthrene-fulvalene dimer. (d) Calculated nucleus-independent chemical shift (NICS) of a fulvalene dimer (left) and calculation of the induced current density (ACID) revealing the  $\pi$ -conjugation of the system (right). The diameter of the circle features corresponds to the qualitative aromatic/antiaromatic (blue/red) character of the ring (see Table in Fig. S6†).

which explains the positive shielding on the benzene rings. The intensity of positive shielding above fulvene and the central benzene rings is much lower than that of proto-typical anti-aromatic molecules, such as cyclobutadiene and pentalene, so they are considered non-aromatic (see Fig. S7† for the quantitative analysis of NICS calculation for the H and H<sub>2</sub> terminated dimer and tetramer).

To gain further insight into the aromatic character of the polymer, we performed calculations of the anisotropy of the induced current density (ACID)<sup>28</sup> (Fig. 4d right panel). The  $\pi$ -ACID (including only pz orbitals) shows a clear conjugation within each bisanthene unit including 26  $\pi$ -electrons in total. The map reveals the interactions of ring currents of each individual ring, enhancing or suppressing the boundary with the neighboring ring, depending on their mutual orientations. Indeed, it reveals that there is aromatic  $\pi$ -conjugation within bisanthene units with the fulvene units excluded. The ACID map shows the clockwise direction of the main current ring on the bisanthene periphery, revealing its aromatic character with all  $\pi$ -electrons involved in this current, in agreement with the  $4n + 2$  rule of aromaticity. We found that it is possible to include the fulvene moieties in the global ring current by passivating the dimer edges with H instead of H<sub>2</sub> (see Fig. S8† for the quantitative analysis of ACID calculation for the H and H<sub>2</sub> terminated dimer and tetramer). However, this leads to the

single bond character of the C–C bond connecting the pentagons and an antiaromatic number of  $\pi$ -electrons, which goes against Glidewell and Lloyd's rule and the experimental observations. Conjugation through the linker shows a higher critical isosurface value for the double-bond linker (CIV 0.0395) than for the single-bond linker (CIV 0.0311, not shown), showing higher electron delocalization between the units. To conclude, the fulvalene polymer is aromatic with non-aromatic linkers, resulting in weak conjugation between units.

Finally, to access the intrinsic electronic characteristics of the bisanthene-fulvalene polymers, we performed a set of scanning tunneling microscopy and spectroscopy experiments. A voltage-dependent differential conductance spectrum ( $dI/dV$  vs.  $V$ ) acquired on 7 revealed peaks in the density of states (DOS) at  $-630$  mV and  $560$  mV (Fig. 5a). Those peaks arise respectively from hybridization of the polymer valence and conduction bands (VB and CB) with the substrate. Spatial mapping of the  $dI/dV$  signal ( $dI/dV$  maps) at peak positions revealed characteristic features (Fig. 5b) that are well reproduced by the corresponding B3LYP-DFT-calculated  $dI/dV$  maps for an oligomer formed by 7 (Fig. 5c). The  $dI/dV$  map of the VB shows maxima at the lateral edge of the bisanthene moiety, with negligible charge density over the bridge (see Fig. 5b). The  $dI/dV$  map of the CB exhibits states on the empty spaces adjacent to the fulvene bridges (see Fig. 5b). Although DFT calculations could not

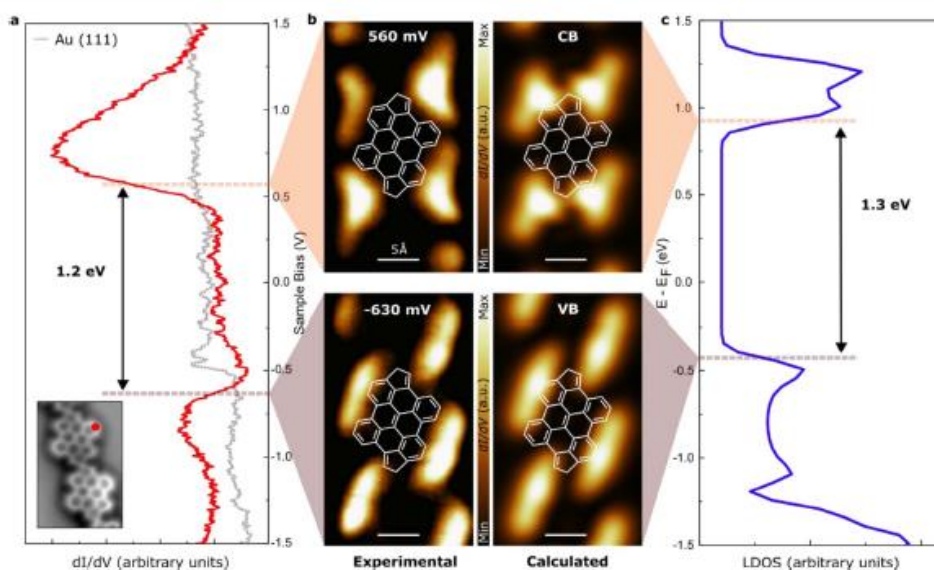


Fig. 5 Electronic structure of fulvalene polymers. (a)  $dI/dV$  conductance spectra of the polymer acquired at the position marked with red in the inset image. The red profile features a gap corresponding to 1.2 eV. (b) Experimental constant current  $dI/dV$  maps (left) and calculated PDOS (right) at the conduction band (top) and valence band (down) onsets. (c) DFT calculated LDOS for fulvalene polymers in the gas phase featuring a bandgap of 1.3 eV.

qualitatively predict the magnitude of the intrinsic bandgap of the polymer<sup>54</sup> (Fig. 5c), they described very well the character of the frontier orbitals of the VB and CB edges of the polymer (cf. Fig. S9†). In fact, the excellent agreement between experimental and simulated dI/dV maps validates the character of the frontier orbitals predicted by DFT. Thus, this results in a low bandgap of ~1.2 eV on Au(111). It should be noted that the bandgap value obtained from STS measurements is typically reduced by an additional electron screening imposed by the proximity of a metallic surface with respect to the intrinsic bandgap of the gas-phase polymer.<sup>60</sup> However, in this case, the perfect agreement between experimental and DFT values of the electronic bandgap indicates a low degree of hybridization of the fulvalene-polymer with the metal support.

## Conclusion

In conclusion, by studying the rearrangement of ethynylarene to cyclopenta fused polycyclic aromatic hydrocarbons on surfaces, we have introduced a novel synthetic strategy for the selective incorporation of five-membered rings into conjugated polymers. In particular, trimethylsilylacetylene protection/deprotection is a well-established strategy in solution-phase chemistry, which we believe also has great potential in the area of on-surface chemistry. The successful realization of bisanthene-fulvalene polymers is confirmed by STM and high-resolution nc-AFM analyses. We found that such a polymer exhibits a measurable low band gap of 1.2 eV and a closed-shell electron configuration on Au(111), as demonstrated by STS supported by DFT calculations. We anticipate that our new synthetic strategy will open avenues to fabricating highly demanded covalent polymers on surfaces incorporating non-benzenoid moieties, which are particularly attractive for organic photovoltaics, photodetectors, and ambipolar field-effect transistors.<sup>61–62</sup>

## Data availability

Data will be available on request. CCDC-2193258 contains the supplementary crystallographic data for this paper. More experimental details can be found in the ESI.†

## Author contributions

A. G. C. and B. T. conceived and designed the experiments. A. G. C. and B. T. supervised the project and led the collaboration efforts. A. J.-M., B. M. and B. T. carried out the SPM experiments, obtained the data and performed on-surface reactions. F. V., J. M. C. and A. G. C. synthesized the precursors. The experimental data were analysed by A. J.-M. and B. T., and discussed by all the authors. S. E., A. M. and P. J. performed the theoretical calculations. The manuscript was written by A. J.-M., A. G. C. and B. T. with contributions from all the authors.

## Conflicts of interest

There are no conflicts to declare.

## Acknowledgements

The authors gratefully acknowledge the support of the Operational Programme for Research, Development, and Education of the European Regional Development Fund (Project No. CZ.02.1.01/0.0/0.0/16\_019/0000754), the European Research Council (ERC) under the European Union's Horizon 2020 research and innovation program (Grant Agreement 677023), and FEDER/Junta de Andalucía-Consejería de Transformación Económica, Industria, Conocimiento y Universidades (B.FQM.428.UGR20). F. V. thanks Ministerio de Universidades (Spain, FPU18/05938). P. J. and S. E. acknowledge the support of the GACR 20-13692X. B. M. and A. M. acknowledge the support from the Internal Student Grant Agency of the Palacký University in Olomouc, Czech Republic IGA\_PrF\_2022\_026 and IGA\_PrF\_2022\_019, respectively. B. M. further acknowledges the Fischer Scholarship.

## References

- Z. Qiu, B. A. G. Hammer and K. Müllen, Conjugated Polymers - Problems and Promises, *Prog. Polym. Sci.*, 2020, **100**, 101179, DOI: [10.1016/j.progpolymsci.2019.101179](https://doi.org/10.1016/j.progpolymsci.2019.101179).
- J. Roncali, Molecular Engineering of the Band Gap of  $\pi$ -Conjugated Systems: Facing Technological Applications, *Macromol. Rapid Commun.*, 2007, **28**(17), 1761–1775, DOI: [10.1002/marc.200700345](https://doi.org/10.1002/marc.200700345).
- Y. Olivier, D. Niedzialek, V. Lemaire, W. Pisula, K. Müllen, U. Koldemir, J. R. Reynolds, R. Lazzaroni, J. Cornil and D. Beljonne, 25th Anniversary Article: High-Mobility Hole and Electron Transport Conjugated Polymers: How Structure Defines Function, *Adv. Mater.*, 2014, **26**(14), 2119–2136, DOI: [10.1002/adma.201305809](https://doi.org/10.1002/adma.201305809).
- R. R. Parkhurst, T. M. Swager, J. S. Siegel and Y.-T. Wu, *Polymers II*, Springer International Publishing, 2014, vol. 350, DOI: [10.1007/978-3-319-07302-6](https://doi.org/10.1007/978-3-319-07302-6).
- Z. Zeng, X. Shi, C. Chi, J. T. López Navarrete, J. Casado and J. Wu, Pro-Aromatic and Anti-Aromatic p-Conjugated Molecules: An Irresistible Wish to Be Diradicals, *Chem. Soc. Rev.*, 2015, **44**(18), 6578–6596, DOI: [10.1039/c5cs00051c](https://doi.org/10.1039/c5cs00051c).
- C. K. Frederickson, B. D. Rose and M. M. Haley, Explorations of the Indenofluorenes and Expanded Quinoidal Analogues, *Acc. Chem. Res.*, 2017, **50**(4), 977–987, DOI: [10.1021/acs.accounts.7b00004](https://doi.org/10.1021/acs.accounts.7b00004).
- J. Liu, S. Mishra, C. A. Pignedoli, D. Passerone, J. I. Urgel, A. Fabrizio, T. G. Lohr, J. Ma, H. Komber, M. Baumgarten, C. Corminboeuf, R. Berger, P. Ruffieux, K. Müllen, R. Fasel and X. Feng, Open-Shell Nonbenzenoid Nanographenes Containing Two Pairs of Pentagonal and Heptagonal Rings, *J. Am. Chem. Soc.*, 2019, **141**(30), 12011–12020, DOI: [10.1021/jacs.9b04718](https://doi.org/10.1021/jacs.9b04718).
- M. Di Giovannantonio, K. Eimre, A. V. Yakutovich, Q. Chen, S. Mishra, J. I. Urgel, C. A. Pignedoli, P. Ruffieux, K. Müllen, A. Narita and R. Fasel, On-Surface Synthesis of Anti-aromatic and Open-Shell Indeno[2,1-b]fluorene Polymers and Their Lateral Fusion into Porous Ribbons, *J. Am. Chem. Soc.*, 2019, **141**(31), 12346–12354, DOI: [10.1021/jacs.9b05335](https://doi.org/10.1021/jacs.9b05335).

- 9 S. Mishra, D. Beyer, R. Berger, J. Liu, O. Grö, J. I. Urgel, K. Müllen, P. Ruffieux, X. Feng and R. Fasel, Topological Defect-Induced Magnetism in a Nanographene, *J. Am. Chem. Soc.*, 2020, **142**(3), 1147–1152, DOI: [10.1021/jacs.9b09212](https://doi.org/10.1021/jacs.9b09212).
- 10 S. Fujii, S. Marqués-González, J.-Y. Shin, H. Shinokubo, T. Masuda, T. Nishino, P. A. Narendra, H. Vázquez and M. Kiguchi, Highly-Conducting Molecular Circuits Based on Antiaromaticity, *Nat. Commun.*, 2017, **8**(1), 1–8, DOI: [10.1038/ncomms15984](https://doi.org/10.1038/ncomms15984).
- 11 G. P. Zhang, Z. Xie, Y. Song, M.-Z. Wei, G.-C. Hu and C.-K. Wang, Is There a Specific Correlation between Conductance and Molecular Aromaticity in Single-Molecule Junctions?, *Org. Electron.*, 2017, **48**, 29–34, DOI: [10.1016/j.orgel.2017.05.032](https://doi.org/10.1016/j.orgel.2017.05.032).
- 12 S. Gil-Guerrero, N. Ramos-Berdullas and M. Mandado, Can Aromaticity Enhance the Electron Transport in Molecular Wires?, *Org. Electron.*, 2018, **61**, 177–184, DOI: [10.1016/j.orgel.2018.05.043](https://doi.org/10.1016/j.orgel.2018.05.043).
- 13 Y. Chujo, *Conjugated Polymer Synthesis: Methods and Reactions*, John Wiley & Sons, 2011.
- 14 L. Grill and S. Hecht, Covalent On-Surface Polymerization, *Nat. Chem.*, 2020, **12**(2), 115–130, DOI: [10.1038/s41557-019-0392-9](https://doi.org/10.1038/s41557-019-0392-9).
- 15 S. Clair and D. G. de Oteyza, Controlling a Chemical Coupling Reaction on a Surface: Tools and Strategies for On-Surface Synthesis, *Chem. Rev.*, 2019, **119**(7), 4717–4776, DOI: [10.1021/ACS.CHEMREV.8B00601](https://doi.org/10.1021/ACS.CHEMREV.8B00601).
- 16 L. Grill, M. Dyer, L. Lafferentz, M. Persson, M. V. Peters and S. Hecht, Nano-Architectures by Covalent Assembly of Molecular Building Blocks, *Nat. Nanotechnol.*, 2007, **2**(11), 687–691, DOI: [10.1038/nnano.2007.346](https://doi.org/10.1038/nnano.2007.346).
- 17 S. Mishra, T. G. Lohr, C. A. Pignedoli, J. Liu, R. Berger, J. I. Urgel, K. Müllen, X. Feng, P. Ruffieux and R. Fasel, Tailoring Bond Topologies in Open-Shell Graphene Nanostructures, *ACS Nano*, 2018, **12**(12), 11917–11927, DOI: [10.1021/acsnano.8b07225](https://doi.org/10.1021/acsnano.8b07225).
- 18 D. G. de Oteyza, P. Gorman, Y.-C. Chen, S. Wickenburg, A. Riss, D. J. Mowbray, G. Etkin, Z. Pedramrazi, H.-Z. Tsai, A. Rubio, M. F. Crommie and F. R. Fischer, Direct Imaging of Covalent Bond Structure in Single-Molecule Chemical Reactions, *Science*, 2013, **340**(6139), 1434–1437, DOI: [10.1126/SCIENCE.1238187](https://doi.org/10.1126/SCIENCE.1238187).
- 19 A. Riss, A. Pérez Paz, S. Wickenburg, H.-Z. Tsai, D. G. de Oteyza, A. J. Bradley, M. M. Ugeda, P. Gorman, H. Sae Jung, M. F. Crommie, A. Rubio and F. R. Fischer, Imaging Single-Molecule Reaction Intermediates Stabilized by Surface Dissipation and Entropy, *Nat. Chem.*, 2016, **8**(7), 678–683, DOI: [10.1038/NCHEM.2506](https://doi.org/10.1038/NCHEM.2506).
- 20 A. Shiotari, T. Nakae, K. Iwata, S. Mori, T. Okujima, H. Uno, H. Sakaguchi and Y. Sugimoto, Strain-Induced Skeletal Rearrangement of a Polycyclic Aromatic Hydrocarbon on a Copper Surface, *Nat. Commun.*, 2017, **8**(1), 1–8, DOI: [10.1038/ncomms16089](https://doi.org/10.1038/ncomms16089).
- 21 J. Li, S. Sanz, M. Corso, D. J. Choi, D. Peña, T. Frederiksen and J. I. Pascual, Single Spin Localization and Manipulation in Graphene Open-Shell Nanostructures, *Nat. Commun.*, 2019, **10**(1), 1–7, DOI: [10.1038/s41467-018-08060-6](https://doi.org/10.1038/s41467-018-08060-6).
- 22 N. Pavliček, P. Gawel, D. R. Kohn, Z. Majzik, Y. Xiong, G. Meyer, H. L. Anderson and L. Gross, Polyene Formation via Skeletal Rearrangement Induced by Atomic Manipulation, *Nat. Chem.*, 2018, **10**(8), 853–858, DOI: [10.1038/s41557-018-0067-y](https://doi.org/10.1038/s41557-018-0067-y).
- 23 B. Schuler, S. Fatayer, F. Mohn, N. Moll, N. Pavliček, G. Meyer, D. Peña and L. Gross, Reversible Bergman Cyclization by Atomic Manipulation, *Nat. Chem.*, 2016, **8**(3), 220–224, DOI: [10.1038/NCHEM.2438](https://doi.org/10.1038/NCHEM.2438).
- 24 Y. Tobe, Non-Alternant Non-Benzenoid Aromatic Compounds: Past, Present, and Future, *Chem. Rev.*, 2015, **15**(1), 86–96, DOI: [10.1002/TCR.201402077](https://doi.org/10.1002/TCR.201402077).
- 25 A. Riss, S. Wickenburg, P. Gorman, L. Z. Tan, H. Z. Tsai, D. G. de Oteyza, Y.-C. Chen, A. J. Bradley, M. M. Ugeda, G. Etkin, S. G. Louie, F. R. Fischer and M. F. Crommie, Local Electronic and Chemical Structure of Oligo-Acetylene Derivatives Formed through Radical Cyclizations at a Surface, *Nano Lett.*, 2014, **14**(5), 2251–2255, DOI: [10.1021/NL403791Q](https://doi.org/10.1021/NL403791Q).
- 26 A. Riss, A. Pérez Paz, S. Wickenburg, H.-Z. Tsai, D. G. de Oteyza, A. J. Bradley, M. M. Ugeda, P. Gorman, H. Sae Jung, M. F. Crommie, A. Rubio and F. R. Fischer, Imaging Single-Molecule Reaction Intermediates Stabilized by Surface Dissipation and Entropy, *Nat. Chem.*, 2016, **8**(7), 678–683, DOI: [10.1038/NCHEM.2506](https://doi.org/10.1038/NCHEM.2506).
- 27 P. Ruffieux, S. Wang, B. Yang, C. Sánchez-Sánchez, J. Liu, T. Dienel, L. Talirz, P. Shinde, C. A. Pignedoli, D. Passerone, T. Dumslaff, X. Feng, K. Müllen and R. Fasel, On-Surface Synthesis of Graphene Nanoribbons with Zigzag Edge Topology, *Nature*, 2016, **531**(7595), 489–492, DOI: [10.1038/nature17151](https://doi.org/10.1038/nature17151).
- 28 M. Orchin and L. Reggel, Aromatic Cyclodehydrogenation. V. A Synthesis of Fluoranthene, *J. Am. Chem. Soc.*, 1947, **69**(3), 505–509, DOI: [10.1021/JA01195A009](https://doi.org/10.1021/JA01195A009).
- 29 B. Mallada, B. de la Torre, J. I. Medieta-Moreno, D. Nachtigallová, A. Matěj, M. Matoušek, P. Mutombo, J. Brabec, L. Veis, T. Cadart, M. Kotora and P. Jelinek, On-Surface Strain-Driven Synthesis of Nonalternant Non-Benzenoid Aromatic Compounds Containing Four- to Eight-Membered Rings, *J. Am. Chem. Soc.*, 2021, **143**(36), 14694–14702, DOI: [10.1021/jacs.1c06168](https://doi.org/10.1021/jacs.1c06168).
- 30 B. Mallada, Q. Chen, T. Chutora, A. Sánchez-Grande, B. Cirera, J. Santos, N. Martín, D. Ecija, P. Jelinek and B. de la Torre, Resolving Atomic-Scale Defects in Conjugated Polymers On-Surfaces, *Chem.-Eur. J.*, 2022, **28**(48), e202200944, DOI: [10.1002/CHEM.202200944](https://doi.org/10.1002/CHEM.202200944).
- 31 L. R. Márquez, N. Ruiz Del Árbol, J. I. Urgel, F. Villalobos, R. Fasel, M. F. López, J. M. Cuerva, J. A. Martín-Gago, A. G. Campaña and C. Sánchez-Sánchez, On-Surface Thermal Stability of a Graphenic Structure Incorporating a Tropone Moiety, *Nanomaterials*, 2022, **12**(3), 488, DOI: [10.3390/NANO12030488](https://doi.org/10.3390/NANO12030488).
- 32 C. Sánchez-Sánchez, T. Dienel, A. Nicolai, N. Kharche, L. Liang, C. Daniels, V. Meunier, J. Liu, X. Feng, K. Müllen, J. R. Sánchez-Valencia, O. Gröning, P. Ruffieux and

- R. Fasel, On-Surface Synthesis and Characterization of Acene-Based Nanoribbons Incorporating Four-Membered Rings, *Chem.-Eur. J.*, 2019, **25**(52), 12074–12082, DOI: [10.1002/CHEM.201901410](https://doi.org/10.1002/CHEM.201901410).
- 33 M. Liu, M. Liu, L. She, Z. Zha, J. Pan, S. Li, T. Li, Y. He, Z. Cai, J. Wang, Y. Zheng, X. Qiu and D. Zhong, Graphene-like Nanoribbons Periodically Embedded with Four- and Eight-Membered Rings, *Nat. Commun.*, 2017, **8**(1), 1–7, DOI: [10.1038/ncomms14924](https://doi.org/10.1038/ncomms14924).
- 34 Q. Fan, D. Martin-Jimenez, D. Ebeling, C. K. Krug, L. Brechmann, C. Kohlmeyer, G. Hilt, W. Hieringer, A. Schirmeisen and J. M. Gottfried, Nanoribbons with Nonalternant Topology from Fusion of Polyazulene: Carbon Allotropes beyond Graphene, *J. Am. Chem. Soc.*, 2019, **141**(44), 17713–17720, DOI: [10.1021/jacs.9b08060](https://doi.org/10.1021/jacs.9b08060).
- 35 J. Deyerling, M. Pörtner, L. Đorđević, A. Riss, D. Bonifazi and W. Auwärter, On-Surface Synthesis of Rigid Benzenoid- and Nonbenzenoid-Coupled Porphyrin-Graphene Nanoribbon Hybrids, *J. Phys. Chem. C*, 2022, **126**(19), 8467–8476, DOI: [10.1021/ACS.JPCA.2C00912](https://doi.org/10.1021/ACS.JPCA.2C00912).
- 36 M. Di Giovannantonio, J. I. Urgel, U. Beser, A. V. Yakutovich, J. Wilhelm, C. A. Pignedoli, P. Ruffieux, A. Narita, K. Müllen and R. Fasel, On-Surface Synthesis of Indeno[fluorene] Polymers by Oxidative Five-Membered Ring Formation, *J. Am. Chem. Soc.*, 2018, **140**(10), 3532–3536, DOI: [10.1021/JACS.8B00587](https://doi.org/10.1021/JACS.8B00587).
- 37 M. Liu, M. Liu, Z. Zha, J. Pan, X. Qiu, T. Li, J. Wang, Y. Zheng and D. Zhong, Thermally Induced Transformation of Nonhexagonal Carbon Rings in Graphene-like Nanoribbons, *J. Phys. Chem. C*, 2018, **122**(17), 9586–9592, DOI: [10.1021/ACS.JPCA.8B02565](https://doi.org/10.1021/ACS.JPCA.8B02565).
- 38 J. I. Urgel, J. Bock, M. Di Giovannantonio, P. Ruffieux, C. A. Pignedoli, M. Kivala and R. Fasel, On-Surface Synthesis of  $\pi$ -Conjugated Ladder-Type Polymers Comprising Nonbenzenoid Moieties, *RSC Adv.*, 2021, **11**(38), 23437–23441, DOI: [10.1039/D1RA03253D](https://doi.org/10.1039/D1RA03253D).
- 39 L. C.-Y. Hou, Q. Sun, K. Eimre, M. Di Giovannantonio, J. I. Urgel, P. Ruffieux, A. Narita, R. Fasel and K. Müllen, On-Surface Synthesis of Unsaturated Carbon Nanostructures with Regularly Fused Pentagon-Heptagon Pairs, *J. Am. Chem. Soc.*, 2020, **142**(23), 10291–10296, DOI: [10.1021/JACS.0C03635](https://doi.org/10.1021/JACS.0C03635).
- 40 H.-Y. Gao, H. Wagner, D. Zhong, J.-H. Franke, A. Studer and H. Fuchs, Glaser Coupling at Metal Surfaces, *Angew. Chem., Int. Ed.*, 2013, **52**(14), 4024–4028, DOI: [10.1002/ANIE.201208597](https://doi.org/10.1002/ANIE.201208597).
- 41 B. de la Torre, A. Matěj, A. Sánchez-Grande, B. Cirera, B. Mallada, E. Rodríguez-Sánchez, J. Santos, J. I. Mendieta-Moreno, S. Edalatmanesh, K. Lauwaet, M. Otyepka, M. Medved, Á. Buendía, R. Miranda, N. Martín, P. Jelinek and D. Ćejić, Tailoring  $\pi$ -Conjugation and Vibrational Modes to Steer on-Surface Synthesis of Pentalene-Bridged Ladder Polymers, *Nat. Commun.*, 2020, **11**(1), 4567, DOI: [10.1038/s41467-020-18371-2](https://doi.org/10.1038/s41467-020-18371-2).
- 42 B. Yang, H. Lin, K. Miao, P. Zhu, L. Liang, K. Sun, H. Zhang, J. Fan, V. Meunier, Y. Li, Q. Li and L. Chi, Catalytic Dealkylation of Ethers to Alcohols on Metal Surfaces, *Angew. Chem.*, 2016, **128**(34), 10035–10039, DOI: [10.1002/ANGE.201602414](https://doi.org/10.1002/ANGE.201602414).
- 43 J. Krüger, F. García, F. Eisenhut, D. Skidin, J. M. Alonso, E. Guitián, D. Pérez, G. Cuniberti, F. Moresco and D. Peña, Decacene: On-Surface Generation, *Angew. Chem., Int. Ed.*, 2017, **56**(39), 11945–11948, DOI: [10.1002/ANIE.201706156](https://doi.org/10.1002/ANIE.201706156).
- 44 W. Fudickar and T. Linker, Why Triple Bonds Protect Acenes from Oxidation and Decomposition, *J. Am. Chem. Soc.*, 2012, **134**(36), 15071–15082, DOI: [10.1021/JA306056X](https://doi.org/10.1021/JA306056X).
- 45 H.-Y. Gao, P. A. Held, S. Amirjalayer, L. Liu, A. Timmer, B. Schirmer, O. Díaz Arado, H. Mönig, C. Mück-Lichtenfeld, J. Neugebauer, A. Studer and H. Fuchs, Intermolecular On-Surface  $\sigma$ -Bond Metathesis, *J. Am. Chem. Soc.*, 2017, **139**(20), 7012–7019, DOI: [10.1021/JACS.7B02430](https://doi.org/10.1021/JACS.7B02430).
- 46 A. Sánchez-Grande, B. de la Torre, J. Santos, B. Cirera, K. Lauwaet, T. Chutora, S. Edalatmanesh, P. Mutombo, J. Rosen, R. Zbořil, R. Miranda, J. Björk, P. Jelinek, N. Martín and D. Ćejić, On-Surface Synthesis of Ethynylene-Bridged Anthracene Polymers, *Angew. Chem.*, 2019, **131**(20), 6631–6635, DOI: [10.1002/ANGE.201814154](https://doi.org/10.1002/ANGE.201814154).
- 47 Q. Sun, X. Yu, M. Bao, M. Liu, J. Pan, Z. Zha, L. Cai, H. Ma, C. Yuan, X. Qiu and W. Xu, Direct Formation of C-C Triple-Bonded Structural Motifs by On-Surface Dehalogenative Homocouplings of Tribromomethyl-Substituted Arenes, *Angew. Chem., Int. Ed.*, 2018, **57**(15), 4035–4038, DOI: [10.1002/ANIE.201801056](https://doi.org/10.1002/ANIE.201801056).
- 48 J. Cioslowski, M. Schimeczek, P. Piskorz and D. Moncrieff, Thermal Rearrangement of Ethynylarenes to Cyclopenta fused Polycyclic Aromatic Hydrocarbons: An Electronic Structure Study, *J. Am. Chem. Soc.*, 1999, **121**(15), 3773–3778, DOI: [10.1021/JA9836601](https://doi.org/10.1021/JA9836601).
- 49 L. Gross, F. Mohn, N. Moll, P. Liljeroth and G. Meyer, The Chemical Structure of a Molecule Resolved by Atomic Force Microscopy, *Science*, 2009, **325**(5944), 1110–1114, DOI: [10.1126/science.1176210](https://doi.org/10.1126/science.1176210).
- 50 B. Lowe, J. Hellerstedt, A. Matěj, P. Mutombo, D. Kumar, M. Ondráček, P. Jelinek and A. Schiffrin, Selective Activation of Aromatic C-H Bonds Catalyzed by Single Gold Atoms at Room Temperature, *J. Am. Chem. Soc.*, 2022, **144**(46), 21389–21397, DOI: [10.1021/jacs.2c10154](https://doi.org/10.1021/jacs.2c10154).
- 51 K. Gilmore and I. V. Alabugin, Cyclizations of Alkynes: Revisiting Baldwin's Rules for Ring Closure, *Chem. Rev.*, 2011, **111**(11), 6513–6556, DOI: [10.1021/CR200164Y](https://doi.org/10.1021/CR200164Y).
- 52 Y.-Q. Zhang, N. Kepčija, M. Kleinschrodt, K. Diller, S. Fischer, A. C. Papageorgiou, F. Allegretti, J. Björk, S. Klyatskaya, F. Klappenberger, M. Ruben and J. V. Barth, Homo-Coupling of Terminal Alkynes on a Noble Metal Surface, *Nat. Commun.*, 2012, **3**(1), 1–8, DOI: [10.1038/ncomms2291](https://doi.org/10.1038/ncomms2291).
- 53 D. Sen, P. Błoński, B. de la Torre, P. Jelinek and M. Otyepka, Thermally Induced Intra-Molecular Transformation and Metalation of Free-Base Porphyrin on Au(111) Surface Steered by Surface Confinement and Ad-Atoms, *Nanoscale Adv.*, 2020, **2**(7), 2986–2991, DOI: [10.1039/D0NA00401D](https://doi.org/10.1039/D0NA00401D).
- 54 C. Glidewell and D. Lloyd, Mn<sup>0</sup> Study of Bond Orders in Some Conjugated Bi- and Tri-Cyclic Hydrocarbons,



- Tetrahedron*, 1984, **40**(21), 4455–4472, DOI: [10.1016/S0040-4020\(01\)98821-0](https://doi.org/10.1016/S0040-4020(01)98821-0).
- 55 L. Gross, F. Mohn, N. Moll, B. Schuler, A. Criado, E. Guitián, D. Peña, A. Gourdon and G. Meyer, Bond-Order Discrimination by Atomic Force Microscopy, *Science*, 2012, **337**(6100), 1326–1329, DOI: [10.1126/science.1225621](https://doi.org/10.1126/science.1225621).
- 56 M. Kertesz, C. H. Choi and S. Yang, Conjugated Polymers and Aromaticity, *Chem. Rev.*, 2005, **105**(10), 3448–3481, DOI: [10.1021/CR990357P](https://doi.org/10.1021/CR990357P).
- 57 P. V. R. Schleyer, C. Maerker, A. Dransfeld, H. Jiao and N. J. van Eikema Hommes, Nucleus-Independent Chemical Shifts: A Simple and Efficient Aromaticity Probe, *J. Am. Chem. Soc.*, 1996, **118**(26), 6317–6318, DOI: [10.1021/JA960582D](https://doi.org/10.1021/JA960582D).
- 58 D. Geuenich, K. Hess, F. Köhler and R. Herges, Anisotropy of the Induced Current Density (ACID), a General Method To Quantify and Visualize Electronic Delocalization, *Chem. Rev.*, 2005, **105**(10), 3758–3772, DOI: [10.1021/cr0300901](https://doi.org/10.1021/cr0300901).
- 59 A. J. Cohen, P. Mori-Sánchez and W. Yang, Insights into Current Limitations of Density Functional Theory, *Science*, 2008, **321**(5890), 792–794, DOI: [10.1126/SCIENCE.1158722](https://doi.org/10.1126/SCIENCE.1158722).
- 60 J. B. Neaton, M. S. Hybertsen and S. G. Louie, Renormalization of Molecular Electronic Levels at Metal-Molecule Interfaces, *Phys. Rev. Lett.*, 2006, **97**(21), 216405, DOI: [10.1103/PHYSREVLETT.97.216405](https://doi.org/10.1103/PHYSREVLETT.97.216405).
- 61 G. Li, R. Zhu and Y. Yang, Polymer Solar Cells, *Nat. Photonics*, 2012, **6**, 153–161, DOI: [10.1038/nphoton.2012.11](https://doi.org/10.1038/nphoton.2012.11).
- 62 R. A. J. Janssen and J. Nelson, Factors Limiting Device Efficiency in Organic Photovoltaics, *Adv. Mater.*, 2013, **25**(13), 1847–1858, DOI: [10.1002/adma.201202873](https://doi.org/10.1002/adma.201202873).
- 63 Y. Zhao, Y. Guo and Y. Liu, 25th Anniversary Article: Recent Advances in n-Type and Ambipolar Organic Field-Effect Transistors, *Adv. Mater.*, 2013, **25**(38), 5372–5391, DOI: [10.1002/adma.201302315](https://doi.org/10.1002/adma.201302315).

## Single-Molecule Identification of the Isomers of a Lipidic Antibody Activator

Benjamin Mallada,<sup>†</sup> Federico Villalobos,<sup>†</sup> Beatriz Donoso, Raquel Casares, Giovanna Longhi, Jesús I. Mendieta-Moreno, Alejandro Jiménez-Martín, Ali Haïdour, Ravin Seepersaud, Lakshmi Rajagopal, Bruno de la Torre,\* Alba Millán,\* and Juan M. Cuerva\*

Cite This: *J. Phys. Chem. Lett.* 2024, 15, 6935–6942

Read Online

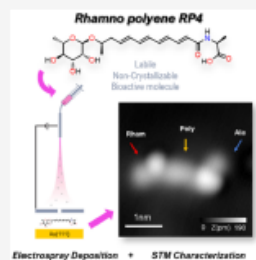
ACCESS |

Metrics & More

Article Recommendations

Supporting Information

**ABSTRACT:** Molecular structural elucidation can be accomplished by different techniques, such as nuclear magnetic resonance or X-ray diffraction. However, the former does not give information about the three-dimensional atomic arrangement, and the latter needs crystallizable solid samples. An alternative is direct, real-space visualization of the molecules by cryogenic scanning tunneling microscopy (STM). This technique is usually limited to thermally robust molecules because an annealing step is required for sample deposition. A landmark development has been the coupling of STM with electrospray deposition (ESD), which smooths the process and widens the scope of the visualization technique. In this work, we present the on-surface characterization of air-, light-, and temperature-sensitive rhamnopolyene with relevance in molecular biology. Supported by theoretical calculations, we characterize two isomers of this flexible molecule, confirming the potential of the technique to inspect labile, non-crystallizable compounds.



One of the most relevant advances in human knowledge has been the understanding of biological processes and its dramatic consequences for human health.<sup>1,2</sup> Such processes usually rely on a fine interplay between organic-based entities, which, in many cases, are labile outside the biological protecting media. The molecular interactions are highly dependent upon functionality and also geometry at the molecular level. Therefore, determining the structure of such organic molecules is critical to rationalizing their mechanism of action. Routinely, nuclear magnetic resonance (NMR) techniques are used to assign the structure of organic compounds. However, these techniques are limited in their capability to discern the constitution and configuration of molecules, which lead on occasions to wrong assignments.<sup>3,4</sup> Furthermore, the outputs come from a myriad of individual molecules, which introduces a notable drawback, as the precise assignment or manipulation of individual structures lies beyond the scope of this methodology. A more precise approach to structural analysis relies on X-ray diffraction of single crystals. In such a case, the distance and relative positions between the atoms are acquired, showing the connectivity (molecular constitution) and three-dimensional (3D) structure (molecular configuration). Despite its undoubted utility, a key limitation remains because it is not always possible to grow high-quality single crystals.<sup>5</sup> Although crystalline sponges (CSs)<sup>6</sup> have been proposed as an alternative, the technique requires a careful selection of the CS, which varies depending upon the target molecule.<sup>7</sup> Moreover, this technique continues to analyze an ensemble

of molecules without any possible molecular manipulation. Cryogenic electron microscopy (cryo-EM) has emerged as another tool allowing for the characterization of macromolecules.<sup>8</sup> Despite the impressive results that can be achieved, atomic manipulation cannot be performed on the samples. Therefore, the development of an alternative technique of general use is of utmost demand for the structural identification and manipulation of organic compounds.

Technological advances have allowed for the imaging of molecules with unprecedented resolution on different surfaces, thus creating a potent tool for electronic and structural analysis.<sup>9–11</sup> In fact, cryogenic scanning tunneling microscopy (STM) allows for real-space imaging of individual molecules deposited on a surface under ultrahigh vacuum (UHV) conditions with sub-nanometer resolution, resulting in a unique instrument for the study of molecular structures, molecular interactions, and reactivity in a controlled environment.<sup>12,13</sup> Remarkably, tip manipulation also makes a direct non-destructive interaction with the substrate possible at the unimolecular level. That characteristic allows for stability or integrity studies among others.<sup>14</sup> Nevertheless, some intrinsic

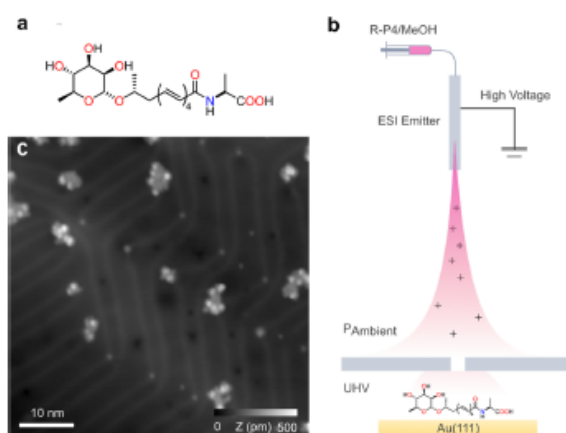
Received: January 17, 2024

Revised: March 29, 2024

Accepted: May 3, 2024

Published: June 27, 2024





**Figure 1.** Electrospray deposition on Au(111) of RP4. (a) Chemical structure of RP4 with the rhamnose group (left), the polyenic chain, and the alanine group (right). (b) Schematic of the ESD from the liquid solution to the Au(111) sample in UHV. (c) Constant-current STM overview of Au(111) after ESD of solution RP4/methanol.

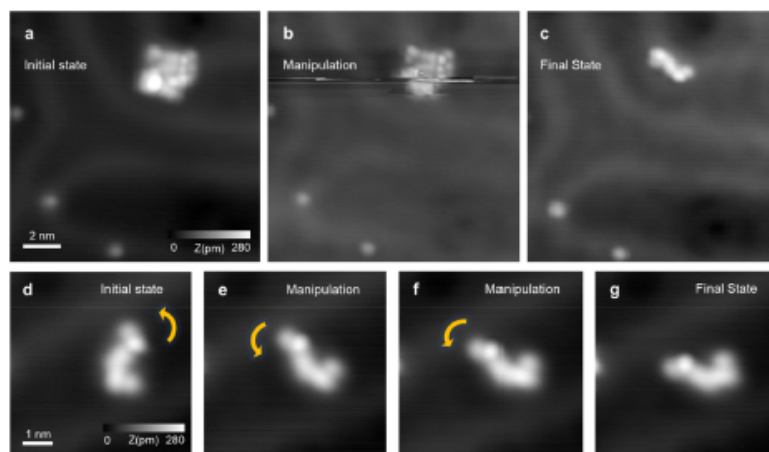
drawbacks related to sample deposition have limited the studies mainly to molecules with high thermal stability as a result of the UHV sublimation process required for sample deposition. Considering the vast number of potential organic structures, innovations capable of dealing with thermally labile or even unstable molecules would be in the forefront of the technique.<sup>15–17</sup> One potential solution is the combination of STM with electrospray deposition (ESD) or electrospray ion beam deposition (ES-IBD),<sup>18,19</sup> which has been demonstrated for the imaging of numerous organic molecules.<sup>20–30</sup> The soft landing of molecules on the atomically clean surface is an excellent alternative for transferring them as a result of its compatibility with many typical organic functional groups. Therefore, the ESD technique presents unique characteristics allowing for the visualization and manipulation of highly sensitive molecular architectures, including those out of the scope of X-ray diffraction techniques, at the unimolecular level in a controlled environment. However, the characteristic exponential decay of the tunneling current with the tip–sample distance still prevents its use for large nonplanar molecular structures where it is more conveniently imaged and characterized using other techniques, such as cryo-EM (e.g.,  $\beta$ -galactosidase).<sup>31</sup>

Although some examples have been reported,<sup>28,32,33</sup> the study of synthetic compounds with relevant biological interest has been less explored and would open new opportunities for this technique. Therefore, we focus on a synthetic lipidic molecule (RP4 in Figure 1a), which mimics a more complex natural product: granadaene.<sup>34,35</sup> This latter longer polyene is cytotoxic/hemolytic and is a key virulence factor promoting all facets of group B *Streptococcus* (GBS) disease.<sup>36–42</sup> Although GBS typically resides in the lower genital tract of healthy women, perinatal GBS infections lead to preterm births, stillbirths, or severe diseases in newborns.<sup>43–45</sup> Currently, no vaccine exists to prevent GBS infections in humans. This is due in part to the difficulty in neutralizing these toxic lipids and challenges in generating non-toxic antigenic lipids. Despite these challenges, we recently showed that RP4 is a non-

hemolytic lipid, and RP4 immunization conferred the production of antibodies that inhibited granadaene-mediated hemolysis and diminished GBS infection in both non-pregnant and pregnant mice.<sup>46,47</sup> RP4 is composed of three distinct components, namely, a rhamnose unit, a terminal amino acid group (alanine), and a main chain consisting of four conjugated double bonds (the acronym RP4 refers to a rhamnopolyene with four double bonds). RP4 shows ideal characteristics for this STM–ESD proof-of-concept study: (i) the structure is known, which is relevant for the validation of the results; (ii) it is polyenic in nature, with RP4 being sensitive to air, temperature, and light and, therefore, labile and ambient unstable; and (iii) it is a non-crystallizable liquid. Moreover, it represents a model for a family of biologically relevant polyenes whose structure is not completely understood, being difficult to manage as a result of its instability. The RP4 determination by this technique paves the way for future structural assignment and understanding of pathogenic behavior of human-threatening GBS bacteria.

Furthermore, the understanding of its structure at the unimolecular level would be a step forward in the understanding of its mode of action as a potential vaccine. Despite the significant difference between the metal surface in UHV and the liquid environment of a vaccine, this exploratory study exemplifies how direct imaging and manipulation of the RP4 molecule by STM allows us to unambiguously discriminate the configuration and structure of individual isomers on the surface.

We first prepared RP4 (Figure 1a) following a stereoselective synthetic approach, affording the all-*E* isomer as the major product (see the Supporting Information for further details). The molecular deposition of RP4 on atomically defined Au(111) was carried out under UHV conditions at room temperature, as illustrated in Figure 1b. The ESD technique was employed to deposit a solution of RP4 in methanol (2 mg/mL) onto the surface, as described in the “Experimental and Computational Methods” section. It is important to note that our setup did not include mass or



**Figure 2.** Isolation and manipulation of the RP4 isomers from clusters. (a–c) Detail in constant current STM of the separation of RP4 clusters by tip manipulation. (d–g) Sequence of STM images displaying a tip-induced manipulation on a single monomer from an initial state (d) to a final state (g) through a sequence of rotations (see the Supporting Information for further examples). Scanning parameters: (a)  $V_t = 501$  mV and  $I = 10$  pA, (b)  $V_t = 1$  mV and  $I = 10$  pA, (c)  $V_t = 51$  mV and  $I = 10$  pA, and (d–g)  $V_t = 501$  mV and  $I = 10$  pA.

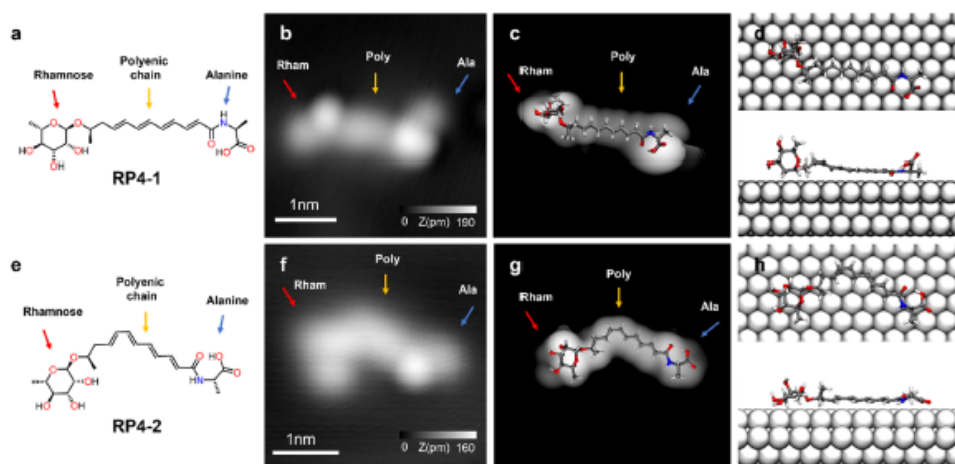
energy selection. The sample was then quickly transferred to a cryogenic scanning tunneling microscope operating at 4.8 K for further examination. The large-scale STM topographs (Figure 1c) revealed that RP4 molecules tend to agglomerate into small and disordered two-dimensional clusters with typical apparent heights ranging from 260 to 500 pm (see the Supporting Information). We postulate that the aggregation of RP4 occurs at the Au surface owing to low surface diffusion barriers and large molecular mobility at room temperature, with the aggregates being stabilized by dispersion forces and hydrogen bonding involving OH of the rhamnose moiety.<sup>28,48</sup> It is important to note that, despite ESD being an ionization process, it is plausible to assume that the ions neutralize rapidly upon contact with the metallic surface as a result of charge transfer with the surface.

To investigate the chemical composition of the clusters, we employed tip-induced manipulations to isolate individual molecular units for a thorough examination. The procedure involved a concise mechanical interaction between the tip and the molecule, resulting in the tip exerting a pulling force on certain parts of the cluster in the direction of fast scanning. Specifically, we deliberately modified the imaging conditions, particularly the tip–sample distance, to separate the molecular aggregates into individual units, as shown in Figure 2 (further details in the “Experimental and Computational Methods” section). Figure 2a illustrates the initial state before cluster manipulation. When the bias voltage was ramped down (from 501 to 1 mV) while scanning the cluster, the tip–sample height was lowered, thus increasing the tip–cluster interaction, as shown in Figure 2b. This step was critical to achieve the separation of the molecular aggregates into individual units. The outcome of cluster manipulation is depicted in Figure 2c, where a single object can be clearly identified. Crucially, this entity possesses a quantifiable length of 2.7 nm, akin to the theoretical extension of the RP4 molecule in the STM-calculated images. This procedure enabled us to discern the

chemical content of the clusters and provided a more comprehensive understanding of the properties and behavior of RP4 on the surface. The procedure was repeated over several aggregates, systematically leading to the isolation of single objects with similar characteristics on the surface. However, this method of isolation does not necessarily preclude the presence of other chemical entities on the surface despite only observing single molecules during the cleaning process. Remarkably, following the manipulation of the cluster, no residual material was observed in the vicinity of the scanned region nor were there any alterations to the tip apex. As a consequence, the complete identification and assignment of structures to single molecules require a careful assessment of the surface chemistry of the clusters.

Next, we conducted controlled molecular manipulations on the single objects using STM to further demonstrate the chemical integrity and stability of the single RP4 molecule. Specifically, we induced rotations and translations of individual RP4 molecules using the STM tip, as illustrated in panels d–g of Figure 2, following isolation of the molecule, as described above. This process was executed sequentially, with each step being imaged to track the position of the molecule from an initial state to a final state. The full manipulation sequence provided compelling evidence that the characteristic functional groups of RP4 remained intact throughout the manipulation process and that the molecule was covalently bonded, with no evidence of tip-induced isomerizations or irreversible changes. These results further reinforce the chemical and stereochemical stability of the RP4 molecule and its potential applicability.

We now shift our focus to examining the stereochemistry of RP4 molecules on the surface. This molecule is relatively complex with a huge number of potential conformations in solution. Full understanding the conformational space of RP4 is crucial to comprehend its potential interactions with other biomolecules and its relevance to biomedical applications.



**Figure 3.** Visualization of RP4 isomers. (a and e) Chemical structures of the visualized RP4 isomers. (b and f) Corresponding constant-current STM images. The RP4-1 isomer displays the rhamnose group in one end, four *E*-alkenes in *s-trans* conformation, and the alanine amino acid in the other end. The RP4-2 isomer presents one of the diene moieties in a *s-cis* conformation. (c and g) STM-simulated images of both RP4 isomers with a superimposed model. (d and h) DFT-calculated conformations for RP4 isomers. Scanning parameters: (b)  $V_s = 51$  mV and  $I = 10$  pA and (f)  $V_s = 501$  mV and  $I = 10$  pA.

Moreover, the main conformer present in solution may not always be involved in molecular recognition or docking processes.

Two different isomers, RP4-1 and RP4-2, were experimentally observed, with the first isomer being much more commonly found (Figure 3). In both RP4 isomer images, we can identify the central polyenic chain flanked by two bright protrusions that correspond to rhamnose and the terminal amino acid. The main difference lies in the more curved central part of RP4-2 (Figure 3f). The structural assignment of such isomers was carried out with the aid of theoretical calculations. A completely unbiased conformational search *in vacuo* with the CREST tool<sup>49</sup> gives a prevalence of folded structures in which the sugar and amino acid terminus are hydrogen-bonded, yielding a curved polyene chain not corresponding to the observed shape (see section 5.1 of the Supporting Information). These curved structures are not likely to be energetically favored on the metallic surface because favorable alkene–surface interactions are avoided. Therefore, it is not surprising that the gold surface was limiting the number of 3D arrangements compared to the vacuum. It is also worth noting that such arrangements may not be more frequent in solution. In that way, we can analyze conformations that are statistically hidden in solution. Considering that molecules arrive to the surface from solution/vacuum, the initially observed aggregates (Figure 2a) could be related with very different RP4 conformers. Nevertheless, manipulations performed to isolate the single molecule drive the system toward RP4 flat isomers to maximize the surface– $\pi$  interactions. To find conformers suitable for testing on a Au surface by the calculations described in the following, a new conformational search for the all *E* isomer was carried out maintaining the *trans*-planar structural characteristic fixed while exploring all conformational possibilities for the two moieties: the rhamnose part and the amino acid (see the “Experimental and Computational

Methods” section for general details and the Supporting Information for the preliminary study of the two independent parts). Two principal conformers were then identified that are partially folded (Table S3 of the Supporting Information), presenting rhamnose parallel to the polyene chain. Although they are challenging for STM elucidation, simple rotations around the rhamnose polyene bridge give a realistic conformation on the surface (see Figure S10 of the Supporting Information for a comparison of the folded geometry versus the extended geometry). This folding is energetically favorable via an energy minimization from the interactions of oxygenated functionalities with the metallic surface. We performed computational simulations with the quantum mechanics (QM)/molecular mechanics (MM) approach<sup>50</sup> to characterize the geometry of the RP4 molecule on the surface for both isomers (panels d and h of Figure 3), and the corresponding STM theoretical images were simulated with a reasonable match to the experimental images (Figure 3c versus Figure 3b and Figure 3g versus Figure 3f) (see the “Experimental and Computational Methods” section for details). Our STM-simulated images accurately replicate the visual representation of the elongated central polyenic chain and the protrusions arising from the out-of-the-surface plane configuration of both rhamnose and the terminal amino acid. Guided by theoretical conformational analysis and supported by simulated images, we elucidate that the major isomer RP4-1 corresponds to the all *s-trans* conformation (Figure 3a), whereas the minor isomer RP4-2 comes from the energetically unfavorable conformation, in which diene closer to rhamnose has a *s-cis* conformation instead of the energetically favored *s-trans* conformation found in isomer RP4-1 (Figure 3e). We cannot discard the fact that the rotation of the single bond that gives *s-cis* diene occurs during the deposition/isolation experiments as a result of the low activation barrier to access such a conformation. Remarkably, as shown in Figure 2, tip-induced manipulations

of the molecule did not promote a conformational change, maintaining the molecule unaltered.

In conclusion, the present study highlights the robust potential in the synergistic application of ESD in conjunction with UHV-STM for probing the intricate understanding of labile and/or non-crystallizable molecular structures on atomically defined surfaces, achieving submolecular resolution. Specifically, we aimed to investigate the chemical structure of the rhamnopolyene lipid RP4 on Au(111). The STM images obtained from our experiments revealed the coexistence of two distinct conformational isomers of RP4 on the surface, which we further confirmed through single-molecule manipulation experiments, thereby establishing the chemical stability of the molecule. Furthermore, we performed density functional theory (DFT) calculations considering flat polyene structures to corroborate our experimental results and used such structures to simulate STM images. Our findings provide novel insights into the chemical structure of a labile complex molecule of biological interest and pave the way for future detailed investigations in this area. Further studies addressing the structural elucidation of more complex polyenes, such as granadaene, or exploring the interaction of RP4 with subsequently electrospray-deposited amino acids or carbohydrates can be envisioned.

#### Experimental and Computational Methods. *Synthesis.*

Unless otherwise stated, all reagents and solvents were purchased from commercial sources and used without further purification. Anhydrous tetrahydrofuran (THF) was freshly distilled over Na/benzophenone. Flash column chromatography was carried out using silica gel 60 (40–63  $\mu\text{m}$ ) as the stationary phase. Analytical thin-layer chromatography (TLC) was performed on aluminum sheets coated with silica gel with fluorescent indicator UV254, observed under UV light (254 nm), and stained with phosphomolybdic acid (5% methanol solution). All  $^1\text{H}$  and  $^{13}\text{C}$  nuclear magnetic resonance (NMR) spectra were recorded on Bruker Avance Neo (400 or 500 MHz) spectrometers at a constant temperature of 298 K. Chemical shifts are reported in parts per million (ppm) and referenced to residual solvent:  $\text{CHCl}_3$  (7.27 and 77.0 ppm for  $^1\text{H}$  and  $^{13}\text{C}$ , respectively), and MeOH (3.31 and 49.0 ppm for  $^1\text{H}$  and  $^{13}\text{C}$ , respectively). Coupling constants ( $J$ ) are reported in hertz. Multiplicities are abbreviated as follows: s, singlet; br s, broad singlet; d, doublet; t, triplet; m, multiplet; dd, doublet of doublets; td, triplet of doublets; ddd, doublet of doublet of doublets; and dt, doublet of triplets. Proton assignment was carried out by two-dimensional (2D) NMR experiments: correlation spectroscopy (COSY), heteronuclear single-quantum correlation (HSQC), and heteronuclear multiple-bond correlation (HMBC), where possible. Assignment of the  $^{13}\text{C}$  NMR multiplicities was accomplished by distortionless enhancement by polarization transfer (DEPT) techniques. Electrospray ionization time-of-flight (ESI-TOF) mass spectra were recorded in a Waters Xevo G2-XS QToF. RP4 was prepared according to the literature,<sup>46</sup> with some modifications detailed in the Supporting Information.

*Scanning Probe Microscopy.* The experiments were conducted within an UHV environment, where the base pressure was maintained below  $5 \times 10^{-10}$  mbar. The setup included a low-temperature scanning tunneling microscope (Createc GmbH) operating at 4.2 K. Imaging was performed using a Pt/Ir tip with the bias voltage applied to the sample. Metallic tips were achieved through controlled indentations on the exposed surface. Au(111) was prepared via standard cycles of Ar<sup>+</sup>

sputtering and annealing. The ESDs were carried out using a commercial system (MolecularSpray, Ltd.) outfitted with several pumping stages. Our ESD setup was run in positive mode; that is, a positive bias is applied to the emitter. The setup was linked to the UHV preparation chamber. RP4 was dissolved in methanol to form a solution with a concentration of 2 mg/mL. The deposition was performed on the sample at ambient temperature. During the spray deposition, the pressure in the chamber was less than  $1 \times 10^{-7}$  mbar. Typically, the voltages applied to the capillary ranged between 2 and 2.3 kV with necessary adjustments to maintain spray stability while keeping an approximate pumping rate of 60  $\mu\text{L}/\text{h}$  for 60 min. After deposition, the sample was immediately transferred to the analysis chamber in UHV and cooled down to 4.2 K. All data were subject to standard processes using the WSxM software<sup>51</sup> without any filtering or smoothing. Approximately, more than 20 RP4 molecules were considered in dozens of STM overviews of  $50 \times 50 \text{ nm}^2$ . The molecular manipulation to separate RP4 from the conglomerated islands was performed by scanning in constant current mode a conglomerate with a bias voltage of 1 mV and a tunneling current of 10 pA. After every manipulation event, the frame was rescanned in constant current mode with a bias voltage of 500 mV and a tunneling current of 10 pA. Single-molecule manipulation has been performed in constant current mode (10 pA) by ranging the bias to 1 mV.

*Theoretical Calculations.* A completely unbiased conformational search *in vacuo* was carried out with the CREST tool.<sup>49</sup> After the CREST conformational search, structures have been optimized at the M06/txvp level with the Gaussian 16 package.<sup>52</sup> RP4 structures on Au(111) have been calculated using a QM/MM approach<sup>50</sup> with the molecules described with Fireball DFT<sup>53</sup> and the surface described with the interface force field.<sup>54</sup> More details are given in the Supporting Information.

## ■ ASSOCIATED CONTENT

### Supporting Information

The Supporting Information is available free of charge at <https://pubs.acs.org/doi/10.1021/acs.jpclett.4c00164>.

General details, synthetic procedures, copy of  $^1\text{H}$  NMR and high-resolution mass spectra, additional figures of the on-surface characterization of RP4, and computational details (PDF)

## ■ AUTHOR INFORMATION

### Corresponding Authors

**Bruno de la Torre** – Regional Centre of Advanced Technologies and Materials, Czech Advanced Technology and Research Institute (CATRIN), Palacký University Olomouc, 78371 Olomouc, Czech Republic; [bruno.de@upol.cz](mailto:bruno.de@upol.cz); orcid.org/0000-0002-6462-6833; Email: [bruno.de@upol.cz](mailto:bruno.de@upol.cz)

**Alba Millán** – Departamento de Química Orgánica, Unidad de Excelencia de Química Aplicada a la Biomedicina y Medioambiente, C. U. Fuentenueva, Universidad de Granada, 18071 Granada, Spain; [amillan@ugr.es](mailto:amillan@ugr.es); orcid.org/0000-0003-2754-270X; Email: [amillan@ugr.es](mailto:amillan@ugr.es)

**Juan M. Cuerva** – Departamento de Química Orgánica, Unidad de Excelencia de Química Aplicada a la Biomedicina y Medioambiente, C. U. Fuentenueva, Universidad de Granada, 18071 Granada, Spain; [jmCuerva@ugr.es](mailto:jmCuerva@ugr.es); orcid.org/0000-0001-6896-9617; Email: [jmCuerva@ugr.es](mailto:jmCuerva@ugr.es)

## Authors

**Benjamin Mallada** – Institute of Physics, Czech Academy of Sciences, 16200 Prague, Czech Republic; Regional Centre of Advanced Technologies and Materials, Czech Advanced Technology and Research Institute (CATRIN), Palacký University Olomouc, 78371 Olomouc, Czech Republic; [orcid.org/0000-0002-8209-9977](https://orcid.org/0000-0002-8209-9977)

**Federico Villalobos** – Departamento de Química Orgánica, Unidad de Excelencia de Química Aplicada a la Biomedicina y Medioambiente, C. U. Fuentenueva, Universidad de Granada, 18071 Granada, Spain

**Beatriz Donoso** – Departamento de Química Orgánica, Unidad de Excelencia de Química Aplicada a la Biomedicina y Medioambiente, C. U. Fuentenueva, Universidad de Granada, 18071 Granada, Spain

**Raquel Casares** – Departamento de Química Orgánica, Unidad de Excelencia de Química Aplicada a la Biomedicina y Medioambiente, C. U. Fuentenueva, Universidad de Granada, 18071 Granada, Spain

**Giovanna Longhi** – Dipartimento di Medicina Molecolare e Traslazionale, Università di Brescia, 25121 Brescia, Italy; [orcid.org/0000-0002-0011-5946](https://orcid.org/0000-0002-0011-5946)

**Jesús I. Mendieta-Moreno** – Instituto de Ciencia de Materiales de Madrid (ICMM), Consejo Superior de Investigaciones Científicas (CSIC), 28049 Madrid, Spain; [orcid.org/0000-0001-8530-3315](https://orcid.org/0000-0001-8530-3315)

**Alejandro Jiménez-Martin** – Institute of Physics, Czech Academy of Sciences, 16200 Prague, Czech Republic; Regional Centre of Advanced Technologies and Materials, Czech Advanced Technology and Research Institute (CATRIN), Palacký University Olomouc, 78371 Olomouc, Czech Republic; Faculty of Nuclear Sciences and Physical Engineering, Czech Technical University, 11519 Prague, Czech Republic

**Ali Haidour** – Unidad de Resonancia Magnética Nuclear, Centro de Instrumentación Científica, Universidad de Granada, 18071 Granada, Spain

**Ravin Sepsersaud** – Center for Global Infectious Disease Research, Seattle Children's Research Institute, Seattle, Washington 98109, United States

**Lakshmi Rajagopal** – Center for Global Infectious Disease Research, Seattle Children's Research Institute, Seattle, Washington 98109, United States; Department of Global Health and Department of Pediatrics, University of Washington, Seattle, Washington 98105, United States

Complete contact information is available at: <https://pubs.acs.org/10.1021/acs.jpcl.4c00164>

## Author Contributions

<sup>†</sup>Benjamin Mallada and Federico Villalobos contributed equally to this work.

## Notes

The authors declare no competing financial interest.

## ACKNOWLEDGMENTS

The authors gratefully acknowledge the support of the National Institutes of Health (U.S.A., R01AI167421) and FEDER/Junta de Andalucía—Consejería de Transformación Económica, Industria, Conocimiento y Universidades (Spain, Grants B-FQM-130-UGR20 and P20\_00028). Federico Villalobos thanks Ministerio de Universidades (Spain, FPU18/05938). Bruno de la Torre acknowledges the financial

support of the Czech Science Foundation (23-06781M) and the CzechNanoLab Research Infrastructure supported by the Ministry of Education, Youth and Sports of the Czech Republic (MEYS CR, LM2023051). Funding for open access charge: Universidad de Granada / CBUA.

## REFERENCES

- (1) Dugas, H. *Biorganic Chemistry. A Chemical Approach to Enzyme Action*; Springer-Verlag: New York, 1996; DOI: 10.1007/978-1-4612-2426-6.
- (2) Van Vranken, D.; Weiss, G. *Introduction to Biorganic Chemistry and Chemical Biology*; Garland Science: New York, 2012; DOI: 10.1201/9780203381090.
- (3) Nicolaou, K. C.; Snyder, S. A. Chasing Molecules That Were Never There: Misassigned Natural Products and the Role of Chemical Synthesis in Modern Structure Elucidation. *Angew. Chem., Int. Ed.* **2005**, *44*, 1012–1044.
- (4) Menna, M.; Imperatore, C.; Mangoni, A.; Della Sala, G.; Tagliatela-Scafati, O. Challenges in the Configuration Assignment of Natural Products. A Case-Selective Perspective. *Nat. Prod. Rep.* **2019**, *36*, 476–489.
- (5) Holton, J. M.; Frankel, K. A. The Minimum Crystal Size Needed for a Complete Diffraction Data Set. *Acta Crystallogr., Sect. D: Struct. Biol.* **2010**, *66*, 393–408.
- (6) Inokuma, Y.; Yoshioka, S.; Ariyoshi, J.; Arai, T.; Hitora, Y.; Takada, K.; Matsunaga, S.; Rissanen, K.; Fujita, M. X-ray Analysis on the Nanogram to Microgram Scale Using Porous Complexes. *Nature* **2013**, *495*, 461–466.
- (7) Zigon, N.; Duplan, V.; Wada, N.; Fujita, M. Crystalline Sponge Method: X-ray Structure Analysis of Small Molecules by Post-Orientation within Porous Crystals—Principle and Proof-of-Concept Studies. *Angew. Chem., Int. Ed.* **2021**, *60*, 25204–25222.
- (8) Cheng, Y. Single-Particle Cryo-EM—How Did It Get Here and Where Will It Go. *Science* **2018**, *361*, 876–880.
- (9) Gross, L. Recent Advances in Submolecular Resolution with Scanning Probe Microscopy. *Nat. Chem.* **2011**, *3*, 273–278.
- (10) Jelinek, P. High Resolution SPM Imaging of Organic Molecules with Functionalized Tips. *J. Phys.: Condens. Matter* **2017**, *29*, No. 343002.
- (11) Bian, K.; Gerber, C.; Heinrich, A. J.; Müller, D. J.; Scheuring, S.; Jiang, Y. Scanning Probe Microscopy. *Nat. Rev. Methods Primers* **2021**, *1*, 36.
- (12) Zhang, X.; Zeng, Q.; Wang, C. On-Surface Single Molecule Synthesis Chemistry: A Promising Bottom-Up Approach towards Functional Surfaces. *Nanoscale* **2013**, *5*, 8269–8287.
- (13) Wang, C.; Chi, L.; Ciesielski, A.; Samori, P. Chemical Synthesis at Surfaces with Atomic Precision: Taming Complexity and Perfection. *Angew. Chem., Int. Ed.* **2019**, *58*, 18758–18775.
- (14) Hla, S.-W.; Rieder, K.-H. STM Control of Chemical Reactions: Single-Molecule Synthesis. *Annu. Rev. Phys. Chem.* **2003**, *54*, 307–330.
- (15) Spong, J.; Mizes, H.; LaComb, L., Jr.; Dovek, M. M.; Frommer, J. E.; Foster, J. S. Contrast Mechanism for Resolving Organic Molecules with Tunnelling Microscopy. *Nature* **1989**, *338*, 137–139.
- (16) Foster, J.; Frommer, J. Imaging of Liquid Crystals using a Tunnelling Microscope. *Nature* **1988**, *333*, 542–545.
- (17) Hansma, P. K.; Elings, V. B.; Marti, O.; Bracker, C. E. Scanning Tunneling Microscopy and Atomic Force Microscopy: Application to Biology and Technology. *Science* **1988**, *242*, 209–216.
- (18) Hamann, C.; Woltmann, R.; Hong, I.-P.; Hauptmann, N.; Karan, S.; Berndt, R. Ultrahigh Vacuum Deposition of Organic Molecules by Electrospray Ionization. *Rev. Sci. Instrum.* **2011**, *82*, No. 033903.
- (19) Rauschenbach, S.; Ternes, M.; Hamau, L.; Kern, K. Mass Spectrometry as a Preparative Tool for the Surface Science of Large Molecules. *Annu. Rev. Anal. Chem.* **2016**, *9*, 473–498.
- (20) Kley, C. S.; Dette, C.; Rinke, G.; Patrick, C. E.; Čechal, J.; Jung, S. J.; Baur, M.; Dürr, M.; Rauschenbach, S.; Giustino, F.; Stephanow,

- S.; Kern, K. Atomic-Scale Observation of Multiconformational Binding and Energy Level Alignment of Ruthenium-Based Photosensitizers on TiO<sub>2</sub> Anatase. *Nano Lett.* **2014**, *14*, 563–569.
- (21) Deng, Z.; Thontasen, N.; Malinowski, N.; Rinke, G.; Harnau, L.; Rauschenbach, S.; Kern, K. A Close Look at Proteins: Submolecular Resolution of Two- and Three-Dimensionally Folded Cytochrome C at Surfaces. *Nano Lett.* **2012**, *12*, 2452–2458.
- (22) Warr, D. A.; Perdigão, L. M. A.; Pinfold, H.; Blohm, J.; Stringer, D.; Leventis, A.; Bronstein, H.; Troisi, A.; Costantini, G. Sequencing Conjugated Polymers by Eye. *Sci. Adv.* **2018**, *4*, No. eaas9543.
- (23) Abb, S.; Harnau, L.; Gutzler, R.; Rauschenbach, S.; Kern, K. Two-Dimensional Honeycomb Network Through Sequence-Controlled Self-Assembly of Oligopeptides. *Nat. Commun.* **2016**, *7*, 10335.
- (24) Rauschenbach, S.; Rinke, G.; Gutzler, R.; Abb, S.; Albarghash, A.; Le, D.; Rahman, T. S.; Dürr, M.; Harnau, L.; Kern, K. Two-Dimensional Folding of Polypeptides into Molecular Nanostructures at Surfaces. *ACS Nano* **2017**, *11*, 2420–2427.
- (25) Abb, S.; Tarrat, N.; Cortés, J.; Andriyevsky, B.; Harnau, L.; Schön, J. C.; Rauschenbach, S.; Kern, K. Carbohydrate Self-Assembly at Surfaces: STM Imaging of Sucrose Conformation and Ordering on Cu(100). *Angew. Chem., Int. Ed.* **2019**, *58*, 8336–8340.
- (26) Abb, S.; Tarrat, N.; Cortés, J.; Andriyevsky, B.; Harnau, L.; Schön, J. C.; Rauschenbach, S.; Kern, K. Polymorphism in Carbohydrate Self-Assembly at Surfaces: STM Imaging and Theoretical Modelling of Trehalose on Cu(100). *RSC Adv.* **2019**, *9*, 35813–35819.
- (27) Wu, X.; Delbianco, M.; Anggara, K.; Michnowicz, T.; Pardo-Vargas, A.; Bharate, P.; Sen, S.; Pristi, M.; Rauschenbach, S.; Schlickum, U.; Abb, S.; Seeberger, P. H.; Kern, K. Imaging Single Glycans. *Nature* **2020**, *582*, 375–378.
- (28) Seibel, J.; Fittolani, G.; Mirhosseini, H.; Wu, X.; Rauschenbach, S.; Anggara, K.; Seeberger, P. H.; Delbianco, M.; Kühne, T. D.; Schlickum, U.; Kern, K. Visualizing Chiral Interactions in Carbohydrates Adsorbed on Au(111) by High-Resolution STM Imaging. *Angew. Chem., Int. Ed.* **2023**, *62*, No. e202305733.
- (29) Anggara, K.; Sršán, L.; Jaroentomechai, T.; Wu, X.; Rauschenbach, S.; Narimatsu, Y.; Clausen, H.; Ziegler, T.; Miller, R. L.; Kern, K. Direct Observation of Glycans Bonded to Proteins and Lipids at the Single-Molecule Level. *Science* **2023**, *382*, 219–223.
- (30) Moro, S.; Siemons, N.; Drury, O.; Warr, D. A.; Moriarty, T. A.; Perdigão, L. M. A.; Pearce, D.; Moser, M.; Hallani, R. K.; Parker, J.; McCulloch, I.; Frost, J. M.; Nelson, J.; Costantini, G. The Effect of Glycol Side Chains on the Assembly and Microstructure of Conjugated Polymers. *ACS Nano* **2022**, *16*, 21303–21314.
- (31) Esser, T. K.; Bohning, J.; Öntür, A.; Chinthapalli, D. K.; Eriksson, L.; Grabarics, M.; Fremdling, P.; Konijnenberg, A.; Makarov, A.; Botman, A.; Peter, C.; Benesch, J. L. P.; Robinson, C. V.; Gault, J.; Baker, L.; Bharat, T. A. M.; Rauschenbach, S. Cryo-EM of Soft-Landed  $\beta$ -Galactosidase: Gas-Phase and Native Structures are Remarkably Similar. *Sci. Adv.* **2024**, *10*, No. ead4628.
- (32) Rodríguez-Galván, A.; Contreras-Torres, F. F. Scanning Tunneling Microscopy of Biological Structures: An Elusive Goal for Many Years. *Nanomaterials* **2022**, *12*, 3013.
- (33) Anggara, K.; Zhu, Y.; Delbianco, M.; Rauschenbach, S.; Abb, S.; Seeberger, P. H.; Kern, K. Exploring the Molecular Conformation Space by Soft Molecule–Surface Collision. *J. Am. Chem. Soc.* **2020**, *142*, 21420–21427.
- (34) Rosa-Fraile, M.; Rodríguez-Granger, J.; Haidour-Benamin, A.; Cuerva, J. M.; Sampedro, A. Granada: Proposed Structure of the Group B Streptococcus Polyenic Pigment. *Appl. Environ. Microbiol.* **2006**, *72*, 6367–6370.
- (35) Paradis, M.; Jurado, R.; Haidour, A.; Rodríguez Granger, J.; Sampedro Martínez, A.; de la Rosa Fraile, M.; Robles, R.; Justicia, J.; Cuerva, J. M. Clarifying the Structure of Granada: Total Synthesis of Related Analogue [2]-Granada and Confirmation of its Absolute Stereochemistry. *Bioorg. Med. Chem.* **2012**, *20*, 6655–6661.
- (36) Whidbey, C.; Harrell, M. I.; Burnside, K.; Ngo, L.; Becraft, A. K.; Iyer, L. M.; Aravind, L.; Hitti, J.; Adams Waldorf, K. M.; Rajagopal, L. A Hemolytic Pigment of Group B Streptococcus Allows Bacterial Penetration of Human Placenta. *J. Exp. Med.* **2013**, *210*, 1265–1281.
- (37) Boldenow, E.; Gendrin, C.; Ngo, L.; Bierle, C.; Vormhagen, J.; Coleman, M.; Merillat, S.; Armistead, B.; Whidbey, C.; Alishetti, V.; Santana-Ufret, V.; Ogle, J.; Gough, M.; Srinouanprachanh, S.; MacDonald, J. W.; Bammler, T. K.; Bansal, A.; Liggitt, H. D.; Rajagopal, L.; Adams Waldorf, K. M. Group B Streptococcus Circumvents Neutrophils and Neutrophil Extracellular Traps during Amniotic Cavity Invasion and Preterm Labor. *Sci. Immunol.* **2016**, *1*, No. eaah4576.
- (38) Siemens, N.; Oehmcke-Hecht, S.; Hofmann, J.; Skorka, S. B.; Nijhuis, R. H. T.; Ruppen, C.; Skrede, S.; Rohde, M.; Schultz, D.; Laik, M.; Itzek, A.; Pieper, D. H.; van den Bout, C. J.; Claas, E. C. J.; Kuijper, E. J.; Mauritz, R.; Sendi, P.; Wunderink, H. F.; Norrby-Teglund, A. Prothrombotic and Proinflammatory Activities of the  $\beta$ -Hemolytic Group B Streptococcal Pigment. *J. Innate Immun.* **2020**, *12*, 291–303.
- (39) Armistead, B.; Quach, P.; Snyder, J. M.; Santana-Ufret, V.; Furuta, A.; Brokaw, A.; Rajagopal, L. Hemolytic Membrane Vesicles of Group B Streptococcus Promote Infection. *J. Cutan. Dis.* **2021**, *223*, 1488–1496.
- (40) Zangwill, K. M.; Schuchat, A.; Wenger, J. D. Group B Streptococcal Disease in the United States, 1990: Report from a Multistate Active Surveillance System. *MMWR CDC Surveill. Summ.* **1992**, *41*, 25–32.
- (41) Francois Watkins, L. K.; McGee, L.; Schrag, S. J.; Beall, B.; Jain, J. H.; Pondo, T.; Farley, M. M.; Harrison, L. H.; Zansky, S. M.; Baumbach, J.; Lynfield, R.; Snippes Vagnone, P.; Miller, L. A.; Schaffner, W.; Thomas, A. R.; Watt, J. P.; Petit, S.; Langley, G. E. Epidemiology of Invasive Group B Streptococcal Infections Among Nonpregnant Adults in the United States, 2008–2016. *JAMA Int. Med.* **2019**, *179*, 479–488.
- (42) Sendi, P.; Johansson, L.; Norrby-Teglund, A. Invasive Group B Streptococcal Disease in Non-Pregnant Adults: A Review with Emphasis on Skin and Soft-Tissue Infections. *Infection* **2008**, *36*, 100–111.
- (43) Lawn, J. E.; Bianchi-Jassir, F.; Russell, N. J.; Kohli-Lynch, M.; Tann, C. J.; Hall, J.; Madrid, L.; Baker, C. J.; Bartlett, L.; Cutland, C.; Gravett, M. G.; Heath, P. T.; Ip, M.; Le Doare, K.; Madhi, S. A.; Rubens, C. E.; Saha, S. K.; Schrag, S.; Sobanjo-ter Meulen, A.; Vekemans, J.; Seale, A. C. Group B Streptococcal Disease Worldwide for Pregnant Women, Stillbirths, and Children: Why, What, and How to Undertake Estimates? *Clin. Infect. Dis.* **2017**, *65*, S89–S99.
- (44) Seale, A. C.; Bianchi-Jassir, F.; Russell, N. J.; Kohli-Lynch, M.; Tann, C. J.; Hall, J.; Madrid, L.; Blencow, H.; Couzens, S.; Baker, C. J.; Bartlett, L.; Cutland, C.; Gravett, M. G.; Heath, P. T.; Ip, M.; Le Doare, K.; Madhi, S. A.; Rubens, C. E.; Saha, S. K.; Schrag, S. J.; Sobanjo-ter Meulen, A.; Vekemans, J.; Lawn, J. E. Estimates of the Burden of Group B Streptococcal Disease Worldwide for Pregnant Women, Stillbirths, and Children. *Clin. Infect. Dis.* **2017**, *65*, S200–S219.
- (45) Gonçalves, B. P.; Procter, S. R.; Paul, P.; Chandna, J.; Lewin, A.; Seadat, F.; Koukounari, A.; Dangor, Z.; Leahy, S.; Santham, S.; John, H. B.; Bramugy, J.; Bardaji, A.; Abubakar, A.; Nasambu, C.; Libster, R.; Sánchez Yanotti, C.; Horváth-Puhó, E.; Sørensen, H. T.; van de Beek, D.; Bijlsma, M. W.; Gardner, W. M.; Kassebaum, N.; Trotter, C.; Bassat, Q.; Madhi, S. A.; Lambach, P.; Jit, M.; Lawn, J. E.; Søgaard, K. K.; van Kassel, M. N.; Snoek, L.; de Gier, B.; van der Ende, A.; Hahne, S. J. M.; Harden, L. M.; Ghoor, A.; Mbatha, S.; Lowick, S.; Loughton, B.; Jaye, T.; Lala, S. G.; Sithole, P.; Msayi, J.; Kumalo, N.; Msibi, T. N.; Arumugam, A.; Murugesan, N.; Rajendraprasad, N.; Priya, M.; Mabrouk, A.; Katana, P. V.; Mwangome, E.; Newton, C. R.; Mucase, H.; Aerts, C.; Massora, S.; Medina, V.; Rojas, A.; Amado, D.; Llapur, C. J.; Hossain, A. K. M. T.; Rahman, Q. S.-u.; Ip, M.; Seale, A.; Heath, P. T.; Le Doare, K.; Khalil, A.; Schrag, S. J.; Sobanjo-ter Meulen, A.; Mason, E.; Blau, D. M.; El Arifeen, S.; Asefa, N.; Onyango, D.; Sow, S. O.; Mandomando, I.; Ogbuanu, I.; Kotloff, K. L.; Scott, J. A. G.; Gurley, E. S.; Barr, B. A. T.; Mahtab, S. Group B Streptococcus Infection During Pregnancy



and Infancy: Estimates of Regional and Global Burden. *Lancet Glob. Health* **2022**, *10*, e807–e819.

(46) Armistead, B.; Herrero-Foncubierta, P.; Coleman, M.; Quach, P.; Whidbey, C.; Justicia, J.; Tapia, R.; Casares, R.; Millán, A.; Haidour, A.; Granger, J. R.; Vornhagen, J.; Santana-Ufret, V.; Merillat, S.; Adams Waldorf, K.; Cuerva, J. M.; Rajagopal, L. Lipid Analogs Reveal Features Critical for Hemolysis and Diminish Granadaene Mediated Group B Streptococcus Infection. *Nat. Commun.* **2020**, *11*, 1502.

(47) Furuta, A.; Coleman, M.; Casares, R.; Seepersaud, R.; Orvis, A.; Brokaw, A.; Quach, P.; Nguyen, S.; Sweeney, E.; Sharma, K.; Wallen, G.; Sanghavi, R.; Mateos-Gil, J.; Cuerva, J. M.; Millán, A.; Rajagopal, L. CDI and iNKT Cells Mediate Immune Responses against the GBS Hemolytic Lipid Toxin Induced by a Non-Toxic Analog. *PLoS Pathog.* **2023**, *19*, No. e1011490.

(48) Cao, N.; Yang, B.; Riss, A.; Rosen, J.; Björk, J.; Barth, J. V. On-Surface Synthesis of Enetriynes. *Nat. Commun.* **2023**, *14*, 1255.

(49) Pracht, P.; Bohle, F.; Grimme, S. Automated Exploration of the Low-Energy Chemical Space with Fast Quantum Chemical Methods. *Phys. Chem. Chem. Phys.* **2020**, *22*, 7169–7192.

(50) Mendieta-Moreno, J. L.; Walker, R. C.; Lewis, J. P.; Gómez-Puertas, P.; Mendieta, J.; Ortega, J. An Efficient Local-Orbital DFT QM/MM Method for Biomolecular Systems. *J. Chem. Theory Comput.* **2014**, *10*, 2185–2193.

(51) Horcas, L.; Fernández, R.; Gómez-Rodríguez, J. M.; Colchero, J.; Gómez-Herrero, J.; Baro, A. M. WSXM: A Software for Scanning Probe Microscopy and a Tool for Nanotechnology. *Rev. Sci. Instrum.* **2007**, *78*, No. 013705.

(52) Frisch, M. J.; Trucks, G. W.; Schlegel, H. B.; Scuseria, G. E.; Robb, M. A.; Cheeseman, J. R.; Scalmani, G.; Barone, V.; Petersson, G. A.; Nakatsuji, H.; Li, X.; Caricato, M.; Marenich, A. V.; Bloino, J.; Janesko, B. G.; Gomperts, R.; Mennucci, B.; Hratchian, H. P.; Ortiz, J. V.; Izmaylov, A. F.; Sonnenberg, J. L.; Williams-Young, D.; Ding, F.; Lipparini, F.; Egidi, F.; Goings, J.; Peng, B.; Petrone, A.; Henderson, T.; Ranasinghe, D.; Zakrzewski, V. G.; Gao, J.; Rega, N.; Zheng, G.; Liang, W.; Hada, M.; Ehara, M.; Toyota, K.; Fukuda, R.; Hasegawa, J.; Ishida, M.; Nakajima, T.; Honda, Y.; Kitao, O.; Nakai, H.; Vreven, T.; Throssell, K.; Montgomery, J. A., Jr.; Peralta, J. E.; Ogliaro, F.; Bearpark, M. J.; Heyd, J. J.; Brothers, E. N.; Kudin, K. N.; Staroverov, V. N.; Keith, T. A.; Kobayashi, R.; Normand, J.; Raghavachari, K.; Rendell, A. P.; Burant, J. C.; Iyengar, S. S.; Tomasi, J.; Cossi, M.; Millam, J. M.; Klene, M.; Adamo, C.; Cammi, R.; Ochterski, J. W.; Martin, R. L.; Morokuma, K.; Farkas, O.; Foresman, J. B.; Fox, D. J. *Gaussian 16, Revision C.01*; Gaussian, Inc.: Wallingford, CT, 2016.

(53) Lewis, J. P.; Jelinek, P.; Ortega, J.; Demkov, A. A.; Trabada, D. G.; Haycock, B.; Wang, H.; Adams, G.; Tomfohr, J. K.; Abad, E.; Wang, H.; Drabold, D. A. Advances and Applications in the FIREBALL Ab Initio Tight-Binding Molecular-Dynamics Formalism. *Phys. Status Solidi B* **2011**, *248*, 1989–2007.

(54) Heinz, H.; Lin, T.-J.; Kishore Mishra, R.; Emami, F. S. Thermodynamically Consistent Force Fields for the Assembly of Inorganic, Organic, and Biological Nanostructures: The INTERFACE Force Field. *Langmuir* **2013**, *29*, 1754–1765.